Accession No. 27382

24

(NASA CR-53675; SID 63-1293)

FINAL REPORT

MARINER B/VOYAGER ENTRY CAPSULE

PRELIMINARY DESIGN STUDY

(~~JPL P.O. No.~~ Contract BE 4-21764)

10 October 1963

Prepared by: M. G. Boobar
M. G. Boobar
Project Manager
Lunar and Planetary Systems

10 Oct. 1963 289p refs

Approved by: M. W. Jack Bell
M. W. J. Bell
Director
Lunar and Planetary Systems

172953R

(1) NORTH AMERICAN AVIATION, INC., Downey, Calif. (2)

(2) SPACE and INFORMATION SYSTEMS DIVISION

Unc

[redacted]

FOREWORD

This document presents the Final Technical Report of the work performed under contract to the Jet Propulsion Laboratories under P. O. No. BE 4-217624 by the members of Advanced Systems and Aerospace Sciences of the Space and Information Systems Division of North American Aviation, Inc.

The program was administered by Mr. James M. Brayshaw, Jr., of JPL. His continued encouragement and sound technical advice were deeply appreciated. Acknowledgment is made of the support and technical contributions of the following S&ID technical personnel to the program and the contents of this report.

B. A. McElhoe
A. S. Musicman
M. J. Whalen
P. A. Leonard
A. F. Cummings
D. H. Wykes

In addition, acknowledgment is given to the support and assistance of the Cook Electric Company Technology Center for their support in the recovery system analysis and the Johns Manville Company Aerospace Division for their cooperation in furnishing data on the composite structural concept and its fabricability.

TABLE OF CONTENTS

	Page
1.0 INTRODUCTION AND SUMMARY	1-1
2.0 PARAMETRIC STUDY	2-1
2.1 ENVIRONMENTAL PARAMETERS	2-1
2.2 TRAJECTORY PARAMETERS	2-5
2.3 HEATING PARAMETERS	2-18
2.3.1 Methods of Analysis	2-18
2.3.1.1 Convective Heating	2-18
2.3.1.2 Radiative Heating	2-20
2.3.1.3 Heating Distributions	2-26
2.3.2 Heating Loads	2-26
2.3.3 Effect of Uncertainties on Heating Loads	2-31
2.3.3.1 Generalized Heating Analysis	2-31
2.3.3.2 Results of Analysis	2-37
2.3.4 References	2-41
2.3.5 Nomenclature	2-44
2.4 MATERIALS CONSIDERATIONS AND CONSTRAINTS	2-46
2.4.1 Sterilization Requirements	2-46
2.4.2 Effects of Space Environment	2-51
2.4.2.1 Radiation Effects	2-51
2.4.2.2 Vacuum Effects	2-52
2.4.2.3 Effects of Meteorites	2-53
2.4.2.4 Effects of Thermal Cycling	2-53
2.4.3 Materials Considerations	2-53
2.4.3.1 Ablators	2-54
2.4.3.2 Structural Materials	2-57
2.4.3.2.1 Metals	2-57

2.4.3.2.2 Non-Metallics 2-57

2.4.3.3 Landing System 2-67

2.4.4 References 2-67

2.5 DESIGN AND GEOMETRIC CONSTRAINTS 2-69

2.5.1 Antenna Considerations 2-78

2.5.2 References 2-83

2.6 STRUCTURAL TRADEOFFS 2-84

2.6.1 Design Criteria 2-84

2.6.1.1 Boost Load Considerations 2-84

2.6.1.2 Space Environmental Considerations 2-85

2.6.1.3 Mars Entry Considerations 2-85

2.6.2 Forebody Structural Design 2-86

2.6.2.1 Forebody Structural Concepts 2-89

2.6.2.1.1 Conventional Structures 2-89
2.6.2.1.2 Composite Structures 2-90

2.6.2.2 Forebody Materials Tradeoffs 2-91

2.6.3 Afterbody Structural Design 2-93

2.6.3.1 Aftcone Structural Analysis 2-94

2.6.4 References 2-95

2.7 HEAT SHIELD TRADEOFFS 2-126

2.7.1 Candidate Materials 2-126

2.7.2 Methodology 2-126

2.7.3 Heat Shield Thicknesses vs Backface Temperatures 2-128

2.7.4 Heat Shield Recommendations 2-129

2.7.5 References 2-130

2.7.6 Nomenclature 2-131

2.8 LANDING SYSTEM TRADEOFFS 2-177

2.8.1 Considerations and Constraints 2-177

2.8.2 Parachute Design Concepts 2-184

2.8.3 Parachute System Deployment Concepts 2-186

2.8.4 Landing System Concepts 2-187

2.8.5 Recovery System Sequencing and Actuation 2-189

2.8.6 Impact Attenuation 2-192

2.9 SYSTEM WEIGHTS TRADEOFFS AND INERTIAL PROPERTIES 2-196

2.9.1 System Weights Tradeoffs 2-196

2.9.2 Preliminary Inertial Properties 2-201

2.10 DYNAMIC CONSIDERATIONS 2-204

2.10.1 Static Stability 2-204

2.10.2 Dynamic Stability 2-204

2.10.3 References 2-214

3.0 PRELIMINARY DESIGN 3-1

3.1 CONFIGURATION SELECTION 3-1

3.1.1 Mariner B Capsule 3-1

3.1.2 Voyager Capsule 3-3

3.2 HEAT SHIELD-STRUCTURAL DESIGN 3-5

3.2.1 Mariner B Capsule 3-5

3.2.1.1 Forebody 3-5

3.2.1.2 Payload Support 3-6

3.2.1.3 Afterbody 3-9

3.2.2 Voyager Capsule 3-9

3.2.2.1 Forebody 3-9

3.2.2.2 Afterbody 3-11

3.3 LANDING SYSTEM DESIGN 3-17

3.3.1 CONCEPT 6 (MARINER B)/MAXIMUM ALTITUDE 3-17

3.3.2 CONCEPT 4 (MARINER B)/MAXIMUM TIME 3-18

3.3.3 CONCEPT 1 (VOYAGER)/RECOVERY 3-21

3.4 CONFIGURATION DRAWINGS 3-25

3.4.1 MARINER B CAPSULE 3-25

3.4.2 VOYAGER CAPSULE 3-29

3.5 WEIGHT AND MASS PROPERTIES 3-31

1.0 INTRODUCTION AND SUMMARY

Company sponsored studies by the Space and Information Systems Division of North American Aviation, Inc., have shown the advantages of employing high drag configurations (e.g., Apollo) for simple ballistic entry into the Martian atmosphere over a wide range of entry angles (i.e., γ = -20° to -90°). These studies indicated that the highest payload to gross weight ratios could be attained with these configurations, as compared to those with a lower drag coefficient, for landing an unmanned, scientific payload on Mars. Recent unpublished findings by L. D. Kaplan of the Jet Propulsion Laboratories indicate that previous reported surface pressures for Mars may be high by an order of magnitude. These findings further emphasize the need for a high drag configuration for ballistic entry.

The objectives of this study were to perform a preliminary design analysis to define the heat shield, structure, and landing system requirements for the Martian entry and lander capsules which have been proposed as integral parts of both the Mariner B and Voyager missions. Because of the backlog of data being developed for the manned lunar mission, the Apollo shape was to be employed as a basepoint configuration. The designs were to be consistent with state of technology available for the late 1966 Mariner B and 1969 Voyager launch opportunities for Mars. In resolving choices of approach, conceptual simplicity as ultimately reflected in enhanced reliability, was always selected as the preferred approach.

The initial ground rules assumed for the study included:

(a) Nominal small capsule gross weight = 400 pounds

(b) Nominal large capsule gross weight = 2,000 pounds

(c) Small capsule compatibility with the Centaur shroud

(d) Large capsule compatibility with the S-VI shroud

(e) Ballistic entry with L/D = 0

(f) Initial entry velocity = 25,000 fps

(g) Range of entry angles = -20° to -90°

(h) JPL (Kaplan) atmospheres

(i) Small capsule "electronic" payload = 100 pounds; inclusive of 12 pound inboard antenna

(j) Payload has its own environmental control system

(k) Large capsule "electronic" payload = 600 pounds; inclusive of 12 pound inboard antenna

(l) Maximum allowable payload acceleration = 1,000 g's

(m) Electronic payload packing density = 30 lb/ft^3; minimum fore and aft payload depth = 9 inches

(n) Landing survival for both small and large capsules

(o) Spacecraft-bus/capsule communication capability required after separation to entry blackout and post parachute deployment

(p) Materials compatibility with 145°C, 3 cycle dry heat sterilization

(q) Small capsule bit rate = 5 B/sec

As the study progressed, modifications to these ground rules were made. The small capsule payload weight was increased to 150 pounds, then allowed to "seek its own level" when the gross capsule weight was lowered to 350 pounds. The feasibility of employing a slot antenna was considered to afford more flexibility in the internal payload and recovery systems arrangements. The requirement for landing survival of the small capsule also was relaxed.

During the first phase of the study, the entry trajectory and heating parameters were investigated as a function of the four atmospheres submitted by JPL. Coupled with the design and geometric constraints, heat shield and structural analyses, various recovery system concepts, materials considerations, and a dynamics analysis, the following tradeoffs and design requirements become apparent.

(1) $\gamma = -90°$ entry into the W_2 atmosphere presented the most severe system constraint. The axial entry decelerations experienced would be in the excess of 160 g's. To deploy a hypersonic parachute, nominally limited by presently demonstrated technology to a deployment velocity of 3750 fps in the Martian atmosphere, will mean penetration into the atmosphere to altitudes as low as 28,000 feet (based on dynamic trajectory analyses) before deployment for a capsule having nominal M/C_DA of 0.2. Assuming that subsonic velocities must be attained before atmospheric sampling can be initiated, the capsule will drop further to approximately 15,000 to 20,000 feet, depending upon whether a single stage or two stage system is employed. The time available for sampling and data transmission from Mach 0.9 to ground impact

will be in the order of 90 to 170 seconds, again depending upon the system selected. If the transmission rate is 5 B/sec, only a very limited number of atmospheric samples can be taken prior to impact, if a large amount of data has been acquired during entry by the capsule instruments (e.g., accelerometer readings, temperatures, etc.) has to be recorded and played back after parachute deployment. A single stage system, although it affords less pre-impact parachute time, can sample a greater height of atmosphere and is inherently more reliable.

Increased chute time can be achieved at the expense of a larger parachute system and consequent reduction in payload weight, if the capsule weight is fixed. Both time and altitude can be bought only by reducing the M/C_DA at the expense of less payload, or by increasing the base diameter and therefore the gross capsule weight.

It should be noted, however, that the data presented are for the "worst" atmosphere and worst possible entry angle. Even if this atmosphere is encountered, entry at any angle other than 90° will increase the time available for sampling and data transmission, accordingly.

Development of an adequate sensor to initiate the deployment sequence is a prerequisite.

(2) Although there is considerable uncertainty regarding the magnitude of the radiative heat load (particularly for high angle entry), the convective loads and time (which can be estimated with reasonable confidence) at -20° entry are of such magnitude that they govern the design of the heat shield. Heat shield thickness requirements at -20° entry angles exceed those for -90° by a factor of two to three, thus providing what appears to be an adequate margin for the uncertainties associated with the high angle radiative pulse.

(3) Review of the candidate materials, particularly those for the small capsule, for compatibility with the sterilization requirements, possible effects of the nominal seven-month space journey, and the entry environment revealed no insurmountable problems.

(4) The heat shield structural tradeoffs yielded the expected result that the amount of insulation required is inversely proportional to the backface temperature. A structural design load of 200 g's was selected for -90° entry into atmosphere W_2. Heating times are so short and the heat shield

thickness required for -20° entry so great, that the backface temperature rise for the maximum load condition is nil and, hence, a cold structure could be assumed. At lower entry angles, the loads are reduced accordingly (i.e., loads are approximately proportional to sin γ).

The forebody represents on the order of 40 to 50 percent of the gross capsule weight and the heat shield is two to three times the weight of the structure. Although most "modern" materials (e.g., Avcoat, Thermo-Lag, SE-28, etc.) appear more efficient, for the small capsule (Mariner B), phenolic-glass is suggested as the heat shield material because the short development time available to meet the January 1967 flight date can be offset by the backlog of available experience, qualification, and flight test data obtained on the Mercury and various ballistic missile programs. Indeed, one Mercury flight test report on this material described essentially the same entry heating profile as was computed for the limiting case (and, indeed, provided an excellant check upon the validity of our calculated heat shield requirements).

Of the several structural arrangements considered, a conventional aluminum sandwich appeared most attractive. However, the weight penalties paid for adhesives in this type of arrangement are high and so the possibility of employing a composite glass-phenolic heat shield structure was explored with several manufacturers. For the Mariner B, 350 pound capsule, the weight saving would afford an increase in payload weight of from 75 to 110 pounds (or an equivalent reduction in M/C_DA of approximately 10 percent). Fabrication of this structure for the small capsule appears to be well within the state-of-the-art and we were informed that the requisite facilities and equipment are available. This concept appears to merit further consideration.

Because of the large sizes required, the composite heat shield structural concept does not appear feasible for the large capsule. However, because of the longer lead times available, more efficient heat shield materials than phenolic-glass were considered applicable (e.g., SE-28, Thermo-Lags, etc). These will afford significant reductions in the unit weight of the forebody.

(5) The dynamic analysis indicated that capsule stability was enhanced as the c.g. was moved forward from 20% to 15% of the base diameter. At a c.g. of 0.15 D_B, sufficient damping will occur to assure acceptably small oscillations during peak heating, parachute deployment, and data transmission for

all entry angles of attack if there is initial tumbling. (Rates to 36 deg/sec were investigated.) However, if the c.g. is moved back to 0.2 D_B, there is neutral static stability in the apex-forward attitude and, for non-tumbling entry, the vehicle may orient heat-shield forward. Stabilization improves with lower c.g. locations, lower entry angles, and lower atmospheric betas.

Center of gravity locations at 0.15 D_B appear attainable for the small capsule; for the large capsule, the c.g. location will be moved significantly forward. A simple active damping system, weighing in the order of 10 pounds appears capable of damping 360°/sec of angular velocity in the small capsule. An equivalent system for the large capsule will weigh approximately 90 pounds; a 45 pound system will provide 180°/sec of damping.

The maximum lateral loads encountered are in the order of 40 g's or less.

(6) Employing JPL Mars-Venus trajectory data (Clark), the possible tradeoffs between entry velocity, flight time, and communication distance were developed between Class I and Class II Mars trajectories.

At the conclusion of the parametric study, a set of summary tradeoff curves were developed which showed the weight of the entry capsule as a function of M/C_DA, base diameter, materials, and payload weight for entry velocities of both 25,000 and 22,000 fps. As was expected, the 22,000 fps entry velocity affords increased payload weights (e.g., 15 pounds increase in the case of the small capsule). These summaries also were employed to select the most promising configurations for further study in the preliminary design phase of study.

For the small capsule, the configuration selected weighed 350 pounds. It had a base diameter of 6.75 feet, a phenolic-glass heat shield, and aluminum forebody structure. The afterbody consisted of a phenolic-glass cone, for pre-entry r.f. transmission, which is jettisoned prior to parachute deployment. Alternatives considered included a metallic afterbody to house a slot antenna in order to afford greater angular coverage and flexibility in payload and parachute system placement. This configuration proved heavier than the one with the inboard antenna configuration suggested by JPL because of the construction and weight of di-electric material required to fill the slots. The other alternative considered the composite forebody which has been discussed previously. Systems for missions which require and do not require impact survival were considered.

In the case of the large capsule, the configuration concepts which were considered included (a) the conventional Apollo shape, wherein the volume included by the 33° aft cone affords a far greater payload volume than is required, (b) a flat plate afterbody, and (c) an open afterbody wherein the

payload and auxilliary systems rest within the forebody cavity and are protected "against the elements" by a suitable contour-fitted enclosure. To achieve the target M/C_DA of 0.2, 17 and 18 foot base diameters were required for compatibility with the gross entry capsule weights of 2160 to 2650 pounds. More advanced heat shield materials were considered for these configurations.

Suitable preliminary design drawings of the configurations and deployment sequencing, as well as summaries of the weight and mass properties for each configuration were developed.

The capsules described for both the Mariner B and Voyager missions appear feasible within the state-of-the-art technology which will be available for each launch date. They are entirely compatible with the mission and vehicle requirements described. The sections which follow describe the parametric and preliminary design phases of the study.

2.0 PARAMETRIC STUDY

2.1 ENVIRONMENTAL PARAMETERS

The atmospheric data used for the trajectory computations are summarized in Table 2.1-1. The data were submitted by JPL as an input to the study and are based on the unpublished work of L. D. Kaplan of JPL. These atmospheres used are characterized by significantly lower surface pressures and lower overall densities than have been reported previously.

The four atmospheres provide consistent models covering a variety of possibilities; they cover a range of uncertainty of an order of magnitude of density at the altitudes of high aerodynamic deceleration (Figure 2.1-1). The uncertainty in temperature is shown in Figure 2.1-2. The range of temperatures leads to uncertainties in the inverse scale height (β) and the speed of sound. Fortunately, absolute velocities, rather than Mach numbers, are employed in most hypersonic aerothermodynamic expressions; thus minimizing the requirement for accurate values for the speed of sound. The uncertainty in β, however, can lead to large variations in expected deceleration loads, heating rates, parachute deployment altitudes, and the dynamic behavior.

Although a nominal atmosphere was defined, the preliminary design study was not based on this atmosphere. The heat shield structure and landing system designs are based on the requirements to successfully accomplish the mission in whichever of the model atmospheres presents the worst condition for that particular system.

TABLE 2.1-1

MARS ATMOSPHERE & UNCERTAINTIES

Property	Worst		Nominal	Best
	W2	W1	N	B
Surface Pressure mb	11	11	15	30
lb/ft^2	23	23	31.4	62.6
Stratosphere Temps. °K	130	230	180	130
°R	234	415	324	234
Surface Temperature °K	260	260	230	210
°R	468	468	415	378
Acceleration of Gravity cm/sec^2	375	375	375	375
at surface ft/sec^2	12.3	12.3	12.3	12.3
Composition, Molar Concentration %				
CO^2	65	65	43	11
A	35	35	32	13
N_2	0	0	25	76
Molecular Weight	42.7	42.7	38.7	31.2
Specific Heat Ratio	1.40	1.40	1.42	1.42
Adiabatic Temp. Lapse Rate °K/KM	-5.30	-5.30	-4.81	-3.93
°R/ft x 10^{-2}	- .291	- .291	- .264	- .216
Tropopause Altitude Km	24.5	5.66	10.4	20.35
Ft	80,500	18,600	34,100	64,600
Inverse Scale Height Km^{-1}	.148	.0838	.0970	.108
Above tropopause ft^{-1} x 10^{-4}	.451	.255	.295	.329
Below tropopause ft^{-1} x 10^{-4}	.228	.171	.187	.192
Surface Density gm/cm^3 x 10^{-5}	2.17	2.17	3.04	5.36
$\#/ft^3$ x 10^{-4}	13.55	13.55	18.95	33.4
$Slugs/ft^3$ x 10^{-5}	4.21	4.21	5.89	10.37
Artificial Surface gm/cm^3 x 10^{-5}	13.2	2.53	4.27	14.1
Density $\#/ft^3$ x 10^{-4}	82.4	15.8	27.3	88.0
$Slugs/ft^3$ x 10^{-5}	25.6	4.9	8.46	25.3
Density at gm/cm^3 x 10^{-5}	.347	1.57	1.60	1.55
Tropopause $\#/ft^3$ x 10^{-4}	2.16	9.87	10.0	9.68
Slugs/ft x 10^{-5}	.671	3.06	3.11	3.0

FIGURE 2.1-1

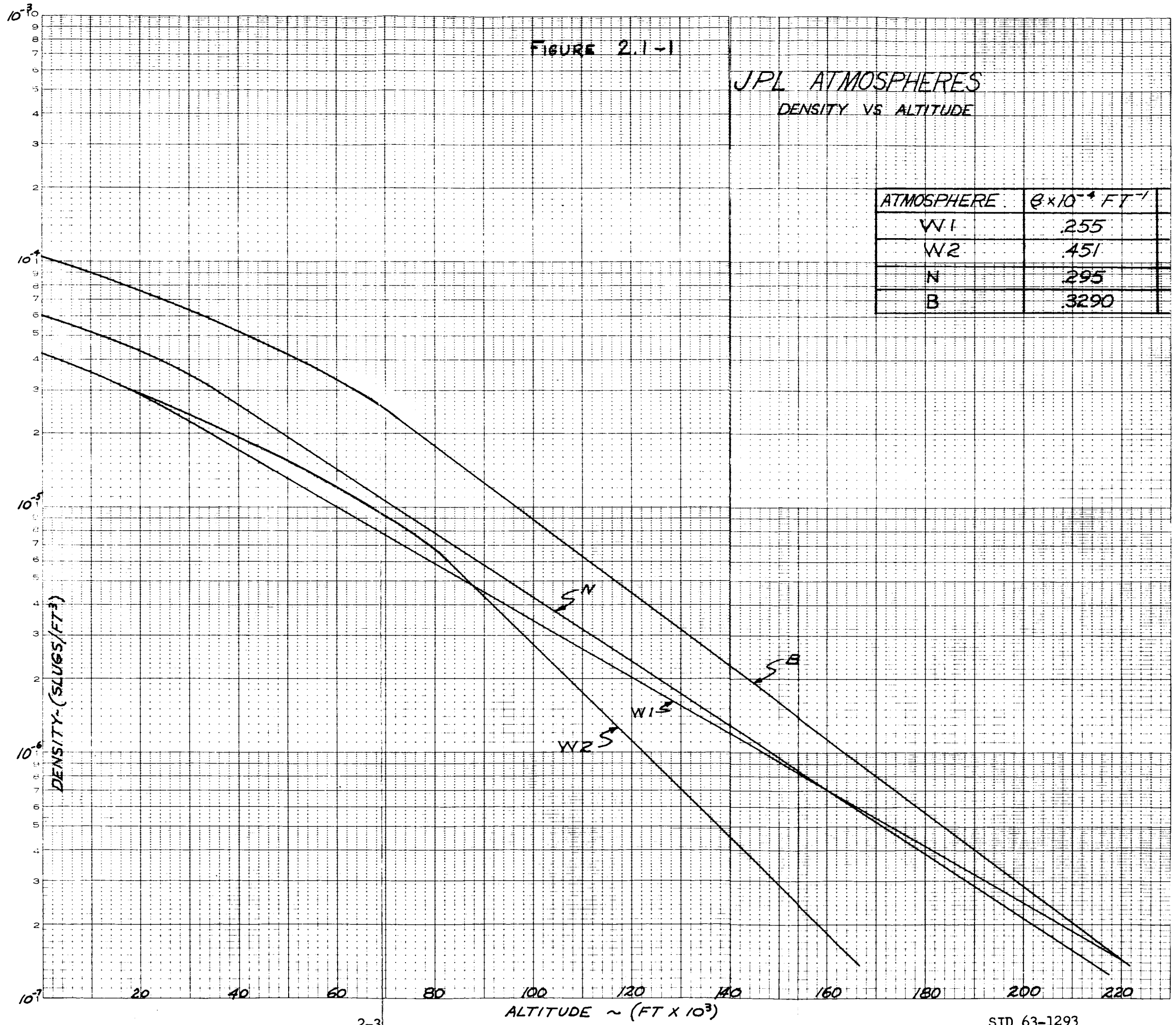
JPL ATMOSPHERES
DENSITY VS ALTITUDE
ATMOSPHERE
$\beta \times 10^{-4}$ FT^{-1}
W1 .255
W2 .451
N .295
B .3290
N
B
W1
W2
DENSITY ~ (SLUGS/FT^3)
ALTITUDE ~ (FT X 10^3)
10^{-3}
10^{-4}
10^{-5}
10^{-6}
10^{-7}
20
40
60
80
100
120
140
160
180
200
220

Figure 2.1-2

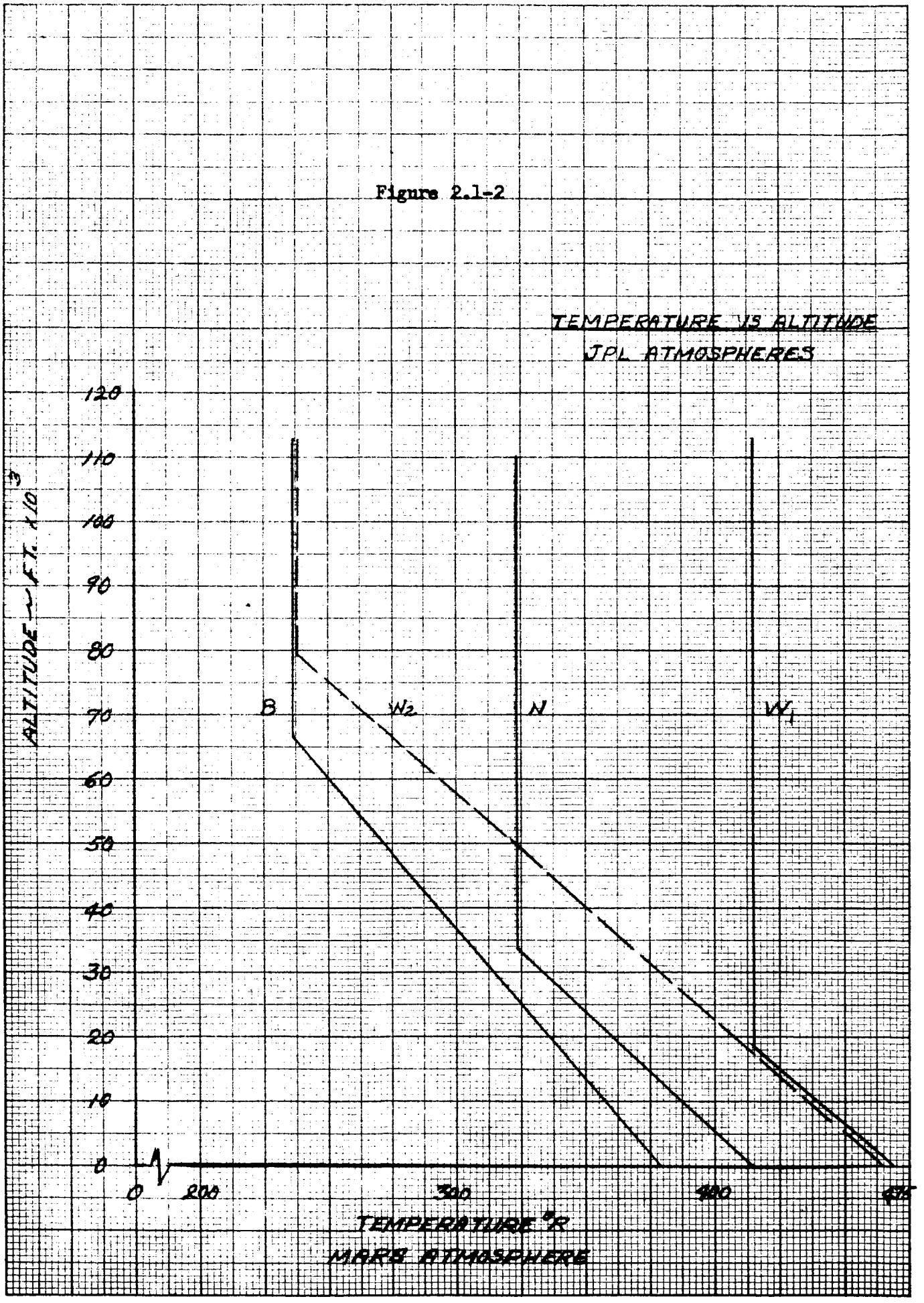
TEMPERATURE VS ALTITUDE
JPL ATMOSPHERES
ALTITUDE ~ FT. X 10³
120
110
100
90
80
70
60
50
40
30
20
10
0
B
W2
N
W1
0
200
300
400
500
TEMPERATURE °R
MARS ATMOSPHERE

2.2 TRAJECTORY PARAMETERS

Heating loads, accelerations, and other trajectory parameters for a range of vehicle ballistic coefficients (M/C_DA) were evaluated early in the study. These data were computed for each of the atmospheric models employing the point mass digital trajectory programs in use at S&ID. With the availability of these data, the tradeoffs on heat-shield materials, structural concepts, and landing systems leading ultimately to the sizing and design of the capsules could be initiated.

The following range of parameters were investigated:

M/C_DA	=	.01 to 1.0 slugs/ft^2
Entry angle (γ_E)	=	-20° to -90°
Entry velocity (V_E)	=	25,000 fps
Entry altitude	=	1,000,000 ft
L/D	=	0
Angle of attack (α)	=	0
Nominal drag coefficient	=	1.5 (see Table 2.2-1)

Several trajectories also were computed using an entry velocity of 22,000 fps to evaluate the potential benefits of the lower entry velocities. The computer data generated include velocity, acceleration, dynamic pressure, convective and radiant heat flux profiles, and integrated heat flux as a function of altitude and time.

The maximum deceleration (aerodynamic) is shown in the table on Figure 2.2-1. The curves show the altitude the maximum deceleration takes place as a function of the vehicle's M/C_DA. In keeping with theoretical results, the altitude of maximum deceleration proved to be independent of the entry velocity for γ_E near -90°.

The relationships between altitude, velocity, and M/C_DA in the lower altitude and velocity regimes for entry angles of both -20° and -90° are shown in Figures 2.2-2 through 2.2-7. These six figures show the altitudes at which the vehicle has slowed to 5,000 fps, 3,000 fps, and 1,000 fps, and are useful for initial approximations (prior to the availability of dynamic data) of parachute deployment requirements. Inspection of the data indicates that entry into atmospheres W_1 and W_2 at -90° requires the deployment of a hypersonic parachute to realize a rational sample of the atmosphere and permit sufficient time to transmit the acquired data prior to impact.

Curves showing typical entry trajectory profiles are shown in Figures 2.2-8 through 2.2-10. Velocity, altitude, acceleration, and dynamic pressure are plotted vs time for a vehicle $M/C_DA = 0.2$ slugs/ft^2. Those trajectories shown requiring a short time are for the straight-in approach; longer times are shown for $\gamma_E = -20°$ (a near-miss approach).

Figure 2.2-9 shows that in atmosphere W_2, a -20° entry angle results in a trajectory which shows a tendency toward skipping out. It was found

that for an M/C_DA of 0.3 slugs/ft^2, an entry angle of -20° results in a definite skip-out from the atmosphere; hence the limit of entry angle and M/C_DA is established.

Figure 2.2-11 summarizes the pertinent trajectory parameters for an M/C_DA of 0.2 and entry velocity of 25,000 fps. Terminal phase altitudes and velocities are shown as a function of the maximum deceleration and entry angle for atmospheres W_1, W_2, and B. As can be seen, peak deceleration forces are encountered in atmosphere W_2 (i.e., >160 g's). The decay in maximum deceleration forces and increase in tolerance for parachute deployment altitude with decrease in initial entry angle is illustrated.

TABLE 2.2-1

NOMINAL C_D VALUES EMPLOYED

IN POINT MASS TRAJECTORIES

($\alpha = 0°$)

MACH NO.	C_D
0.4	0.9
0.7	1.0
0.9	1.13
1.1	1.31
1.2	1.34
1.35	1.39
1.65	1.43
2.0	1.475
2.4	1.48
3.0	1.47
4.0	1.46
6.0	1.48
10.0	1.51
Free Molecular Flow Regime	2.0

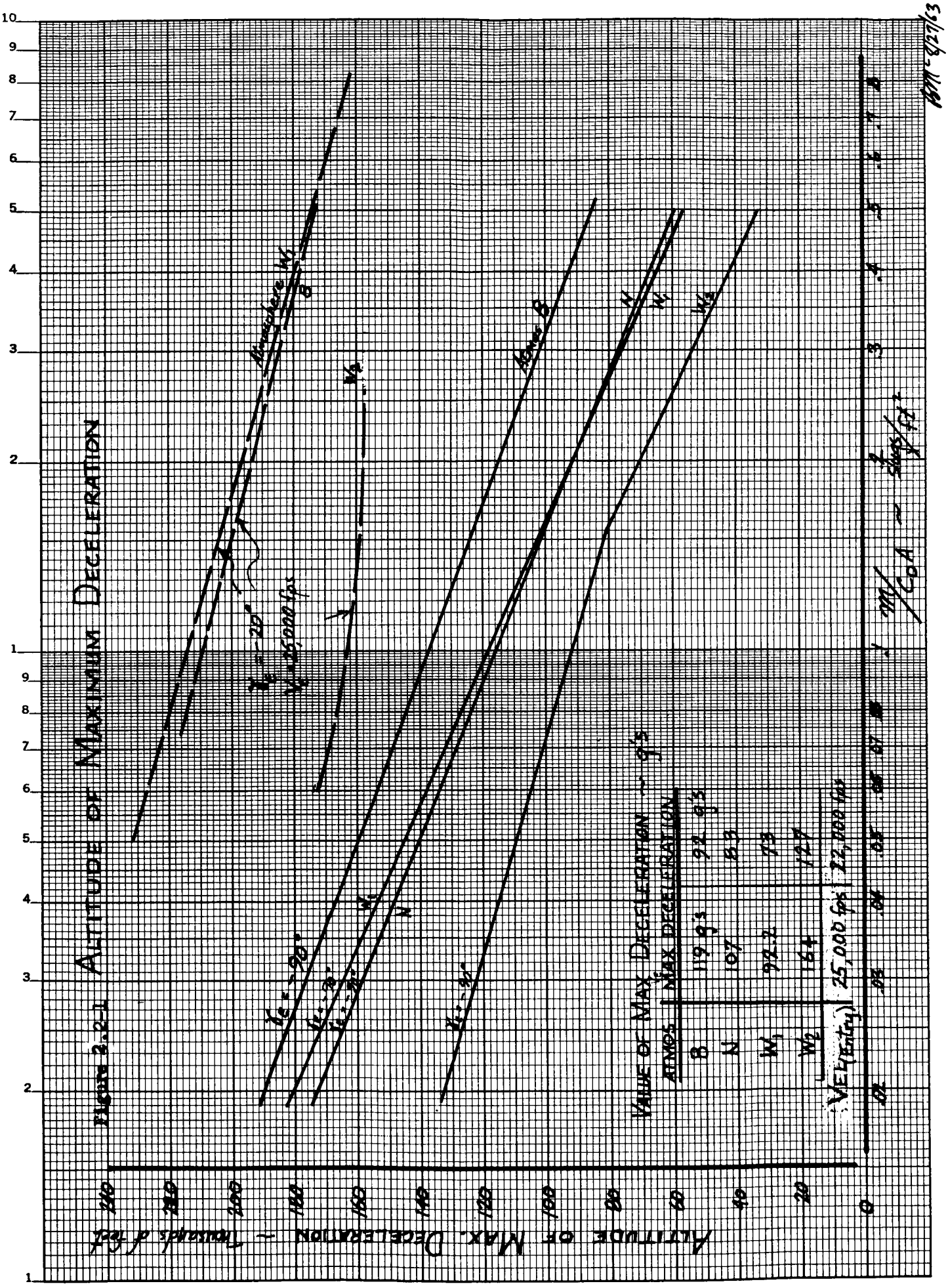
Altitude of Maximum Deceleration
Atmosphere W1
B
W2
Atmos B
N
W1
W2
γE = -20°
γE = -25,000 fps
γE = -20°
γE = -30°
γE = -40°
Value of Max Deceleration ~ g's
Atmos
Max Deceleration
B 119 g's
N 107
W1 92.2
W2 164
VE (Entry) 25,000 fps
22,700 fps
Altitude of Max. Deceleration ~ Thousands of feet
m/CDA ~ slugs/ft²

Figure 2.2-1

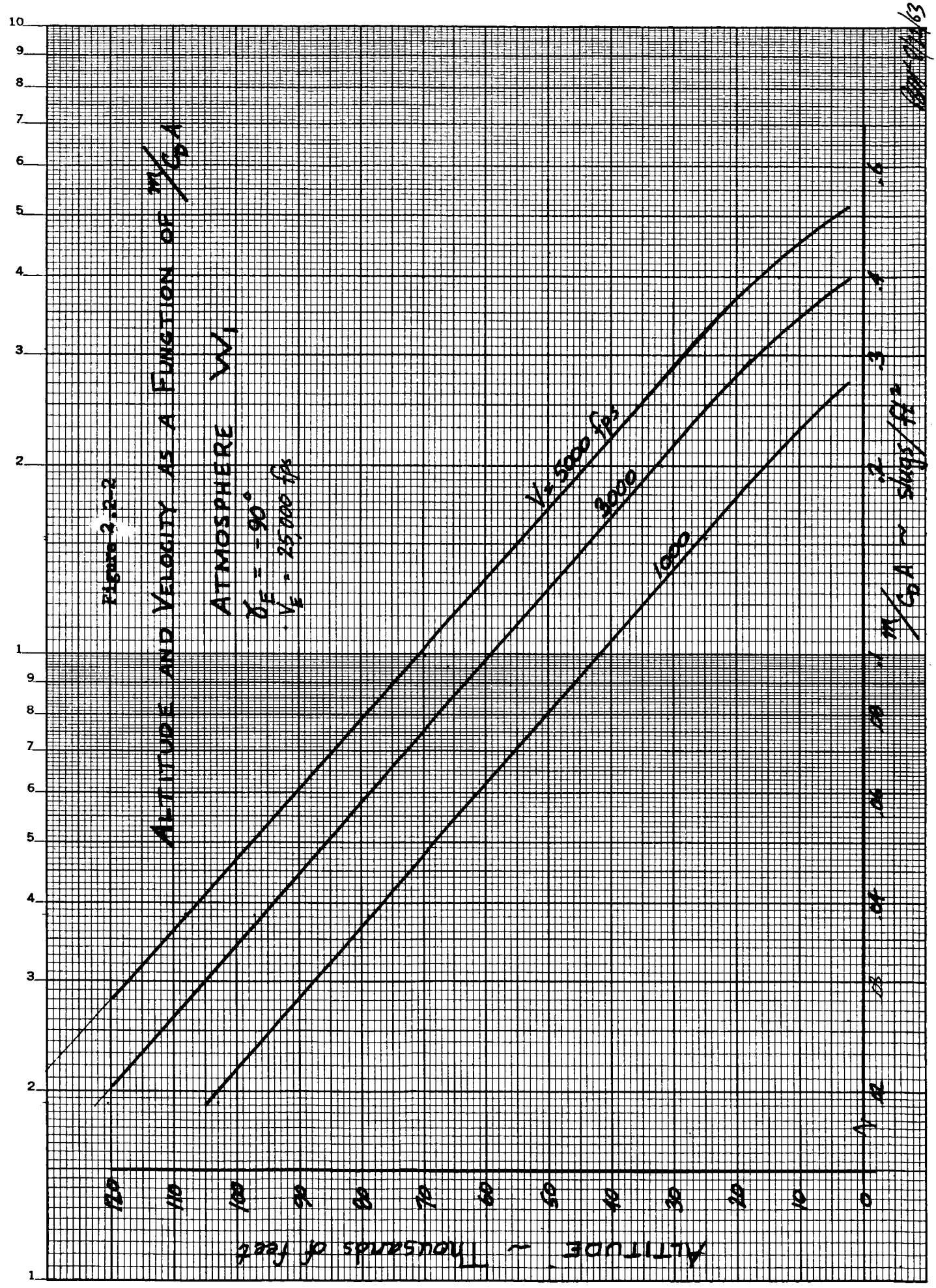
ALTITUDE AND VELOCITY AS A FUNCTION OF m/C_DA
ATMOSPHERE W_1
$\gamma_E = -90°$
$V_E = 25{,}000$ fps
$V_1 = 5000$ fps
3000
1000
m/C_DA ~ slugs/ft²
ALTITUDE ~ Thousands of feet

Figure 2.2-2

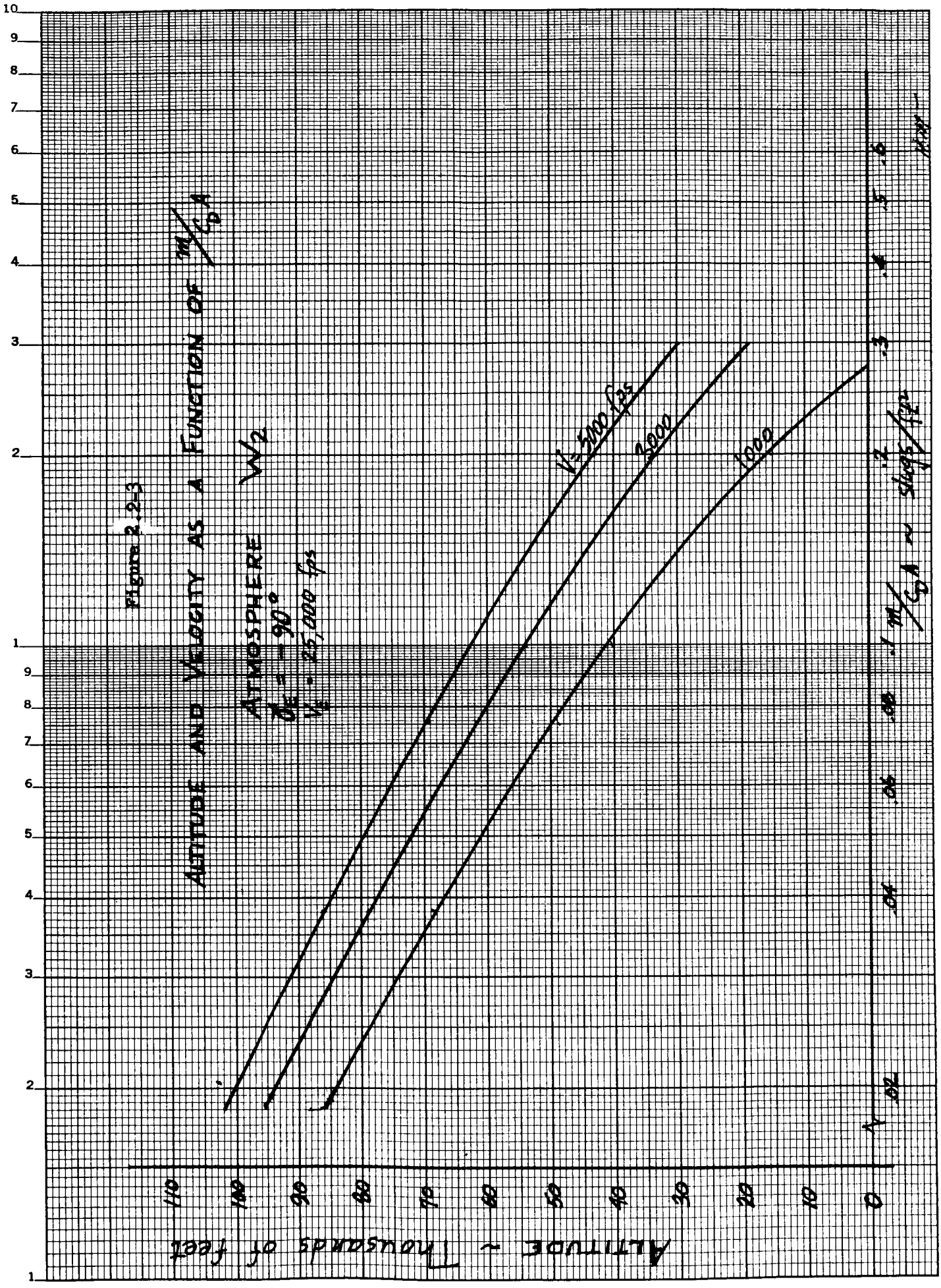
ALTITUDE AND VELOCITY AS A FUNCTION OF m/C_DA
ATMOSPHERE
$\gamma_E = -90°$
$V_E = 25,000$ fps
$W/2$
V = 500 fps
2000
1000
m/C_DA ~ slugs/ft²
ALTITUDE ~ Thousands of feet
110
100
90
80
70
60
50
40
30
20
10
0
.02
.04
.06
.08
.1
.2
.3
.4
.5
.6

Figure 2.2-3

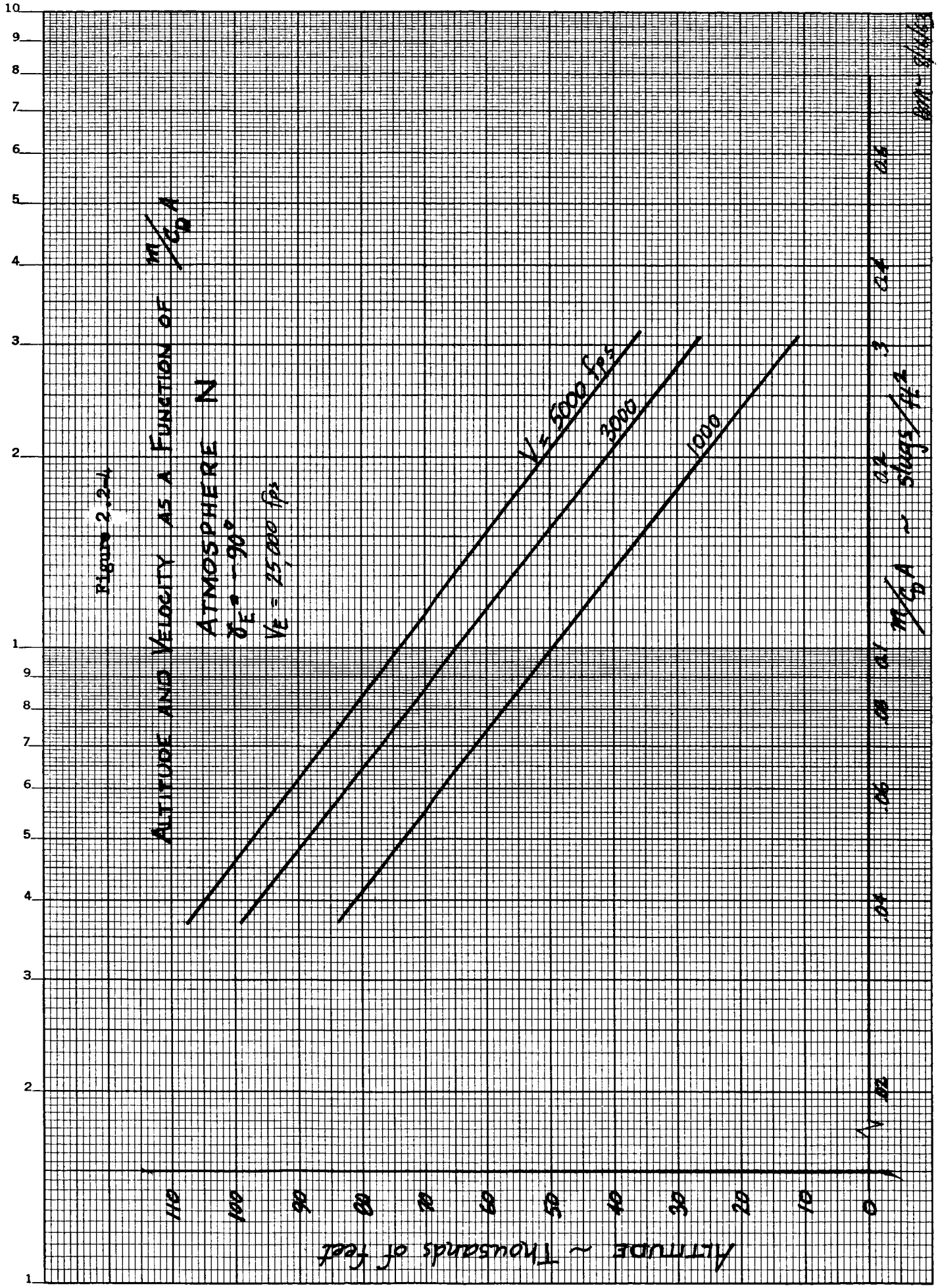
ALTITUDE AND VELOCITY AS A FUNCTION OF $m/C_D A$
ATMOSPHERE N
$\gamma_E = -90°$
$V_E = 25{,}000$ fps
$V = 5000$ fps
3000
1000
ALTITUDE ~ Thousands of feet
$m/C_D A$ ~ slugs/ft²
.02
.04
.06
.08
.1
.2
.3
.4
.6
0
10
20
30
40
50
60
70
80
90
100
110

Figure 2.2-4

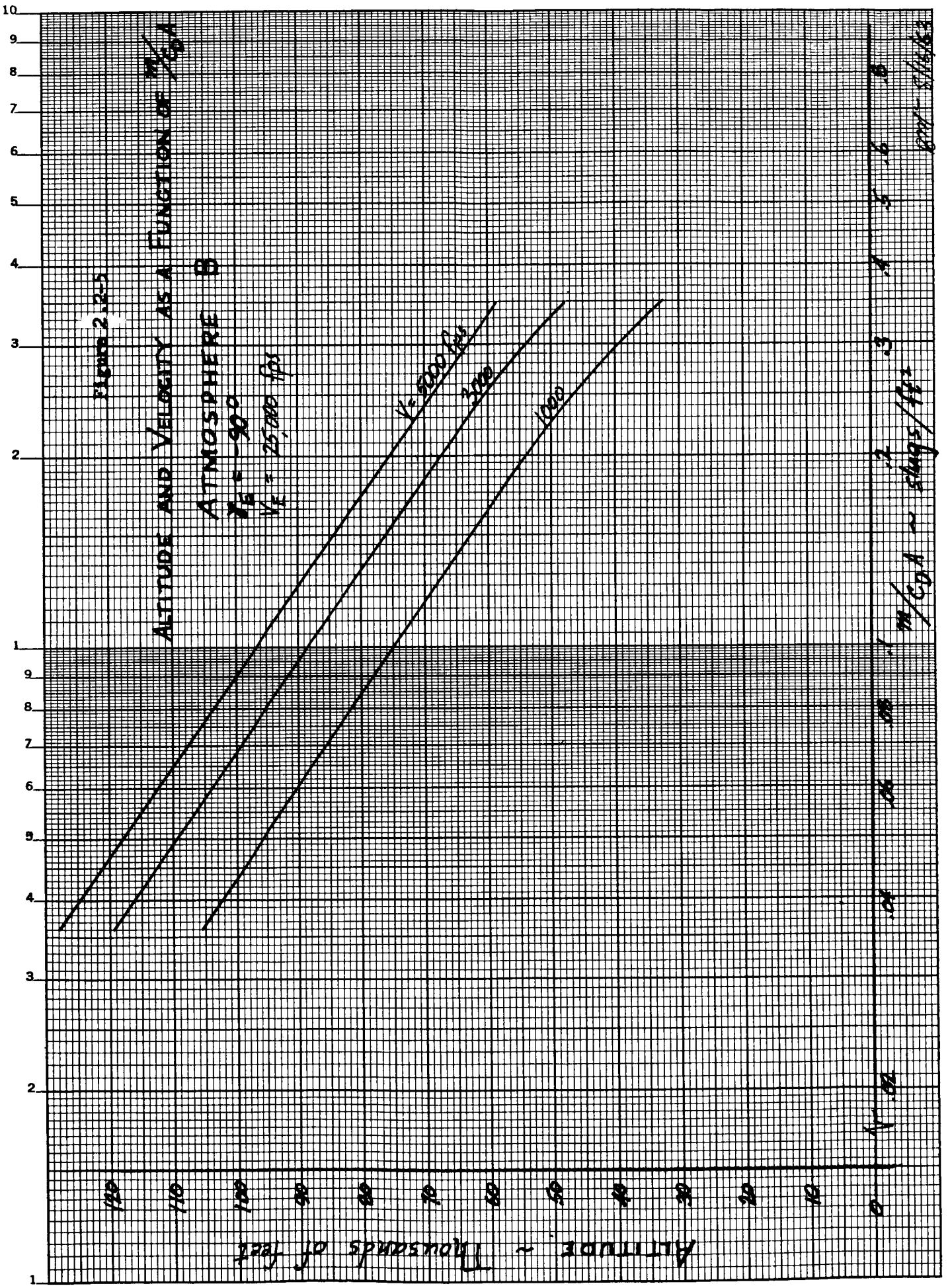
ALTITUDE AND VELOCITY AS A FUNCTION OF m/C_DA
ATMOSPHERE B
$\gamma_E = -90°$
$V_E = 25{,}000$ fps
$V_E = 200$ fps
300
1000
m/C_DA ~ slugs/ft²
ALTITUDE ~ Thousands of feet

FIGURE 2.2-5

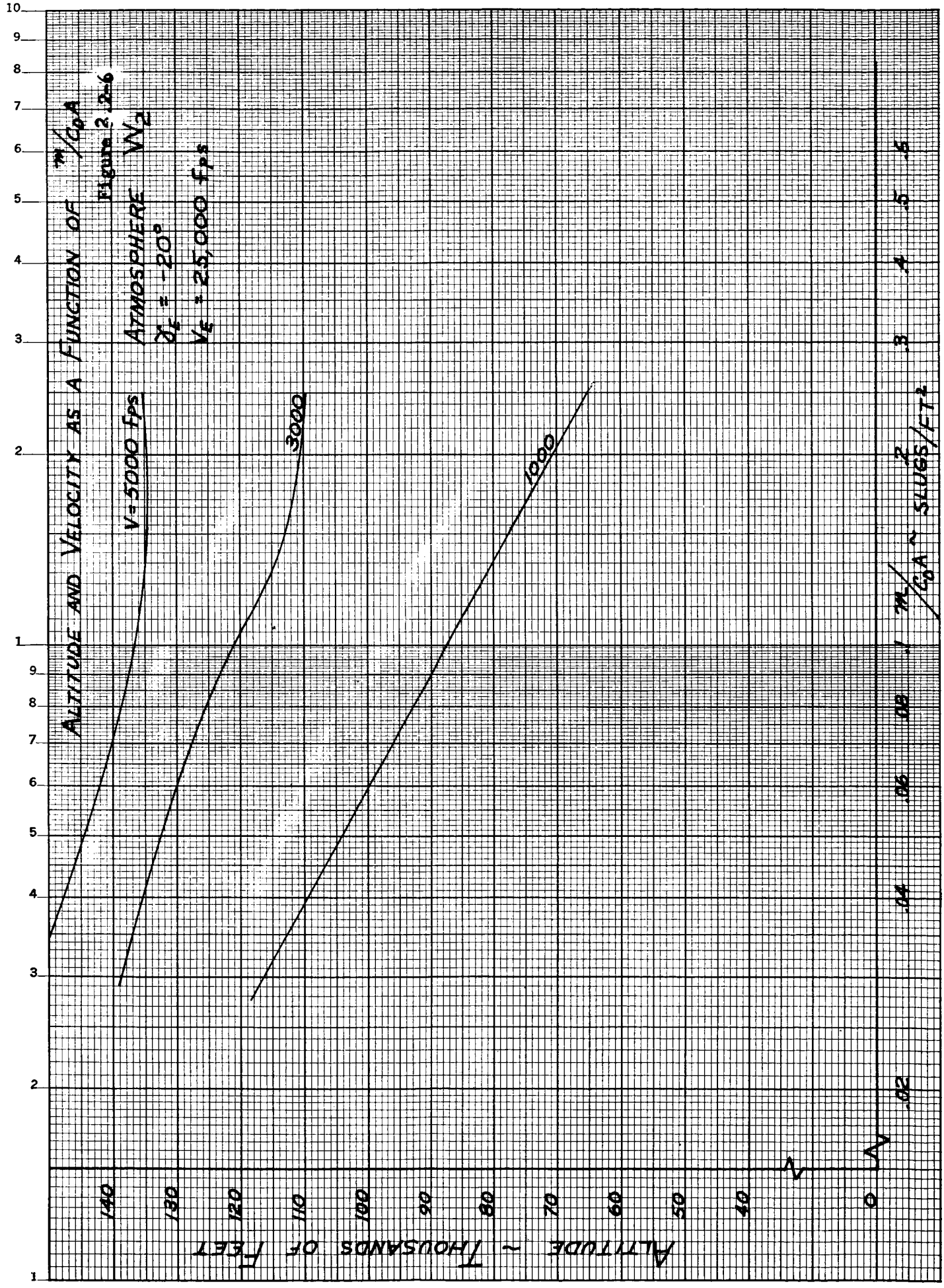
ALTITUDE AND VELOCITY AS A FUNCTION OF m/C_DA
Figure 2.2-6
ATMOSPHERE
$\gamma_E = -20°$
$V_E = 25,000$ fps
W_2
V=5000 fps
3000
1000
m/C_DA ~ SLUGS/FT^2
.02
.04
.06
.08
.1
.2
.3
.4
.5
.6
ALTITUDE ~ THOUSANDS OF FEET
140
130
120
110
100
90
80
70
60
50
40
0

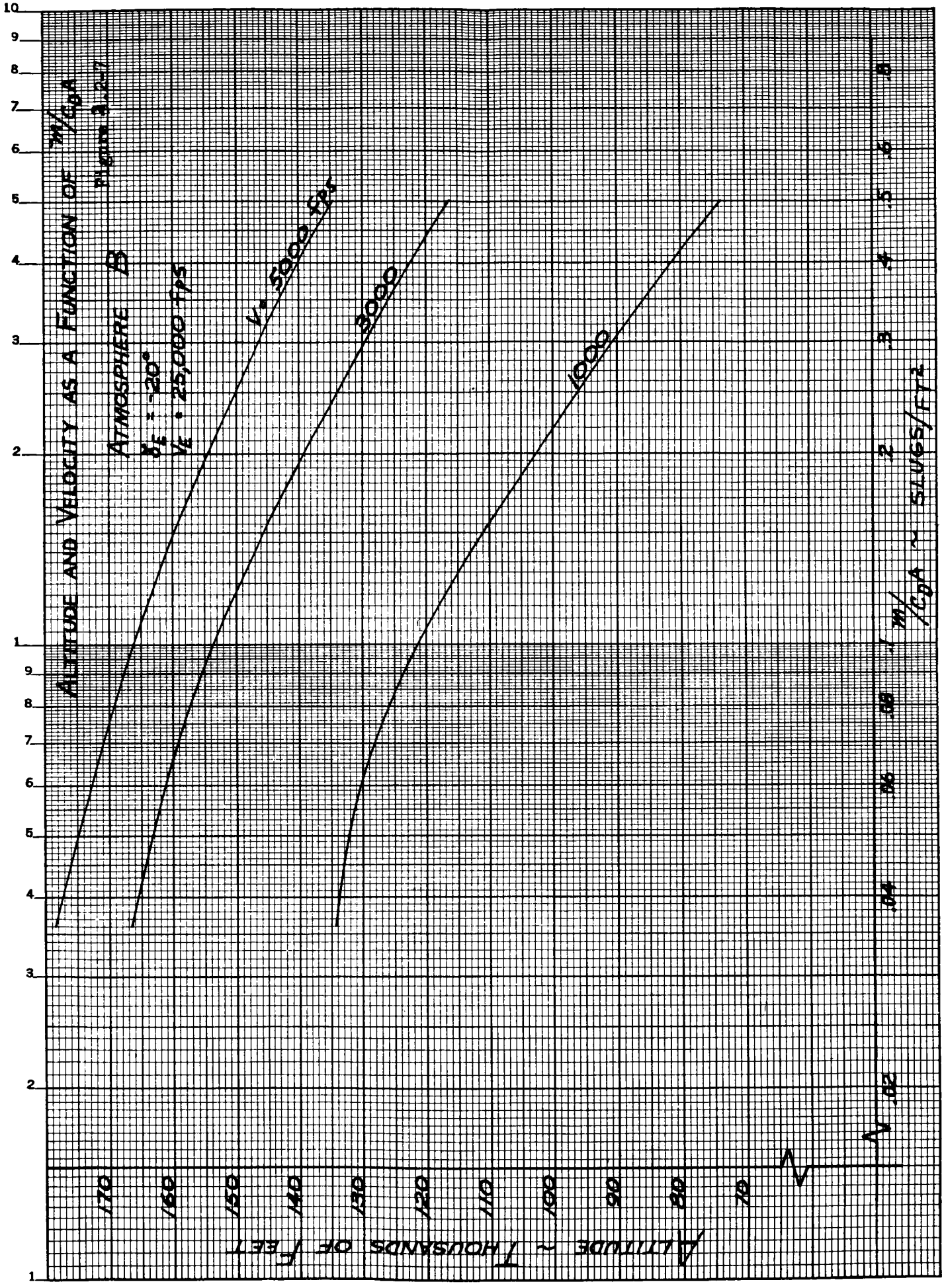
ALTITUDE AND VELOCITY AS A FUNCTION OF W/C_DA
FIGURE 2.2-7
B
ATMOSPHERE B
γ_E = -20°
V_E = 25,000 FPS
V = 5000 FPS
3000
1000
W/C_DA ~ SLUGS/FT²
.8
.6
.5
.4
.3
.2
.08
.06
.04
.02
ALTITUDE ~ THOUSANDS OF FEET
170
160
150
140
130
120
110
100
90
80
70

FORM M 113-N-3 (REV. 5-61)

PREPARED BY: TW	NORTH AMERICAN AVIATION, INC. SPACE and INFORMATION SYSTEMS DIVISION	PAGE NO. OF
CHECKED BY: [illegible]		REPORT NO.
DATE: 9-9-63		MODEL NO.

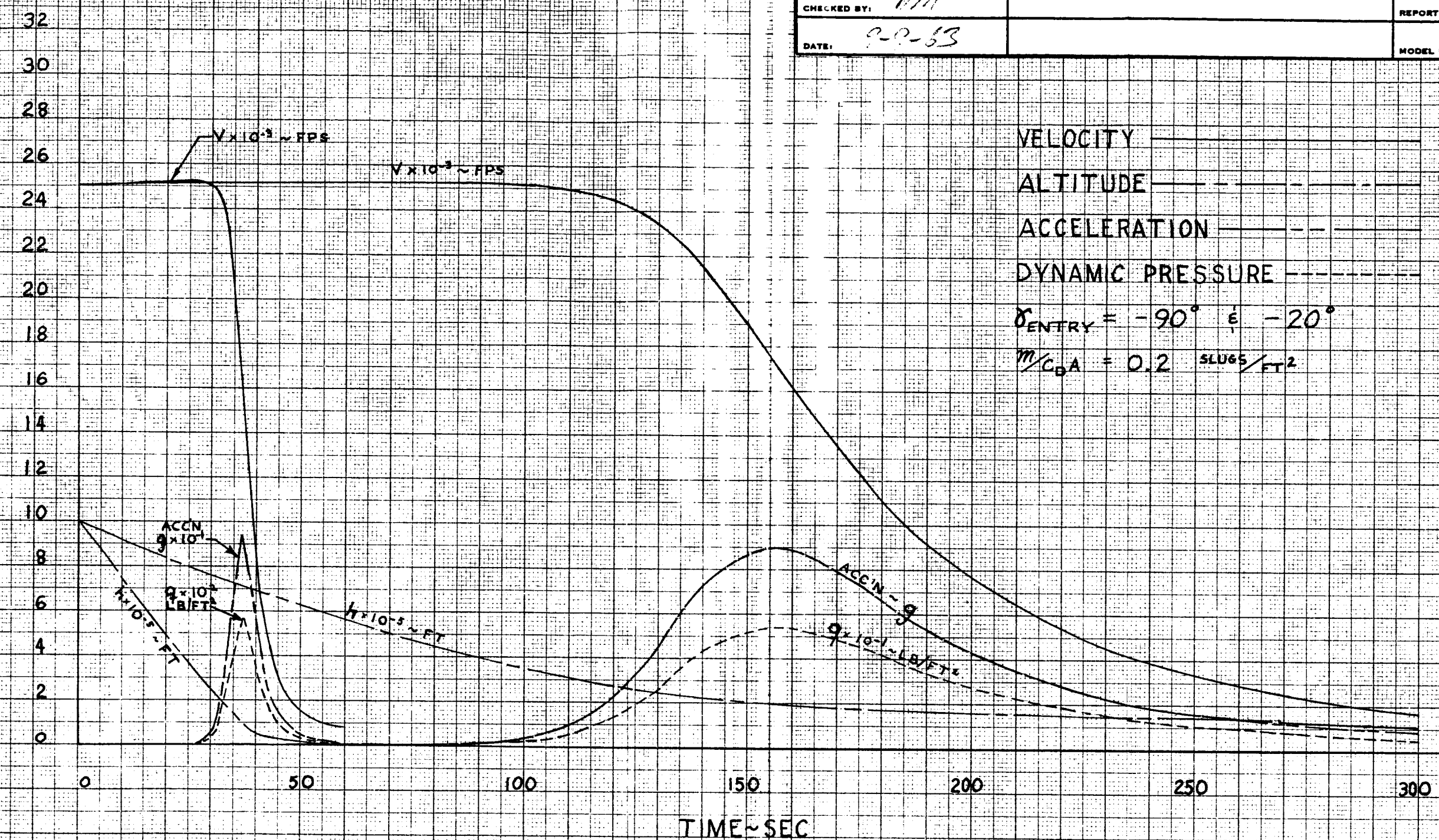

FIGURE 2.2-8 TRAJECTORY VARIABLES — ATMOSPHERE W_1

FORM M-113-N-3 (REV. 5-61)

PREPARED BY: T.K.	NORTH AMERICAN AVIATION, INC. SPACE and INFORMATION SYSTEMS DIVISION	PAGE NO OF
CHECKED BY:		REPORT NO
DATE: 9-9-62		MODEL NO.

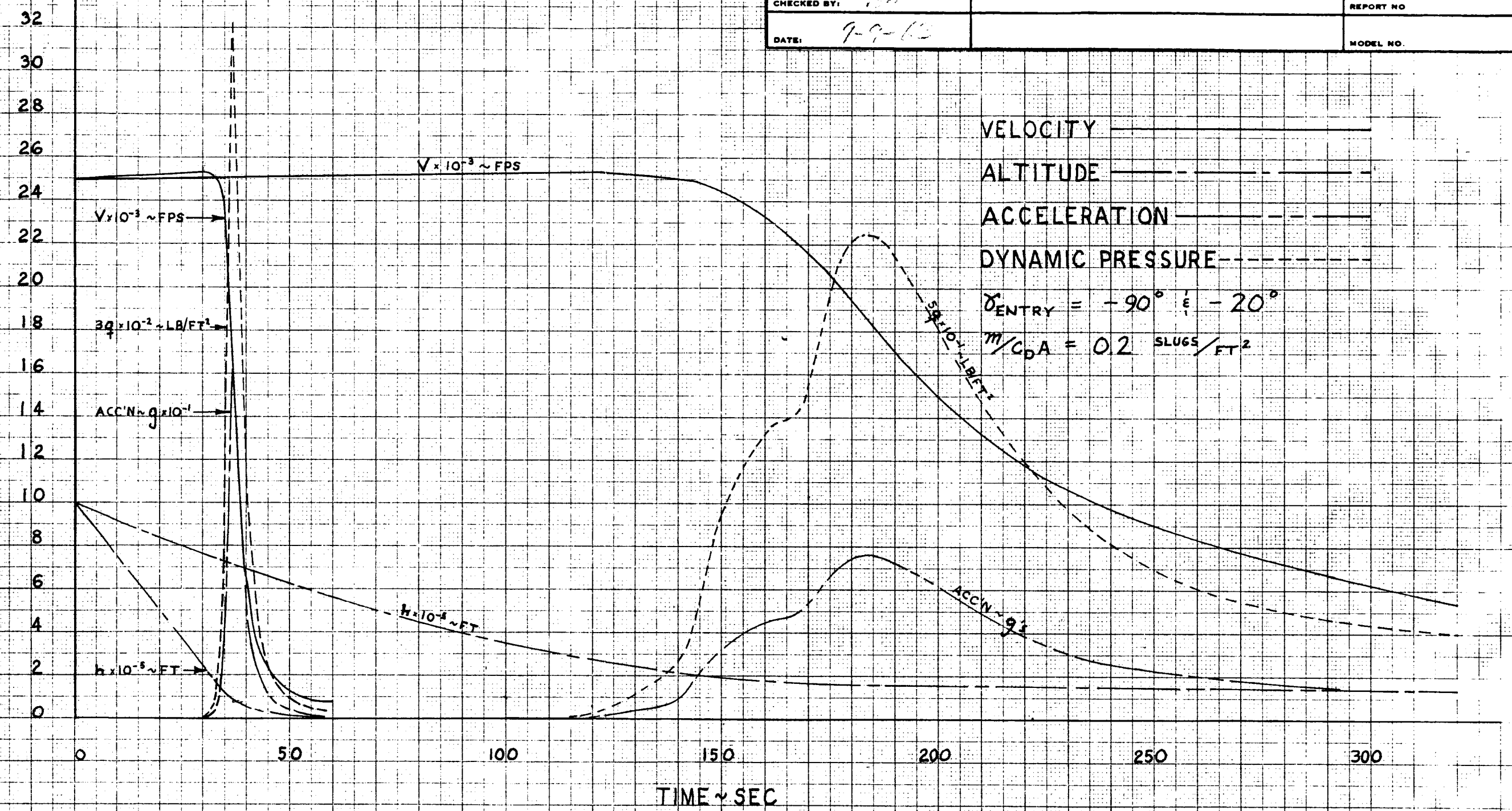

FIGURE 2.2-9 TRAJECTORY VARIABLES – ATMOSPHERE W_2

FORM M-113-N-3 (REV. 5-61)

PREPARED BY: TVW	NORTH AMERICAN AVIATION, INC. SPACE and INFORMATION SYSTEMS DIVISION	PAGE NO. OF
CHECKED BY: BMC		REPORT NO.
DATE: 7-9-63		MODEL NO.

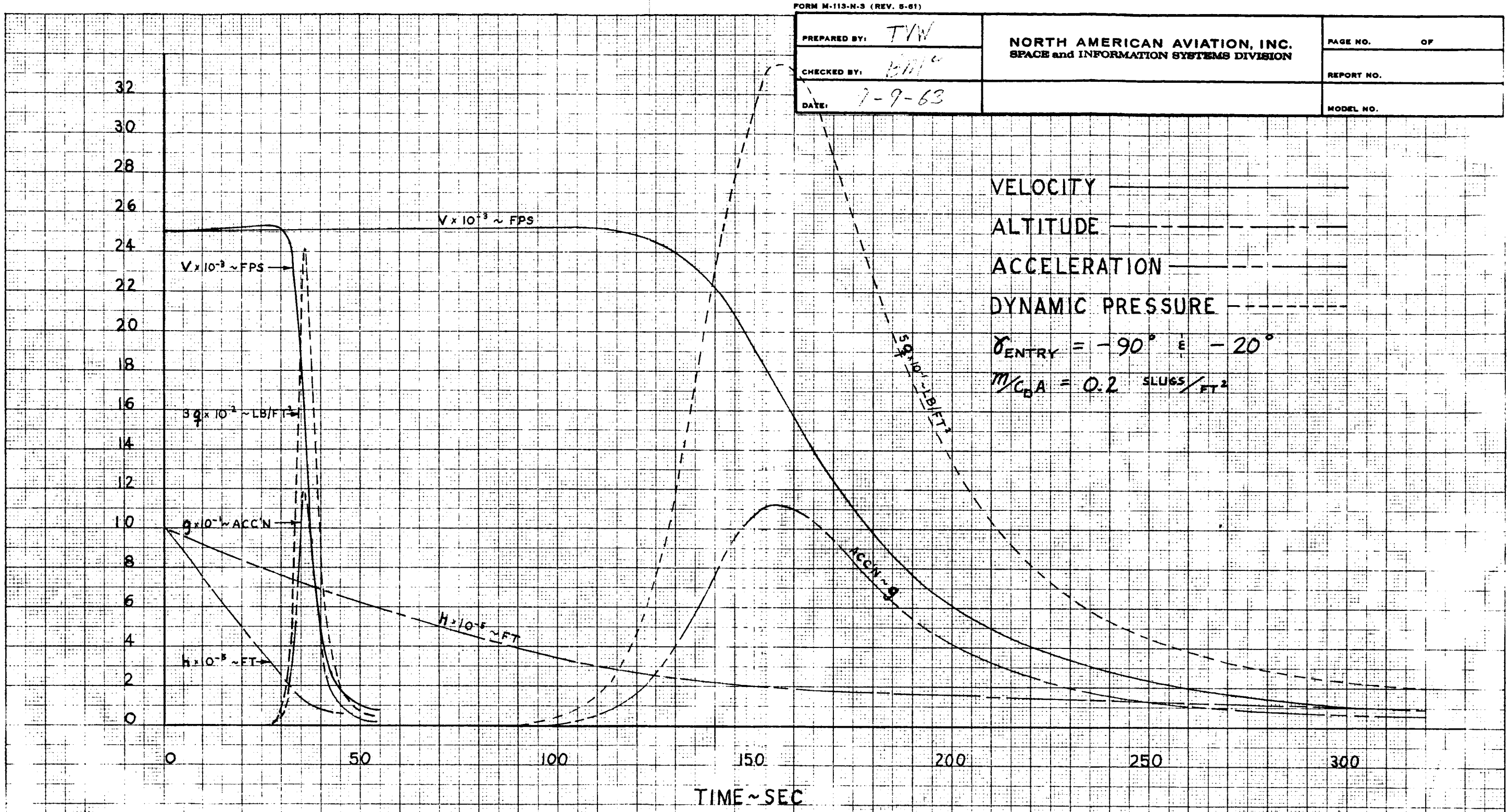

FIGURE 2.2-10 TRAJECTORY VARIABLES – ATMOSPHERE B

PREPARED BY: BM	NORTH AMERICAN AVIATION, INC. SPACE and INFORMATION SYSTEMS DIVISION	PAGE NO. OF
CHECKED BY:		REPORT NO.
DATE: 9/6/63	FIGURE 2.2-11	MODEL NO.

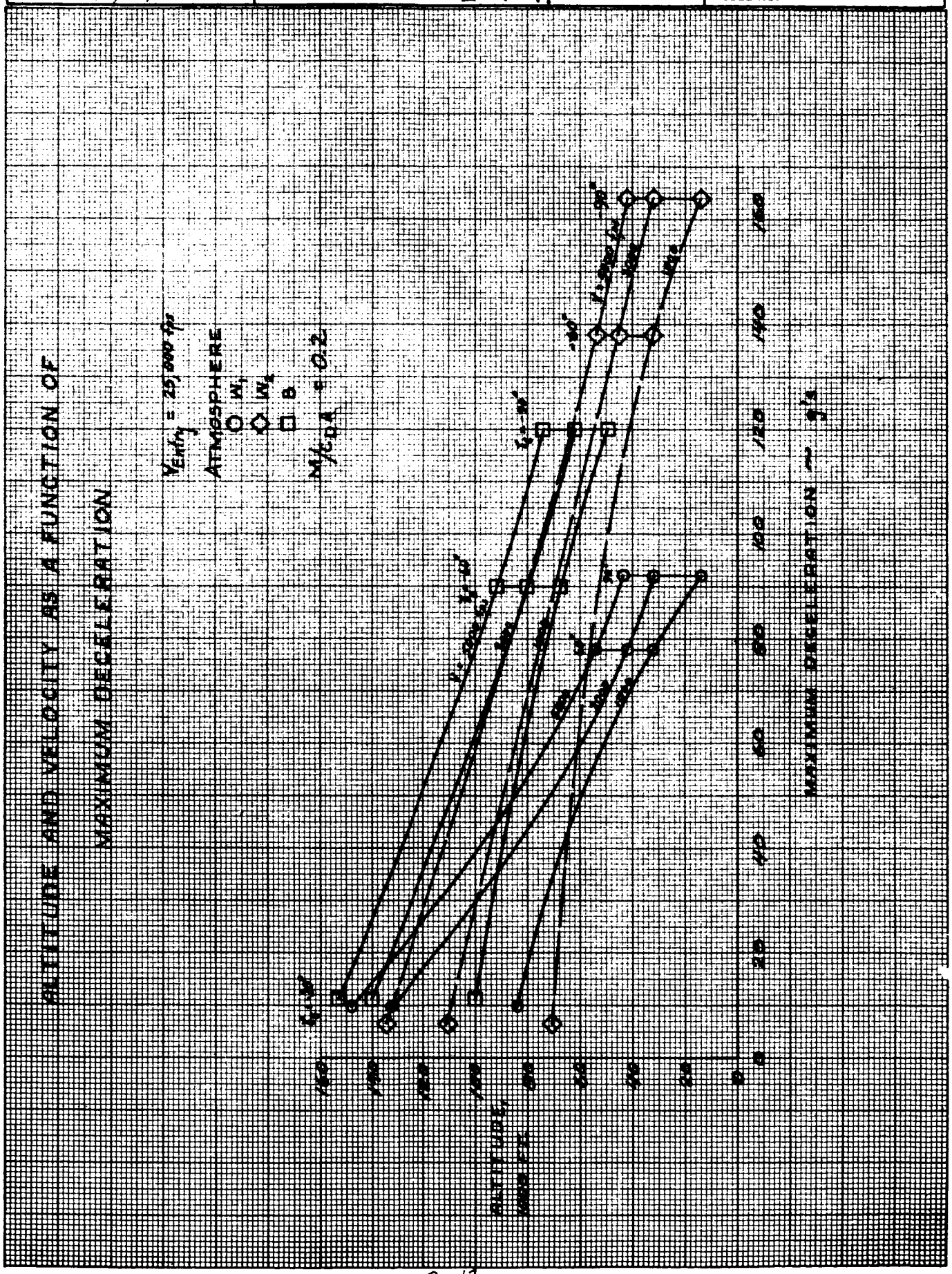

2.3 HEATING PARAMETERS

The methods developed for predicting aerodynamic heating in the Earth's atmosphere can be applied to Mars entry by modification of the applicable parameters and constants to account for differences in atmospheric properties. These include enthalpy, specific heat ratio, viscosity, thermal conductivity, etc. A discussion of the methods of prediction currently used and the application of these methods to the present study follows.

2.3.1 Methods of Analysis

2.3.1.1 Convective Heating

Hoshizaki (Reference 1) has expressed laminar convective stagnation point heating as follows:

$$(1)\ \dot{q}_{cs} = 4.32 \times 10^4 \sqrt{\left(\frac{dU_e}{dx}\right)_{sp} \rho_W \mu_W \left(\frac{T_W}{900}\right)^{0.4}} \left(\frac{U_\infty}{10^4}\right)^{1.69} \left(1 - \frac{h_W}{h_\infty}\right) \frac{BTU}{ft^2 sec}$$

Applying the transport properties reported by Hansen (Reference 2), Equation (1) may be expressed as:

$$(2)\ \dot{q}_{cs} = 2.59 \times 10^2 \sqrt{\rho_\infty \left(\frac{dU_e}{dx}\right)_{sp}} \left(\frac{U_\infty}{10^4}\right)^{2.69} \left(1 - \frac{h_W}{h_\infty}\right) \frac{BTU}{ft^2\ sec}$$

The stagnation point velocity gradient $\left(\frac{dU_e}{dx}\right)_{sp}$ may be determined by the solution of the stagnation region flow field (e.g., Li and Geiger (Reference 3) for an equilibrium, adiabatic, and constant density flow field, i.e.,

$$(3)\quad \left(\frac{dU_e}{dx}\right)_{sp} = \frac{U_\infty}{R_n} \sqrt{\frac{\rho_\infty}{\rho_2} \left(2 - \rho_\infty/\rho_2\right)}$$

However, for the velocities of concern in this study, the density ratio across the shock wave ρ_∞/ρ_2 is approximately 1/15. This assumption, along with the cold wall approximation, yields the following expression for laminar heating at the stagnation point in air:

$$(4)\ \dot{q}_{cs} \sqrt{R_n} = 2.7 \times 10^{-9} \rho_\infty^{1/2}\ U_\infty^{3.19}$$

For carbon dioxide, the same form of Equation (4) is employed; however, the constant becomes 2.94×10^{-9} rather than 2.7×10^{-9} because of the change in thermodynamic and transport properties.

Comparisons of Hoshizaki's theory with test data are shown on Figure 2.3-1 (Reference 6) for various carbon dioxide and nitrogen mixtures. Due to the uncertainties involved in the composition of the Martian atmosphere

FIGURE 2.3-1 COMPARISON OF STAGNATION POINT CONVECTIVE HEATING THEORY AND EXPERIMENTAL DATA (FROM REF. 5)

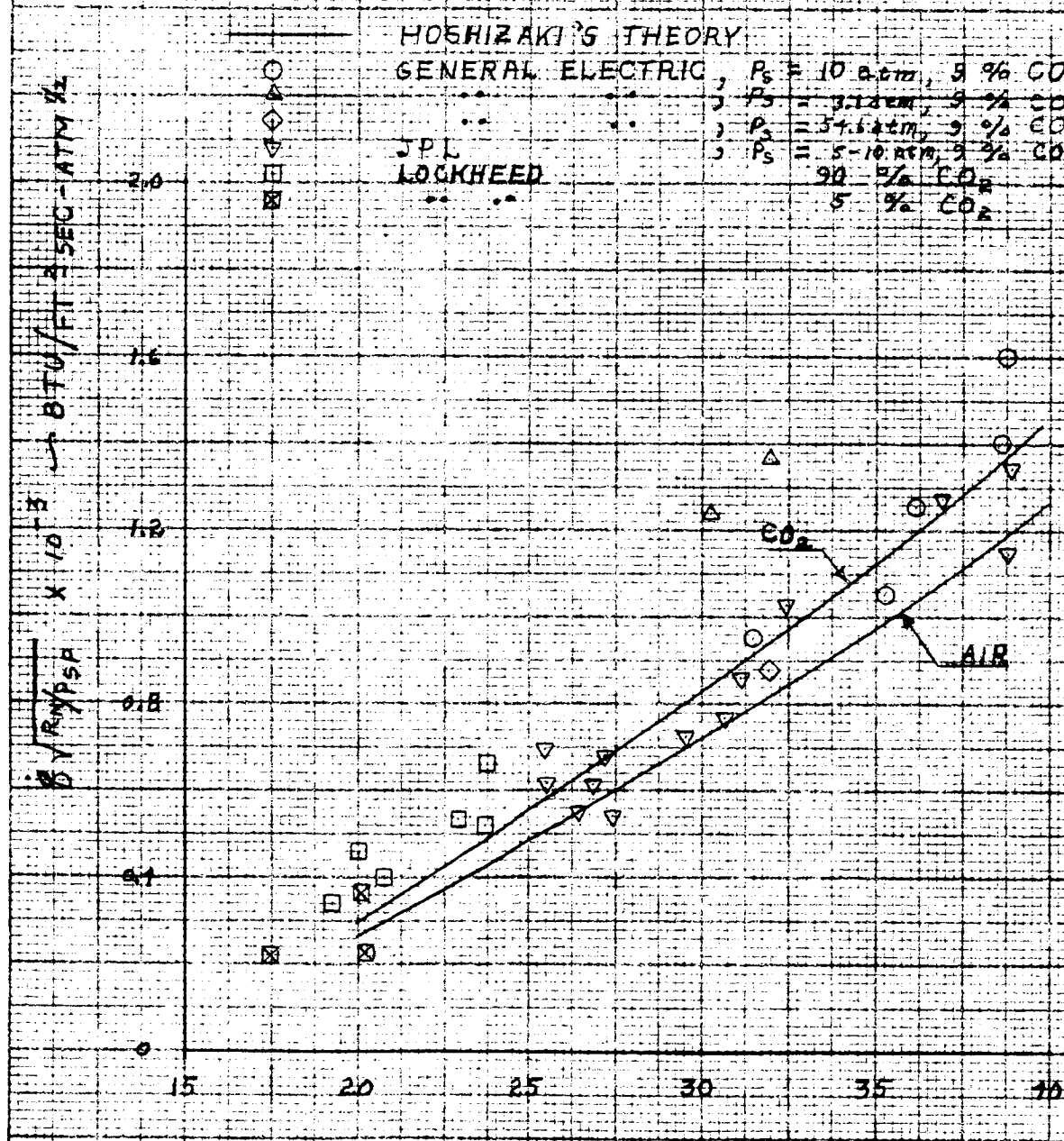

and experimental scatter, the heating rates predicted by Equation (4) arbitrarily were increased by 25% (Reference 6). Thus, the convective heating rates were calculated employing the following expression:

$$(5)\ \dot{q}_{cs} \sqrt{Rn} = 3.37 \times 10^{-9} \rho_\infty^{1/2} U_\infty^{3.19}$$

The equation for maximum turbulent heating on a body in air may be expressed as (Reference 7):

$$(6)\ \dot{q}_{ct} \ (R_n)^{0.2} = 2.86 \times 10^{-8} \ \rho_\infty^{0.8} \ U_\infty^{3.35}$$

Maximum and integrated laminar and turbulent heating rates for entry velocities of 22,000 and 25,000 fps are shown as a function of M/C_DA in Figures 2.3-2 to 2.3-6. It may be seen that laminar heating is higher than the turbulent heating at M/C_DA values below 0.2. This appears due to the low Reynolds' numbers encountered at peak heating for the low M/C_DA's for the entry vehicles. Since the boundary layer is expected to remain laminar during the maximum heating period, the laminar equation was used for all preliminary design calculations.

2.3.1.2 Radiative Heating

The radiative heating rate at the stagnation point is usually determined by assuming the stagnation region to be approximated by a semi-infinite slab. Under this assumption, the heating rate is written as

$$(7)\ \dot{q}_{Rad.\ S.P.} = I\ \delta/2$$

where I is the radiant intensity of the shock layer gas and δ is the shock stand-off distance. Various studies of shock layer intensity have shown that analytically derived values for intensity (References 8, 9) are still uncertain, even for air. James (Reference 10) has studied CO_2-N_2 mixtures simulating the Martian atmosphere. Spiegel (Reference 5) used the intensity data given in Reference 8 for the various species assumed to exist in the Martian atmosphere and obtained a correlation equation of the form:

$$(8)\ \ I = 1.7 \times 10^{-11} \ \rho_\infty^{1.4} \ U_\infty^{5} \ \frac{BTU}{Ft^2\text{-sec-ft}}$$

This equation was used to determine the intensity values for this study. The shock detachment distance was assumed to be approximately equal to the density ratio, ρ_∞/ρ_2, for which a value of 1/15 was chosen. Although there is some question as to the accuracy of this equation, the form is quite convenient for a preliminary design study and appears sufficiently accurate considering the lack of experimental data in this area. The effect of uncertainties in this equation on heat shield weight is discussed in a following section.

Figure 2.3-2

STAGNATION POINT
MAXIMUM CONVECTIVE-LAMINAR
HEATING RATE vs. m/C_DA

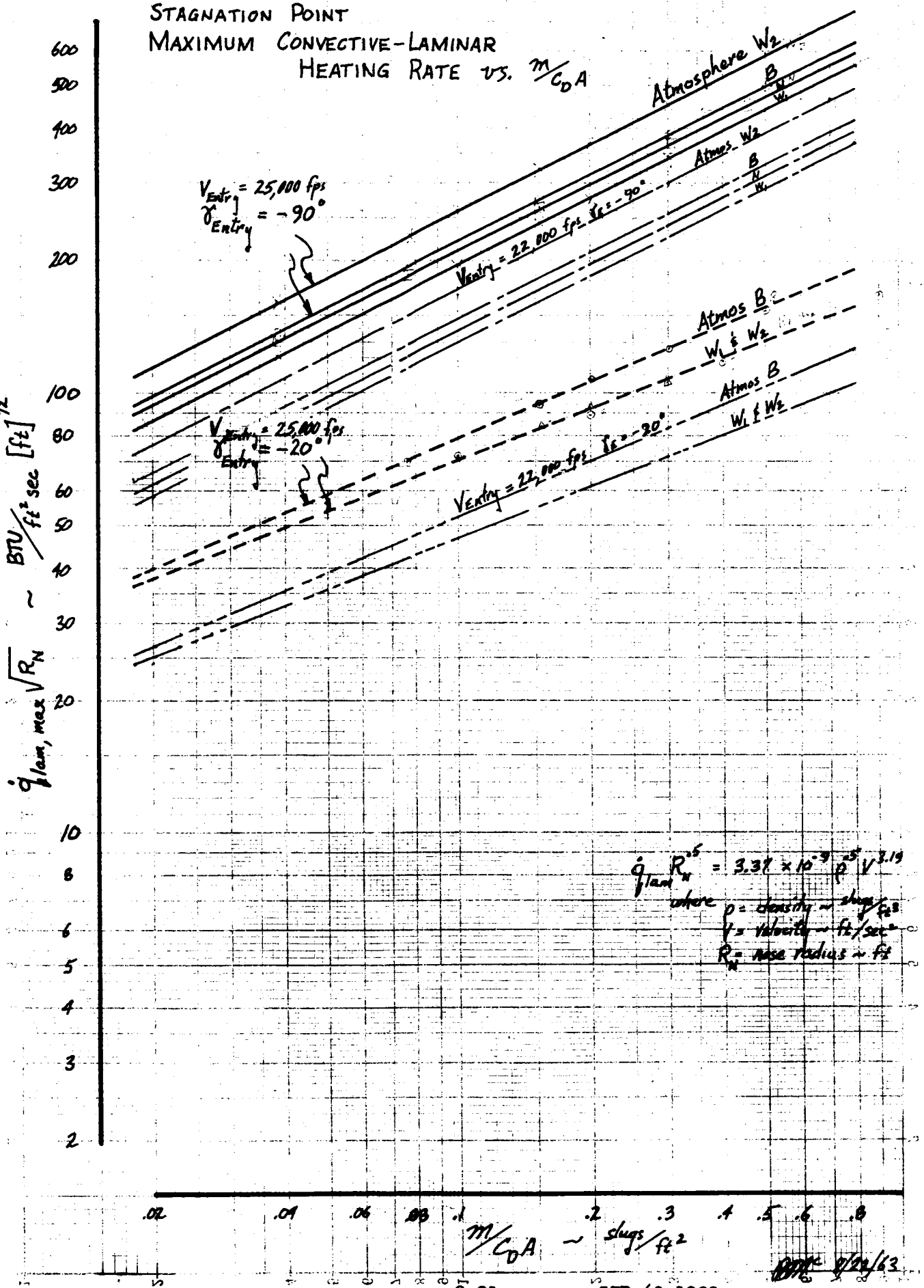

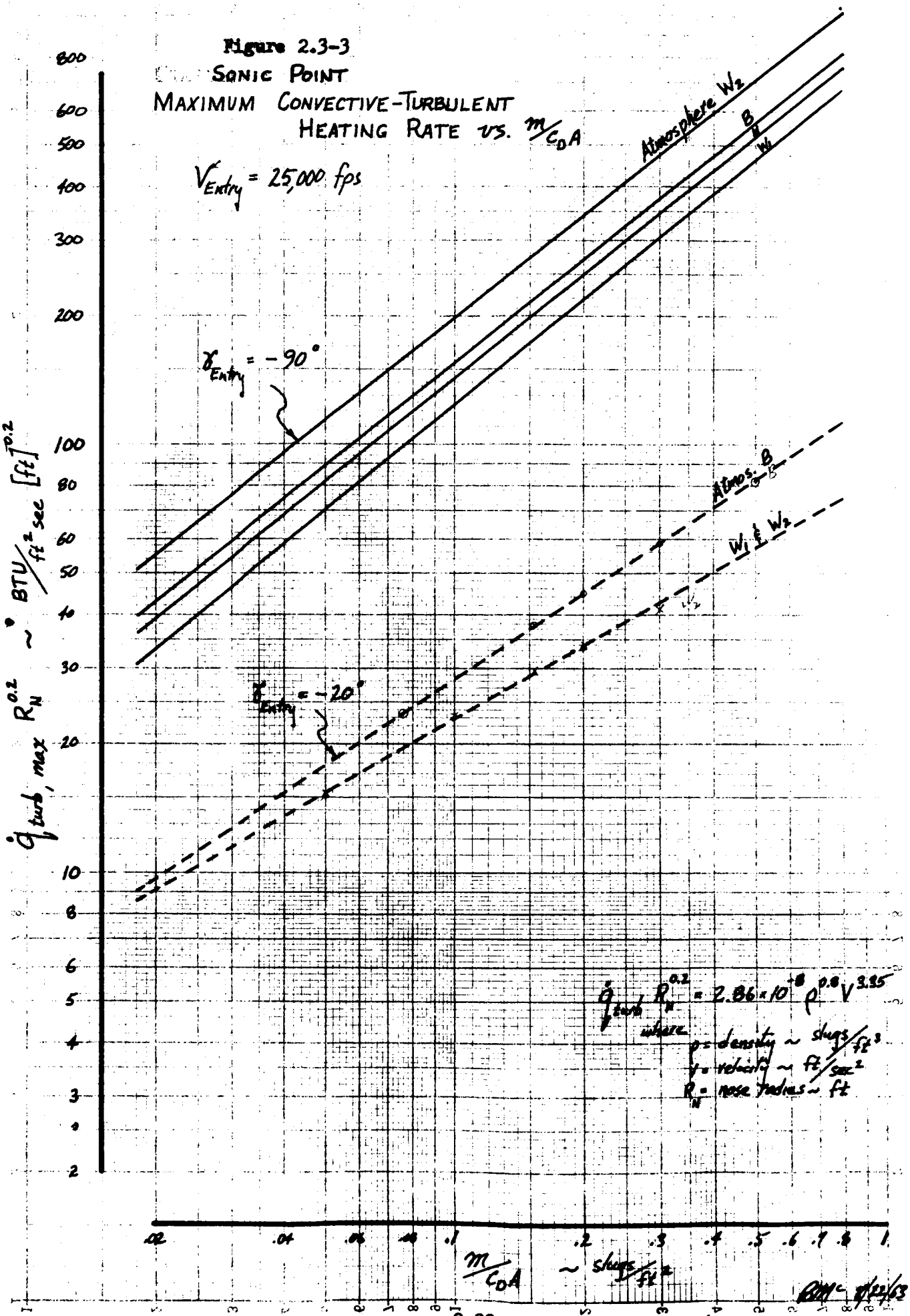
Figure 2.3-3
SONIC POINT
MAXIMUM CONVECTIVE-TURBULENT
HEATING RATE vs. m/C_DA
V_Entry = 25,000 fps
Atmosphere W2
B
W1
γ_Entry = -90°
Atmos. B
W1 & W2
γ_Entry = -20°
q̇_turb, max R_N^0.2 ~ BTU/ft² sec [ft]^0.2
q̇_turb R_N^0.2 = 2.86×10^-8 ρ^0.8 V^3.35
where
ρ = density ~ slugs/ft³
V = velocity ~ ft/sec²
R_N = nose radius ~ ft
m/C_DA ~ slugs/ft²

Figure 2.3-4

INTEGRATED HEATING FLUX

$\gamma_{Entry} = -90°$

$V_{Entry} = 25{,}000$ fps

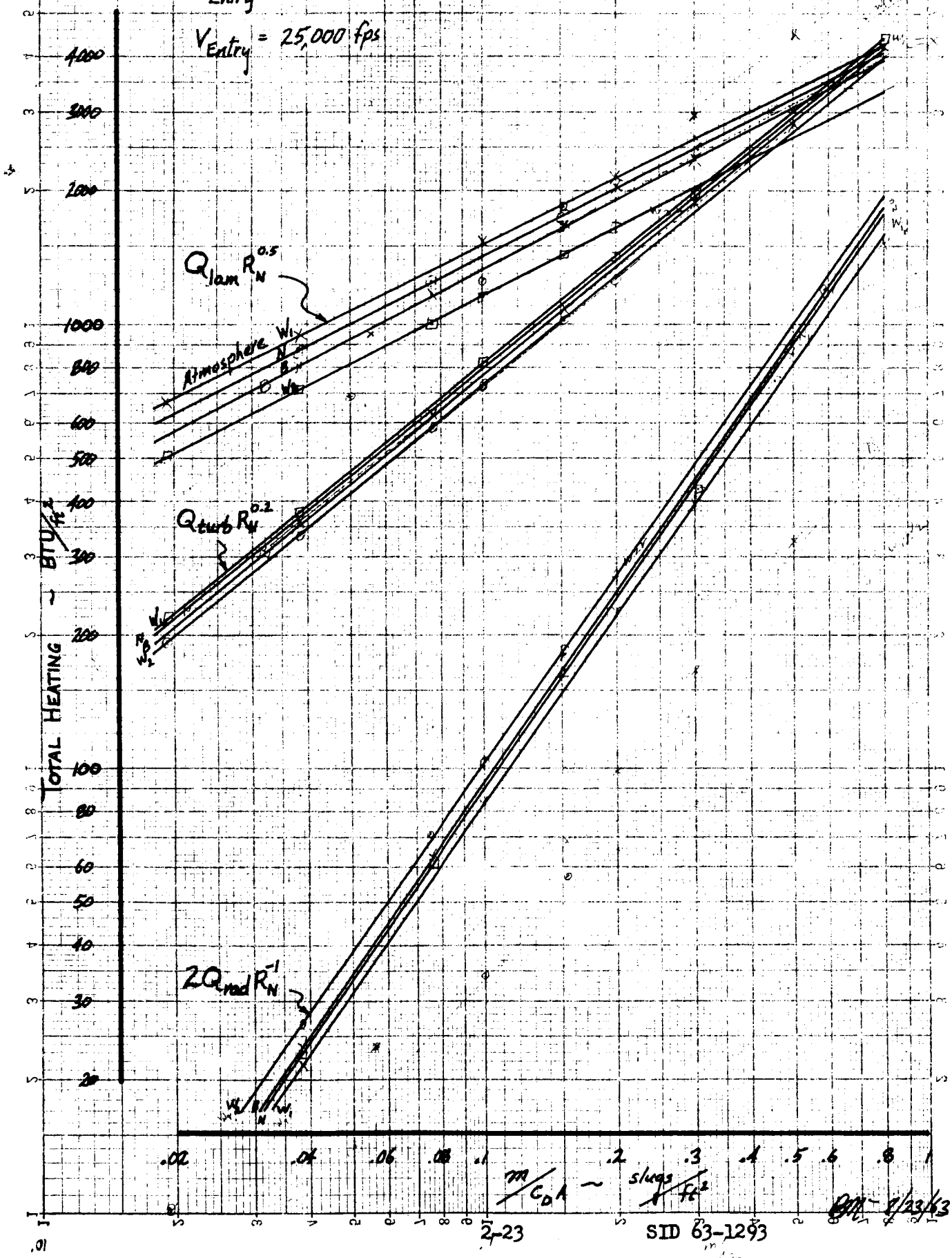

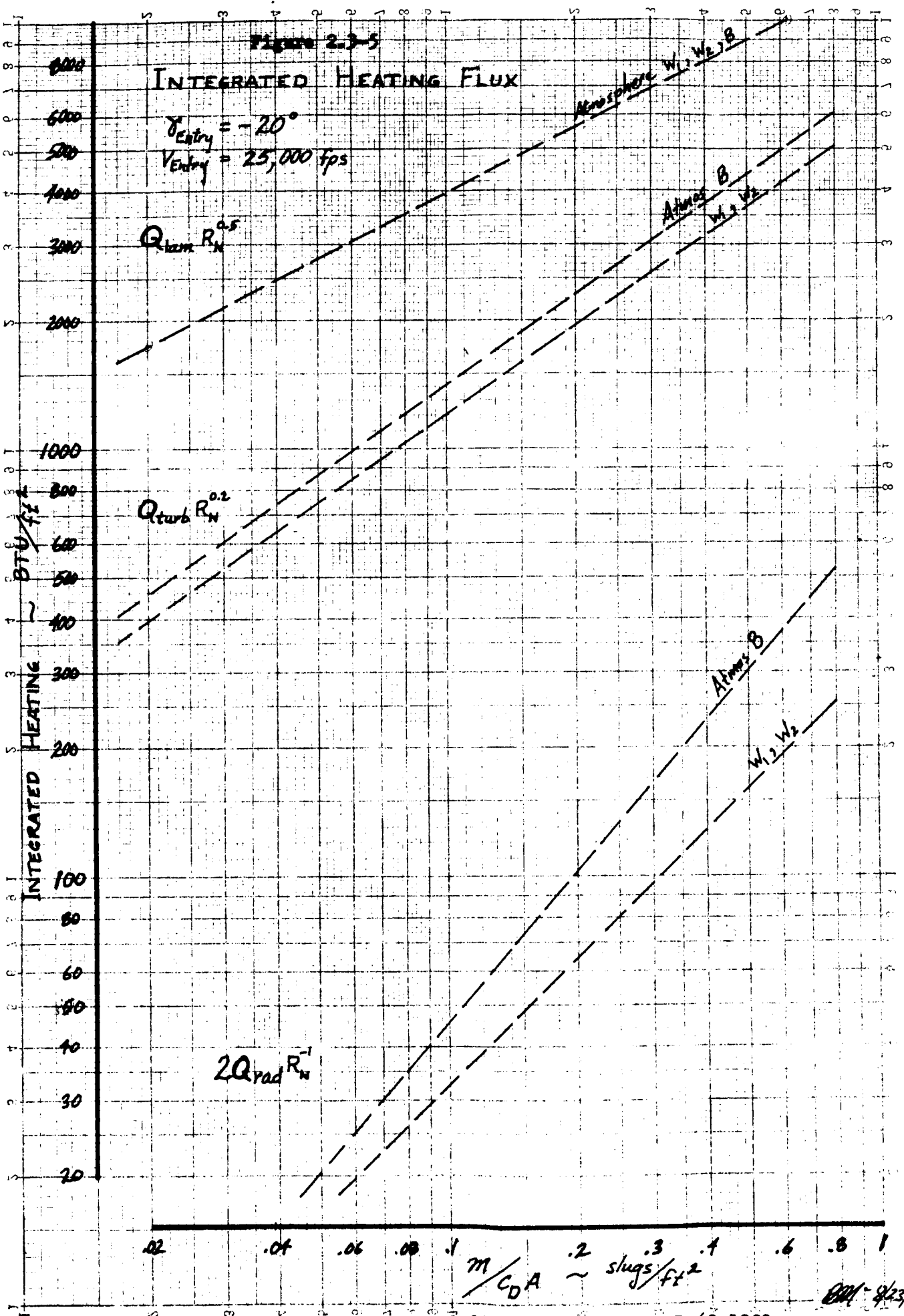
Figure 2.3-5
INTEGRATED HEATING FLUX
$\gamma_{Entry} = -20°$
$V_{Entry} = 25{,}000$ fps
$Q_{lam} R_N^{0.5}$
$Q_{turb} R_N^{0.2}$
$2Q_{rad} R_N^{-1}$
Atmosphere W_1, W_2, B
Atmos B
W_1, W_2
Atmos B
W_1, W_2
INTEGRATED HEATING ~ BTU/ft²
6000
5000
4000
3000
2000
1000
800
600
500
400
300
200
100
80
60
50
40
30
20
.02
.04
.06
.08
.1
.2
.3
.4
.6
.8
1
$m/C_D A$ ~ slugs/ft²

BM - 8/23/63

Figure 2.3-6

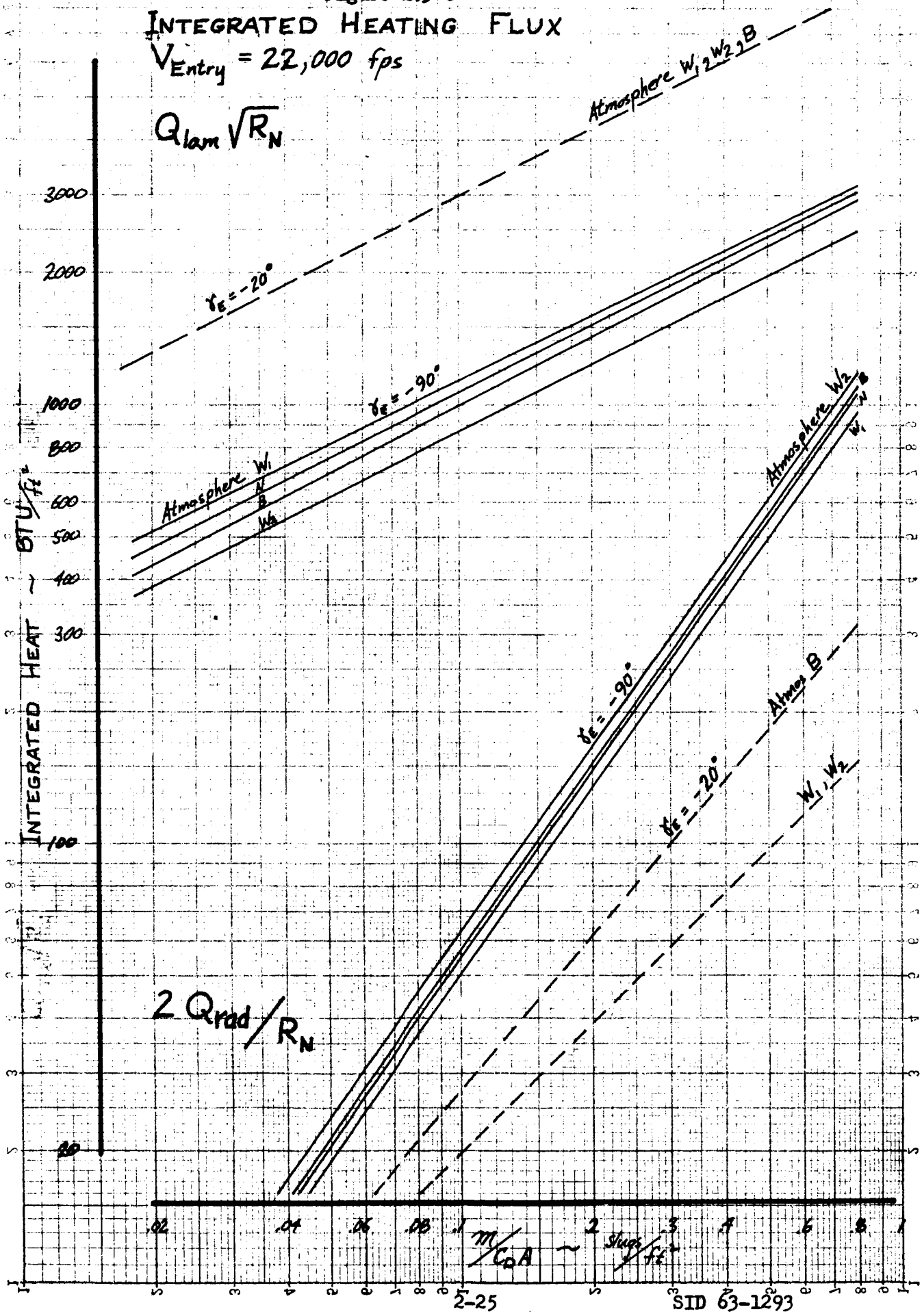
INTEGRATED HEATING FLUX
V_{Entry} = 22,000 fps
$Q_{lam}\sqrt{R_N}$
Atmosphere W_1, W_2, B
$\gamma_E = -20°$
$\gamma_E = -90°$
Atmosphere W_1
B
W_2
Atmosphere W_2
B
W_1
$\gamma_E = -90°$
Atmos B
$\gamma_E = -20°$
W_1, W_2
$2\,Q_{rad}/R_N$
INTEGRATED HEAT ~ BTU/ft²
3000
2000
1000
800
600
500
400
300
100
80
.02
.04
.06
.08
.1
.2
.3
.4
.6
.8
1
m/C_DA ~ slugs/ft²

2.3.1.3 Heating Distributions

The distribution of both convective and radiative heating on the front face of an Apollo-type vehicle at zero angle-of-attack is almost constant. This has been confirmed by experimental data obtained from the Apollo program (Reference 4). Typical heating variations on the front face are presented in Figure 2.3-7. The small error introduced by assuming that the stagnation point heating values apply over the entire front face of the capsule is well within the overall accuracy of the analysis. It is expected that oscillations in angle-of-attack not exceeding $\pm 30°$ during the 90° entry trajectory will not result in average forebody heating rates in excess of vehicle design values.

The heating on the afterbody is essentially due only to convection and drops off quite rapidly near the shoulder to a fairly constant level from the shoulder to the apex of the conical afterbody as shown on Figure 2.3-7. The heating rates on the conical afterbody are about 5% of the stagnation point heating rates, and should not pose a problem providing the vehicle's attitude is stabilized soon after initial entry and large oscillations in angle-of-attack do not occur which would expose the afterbody to attached boundary layer heating conditions.

It should be noted that in determining the heating to the front face of an Apollo type vehicle, an effective nose radius must be used rather than the actual geometrical radius. This is due to the fact that the front face is not absolutely spherical shape. Experimental results from the Apollo program shows that the effective nose radius is equal to the maximum diameter divided by 1.15.

2.3.2 Heating Loads

The atmosphere and trajectories chosen for this study are described in another section of this report. Entry angles from 90° to 20° and range of M/C_DA values of from .02 to .8 slugs/ft^2 were considered. The previously described expressions for laminar, turbulent, and radiative heating were inserted into the point mass trajectory programs to develop initial heating rate data. Figures 2.3-8 to 2.3-10 show the time history of the heating rates for atmospheres W_1, W_2, and B for U_i = 25,000 fps and M/C_DA = 0.2.

The maximum laminar convective stagnation point heating rates as a function of R_n and M/C_DA for entry angles of 90° and 20°, entry velocities of 25,000 and 22,000 fps, and four different atmospheres have been presented in Figures 2.3-2 and 2.3-3. It can be seen that increasing M/C_DA an order of magnitude, increases the peak heating rate by approximately a factor of three. If the entry velocity is reduced from 25,000 to 22,000 fps, the peak heating rate is decreased

Figure 2.3-7 Typical Heating-Rate Distribution Over An Apollo-Type Capsule

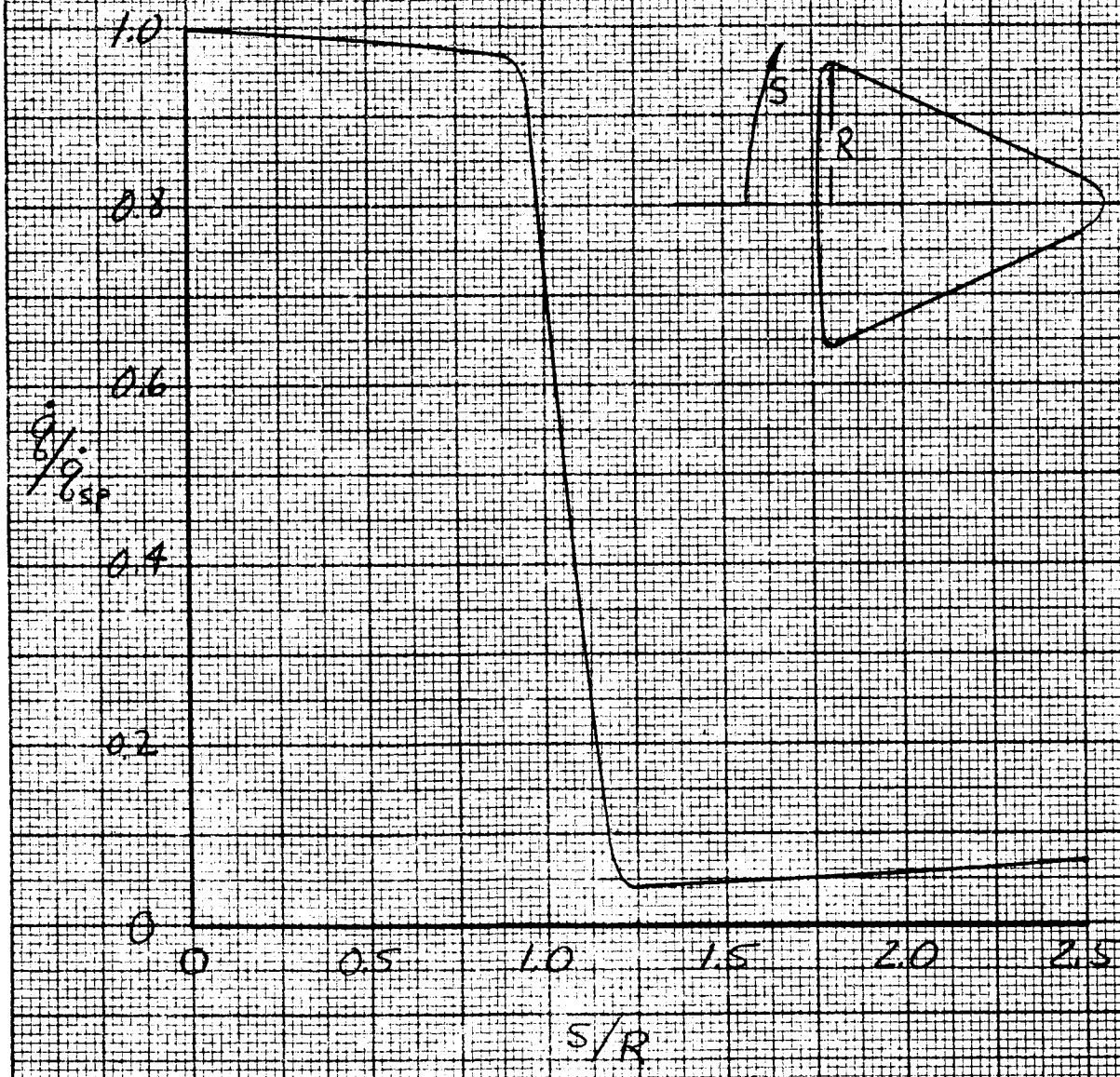

Figure 2.3-8

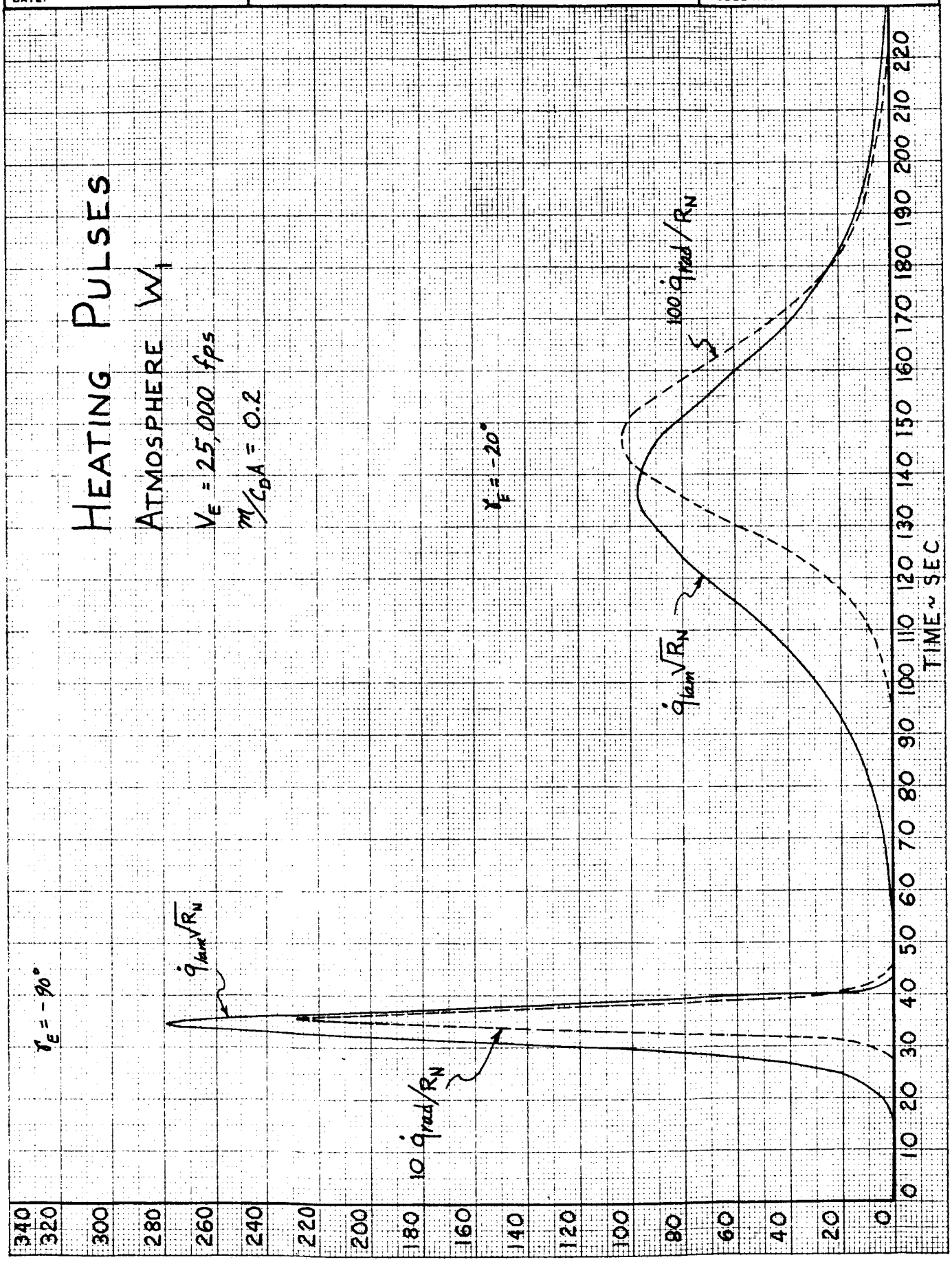
HEATING PULSES
ATMOSPHERE W1
V_E = 25,000 fps
m/C_DA = 0.2
γ_E = -90°
γ_E = -20°
$\dot{q}_{lam}\sqrt{R_N}$
$10\,\dot{q}_{rad}/R_N$
$100\,\dot{q}_{rad}/R_N$
TIME ~ SEC
0 10 20 30 40 50 60 70 80 90 100 110 120 130 140 150 160 170 180 190 200 210 220
0 20 40 60 80 100 120 140 160 180 200 220 240 260 280 300 320 340

PREPARED BY:	NORTH AMERICAN AVIATION, INC. SPACE and INFORMATION SYSTEMS DIVISION	PAGE NO. OF
CHECKED BY:		REPORT NO.
DATE:	Figure 2.3-9	MODEL NO.

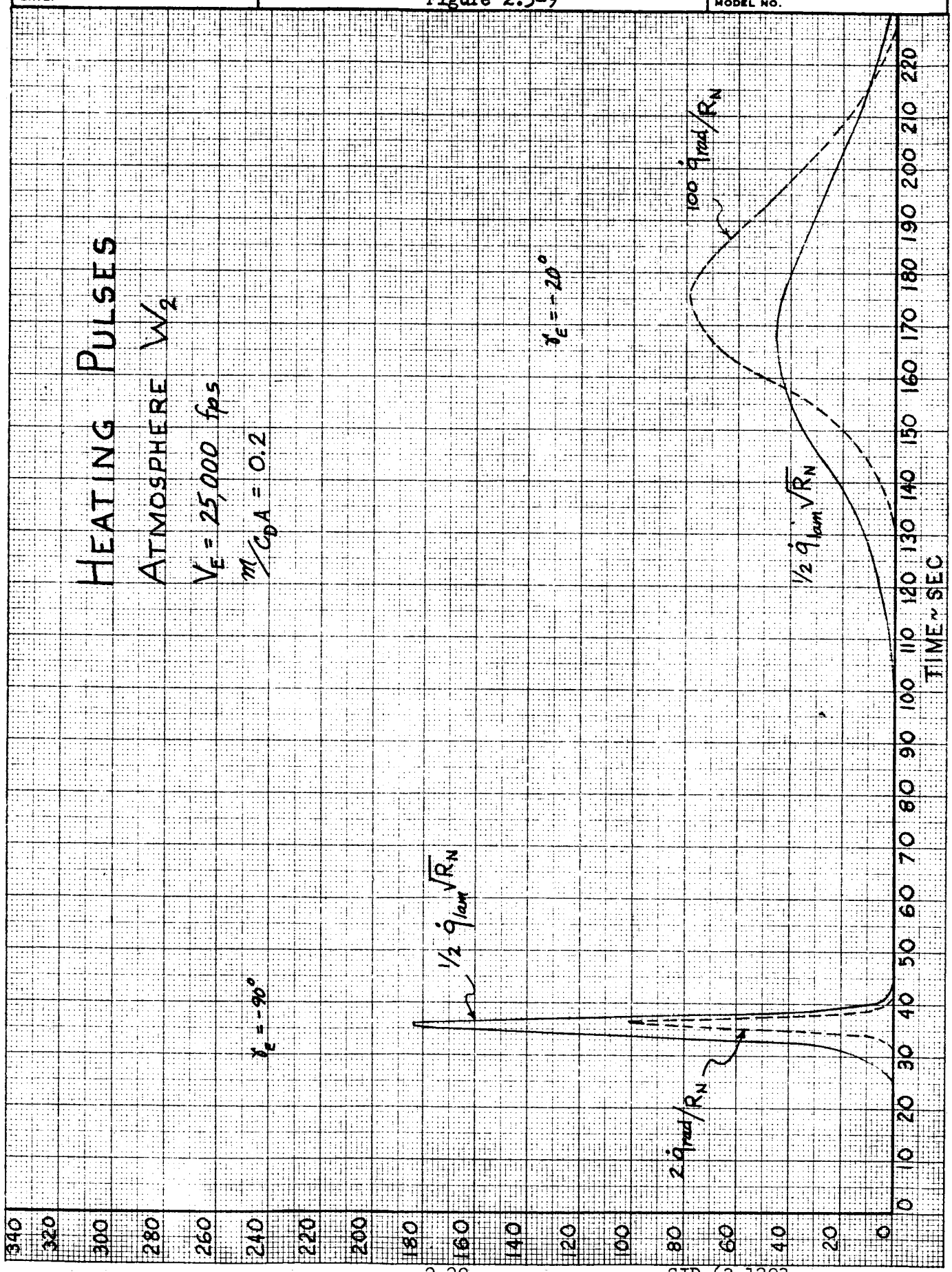

Figure 2.3-10

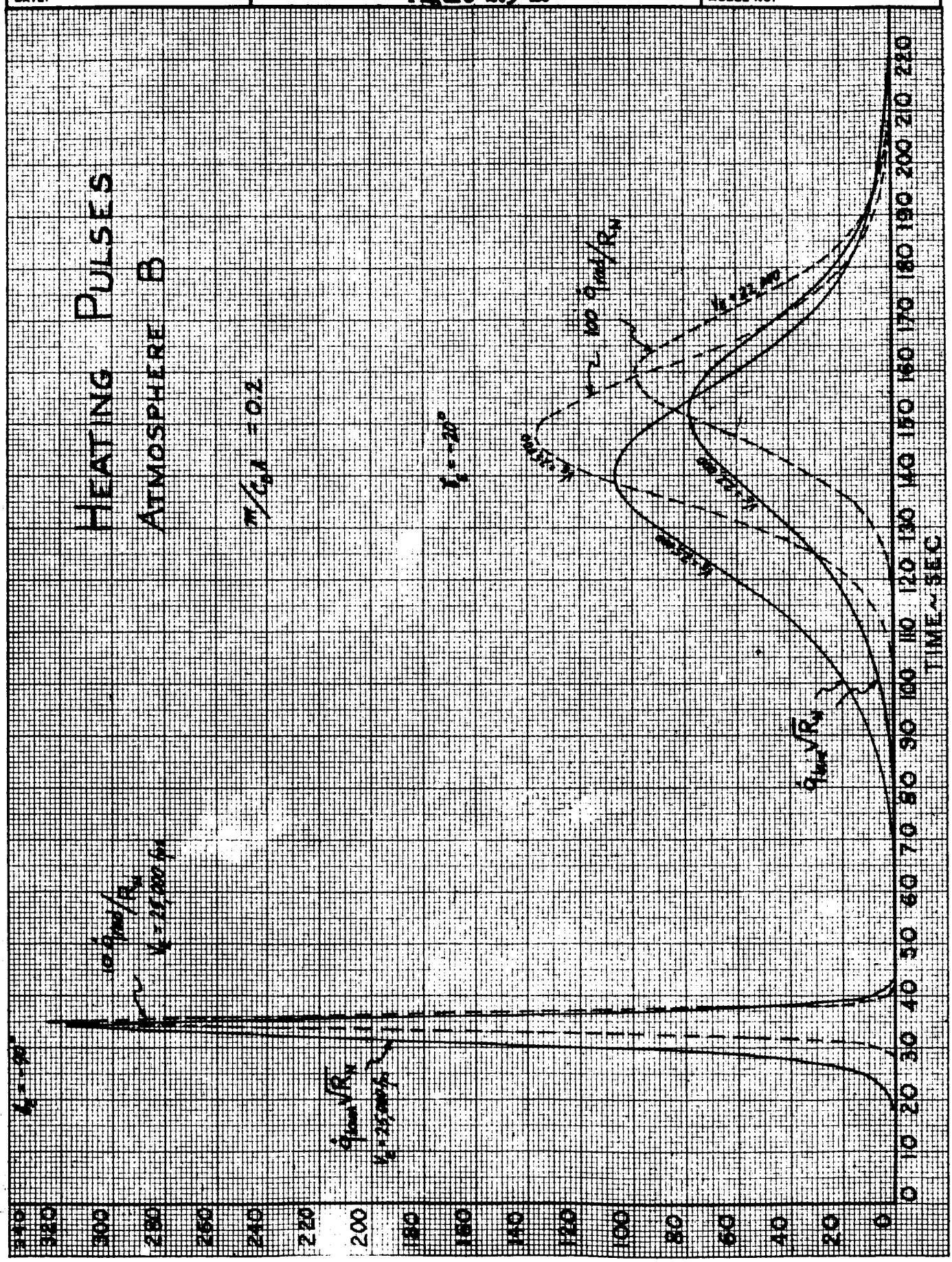
HEATING PULSES
ATMOSPHERE B
TIME ~ SEC
0 10 20 30 40 50 60 70 80 90 100 110 120 130 140 150 160 170 180 190 200 210 220
0 20 40 60 80 100 120 140 160 180 200 220 240 260 280 300 320 340

approximately 33%. The peak heating rate associated with a 20° entry is about 1/3 that for a 90° entry at the same velocity. As shown in Figures 2.3-4, 2.3-5, and 2.3-6, however, the integrated heating associated with a 20° entry is about 2½ times that for a 90° entry at the same velocity.

Figure 2.3-11 presents the peak radiative heating rates at 25,000 fps. Radiative heating rates at 22,000 fps are approximately half those encountered at 25,000 fps. The effect of the atmospheres enters only through the trajectory variables since the intensity curve fit used to obtain these heating rates was for a constant composition of 7½% CO_2 and 92½% N_2. The effect of composition is discussed in the following section. It is interesting to note again that the 20° entry results in quite small peak heating rates compared to the 90° entry.

The effect of entry angle on peak and integrated heating for an M/C_DA of 0.2 are summarized in Figures 2.3-12 and 2.3-13 for atmospheres W_2 and B. The peak laminar and radiative heating rates decrease rapidly below entry angles of -40°. As expected, the integrated laminar rates vary inversely with the peak rates whereas the integrated radiant flux increases because of the relative effective times associated with each heat transfer mode. An analytical expression is shown in the following section which describes the effect of entry angle.

Figures 2.3-4, 2.3-5, and 2.3-6 present the integrated heat loads to the stagnation point as a function of M/C_DA, entry angle, entry velocity, and atmosphere. As mentioned previously, the integrated heat load for the 20° entry is about 2½ times that for the 90° entry. Inasmuch as the heat protection system weight required is very nearly proportional to the integrated heat load for the conditions of this study, integrated heating rather than heating rate becomes the governing parameter. As indicated in Section 2.7, the 20° entry trajectory should be considered as the design case inasmuch as it results in the highest heat shield weights.

2.3.3 Effect of Uncertainties on Heating Loads

2.3.3.1 Generalized Heating Analysis

The effects of uncertainties in the Martian atmospheric environment and in the state-of-the-art methods of calculating radiative heat transfer on required heat shield weights quite properly should be the object of a full scale research effort. Only gross effects are considered here to indicate the trends to be expected and to define the region of validity of the heating data generated for the study.

The aerodynamic heating rate (convective or radiative) may be expressed in the form:

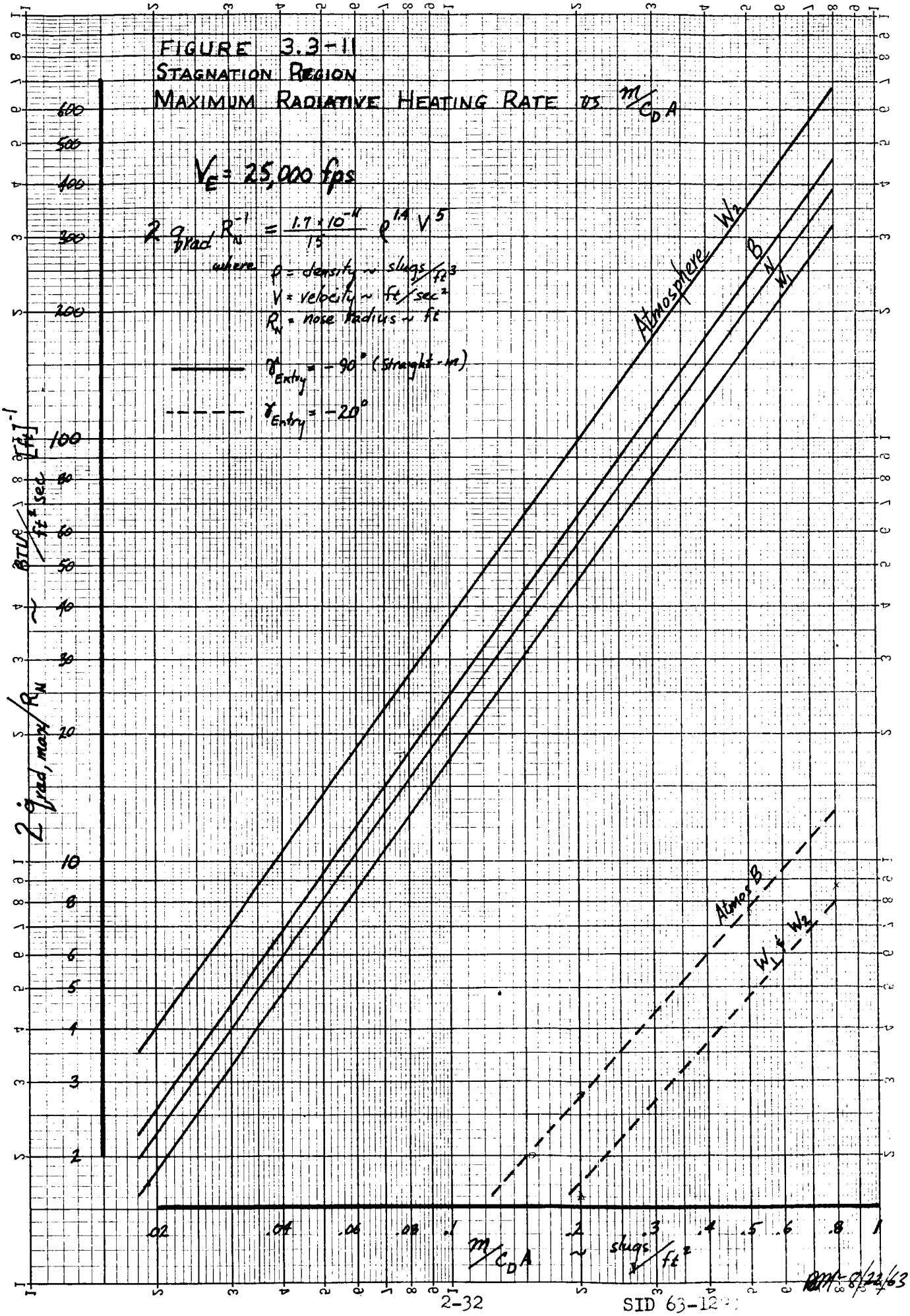
FIGURE 3.3-11
STAGNATION REGION
MAXIMUM RADIATIVE HEATING RATE VS $m/C_D A$
$V_E = 25{,}000$ fps
$2\dot{q}_{rad} R_N^{-1} = \frac{1.7 \times 10^{-4}}{15} \rho^{1.4} V^5$
where ρ = density ~ slugs/ft³
V = velocity ~ ft/sec²
R_N = nose radius ~ ft
$\gamma_{Entry} = -90°$ (Straight-in)
$\gamma_{Entry} = -20°$
Atmosphere W_2
B
N
W_1
Atmos B
W_1 & W_2
$2\dot{q}_{rad,max}/R_N$ ~ BTU/ft² sec [ft]⁻¹
$m/C_D A$ ~ slugs/ft²

RM-8/22/63

FIGURE 2.3-12

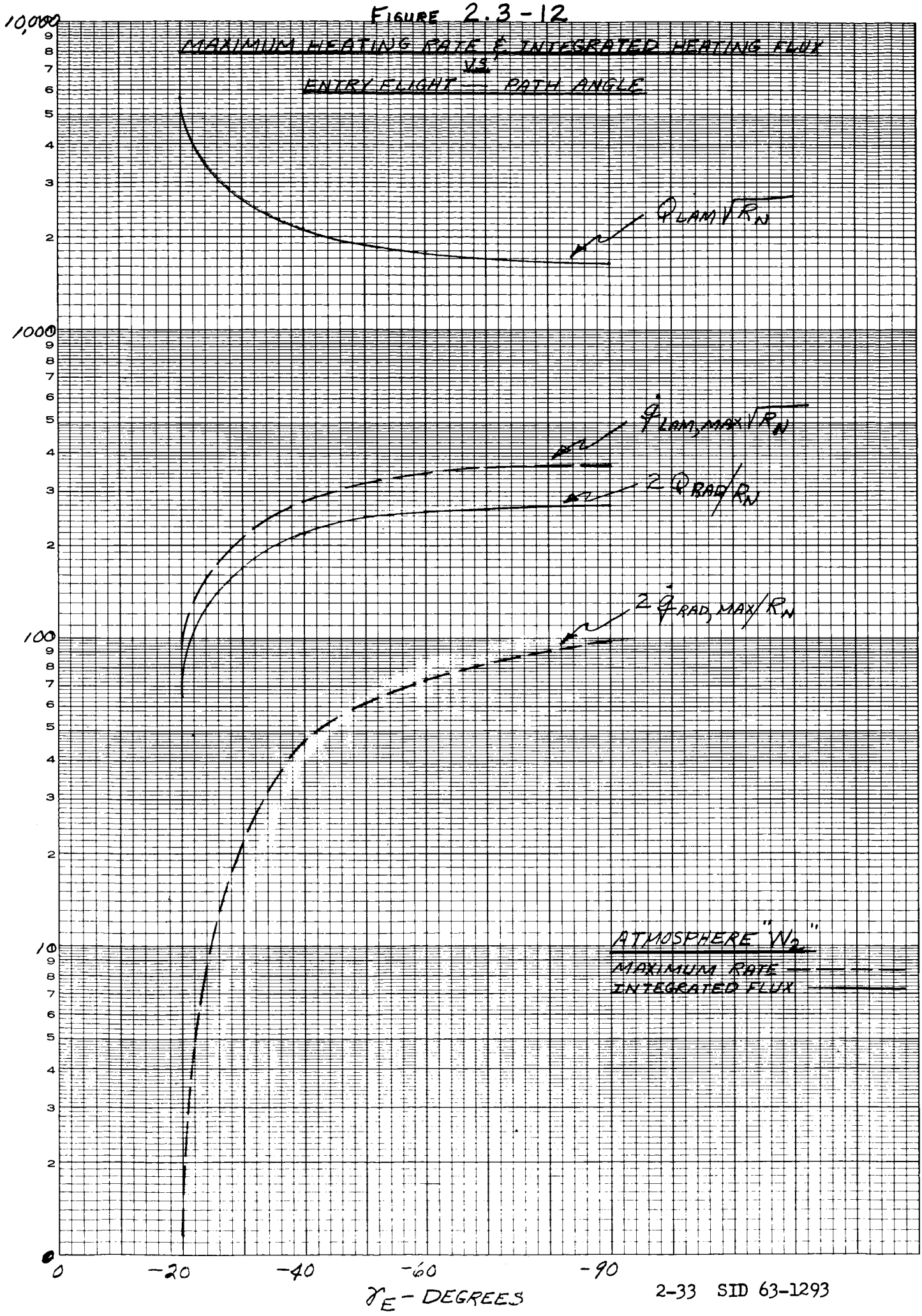
MAXIMUM HEATING RATE & INTEGRATED HEATING FLUX
VS.
ENTRY FLIGHT — PATH ANGLE
$Q_{LAM}\sqrt{R_N}$
$\dot{q}_{LAM,MAX}\sqrt{R_N}$
$2\,Q_{RAD}/R_N$
$2\,\dot{q}_{RAD,MAX}/R_N$
ATMOSPHERE "N_2"
MAXIMUM RATE
INTEGRATED FLUX
10,000
1000
100
10
0
-20
-40
-60
-90
γ_E - DEGREES

FIGURE 2.3-13

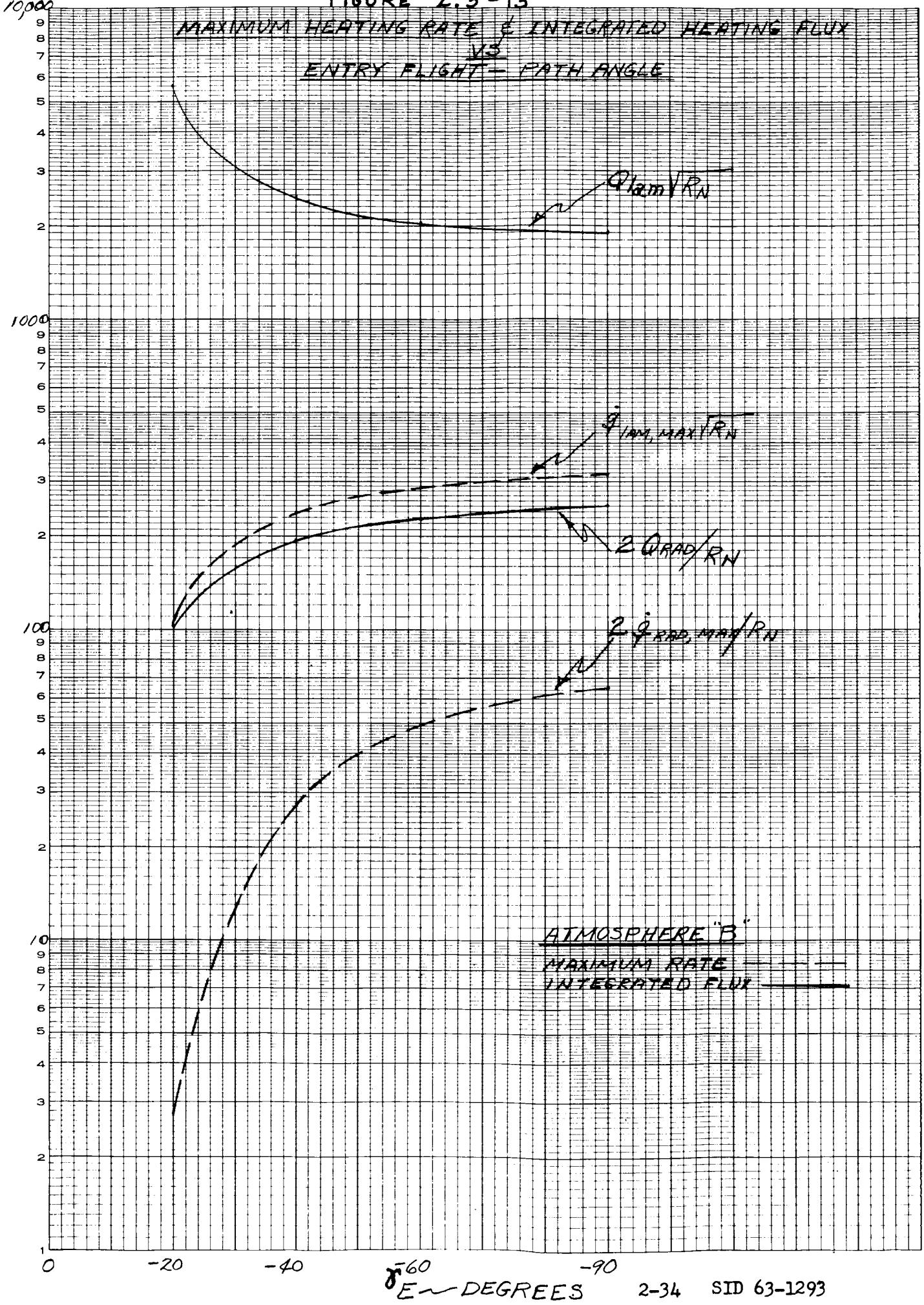
MAXIMUM HEATING RATE & INTEGRATED HEATING FLUX
VS
ENTRY FLIGHT - PATH ANGLE
$Q_{lam}\sqrt{R_N}$
$\dot{q}_{lam,max}\sqrt{R_N}$
$2\,Q_{RAD}/R_N$
$2\,\dot{q}_{RAD,max}/R_N$
ATMOSPHERE "B"
MAXIMUM RATE
INTEGRATED FLUX
10,000
1000
100
10
1
0
-20
-40
-60
-90
γ_E ~ DEGREES

$$(9) \quad \dot{q} = \frac{K \ \rho_\infty^j \ U_\infty^n}{L^m}$$

where K, j, and n depend on the type of heating considered and L is a characteristic length of the body, such as nose radius. Table 2.3-1 lists the values of the parameters in Equation (8) for the modes of heating considered in this study. It is to be noted that in Equation (8), it is assumed that the recovery enthalpy is much greater than the wall enthalpy.

TABLE 2.3-1

VALUES OF HEATING PARAMETERS

TYPE OF HEATING	K	j	n	L	m
Convective Stagnation Point (Equation 5)	3.37×10^{-9}	.50	3.19	R_{nose}	.50
Radiative Stagnation Point (Equation 7)	5.67×10^{-13}	1.4	5.0	R_{nose}	-1.0

The total heat transfer to a unit area of the body during an entry trajectory is given by:

$$(10) \quad Q = \int_o^t \dot{q} \, dt \text{ or } \int_v^{v_f} \dot{q} \left(\frac{dt}{du}\right) du$$

The drag equation for ballistic entry is simply:

$$(11) \quad D/W = -\dot{V}/g \qquad \text{or}$$

$$\frac{C_D \ A \ \rho_\infty U_\infty^{\ 2}}{2W} = -1/g \ \frac{du}{dt}$$

Since the entry angle does not change significantly over the critical portion of the trajectory,

$$\frac{-du}{dt} = -\sin \gamma_i \ \frac{d(u^2/2)}{dh}$$

Substituting into (11) using the hydrostatic equation gives:

$$\frac{C_D A}{M \sin \gamma_i} \frac{dP}{g} = \frac{d\,(U_\infty^2/2)}{U_\infty^2/2}$$

Integrating and recognizing that P_i is much smaller than the pressure at maximum heating yields:

$$(12) \quad \frac{C_D A}{M \sin \gamma_i} \frac{P}{g} = \frac{U_\infty^2}{U_i^2}$$

Assuming an isothermal atmosphere this becomes:

$$(13) \quad \frac{C_D A}{M \sin \gamma_i} \rho_\infty = \ln \frac{U_\infty^2}{U_i^2} \quad \text{or} \quad \frac{\rho_\infty}{\beta \Delta \sin_i} = \ln \frac{U_\infty^2}{U_i^2}$$

Now substituting (9), (11), and (13) into (10), there results:

$$(14) \quad Q = \frac{-2kU_i^{n-1}(-\beta \sin \gamma_i)^{j-1} \Delta^j}{L^m} \int^{U_f/U_i} \left(\frac{U_\infty}{U_i}\right)^{n-2} \left(-\ln \frac{U_\infty^2}{U_i^2}\right)^{j-1} d(U_\infty/U_i)$$

This expression shows how the integrated heat load varies with the ballistic coefficient, Δ, the inverse scale height, β, and the characteristic length, L. In the analyses that follow, this expression is used to assess the effects of various uncertainties associated with the Martian atmosphere and radiant heating state-of-the-art.

Another interesting result that can be obtained utilizing the above analysis, is an analytical expression for the ratio of radiative to convective heating. Using the coefficients given in Table 2.3-1, the integral in equation (6) can be solved to obtain:

$$\int_0^\infty \left(\frac{2}{n-1}\right)^j \eta^{2j-1} e^{-\eta^2} \begin{cases} = .847 \text{ for convection} \\ = .168 \text{ for radiation} \end{cases}$$

Forming the ratio of radiative to convective heating

$$\frac{Q_{rad}}{Q_{conv}} = \frac{1.92 \times 10^3}{3.08} \frac{(U_i/10^4)^4 (-\beta \sin \gamma_i)^{0.4} (M/C_D A)^{1.4} R_n}{(U_i/10^4)^{2.19} (-\beta \sin \gamma_i)^{-0.5} (M/C_D A)^{0.5} R_n^{-0.5}}$$

or

$$(15)\quad \frac{Qrad}{Qconv} = 6.24\text{x}10^2 \left(\frac{U_i}{10^4}\right)^{1.81} \left(\frac{M}{C_D A}\right)^{0.9} R_n^{1.5} \left(-\beta \sin \gamma_i\right)^{0.9}$$

Equation (15) gives the ratio of radiative to convective heating as a function of β, $M/C_D A$, U_i, γ_i, and R_n.

2.3.3.2 Results of Analysis

Radiative heating, by its very nature, depends quite strongly on the composition of the atmosphere considered. In addition, the atmospheric density and entry velocity are quite important, as indicated in the previous section. Figure 2.3-14 shows the effect on heat shield weight of changing the composition from $7\frac{1}{2}$ % CO_2 and $91\frac{1}{2}$% N_2 to various other combinations for two entry trajectories, both having initial velocities of 25,000 fps and ballistic parameters of 0.2 slugs/ft^2. The entry angles considered were 20° and 90°, and each curve was normalized to the corresponding heat shield weight at $7\frac{1}{2}$% CO_2. It is to be noted that the peaks on the curves occur at a CO_2 concentration of about 15%. The probable CO_2 concentration in the Martian atmosphere ranges from about 5% to 65% CO_2 by volume. As can be seen from the figure, this range of compositions can result in extremely large changes in required heat shield weights. Figure 2.3-14 shows that the heat shield weight for the 90° trajectory is more strongly affected by changes in the CO_2 concentration than the 20° trajectory. However, since the overall heat load is higher for the 20° entry trajectory, the vehicle is designed for this case, and the resulting uncertainty in heat shield weight ranges from about +5% (at 15% CO_2) to -30% (at 65% CO_2).

The data shown on Figure 2.3-14 were obtained using intensity data given by Spiegel (Reference 1) and James (Reference 2). These two sets of data agree fairly well; however, a fairly large uncertainty exists as to the absolute values obtained by both James and Spiegel.

Figures 2.3-15 and 2.3-16 indicate the effect of uncertainties in the intensities on required heat shield weight, as a function of nose radius, for the two trajectories considered. Spiegel's intensity values were used as the reference values. The range of intensities shown, +50% and -33%, were arbitrarily chosen to indicate the sensitivity of heat shield weight to intensity uncertainties. As shown on Figures 2.3-15 and 2.3-16, the effect of intensity uncertainties is magnified as the nose radius is increased. This is because the radiative heating varies directly as the nose radius, while the convective heating varies inversely as the square root of the nose radius

PREPARED BY: EMR	NORTH AMERICAN AVIATION, INC. SPACE and INFORMATION SYSTEMS DIVISION	PAGE NO. OF
CHECKED BY:		REPORT NO. FS/63-327
DATE: 25 Sept 63	Figure 2.3-14	MODEL NO. 2.3-14

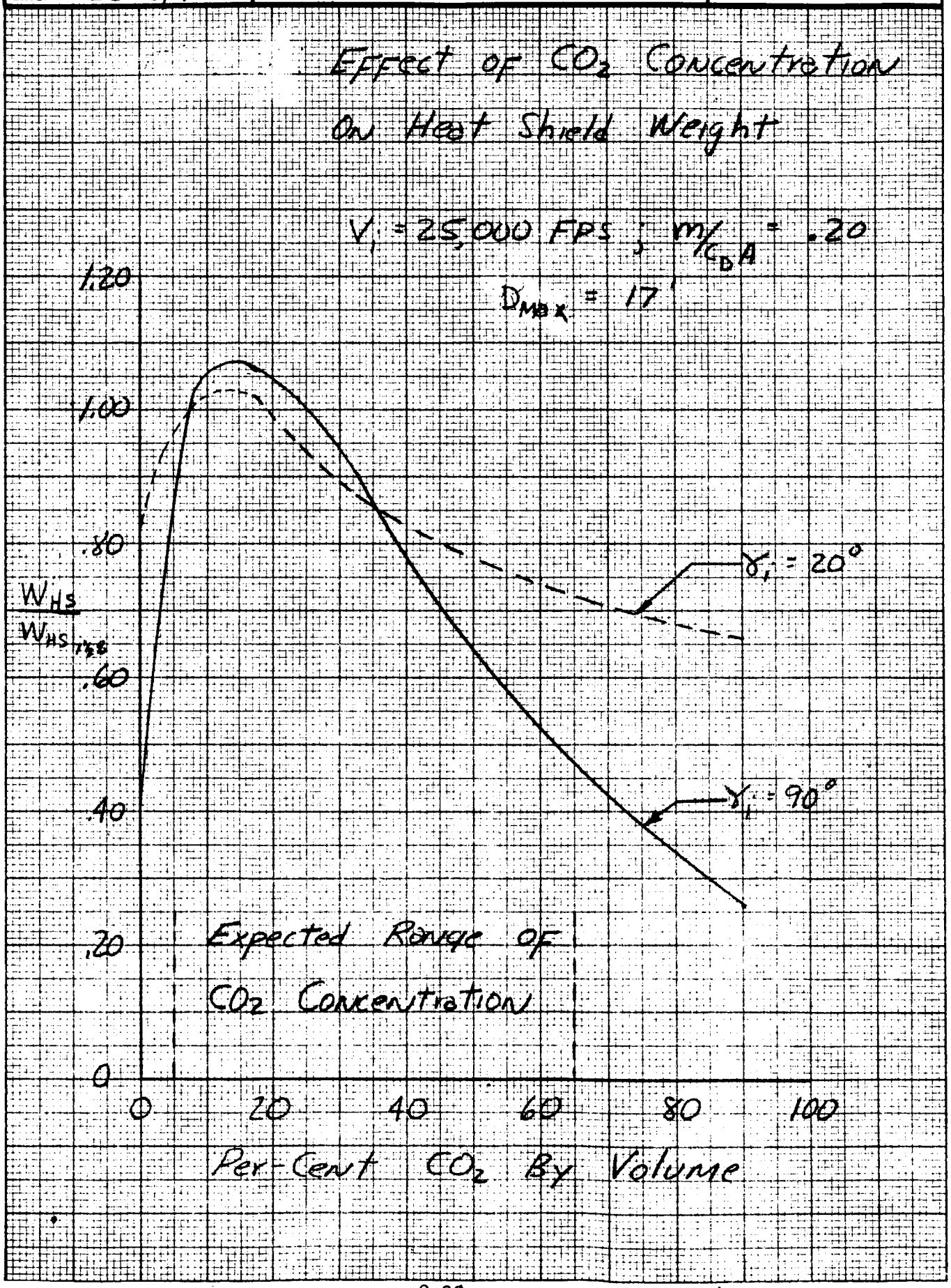

FORM M-113-N REV. 5-61

PREPARED BY: EMR	NORTH AMERICAN AVIATION, INC. SPACE and INFORMATION SYSTEMS DIVISION	PAGE NO. OF
CHECKED BY:		REPORT NO. FS/63-327
DATE: 25 Sept 63	Figure 2.3-15	MODEL NO. 2.3-15

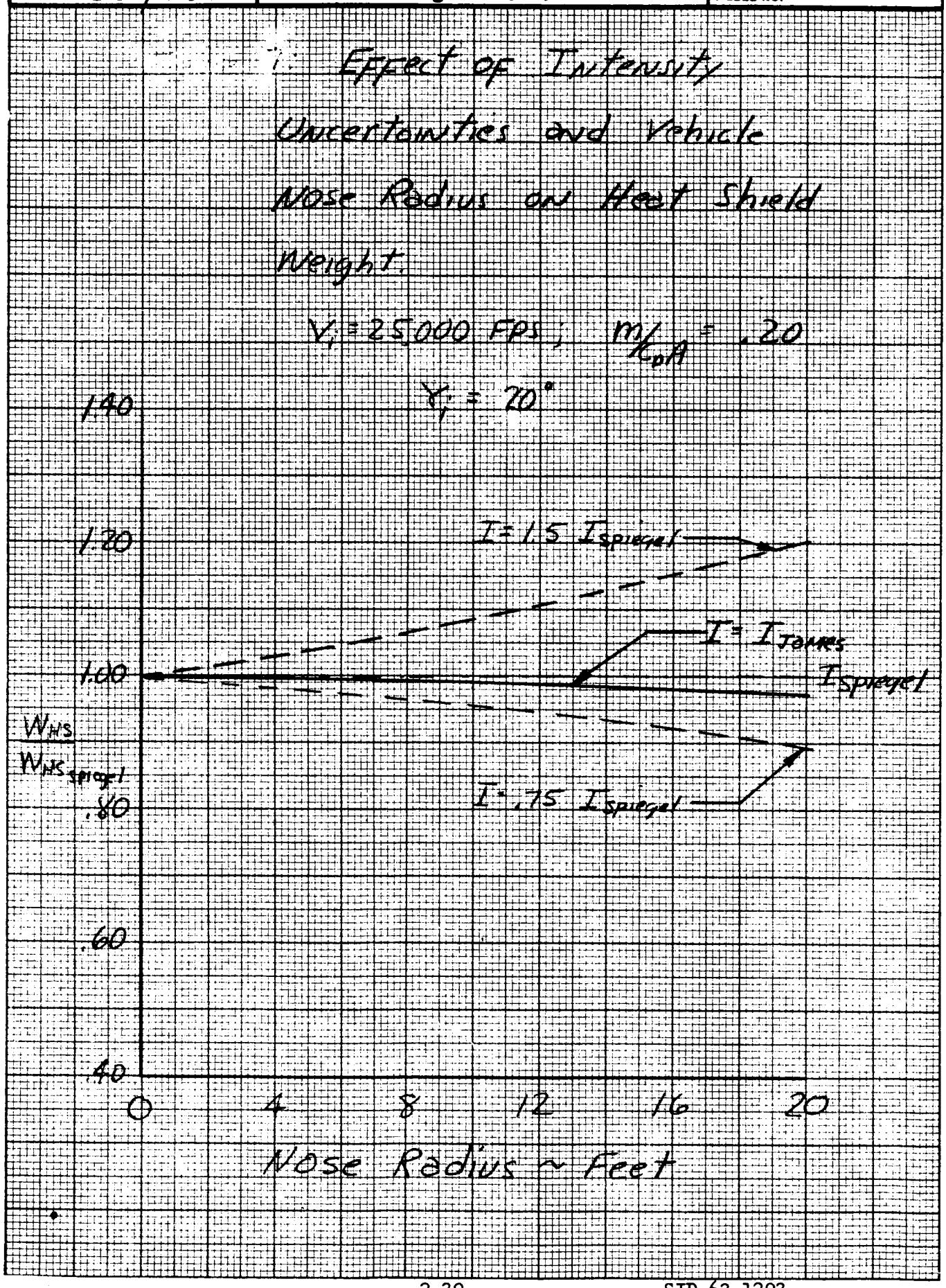

Figure 2-3-16

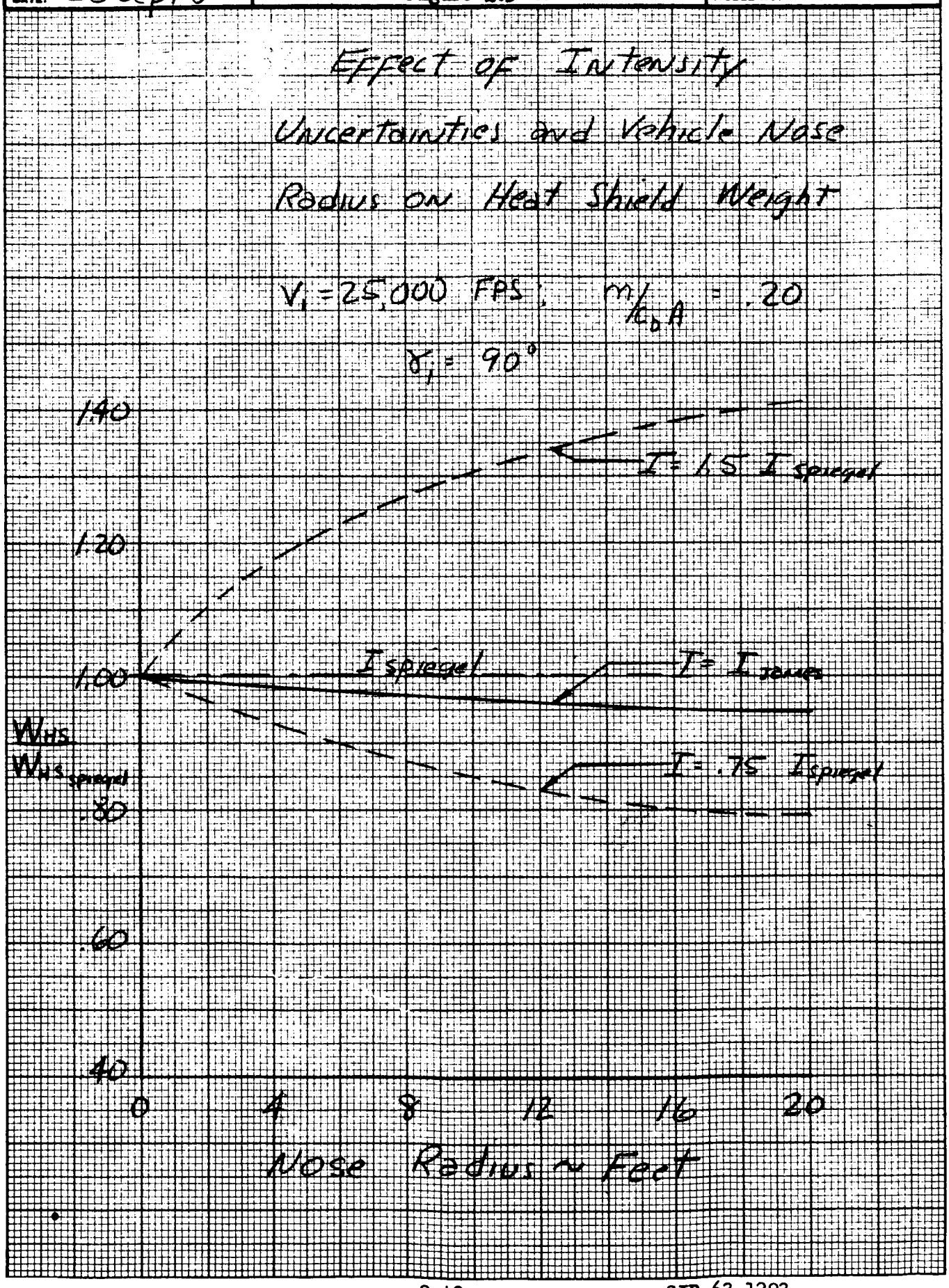
Effect of Intensity Uncertainties and Vehicle Nose Radius on Heat Shield Weight
$V_i = 25{,}000$ FPS ; $m/C_D A = .20$
$\gamma_i = 90°$
1.40
1.20
1.00
.80
.60
.40
$I = 1.5\ I_{spiegel}$
$I_{spiegel}$
$I = I_{James}$
$I = .75\ I_{spiegel}$
$W_{HS} / W_{HS\ spiegel}$
0
4
8
12
16
20
Nose Radius ~ Feet

(see Section 2.3.2.1). The effect of intensity uncertainties is seen to be greater for the 90° trajectory than for the 20° trajectory, since the vehicle travels at lower altitudes for the 90° case.

Figures 2.3-17 and 2.3-18 present the effect of uncertianties in the inverse scale height β, on the required heat shield weights, again for both 20° and 90° entry trajectories. The effect is determined directly from Equation (6) of Section 2.3.2.1. Four atmospheres were considered in the analysis (W_1, W_2, N, and B). The nominal atmosphere, N, was chosen as the reference point. In these calculations, the value of β above the tropopause was used because maximum heating occurs at altitudes well above the tropopause. Two nose radii were considered for each trajectory, corresponding to capsule diameters of 17 ft. and 6.75 ft. For the 20° trajectory, changing β from one extreme to the other (W_1 to W_2) causes heat-shield weight changes of from +2 to -6% for the 17 ft. vehicle, while changes of from +6 to -14% are incurred by the smaller vehicle. For the 90° trajectory, the effect of vehicle size is different for the larger vehicle. From Figure 2.3-18, it is seen that the larger vehicle undergoes changes from -4 to +11%, while the smaller vehicle undergoes changes from +1 to -10% as the scale height is changed from the W_1 to W_2 value. The influence of vehicle size on the effects of β reflects both the different effects of β on radiative and convective heating, and the magnitude of the ratio of convective to radiant heating. Again, since the 20° trajectory is the design case, the 90° trajectory serves only to illustrate the influence of entry angle. Unless very large increases are indicated for the 90° entry trajectory, the sensitivity of the design heat shield weight to each uncertainty considered is illustrated by the 20° entry angle curves.

2.3.4 References

1. Hoshizaki, H., Heat Transfer in Planetary Atmospheres at Super-Satellite Speeds, ARS Journal, Vol. 32, No. 10, October 1962.

2. Hansen, C. F., Approximations for the Thermodynamic and Transport Properties of High Temperature Air, NASA TR R-50, 1959

3. Li, T. Y. and R. E. Geiger, Stagnation Point of a Blunt Body in Hypersonic Flow, IAS Journal, Vol. 24, No. 1, January 1957

4. Experimental Heat-Transfer and Pressure Distribution Over Entry Configurations of .02 Scale Apollo Models at Zero Angle of Attack, SID 63-623, June 1963 (Confidential)

5. Spiegel, J. M., et al Aerothermodynamics of Planetary Entry, Jet Propulsion Laboratory, SPS 37-22, Vol. IV, Section 354

6. Private Communication: J. M. Spiegel, Jet Propulsion Laboratory.

7. Private Communication: G. M. Hanley, S&ID

Figure 2.3-17

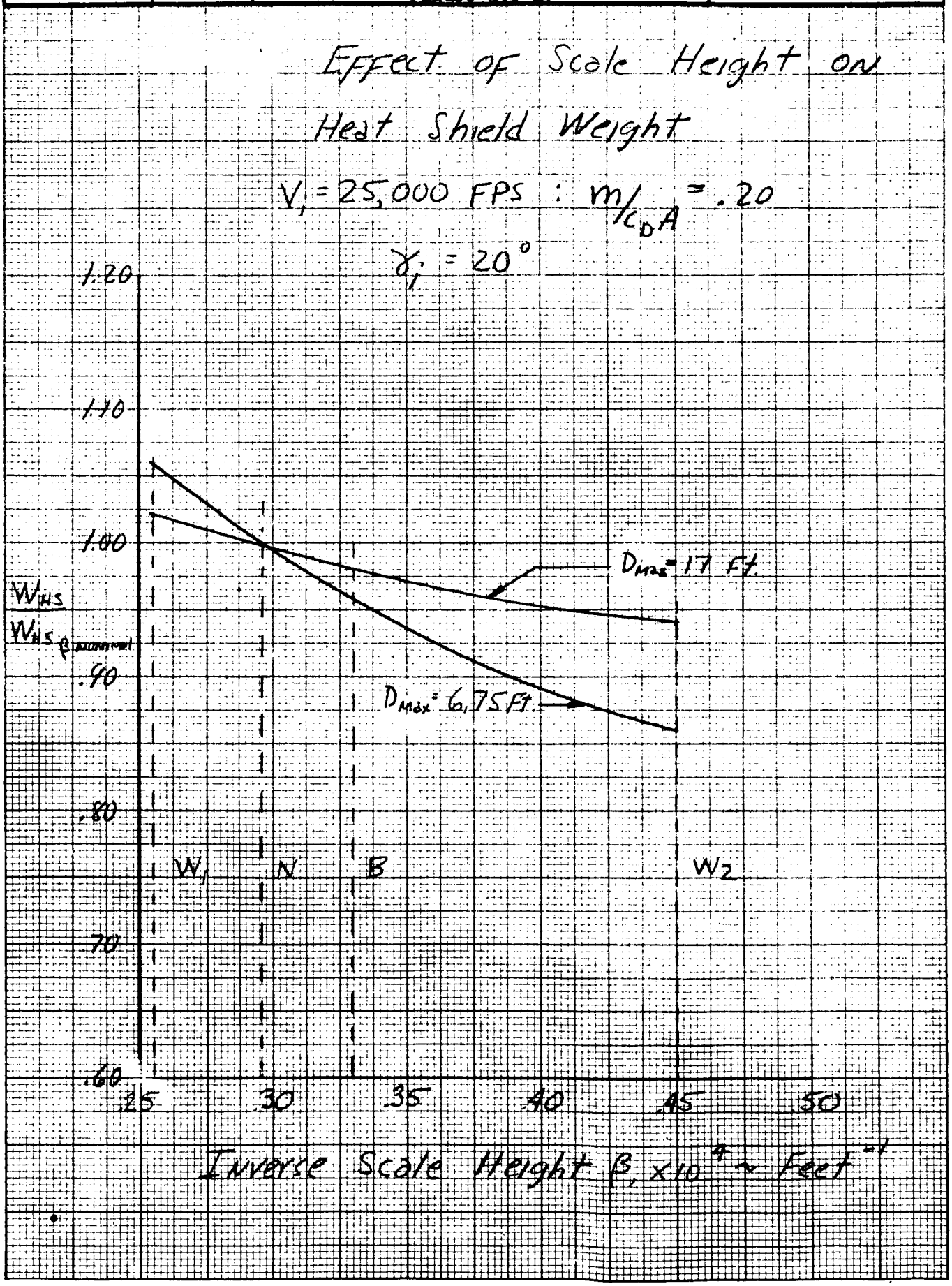
Effect of Scale Height on
Heat Shield Weight
$V_1 = 25{,}000$ FPS : $m/C_DA = .20$
$\gamma_1 = 20°$
1.20
1.10
1.00
.90
.80
.70
.60
W_{HS}
$W_{HS_{\beta\,nominal}}$
$D_{Max} = 17$ Ft
$D_{Max} = 6.75$ Ft
W_1
N
B
W_2
.25
.30
.35
.40
.45
.50
Inverse Scale Height β, $\times 10^4$ ~ Feet^{-1}

PREPARED BY: EMR	NORTH AMERICAN AVIATION, INC. SPACE and INFORMATION SYSTEMS DIVISION	PAGE NO. OF
CHECKED BY:		REPORT NO. FS/63-327
DATE: 26 Sept 63	Figure 2.3-18	MODEL NO. 2-3-18

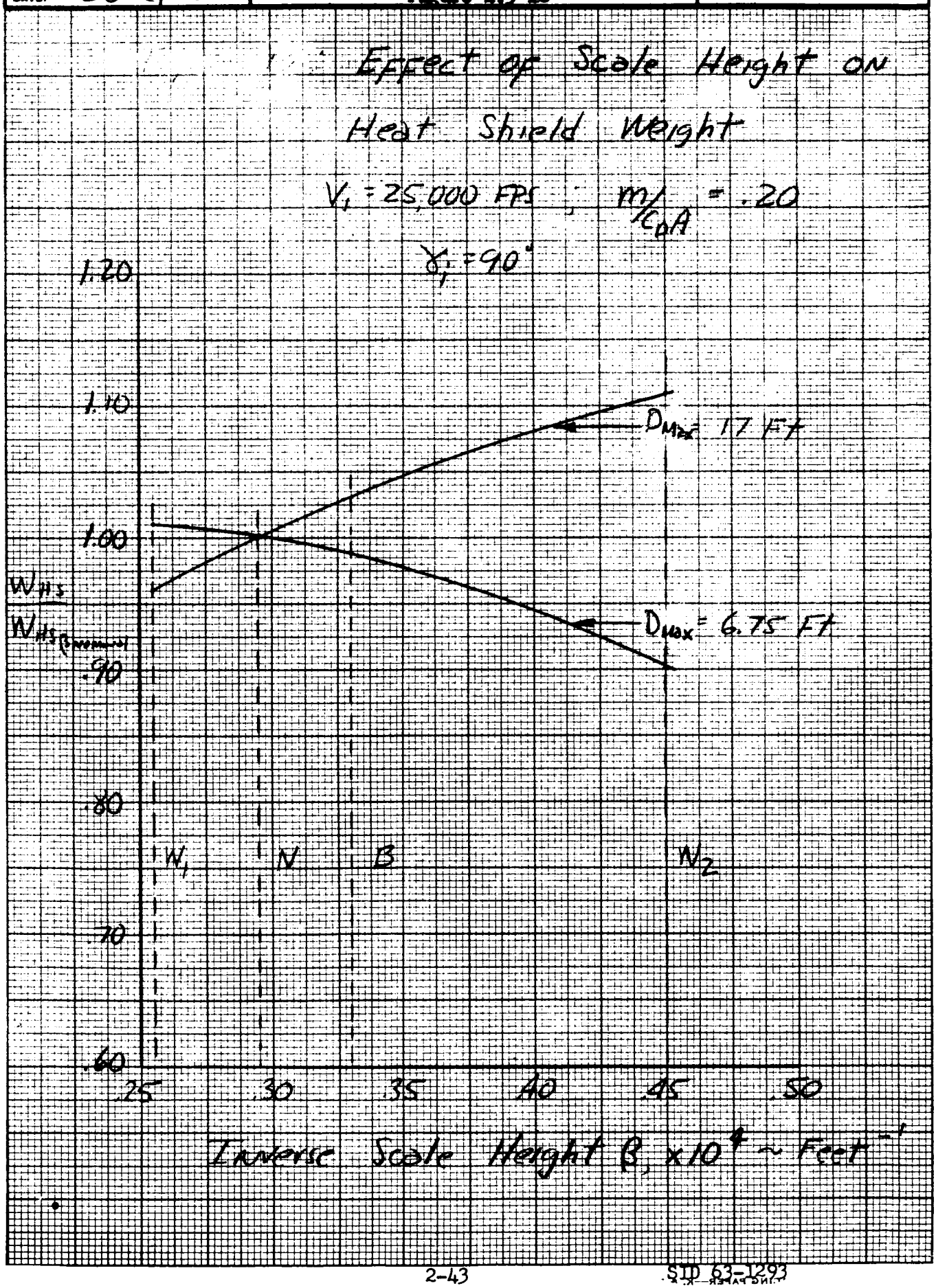

8. Kivel, B and K. Bailey, Tables of Radiation from High Temperature Air, Avco-Everett Research Lab., Rep. 121, December 1957.

9. Meyerott, R. E., J. Sokoloff and R. W. Nicholls, Absorption Coefficients of Air, Geophysical Research Papers No. 68, July 1960.

10. James, C. S., Experimental Studies of Radiative Transport from Hot Gases Simulating in Composition the Atmospheres of Mars and Venus, AIAA Preprint 63-455, August 1963.

2.3.5 Nomenclature

M - Mass, Slugs

C_D - Drag Coefficient

A - Reference Area, $\frac{D_{Max}^2}{4}$, Ft^2

D_{Max} - Maximum Vehicle Diameter, Feet

R_n - Nose Radius, Feet

I - Intensity

$\dot{q}$ - Heating Rate

Q - Integrated Heat Load

U - Velocity, Ft/Sec

T - Temperature, °R

h - Static Enthalpy, $\frac{BTU}{Lb}$; Altitude, Feet

K - Constant

g - Acceleration Due to Gravity, Ft/Sec^2

P - Pressure, PSF

γ - Flight Path Angle, Degrees

β - Inverse Scale Height, Ft^{-1}

ρ - Density, $Slugs/Ft^3$

Subscripts

CS - Convective, Stagnation Point

CT - Convective, Turbulent

Rad. - Radiative

i - Initial

f - Final

S.P. - Stagnation Point

∞ - Free-Stream

W - Wall

2.4 MATERIALS CONSIDERATIONS AND CONSTRAINTS

The following section discusses the materials considerations and constraints imposed by the sterilization requirements, the effects of the space environment, and, finally, the materials considered to satisfy the requirements imposed by entry (e.g., heating, loads, impact, etc.).

2.4.1 Sterilization Requirements

Materials compatibility with a requirement for sterilization is perhaps the first constraint which should be considered in a survey of suitable spacecraft materials. The compatibility of the various candidate materials with various sterilization processes are dependent upon their inherent properties.

Several methods, either singly or combined, may be used for sterilization of the spacecraft. Dry heat, gas (ethylene oxide), and X- or gamma-radiation are being considered. Dependent on the materials and assemblies, any one method, or combination of methods may be advisable.

The method considered for sterilizing the entry capsule was confined to dry heat (e.g., nitrogen) at 145°C (= 300°F) through three, 36 hour cycles. Inasmuch as the scope of this study was limited to the heat shield, structure and landing systems, no concern was given to sterilizing the total entry system, i.e., capsule and payload. It should be noted, however, that if the electronic payload assembly cannot withstand the dry heat sterilization cycle assumed for the "vehicle subsystems", sterilization might have to be violated when the payload and vehicle are mated and the entire system then re-sterilized in some compatible manner. This latter phase sterilization was not considered in this study.

With regard to the sterilization compatibility of the materials considered for the recommended designs discussed in Section 3.0, they are as follows:

(1) Heat Shield Material: 91-LD phenolic glass laminate This material can withstand with little effect upon material properties, the 300 F for 106 hours required by dry heat sterilization (see Figure 2.4-1).

(2) Shell Structure Materials: Honeycomb structure consisting of HT-424 epoxy-phenolic adhesive - aluminum skin - aluminum core

(a) Aluminum used for skin and core: aluminum foil, Al 5052 or similar, will not be affected by heat treatment of 300F.

(b) HT424 Epoxy-phenolic adhesive. Withstands temperatures up to 500F. Strength reduced from 2500 to 1800 psi when heated to 300F. Strength is regained almost completely after cooling.

(3) Erection Shield Materials: Honeycomb structure consisting of phenolic glass core, phenolic glass laminate skin, and high temperature epoxy adhesive. (An adhesive of nitrile phenolic is the alternate choice).

(a) The phenolic-glass facings of the honeycomb structure will not be significantly affected as shown in Figure 2.4-1.

(b) The phenolic-glass honeycomb core is basically made from the same type of phenolic resin and glass fiber material as those discussed for the heat shield (see also Figure 2.4-2) and can withstand the effects of dry heat sterilization.

(c) High temperature resistant epoxies (NOVALAC epoxy, curer with an anhydride curing agent) or a nitrile phenolic adhesive: these materials are suggested for their radio-transparency and ability to withstand high temperature for prolonged periods.

It should be noted that the data and curves showing behavior of plastics under prolonged heating apply to heating in air. The deterioration of the plastics is partially caused by the oxidizing atmosphere; therefore, it can be assumed that less deterioration will be encountered in nitrogen. The data supplied may therefore be conservative.

(4) Parachute and Drogue Chute Material: HT-1 nylon (NOMEX) This high temperature yarn, a DuPont development, will withstand temperatures up to 500F. Test data for exposure up to 24 hours by the Fibrous Metals Branch of ASD are shown in Figure 2.4-3. The data indicate a slight increase in strength after 24 hours exposure at elevated temperature of 400F and re-cooling. NOMEX yarn is degraded by the presence of water vapor at elevated temperatures and has reportedly lost 70% of its tenacity after 1000 hours at 300F. Damage could result to chute and lines which are packaged in containers which will not allow the moisture given off by the nylon to escape during the dry heat sterilization cycle.

FIGURE 2.4-1

THE EFFECT OF ELEVATED TEMPERATURE AGING UPON PHENOLIC-GLASS LAMINATE

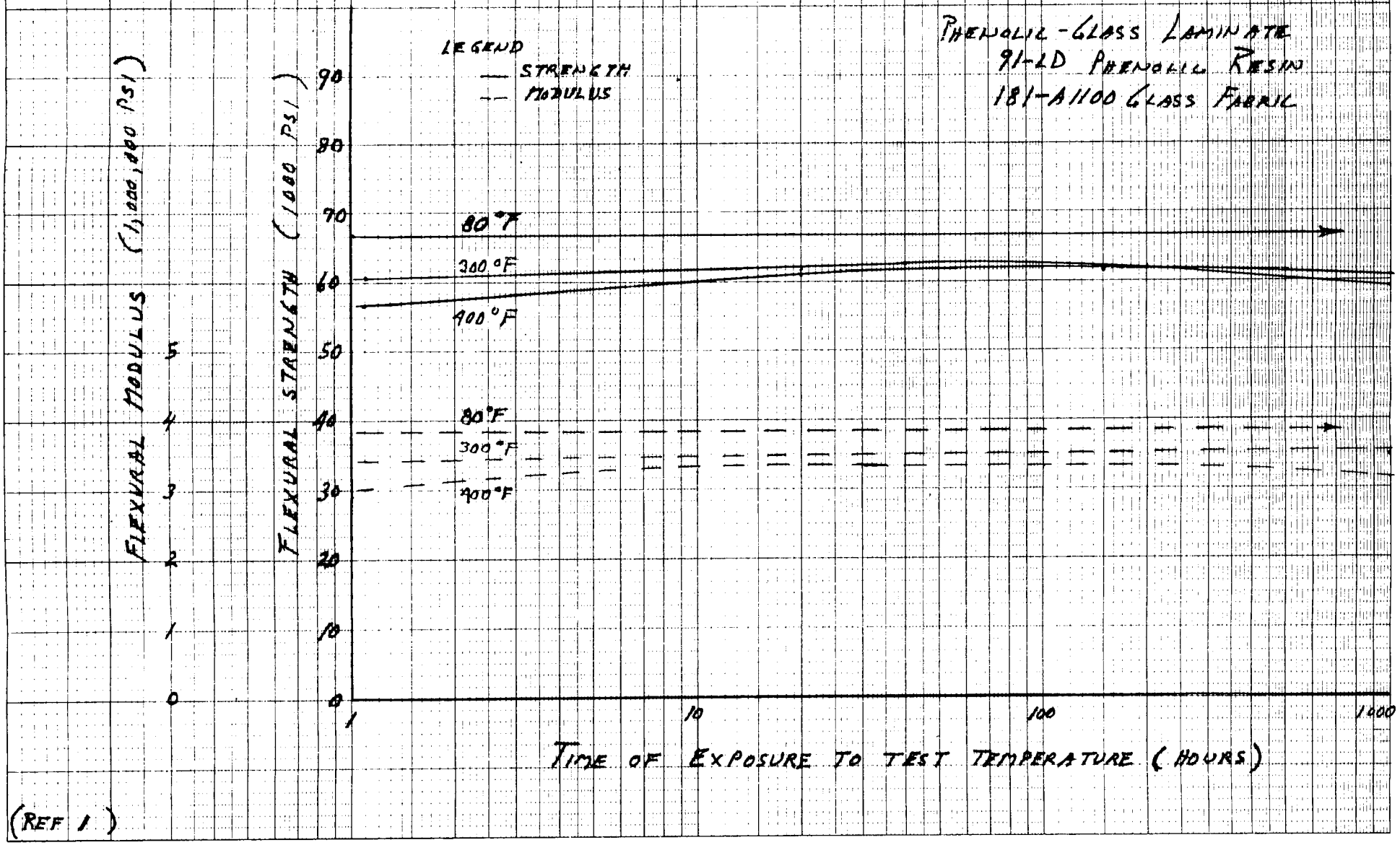

(REF 1)

(b) HT424 Epoxy-phenolic adhesive. Withstands temperatures up to 500F. Strength reduced from 2500 to 1800 psi when heated to 300F. Strength is regained almost completely after cooling.

(3) Erection Shield Materials: Honeycomb structure consisting of phenolic glass core, phenolic glass laminate skin, and high temperature epoxy adhesive. (An adhesive of nitrile phenolic is the alternate choice).

(a) The phenolic-glass facings of the honeycomb structure will not be significantly affected as shown in Figure 2.4-1.

(b) The phenolic-glass honeycomb core is basically made from the same type of phenolic resin and glass fiber material as those discussed for the heat shield (see also Figure 2.4-2) and can withstand the effects of dry heat sterilization.

(c) High temperature resistant epoxies (NOVALAC epoxy, curer with an anhydride curing agent) or a nitrile phenolic adhesive: these materials are suggested for their radio-transparency and ability to withstand high temperature for prolonged periods.

It should be noted that the data and curves showing behavior of plastics under prolonged heating apply to heating in air. The deterioration of the plastics is partially caused by the oxidizing atmosphere; therefore, it can be assumed that less deterioration will be encountered in nitrogen. The data supplied may therefore be conservative.

(4) Parachute and Drogue Chute Material: HT-1 nylon (NOMEX) This high temperature yarn, a DuPont development, will withstand temperatures up to 500F. Test data for exposure up to 24 hours by the Fibrous Metals Branch of ASD are shown in Figure 2.4-3. The data indicate a slight increase in strength after 24 hours exposure at elevated temperature of 400F and re-cooling. NOMEX yarn is degraded by the presence of water vapor at elevated temperatures and has reportedly lost 70% of its tenacity after 1000 hours at 300F. Damage could result to chute and lines which are packaged in containers which will not allow the moisture given off by the nylon to escape during the dry heat sterilization cycle.

FIGURE 2.4-1

THE EFFECT OF ELEVATED TEMPERATURE AGING UPON PHENOLIC-GLASS LAMINATE

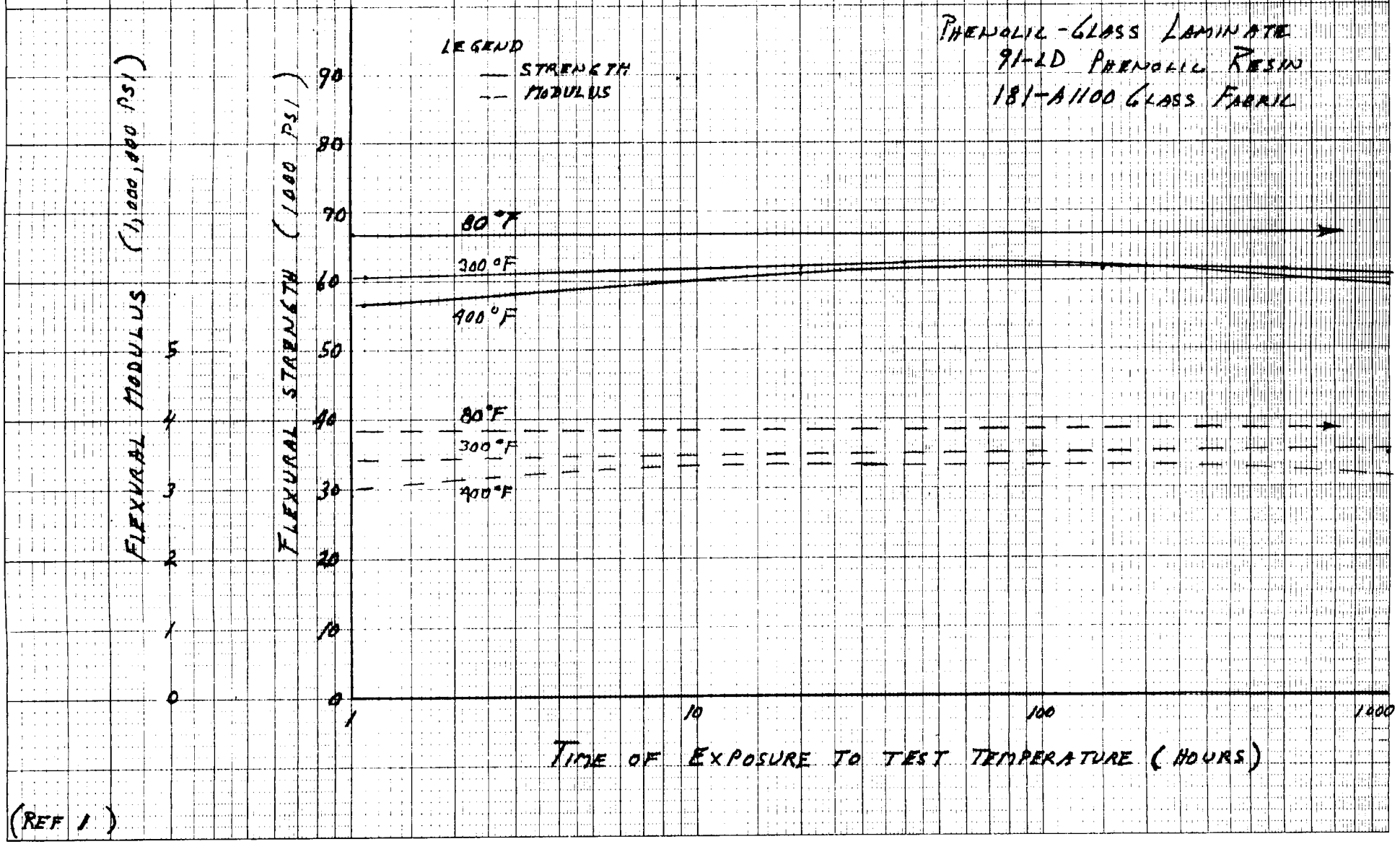

(REF 1)

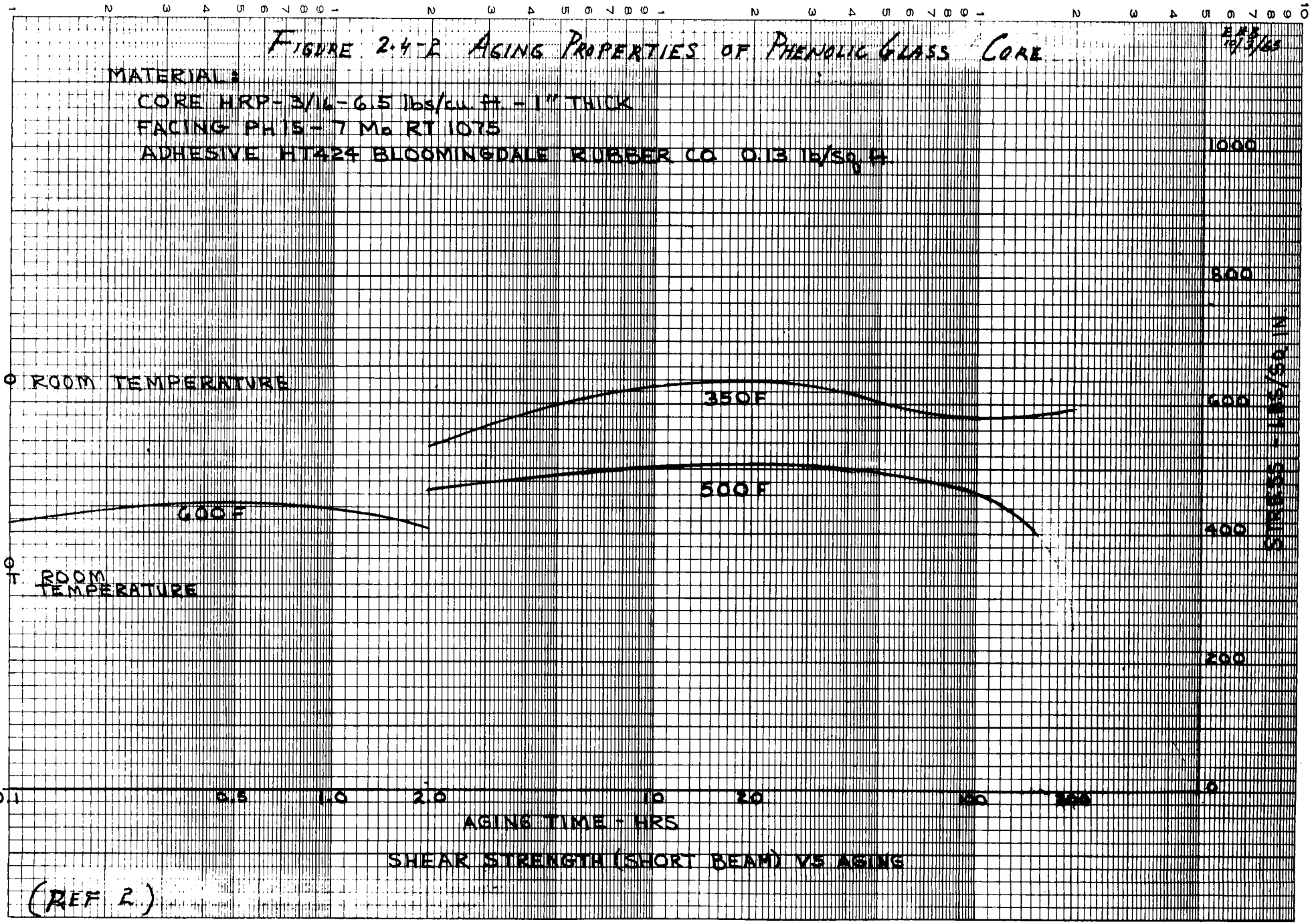

FIGURE 2.4-2 AGING PROPERTIES OF PHENOLIC GLASS CORE

SHEAR STRENGTH (SHORT BEAM) VS AGING

(REF 2)

FIGURE 2.9-3

DEGRADATION OF NOMEX® (HT-1) NYLON FABRIC*
AFTER EXPOSURE TO ELEVATED TEMPERATURES

DRN 10/4/3

* (MIL-C-8021 TYPE 1)

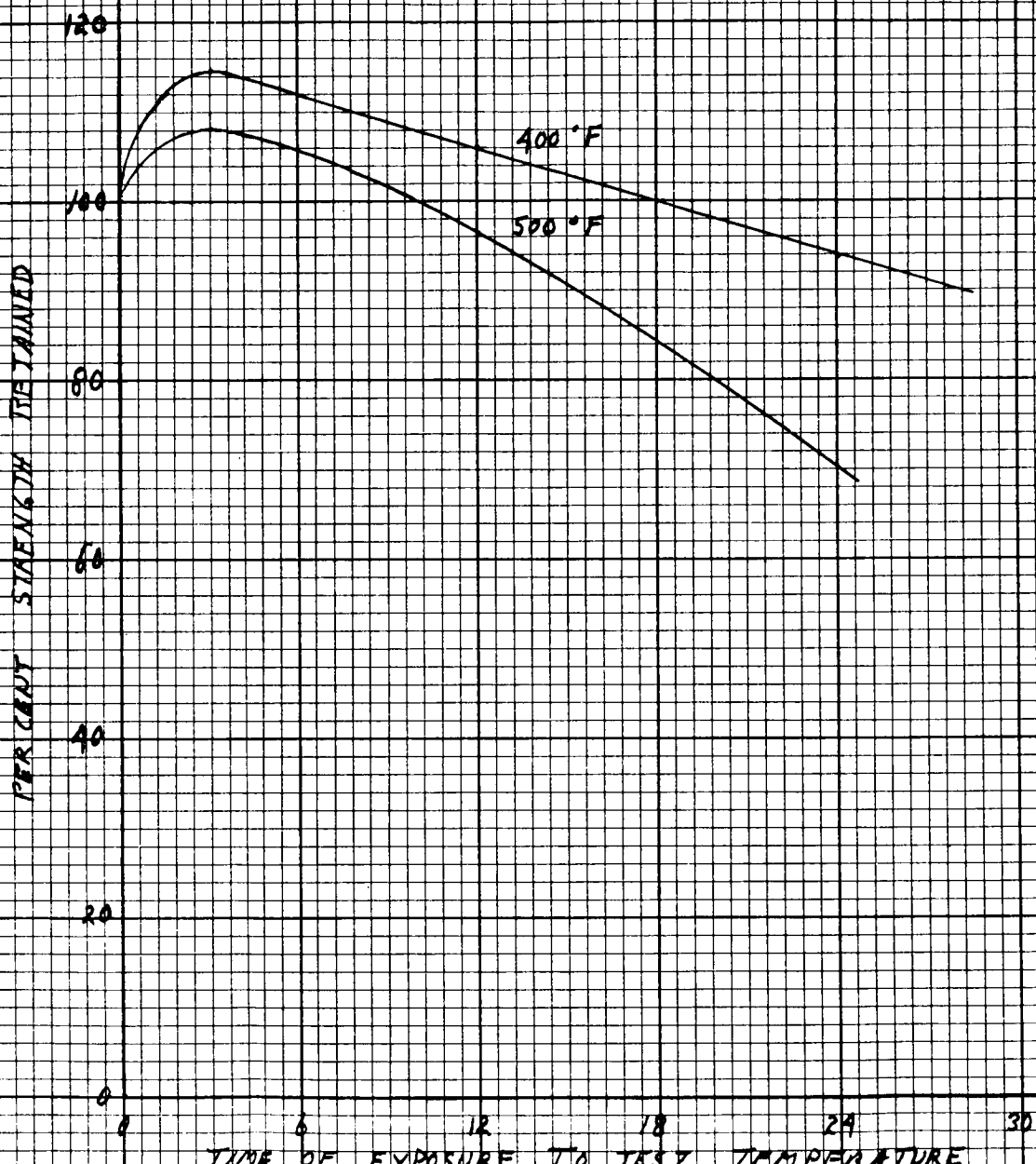

(REF 3)

(5) Chute Container: Aluminum sheet
No problems anticipated in heating during sterilization.

(6) Explosives used for Release of Heat Shield and Parachutes
Material suggested: Flexible linear charge of "TACOT" explosive.

This DuPont explosive will stand service temperatures up to 350C. The explosive is packed in a lead sheath which will give extra protection against radiation damage to the explosive.

A Primacord of RDX or similar explosive has an ignition temperature of 285F and cannot be sterilized by dry heat. If Primacord were established, a different method of sterilization and assembly would be necessary.

In summary, it appears that all materials suggested for the fabrication of the space capsule are compatible with a dry heat treatment of 145C for three, 36 hour cycles without significant change in their properties. It can therefore be assumed that sterilization of the capsule appears feasible.

2.4.2 Effects of Space Environment

The trans-Mars phase of the journey will be in the order of 200 days duration. During this time, the capsule materials will encounter the varied radiation, vacuum, meteorite and thermal cycling stresses of the space environment. The paragraphs which follow discuss these effects.

2.4.2.1 Radiation Effects

Concern for the effects of high energy charged particles of solar and cosmic origin has generally been primarily for personnel protection. Highly energetic radiation can also affect material properties and cause radiation damage if absorbed in the material. Metallic materials are generally stable in space at normal temperatures and are essentially unaffected by ionizing radiation except for transient radiation effects on semiconductor materials and electronic components. The metallic materials to be used in the capsule package should be unaffected structurally even by solar flares with the possible exception of any functioning electronic sequencing or control devices associated with the landing or control subsystem. Organic polymers (such as the nylon which must be employed for parachutes and which also is a candidate ablator) are more susceptible to degradation than metals and may be subject to loss of flexibility from exposure to soft X-rays and ultra-violet radiation over an extended period. The parachutes are adequately shielded from UV and soft X-radiation by their containers and location in the capsule. Additional shielding to radiation may be provided by such structural components as the bus and booster. Experimental evidence (Reference 4) indicates that HT-1 nylon, when exposed to gamma radiation and

concurrent temperatures up to 650F, displays superior performance and shows no evidence of degradation under the test conditions.

2.4.2.2 Vacuum Effects

In general, engineering properties are little affected in vacuum unless appreciable loss of mass occurs. The amount of metal loss due to evaporation, for the capsule metals considered at the maximum temperatures anticipated, should be insignificant from a structural viewpoint. A possible source of concern is the tendency for similar metals in rubbing contact under pressure to experience cold-welding. This is even more likely to occur in the ultra-high vacuum of outer space and at elevated temperatures. This tendency can be reduced by using dissimilar metals at contact points under little or no pressure. One place this might happen is at the explosive nuts, if separation of the heat shield is not complete. Whether cold welding will occur is purely speculation at this time inasmuch as no data from comparable space environmental conditions for equivalent times are available for reliable evaluation. As a precautionary measure, the addition of a dry lubricant would be advisable. A thorough discussion of the outgassing characteristics of dry lubricant materials in a vacuum is given in Reference 5.

Vacuum has greater effect upon organic compounds and fluids. Roles of volatilization and sublimation of surface polymers become appreciable at low pressures for organic materials of relatively high vapor pressure. According to classical concepts, the rate at which molecules escape from a surface into an infinite vacuum is given by the Langmuir equation:

$$\dot{W} = \frac{P}{17.14} \left(\frac{M}{T_{sp}}\right)^{\frac{1}{2}}$$

Where $\dot{W}$ = rate of evaporation of sublimation in grams per square centimeter per second.

P = vapor pressure of the material in Torr.

M = molecular weight of the material in the gas phase.

T_{sp} = wall temperature of the material in degrees Kelvin.

It should be noted that the Langmuir equation predicts a dependence of mass loss on both wall temperature and the weight of the gas phase material. The vapor pressure and molecular weight in the gas phase for most elements and molecular compounds are well known, however, organic plastics are long chain compounds which when exposed to a high vacuum decompose into smaller more volatile fragments, the molecular weight of which has not been well established. Accordingly, the Langmuir equation is not particularly useful

in calculating the mass loss rate of organic plastics intended for space application. For this reason, it is necessary to measure directly the weight loss per unit of time for various materials and configurations exposed not only to vacuum conditions, but also simulated solar radiation or other space environmental parameters which tend to effect surface temperature. Work has been initiated to study the resistance of many polymers to space environments, but the effort is limited and does not include exposure times of 6,000 to 7,000 hours (Reference 6).

2.4.2.3 Effects of Meteorites

Little practical protection against large meteorite penetrations of space vehicle structures can be afforded from a weight standpoint. Puncture of the unpressurized conical afterbody may not be critical if the payload remains undamaged, but perforation of the heat shield might make it unfit to resist the entry environment. Meteoroid and dust erosion can seriously affect the optical and emissive properties of highly reflecting thin films such as might be used for thermal control, but generally have little structural effect. For this reason, the passive thermal control films should be diffuse and unpolished coatings, (e.g., MgO).

2.4.2.4 Effects of Thermal Cycling

The spacecraft temperature in space will be derived essentially from solar radiation except as modified by the absorptance and emittance (a/e ratio) of the outer surface coating. Although the temperatures to be encountered during the trans-Martian flight will probably vary between -100F and about 250F, both passive and active thermal control techniques (e.g., coatings, sun-shielding, louvres, heaters, etc.) may be expected to be applied to maintain acceptable surface and internal capsule temperatures. (Design of a trans-Martian thermal control system is beyond the scope of this study.) No significant degradation of properties is anticipated due to temperature cycling if the temperatures could be maintained between 0 and 150F for the candidate metallic and non-metallic materials considered. Should the temperature limits be lowered significantly, there will be some concern for the heat shield structural bond. Delamination of the bond could compromise the effectiveness of the heat shield during entry.

2.4.3 Materials Considerations

The materials selected for the several subsystems investigated will have to withstand both the thermal and mechanical stresses imposed by the entry environment. These have been categorized and are presented in the paragraphs which follow.

2.4.3.1 Ablators

Based on the type and degree of heating the design of the heat shield was limited to the use of an ablative type of thermal control system. The heating times are defined by the entry angle (-20° and -90°). If capsule release conditions dictate a low entry angle, the material must perform as an insulator as well as an ablator. The time period for the higher angle entry is much shorter, therefore, the ablation properties of the material are of primary consideration. It was therefore decided that because of the entry uncertainties, that a homogeneous material (ablator-insulator) would be employed. The ablation materials considered include the following:

(1) Cork: Cork is a low temperature ablator which performs very well when subjected to the heating environment for this mission. It is a good insulator and provides ample efficiency in the ablation process. The disadvantages include low char layer strength, sterilization limitations, and storability. Char layer strength is necessary in order to provide heat dissipation by radiation. Sterilization procedures, at the present time, include the use of temperatures in the range of 300F. At 300F cork begins to decompose, therefore, an alternate sterilization procedure would be required. In storing the material, moisture and fungus growth can present problems. Coatings are available which can be used to retard fungus growth and moisture absorption.

(2) Teflon: Teflon is referred to as a subliming ablator. It performs satisfactorily when the allowable backface temperature is in the range of 700F. The higher backface temperature places greater emphasis on the ablative quality of the material and less on the insulative abilities. At low allowable backface temperatures, the weight requirement for insulation is too great for teflon to provide competition for the other materials. Another factor which warrants consideration is the transmissivity to thermal radiation. Some compositions of teflon are not opaque to thermal radiation, therefore, they are limited to use in a convective heating requirement.

(3) Phenolic Glass: Phenolic glass is a relatively high temperature ablator. It combines the ablation and reradiation method of heat blockage into an efficient thermal protection shield. The high ablation temperature results in an appreciable quantity of heat being reradiated. The char layer is strong and the material itself is suitable for structural purposes. The major deterrent to phenolic glass is the insulative requirements imposed by a low allowable backface temperature or long periods of heat flux.

The material is available in various compositions, therefore, the properties are affected somewhat by the percentages of reinforcement or resin in a specific type. In the analysis conducted here, it was assumed that the composition was 70% reinforcement and 30% resin. The effects of increasing the percentage of resin would be to decrease structural properties; however, the thermal efficiency would be increased. For instance, if the composition were 40% reinforcement and 60% resin, the thermal efficiency is approximately 6,000 Btu/lb; if the composition were 70% reinforcement and 30% resin, the thermal efficiency is about 4,900 Btu/lb (Reference 6). For structures which maintain structural integrity in the 500F to 700F range, phenolic glass is a prime candidate. It has the added feature of being used previously and extensively tested; therefore, its performance is predicted more accurately.

(4) Avcoat: Avcoat is available in various compositions; two types were considered in this study. Some of the components in an Avcoat material are micro-quartz fibers, glass fibers, phenolic microballoons, and an epoxy filler. Avcoat II, a castable resin which was analyzed as a heat shield material, appeared satisfactorily from a weight standpoint. Its major disadvantage, encountered during the Minuteman Program, was the cracking and falling apart of the material due to thermal stresses. To combat this difficulty, a new composition, developed for the Apollo program, is being considered. Avcoat 5026-39, a proprietary material, is used in conjunction with a phenolic glass honeycomb matrix. The Avcoat material is used to fill the honeycomb core and the composite is bonded to a substructure. The honeycomb serves to inhibit erosion of the char layer and minimizes the effect and propagation of thermal stress cracks.

(5) Thermo-lag T-500: Thermo-lag is a moldable compound formulated in various compositions which in turn provide a range of thermal properties. The compounds included in this analysis were T-230 and T-500. The T-230 was not examined extensively due to the lack of data pertinent to its performance. The T-500 can be used in conjunction with a phenolic glass honeycomb in the same manner as the Avcoat material. It exhibits good thermal properties and ablates at approximately 530F. The major difficulty experienced with this material is failure in a severe cold environment. Apollo tests indicated that the material fell away from the honeycomb; however, the Emerson Electric Manufacturing Company, (holder of proprietary rights to

the Thermo-lag compounds), has developed new variations which are more stable in a cold environment. Although thermo-lag is a subliming ablator, it forms a char layer and re-radiation is utilized as a part of the overall efficiency. Some of the projects which have utilized the Thermo-lag compounds are: Little Joe capsule, Argo and Honest John nose cones, and the Thor Delta nose cone.

(6) SE-28: SE-28 is an NAA-developed material made up of a castable resin system with a microballoon filler. It was developed during the Minuteman Program. It has not been used for reentry vehicles, as of this writing, but the properties of the material are such that it warrants consideration. System weights are comparable or better than those derived for the other materials studied.

(7) Phenolic Nylon: Phenolic nylon is a composite material made up of nylon fibers and a phenolic resin. It is available in densities ranging from approximately 36 lb/ft^3 to 80 lb/ft^3. The reinforcement and the resin can be proportioned depending on the desired properties. A 60% resin content results in a thermal efficiency of approximately 7,200 Btu/lb while a 30% resin content provides a thermal efficiency of approximately 6,400 Btu/lb. The nylon and resin can be used in conjunction with a phenolic glass honeycomb. As stated previously, the honeycomb aids in reducing the effects of thermal stresses and provides greater char strength. One of the problem areas in the use of phenolic nylon is the gas formation which can result from long, low flux heating environments. This has been nullified to some extent by changing the method of preparing the nylon and information available at present indicates that a powdered nylon used with the phenolic resin performs more satisfactorily. The gas formation may cause a "blowing off" of the char, thereby removing the possibility of dissipating heat by radiation. Gas formation can be controlled by substituting DuPont's new high temperature resistant NOMEX HT-1 nylon for present nylon formulations. This material change would also improve the ablator's resistance to the combined effects of elevated temperatures, radiation and vacuum. Such a new material requires considerable laboratory investigation and is not a state-of-the-art material. It is worthy, however, of consideration for application on future deep-space vehicles in light of the ablative efficiency and low weight of phenolic nylon type of ablators.

2.4.3.2 Structural Materials

2.4.3.2.1 Metals

A comparison of the design properties of a number of proposed metals and alloys at room temperature and over a wide range of temperatures is presented in Table 2.4-1 and Figure 2.4-4. From the value of the modulus to density ratio for the beryllium alloys, it is obvious that they are superior to all the other alloys in that regard. However, the ductility and fabricability of the beryllium alloys are quite poor and have not been adequately improved by such production techniques as cross-rolling and hot-upsetting. Most of the other materials show an approximately equivalent modulus/density ratio although Rene' 41, PH15-7Mo and the 4130 alloy lead the others over a wider temperature range. From Figure 2.4-4 the highest compressive yield strength/density values shown are for Ti-6Al-4V, 18-8, QMV-Be and PH15-7Mo in that order. The values for Ti-6Al-4V decrease rapidly and approach the other materials at about 400F, while the 18-8, Be and PH15-7Mo are more gradual in reduction with temperature. The aluminum alloys show excellent properties at the lower temperatures and combined with good fabricability are useful materials for such application. The beryllium alloys are too difficult to fabricate and are brittle in behavior. The maraging steels are showing excellent properties and with further development should find good application. The PH15-7Mo alloy shows excellent promise because of its ease of fabrication, weldability and ready availability treated to higher strength values than the 17-7PH alloy and is finding increasing use at temperatures up to 1000F.

A graphical representation of the variation with temperature of the design properties given in Figure 2.4-4 in which the upper curves represent the strength/density ratio while the lower group shows the modulus/density variation. The Rene' 41 curves in both groups are quite stable and change very gradually over the temperature range indicated. This alloy has a very desirable strength characteristic but many problems are encountered in fabrication. As noted previously, the Ti-6Al-4V alloy shows good strength at the lower temperatures but which decreases rapidly with increasing temperatures to the operational range of the PH15-7Mo alloy and below that the 4130 low-alloy steel. The anticipated service requirements will have to dictate the application of the presently available structural materials.

2.4.3.2.2 Non Metallics

Laminates. Polyester-glass, epoxy glass, silicone glass and phenolic glass laminates were studied for possible application in the design of the conical afterbody and the self erection/protection shell. However, only phenolic-glass had the combination of radio transparency, good retention of mechanical properties at elevated temperatures, high strength to weight ratio, and above average resistance to the effect of a space environment; polyester and epoxy laminates have poor resistance to prolonged high temperature exposure and silicone laminates have a poor strength to weight ratio in the anticipated working temperature range (-100 to 300) of the

TABLE 2.4-1

ROOM TEMPERATURE PROPERTIES OF STRUCTURAL METALS

System	Alloy	Density #/in.^{3}	F_{cy}, ksi	$E_c \times 10^{-6}$ psi	$\frac{F_{cy} \times 10^{-4}}{p}$	$\frac{E_c \times 10^{-7}}{p}$
Al	2014-T6	0.101	60	10.7	59.4	10.6
	7075-T6	0.101	68	10.5	67.3	10.4
Ti	Ti-6Al-4V	0.160	145	15.2	90.6	9.5
	Ti-5Al-2.5 Sn	0.161	127	15.0	78.9	9.3
Mg	HM21A	0.064	22	6.5	34.4	10.1
	HK31A	0.064	20	6.5	31.3	10.1
W	W	0.697	200	59.0	28.7	8.5
	50W-50Mo	0.478	108	53.0	22.6	11.1
Mo	Mo-.5Ti	0.369	65	45.5	17.6	12.7
Be	QMV (H.P.)	0.066	42	42.0	63.7	63.8
	C.R. Sheet	0.067	58	42.5	86.5	63.4
Steel	4130 4140 4340	0.283	165	29.0	58.3	10.2
Maraging	18 Ni	0.289	240	26.2	83.0	9.1
Stainless Steel	18-8 (FH)	0.286	235	28.6	82.2	10.0
	18-8 (1/2 H)	0.286	85	26.0	29.8	9.1
	PH 17-7	0.282	155	26.0	55.0	9.2
	PH 15-7 Mo.	0.282	185	30.0	65.6	10.6
Superalloy	Rene 41	0.298	135	31.6	45.3	10.6

FIGURE 2.4-4
ELEVATED TEMPERATURE PROPERTIES OF METALLIC MATERIALS

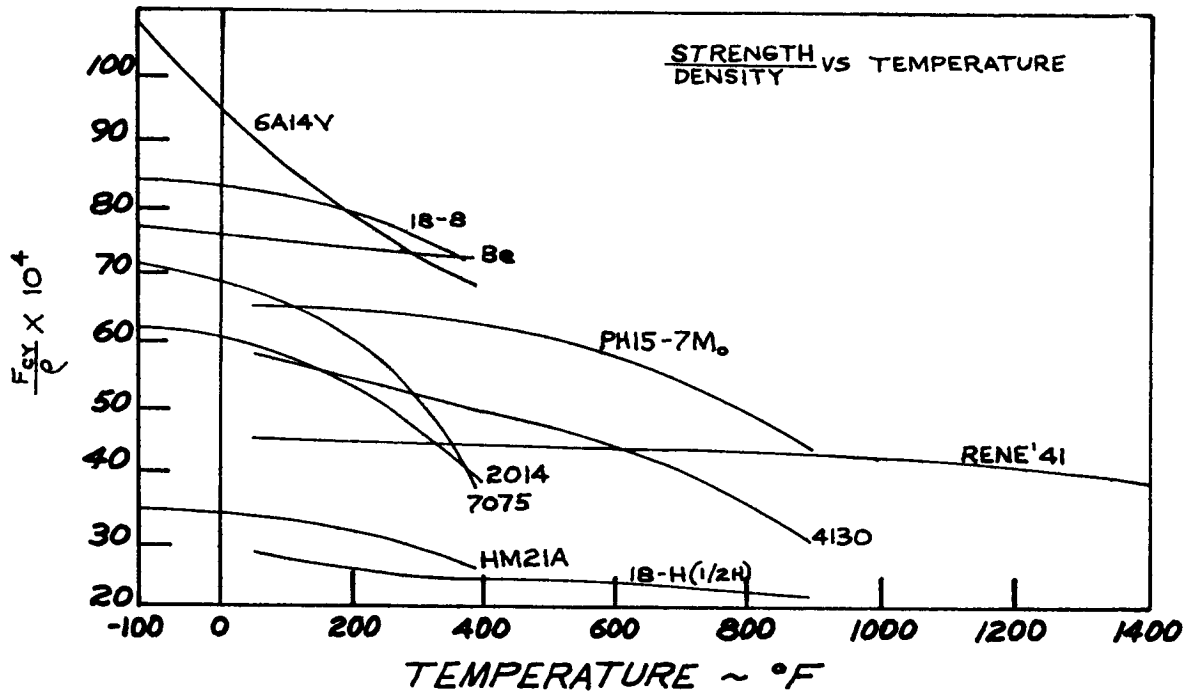

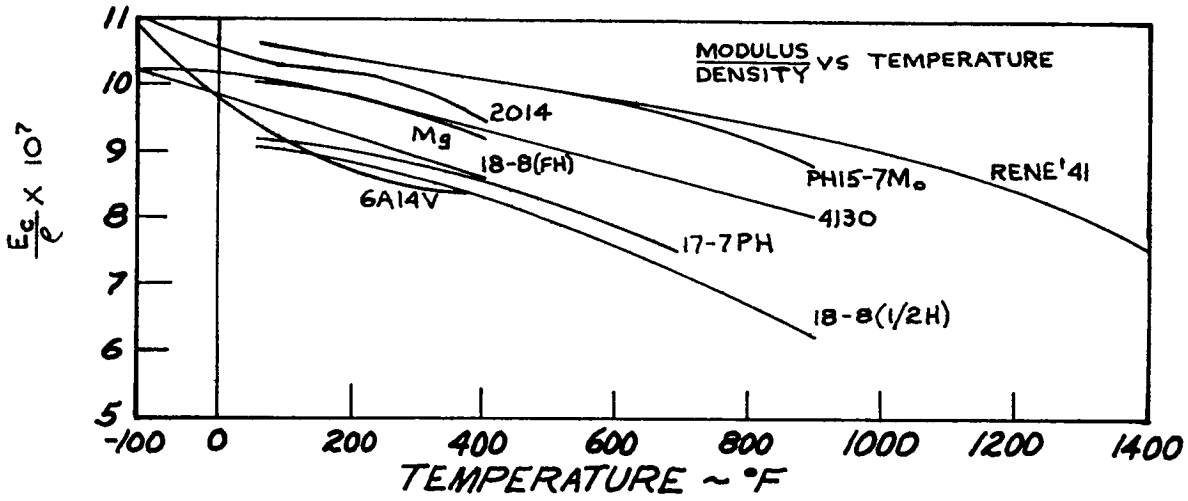

"Lander" vehicle. Phenolic-glass laminate has a long history of reliability. Mechanical properties of this material for this study, taken from Reference 1, indicate excellent retention of properties after long time exposure to temperatures as high as 500F and for shorter exposure periods up to temperatures of 800F.

A promising new material which appears to be an improved alternate to phenolic resins is polybenzimidazole (PBI) manufactured by Narmco materials under the trade name of Imidite. PBI, developed under an Air Force contract, has exhibited outstanding properties at elevated temperatures. When heated in a nitrogen atmosphere, PBI materials incurred virtually zero weight loss at temperatures up to approximately 800F, giving an indication of its ability to resist boil-off of polymer molecules in a vacuum. Because of the linear molecular structure, PBI polymers display extremely high cohesive strength and as an adhesive have high affinity for any wettable surface, matching the adhesive qualities of epoxies. The linear molecular structure also provides a high degree of toughness enabling the material, when used as a composite binder, to relieve local stresses that would normally crack more brittle phenolic binders. Typical PBI laminate properties are shown in Figure 2.4-5. While the improved mechanical and physical properties of PBI make it an inviting substitute for phenolic resins in laminates, adhesives, ablators, etc., it is a new unproven material which should be evaluated more extensively before it can be given serious consideration for space vehicle application.

Honeycomb Core. Both aluminum and phenolic-glass honeycomb core materials will be employed in the various design concepts. The 5052-H39 aluminum honeycomb is recommended for use in the aluminum heat shield back-up structure because of its proven reliability, strength to weight ratio, good fatigue properties and availability. Non-perforated core will be utilized to minimize the effect of hard vacuum upon the adhesives used in the fabrication of the core and the bonding of the facing sheets to the core. The epoxy-phenolic adhesive system which will bond the facings to the core has better than **average** resistance to a space environment, but little is known about the effect of hard vacuum upon the **core**-bond adhesive of the aluminum core. It's particular resin formulation is proprietary, but it is believed to be made from either vinyl-phenolic or an epoxy-nylon polymer. These latter materials are to the best information available, only considered marginal as far as prolonged resistance to a space environment is concerned. The properties of adhesively bonded honeycomb core in a vacuum are being studied at NAA for the Apollo program but will not be studied for the length of time required for the trans-Mars mission (i.e., 6,000 to 7,000 hours). Table 2.4-2 lists NAA established room temperature design allowables for 5052-H39 alloy aluminum core. Other core properties used in this study were taken from References 8 and 9.

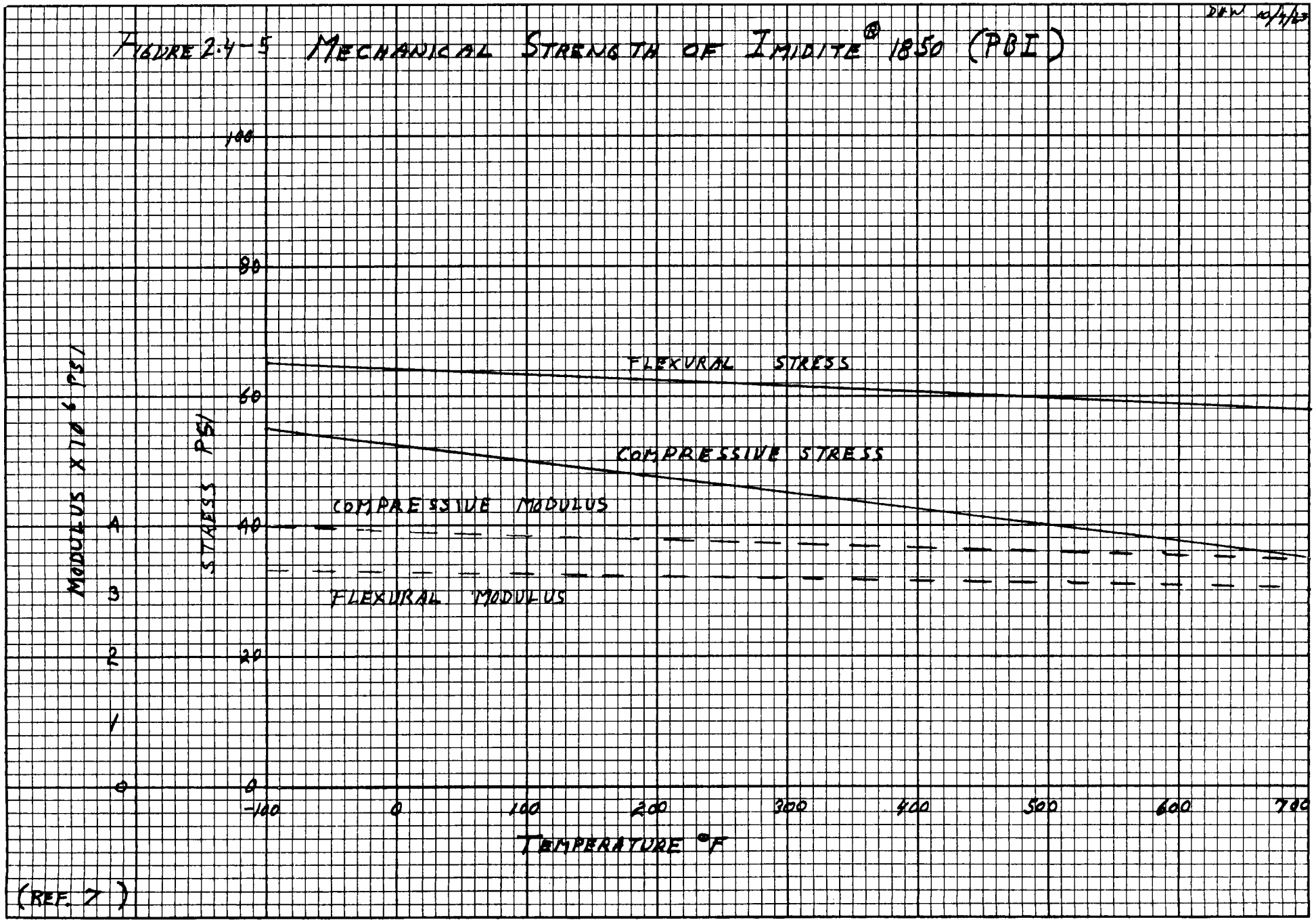
DHW 10/4/63
FIGURE 2.4-5 MECHANICAL STRENGTH OF IMIDITE® 1850 (PBI)
FLEXURAL STRESS
COMPRESSIVE STRESS
COMPRESSIVE MODULUS
FLEXURAL MODULUS
MODULUS X 10⁶ PSI
STRESS PSI
TEMPERATURE °F
0
1
2
3
4
0
20
40
60
80
100
-100
0
100
200
300
400
500
600
700
(REF. 7)

TABLE 2.4-2 ALUMINUM HONEYCOMB CORE PROPERTIES

Honeycomb Cell Size - Inches	Core Density lb/ft^3	Block Shear Strength Long lb/in^2	Block Shear Strength Trans. lb/in^2	Flatwise compression Strength lb/in^2
3/16	3.1	220	120	230
3/16	4.4	340	190	460
1/4	1.6	100	50	40
1/4	2.3	150	80	140
1/4	3.4	250	140	310

Heat resistance phenolic glass core, as manufactured by Hexcel Products, Inc., are suggested for the self erection/protection shell segments because of its transparency to electromagnetic radiation. This plastic core is manufactured from woven glass cloth which has been impregnated with a high temperature phenolic resin. It is manufactured into honeycomb and then brought to the required density by successive dipping into the phenolic resin. The aging characteristics of HRP-3/16-6.5 phenolic glass core at 350, 500 and 600F for various periods of exposure are indicated in Figure 2.4-2. It is anticipated that the core will not be affected by the environments of a trans-Mars mission more than the other phenolic-glass materials incorporated into the Lander design. The properties of phenolic core taken from Reference 2 have been substantiated at NAA during evaluation programs conducted for Saturn and Apollo projects.

Adhesives. Three areas in the structure potentially will require the use of structural adhesives. These are: (1) bonding of the aluminum facing sheets to the aluminum core, (2) bonding of the heat shield to the aluminum sandwich structure, and (3) bonding of the phenolic-glass honeycomb core. Epoxy-phenolic adhesives such as those produced by Shell Chemical Company (422J), Adhesives Engineering (422J) and Bloomingdale Rubber Company (HT424) can be efficiently employed in area (1). This adhesive material as shown in Figure 2.4-6 offers consistently good properties over wide temperature ranges and because of the phenolic resin used in its formulation should have good retention of properties in a space environment. The closed nature of the sandwich panel should also help minimize the deterioration of adhesive properties due to hard vacuum and solar radiation. Considerable experience, test data, and bonding experience is available on this adhesive system; consequently no problems are anticipated in the manufacture of space hardware with epoxy-phenolic adhesives.

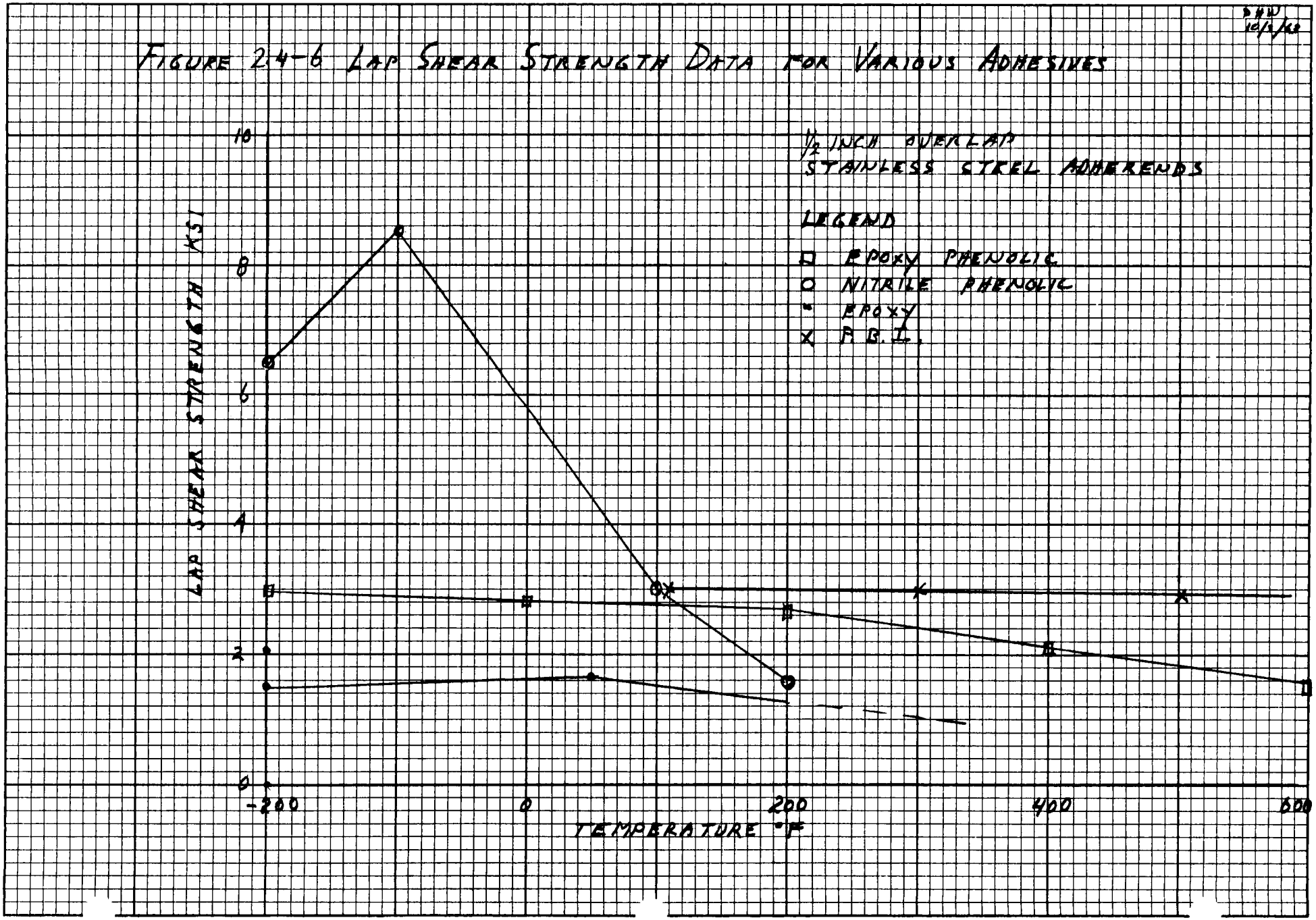
DHW 10/1/62
FIGURE 24-6 LAP SHEAR STRENGTH DATA FOR VARIOUS ADHESIVES
1/2 INCH OVERLAP
STAINLESS STEEL ADHEREND
LEGEND
EPOXY PHENOLIC
NITRILE PHENOLIC
EPOXY
P.B.I.
LAP SHEAR STRENGTH KSI
10
8
6
4
2
0
-200
0
200
400
600
TEMPERATURE °F

TABLE 2.4-3

IMPACT ATTENUATING MATERIAL CHARACTERISTICS

MATERIAL	DENSITY	COMPRESSIVE STRENGTH	ENERGY ABSORBED	
	(lb/ft^3)	(lb/in^2)	(ft-lb/lb)	(ft-lb)/ft^3
Balsa Wood	6 to 12	750 to 2950	24,000	144,000 to 288,000
Alum. Honeycomb Core 1/8 - 3003 - .0015P	6.48	320 to 400	5,350 to 6,700	34,700 to 43,300
Alum. Honeycomb Core 1/8 - 3003 - .0015P with 16 lb/ft^3 Lockfoam filler	19.14	1,400 to 2,300	7,900 to 13,000	151,000 to 249,000
Alum. Honeycomb Core 1/8 - 3003 - .0015P with Balsa Wood Filler	13.5	1,200 to 1,360	9,600 to 10,900	130,000 to 147,000
Alum. Honeycomb Core 1/8 - 3003 - .002P	8.02	540	7,260	58,200
Alum. Honeycomb Core 1/8 - 3003 - .002P with 16 lb/ft^3 Lockfoam Filler	18.2	2,250	13,300	242,000
Alum. Honeycomb Core 1/8 - 3003 - .002P with Balsa Wood Filler	14.25	1,340	10,200	145,000

TABLE 2.4-4

SHOCK ABSORBING SYSTEM

COMPARATIVE EFFICIENCIES OF VARIOUS

CRUSHABLE ALUMINUM HONEYCOMB CORES

HONEYCOMB TYPE	WT. PER FOOT OF THICKNESS PER 1000# OF PAYLOAD PER G DECELERATION
AL 1/8 - 3003 - .0015	.131
AL 3/16 - 3003 - .002	.138
AL 1/8 - 3003 - .001	.150
AL 1/4 - 3003 - .004	.151
AL 1/4 - 3003 - .003	.151
AL 3/8 - 3003 - .003	.183
AL 3/16 - 3003 - .001	.214

Bonding of the ablative heat shield to aluminum sandwich backup structure can be accomplished with the epoxy-phenolic adhesive systems previously discussed, but careful consideration will have to be given to differences which exist between the coefficient of thermal expansion of the glass phenolic ablator and aluminum sandwich backup structure. The difference is almost 3 to 1. Failure in the bond between these two materials is more likely to result as the structure approaches a low thermal environment for the following reason: the bond is made between the materials at approximately 250 to 350F; as the structure cools to room temperature the bonded parts are prestressed and any further lowering of the temperature will increase the level of stress. Rupturing of the bond is therefore possible in space where temperatures as low as -100° may be encountered if the bond is not suitably protected. Conversely, as the temperature of the parts are increased stress is decreased until equilbrium is reached when both materials are at the bonding temperature. Rupturing of the bond between the heat shield and the sandwich panel is also dependent upon the strength of the weakest element in the system, which is in this case either the bond between the adhesive and the phenolic resin in the laminate or the bond between the phenolic resin and the glass reinforcement in the laminate. Should an analysis indicate that the problem just discussed exists, a high modulus silicone rubber adhesive will have to be employed. The adhesive which will be required to structurally bond the phenolic glass core to the phenolic-glass laminate facings will also have to be transparent to r.f., posing a difficult material selection problem. HT424 epoxy-phenolic adhesive would be the best bonding agent but because of the aluminum powder/flake used in its manufacture, would readily attenuate radio waves. Alternate adhesives for the application are shown in Figure 2.4-6. High temperature epoxies and nitrile phenolic adhesive are critical for this application because of their relatively poor aging characteristics and undefined properties after prolonged exposure to space. A more suitable alternate to HT424 would be PBI but, as previously indicated, this material is new and cannot be considered state-of-the-art as yet.

Considerable work has been done on the evaluation of materials and their energy absorbing characteristics. Table 2.4-3 tabulates the most efficient of the energy absorbing materials studied. As indicated, balsa wood is the most efficient of the materials listed. Balsa, unfortunately, is an inconsistent product. Its density varies extensively throughout any single log and as a result, tests show unusually wide variations in crushing strength and failure mode. These variations have been satisfactorily controlled by tailoring or homogenizing the wood. It still, however, cannot be utilized because of the charring of the material which would take place during dry heat sterilization of the vehicle. An energy absorbing material which has more potential for space application is aluminum honeycomb core. Table 2.4-3 shows how aluminum core energy absorbing efficiency can be improved by the addition of filler materials. The space resistance of this type of core would certainly be equal to that of the core material used in the heat shield backup structure. The comparative efficiency of various unfilled cores are shown in Table 2.4-4.

2.4.3.3 Landing System

The landing system is comprised basically of a parachute system and any crushable material which may be required to attenuate the landing impact for a mission having post-impact requirements.

Considering the requirements for the parachute system, it is recommended that DuPont's HT-1 nylon yarn, recently given the trade name of NOMEX, be used in the fabrication of the drogue and main chute as well as extension, lanyard, and riser lines. NOMEX (HT-1) yarn has properties similar to those of industrial yarns of 66 nylon and Dacron polyester fiber at room temperature, except for its somewhat lower tenacity and exceptionally high modulus. At the melting temperature of the other two fibers (428F), NOMEX still retains well over half its room temperature strength and continues to have good electrical properties. NOMEX does not melt, is self-extinguishing, and decomposes into a friable char when exposed to excessive heat. These properties will minimize the possibility of the chute and associated lines fusing together, should the melting point of the material be reached by unanticipated heating prior to deployment. This non-fusing property will minimize the possibility of the chute adhering to the chute containers and causing a malfunction of the landing system.

NOMEX yarn has one disadvantage which must be considered carefully; it degrades slowly in the presence of water vapor at elevated temperature. In a sealed tube test, NOMEX yarn exhibited a tenacity loss of about 70% after 1000 hours at 300°F. Damage could result to chute and lines which are placed in containers which will not allow moisture given off by the nylon itself to escape during the dry heat sterilization cycle, or during flight to Mars. DuPont reports that, in the same test, DuPont Type 272 rayon, Type 300 nylon, and Type 51 Dacron polyester fiber were completely degraded in fewer than 100 hours; Type 42 Orlon acrylic fiber was degraded after about 300 hours (Reference 10).

2.4.4 References

1. "Plastics for Flight Vehicles" MIL-HDBK-17 Armed Forces Supply Support Center, Washington 25, D. C., November 1959

2. Aging Properties of Phenolic Glass Core, unpublished Northrop Norair report, Donald H. Wykes, March 1958

3. Thermal and Gamma Radiation Behavior of New High Temperature Organic Fiber, WADC Technical Note 60-299, C. O. Little, Jr., ASD, Wright-Patterson Air Force Base, Ohio, June 1961

4. Thermal and Gamma Radiation Behavior of a New High Temperature Inorganic Fiber, WADD Technical Note 60-299, June 1961, ASD, Wright-Patterson Air Force Base, Ohio

5. Outgassing Characteristics of Dry Lubricant Materials in a Vacuum

D. H. Bowen and W. A. Hickam, Machine Design, July 4, 1960

6. The Effects of Space Environment on Material, Society of Aerospace Material and Process Engineers Symposium, St. Louis, May 7-9, 1962

7. "IMIDITE: A Commercial Realization of a Recent Laboratory Curiosity" L. P. Suffredini, Narmco Materials

8. "Engineering Data Handbook" Hecell Products Inc., Berkeley, California

9. "The Design and Analysis of Sandwich Construction" SL 100, Space & Information Systems Division, April 1962

10. "Physical and Chemical Properties of HT-1" W. R. Clay and W. C. Long, E. I. DuPont de Nemours & Co., Inc., Textile Research Laboratory, Wilmington, Delaware, May 1961

2.5 DESIGN AND GEOMETRIC CONSTRAINTS

The design of the capsule is constrained by two basic requirements. They are:

(a) The size of the capsule required to meet the nominal M/C_DA with a given aerodynamic configuration and gross target weight.

(b) Compatibility with the booster-shroud dimensions and available volumes, as well as the spacecraft bus.

Items (a) and (b) obviously are inter-related. Item (a), in itself, cannot be expressed uniquely inasmuch as the minimum size must be large enough to at least house the payload and other inboard systems; on one hand, in striving for an M/C_DA of 0.2, or less, the increase in size (as reflected by an increase in base diameter and, hence, projected area) must be traded off against the increase in surface area (which ultimately is reflected in higher structural and heat shield weights).

Some preliminary payload constraints were presented at the beginning of the study in a letter by J. M. Brayshaw, Jr. of JPL (31 July 1963) for the two sized capsules considered. The constraints included:

1. Gross capsule weights: 400 lbs. (later reduced to 350 lbs.) and 2000 lbs.

2. Capsule payload is instrumentation, power, control and communications systems with the following characteristics:

Initial Capsule Target Weights	Electronic Payload Wt.	Packaging Density (lb/ft^3	Internal Heat (Elec. Watts)
400	150	30	65
2000	600	30	450

(a) Communication antenna 32 inches in diameter and 16 inches deep (its weight of 12 lbs. included in payload.

(b) Minimum fore and aft dimension of payload is 9 inches

(c) Operating bulk temperature of payload is 10° to 55°C.

(d) Maximum allowable payload acceleration is 1000 earth g's

3. Centaur shroud constraints for the small capsule

4. Saturn VI shroud constraints for the large capsule

Using these data, a study was made to determine the capsule minimum and maximum sizes. Figure 2.5-1 shows the minimum size required for the small capsule using the cylindrical antenna and the minimum electronic payload height of 9 inches. This results in a capsule with a base diameter of 60 inches which may be located in the Centaur shroud in a manner to leave in excess of 300 cu. ft. for the spacecraft bus.

In the case of the larger capsule, Figure 2.5-2 shows a minimum size capsule with a base diameter of 70 inches. The cylindrical antenna is used and the electronic payload is packaged to use the volume most efficiently. This configuration leaves a volume in excess of 4000 cu.ft. for the spacecraft bus within the Saturn shroud.

The maximum size capsules are constrained by the envelope dimensions of the Centaur and Saturn shrouds. Figure 2.5-3 illustrates the arrangement of the small capsule where the maximum base diameter of 98 inches is placed within the Centaur shroud. This arrangement leaves a volume of 187 cu. ft. for the spacecraft bus. The arrangement for the larger capsule is shown in Figure 2.5-4. This configuration yields a maximum base diameter of 230 inches inside the Saturn shroud and provides a volume of 1760 cu. ft. for the spacecraft bus.

All of the configurations were represented by the Apollo shape. Figure 2.5-5 defines the geometric characteristics of the configuration and presents the derived surface areas and volumes as a function of capsule base diameter. Figure 2.5-6 shows the variation of M/C_DA as a function of base diameter and capsule weight for a C_D of 1.5. For the small capsule, the M/C_DA varies from 0.35 slugs/ft^2 for the 60 inch diameter capsule to 0.165 slugs/ft^2 for the 98 inch diameter capsule. The larger capsule could have an M/C_DA range of 1.9 slugs/ft^2 for the 70 inch diameter capsule to 0.135 slugs/ft^2 for the 230 inch diameter capsule.

The smaller capsule can be configured to the standard Apollo shape with reasonably efficient use of the available internal volume for the range of base diameters under consideration. The larger capsule, however, has poor volumetric efficiency for the base diameters required to achieve an M/C_DA of 0.2 slugs/ft^2, or lower. Inasmuch as the total capsule weight is dependant on the relationship of internal volume to surface area, maximum volumetric efficiency is desired. Therefore, tradeoff studies were made to modify the Apollo shape and reduce the afterbody volume by changing the slope or truncating the cone.

The effects of these changes on the structure and dynamic characteristics are given in Sections 2.7 and 2.10. Section 3.0 discusses the design implications and presents several alternate configuration drawings.

MARINER 400 LB. ENTRY CAPSULE MINIMUM CONFIGURATION
138 LB (4.6 CU FT) CYLINDRICAL E.P. WITH J.P.L. CYL. ANTENNA
& NO IMPACT ATTENUATION

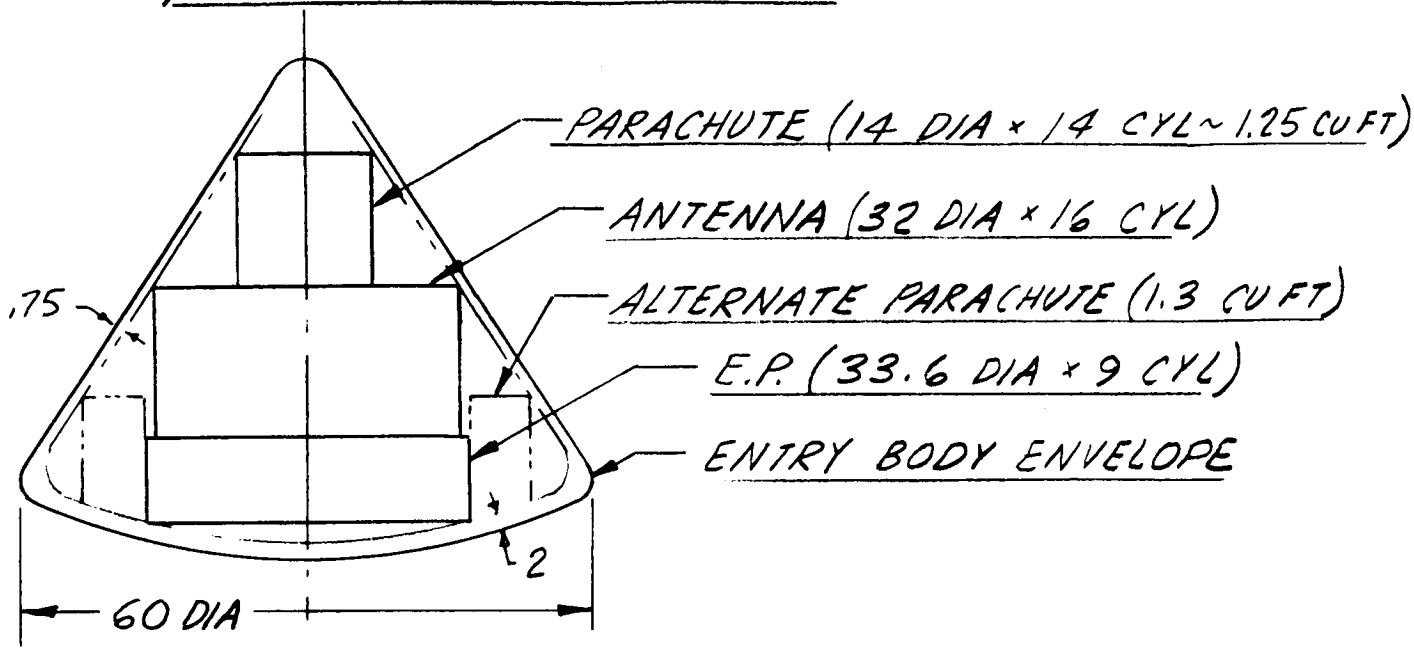

ENTRY CAPSULE CONFIG. (1/20 SCALE)

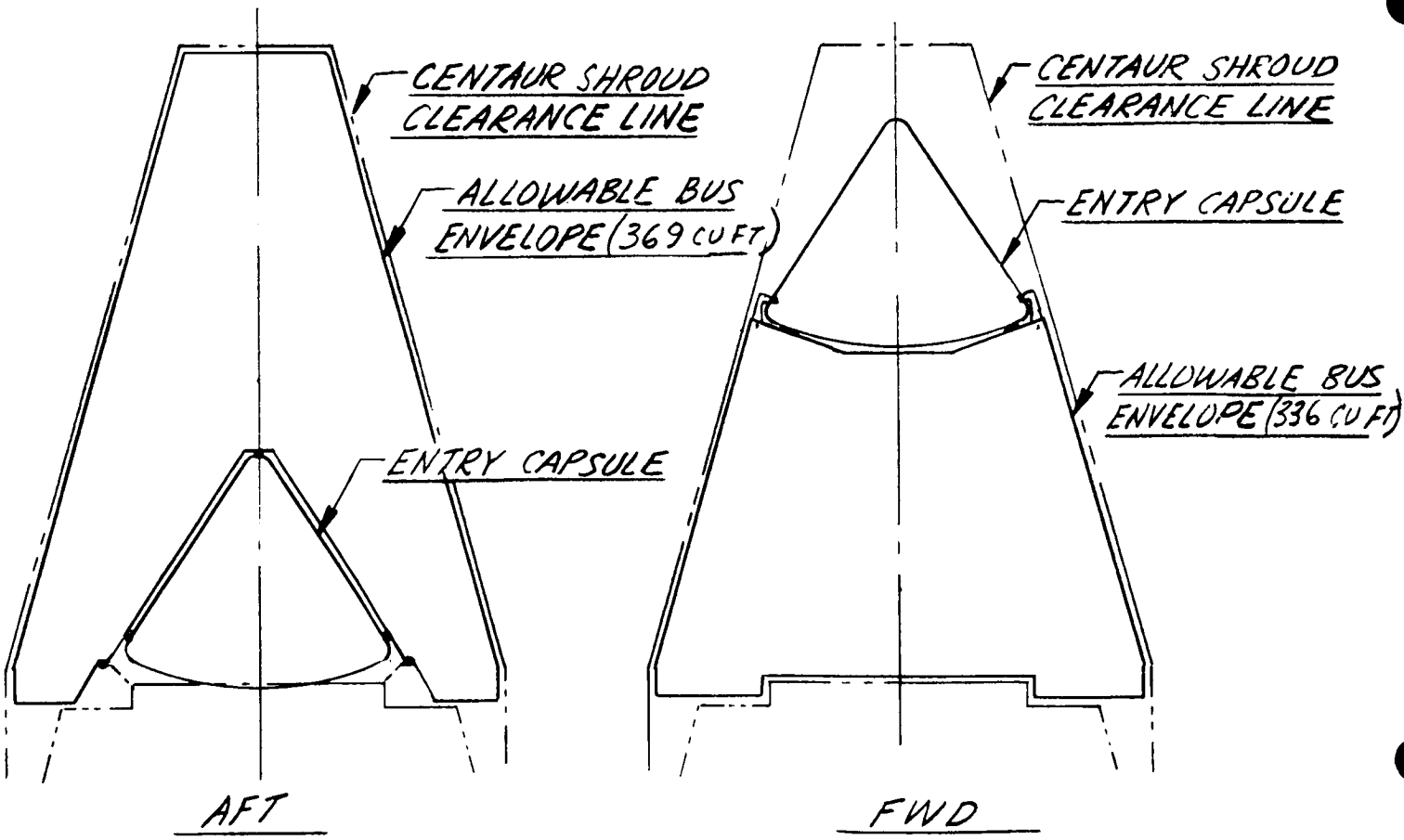

TYPICAL INSTALLATIONS (1/40 SCALE)

FIGURE 2.5-2

VOYAGER 2000 LB ENTRY CAPSULE MINIMUM CONFIGURATION
588 LB (19.6 CU FT) CYLINDRICAL E.P. WITH JPL CYL. ANTENNA
& NO IMPACT ATTENUATION

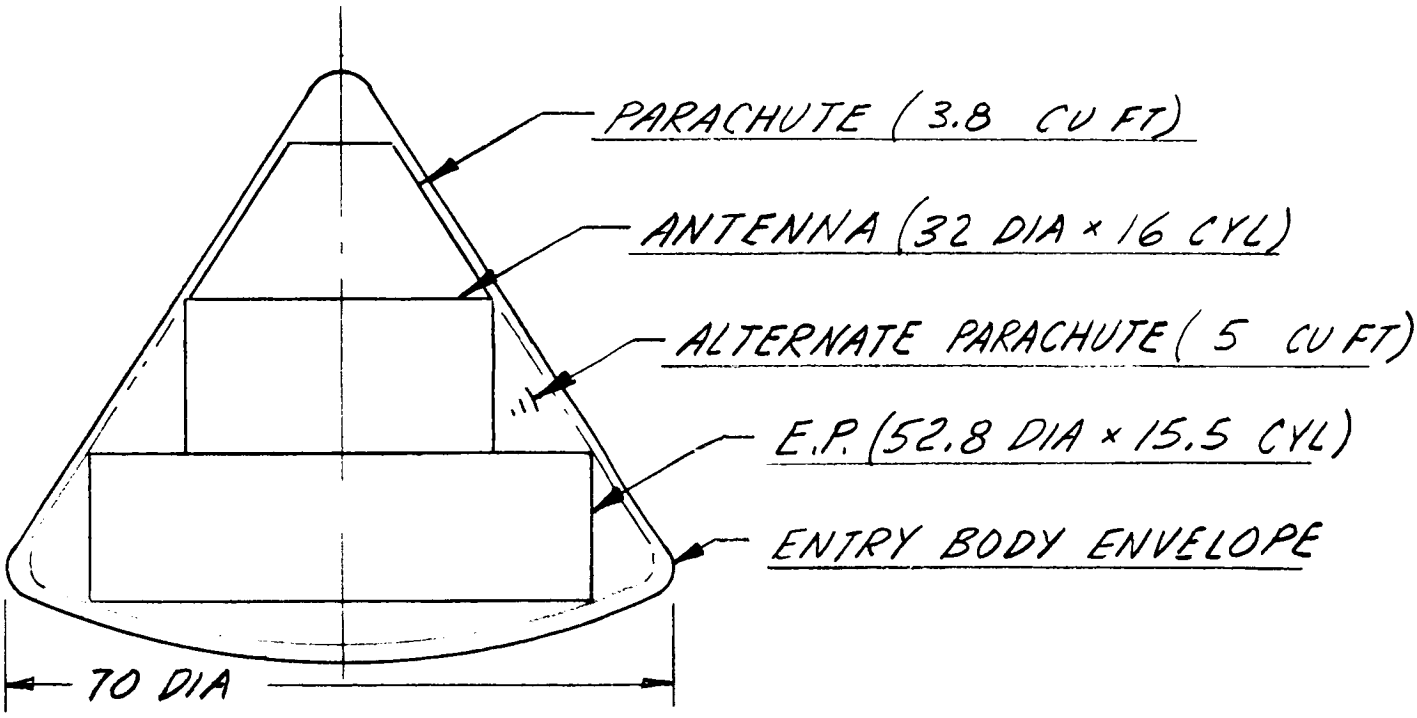

ENTRY CAPSULE CONFIG. (1/20 SCALE)

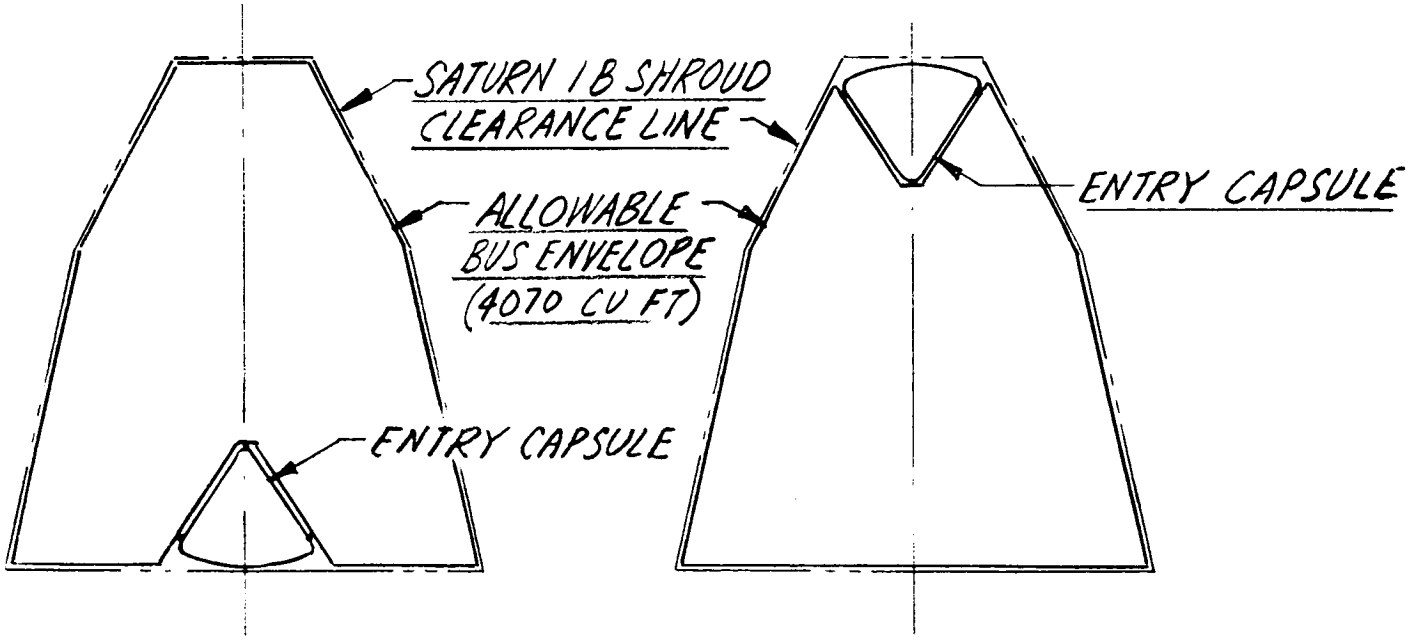

AFT FWD

TYPICAL INSTALLATIONS (1/100 SCALE)

FIGURE 2.5-3

MARINER 400 LB ENTRY CAPSULE MAXIMUM CONFIGURATION
135 LB (4.6 CU FT) CYLINDRICAL E.P. WITH J.P.L. CYL. ANTENNA
& NO IMPACT ATTENUATION

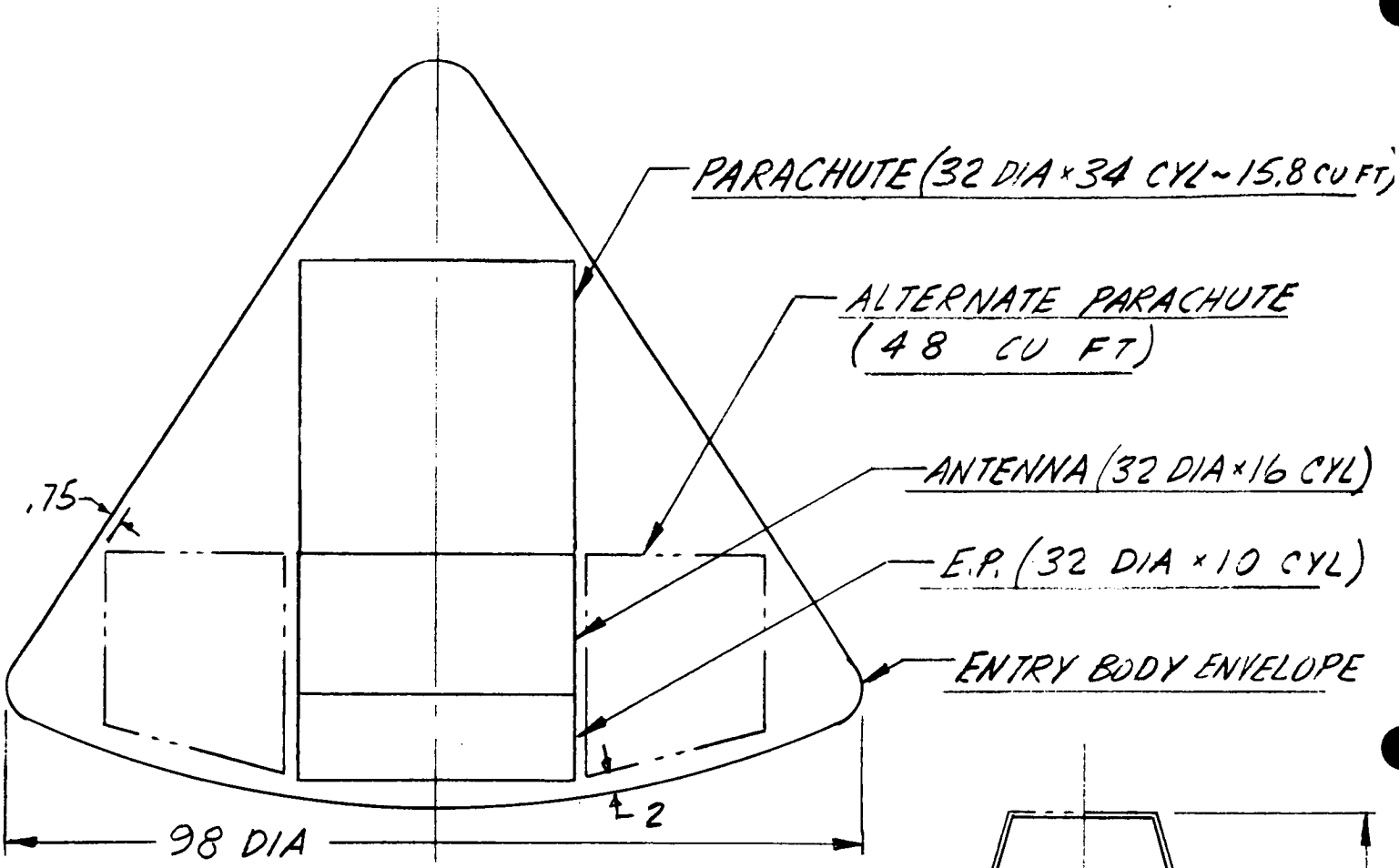

ENTRY CAPSULE CONFIG. (1/20 SCALE)

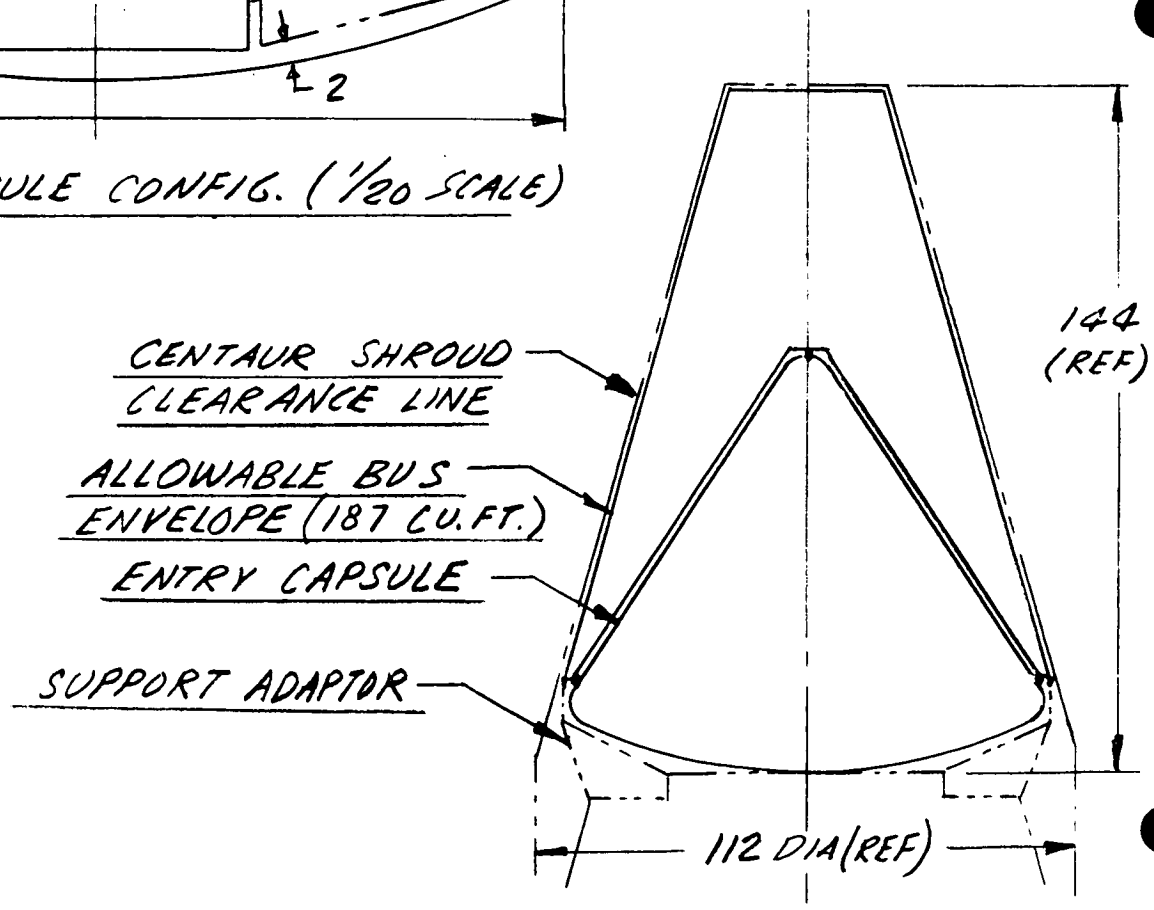

TYPICAL INSTALLATION (1/40 SCALE)

FIGURE 2.5-4

VOYAGER 2000 LB ENTRY CAPSULE MAXIMUM CONFIGURATION
588 LB (19.6 CU FT) CYLINDRICAL E.P. WITH JPL CYL. ANTENNA
& NO IMPACT ATTENUATION

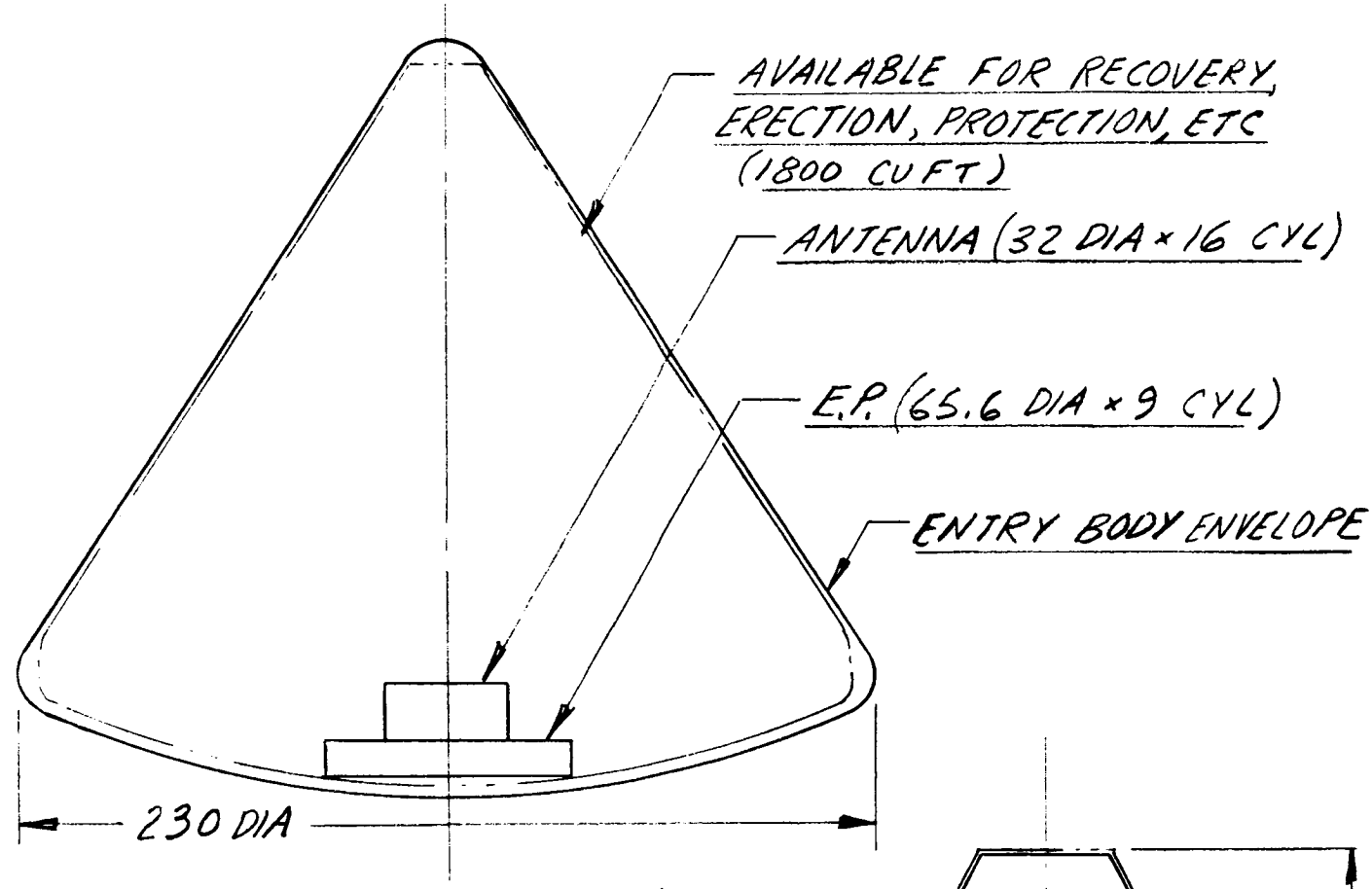

ENTRY CAPSULE CONFIG. (1/50 SCALE)

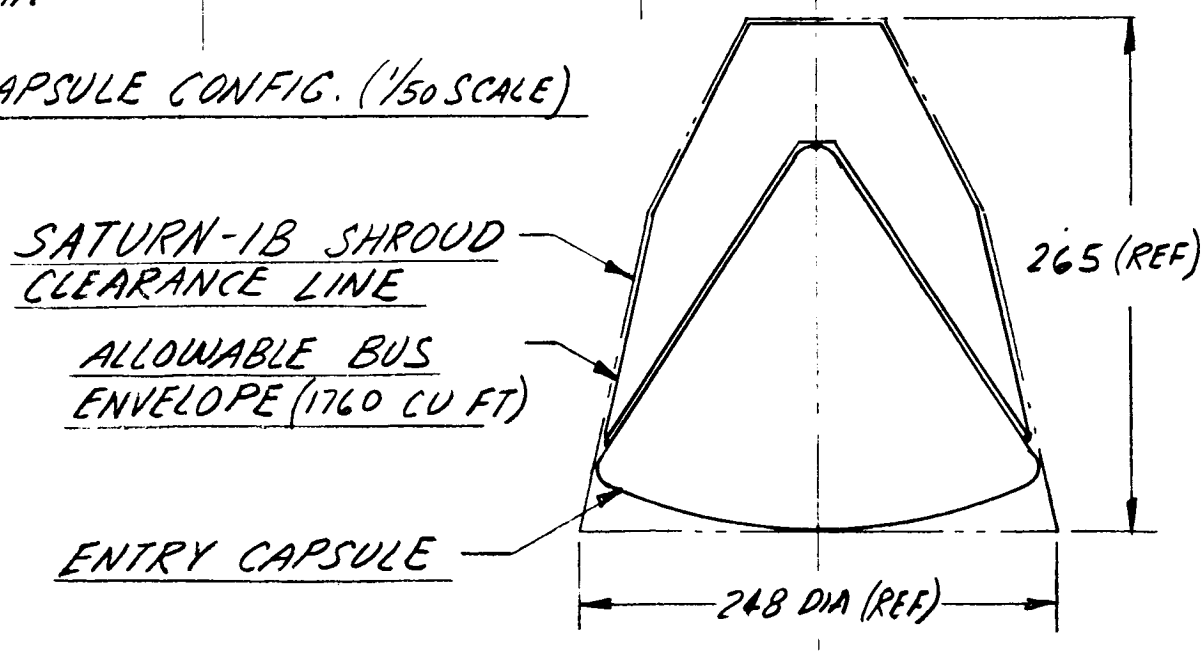

TYPICAL INSTAL. (1/100 SCALE)

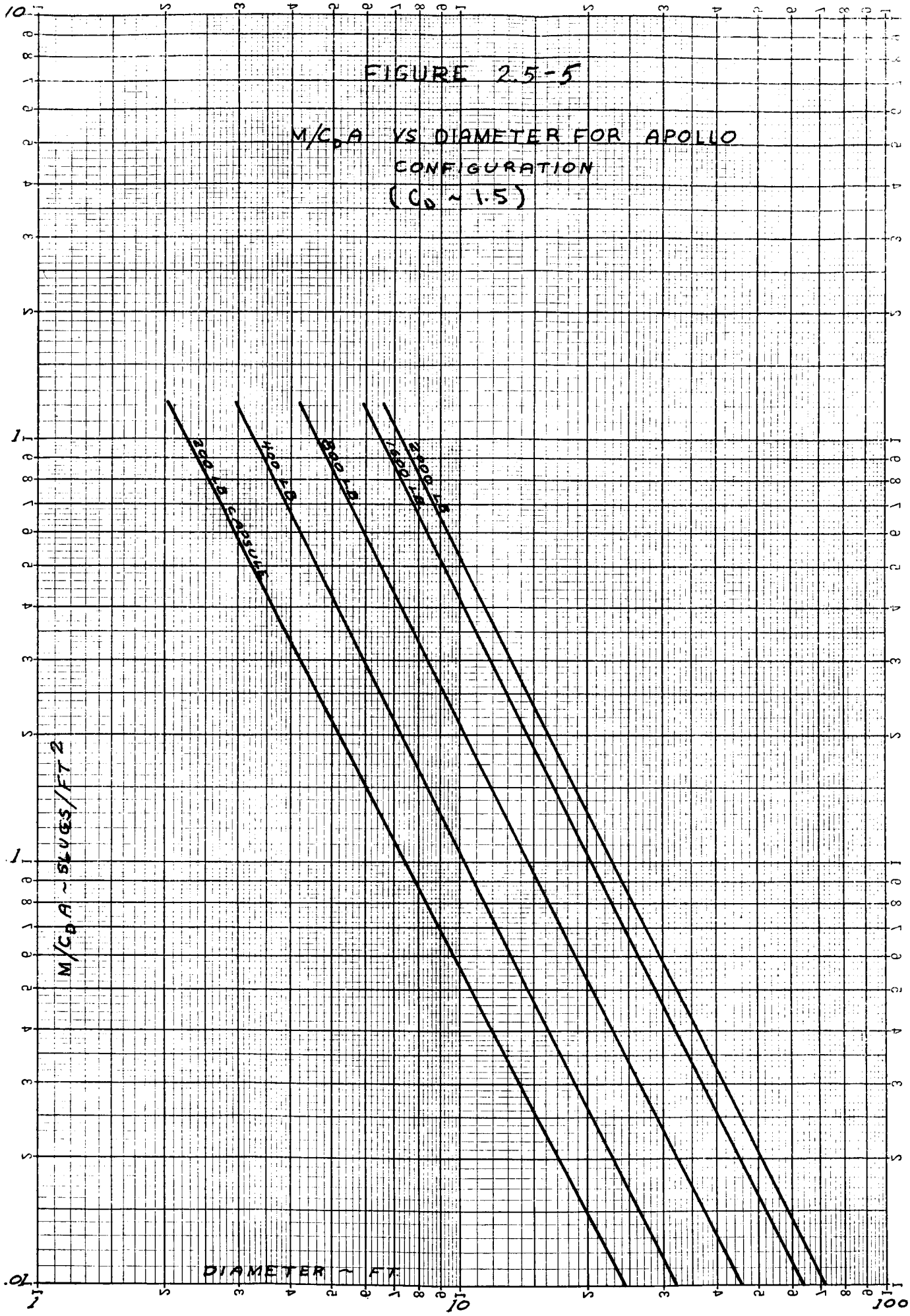

FIGURE 2.5-5

M/CDA VS DIAMETER FOR APOLLO CONFIGURATION ($C_D \sim 1.5$)

VOLUME & AREA VS DIAMETER FOR APOLLO CONFIGURATION

FIGURE 2.5-7

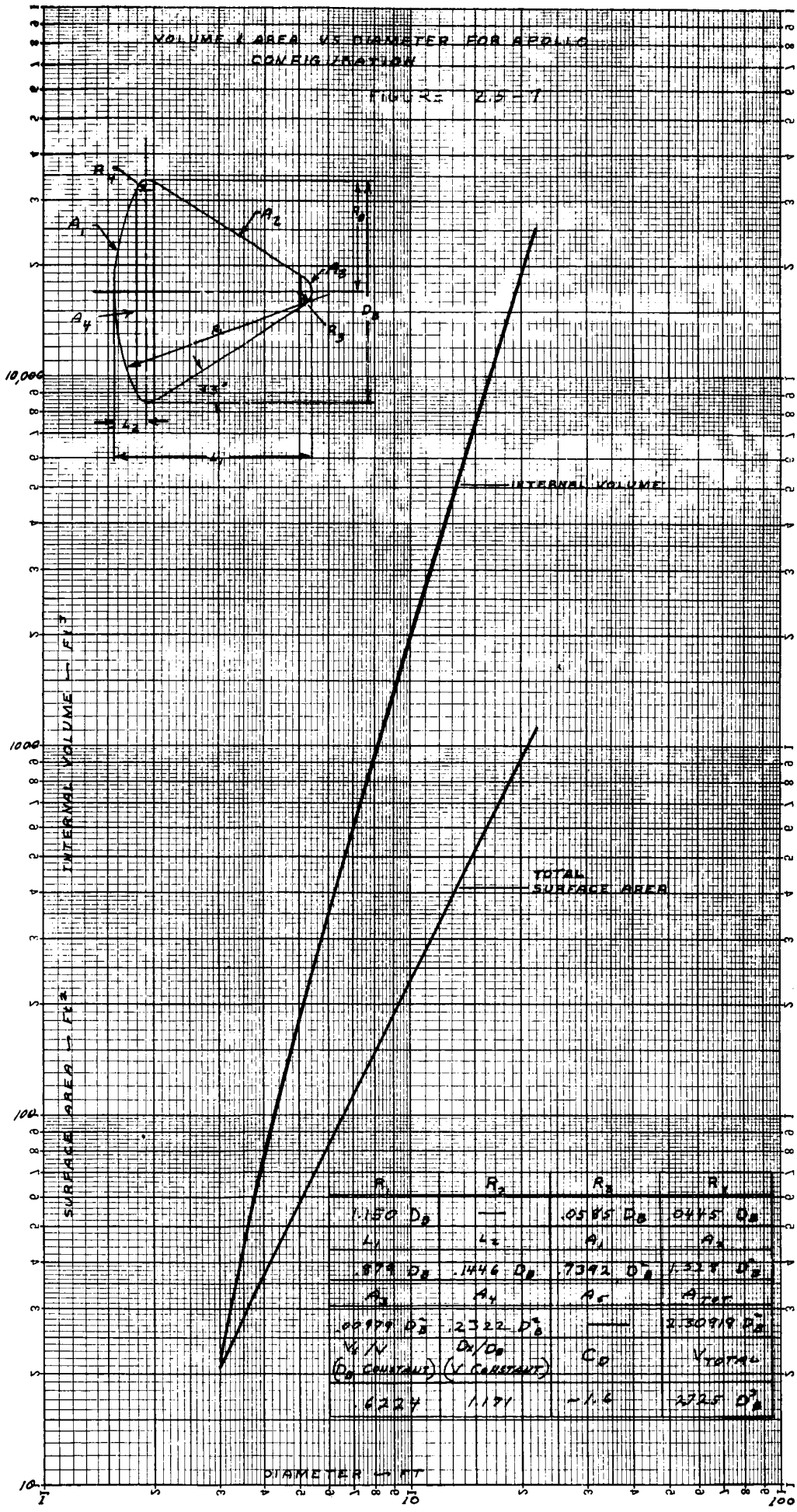

R_1	R_2	R_3	R_4
$1.150\ D_B$	—	$.0585\ D_B$	$.0445\ D_B$
L_1	L_2	A_1	A_2
$.879\ D_B$	$.1446\ D_B$	$.7392\ D_B^2$	$1.328\ D_B^2$
A_3	A_4	A_5	A_{TOT}
$.00979\ D_B^2$	$.2322\ D_B^2$	—	$2.30918\ D_B^2$
V_i/V (D_B CONSTANT)	D_x/D_B (V CONSTANT)	C_D	V_{TOTAL}
.6224	1.171	−1.6	$.2725\ D_B^3$

2.5.1 Antenna Considerations

The inboard antenna configuration suggested by JPL imposed certain design constraints on the capsule (e.g., requires radar transparent afterbody for pre-entry data transmission, limitations on parachute system placement; probable requirements for jettisoning afterbody to deploy chutes and transmit data, particularly if charring ablator material is employed for cone, etc.). A preliminary effort was made to assess the merits of an alternate 200 mc antenna system (to the one suggested) which would afford greater design flexibility and antenna capability. The antenna system considered would have full azimuthal coverage and a ± 100-degree/10 db beamwidth in elevation. It would consist of one or two concentric rings of four slots on the aft cone surface. A phase progression will be used in energizing these slots; if two rings are employed, the second ring will have a phase advance with respect to the first one in order to obtain a beam tilt of 30 degrees, thus providing maximum energy along the axis of the cone.

Since protrusions on the cone are undesirable, attention was directed to a flush mounting. One technique for flush mounting an antenna is to use a printed circuit on the dielectric material. Because of environmental considerations, this idea was abandoned. The next solution considered was half wave resonant slots cut in the skin of the cone.

Both circumferential and longitudinal slot orientations were considered. Longitudinal slots were rejected in favor of circumferential ones because the latter will direct more energy toward the apex of the cone and maximum on-axis energy is required.

The direction of radiation along the axis of a cone is determined by the position of the radiating elements of the cone and the nature of the bounding surfaces. The finite extent of the cone and the fact that the cone is probably truncated or at least rounded will introduce radiation components not entirely predictable; however, the antenna configuration selected provides maximum control of the radiation pattern.

In order to maximize radiation on the axis, two concentric rings having four slots each are positioned in the cone as shown in Figure 2.5-7. The slots in each ring will be fed in phase progression: 0 deg, 90 deg, 180 deg. The second ring of four slots, fed also in phase progression but with an advance in phase δ degrees with respect to the first is positioned at a distance m away from it to produce a beam tilt. By choosing m and δ properly, following the equation $2\pi(m/\lambda \cos\theta + n) = \delta$, where n is an integer and λ is the wave length, one can obtain a 30 degree beam tilt which theoretically will bring the maximum radiation in the same direction as the axis of the cone. The necessary phasing for different values of ring spacing, m, is as follows:

δ ~ degrees	m ~ inches
30	5.6
10	1.8
1.58	3

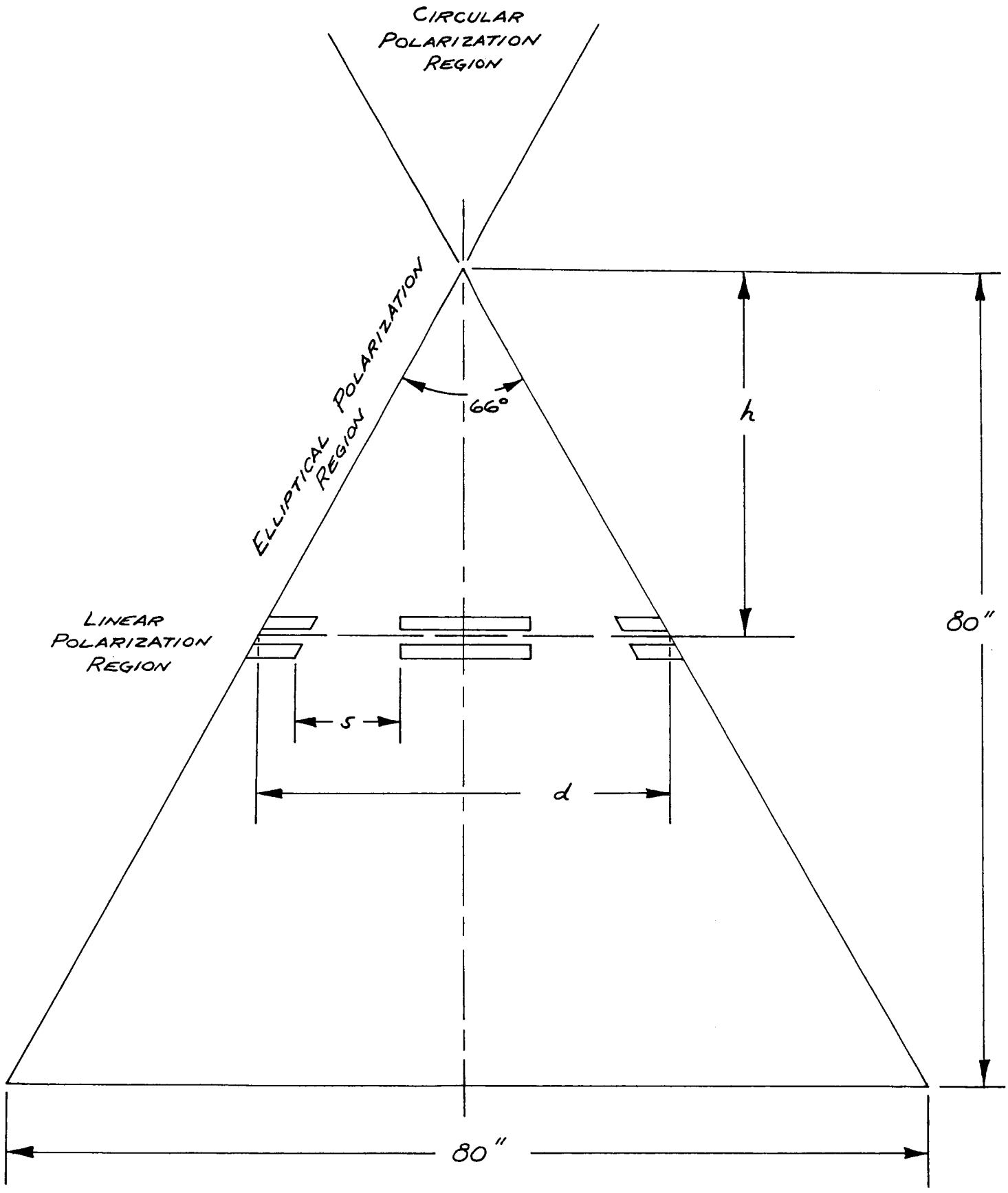

ANTENNA ELEMENT LOCATION

FIGURE 2.5-7

Because of weight considerations, a two-ring array was set aside in favor of a simple ring array. This ring alone will produce an omnidirectional pattern in azimuth. An observer situated in the far field of the antenna and on the axis of the cone will detect a circular polarization. As he moves off the axis, he will detect a gradual change from circular polarization to elliptical polarization and finally, in the plane of the slots, a linear polarization. Because the radiating slots are mounted on a curved surface, energy will have a tendency to creep on the surface and create disturbances in the pattern. Part of this disturbance can be predicted by matchint the field at the boundaries, as shown by S. Silver and L. L. Bailin (Reference 1).

Particular attention was given to the position of the slots along the axis of the cone, for the closer they are to the apex the better the radiation pattern on the axis. The lateral spacing, s, between slots versus their position in height, h, are shown below. It should be noted that the spacing, d, between slots has to be less than the wavelength to prevent multilobing.

d/λ	s ~ inches	h ~ inches
1.0	18.3	51
.796	9	40.7
.712	5	36.4

If after pattern calculations or experimental test it is found that the ring is not close enough to the apex of the cone, then it is suggested that the ring contain only three slots instead of four. This will allow the ring to be moved closer to the nose. Further help in this direction can be obtained by loading the slots, for example by using a dumbbell shape, in order to decrease the resonant length.

Each slot can either be backed by a ground plane to form a triplate antenna (See Figure 2.5-8) or be boxed in a cavity. In the case of a boxed-in slot the depth of the cavity must be $\frac{\lambda_g}{4}$. To reduce this dimension, it is suggested that the cavity be filled with a dielectric. This will serve two purposes; no radome is then necessary, and breakdown across the slot is reduced. The depth then becomes $\lambda_g = \lambda_0 / [E_r - (\lambda_0/\lambda_c)^2]^{1/2}$; where E_r is the relative dielectric chosen, λ_g is the wavelength in the cavity, and λ_c is the cutoff wavelength equal to 2a. The best suitable dielectric recommended for this application appears to be fused quartz foam of the type manufactured by Emerson and Cuming. Its dielectric constant is 1.4, its dissipation factor is 0.0005 across the frequency band of 60 to 10^{10} cps, and it can be used at 2000°F maximum for a long period of time without deterioration. Using this technique, the dimensions of the slot and the cavity then are:

slot length	=	ℓ	=	28 inches
slot width	=	w	=	6 inches
cavity depth	=	d	=	35 inches

GEOMETRY OF THE SLOT IN TRI-PLATE

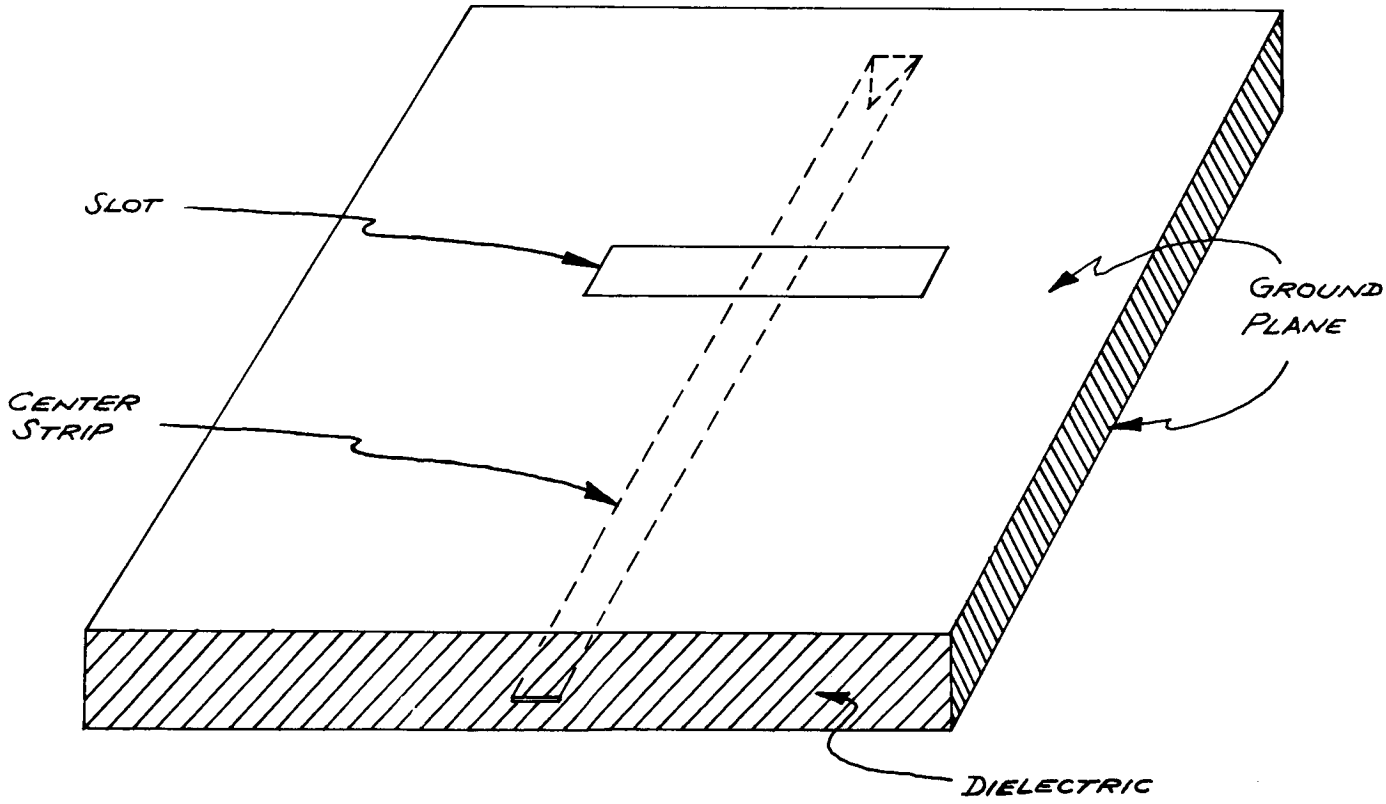

FIGURE 2.5-8

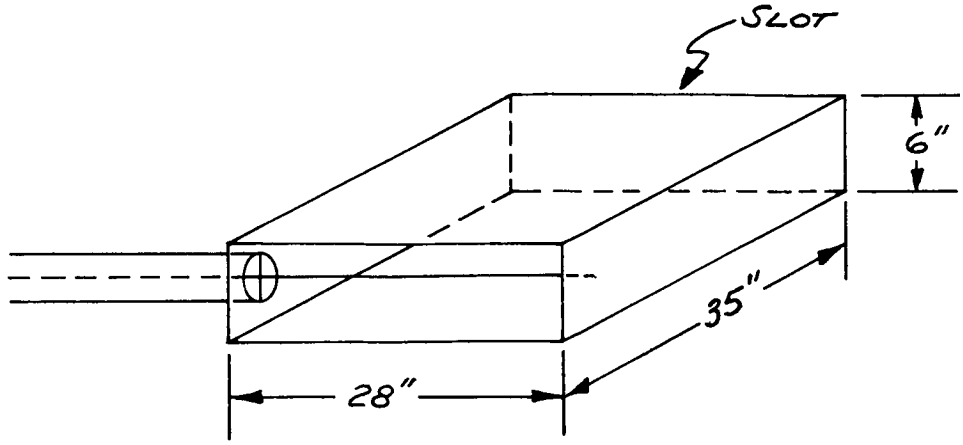

COAX FOR TE_{10} MODE EXCITATION

FIRST METHOD

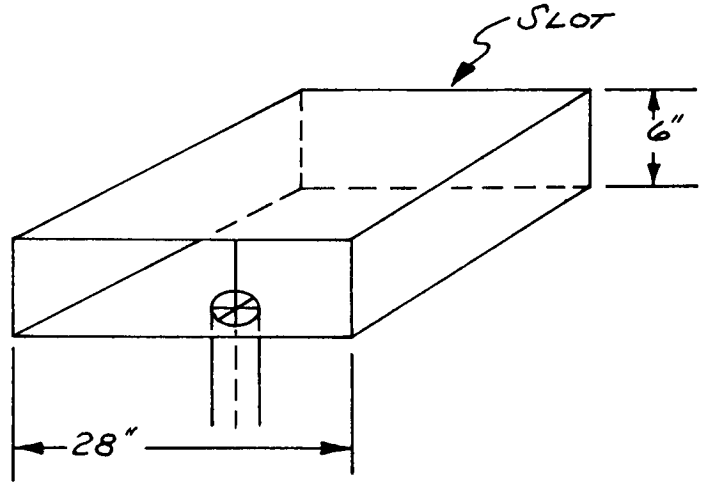

COAX FOR TE_{10} MODE EXCITATION

SECOND METHOD

ALTERNATE FEED METHOD FOR CAVITY BACKED SLOT

FIGURE 2.5-9

Although the use of a cavity having a quarter-guide wavelength depth gives the greatest bandwidth, the rather large dimensions involved make the configuration somewhat unattractive. A more useful cavity is attained if some reactive loading of the slot is employed. In this case, the cavity shortened so that it produces an inductive reactance at the slot. The slot is then loaded with parallel plates to create a compensating capacitive reactance and resonant the slot. Such a configuration would require only a six-inch depth of cavity rather than the 35 inches indicated with a quarter wavelength cavity. The price is a reduction of bandwidth and an increase in the field intensity in the slot. The bandwidth reduction is probably not serious since the system does not require all the available bandwidth but the increase in field intensity must be dealt with carefully if breakdown problems are to be avoided.

An attractive way to feed the slot would be with a tripline embedded in the same fused-quartz foam dielectric, as shown in Figure 2.5-3. The advantage of this technique is that the antenna becomes very thin in depth, approximately $\frac{1}{2}$ inch. The dimensions of the slot will remain the same, however.

It should be observed that the six-inch slot width is cited as being desirable from a bandwidth and field intensity standpoint. As noted above, the bandwidth is probably not required. Therefore, the slot width can be reduced if care is taken to solve the breakdown problem by suitable loading techniques. The feed system can utilize either printed circuit techniques on ceramic dielectric, or coaxial cables with proper length to obtain the desired phasing.

The relative weights of the slot versus the inboard antenna are presented in Section 3.5

2.5.2 References

1. S. Silver and L. L. Bailin, Boundries Value Pattern for Sphere and Cone, Trans. IRE, PGAP, Jan 1956

2.6 STRUCTURAL TRADEOFFS

2.6.1 Design Criteria

Nominal gross weights of 400 and 2000 pounds, respectively, were assumed initially for the smaller and larger capsules. (The small capsule weight was changed during the final selection to 350 pounds.) Since a range of capsule diameters from 4 ft. to approximately 20 ft. were considered, the structural study was conducted on a parametric basis, to determine structure weights compatible with the design requirements. Current materials and manufacturing techniques were considered for the end product.

The structure was designed as two elements: i.e., a forebody to carry the payload and systems and an afterbody to provide entry stability and payload protection. Both members were designed as compression carrying elements to fail in buckling under ultimate loads. The design conditions were defined by applying a 25% margin of safety to the ultimate loads or accelerations (Reference 1, and personal discussion with Herman Bank, JPL, on 9-27-63).

Loads resulting from boost, space flight, and Mars entry (including deceleration and impact) all were considered. The effects of these loading conditions are discussed below.

2.6.1.1 Boost Load Considerations

The load level imposed during launch on the vehicle and vehicle's components are below 10 g's and noncritical. The loads imposed on the entry vehicle structure by the bus will depend on the final design of the lander and bus supports within the booster's shroud. Since this condition was not defined, these loads could not be considered.

An Atlas-Centaur booster was assumed to be available for the Mariner B mission. Current data on this vehicle with a sandwich type shroud shows an accoustic pressure of 144 db on the external surface during boost. Assuming that the shroud will provide an attenuation of 20 db, the vehicle will sense an overall pressure level of 124 db. These pressures are equivalent to static pressure of about .0044 Psi to .044 Psi (Reference 2). After the spacecraft bus and lander are designed and load paths to the booster are determined, an analysis of natural frequencies of these bodies and components should be performed to check the effects of vibration input during boost. This investigation obviously is beyond the scope of this program. (Acoustic data for the advanced Saturn research vehicle, including the S-VI stage, are not available.)

The static pressures resulting from acoustic vibration do not design the structural components of the entry capsule.

2.6.1.2 Space Environmental Considerations

During flight the vehicle will not be subjected to any significant structural loads. Effects of thermal cycling, outgassing, meteoroid exposure, etc., on the structural materials used is discussed in Section 2.4.

Considerable data are available on the effects of size, frequency, velocity, density and impact of meteoroids in the vicinity of the Earth. The Mariner II flight to Venus indicated that the meteoroid hazard of interplanetary space may be four orders of magnitude lower. However, because of the asteroid belt, higher meteoroid concentrations may be encountered as Mars is approached.

The capsule is part of a bus/lander spacecraft for much of the mission. It is assumed that the bus will provide protection against meteoroid impact to part of the capsule. Until the vehicle arrangement is defined, an analysis of meteoroid protection requirements for the capsule appears unjustified.

2.6.1.3 Mars Entry Considerations

Two entry angles were considered: -90° and -20°. During entry, the vehicle is subjected to a condition of maximum heating, followed by a condition of maximum load. These conditions are out of phase with respect to time. For -20° entry, the maximum load (design load factor of 14 g's) is supported by a structure at less than 300° F. At the end of heating (240 seconds), this load is reduced to about 2.0 g's.

For -90° entry, the load factor can approach 200 g's; however, the entry time is so short that the structural temperature rise does not exceed 100° F. Symmetric entry (i.e., zero angle of attack) at $\gamma_c = -90°$ was selected as the critical condition for structural design. The lateral loads induced by such dynamic effects as oscillations, tumbling, etc. were included in the analysis.

After maximum deceleration, the afterbody may be jettisoned thus exposing the payload and landing system. The chute then will be deployed. After initial deployment and subsonic velocities are attained, the joint between the payload and forebody structure will be destroyed and the heat shield jettisoned. The parachute attachments are designed to apply the chute loads directly to the payload structure. Hence, load paths in the payload must be provided from the chute attach points to the support ring on the forebody.

Both the symmetrical entry loads and the lateral loads due to unsymmetrical and/or oscillatory entry impose compression loads on the forebody shell. If sandwich construction is used, a detailed study

is required to demonstrate core stability. This detailed analysis was considered beyond the scope of this contract.

The afterbody also was studied parametrically assuming symmetrical entry loads. Resulting thicknesses and weights for the selected designs were increased to allow for the effects of aerodynamic heating, vibration, and side loads, assuming that suitable stiffening webs and rings could be introduced.

2.6.2 Forebody Structural Design

The forebody was analyzed parametrically as a section of a spherical shell supporting a uniformly distributed pressure on the external surface. The pressure is reacted along a freely supported edge by the inertia of payload and structure. This loading corresponds to symmetric entry at zero angle of attack. For sandwich construction, the facings are supposed to fail under buckling stresses, while the core takes only the compressive load needed to transfer part of the pressure load to the inner face. The validity of this approach is questionable when shear or bending is introduced in the core. The stresses introduced in the edge support and load distribution when the design configurations were selected required local reinforcement of core and facings. The increase in weight due to these changes does not appear to be significant when compared with the capsule gross weight.

In the parametric study, the weight of the forebody structure was determined as a function of "Wg", the inertia load imposed on the structure by the mass of payload, landing system, and structure when decelerated during atmospheric entry.

If p is the external aerodynamic pressure on the dome, the following expressions have been developed to define the structure:

(1) $p = \dfrac{W \quad g}{\frac{\pi}{4} D_B^2}$

(2) $\sigma_{cr} = 0.54 \, E \, \dfrac{p}{R}$ (Reference 3)

(3) $\sigma = \dfrac{pR}{2 \, t_f}$ (Reference 1)

(4) $\rho = \sqrt{\dfrac{I}{A}} = \dfrac{h}{2}$ Radius of gyration

Combining (2), (3), and (4)

(5) $$t_f\, h = \frac{pR^2}{0.54\, E}$$

$$w_A = \gamma_c\, h + \gamma_f\, t_f + \gamma_G$$

$$= C\, \gamma_c\, h + \gamma_f\, t_f + \gamma_G$$

$$= C\, \gamma_f\, \frac{pR^2}{0.54E}\, t_f + \gamma_f\, t_f + \gamma_G$$

$$= C\, \gamma_f\, \frac{Wg}{\frac{\pi}{4} D_B^2}\, \frac{(1.15)^2\, D_B^2}{0.54\, E\, t_f} + \gamma_f\, t_f + \gamma_G$$

(6) $$= C\, \gamma_f\, \frac{W\, g}{E\, t_f}\, 3.13 + \gamma_f\, t_f + \gamma_G$$

$$\frac{dw}{dt_f} = - \frac{C\, \gamma_f\, W\, g\, 3.13}{E\, t_f^2} + \gamma_G$$

$$\frac{dw}{dt_f} = \gamma_f \left(1 - \frac{C\, W\, g}{E\, t_f^2}\, 3.13\right) = 0$$

(7) $$t_f = \frac{3.13\, C}{E}\, W\, g$$

from (6) $$h = 3.13\, \frac{Wg}{Et_f}$$

$$= 3.13\, \frac{Wg}{E} \sqrt{\frac{E}{\frac{3.13\, C}{Wg}}}$$

(8) $$w = 2\, \gamma_f \sqrt{\frac{3.13\, C}{E}\, Wg} + \gamma_G$$

Where:

w = structural weight (lb/ft^2)

$C = \frac{\gamma_c}{\gamma_f}$ = weight ratio of core to facing

γ_f = weight density ($lb/ft^2/in$) of faces

γ_c = weight density of core ($lb/ft^2/in$)

h = core depth (in)

t_f = $t_1 + t_2$ = total facing thickness (in)

γ_G = bond or brazing weight (lb/ft^2)

g = load factor

E = modulus of elasticity of sandwich facings

Equation (8) shows that:

(a) The weight per ft^2 of forebody structure is independent of the capsule diameter.

(b) w is directly proportional to $\sqrt{Wg}$, that is, to $\sqrt{\eta}$ where η is the load factor measured in earth g's.

(c) The structural unit weight is dependent on the operating temperature as it affects E and C. Both core density and facing thicknesses are limited by minimum values that reflect current manufacturing practice.

(d) γ_G, the adhesive bond weight, is a constant value independent of loading considerations.

The study was conducted for "Wg" values from 40 x 10^3 (η = 100 g's for a 400 lb capsule) to 70 x 10^4 (η = 350 g's for a 2000 lb capsule).

The weight of the forebody is given by:

$$w = c\,\gamma_f\,h + \gamma_f t_f + \gamma_G$$

Obviously, the results obtained by applying Equations (7) and (8) have to be rationalized by reviewing the minimum thicknesses allowed by current manufacturing practice.

Total weight of the dome structure is given by:

$$W_t = w\,A_d$$

$$A_d = .8553\,D^2 \text{ base}$$

A curve can be drawn to represent the dependency between weight per square foot and load, since Equation (8) may be rewritten as,

$$w = K_1\sqrt{Wg} + \gamma_G,$$

where K_1 is a function of amterial properties at the operating temperature considered. Furthermore, γ_G can be assumed as .260 lb/sq. ft.

(Reference 4) for HT 424 adhesive material 15 mills thick on both faces. Thus

$$w = K_1 \sqrt{Wg} + .260$$

where:

$$K_1 = 2 \sqrt{\frac{3.13\ C}{E}}$$

For brazed sandwich construction of high temperature materials, current practice indicates a value of 0.210 lb/ft^2 for γ_G.

2.6.2.1 Forebody Structural Concepts

2.6.2.1.1 Conventional Structures

The conventional forebody construction studied consists of a sandwich shell, with metallic facings and core, brazed or bonded with high temperature adhesive. The heat shield is attached to the base structure with a resilient type bond (e.g., silicone rubber) to reduce the effects of differential expansion between structure and heat shield. This type of structure is employed on Apollo and Gemini.

The core density has been kept to a minimum value consistent with the assumption that the core will transfer part of the aerodynamic pressure loads to the inner face sheet. If end constraints or payload support details should apply shear or bending loads, local reinforcements of the core and/or facings may be needed. Such reinforcements will not substantially increase the weight of the vehicle significantly, because the entire forebody structural weight is less than 10 percent of the gross weight.

There are two major disadvantages to the conventional type structure:

(a) The weight of adhesive and/or brazing material needed to bond the facings to the core and the heat shield to the structure represents a significant fraction of the structural weight. The weight of adhesive, e.g., type HT 424 for a .015 film thickness, is .260 lb/ft^2 (Reference 4), and the weight of the resilient silicone rubber required to attach the heat shield to the structure is calculated to be .335 lb/ft^2 if a thickness of 0.05 inches is employed.

(b) For sandwich construction using high-temperature resistant metals (beryllium, steel, titanium) or plastic laminates, the temperature limitations of the joint imposes a constraint,

which makes it impossible to realize the full strength potential of the structural materials.

The analyses performed during the parametric tradeoffs show the bonded aluminum construction for operating temperatures below 530° F and brazed PH 17-7 Mo steel for temperatures up to 900° F as the lightest for conventional metallic sandwich structures.

2.6.2.1.2 Composite Structures

Two non-metallic structures were analyzed. The first used asbestos reinforced facings with a structural insulation filler contained by glass phenolic webs, similar to Johns-Manville Min-K Interlock. This concept shows a weight advantage when compared to metal sandwich at high temperatures because of the excellant insulating properties of Min-K. It does not, however, solve the problem imposed by the bond-line temperature limit. Since there was no design requirement to limit the internal temperature of the capsule, the insulating properties of Min-K were not utilized.

The second composite construction is a new design conceived to answer the problems imposed by the adhesives; i.e., weight and temperature limitations. Basically, this concept involves the lamination of both facings of the sandwich and the core, or internal structure, together (Figure 2.6-1). To provide adequate common surfaces for lamination, the core was designed using square tubing, or hat sections with flanges, laminated to the fiber-reinforced resin shells by lay-up in a circular, or spiral pattern, to maintain symmetry about the capsule axis. The outer shell would be thick enough to serve as both the heat shield and structural element. This can be done quite efficiently with phenolic glass. If other materials, with radical differences between the resin content of the structural and ablative materials are employed, a first lamination between heat shield and outer shell, is required. This would eliminate the need for a resilient bond between these layers, since they are fabricated of one material.

Although this type of structure has not been fabricated previously in comparable sizes, the design merits further consideration because it offers the promise of being the lightest weight. Two experienced reinforced plastics manufacturers (Raybestos-Manhattan and Johns-Manville) who have developed commercial materials applying this principle have been approached and both agree on the feasibility of manufacture. Johns-Manville claims to have the tooling and appears willing to accept the responsibility of delivering a useful final product. (This type of construction is proposed only for the small capsule, because of present manufacturing facilities limit the size of dome which can be satisfactorily handled.) The weights analysis performed during the

parametric study of this construction employed material properties consistent with Johns-Manville data.

The properties of the material considered correspond to 30% resin content and 70% glass fiber. They are:

Coefficient of Thermal Expansion	=	5.0 to 6.0 x 10^{-6}
Specific gravity (maximum)	=	1.80
Flexural Strength	=	43000 psi
Tensile Strength	=	29000 psi
Compressive Strength	=	25000 psi
E (compression)	=	3.9 x 10^{6} psi

The following manufacturing process is proposed (Reference 6):

(a) Mold the outer shield by lay-up in a female die with vacuum draw, augmented by autoclave to 100 psi pressure.

(b) Mold the inner structure similarly except lay-up over a male die.

(c) The center labyrinth core to be of the same material as the outer shield; form, cure, and then bond to the outer and inner shells. Further studies of the lamination of this core to the shells is recommended to minimize bond weight.

(d) Initial material considered is glass fabric 181 with 91 LD resin because of previous space vehicle experience with this material (e.g., Mercury program).

2.6.2.2 Forebody Materials Tradeoffs

The following materials have been considered for the forebody sandwich construction:

(a) 5052 H39 aluminum facings and core, joined with high temperature adhesive film.

(b) PH 17-7 Mo steel facings and core, brazed.

(c) PH 17-7 Mo steel facings and 5052 H39 aluminum core, joined with high temperature adhesive film.

(d) 6 Al 4V titanium facings (both in annealed and fully aged S.T.A. conditions) and PH 17-7 Mo steel core, joined with high temperature adhesive film.

(e) 6 Al-4V titanium facings with 5052 H39 aluminum core.

(f) Cross rolled beryllium facings and core, brazed.

(g) Cross rolled beryllium facings and PH 17-7 Mo steel core, brazed.

(h) Composite structure of Min-Klad interlock with reinforced asbestos facings; reinforced glass webs and Min-K insulation.

(i) Composite structure, with facings and core of a material able to perform both as ablator, insulator, and load-carrying member. 91 LD resin with #181 glass fabric was the material considered for this type of construction. Materials trade-offs are done on a weight and temperature limitation basis.

Table 2.6-1 (a) through (f) present the structural analyses for the several materials and concepts. Parts (g) through (i) of Table 2.6-1 describe the sandwich core depth and facing thickness requirements for Wg = 70,000 lb. Figures 2.6-1, -2, and -3 summarize these results and show the unit weight as a function of Wg and temperature for the various structural concepts. In all cases, the core density has been kept to minimum values compatible with manufacturing practices (e.g., .0007 minimum thickness for aluminum foil, or .001 in thickness of steel foil with cell sizes of 1/8 to 3/8" (Reference 7). For the model developed in the parametric study, with simply supported edges and no concentration of loads, the core will only work under compression. If, during the design phase it is found that concentrated loads are applied to the shell, the facings and core will have to be reinforced locally by deepening of the sandwich, densifying the core and the use of doublers on the skins in order to take into account the shear and moments thus introduced.

The parameter $C = \gamma_c / \gamma_f$ has been chosen in all cases to reflect minimum core density at room temperature and was corrected at higher temperatures to reflect the reduction of Fcy and the increase in core weight required to keep the compression stresses in the core constant. For the glass phenolic composite structure, no value has been entered for γ_c (weight per ft^2 of adhesive film) since the facings and core are laminated together.

Because of the experience accumulated to date with conventional aluminum sandwich structures, this type of construction was chosen as a design basepoint for both the large and small capsules. It is temperature limited to applications below 525°F (Reference 5). At this temperature, the core weight penalty required to keep compressive stresses in the core equal to those on a minimum density core at room temperature are excessive. From 525°F to 900°F brazed PH 17-7 Mo steel is the lightest sandwich. For all sandwich structures bonded with epoxy-phenolic adhesive, structural temperatures are limited to 800°F for the short time exposures to be encountered. For brazed joints, the limiting temperature exceeds that of the metallic materials considered (Reference 7). However, all of the metallic constructions have the drawback of the weight and temperature limitations imposed by the adhesive and brazing compounds used to join facings to core.

Of all metallics considered, the cross rolled beryllium is the lightest for use at moderately high temperatures. Present technology of beryllium is being advanced at S&ID through company-funded studies; means of obtaining the thicknesses required in the sheet and plate sizes needed, as well as the joining and forming techniques that will allow fabrication of the forebody as a corrugated sandwich structure, are expected to be available in the near future. Further investigation of this approach is recommended. The gages indicated for beryllium-beryllium and beryllium-steel sandwich are shown in Table 2.6-1(e) to (f); however, they obviously can not be fabricated practically at this time.

Two non-metallic composite structures also have been studied. These include a Johns-Manville Min-K Interlock type (Reference 8) using the properties for low pressure molded reinforced facings (Reference 9) and a Min-K filled reinforced plastic interlock core. This type of sandwich was too heavy since the insulating properties of Min-K are not needed in this design.

An integrated type of construction also was considered where the structural and heat shield subsystems are composed of the same homogeneous material by integrally laminating the inner facing, core, and/or stabilizing webs, outer facing and heat shield (Table 2.6-1(e) and (f). This system obviously mitigates the problem of differential expansion coefficients between the shield and structure and also can result in a net weight saving by eliminating the bonding requirements. As indicated previously, the fabricability has been investigated for #181 glass fiber reinforced 91LD phenolic resin. The results of these surveys indicate that manufacture of such a composite having the desired structural and thermal properties appears feasible for the small capsule.

In summary, aluminum sandwich construction was chosen as a design basepoint for the forebodies of both the large and small capsules because of the backlog of accumulated experience with this type of structure. However, investigation of the composite material concepts and beryllium for the forebody design should be continued because of the considerable potentials they offer in weight reduction and amelioration of thermal expansion and bond temperature problems.

2.6.3 Afterbody Structural Design

The function of the afterbody is both to enhance stability and to protect the inboard capsule systems (e.g., payload and landing system) from the space and entry environment. The basepoint design includes an inboard antenna and thus the afterbody must be made of r.f. transparent material (e.g., reinforced fiberglass). It was assumed further that the fiberglass afterbody would char during entry and, therefore, it would be jettisoned prior to initiation of data transmission after parachute deployment. (Details of the afterbody release mechanism are presented in another section of this report.) An alternate antenna design considered had flush-mounted slot antennas on the afterbody, employing an aluminum afterbody structure.

The small capsule studies were confined to the Apollo configuration and, therefore, the aft cone included angle was 66°. In the case of the large capsule, there was an obvious excess of volume over that required to house the payload and landing systems. Three afterbody configurations therefore were considered in an attempt to reduce the weight of the large capsule by eliminating the aft cone. These included a) a 66° Apollo-type aft cone to serve as a basepoint, b) a 180° flat plate enclosing the backface of the forebody, and c) enshrouding the payload with a "form-fitting" protective cover. The third concept, (c), obviously offers the greatest potential for weight saving. Only the aft cone configuration was analyzed. Stability considerations are discussed in Section 2.10.

2.6.3.1 Aft Cone Structural Analysis

The wall of the cone was sized to support its own weight under the load factors given by the maximum aerodynamic deceleration forces encountered during entry (i.e., 200 g's). Under these conditions, a section of the base of the cone will be critical in buckling. Calculations were made for a long cylinder of the same radius, as a monocoque shell (Reference 10). A previous analysis shows that, at least for the small capsule, monocoque construction is lighter than sandwich. The study was performed parametrically for radii of 18 inches to 120 inches and for thicknesses of at least 0.010 inches. Aluminum and plastic materials, at diffferent temperatures, were considered.

The weight of the cone, for a constant wall thickness t, is:

$$W_c = \delta t \quad A_c$$

where

A_c, the wall area for the Apollo shape, is

$$A_c = A_3 + A_2 + 1/2\ A_4 = 1.454\ D_B^2 (ft^2)$$

$$\therefore W_c = \delta t (1.454) D_B^2$$

The load is $(W_c \times \eta)$, where η is the load factor as measured in earth g's. The analysis of the aluminum afterbody was based on room temperature properties. For high temperature conditions, the allowable load factors η are ratioed down according to the following scale:

$$200° = \eta_{RT} \frac{E_{200}}{E_{RT}} = 98\% \ \eta_{RT}$$

$$400° = 90\% \ \eta_{RT}$$

$$600° = 70\% \ \eta_{RT}$$

A similar analysis was performed for a glass reinforced afterbody made of 91LD resin and #181 glass fiber. The material properties employed are de-

scribed in References 5 and 11.

Figures 2.6-5 and 2.6-6 show the plastic aft cone thicknesses required and weights as a function of base diameter load factor and temperature. Figures 2.6-7 shows the weights of an aluminum monocoque aft cone. Figures 2.6-8 and 2.6-9 are similar to 2.6-5 and 2.6-6, except that they are for aluminum. (Although the r.f. transparency requirement precludes the use of an aluminum afterbody, these data were employed in the design of the slotted antenna configuration.) The detailed aft cone engineering calculations are presented in Tables 2.6-2(a) to (f) for the plastic and Tables 2.6-2(g) to (l) for the aluminum.

Time limitations did not permit a detailed analysis to account for the effects on the aft cone of acoustic vibrations, buffeting, and the dynamic oscillations encountered during entry. Provision, however, is made for the weight of reinforcing rings and webs in the weights analysis.

2.6.4 References

1. R. J. Roark, "Formulas for Strain & Stress" McGraw Hill Company, 1954

2. NASA TN D 1502 - "Noise Measurements During Captive and Launch Firings of a Large Rocket-Powered Vehicle," W. H. Mayer & P. M. Edge, Jr., Nov. 1962

3. MM 62/19/5 "The Buckling of Domed Bulkheads Subjected to Collapsing Pressure" F. Rish, NAA, S&ID, 9 Jan 62

4. The Bloomingdale Rubber Adhesive Handbook

5. MIL-HDBK5 "Strength of Metal Aircraft Elements" March 1961

6. P. J. Paetzold, Johns-Manville letter to M. G. Boobar, 30 Sept 1963

7. NAA/S. L100 "The Design and Analysis of Sandwich Construction, 10 April 1962

8. Johns-Manville Insulation Handbook

9. Raybestos Manhattan Data Sheets

10. NACA TN 3783 - Handbook of Structural Stability, Part III, Buckling of Curved Plates and Shells - G. Gerard & H. Becker, 1957

11. MIL-HDBK 17 "Plastics for Flight Vehicles," Nov 1959

Weight of Dome Structure per ft²

$$\omega = K_1\sqrt{Wg} + \gamma_G = 2\gamma_f\sqrt{\frac{3.13\,C}{E}}\sqrt{Wg} + \gamma_G$$

NORTH AMERICAN AVIATION, INC.
SPACE and INFORMATION SYSTEMS DIVISION

Prepared By: ASM
Checked By:
Date: 9/19/63
Page No. of
Report No.
Model No. Voyager

1	2	3	4	5	6	7	8	9	10	11	12	13	14	15
Mat'l Facing	δ_f Lb/in²	γ_f Lb/Ft²in	Mat'l Core	C γ_c/γ_f	E_T $\times 10^{-6}$	$\sqrt{\frac{3.13C}{E}}$ $\times 10^4$	③ × ⑦ $\times 10^4$	K_1 2 × ⑧ $\times 10^3$	Type of Joint	γ_G Lb/Ft²	$Wg = 40000$ $\sqrt{Wg} = 200$ $K_1\sqrt{Wg}$	ω_{40K} Lb/Ft² ⑪ + ⑫	$Wg = 60000$ $\sqrt{Wg} = 245$ $K_1\sqrt{Wg}$	ω_{60000} Lb/Ft² ⑪ + ⑭
5052 H39 Aluminum	.100	14.4	5052 H39 Aluminum	.015	RT & 100 10	.685	9.85	1.97	HR Bonded	.260	.394	.654	.482	.742
				.015	200 9.8	.692	9.96	1.99			.398	.658	.488	.748
				.015	300 9.5	.704	10.15	2.03			.406	.666	.497	.757
				.015	400 9.0	.720	10.38	2.07			.414	.674	.506	.766
				.017	500 8.0	.810	11.65	2.33			.466	.726	.571	.831
5052 H39 Aluminum	.100	14.4	5052 H39 Aluminum	.019	530 7.8	.874	12.58	2.52	HR Bonded	.260	.504	.764	.617	.877
PH 17-7Mo Steel	.276	39.7	PH 17-7Mo Steel	.015	RT & 100 30	.396	15.6	3.12	Brazed	.210	.624	.834	.766	.976
				.0156	200 30	.404	15.9	3.18			.636	.846	.780	.990
				.0163	300 29.6	.415	16.35	3.27			.654	.864	.803	1.013
				.0169	400 28.9	.428	16.9	3.38			.676	.886	.830	1.040
				.0177	500 28.2	.442	17.4	3.48			.696	.906	.854	1.064
				.0187	600 27.0	.465	18.3	3.66			.732	.942	.899	1.109
				.0203	700 25.8	.496	19.6	3.92			.784	.994	.962	1.172
				.0235	800 24.6	.545	21.45	4.29			.858	1.018	1.055	1.265
PH 17-7Mo Steel	.276	39.7	PH 17-7Mo Steel	.030	900 23.1	.636	25.1	5.02	Brazed	.210	1.004	1.214	1.230	1.440
PH 17-7Mo Steel	.276	39.7	5052 H39 Aluminum	.006	RT & 100 30	.250	9.92	1.984	Bonded	.260	.397	.657	.486	.746
				.006	200 30	.250	9.92	1.984			.397	.657	.486	.746
				.006	300 29.6	.252	10.00	2.000			.400	.860	.490	.750
				.006	400 28.9	.256	10.30	2.060			.412	.672	.505	.765
				.007	500 28.2	.279	11.05	2.210			.442	.702	.542	.802
PH 17-7Mo Steel	.276	39.7	5052 H39 Aluminum	.008	530 27.6	.301	11.95	2.390	Bonded	.260	.478	.738	.586	.846

TABLE 2.6-1.(a)

Weight of Dome (Forebody) Struct. Lb/ft²

$$\omega = K_1\sqrt{W_g} + \gamma_G = 2\gamma_f\sqrt{\frac{3.13C}{E}}\sqrt{W_g} + \gamma_G$$

NORTH AMERICAN AVIATION, INC.
SPACE and INFORMATION SYSTEMS DIVISION

Prepared By: | Page No. of
Checked By: | Report No.
Date: | Model No.

1	2	3	4	5	6	7	8	9	10	11	12	13	14	15
Mat'l Facing	Mat'l Core	γ_G	K_1 $\times 10^3$	$W_g = 100000$ $\sqrt{W_g} = 316$ $K_1\sqrt{W_g}$	ω_{100K} Lb/ft² ③+⑤	$W_g = 150000$ $\sqrt{W_g} = 387$ $K_1\sqrt{W_g}$	ω_{150K} Lb/ft² ③+⑦	$W_g = 300000$ $\sqrt{W_g} = 547$ $K_1\sqrt{W_g}$	ω_{300K} Lb/ft² ③+⑨	$W_g = 500000$ $\sqrt{W_g} = 706$ $K_1\sqrt{W_g}$	ω_{500K} Lb/ft² ③+⑪	$W_g = 700000$ $\sqrt{W_g} = 836$ $K_1\sqrt{W_g}$	ω_{700000} Lb/ft² ③+⑬	Temp °F
5052 H39 Al Alloy	5052 H39 Al Alloy	.260	1.97	.623	.883	.762	1.022	1.079	1.339	1.392	1.652	1.650	1.910	RT
			1.99	.630	.890	.770	1.030	1.090	1.350	1.408	1.668	1.665	1.925	200
			2.03	.642	.902	.785	1.045	1.111	1.371	1.435	1.695	1.700	1.960	300
			2.07	.655	.915	.802	1.062	1.133	1.393	1.465	1.725	1.730	1.990	400
			2.33	.736	.996	.900	1.160	1.275	1.535	1.645	1.905	1.950	2.210	500
5052 H39 Al Alloy	5052 H39 Al Alloy	.260	2.52	.796	1.056	.975	1.235	1.380	1.640	1.780	2.040	2.110	2.370	530
PH17-7Mo Steel	PH17-7Mo Steel	.210	3.12	.986	1.196	1.210	1.420	1.710	1.920	2.210	2.420	2.610	2.820	RT
			3.18	1.008	1.218	1.230	1.440	1.745	1.955	2.250	2.460	2.660	2.870	200
			3.27	1.035	1.245	1.265	1.475	1.790	2.000	2.310	2.520	2.735	2.945	300
			3.38	1.070	1.280	1.310	1.520	1.850	2.060	2.390	2.600	2.830	2.940	400
			3.48	1.100	1.310	1.350	1.560	1.910	2.120	2.460	2.670	2.910	3.120	500
			3.66	1.160	1.370	1.415	1.625	2.000	2.210	2.590	2.800	3.060	3.270	600
			3.92	1.240	1.450	1.520	1.730	2.150	2.360	2.770	2.980	3.280	3.490	700
			4.29	1.358	1.568	1.660	1.870	2.350	2.560	3.030	3.240	3.580	3.790	800
PH17-7Mo Steel	PH17-7Mo Steel	.210	5.02	1.590	1.800	1.945	2.155	2.750	2.960	3.550	3.760	4.200	4.410	900
PH17-7Mo Steel	5052 H39 Aluminum	.260	1.984	.626	.886	.769	1.029	1.085	1.345	1.405	1.665	1.660	1.920	RT
			1.984	.626	.886	.769	1.029	1.085	1.345	1.405	1.665	1.660	1.920	200
			2.000	.633	.893	.775	1.035	1.095	1.355	1.415	1.675	1.675	1.935	300
			2.060	.650	.910	.798	1.058	1.155	1.415	1.455	1.735	1.725	1.985	400
			2.210	.700	.960	.855	1.115	1.210	1.470	1.560	1.820	1.850	2.110	500
PH17-7Mo Steel	5052 H39 Aluminum	.260	2.390	.755	1.015	.925	1.185	1.310	1.570	1.690	1.950	2.000	2.260	530

TABLE 2.6-1 (b)

Weight of Dome (Forebody) Struct. per ft²

$\omega = K_1\sqrt{Wg} + \gamma_G = 2\gamma_f\sqrt{\frac{3.13C}{E}}\sqrt{Wg} + \gamma_G$

NORTH AMERICAN AVIATION, INC.
SPACE and INFORMATION SYSTEMS DIVISION

Prepared By: A.S.M. | Page No. of
Checked By: | Report No.
Date: 9/19/63 | Model No. Voyager

1 Mat'l Facing	2 δ_f Lb/in³	3 γ_f Lb/Ft²in	4 Mat'l Core	5 C γ_c/γ_f	6 E_T ×10⁻⁶	7 $\sqrt{\frac{3.13C}{E}}$ ×10⁴	8 (3)×(7) ×10⁴	9 K_1 2×(8) ×10³	10 Type of Joint	11 γ_G Lb/Ft²	12 Wg=40000 √Wg=200 $K_1\sqrt{Wg}$	13 ω_{40000} Lb/Ft² (11)+(12)	14 Wg=60000 √Wg=245 $K_1\sqrt{Wg}$	15 ω_{60000} Lb/Ft² (11)+(14)
6Al 4V Ti Annealed	.160	23.0	PH 17-7Mo Steel	.029	RT 15.0	.779	17.90	3.58	Bonded	.260	.716	.976	.873	1.133
				.030	200 14.1	.815	18.75	3.75			.750	1.010	.920	1.180
				.031	300 13.65	.844	19.40	3.88			.776	1.036	.952	1.212
				.033	400 13.2	.885	20.15	4.03			.806	1.066	.990	1.250
				.034	500 12.6	.920	21.15	4.23			.846	1.106	1.040	1.300
				.036	600 12.15	.964	22.15	4.43			.886	1.146	1.085	1.345
				.039	700 11.70	1.020	23.45	4.69			.938	1.198	1.150	1.410
6Al 4V Ti Annealed	.160	23.0	PH 17-7Mo Steel	.045	800 11.1	1.125	25.80	5.16	Bonded	.260	1.032	1.292	1.265	1.515
6Al 4V Ti STA.	.160	23.0	PH 17-7Mo Steel	.029	RT 16.3	.746	17.15	3.43	Bonded	.260	.686	.946	.841	1.101
				.030	200 15.9	.770	17.70	3.54			.708	.968	.868	1.128
				.031	300 15.5	.791	18.20	3.64			.728	.988	.892	1.152
				.033	400 15.1	.829	19.05	3.81			.762	1.022	.935	1.195
				.034	500 14.7	.852	19.60	3.92			.784	1.044	.961	1.221
				.036	600 14.3	.889	20.45	4.09			.818	1.078	1.000	1.260
				.039	700 13.9	.938	21.55	4.31			.862	1.122	1.058	1.318
6Al 4V Ti STA	.160	23.0	PH 17-7Mo Steel	.045	800 13.5	1.020	23.50	4.70	Bonded	.260	.940	1.200	1.155	1.415
6Al 4V Ti STA	.160	23.0	5052 H39 Aluminum	.010	RT 16.3	.438	10.10	2.02	Bonded	.260	.404	.664	.495	.755
				.010	200 15.9	.444	10.20	2.04			.408	.668	.500	.760
				.010	300 15.5	.450	10.34	2.07			.414	.674	.508	.768
				.010	400 15.1	.455	10.48	2.10			.420	.680	.515	.775
				.0113	500 14.7	.490	11.25	2.25			.450	.710	.552	.812
6Al 4V Ti STA	.160	23.0	5052 H39 Aluminum	.0127	530 14.5	.524	12.05	2.41	Bonded	.260	.482	.742	.590	.850

TABLE 2.6.1.(C)

Weight of Dome (Forebody) Structure Lb/ft²

$$W = K_1\sqrt{Wg} + \gamma_G = 2\gamma_F\sqrt{\frac{313C}{E}}\sqrt{Wg} + \gamma_G$$

NORTH AMERICAN AVIATION, INC.
SPACE and INFORMATION SYSTEMS DIVISION

Prepared By: | Page No. of
Checked By: | Report No.
Date: | Model No.

1	2	3	4	5	6	7	8	9	10	11	12	13	14	15
Mat'l Facing	Mat'l core	γ_G Lb/ft²	K_1 ×10³	$Wg = 10^5$, $\sqrt{Wg} = 316$, $K_1\sqrt{Wg}$	ω_{10^5} Lb/ft² (3)+(5)	$Wg = 15\times10^4$, $\sqrt{Wg} = 387$, $K_1\sqrt{Wg}$	$\omega_{15\times10^4}$ Lb/ft² (3)+(7)	$Wg = 30\times10^4$, $\sqrt{Wg} = 547$, $K_1\sqrt{Wg}$	$\omega_{30\times10^4}$ Lb/ft² (3)+(9)	$Wg = 50\times10^4$, $\sqrt{Wg} = 706$, $K_1\sqrt{Wg}$	$\omega_{50\times10^4}$ Lb/ft² (3)+(11)	$Wg = 70\times10^4$, $\sqrt{Wg} = 836$, $K_1\sqrt{Wg}$	$\omega_{70\times10^4}$ Lb/ft² (3)+(13)	Temp. °F
6Al 4V Ti Annealed	PH 17-7Mo Steel	.260	3.58	1.132	1.392	1.387	1.647	1.960	2.220	2.530	2.790	3.000	3.260	RT
			3.75	1.185	1.445	1.455	1.715	2.055	2.315	2.650	2.910	3.140	3.400	200
			3.88	1.225	1.485	1.505	1.765	2.125	2.385	2.750	3.010	3.250	3.510	300
			4.03	1.275	1.535	1.560	1.820	2.210	2.470	2.850	3.110	3.380	3.640	400
			4.23	1.340	1.600	1.640	1.900	2.320	2.580	2.990	3.250	3.540	3.800	500
			4.43	1.400	1.660	1.715	1.975	2.430	2.690	3.130	3.390	3.710	3.970	600
			4.69	1.480	1.740	1.815	2.075	2.570	2.830	3.320	3.580	3.920	4.180	700
6Al 4V Ti Annealed	PH 17-7Mo Steel	.260	5.16	1.630	1.890	2.000	2.260	2.825	3.085	3.650	3.910	4.320	4.580	800
6Al 4V Ti STA	PH 17-7Mo Steel	.260	3.43	1.085	1.345	1.330	1.590	1.880	2.140	2.425	2.685	2.870	3.130	RT
			3.54	1.120	1.380	1.370	1.630	1.940	2.200	2.500	2.760	2.960	3.220	200
			3.64	1.150	1.410	1.410	1.670	1.995	2.255	2.570	2.830	3.050	3.310	300
			3.81	1.205	1.465	1.475	1.735	2.085	2.345	2.695	2.955	3.190	3.450	400
			3.92	1.240	1.500	1.520	1.780	2.150	2.410	2.770	3.030	3.280	3.540	500
			4.09	1.290	1.550	1.585	1.845	2.240	2.500	2.890	3.150	3.420	3.680	600
			4.31	1.365	1.625	1.670	1.930	2.360	2.620	3.050	3.310	3.610	3.870	700
6Al 4V Ti STA	PH 17-7Mo Steel	.260	4.70	1.485	1.745	1.820	2.080	2.570	2.830	3.325	3.585	3.930	4.190	800
6Al 4V Ti STA	5052 H39 Al	.260	2.02	.640	.900	.784	1.044	1.105	1.365	1.430	1.690	1.690	1.950	RT
			2.04	.645	.905	.790	1.050	1.118	1.378	1.445	1.705	1.710	1.970	200
			2.07	.655	.915	.802	1.062	1.135	1.395	1.465	1.725	1.730	1.990	300
			2.10	.665	.925	.814	1.074	1.150	1.410	1.485	1.745	1.755	2.015	400
			2.25	.712	.972	.872	1.132	1.230	1.490	1.590	1.850	1.880	2.140	500
6Al 4V Ti STA	5052 H39 Al	.260	2.41	.760	1.020	.935	1.195	1.320	1.580	1.700	1.960	2.020	2.280	530

TABLE 2.6r/(d)

Weight of Dome Structure per ft²

$\omega = K_1\sqrt{W_g} + \gamma_g = 2\gamma_f\sqrt{\frac{3.13C}{E}}\sqrt{W_g} + \gamma_G$

NORTH AMERICAN AVIATION, INC.
SPACE and INFORMATION SYSTEMS DIVISION

Prepared By: A.S.M. | Page No. of
Checked By: | Report No.
Date 9-13-63 | Model No. Voyager

1	2	3	4	5	6	7	8	9	10	11	12	13	14	15
Mat'l facing	γ_f Lb/in³	γ_f Lb/Ft²in	Mat'l Core	C γ_c/γ_f	E_t $\times 10^{-6}$	$\sqrt{\frac{3.13C}{\times 10^{-4}E}}$	(3)×(7) $\times 10^{-4}$	K_1 $2\times$(8) $\times 10^{-3}$	Type of Joint	γ_G Lb/Ft²	$W_g = 40000$, $\sqrt{W_g} = 200$, $K_1\sqrt{W_g}$	ω_{40000} Lb/Ft² (11)+(12)	$W_g = 60000$, $\sqrt{W_g} = 245$, $K_1\sqrt{W_g}$	ω_{60000} Lb/Ft² (11)+(14)
#181 PG 91-LD	.064	9.25	Reinf	.030	100°F 3.2	1.715	15.81	3.162	Laminated	—	.632	.632	.776	.776
			Glass	.033	200°F 3.15	1.810	16.75	3.350		—	.670	.670	.821	.821
				.035	300°F 3.05	1.895	17.55	3.510		—	.702	.702	.860	.860
				.039	400°F 2.90	2.050	19.00	3.800		—	.760	.760	.931	.931
				.050	500°F 2.70	2.410	22.30	4.460		—	.892	.892	1.092	1.092
#181 PG 91-LD	.064	9.25		.066	550°F 2.60	2.820	26.15	5.239	Laminated	—	1.046	1.046	1.281	1.281
Cross Rolled Beryllium	.067	9.65	PH17-7Mo Steel	RT .062	RT 42	.680	6.49	1.298	Brazed	.210	.260	.470	.318	.528
				300 .067	300 42	.706	6.75	1.350			.270	.480	.331	.541
				500 .073	500 41.5	.741	7.07	1.414			.283	.493	.347	.557
				700 .083	700 39.4	.810	7.73	1.546			.309	.519	.379	.589
Cross Rolled Beryllium	.067	9.65	Steel	900 .123	900 35.6	1.040	9.93	1.986	Brazed	.210	.398	.608	.486	.696
CR Be	.067	9.65	CR Be	* .015	RT 42	.334	3.22	.644	Brazed	.210	.129	.339	.157	.367
				.018	200 42	.366	3.53	.706			.141	.351	.173	.383
				.020	400 42	.386	3.72	.744			.149	.359	.182	.392
				.022	600 41	.410	3.96	.792			.158	.368	.194	.402
				.025	800 37.5	.457	4.41	.882			.177	.387	.216	.426
CR Be	.067	9.65	CR Be	.035	1000 33.7	.570	5.50	1.100	Brazed	.210	.220	.430	.270	.480
Reinf. Asbestos AIRPO TYPE	.058	8.40	MINK Type Struct. Insul. Interlock	.200	RT 3.8	4.060	34.20	6.84	Bonded	.260	1.368	1.628	1.675	1.935
					500 3.8	4.060	34.20	6.84			1.368	1.628	1.675	1.935
					800 2.9	4.650	39.00	7.80			1.560	1.820	1.915	2.175
Reinf. Asbestos AIRPO Type	.058	8.40	MINK Type Struct. Insul Interlock	.200	1000 2.1	5.460	45.90	9.18	Bonded	.260	1.836	2.096	2.250	2.510

* This value of C is high, but assumed equal to Al & steel because of manufacturing considerations

TABLE 2.6-1 (e)

Weight of Dome Structure

$w = K_1\sqrt{W_g} + \gamma_g = 2\gamma_f\sqrt{\frac{C\,3.13}{E}}\sqrt{W_g} + \gamma_g$

NORTH AMERICAN AVIATION, INC.
SPACE and INFORMATION SYSTEMS DIVISION

Prepared By: ASM
Checked By:
Date: 9/16/63
Page No. of
Report No.
Model No.

1	2	3	4	5	6	7	8	9	10	11	12	13	14	15
Mat'l facing	Mat'l Core	γ_g LL/FT²	$K_1 \times 10^3$	$W_g = 80000$, $\sqrt{W_g} = 283$, $K_1\sqrt{W_g}$	W_{80000} LB/FT² (3)+(5)	$W_g = 100000$, $\sqrt{W_g} = 316$, $K_1\sqrt{W_g}$	W_{100000} LB/FT² (3)+(7)	$W_g = 200000$, $\sqrt{W_g} = 446$, $K_1\sqrt{W_g}$	W_{200000} LB/FT² (3)+(9)	$W_g = 300000$, $\sqrt{W_g} = 547$, $K_1\sqrt{W_g}$	W_{300000} LB/FT² (3)+(11)	$W_g = 400000$, $\sqrt{W_g} = 632$, $K_1\sqrt{W_g}$	W_{400000} LB/FT² (3)+(13)	T °F
#181 PG 91-LD	Reinf Glass	–	3,162	.896	.896	.999	.999	1.410	1.410	1.731	1.731	1.998	1.998	100
		–	3,550	.948	.948	1.059	1.059	1.494	1.494	1.835	1.835	2.117	2.117	200
		–	3,570	.993	.993	1.109	1.109	1.565	1.565	1.920	1.920	2.218	2.218	300
		–	3,800	1.075	1.075	1.200	1.200	1.695	1.695	2.080	2.080	2.401	2.401	400
		–	4,460	1.262	1.262	1.409	1.409	1.989	1.989	2.445	2.445	2.819	2.819	500
#181 PG 91-LD	Reinf Glass	–	5,230	1.480	1.480	1.653	1.653	2.333	2.333	2.860	2.860	3.305	3.305	550
Cross Rolled Beryllium	PH 17-7 Mo	.210	1.298	.367	.577	.410	.620	.580	.790	.710	.920	.820	1.030	RT
			1,350	.382	.592	.426	.636	.604	.814	.740	.950	.853	1.063	300
			1.414	.400	.610	.447	.657	.634	.844	.775	.985	.894	1.104	500
			1.546	.437	.647	.488	.698	.690	.900	.846	1.056	.976	1.186	700
Cross Rolled Beryllium	PH 17-7 Mo	.210	1.986	.562	.772	.627	.837	.886	1.096	1.086	1.296	1.255	1.465	900
Cross Rolled Be	Cross Rolled Be	.210	.644	.183	.393	.203	.413	.277	.487	.353	.563	.407	.617	RT
			.706	.200	.410	.223	.433	.315	.525	.387	.597	.446	.656	200
			.744	.211	.421	.235	.445	.332	.542	.407	.617	.470	.680	400
			.792	.224	.434	.250	.460	.353	.563	.434	.644	.500	.710	600
			.882	.250	.460	.279	.489	.394	.604	.483	.693	.558	.768	800
Cross Rolled Be	Cross Rolled Be	.210	1.100	.311	.521	.347	.557	.490	.700	.602	.812	.695	.805	1000
Reinf. Asbestos 41RPD Type	Mink Type struct. insul. Interlock	.260	6.84	1.935	2.195	2.160	2.420	3.060	3.320	3.745	4.005	4.320	4.580	RT
			6.84	1.935	2.195	2.160	2.420	3.060	3.320	3.745	4.005	4.320	4.580	500
			7.80	2.205	2.465	2.465	2.725	3.485	3.745	4.260	4.520	4.940	5.200	800
Reinf Asbestos 41RPD Type	Mink Type Struct. Ins. Interlock	.260	9.18	2.595	2.855	2.905	3.165	4.110	4.370	5.040	5.300	5.810	6.070	1000

TABLE 2.6-1 (F)

TABLE 2.6-1.(g)

$$h = \sqrt{\frac{3.13}{CE}}\sqrt{Wg}$$

$$t_f = \sqrt{\frac{3.13\,C}{E}}\sqrt{Wg} \quad \text{(two facings)}$$

Forebody - Sandwich Core Depth & Facings Thickness as a function of material & temperature for Wg = 70000 lb

①	②	③	④	⑤	⑥	⑦	⑧	⑨	⑩
Mat'l Facing	Mat'l Core	Temp	$E \times 10^{-6}$	$C = \sigma_c/\gamma$	$\sqrt{\frac{3.13C}{E}}$	$\sqrt{3.13/CE}$	$Wg = 70 \times 10^3$	t_{70000}	h_{70000}
		°F	psi		$\times 10^4$	$\times 10^2$	$\sqrt{Wg}$	⑥×⑧	⑦×⑧
5052 H39 Aluminum	5052 H39 Aluminum	RT & 100	10	.015	.685	.457	264.5	.0181	1.21
		200	9.8	.015	.692	.461		.0183	1.22
		300	9.5	.015	.704	.469		.0186	1.24
		400	9.0	.015	.720	.480		.0191	1.27
		500	8.0	.017	.810	.476		.0214	1.26
5052 H39 Aluminum	5052 H39 Aluminum	530	7.8	.019	.874	.460		.0231	1.22
PH 17-7 Mo Steel	PH 17-7 Mo Steel	RT & 100	30	.015	.396	.264		.012 min	.70
		200	30	.0156	.404	.259		.012 min	.685
		300	29.6	.0163	.415	.255		.012 min	.675
		400	28.9	.0169	.428	.253		.012 min	.670
		500	28.2	.0177	.442	.249		.012 min	.660
		600	27.0	.0187	.465	.249		.0123	.660
		700	25.8	.0203	.496	.244		.0132	.647
		800	24.6	.0235	.545	.232		.0144	.615
PH 17-7 Mo Steel	PH 17-7 Mo Steel	900	23.1	.030	.636	.212		.0168	.560
PH 17-7 Mo Steel	5052 H39 Aluminum	RT & 100	30	.006	.250	.400		.012 min	1.060
		200	30	.006	.250	.400			1.060
		300	29.6	.006	.252	.403			1.070
		400	28.9	.006	.256	.410			1.075
		500	28.2	.007	.279	.399			1.060
PH 17-7 Mo Steel	5052 H39 Aluminum	530	27.6	.008	.301	.376	264.5	.012 min	1.000

PREPARED BY: ASM	NORTH AMERICAN AVIATION, INC. SPACE and INFORMATION SYSTEMS DIVISION	PAGE NO. OF
CHECKED BY:		REPORT NO.
DATE: 9/25/63	Voyager Entry Capsule Design Study	MODEL NO. Voyager

TABLE 2.6-1(h)

$$h = \sqrt{\frac{3.13}{CE}}\sqrt{Wg}$$

$$t = \sqrt{\frac{3.13\,C}{E}}\sqrt{Wg} \quad \text{(two facings)}$$

Forebody - Sandwich Core Depth & Facing Thickness as a function of mat'l & temperature for Wg = 70000 lb

①	②	③	④	⑤	⑥	⑦	⑧	⑨	⑩
Mat'l facing	Mat'l Core	Temp	$E \times 10^{-6}$	$C = \gamma_c/\gamma_f$	$\sqrt{\frac{3.13\,C}{E}}$	$\sqrt{3.13/CE}$	$Wg = 70000$	t_{70000}	h_{70000}
		°F	psi		$\times 10^4$	$\times 10^2$	$\sqrt{Wg}$	⑥×⑧	⑦×⑧
6Al 4V Ti Annealed	PH 17-7Mo Steel	RT	15.0	.029	.779	.268	264.5	.0206	.705
		200	14.1	.030	.815	.271		.0216	.720
		300	13.65	.031	.844	.272		.0223	.720
		400	13.2	.033	.885	.269		.0234	.710
		500	12.6	.034	.920	.271		.0244	.715
		600	12.15	.036	.964	.267		.0256	.705
		700	11.70	.039	1.020	.261		.0270	.690
6Al 4V Ti	PH 17-7Mo Steel	800	11.1	.045	1.125	.250		.0300	.660
6Al 4V Ti STA	PH 17-7Mo Steel	RT	16.3	.029	.746	.258		.0198	.685
		200	15.9	.030	.770	.257		.0204	.680
		300	15.5	.031	.791	.255		.0209	.675
		400	15.1	.033	.829	.251		.0220	.665
		500	14.7	.034	.852	.251		.0225	.665
		600	14.3	.036	.889	.246		.0235	.650
STA		700	13.9	.039	.938	.240		.0248	.635
6Al 4V Ti	PH 17-7Mo Steel	800	13.5	.045	1.020	.200		.0270	.530
6Al 4V Ti STA	5052 H39 Aluminum	RT	16.3	.010	.438	.438		.0120	1.160
		200	15.9	.010	.444	.444		.0120	1.175
		300	15.5	.010	.450	.450		.0120	1.190
		400	15.1	.010	.455	.455		.0120	1.200
		500	14.7	.0113	.490	.435		.0130	1.150
6Al 4V Ti STA	5052 H39 Aluminum	530	14.5	.0127	.524	.412	264.5	.0140	1.090

PREPARED BY: AGM	NORTH AMERICAN AVIATION, INC. SPACE and INFORMATION SYSTEMS DIVISION	PAGE NO. OF
CHECKED BY:		REPORT NO.
DATE: 9/25/63	Voyager Entry Capsule Design Study	MODEL NO. Voyager

TABLE 2.6-1 (1)

$$h = \sqrt{\frac{3.13}{CE}}\ \sqrt{Wg}$$

$$t = \sqrt{\frac{3.13C}{E}}\ \sqrt{Wg} \quad \text{(two facings)}$$

Forebody - Sandwich Core Depth & Facing Thickness as a function of mat'l and temperature for Wg = 70000 lb.

①	②	③	④	⑤	⑥	⑦	⑧	⑨	⑩
Mat'l Facing	Mat'l Core	Temp	$E \times 10^{-6}$	$C = {}^{BC}/_{BF}$	$\sqrt{\frac{3.13C}{E}}$	$\sqrt{3.13/CE}$	$Wg = 70000$	t_{70000}	h_{70000}
		°F	psi	—	$\times 10^{4}$	$\times 10^{2}$	$\sqrt{Wg}$	⑥×⑧	⑦×⑧
#181 PG 91 LD	Reinf Glass	RT	3.2	.030	1.715	.572	264.5	.0454	1.510
		200	3.15	.033	1.810	.549		.0480	1.450
		300	3.05	.035	1.895	.541		.0500	1.430
		400	2.90	.039	2.050	.525		.0542	1.390
		500	2.70	.050	2.410	.482		.0639	1.275
#181 PG 91 LD	Reinf Glass	550	2.60	.065	2.82	.435		.0746	1.150
Cross Rolled Beryllium	PH 17-7 Mo Steel	RT	42	.062	.680	.110		.0180	.292
		300	42	.067	.706	.106		.0187	.280
		500	41.5	.073	.741	.099		.0197	.260
		700	39.4	.083	.810	.098		.0214	.259
Cross Rolled Beryllium	PH 17-7 Mo Steel	900	35.6	.123	1.040	.085		.0270	.225
Cross Rolled Beryllium	Cross Rolled Beryllium	RT	42	.015	.334	.223		.0088	.590
		200	42	.017	.366	.216		.0097	.571
		400	42	.020	.386	.193		.0104	.510
		600	41	.022	.410	.186		.0109	.494
		800	37.5	.025	.457	.183		.0121	.485
Cross Rolled Beryllium	Cross Rolled Beryllium	1000	33.7	.035	.570	.163		.0151	.431
Reinf. Asbestos 41RPD Type	MIN-K Type Struct. Insulation Interlock	R.T.	3.8	.200	4.060	.203		.1075	.536
		500	3.8		4.060	.203		.1075	.536
		800	2.9		4.650	.232		.1230	.615
Reinf Asbest. 41RPD Type	MIN-K Type Struct. Insul. Interlock	1000	2.1	.200	5.460	.273	264.5	.1445	.725

FIG. 2.6-1

Two possible configurations of a Composite Type Structure

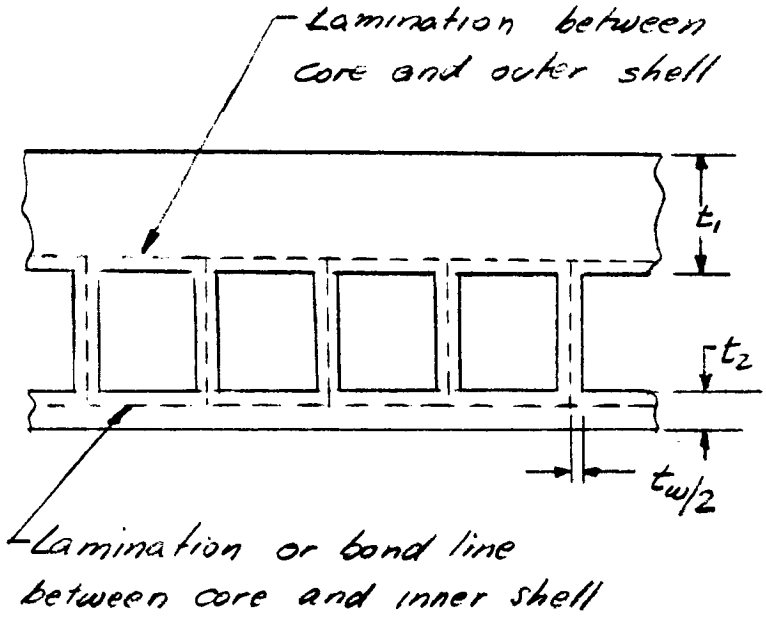

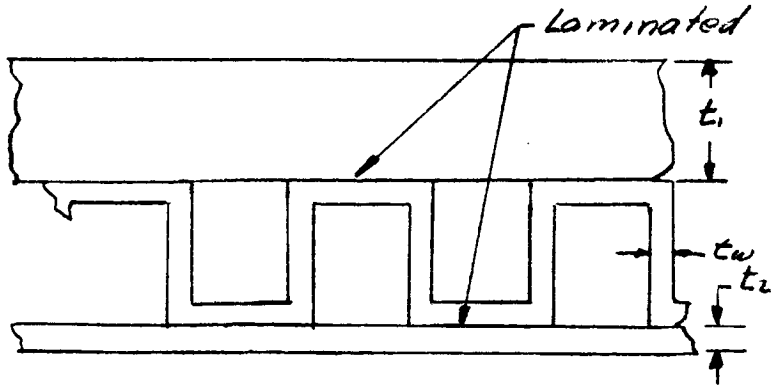

Notes:

t_1 = minimum thickness required for outer shell (heat shield and structural requirements)

t_2 = minimum thickness req'd for inner shell (structural)

t_w = Minimum core wall thickness

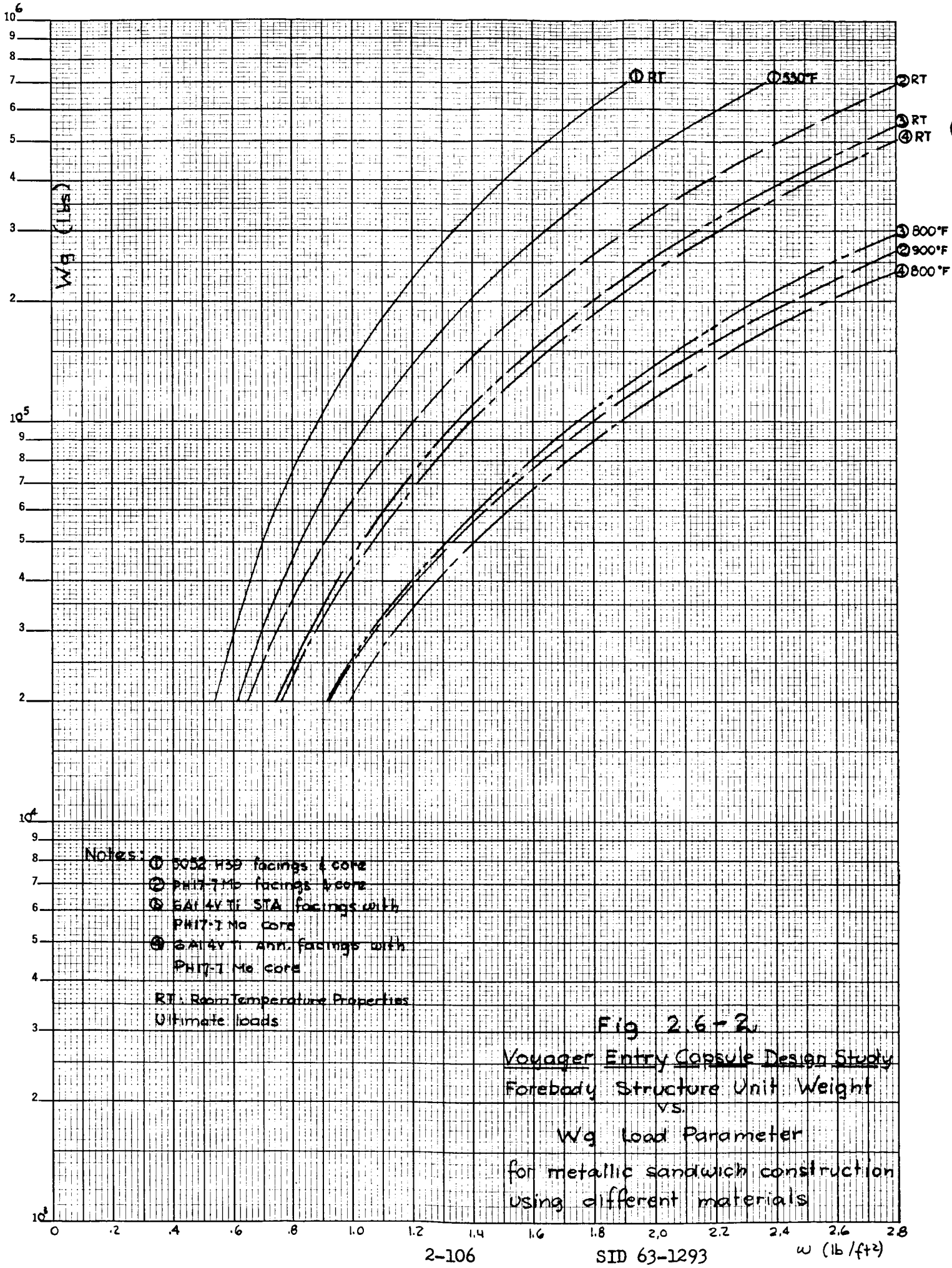

Fig 2.6-2

Voyager Entry Capsule Design Study

Forebody Structure Unit Weight

v.s.

Wg Load Parameter

for metallic sandwich construction using different materials

PREPARED BY: ASM	NORTH AMERICAN AVIATION, INC. SPACE and INFORMATION SYSTEMS DIVISION	PAGE NO. OF
CHECKED BY:		REPORT NO.
DATE: 10/4/63	VOYAGER ENTRY CAPSULE DESIGN STUDY Forebody Unit Weight Vs. Temperature	MODEL NO.

Fig 2.6-3

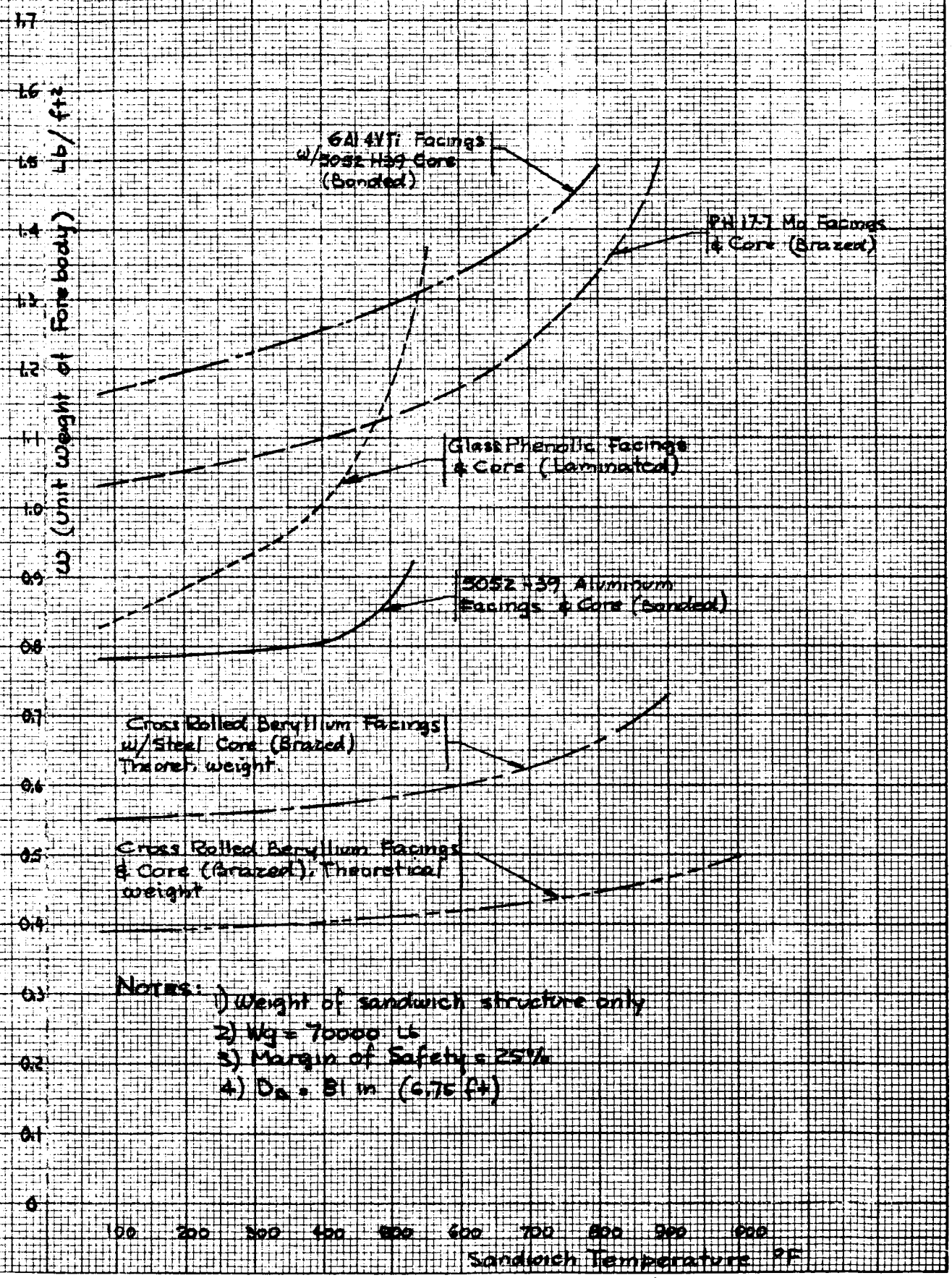

Fig. 2.6-A

Total Weight per Ft² of Structure & Heat Shield vs. Heat Shield Back Face Temperature

Wg = 70000 lb

Weight of H.S./Structure bond (.333 lb/ft²) added to metallic sandwich structures.

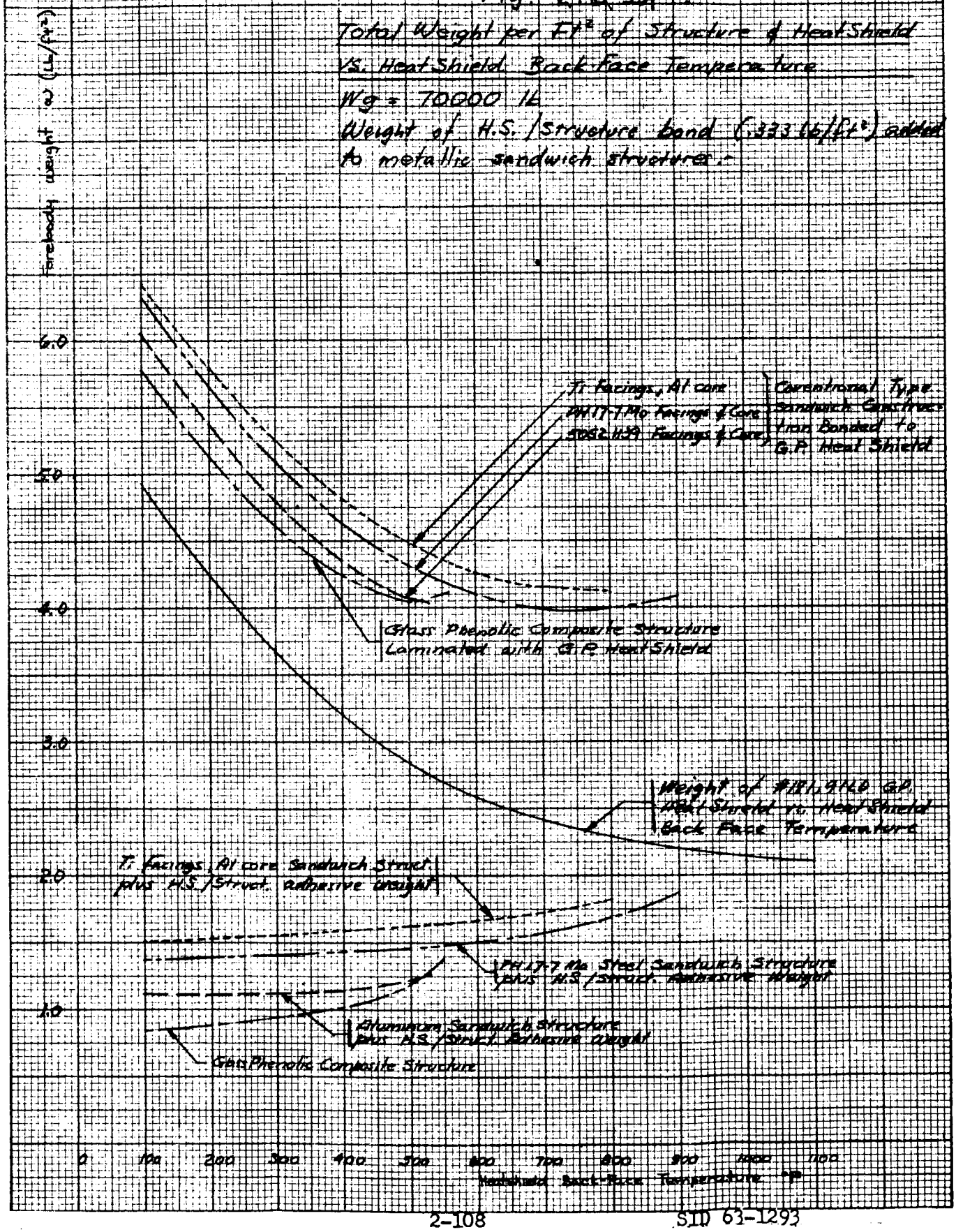

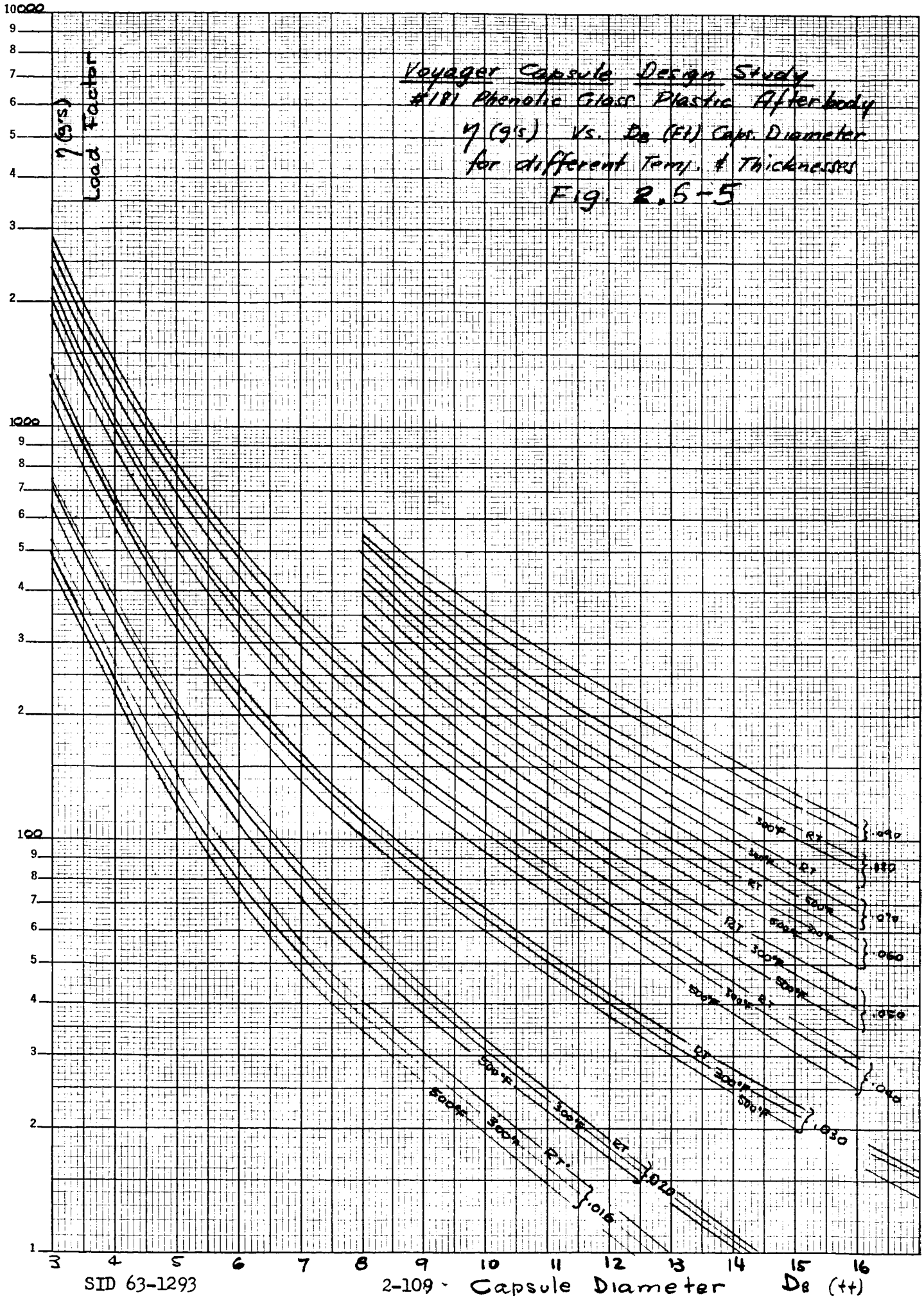
Voyager Capsule Design Study
#181 Phenolic Glass Plastic Afterbody
η (g's) Vs. DB (Ft) Capsule Diameter
for different Temp. & Thicknesses
Fig. 2.5-5
η (g's)
Load Factor
Capsule Diameter DB (ft)
500°F
300°F
RT
.090
.080
.070
.060
.050
.040
.030
.020
.016

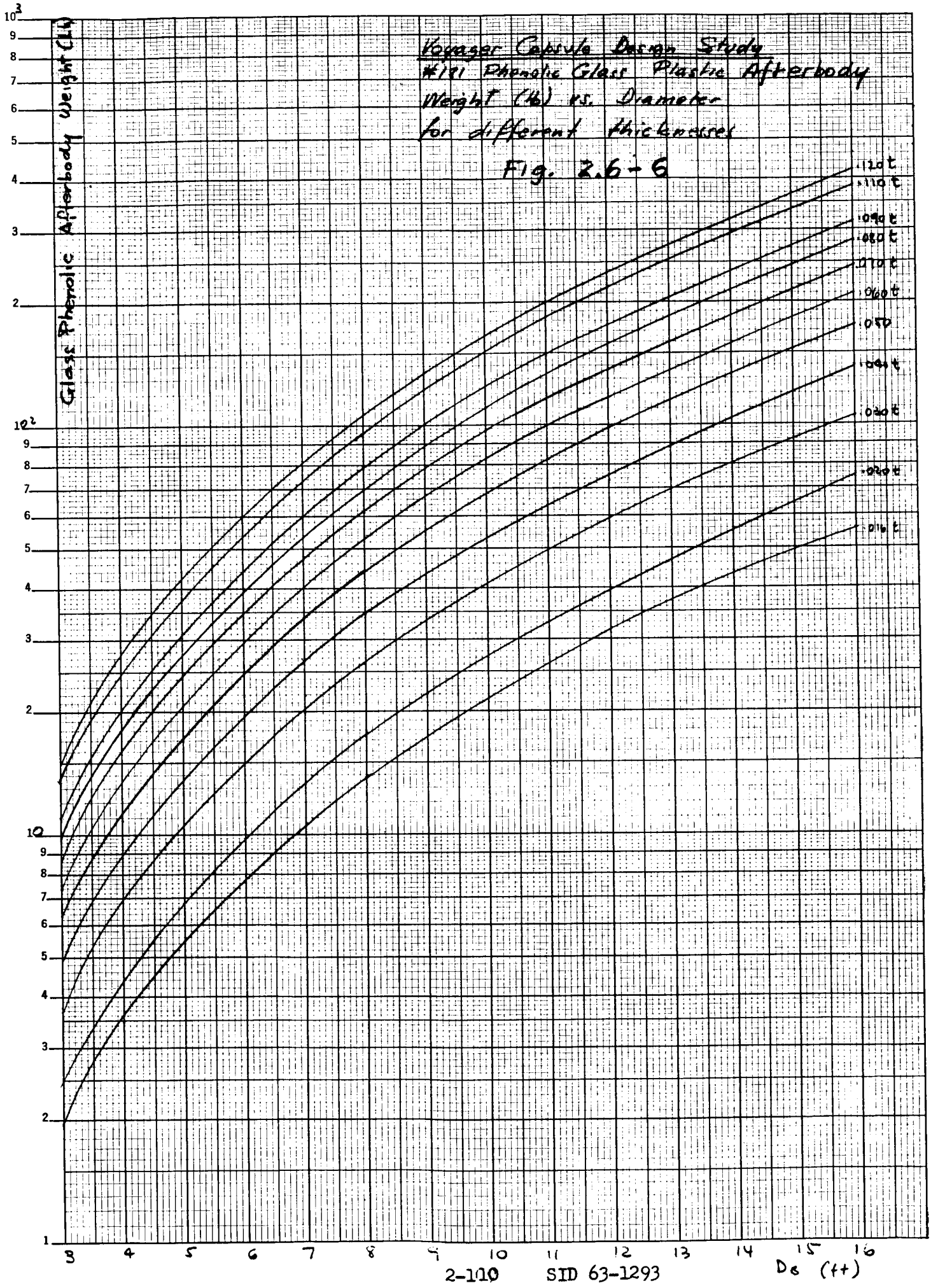
Voyager Capsule Design Study
#181 Phenolic Glass Plastic Afterbody
Weight (lb) vs. Diameter
for different thicknesses
Fig. 2.6-6
Glass Phenolic Afterbody Weight (lb)
.120 t
.110 t
.090 t
.080 t
.070 t
.060 t
.050
.040 t
.030 t
.020 t
.016 t
Dc (ft)

VOYAGER ENTRY CAPSULE DESIGN STUDY

Weight of Afterbody Vs Load Factor

Aluminum Afterbody of Monocoque Construction

Fig. 2.6-7

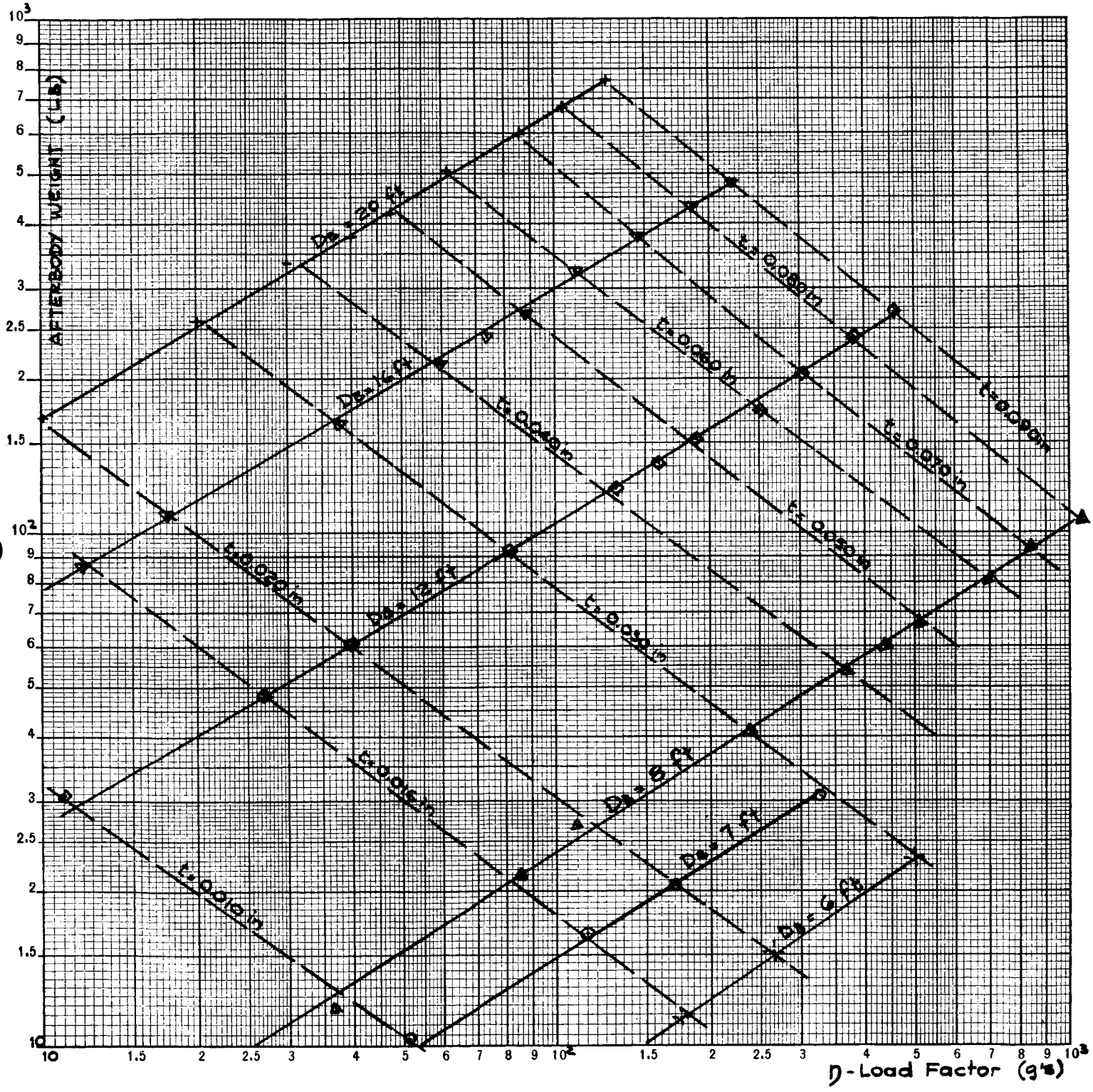

Notes: a) Ultimate loads
b) No local reinforcements

Fig. 26-8

Voyager Capsule Design Study
Aluminum Afterbody Load Factor η (g's)
vs.
Dβ Capsule Diameter (ft)
for different Temperatures & Wall thicknesses

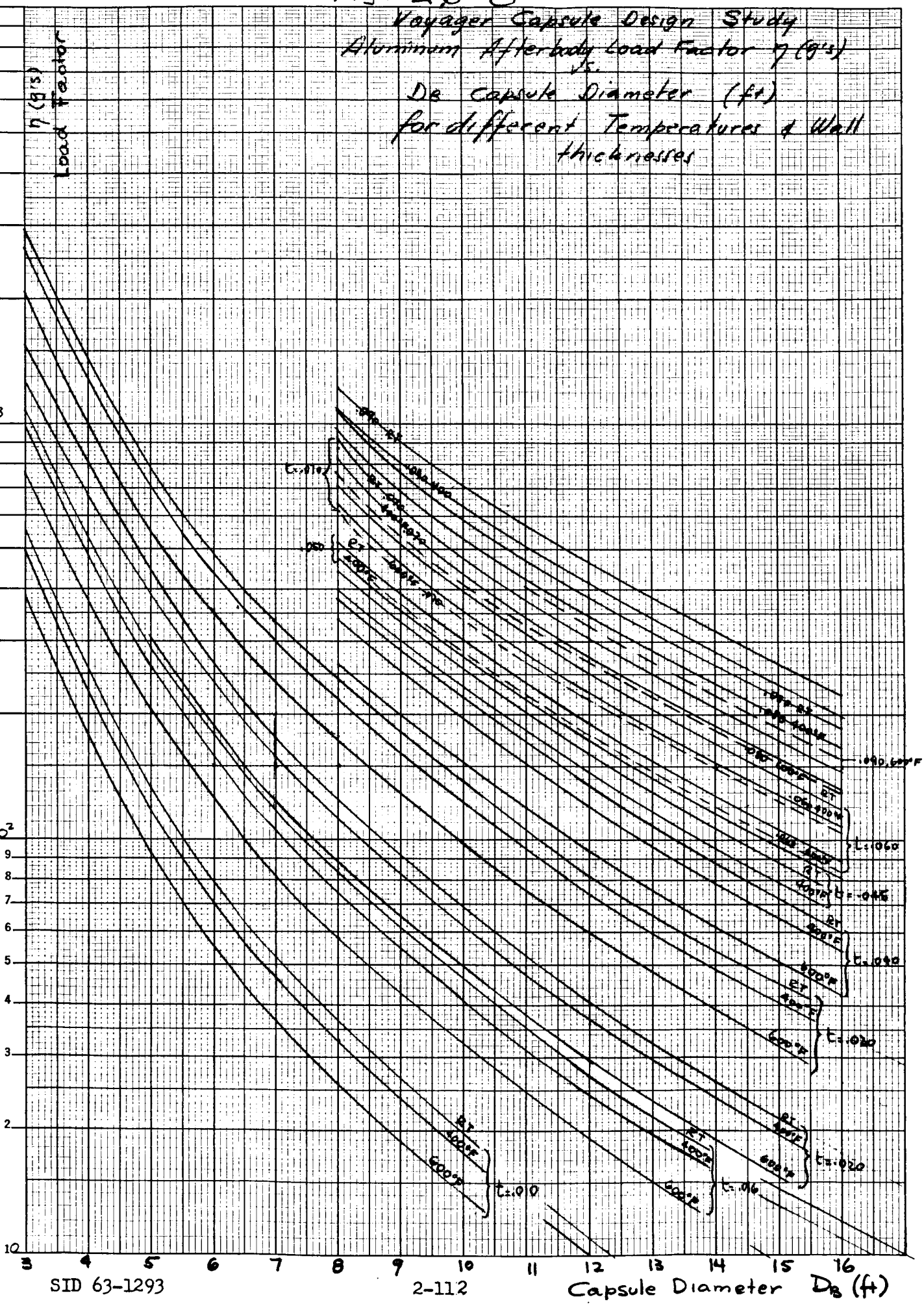

Fig. 2.6-9

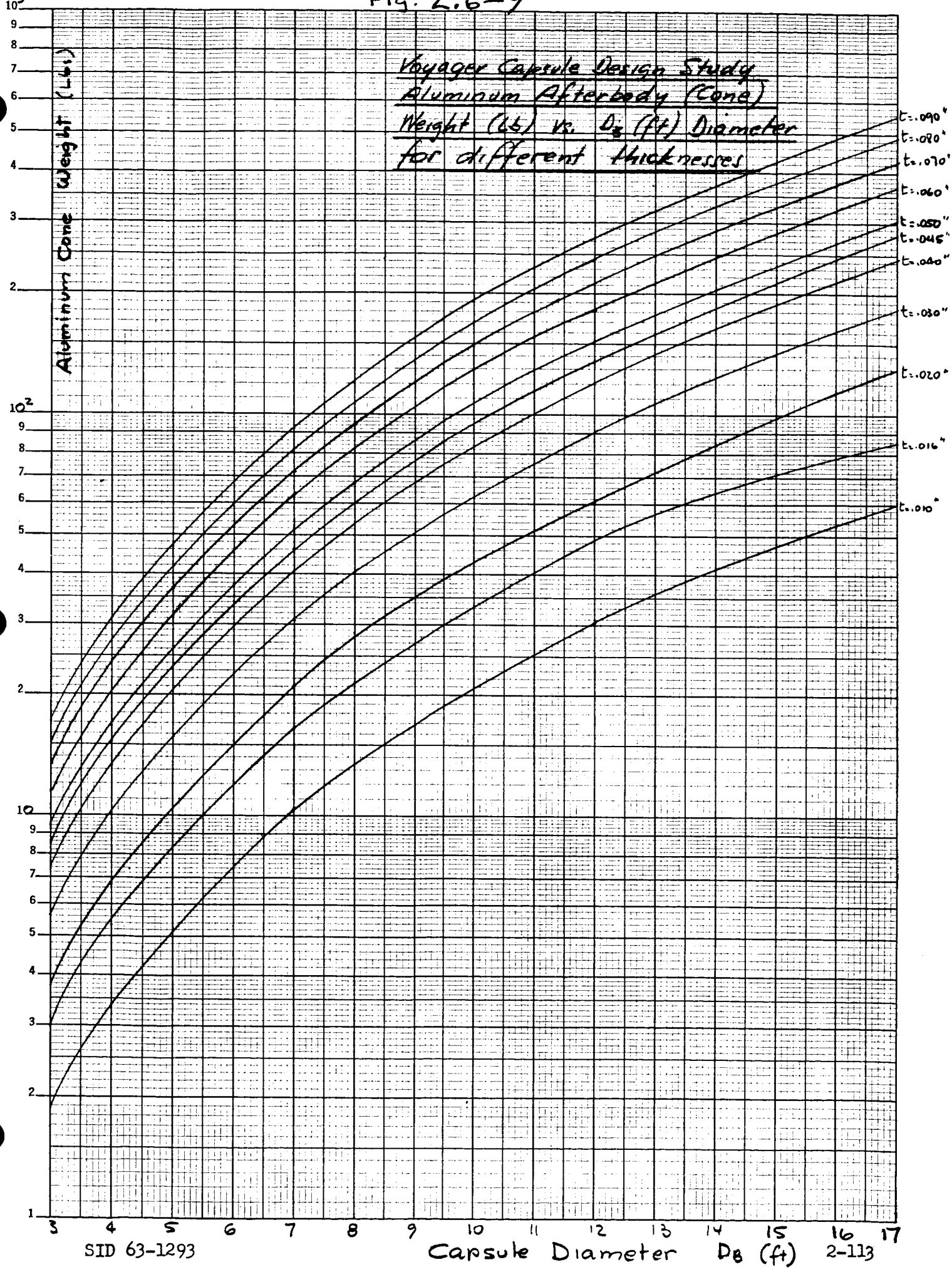
Voyager Capsule Design Study
Aluminum Afterbody (Cone)
Weight (Lb) vs. D_B (ft) Diameter
for different thicknesses
Aluminum Cone Weight (Lbs)
Capsule Diameter D_B (ft)
t=.090"
t=.080"
t=.070"
t=.060"
t=.050"
t=.045"
t=.040"
t=.030"
t=.020"
t=.016"
t=.010"

TABLE 2.6-2 (a)

$\sigma_{cr} = CE\frac{t}{R}$ Plastic Afterbody #181 Ph. Glass

NORTH AMERICAN AVIATION, INC.
SPACE and INFORMATION SYSTEMS DIVISION

Prepared By: ASM
Checked By:
Date: 8/31/63
Page No. of
Report No.
Model No.

1	2	3	4	5	RT 6100	7	8	9	10	11	12	13	14	15
D_B ft	R in	t in	R/t	C σ_{min}	$E_{RT}=3.2\times10^6$ $\sigma_{cr}=\frac{②\times3.2}{④\times10^{-6}}$	Area ② $2\pi t$ in^2	Weight $.218\,D_B^2$ Lb	P_{cr} Lb ⑥×⑦	$\eta_{cr\,RT}$ ⑨ ÷ ⑧	$E_{200}=3.15\times10^6$ $\eta_{cr\,200}$	$E_{300}=3.0\times10^6$ $\eta_{cr\,300}$	$E_{400}=2.9\times10^6$ $\eta_{cr\,400}$	$E_{500}=2.7\times10^6$ $\eta_{cr\,500}$	
3	18	.016	1125	.20	569	1.81	1.95	1030	529	520	495	480	446	
4	24		1500	.18	384	2.42	3.48	930	267	263	250	242	225	
5	30		1875	.15	254	3.02	5.44	766	141	139	132	128	119	
6	36		2250	.135	192	3.62	7.85	695	88	86	82	80	74	
7	42		2625	.12	145	4.22	10.69	610	56	55	52	51	47	
8	48		3000	.11	117	4.83	13.90	565	40	39	37	36	34	
12	72		4500	.08	57	7.25	31.4	410	13	13	12	12	11	
16	96		6000	.065	34	9.65	55.5	320	5	5	4	4	3	
20	120	.016	7500	.055	24	12.06	87.1	290	3	3	3	3	2	

TABLE 2.6-2 (b)
$\sigma_{cr} = CE\frac{t}{R}$ Plastic Afterbody

NORTH AMERICAN AVIATION, INC.
SPACE and INFORMATION SYSTEMS DIVISION

Prepared By: ASM
Checked By:
Date: 8/31/63

Page No. of
Report No.
Model No.

1	2	3	4	5	RT 6100 $E=3.2\times10^6$	7	8	9	10	11	12	13	14	15
D_B ft	R in	t in	R/t	C Umin	$\sigma_{cr}=$ (5)x3.2 / (4)x10^{-6}	Area (2) $2\pi t$ in^2	Weight $.272 D_B^2$ Lb	Pcr Lb (6)x(7)	η_{cr} RT (9)%(1)	$E_{200}=3.1\times10^6$ η_{cr200}	$E_{300}=3.0\times10^6$ η_{cr300}	$E_{400}=2.9\times10^6$ η_{cr400}	$E_{500}=2.7\times10^6$ η_{cr500}	
3	18	.020	900	.22	785	2.36	2.45	1850	755	745	710	684	636	
4	24		1200	.20	532	3.01	4.35	1600	368	362	345	334	310	
5	30		1500	.18	384	3.77	6.80	1450	213	209	200	192	180	
6	36		1800	.16	285	4.52	9.80	1290	131	129	123	119	110	
7	42		2100	.14	214	5.28	13.30	1130	85	83	80	77	72	
8	48		2400	.13	173	6.03	17.40	1040	60	59	56	54	50	
12	72		3600	.095	85	9.04	39.40	765	19	18	18	17	16	
16	96		4800	.010	53	12.06	74.50	640	8.8					
20	120	.020	6000	.065	35	15.05	109.0	530						

TABLE 2.6-2(c)

$\sigma_{cr} = CE\frac{t}{R}$ Plastic Afterbody

NORTH AMERICAN AVIATION, INC.
SPACE and INFORMATION SYSTEMS DIVISION

Prepared By: ASM.
Checked By:
Date: 8/31/63

Page No. of
Report No.
Model No.

1	2	3	4	5	6	7	8	9	10	11	12	13	14	15
D_b ft	R in	t in	R/t	C Unitless	$E = 3.2\times10^6$ $\sigma_{cr} = (5)\times 3.2 / (4)\times10^{-6}$	Area (2) $2\pi t$ in^2	Weight $.49 D_b^2$ lb	Pcrit (6)×(7) lb	η_{cr} (9)/(8)	$E_{200} = 3.15\times10^6$ η_{cr200}	$E_{300} = 3.0\times10^6$ η_{cr300}	$E_{400} = 2.9\times10^6$ η_{cr400}	$E_{500} = 2.7\times10^6$ η_{cr500}	
3	18	.030	600	.29	1550	3.39	3.65	5250	1440	1420	1350	1305	1215	
4	24		800	.25	1000	4.52	6.90	4510	655	644	615	594	550	
5	30		1000	.22	704	5.65	10.40	3980	380	374	357	345	320	
6	36		1200	.20	534	6.77	14.70	3610	245	240	230	222	207	
7	42		1400	.18	410	7.91	20.10	3260	160	157	150	145	135	
8	48		1600	.17	340	9.05	26.20	3090	118	116	110	107	100	
12	72		2400	.13	172	13.58	58.90	2450	41	39	37	36	34	
16	96		3200	.11	108	18.10	104.50	1965	19	18	18	17	16	
20	120	.030	4000	.09	72	22.60	163.0	1630	10	9	9	8	8	

TABLE 2.6-2(d)

$\sigma_{cr} = CE\frac{t}{R}$. Plastic Afterbody

NORTH AMERICAN AVIATION, INC.
SPACE and INFORMATION SYSTEMS DIVISION

Prepared By: A.S.M.
Checked By:
Date: 8/31/63

Page No. of
Report No.
Model No.

1	2	3	4	5	RT 6100 $E = 3.2 \times 10^6$	7	8	9	10	11	12	13	14	15
D_B Ft	R in	t in	R/t	C σ_{min}	$\sigma_{cr} = \frac{①}{④} E$	Area ② $2\pi t$ in^2	Weight $.545 D_B^2$ Lb	Pcr ⑥ × ⑦ Lb	$\eta_{cr_{RT}}$ ⑨ ÷ ⑧	$E_{200} = 3.15 \times 10^6$ $\eta_{cr_{200}}$	$E_{300} = 3.0 \times 10^6$ $\eta_{cr_{300}}$	$E_{400} = 2.8 \times 10^6$ $\eta_{cr_{400}}$	$E_{500} = 2.7 \times 10^6$ $\eta_{cr_{500}}$	
3	18	.040	450	.32	2275	4.51	4.90	10500	2140	2110	2010	1940	1805	
4	24		600	.28	1490	6.03	8.72	9000	1030	1020	965	934	870	
5	30		750	26	1110	7.53	13.65	8350	612	600	575	565	515	
6	36		900	.23	818	9.04	19.65	7380	375	365	352	340	315	
7	42		1050	.21	640	10.53	26.70	6750	252	247	236	228	212	
8	48		1200	.20	530	12.10	34.90	6440	184	180	173	167	155	
12	72		1800	.16	284	18.10	73.40	5150	70	69	65	63	59	
16	96		2400	.13	172	24.15	139.50	4160	30	29	28	27	25	
20	120	.040	3000	.11	117	30.18	216.50	3540	16	15	15	14	13	

Table 2.6-2(e)
$\sigma_{cr} = CE\frac{t}{R}$ Plastic Afterbody

NORTH AMERICAN AVIATION, INC.
SPACE and INFORMATION SYSTEMS DIVISION

Prepared By: A.S.M
Checked By:
Date: 8/31/63

Page No. of
Report No.
Model No.

1	2	3	4	5		7	8	9	10	11	12	13	14	15
D_B ft	R in	t in	R/t	C U_{min}	RT 6100Z $E_{RT} = 3.2\times10^6$ $\sigma_s = ⑤E$	Area ② $2\pi t$ in^2	Weight $.681 D_B^2$ LB	Pcr ⑥ × ⑦ LB	η_{cr} ⑨ × ⑧	$E_{200} = 5.15\times10^6$ $\eta_{cr_{200}}$	$E_{300} = 3.0\times10^6$ $\eta_{cr_{300}}$	$E_{400} = 2.9\times10^6$ $\eta_{cr_{400}}$	$E_{500} = 2.7\times10^6$ $\eta_{cr_{500}}$	
3	18	.050	360	.340	3020	5.65	6.13	17080	2790	2750	2615	2530	2350	
4	24		480	.310	2070	7.53	10.90	15600	1430	1405	1340	1295	1205	
5	30		600	.290	1545	9.42	17.00	14550	858	845	805	775	724	
6	36		720	.250	1110	11.30	24.50	12530	511	505	480	465	430	
7	42		840	.230	875	13.18	34.30	11570	335	330	315	290	280	
8	48		960	.220	734	15.06	43.60	11050	254	250	238	230	215	
12	72		1440	.150	406	22.60	98.10	9200	93	92	87	84	79	
16	96		1920	.150	250	30.80	174.30	7700	44	41	39	38	35	
20	120	.050	2400	.130	173	37.70	272.00	6520	24	23	22	22	80	

TABLE 2.6-2 (f.)

$\sigma_{cr} = CE\frac{t}{R}$ Plastic Afterbody

NORTH AMERICAN AVIATION, INC.
SPACE and INFORMATION SYSTEMS DIVISION

Prepared By: ASM | Page No. of
Checked By: | Report No.
Date: 9/4/3 | Model No.

1	2	3	4	5	RT 6100 $E_{RT}=3.2\times10^6$	7	8	9	10	11	12	13	14	15
D_B ft	R in	t in	R/t	C U min	$\sigma_{cr}=C\,E$	Area ② $2\pi t$ in^2	Weight lb	Pcr ⑥×⑦ lb	η_{cr} ⑤×⑧	$E_{200}=3.15\times10^6$ $\eta_{cr_{200}}$	$E_{300}=3.00\times10^6$ $\eta_{cr_{300}}$	$E_{400}=2.9\times10^6$ $\eta_{cr_{400}}$	$E_{500}=2.7\times10^6$ $\eta_{cr_{500}}$	
						.3775R	.819 D_B^2							
8	48	.060	800	.25	999	18.21	52.50	18200	347	342	325	315	293	
12	72	|	1200	.20	532	27.15	118.0	14450	122	121	114	111	103	
16	96	|	1600	.17	339	36.25	210.0	12250	58	57	54	52	49	
20	120	.060	2000	.14	224	45.20	327.0	10100	31	30	29	27	26	
						.440R	.956 D_B^2							
8	48	.070	680	.28	1315	21.10	61.20	27800	454	446	425	402	384	
12	72	|	1030	.22	683	31.70	137.50	21650	157	155	147	142	133	
16	96	|	1370	.18	421	42.10	244.0	17700	72	71	67	65	61	
20	120	.070	1720	.165	307	52.90	382.0	16200	42	41	39	38	35	
						.502R	1.092 D_B^2							
8	48	.080	600	.29	1545	24.05	69.90	37100	530	522	496	480	438	
12	72	|	900	.23	815	36.10	157.10	29500	188	185	176	170	159	
16	96	|	1200	.20	533	48.10	279.50	25600	91	89	85	82	77	
20	120	.080	1500	.175	373	60.20	436.0	22500	51	50	48	46	43	
						.565R	1.229 D_B^2							
8	48	.090	534	.29	1740	27.15	78.60	47200	600	591	562	544	507	
12	72	|	800	.25	999	40.60	176.50	40500	230	226	215	208	194	
16	96	|	1065	.21	630	54.30	315.20	34200	108	106	101	98	91	
20	120	.090	1335	.19	455	67.90	491.0	31000	63	62	59	57	53	
							1.500 D_B^2							
16	96	.110	870	.23	848	66.40	383.0	56400	148	145	138	133	124	
16	96	.120	800	.25	1000	72.50	419.0	72500	173	170	162	157	146	

TABLE 2.6 - 2(8)

$\sigma_{cr} = CE\frac{t}{R}$ Aluminum Afterbody

NORTH AMERICAN AVIATION, INC.
SPACE and INFORMATION SYSTEMS DIVISION

Prepared By: ASM
Checked By:
Date: 8/21/63

Page No. of
Report No.
Model No.

1	2	3	4	5	6	7	8	9	10	11	12	13	14	15
D_B	R	t	R/t	C umin	$E = 10^7$ $\sigma_{cr} = \frac{(5) \times 10^7}{(4)}$	Area (2) $2\pi t$ in^2	Weight $.210 D_B^2$ LB	P_{cr} (6) x (7)	η_{cr} (9) ÷ (8)	$\eta_{cr_{200}}$ (10) x .98	$\eta_{cr_{400}}$ (10) x .9	$\eta_{cr_{600}}$ (10) x .7		
3	18	.010	1800	.165	.918	1.13	1.89	1040	550	540	495	385		
4	24		2400	.135	560	1.51	3.36	845	252	247	227	176		
5	30		3000	.110	370	1.88	5.25	695	132	129	119	92		
6	36		3600	.095	264	2.26	7.55	596	79	77	71	55		
7	42		4200	.085	200	2.64	10.30	528	51	50	46	36		
8	48		4800	.078	162	3.01	13.45	490	37	36	33	26		
12	72		7200	.055	76	4.55	30.20	346	11	10	10	8		
16	96		9600	.051	53	6.03	53.70	330	6	6	5	4		
20	120	.010	12000											

TABLE 2.6-2(h)

$\sigma_{cr} = C E \frac{t}{R}$, Aluminum Afterbody

NORTH AMERICAN AVIATION, INC.
SPACE and INFORMATION SYSTEMS DIVISION

Prepared By: A.S.M
Checked By:
Date: 8/21/63

Page No. of
Report No.
Model No.

1	2	3	4	5	6	7	8	9	10	11	12	13	14	15
D_B ft	R in	t in	$\frac{R}{t}$	C U=MIN	$E=10^7$ $\sigma_{cr}=\frac{(5)\cdot 10^7}{(4)}$	Area (2) $2\pi t$ in^2	Weight $.335 D_B^2$ Lb	P_{cr} (6) × (7)	η_{cr} (9) % (8)	$\eta_{cr_{200}}$ .98 (10)	$\eta_{cr_{400}}$ .90 (10)	$\eta_{cr_{600}}$ .70 (10)		
3	18	.016	1125	.20	1775	1.81	3.0	3210	1070	1050	964	750		
4	24		1500	.18	1200	2.42	5.35	2910	545	535	481	381		
5	30		1875	.15	800	3.02	8.36	2420	289	284	256	202		
6	36		2250	.135	600	3.62	12.08	2170	180	176	158	126		
7	42		2625	.12	455	4.22	16.42	1920	117	115	103	82		
8	48		3000	.11	367	4.83	21.4	1775	83	81	74	58		
12	72		4500	.08	178	7.25	48.2	1290	27	26	24	19		
16	96		6000	.065	108	9.65	85.6	1030	12	12	10	8		
20	120	.016	7500	.055	75	12.06	134.0	880	7	7	6	5		

TABLE 2.6-2(i).

$\sigma_{cr} = CE\frac{t}{R}$, Aluminum Afterbody

NORTH AMERICAN AVIATION, INC.
SPACE and INFORMATION SYSTEMS DIVISION

Prepared By: ASM
Checked By:
Date: 8/21/63

Page No. of
Report No.
Model No.

1	2	3	4	5	6	7	8	9	10	11	12	13	14	15
D_B ft	R in	t in	R/t	C C=MIN	$E=10^7$ $\sigma_{cr}=\frac{(1)E}{(4)}$	Area (2) $2\pi t$ in²	Weight $.419 D_B^2$ Lb	P_{cr} (6)×(7)	η_{cr} (9)÷(8)	$t_{AVER}=.018$ Weight= $.376 D_B^2$	η'_{cr} (9)÷(11)	η_{cr200} (10)×.98	η_{cr100} (10)×.90	η_{cr60} (10)×.70
3	18	.020	900	.22	2450	2.36	3.77	5780	1530	3.39				
4	24		1200	.20	1665	3.01	6.70	5000	750	6.01	835	735	675	525
5	30		1500	.18	1200	3.77	10.48	4530	435	9.40	482	426	391	304
6	36		1800	.16	890	4.52	15.10	4020	266	13.55	297	261	240	186
7	42		2100	.14	670	5.28	20.50	3540	173	18.40	192	169	156	121
8	48		2400	.13	540	6.03	26.8	3250	121	24.10	135	118	109	85
12	72		3600	.095	265	9.04	60.3	2390	40	54.0	44.5	39	36	28
16	96		4800	.08	166	12.06	114.5	2000	17.5	102.5	19.5	17	16	12
20	120	.020	6000	.065	110	15.05	167.5	1655	10	150.5	11	10	9	7

TABLE 2.6-2(j)

$\sigma_{cr} - CE\frac{t}{R}$, Aluminum, Afterbody

NORTH AMERICAN AVIATION, INC.
SPACE and INFORMATION SYSTEMS DIVISION

Prepared By: ASM
Checked By:
Date: 8/21/3
Page No. of
Report No.
Model No.

1	2	3	4	5	6	7	8	9	10	11	12	13	14	15
D_B ft	R in	t in	R/t	C U_{min}	$E \cdot 10^7$ $\sigma_{cr} = \frac{(5)E}{(4)}$ psi	Area (2) $2\pi t$ in^2	Weight $.629\, D_B^2$ LB	Pcr (6) x (7)	η_{cr} (9) ÷ (8)	23% for $t_{AVE} = .025$ Weight = $.481\, D_B^2$ LB	η'_{cr} (9) ÷ (11)	$\eta_{cr\,200}$ (10) x .98	$\eta_{cr\,400}$ (10) x .90	$\eta_{cr\,600}$ (10) x .70
3	18	.030	600	.29	4840	3.39	5.61	16,400	2920	4.30		2850	2630	2040
4	24		800	.25	3120	4.52	10.06	14100	1400	7.70		1370	1260	980
5	30		1000	.22	2200	5.65	15.72	12420	790	12.10		775	711	555
6	36		1200	.20	1665	6.77	22.65	11300	500	17.35	650	490	450	350
7	42		1400	.18	1290	7.91	30.85	10200	330	23.65	430	323	297	231
8	48		1600	.17	1065	9.05	40.30	9650	240	30.90	310	235	216	168
12	72		2400	.13	540	13.58	90.50	7330	81	69.30	106	79	73	57
16	96		3200	.11	340	18.10	161.0	6150	38	123.30	50	37	34	26
20	120	.030	4000	.09	225	22.60	251.5	5090	20	192.50	26	25	23	18

TABLE 2.6-2(R)

$\sigma_{cr} = CE\frac{t}{R}$, Aluminum, Afterbody

NORTH AMERICAN AVIATION, INC.
SPACE and INFORMATION SYSTEMS DIVISION

Prepared By: ASM
Checked By:
Date: 8/21/63

Page No. of
Report No.
Model No.

1	2	3	4	5	6	7	8	9	10	11	12	13	14	15
D_b ft	R in	t in	R/t	C Umin	$E=10^7$ $\sigma_{cr}=\frac{(5)E}{(4)}$	Area (2)2πt in²	Weight	Per (6)(7)	η_{cr} (9)×(8)	$t_{ave}=.028$ Weight $=.585 D_b^2$	η'_{cr} (9)÷(11)	η_{cr200} (10)×.98	η_{cr400} (10)×.90	η_{cr600} (10)×.70
						.251R	.839 D_b^2							
8	48	.040	1200	.20	1660	12.10	53.5	20100	375	37.5	539	367	337	262
12	72		1800	.16	890	18.10	120.5	16100	133	84.2	190.5	130	120	93
16	96		2400	.13	540	24.15	214.5	13000	60	149.6	86	59	54	42
20	120	.040	3000	.11	367	30.18	335.0	11080	30	234	43	29	27	21
										$t_{ave}=.031$ $W=.649 D_b^2$				
						.283R	.943 D_b^2							
8	48	.045	1066	.21	1970	13.58	60.3	26700	440	41.5	640	430	395	308
12	72		1600	.17	1060	20.38	135.5	21600	160	93.5	230	157	144	112
16	96		2130	.14	660	27.20	241.0	17900	74	166	108	72	66	52
20	120	.045	2670	.12	450	34.0	377.0	15300	40	259	58	39	36	28
						.314R	1.048 D_b^2			$t_{ave}=.050$ $W=.690 D_b^2$				
8	48	.050	960	.22	2290	15.20	67.0	34800	520	44.2	790	510	467	364
12	72		1420	.18	1270	22.65	151.0	28800	190	99.4	290	186	171	133
16	96		1920	.15	783	30.20	268.0	23600	88	177	130	86	79	61
20	120	.050	2400	.13	540	37.70	418.0	20350	48	276	73	46	43	34

TABLE 2.6-2 (L)

$\overline{\sigma_{cr}} = CE\frac{t}{R}$ Aluminum Afterbody

NORTH AMERICAN AVIATION, INC.
SPACE and INFORMATION SYSTEMS DIVISION

Prepared By: ASM
Checked By:
Date: 9-4-3
Page No. of
Report No.
Model No.

1	2	3	4	5	6	7	8	9	10	11	12	13	14	15
D_e ft	R in	t in	R/t	C Umin	$E=10^7$ $\overline{\sigma_{cr}}=\frac{5}{4}E$	Area 2πrt	Weight lb	P_{cr} 6×7/16	η_{cr} 9×8	tare .038 Weight lb	η'_{cr} 9×11	η_{cr200} 12×.98	η_{cr400} 10×.90	η_{cr600} 10×.70
						.3775 R	1.260 D_e^2			.797 D_e^2				
8	48	.060	800	.25	3120	18.21	80.60	56900	705	51.00	1130	691	635	494
12	72		1200	.20	1665	27.15	181.50	45200	250	115.0	393	245	225	175
16	96		1600	.17	1060	36.25	323.0	38400	119	204.0	188	116	107	83
20	120	.060	2000	.14	700	45.20	504.0	31600	62	319.0	99	60	56	43
						.440 R	1.470 D_e^2			t_A = .043 .903 D_e^2				
8	48	.070	680	.28	4120	21.10	94.10	87000	923	57.9	1500	905	830	645
12	72		1030	.22	2135	31.70	211.50	67700	306	130.0	520	300	275	214
16	96		1370	.18	1315	42.10	376.0	55400	147	231.0	239	144	132	106
20	120	.070	1720	.165	960	52.90	588.0	50600	86	361.0	140	84	77	60
						.502 R	1.680 D_e^2			t_A = .048 1.008 D_e^2				
8	48	.080	600	.29	4830	24.05	107.50	116000	1075	64.5	1800	1051	966	750
12	72		900	.23	2550	36.10	242.0	92300	382	145.0	636	374	343	267
16	96		1200	.20	1665	48.10	430.0	80000	186	258.0	310	182	167	130
20	120	.080	1500	.175	1165	60.20	671.0	70300	105	403.0	174	103	94	73
						.565 R	1.890 D_e^2			t_A = .053 1.112 D_e^2				
8	48	.090	534	.29	5430	27.15	121.0	147500	1220	71.3	2070	1200	1095	855
12	72		800	.25	3120	40.60	272.0	126800	465	160.0	790	455	418	326
16	96		1065	.21	1970	54.30	484.0	107000	221	285.0	375	217	198	155
20	120	.090	1335	.19	1425	67.90	755.0	96800	128	445.0	219	125	115	89

2.7 Heat Shield Tradeoffs

The derivation of the entry heating rates and loads are described in Section 2.3. Table 2.7-1 summarizes these values in the stagnation region for the range of base diameters of interest for an M/C_DA of 0.2. For other values of the ballistic coefficient, the scaling relationships described in Section 2.3 apply. The times associated with entry at -20° are in the order of 150 to 200 seconds; at -90° they are in the order of 20 seconds.

The variation in magnitude and nature of the heat input requires a careful screening of materials which will satisfy the spectrum of possible entry requirements. To satisfy this wide range of possible entry heating conditions, one basic assumption of the study was that only homogeneous materials (e.g., ablator-insulators) would be considered.

Although the heating rates described represent those for stagnation conditions, heating is assumed to be uniform over the entire forebody. The results of the flight test program for the Mercury capsule indicated that this assumption was valid for a similar shape (Reference 1). Heating rates for the conical afterbody section of the capsule are expected to average approximately 5% of those for the forebody and, furthermore, no radiative contribution is anticipated. Figures 2.7-1 through 2.7-8 indicate the approximate heating rates for the -20° and -90° entry on the forebodies and afterbodies of the capsules.

2.7.1 Candidate Materials

The characteristics of the ablation materials considered in this study are discussed in Section 2.4; the materials and their thermal properties are summarized in Table 2.7-2. The heat of ablation used in the analysis is the thermo-chemical heat of ablation and is closely approximated by the relationship:

$$\overline{H_{eff}} \sim \frac{q_o - q_r}{\dot{m}} \qquad \text{(Ref. 2)}$$

This value was employed because it is independent of the incident heating rate and surface re-radiation effects. These are considered separately in the analysis.

Although it is recognized that the list of candidate materials is not complete, it was felt that the present list is representative of the classes of materials most likely to perform satisfactorily.

2.7.2 Methodology

A preliminary analysis was performed to derive the unit weight of material required for a specified allowable backface temperature. These results were compared with those derived by the use of an IBM computer program. Con-

stant values for the thermal and ablation properties were used except that, in the computer analysis, the variation of heat of ablation with enthalpy difference across the boundary layer was taken into consideration by employing the data shown in Figures 2.7-9 through 2.7-11. The weight per unit area was calculated for each material for a 7 ft diameter capsule with $M/C_DA = 0.2$ entering the martian atmosphere with $V_E = 25{,}000$ fps at 20° and 90° angles.

The first analytical method employed was that of Mac C. Adams (Reference 3) wherein:

$$t = t_{ae} - \frac{V_w A}{\alpha} \qquad V = \frac{\dot{q}}{H_a P}$$

$$A = \frac{\left(\ln \frac{ta}{t}\right)\alpha}{V_w} \qquad B = V_w \theta$$

$$W = (A + B)\, P$$

These equations assume that steady state heating and ablation prevail after an equilibrium exponential distribution has been established through the material.

The second analytical method employed was that of Swann (Reference 4) wherein:

$$W = \frac{Q}{2H_a}\left[1 - \left(\frac{Ta}{Te}\right)^4\right]\left\{1 + \sqrt{1 + \frac{8kp\theta}{c_p}\left[\ln \frac{ta-ti}{Ta-T_b}\right]^{-1}\left[\frac{Ha}{Q\left[1-\left(\frac{Ta}{Te}\right)^4\right]}\right]^2}\right\}$$

This method incorporates the assumption that the heating rates are constant, that a linear temperature distribution exists through the material, and that the outer surface is at a constant ablation temperature.

The results of the analytic calculations are summarized in Figures 2.7-12 and 2.7-13 and in Tables 2.7-3 through 2.7-6. In comparing the results of the two methods of calculation, Swann's method in all cases yields a greater unit weight than Adams'. Although the unit weights predicated at low backface temperatures differed significantly, the methods are in good agreement at the higher backface temperatures. The difference in the results appears to be in the temperature distribution assumed through the material. As indicated, Adams assumes an exponential temperature gradient, whereas Swann's method is based on a linear temperature profile.

Because of the difference between these approaches, the study was expanded to include analyses of the materials when subjected to transient heating, simulated by use of the IBM program described in Reference (5). This program solves a one-dimensional heat balance equation, on a slab of material(s) using the Dusinberre finite-difference, lumped-parameter method (Reference 6).

In use, the slab of material(s) to be analyzed is divided into a number of sections and a heat balance is written for each section. The program considers:

(1) Heat accumulated in the section.

(2) Heat conduction to or from adjacent sections.

(3) Forced-convection heat transfer from the aerodynamic boundary layer to the outside section.

(4) Radiation to space from the outside section.

$$\frac{(C_p \rho XYZ)_n}{\Delta\theta}(T_n' - T_n) = \frac{K_{n-1} X_n Z_n}{L_{n-1}}(T_{n-1} - T_n) + \frac{K_{n+1} X_n Z_n}{L_{n+1}}(T_{n+1} - T_n) + h_{BL} X_n Z_n (T_{BL} - T_n) - \epsilon \sigma X_n Z_n T_n^4 + \alpha X_n Z_n G$$

The program solves the equation at specified time increments over the entire trajectory. The heating process is handled in the following manner: A temperature rise is determined for the outside section at each interval. After the section reaches ablation temperature, the amount of heat represented by the temperature rise is determined and summed with that of previous intervals. The total is then compared with the effective heat of ablation of a section of material. When the integrated heat input equals or exceeds the effective heat of ablation, the section is removed from further consideration in the problem and the temperature of the next section in the material is set to the ablation temperature. This process continues until the complete trajectory has been analyzed. The results indicate the temperature of each section and the amount of material ablated.

2.7.3 Heat Shield Thicknesses vs Backface Temperatures

Forebody shield thicknesses and corresponding backface temperatures are shown on Figures 2.7-14 through 2.7-27 for each of the candidate materials. (The data on phenolic-glass are presented in Section 3.0 - Preliminary Design.) Comparisons between the computer, Swann, and Adam analyses are indicated for the individual materials.

For example, Figures 2.7-21 through 2.7-24 describe the performance of Thermo-lag T-500. Figure 2.7-21 indicates the thickness and weight of Thermo-lag T-500 when used on the large capsule and subjected to the heating of both a 20° and 90° entry. The weight requirement is greater for the 20° entry. A thickness of approximately .18" is necessary to maintain a 500°F substructure temperature; the resulting weight is approximately 1.2 lb/ft^2. The same amount of material will provide a backface temperature of 160°F when used on the capsule entering at 90°. Figure 2.7-22 shows the temperature history of the structure for an entry of 20°. Although maximum heating occurs near the middle of the entry period, the backface temperature rises to a maximum value near the end of the flight. This is due to a soak-

ing effect, wherein heat stored in the surface layers of the shield continues to flow to the cooler substructure. Figure 2.7-23 shows the structure temperature history for the 90° entry. The shorter time period limits the backface temperature rise to a lower value. These curves demonstrate the load maxima occur prior to the maximum temperature rise and indicate that the structure may be designed employing low temperature criteria. Figure 2.7-24 shows the effects of entry angle on the ablation of material. The material is consumed more rapidly in the 90° entry. The total amount of ablated material is also greater for the 90° entry. The reason for the difference again is that the shorter time period does not permit the conduction of heat away from the surface.

Figure 2.7-25 shows the weights and thicknesses required when using Avcoat 5026-39 on both the small and large capsules entering at 20°. The thickness and weight required is approximately the same for the 7 ft as for the 17 ft capsule. Changing the entry angle to 90° would produce the same type of variation of thickness and weight except that the amounts required would be decreased. The temperature history of the backface is similar to that derived for Thermo-lag T-500. The maximum temperature occurs at the end of the time period, as shown in Figures 2.7-26 and 2.7-27 for the large and small capsules.

Figures 2.7-28 through 2.7-38 indicate the thicknesses and weights for the afterbody of the small capsule. Figures 2.7-28 through 2.7-32 are for an afterbody using a .02" aluminum substructure with phenolic glass protection; Figures 2.7-33 through 2.7-38 are for a phenolic glass afterbody. The configuration with the aluminum substructure results in lower backface temperatures due to the heat capacity of the aluminum. The heating rates to the afterbody were not high enough to produce ablation of the phenolic glass. Figure 2.7-38 indicates the maximum surface temperatures attained by the phenolic glass. Figures 2.7-31, 2.7-32, 2.7-36, and 2.7-37 indicate the temperature of .15" of phenolic glass when used on the large capsule entering at 20° and 90°. Entry at 20° results in a higher temperature for the structure in all cases.

2.7.4 Heat Shield Recommendations

In reviewing the materials, their advantages and disadvantages, and the weights derived from the analysis, phenolic glass is recommended as a prime candidate material for the forebody heat shield on the small capsule. A thorough backlog of experience has been developed in qualifying this material for the ballistic missile and satellite programs and a thorough literature search could conceivably reduce many requirements for a test program and, hence, mitigate the program costs.

A Mercury flight-test report (Reference 1) presents data on a phenolic glass shield subjected to heat inputs very nearly identical to those anticipated for the small capsule at 20° entry. These data confirm the temperatures predicted in this analysis. The analysis indicates that the unit weight required would be approximately 3.2 lb/ft^2 for a 300°F backface tem-

perature, 3 lb/ft^2 for a 500°F backface, and approximately 2.6 lb/ft^2 for a 700°F backface temperature.

Several other materials could be considered to advantage. For example, Avcoat 5026-39 appears much lighter for all temperature regimes. Unit weights would be approximately 1.5 lb/ft^2 at a 300°F backface temperature and 1.0 lb/ft^2 at 700°F. Thermo-lag T-500 and SE-28 offer comparable weight advantages. However, though these and other candidate materials offer lower unit weights than phenolic glass, a more extensive test program would be required to qualify them in time for the project January 1967 launch date.

The forebody heat shield for the large capsule centers about the application of Avcoat 5026-30, Thermo-lag T-500, SE-28, and, perhaps, phenolic nylon. The large capsule is to be flown at a later date than the small capsule (i.e., March 1969), so more development time is available and the various materials can be studied more closely. Data from such programs as Apollo, FIRE, etc., will become available. The size of the large capsule also restricts the choice of materials. Those materials requiring high molding pressures (e.g., phenolic glass) and/or high curing temperatures become less attractive because of the fabrication difficulties presented. A specific recommendation for a material for the large capsule heat shield will not be presented at this time. As stated previously, the weights of the materials analyzed appear reasonable; however, a more extensive analysis of other factors must be conducted before an intelligent selection can be made.

The selection of materials for use on the afterbody does not appear to be restricted by thermal performance but rather by the structural requirements and such factors as payload arrangement (e.g., r.f. transparency). It appears at this time that the thermal capacity (i.e., heat sink properties) of the materials considered can very nearly accommodate the heat loads anticipated.

2.7.5 References

1. O'Neal, R. L., and Rabb, L., "Heat-Shield Performance During Atmospheric Entry Off Project Mercury Research and Development Vehicle," NASA Technical Memo X-490, May 1961 (Confidential)

2. Schmidt, D. L., "Behavior of Plastics in Re-entry Environments," Modern Plastics, November 1960, pp 625-632

3. Adams, M. C., "Recent Advances in Ablation," ARS Journal, September 1959

4. Swann, R. T., "An Engineering Analysis of the Weights of Ablating Systems for Manned Re-entry Vehicles," Ballistic Missile and Space Technology, Vol IV, Academic Press, 1960

5. "The Analysis of Transient One-Dimensional Heat Transfer with Material Ablation Using the IBM 704," NAA Report MD 60-193, June 1960

6. Dusinberre, G. M., "Numerical Analysis of Heat Flow," McGraw Hill Book Company, New York, N. Y., 1949

2.7.6 Nomenclature

Heff - Thermo-chemical Heat of Ablation, BTU/lb

$\dot{q}_o$ - Surface Heating Rate to Non-ablating Calorimeter, BTU/ft^2-sec

$\dot{q}_r$ - Radiant Emission Rate from the Ablating Surface, BTU/ft^2-sec

$\dot{m}$ - Mass Rate of Ablation, lb/ft^2-sec

Heff - Effective Heat of Ablation, BTU/lb

t - Allowable Backface Temperature, °F

t_a - Temperature of Ablation, °F

V_w - Velocity of Ablation, ft/hr

$\dot{q}$ - Average Heating Rate, BTU/ft^2-hr

H_a - Heat of Ablation, BTU/lb

ρ - Density, ft^3/lb

θ - Time, hr

α - Thermal Diffusivity, ft^2/hr

A - Insulation Thickness, ft

B - Thickness Ablated, ft

W - Weight per Unit Area, lb/ft^2

Q - Total Heat Input, BTU/ft^2

T_a - Temperature of Ablation, °R

T_e - Equilibrium Temperature for Average Heating Rate, °R

k - Thermal Conductivity, BTU/ft-hr-°F

C_p - Specific Heat, BTU/lb-°F

T_i - Initial Backface Temperature, °R

T_b - Final Backface Temperature, °R

X - Section Width, ft

Y - Section Thickness, ft

Z - Section Depth, ft

$\Delta\theta$ - Time Interval, sec, min, hr

T_n^1 - Temperature at end of Time Interval

T_n - Temperature at Beginning of Time Interval, °R

K - Thermal Conductivity, BTU/ft^2-hr-°R

$n-1$ - Neighboring Section Numbered one Low than n^{th}

$n+1$ - Neighboring Section Numbered one Higher than n^{th}

L - Conduction Path Length, ft

h_{BL} - Boundary Layer Heat Transfer Coefficient, BTU/ft^2-sec

T_{BL} - Boundary Layer Temperature, °R

ϵ - Emissivity of Section for Radiant Heat Transfer

σ - Stefan-Boltzmann Constant ($.173 \times 10^{-8}$), BTU/hr-ft^2-°R^4

d - Absorptivity of Section for Radiant Heat Transfer

G - Radiation Heat Load from External Source, BTU/ft^2-sec

Table 2.7-1

FOREBODY HEATING LOADS

$\gamma_E = -20°$				
D_B (Ft)	Q_c (1) Btu/Ft^2	Q_c (2) Btu/Ft^2	$\dot{q}_c$ (Max) (1) Btu/Ft^2-Sec	$\dot{q}_R$ (Max) (2) Btu/Ft^2-Sec
5	2680	222	51.9	5.6
6	2440	266	47.4	6.8
7	2270	310	43.9	7.9
8	2120	354	41.0	9.0
14	1600	621	31.0	15.9
16	1500	710	28.9	18.1
18	1420	795	27.2	20.3
20	1340	886	25.9	22.6

$\gamma_E = -90°$				
D_B (Ft)	Q_c (1) Btu/Ft^2	Q_c (2) Btu/Ft^2	q_c (Max) (1) Btu/Ft^2-Sec	$\dot{q}_R$ (Max) (2) Btu/Ft^2-S
5	1005	586	145.0	141.
6	915	704	133.0	170.
7	850	820	123.0	197.
8	795	936	114.5	226.
14	600	1640	86.8	396.
16	562	1880	81.0	452.
18	532	2100	76.2	508.
20	503	2340	72.4	567.

(1) Atmosphere W_1, W_2, B

(2) Atmosphere B

$R_{eff} = D_B / 1.15$

$V_E = 25000$ fps

$M/C_DA = .2$

Table 2.7-2

MATERIAL PROPERTIES

MATERIAL	C_p Btu/Lb-°F	K Btu/Ft-c Hr-°F	ρ Lb/Ft^3	α Ft^2/Hr	T_a °F	ϵ	H_a* Btu/Lb
Cork	.4	.04	30	.0033	500	.9	1300
SE-28	.5	.07	47	.00298	800	.9	2000
Thermo-Lag T-230	.29	.08	90	.00307	230	.8	1550
Thermo-Lag T-500	.35	.15	80	.00535	530	.8	2800
Phenolic Nylon 50% P/50% N	.35	.14	36	.0111	1860	.8	3000
Phenolic Glass 30% P/70% G	.28	.12	100-110	.00429	2000	.8	1600
Avcoat II	.42	1.2	63	.00454	1000	.9	1000
Avcoat 5026-39	.36	.07	35	.00555	800	.8	2000
Teflon	.24	.15	134	.00467	800	.8	2000

* Used in hand calculations or when constant value was assumed.

Figure 2.7-1

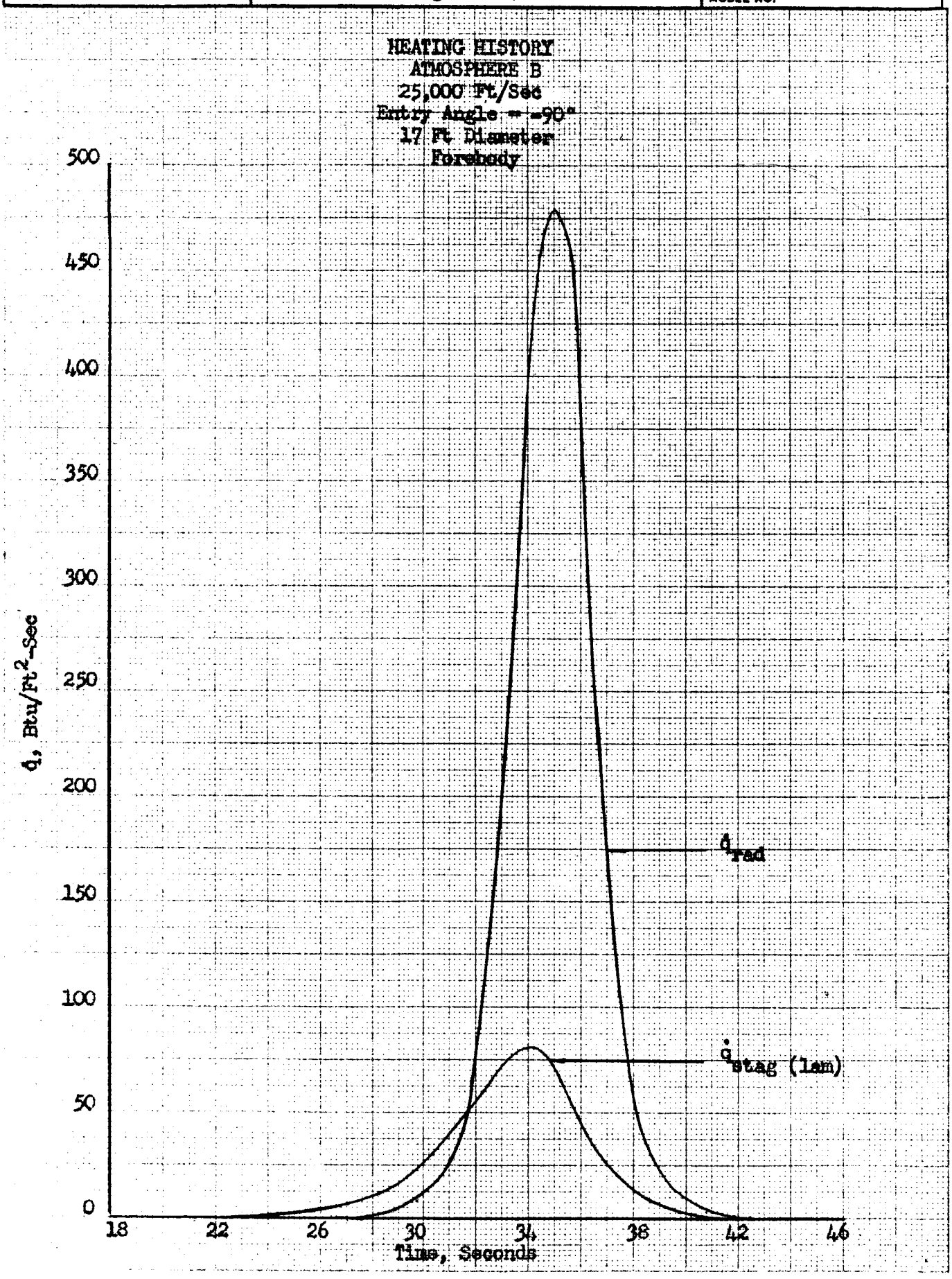
HEATING HISTORY
ATMOSPHERE B
25,000 Ft/Sec
Entry Angle = -90°
17 Ft Diameter
Forebody
500
450
400
350
300
250
200
150
100
50
0
q, Btu/Ft²-Sec
18
22
26
30
34
38
42
46
Time, Seconds
q̇rad
q̇stag (lam)

Figure 2.7-2

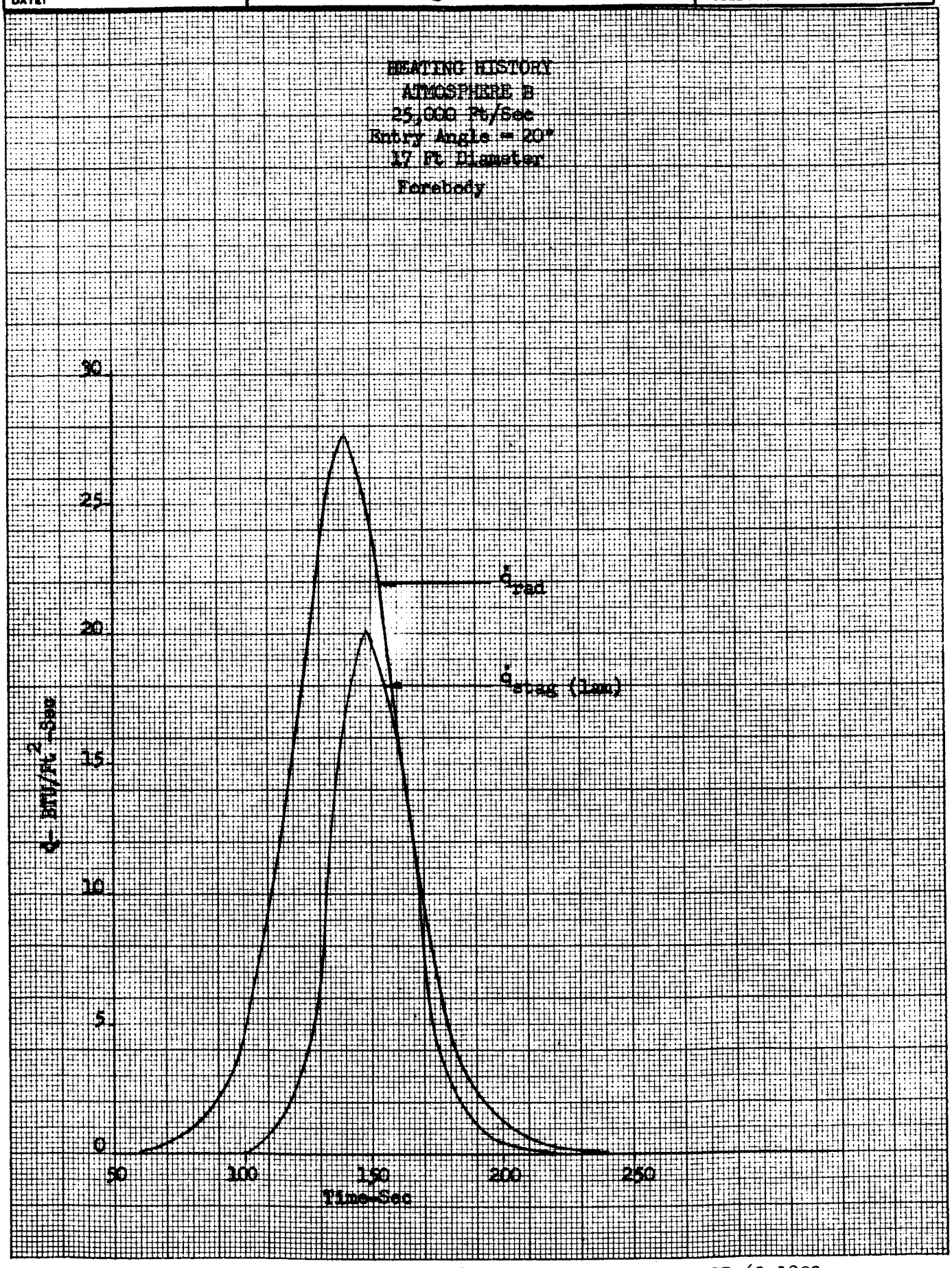
HEATING HISTORY
ATMOSPHERE B
25,000 Ft/Sec
Entry Angle = 20°
17 Ft Diameter
Forebody
$\dot{q}_{rad}$
$\dot{q}_{stag}$ (Lam)
$\dot{q}$ - BTU/Ft^2-Sec
30
25
20
15
10
5
0
50
100
150
200
250
Time-Sec

PREPARED BY:	NORTH AMERICAN AVIATION, INC. SPACE and INFORMATION SYSTEMS DIVISION	PAGE NO. OF
CHECKED BY:		REPORT NO.
DATE:	Figure 2.7-3	MODEL NO.

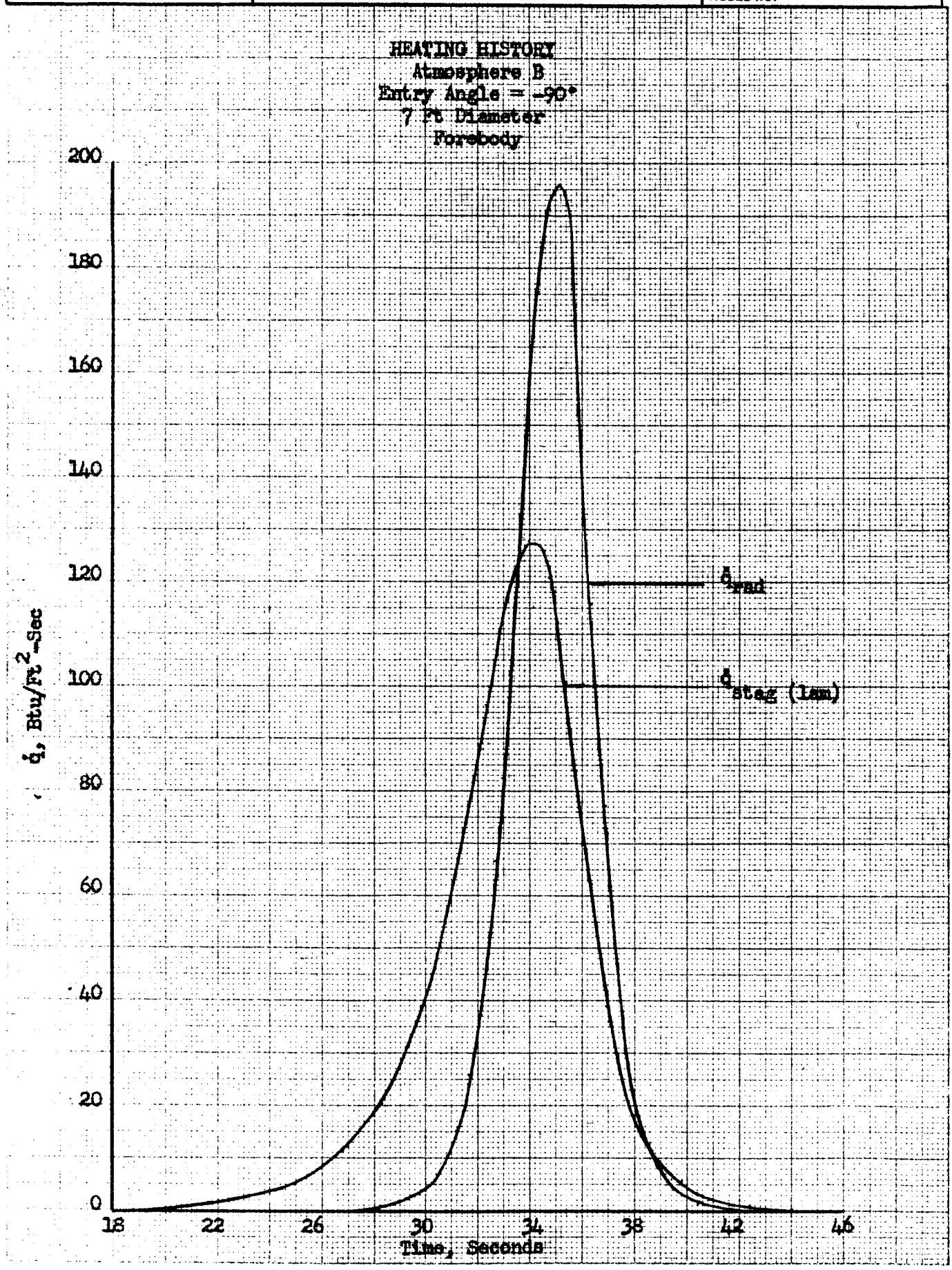

PREPARED BY:	NORTH AMERICAN AVIATION, INC. SPACE and INFORMATION SYSTEMS DIVISION	PAGE NO. OF
CHECKED BY:		REPORT NO.
DATE:	Figure 2.7-4	MODEL NO.

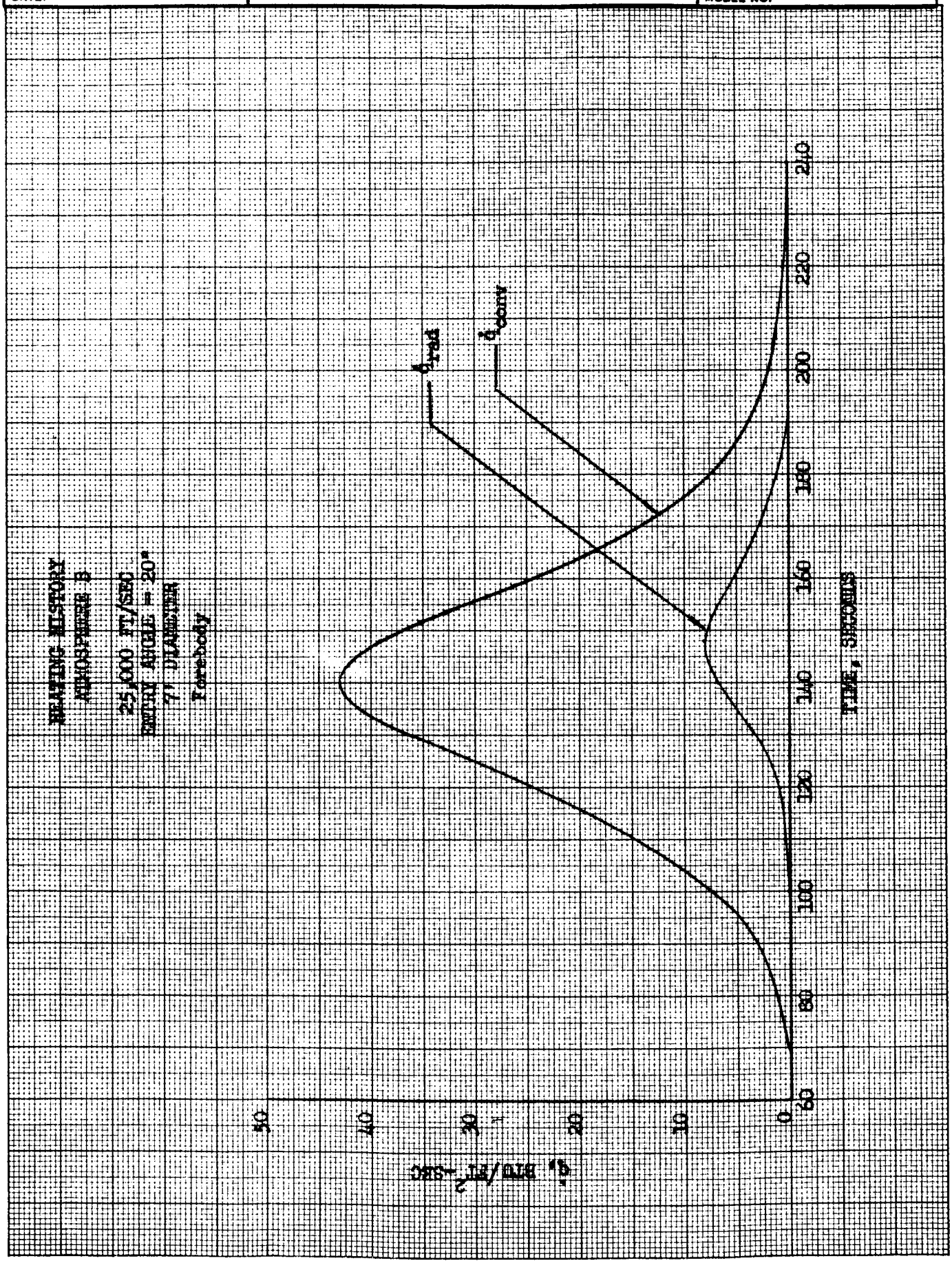

HEATING HISTORY
Atmosphere B
25,000 Ft/Sec
Entry Angle = -20°
7 Ft Diameter
Afterbody

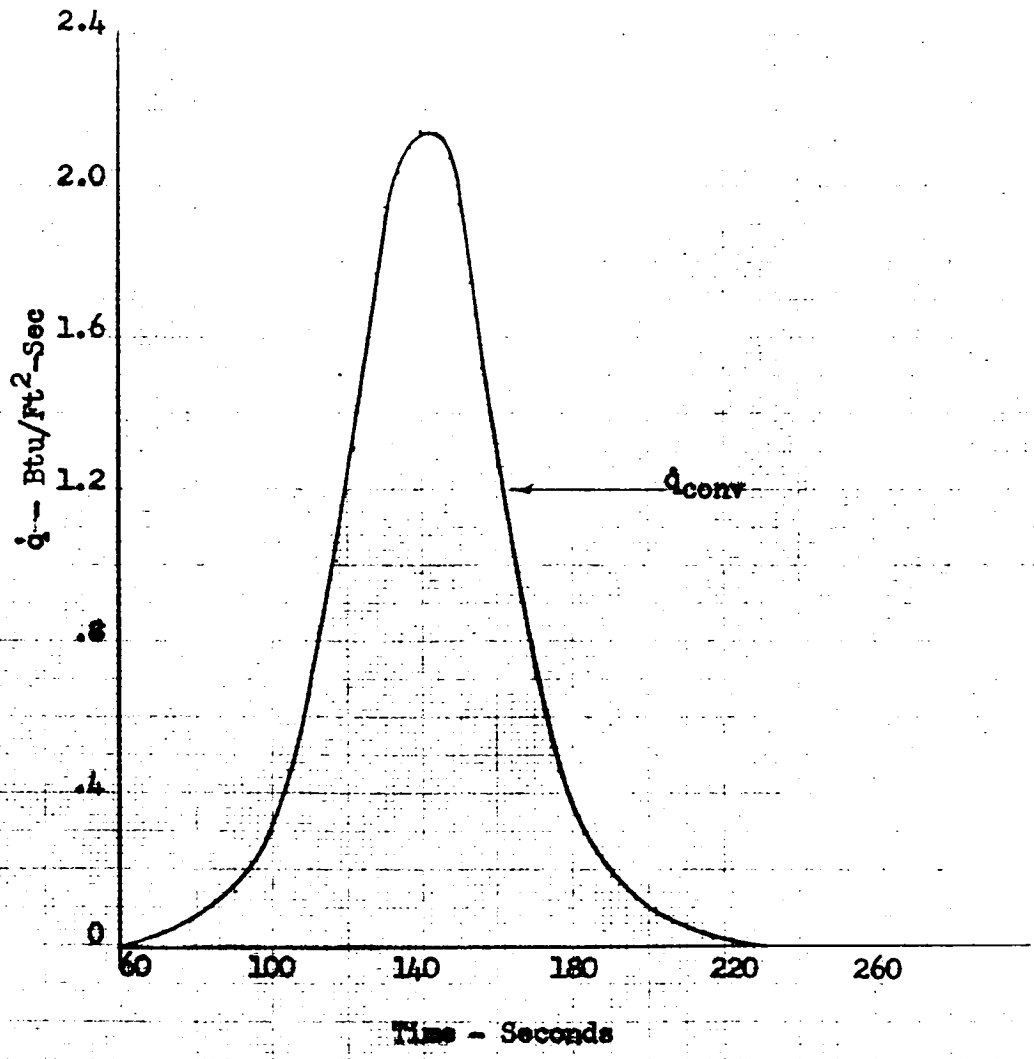

HEATING HISTORY
ATMOSPHERE B
25,000 Ft/Sec
Entry Angle = 90°
7 Ft Diameter
Afterbody

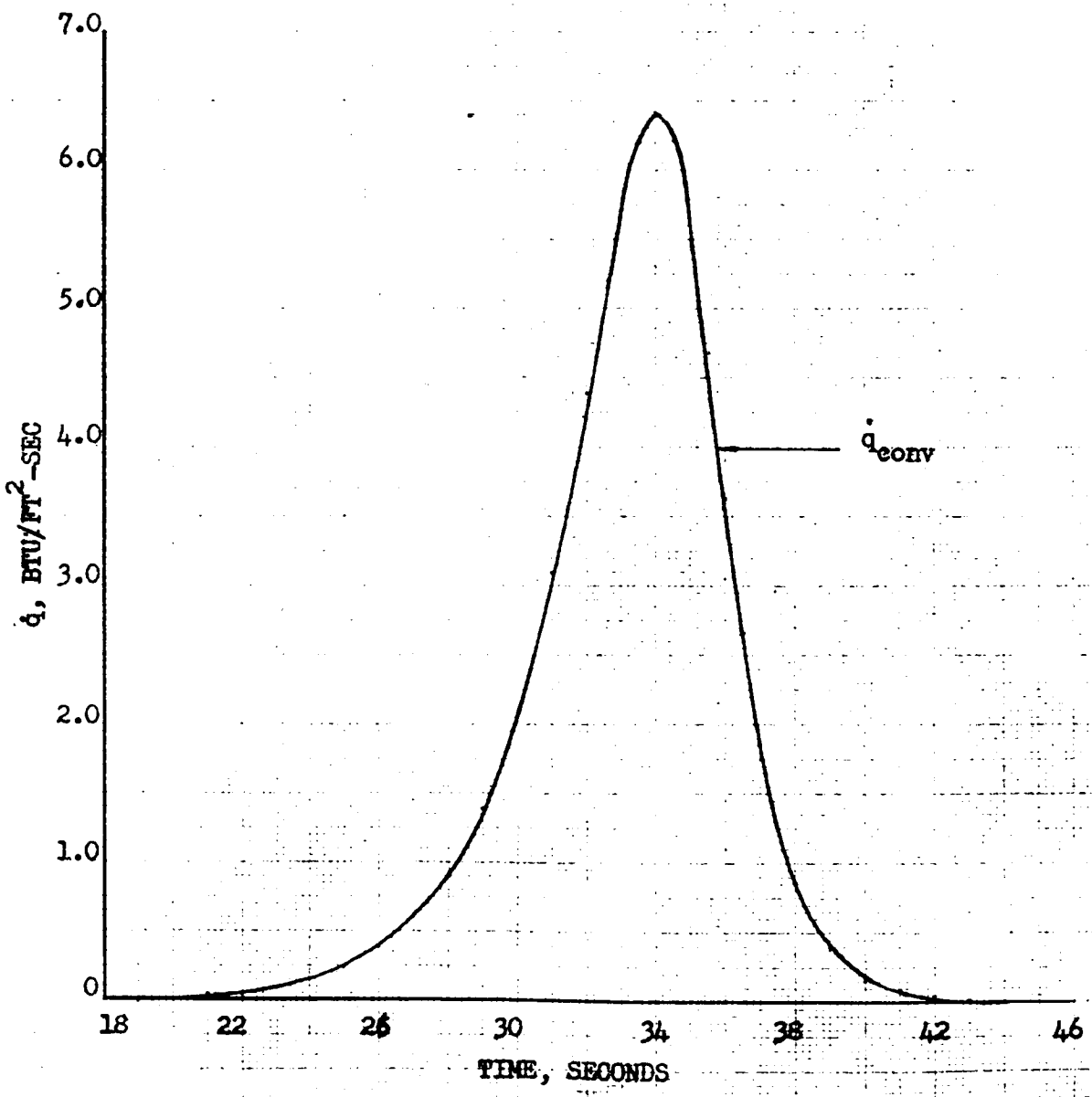

HEATING HISTORY
ATMOSPHERE B
25,000 Ft/Sec
Entry Angle = 20°
17 Ft Diameter
Afterbody

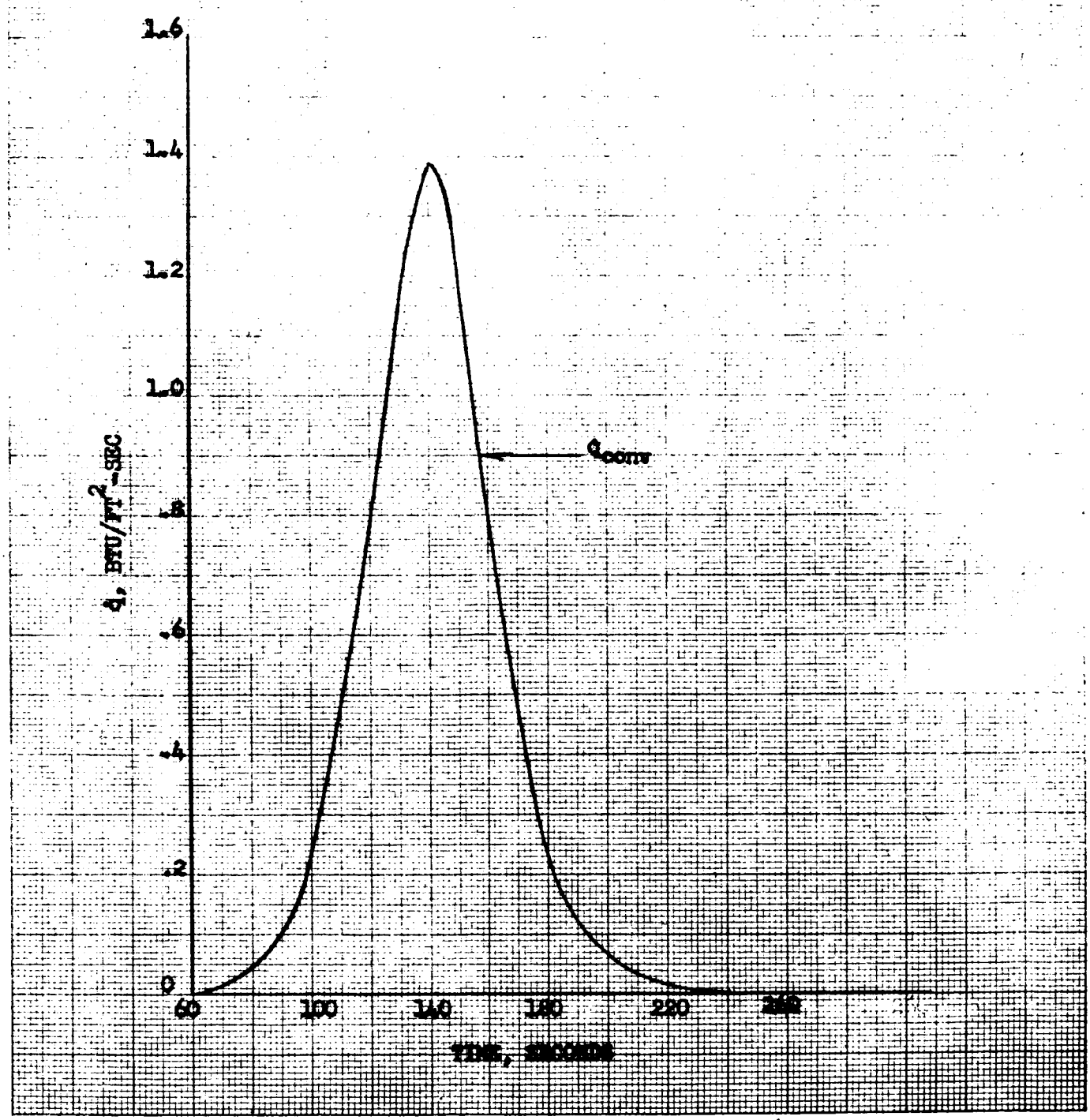

Figure 2.7-8

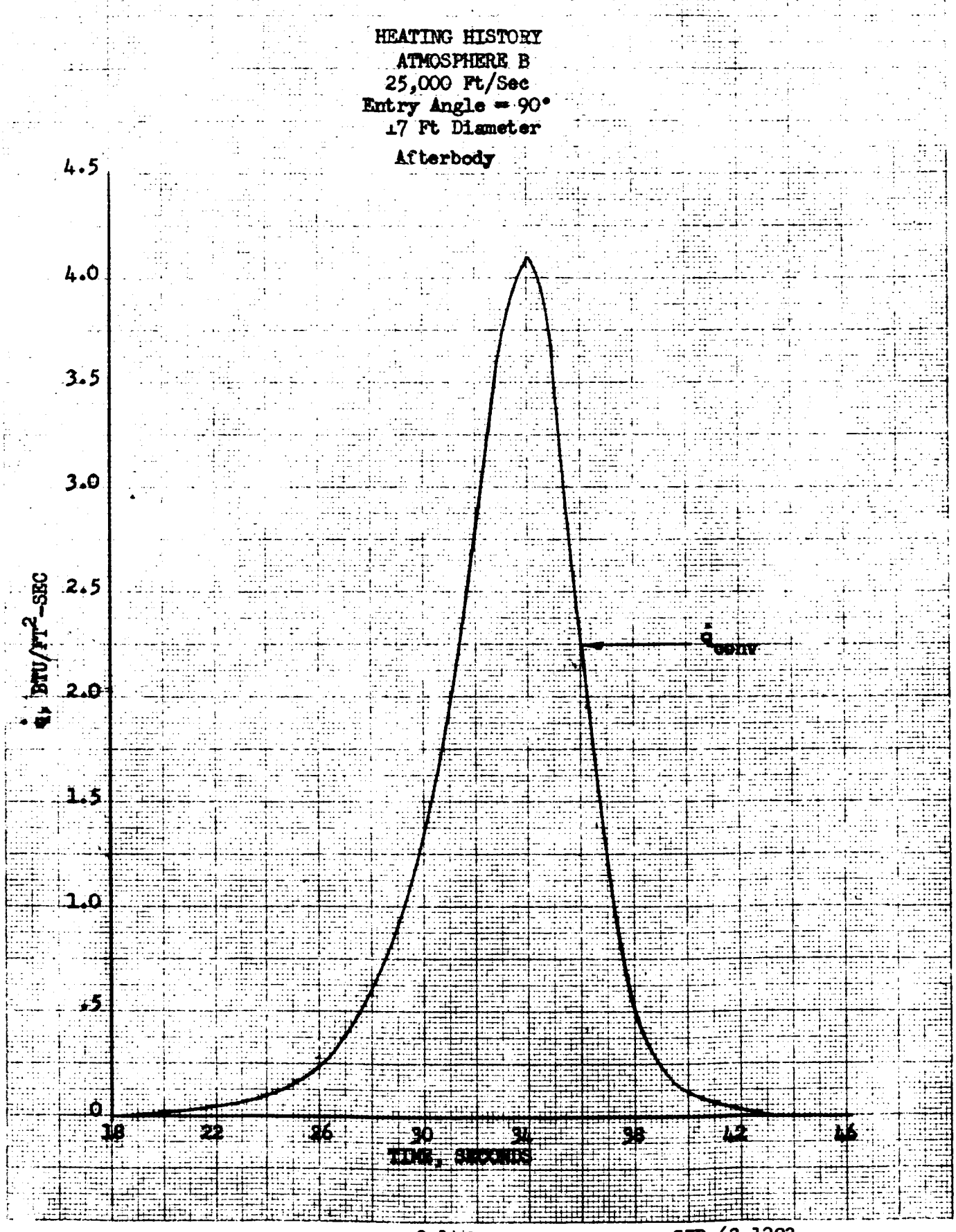
HEATING HISTORY
ATMOSPHERE B
25,000 Ft/Sec
Entry Angle = 90°
17 Ft Diameter
Afterbody
4.5
4.0
3.5
3.0
2.5
2.0
1.5
1.0
.5
0
$\dot{q}$, BTU/FT^2-SEC
$\dot{q}_{CONV}$
18
22
26
30
34
38
42
46
TIME, SECONDS

PREPARED BY:	NORTH AMERICAN AVIATION, INC. SPACE and INFORMATION SYSTEMS DIVISION	PAGE NO. OF
CHECKED BY:		REPORT NO.
DATE:	Figure 2.7-9	MODEL NO.

THERMO-CHEMICAL HEAT OF ABLATION VS ENTHALPY DIFFERENCE

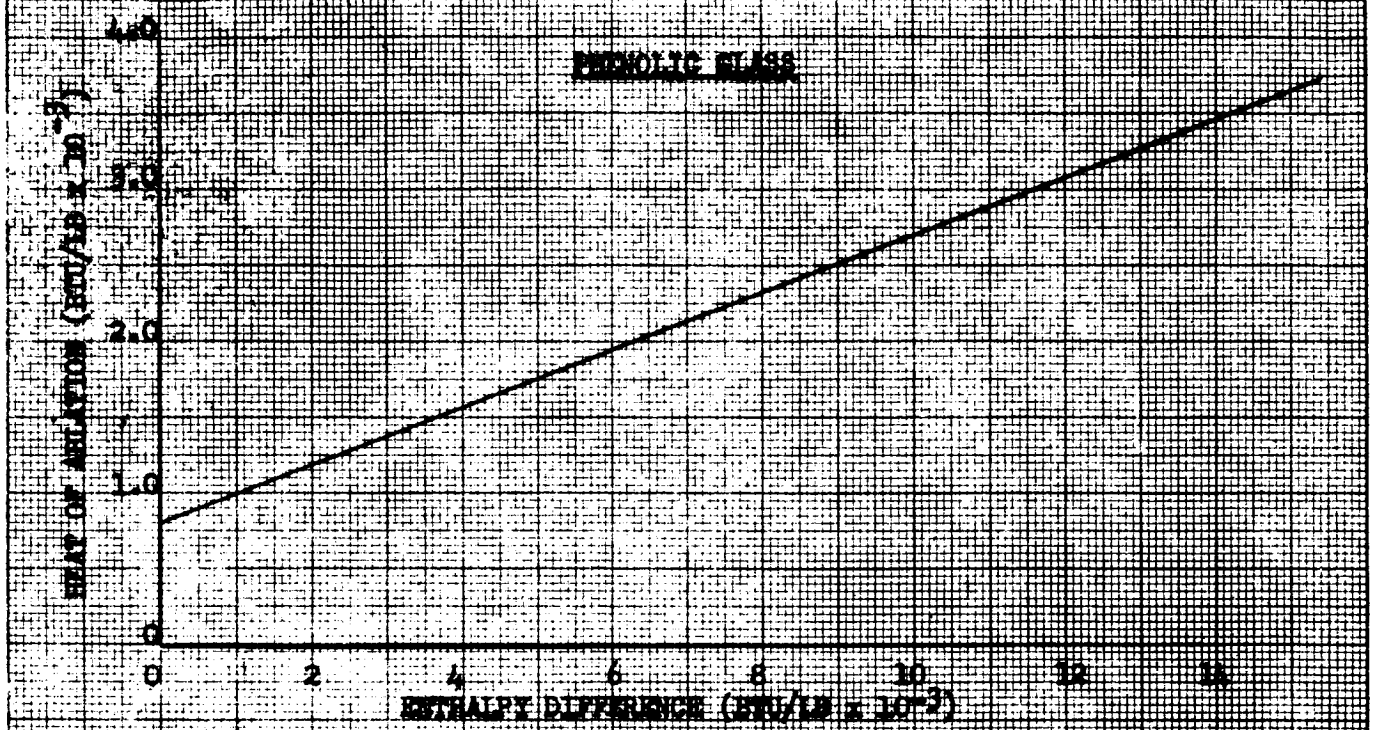

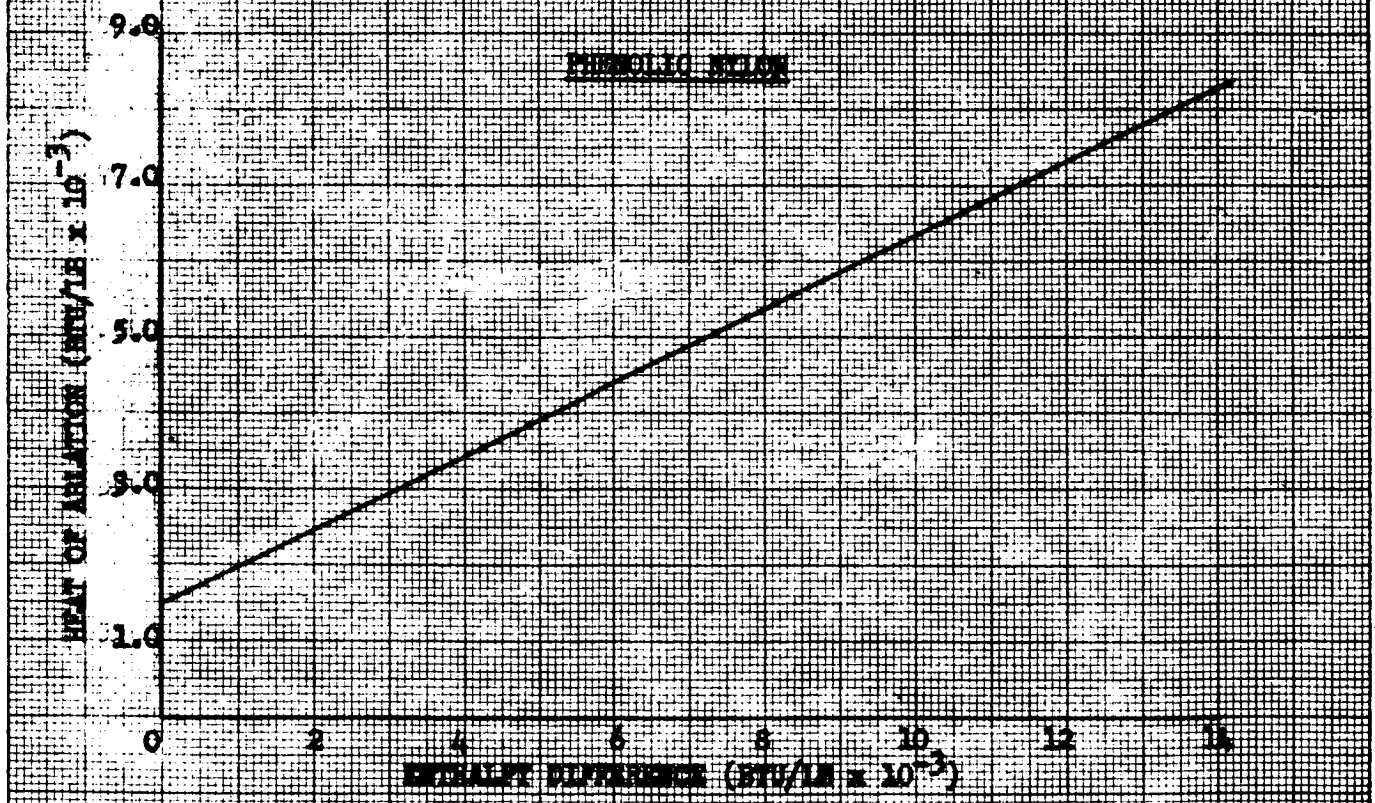

Figure 2.7-10

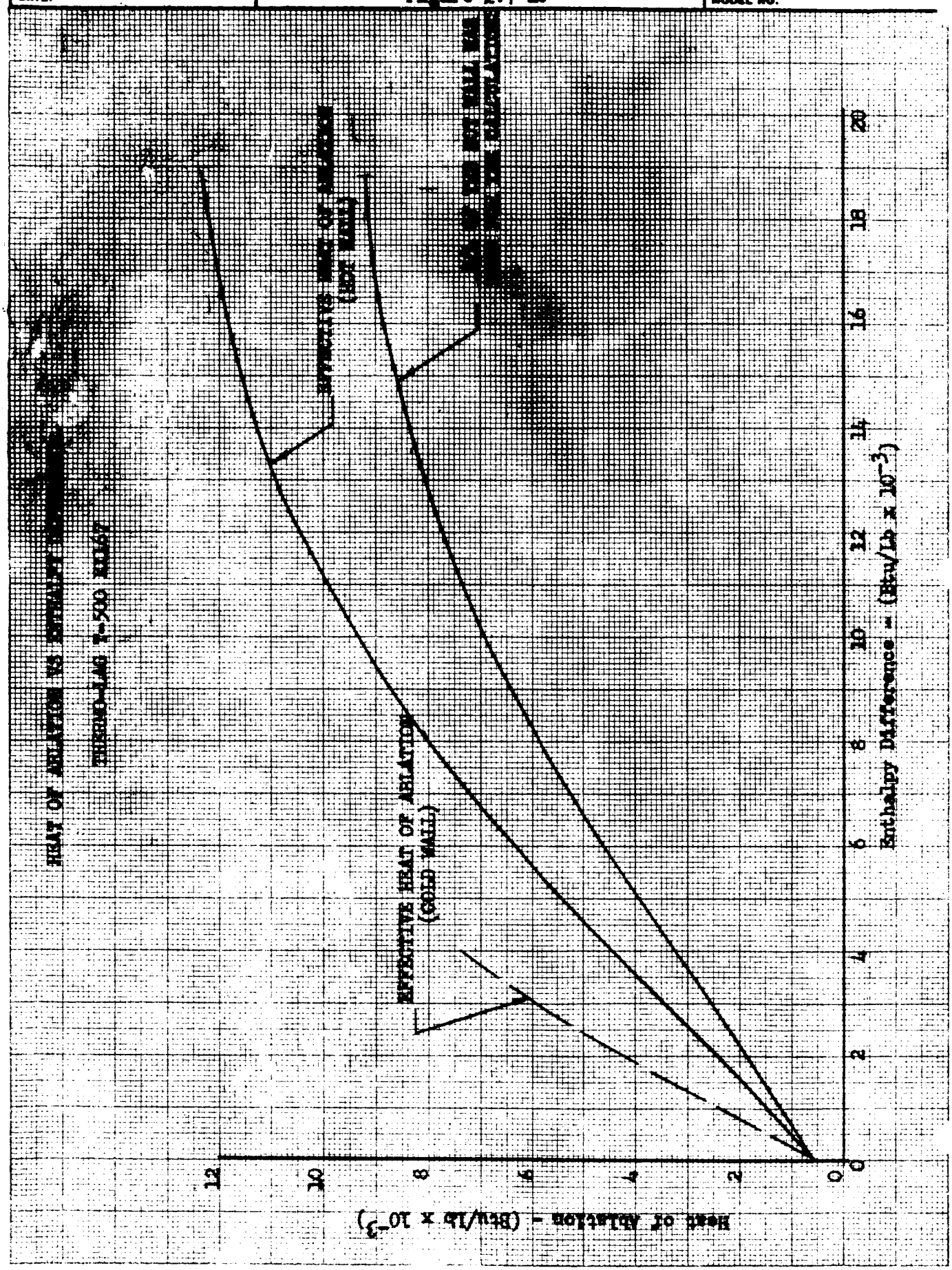
HEAT OF ABLATION VS ENTHALPY
THERMO-LAG T-500 EQ67
EFFECTIVE HEAT OF ABLATION
(HOT WALL)
EFFECTIVE HEAT OF ABLATION
(COLD WALL)
Heat of Ablation - (Btu/Lb x 10^-3)
Enthalpy Difference - (Btu/Lb x 10^-3)
0
2
4
6
8
10
12
14
16
18
20

Figure 2.7-11

THERMO-CHEMICAL HEAT OF ABLATION VS ENTHALPY DIFFERENCE

AVCOAT 5026-39

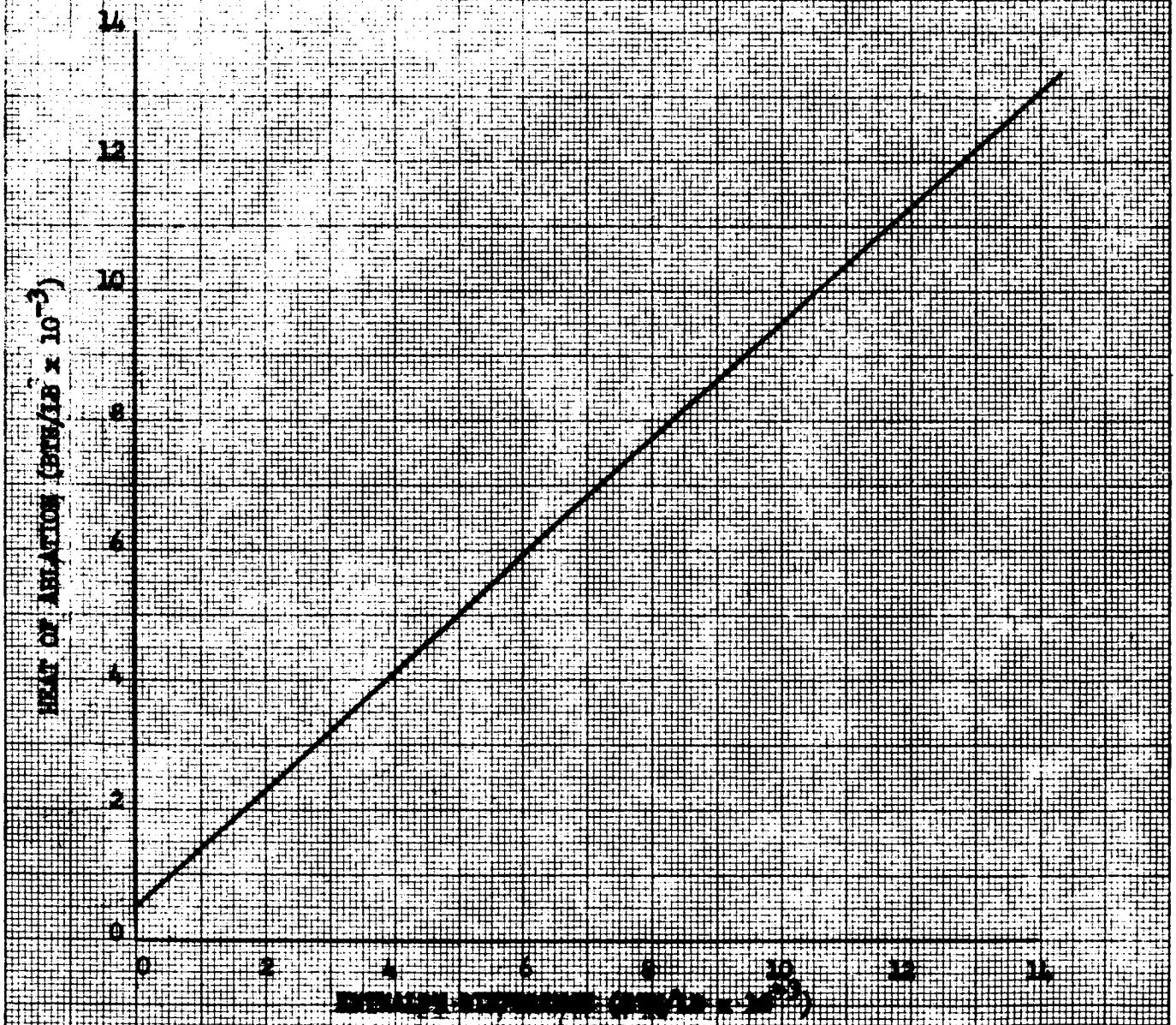

Figure 2.7-12

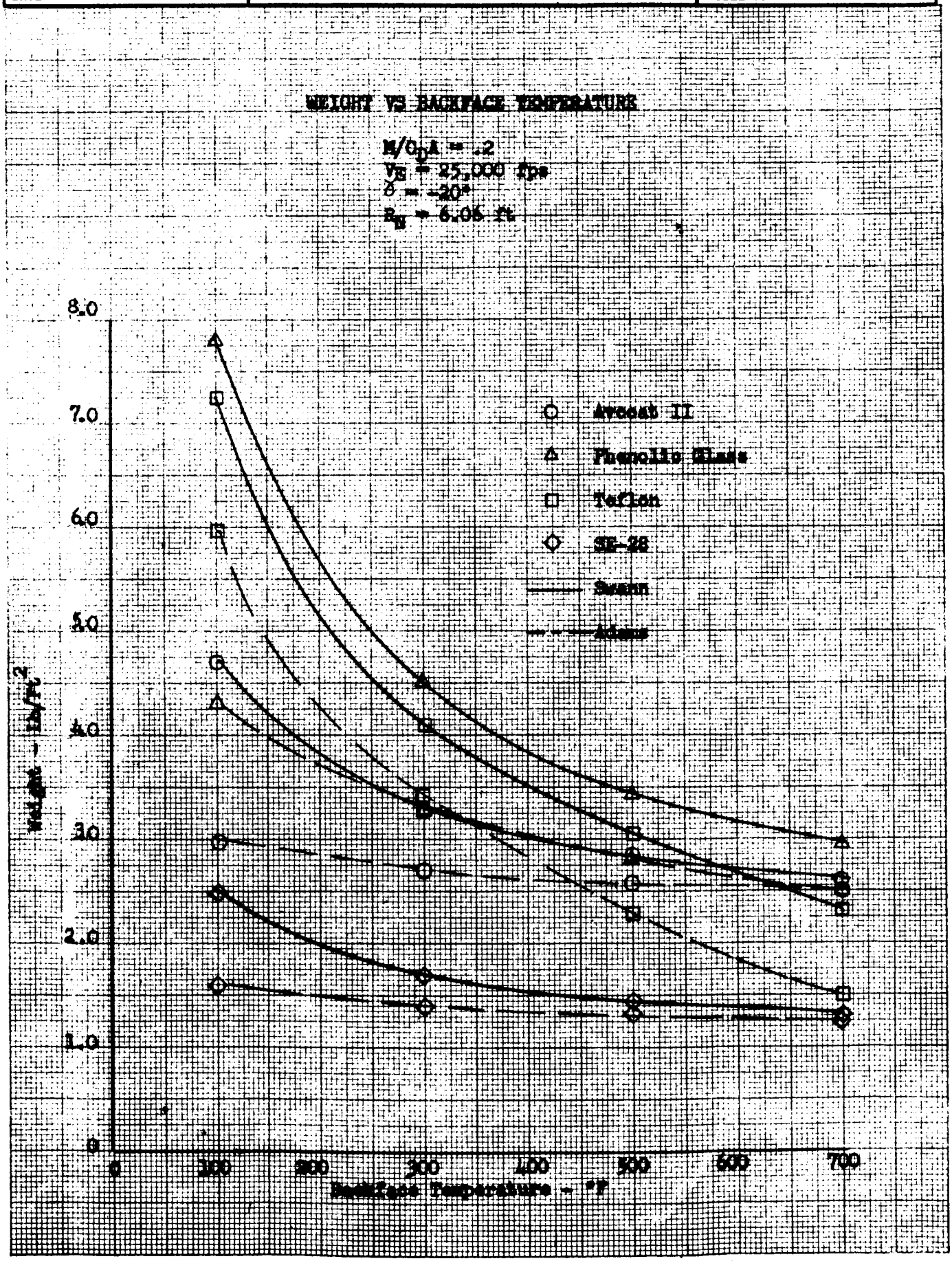
WEIGHT VS BACKFACE TEMPERATURE
M/C_DA = .2
V_E = 25,000 fps
δ = -20°
R_N = 6.06 ft
Avcoat II
Phenolic Glass
Teflon
SE-28
Swann
Adams
Weight - lb/ft²
Backface Temperature - °F
8.0
7.0
6.0
5.0
4.0
3.0
2.0
1.0
0
0
100
200
300
400
500
600
700

Figure 2.7-13

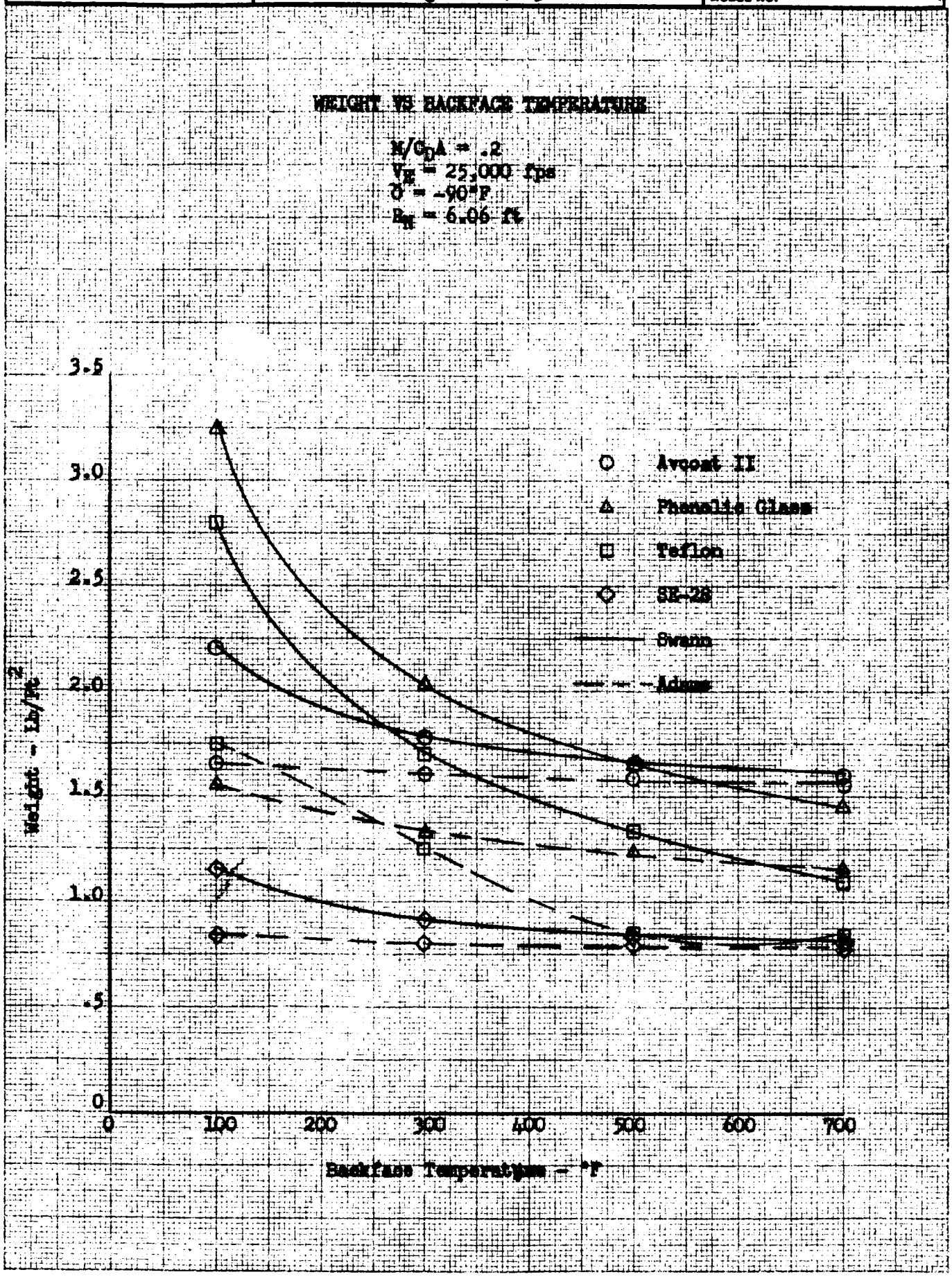
WEIGHT VS BACKFACE TEMPERATURE
M/C_DA = .2
V_E = 25,000 fps
θ = -90°F
R_N = 6.06 ft
Avcoat II
Phenolic Glass
Teflon
SE-28
Swann
Adams
Weight - Lb/ft²
Backface Temperature - °F
0
.5
1.0
1.5
2.0
2.5
3.0
3.5
100
200
300
400
500
600
700

Table 2.7-3

Conditions

Mac Adams Equation

$M/C_DA = .2$
$V_E = 25{,}000$ fps
$\gamma = -20°$
$R_N = 6.06$ Ft

MATERIAL	CORK	AVCOAT II	GLASS PHENOLIC	TEFLON	T-L* 230	T-L* 500	SE-28
Assumed H_a Btu/#	1300	1000	1600	2000	1550	2800	2000
Thermal Diffusivity Ft^2/Hr	.0033	.00454	.00429	.00467	.00307	.00535	.00298
Average Ht. Rate Btu/Ft^2-Sec	20.3	20.3	20.3	20.3	20.3	20.3	20.3
Temp. of Ablation °F	500	1000	2000	800	230	500	800
Ablator Thickness Inches	.748	.459	.187	.109	.20	.129	.317
Insulation Thickness Inches 100°F	.034	.109	.33	.425	.0608	.318	.094
Combined Thickness Inches 100°F	.782	.568	.517	.534	.260	.447	.411
Wt. of Ablator $\#/Ft^2$	1.86	2.41	1.56	1.22	1.50	.86	1.24
Wt. of Insulation $\#/Ft^2$ 100°F	.08	.57	2.75	4.75	.45	2.12	.37
Combined Weight $\#/Ft^2$ 100°F	1.94	2.98	4.31	5.97	1.95	2.98	1.61
Combined Weight $\#/Ft^2$ 300°F	1.89	2.71	3.29	3.40	——	1.54	1.41
Combined Weight $\#/Ft^2$ 500°F	——	2.58	2.80	2.29	——	——	1.32
Combined Weight $\#/Ft^2$ 700°F	——	2.50	2.50	1.50	——	——	1.26
Density $\#/Ft^3$	30	63	100	134	90	80	47

* THERMO-LAG

Table 2.7-4

Conditions

Swann Equation

$M/C_DA = .2$
$V_E = 25{,}000$ fps
$\gamma = -20°$
$R_N = 6.06$ Ft

MATERIAL	CORK	AVCOAT II	GLASS PHENOLIC	TEFLON	T-L* 230	T-L* 500	SE-28
Assumed H_a Btu/#	1300	1000	1600	2000	1550	2800	2000
Thermal Diffusivity Ft^2/Hr	.0033	.00454	.00429	.00467	.00307	.00535	.00298
Average Height Rate Btu/Ft^2-Sec	20.3	20.3	20.3	20.3	20.3	20.3	20.3
Temp. of Ablation °F	500	1000	2000	800	230	500	800
Density $\#/Ft^3$	30	63	100	134	90	80	47
Combined Weight $\#/Ft^2$ 100°F	2.19	4.71	7.81	7.25	2.69	3.69	2.50
Combined Weight $\#/Ft^2$ 300°F	1.91	3.28	4.54	4.09	——	2.06	1.71
Combined Weight $\#/Ft^2$ 500°F	——	2.85	3.45	3.04	——	——	1.46
Combined Weight $\#/Ft^2$ 700°F	——	2.63	2.96	2.30	——	——	1.32

* THERMO-LAG

Table 2.7-5

Conditions

Mac Adams Equation

$M/C_DA = .2$
$V_E = 25{,}000$ fps
$\gamma = -90°$
$R_N = 6.06$ Ft

MATERIAL	CORK	AVCOAT II	GLASS PHENOLIC	TEFLON	T-L* 230	T-L* 500	SE-28
Ablator Thickness Inches	.48	.296	.117	.069	.134	.083	.198
Insulation Thickess Inches	.0071	.022	.072	.089	.012	.066	.019
Combined Thickness Inches	.487	.318	.189	.158	.146	.149	.217
Weight of Ablator #/Ft^2	1.19	1.55	.974	.78	1.0	.55	.78
Weight of Insulator #/Ft^2	.017	.11	.587	.98	.091	.44	.078
Combined Weight #/Ft^2 100°F	1.207	1.66	1.56	1.76	1.09	.99	.85
Combined Weight #/Ft^2 300°F	1.20	1.61	1.34	1.25	——	.70	.81
Combined Weight #/Ft^2 500°F	——	1.59	1.24	.87	——	——	.79
Combined Weight #/Ft^2 700°F	——	1.57	1.17	.84	——	——	.78
Average Height Rate	97.5	97.5	97.5	97.5	97.5	97.5	97.5

* THERMO-LAG

Table 2.7-6

Conditions

Swann Equation

$M/C_DA = .2$
$V_E = 25{,}000$ fps
$\gamma = -90°$
$R_N = 6.06$ Ft

MATERIAL	CORK	AVCOAT II	GLASS PHENOLIC	T-L* 230	T-L* 500	TEFLON	SE-28
Assumed H_a Btu/#	1300	1000	1600	1550	2800	2000	2000
Thermal Diffusivity Ft^2/Hr	.0033	.00454	.00429	.00307	.00535	.00467	.00298
Average Height Rate Btu/Ft^2-Sec	97.5	97.5	97.5	97.5	97.5	97.5	97.5
Temp. of Ablation °f	500	1000	2000	230	500	800	800
Density $\#/Ft^3$	30	63	100	90	80	134	47
Combined Weight $\#/Ft^2$ 100°F	1.29	2.21	3.25	0.30	1.42	2.80	1.16
Combined Weight $\#/Ft^2$ 300°F	1.22	1.78	2.04	—	.869	1.70	0.91
Combined Weight $\#/Ft^2$ 500°F	—	1.67	1.65	—	—	1.34	.843
Combined Weight $\#/Ft^2$ 700°F	—	1.61	1.45	—	—	1.10	.809

* THERMO-LAG

Figure 2.7-14

MAXIMUM BACKFACE TEMPERATURE AS A FUNCTION OF TOTAL THICKNESS

PHENOLIC NYLON

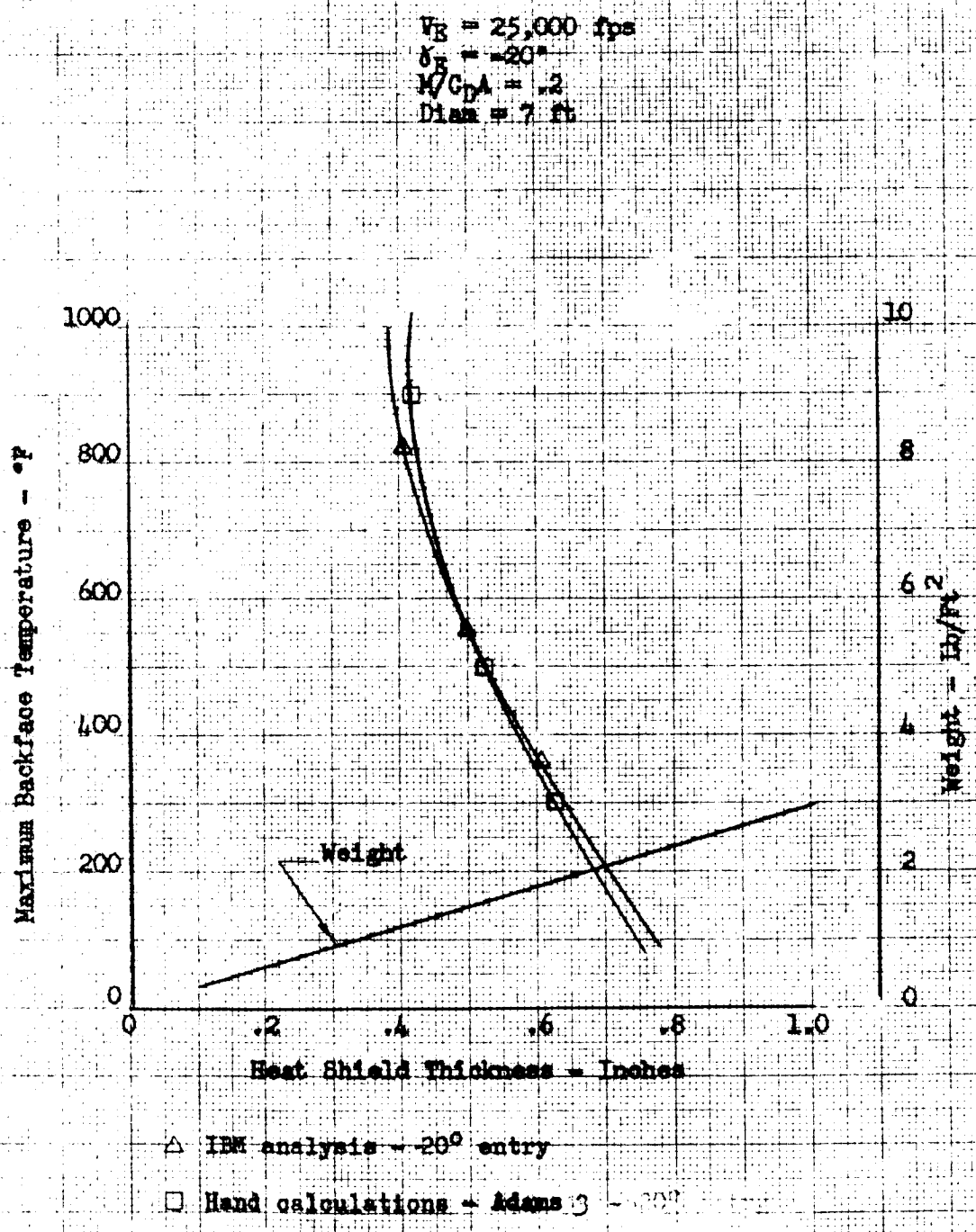

Figure 2.7-15 (Sheet 1)

STRUCTURE TEMPERATURE VS. PHENOLIC NYLON THICKNESS

V_E = 25,000 fps
γ_E = -20°
M/C$_D$A = .2
Diam = 7 ft

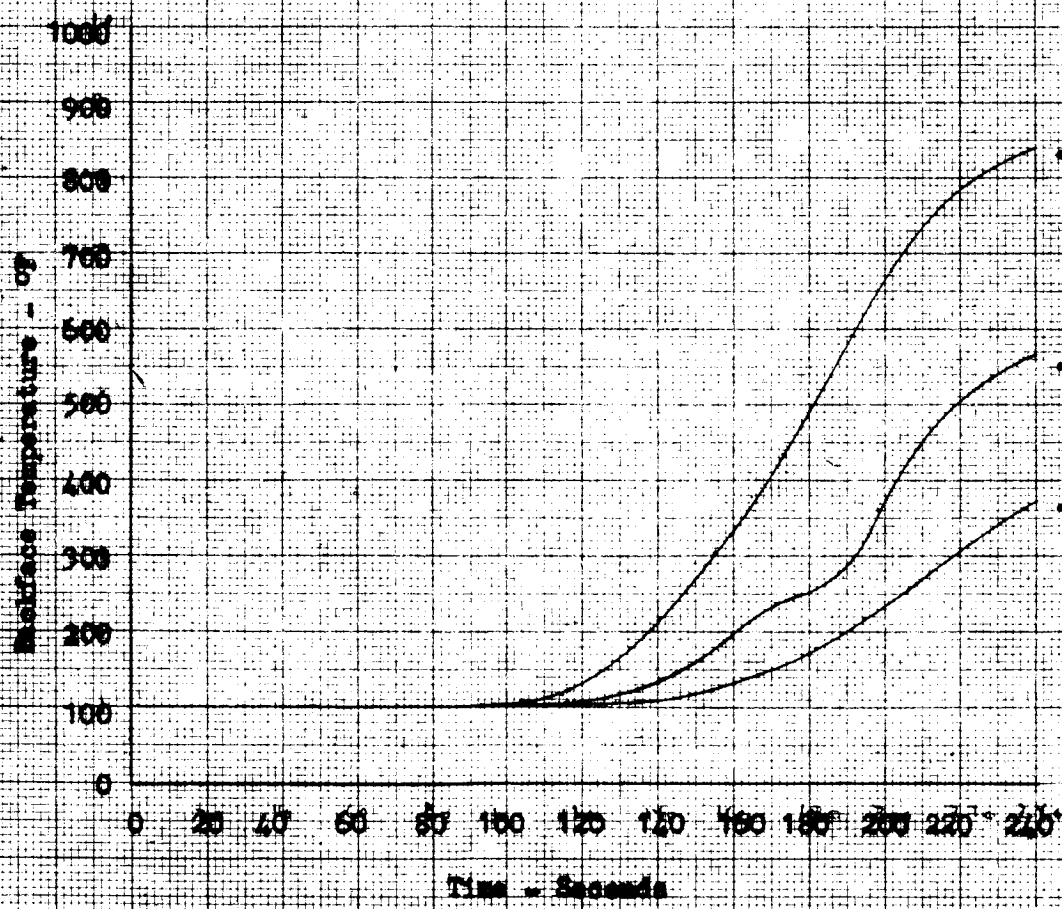

Figure 2.7-16

MAXIMUM BACKFACE TEMPERATURE AS A FUNCTION OF TOTAL THICKNESS

AVCOAT II

V_E = 25,000 fps
γ_E = -20° & -90°
M/C_DA = .2
Diam = 7 ft

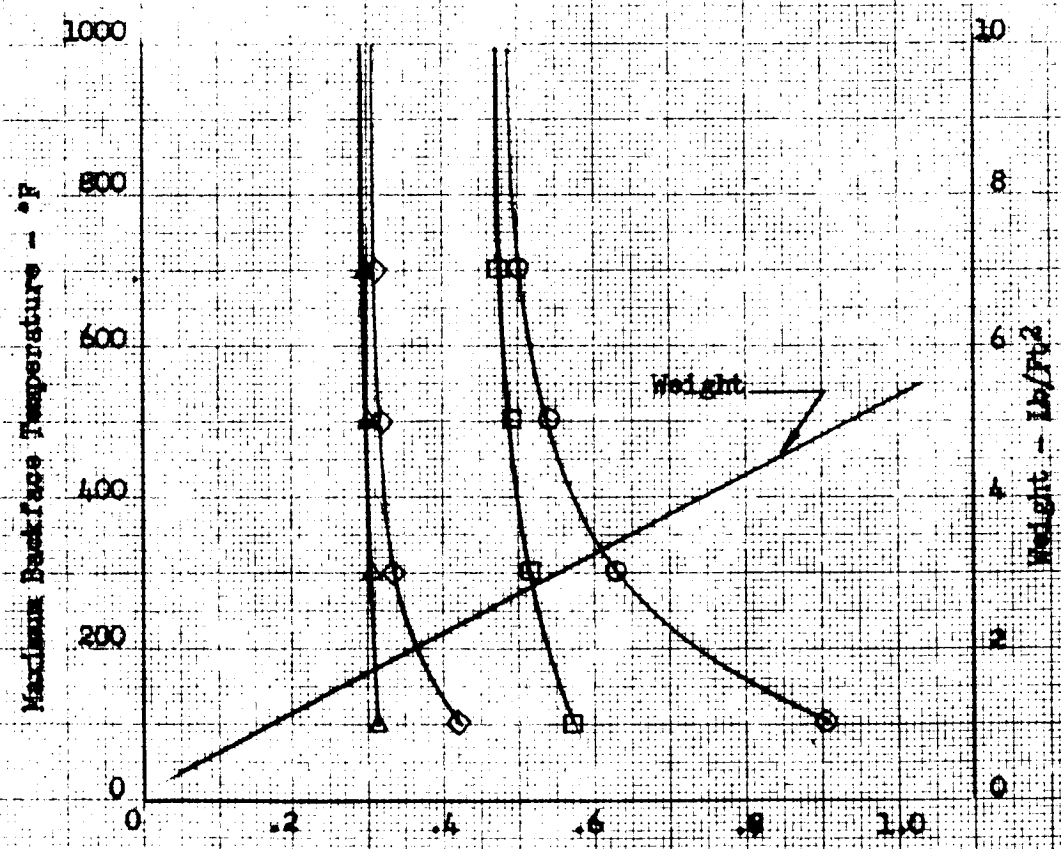

Hand Calculations - Swann (-20° Entry)

Hand Calculations - Adams (-20° Entry)

Hand Calculations - Swann (-90° Entry)

Hand Calculations - Adams (-90° Entry)

Figure 2.7-17

MAXIMUM BACKFACE TEMPERATURE AS A FUNCTION OF TOTAL THICKNESS

TEFLON

V_E = 25,000 fps
γ_E = -20° & -90°
W/CpA = .2
Diam = 7 ft

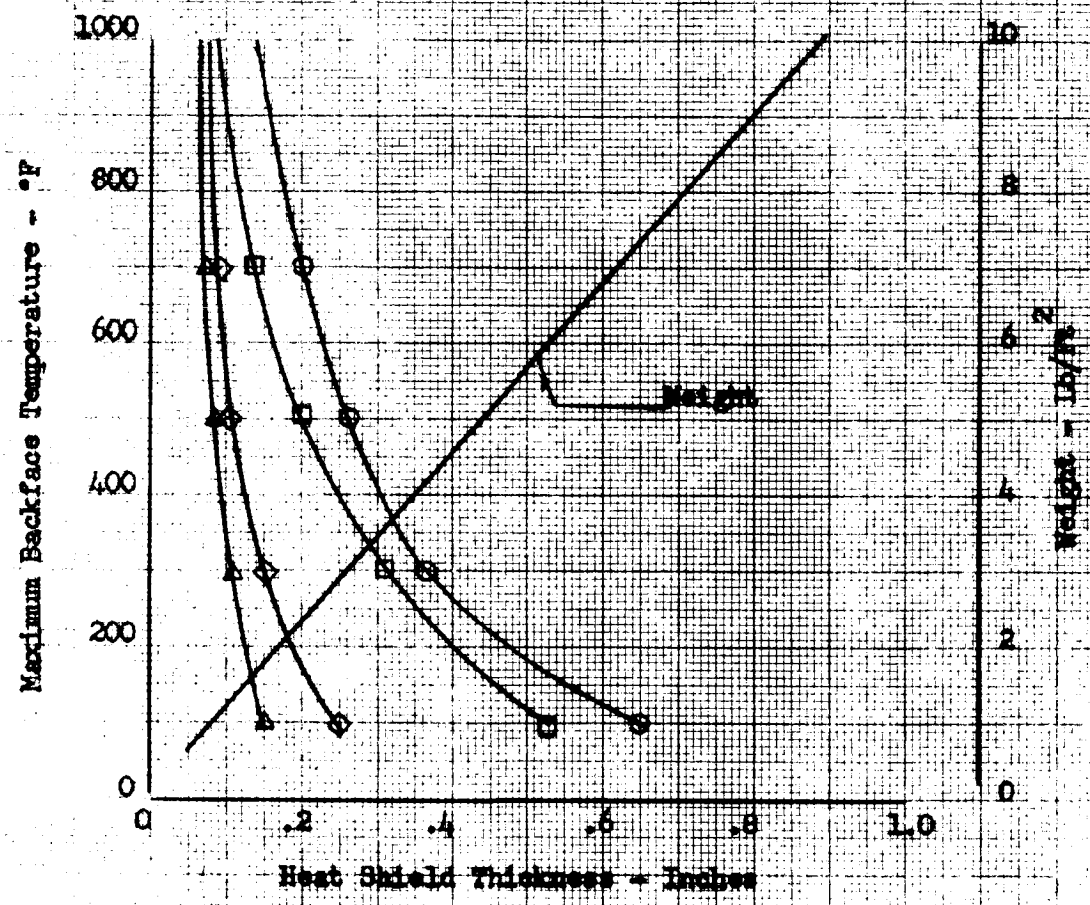

○ Hand Calculations - Swann (-20° Entry)

□ Hand Calculations - Adams (-20° Entry)

◇ Hand Calculations - Swann (-90° Entry)

△ Hand Calculations - Adams (-90° Entry)

Figure 2.7-18

MAXIMUM BACKFACE TEMPERATURE AS A FUNCTION OF TOTAL THICKNESS

SE-28

V_E = 25,000 fps
γ_E = -20° & -90°
M/C_DA = .2
Diam = 7 ft

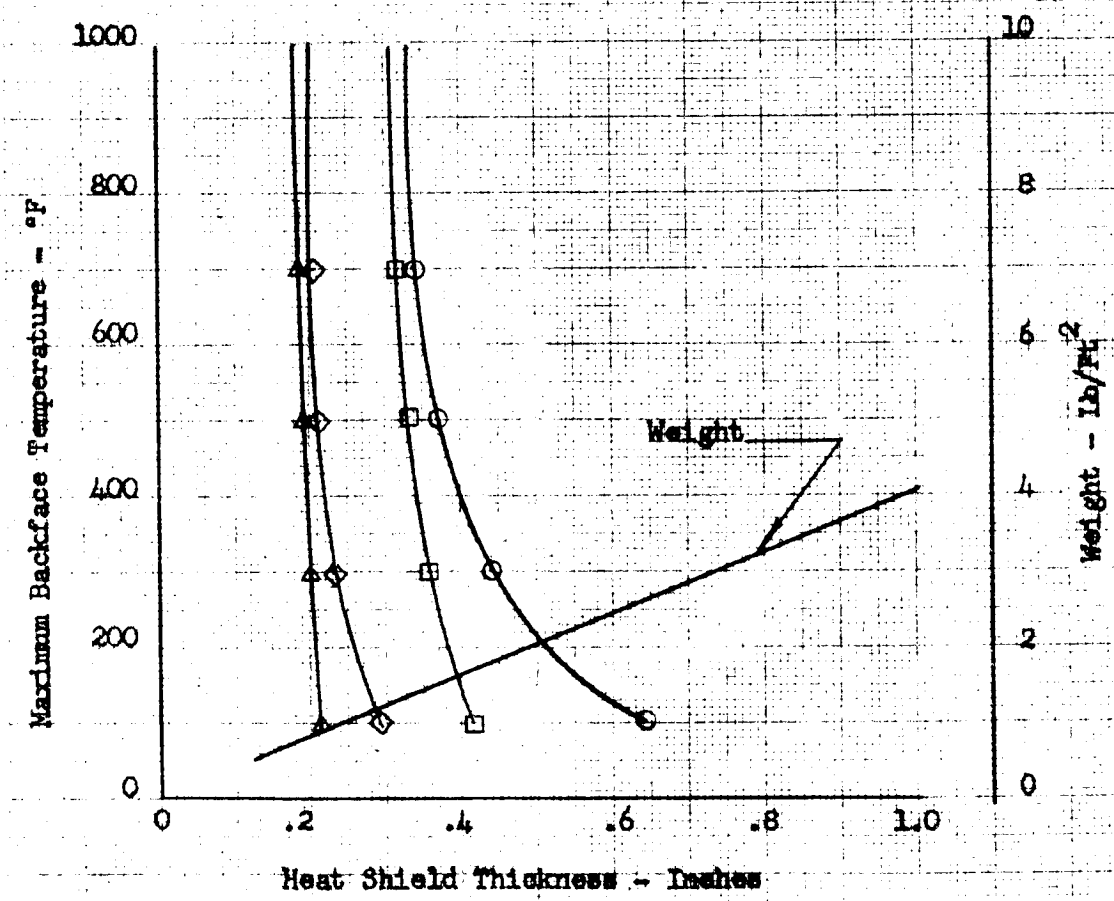

○ Hand Calculations - Swann (-20° Entry)

□ Hand Calculations - Adams (-20° Entry)

◇ Hand Calculations - Swann (-90° Entry)

△ Hand Calculations - Adams (-90° Entry)

Figure 2.7-19

MAXIMUM BACKFACE TEMPERATURE AS A FUNCTION OF TOTAL THICKNESS

SE - 2B

V_B = 25,000 fps
γ_E = -20°
M/C_DA = .2
Diam = 17 ft

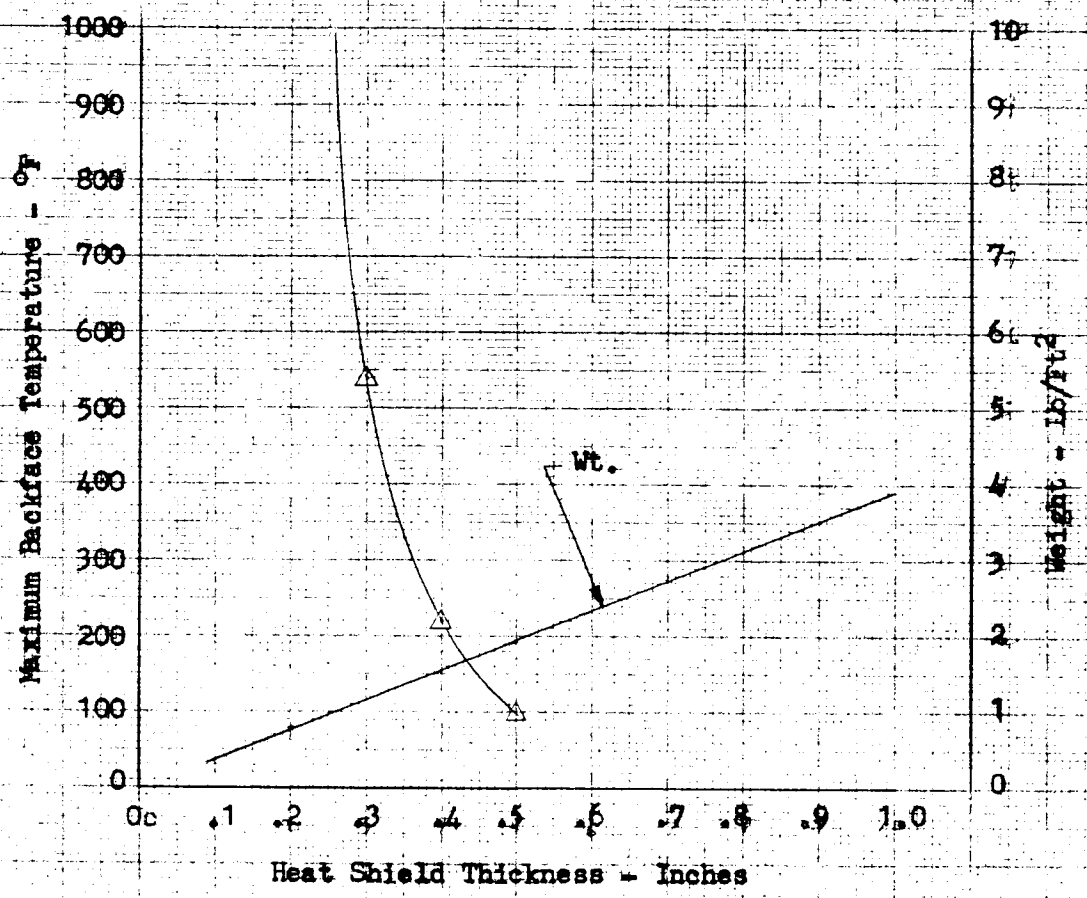

IBM analysis -

Figure 2.7-29

STRUCTURE TEMPERATURE VS SE-28 THICKNESS

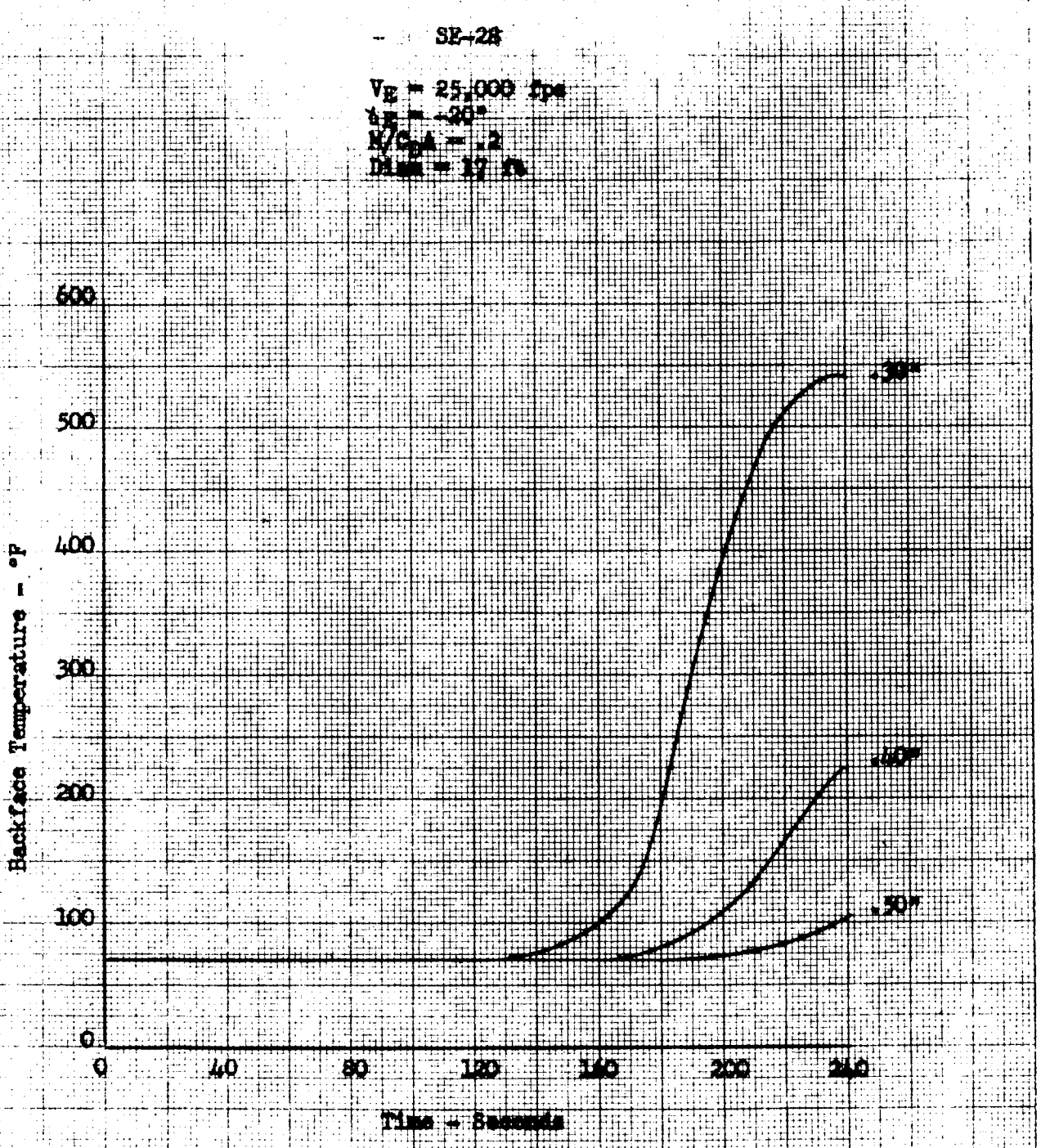

MAXIMUM BACKFACE TEMPERATURE AS A FUNCTION OF TOTAL THICKNESS

THERMO-LAG T-500

V_E = 25,000 fps
γ_E = -20° & -90°
M/C_DA = .2
Diam = 17 ft

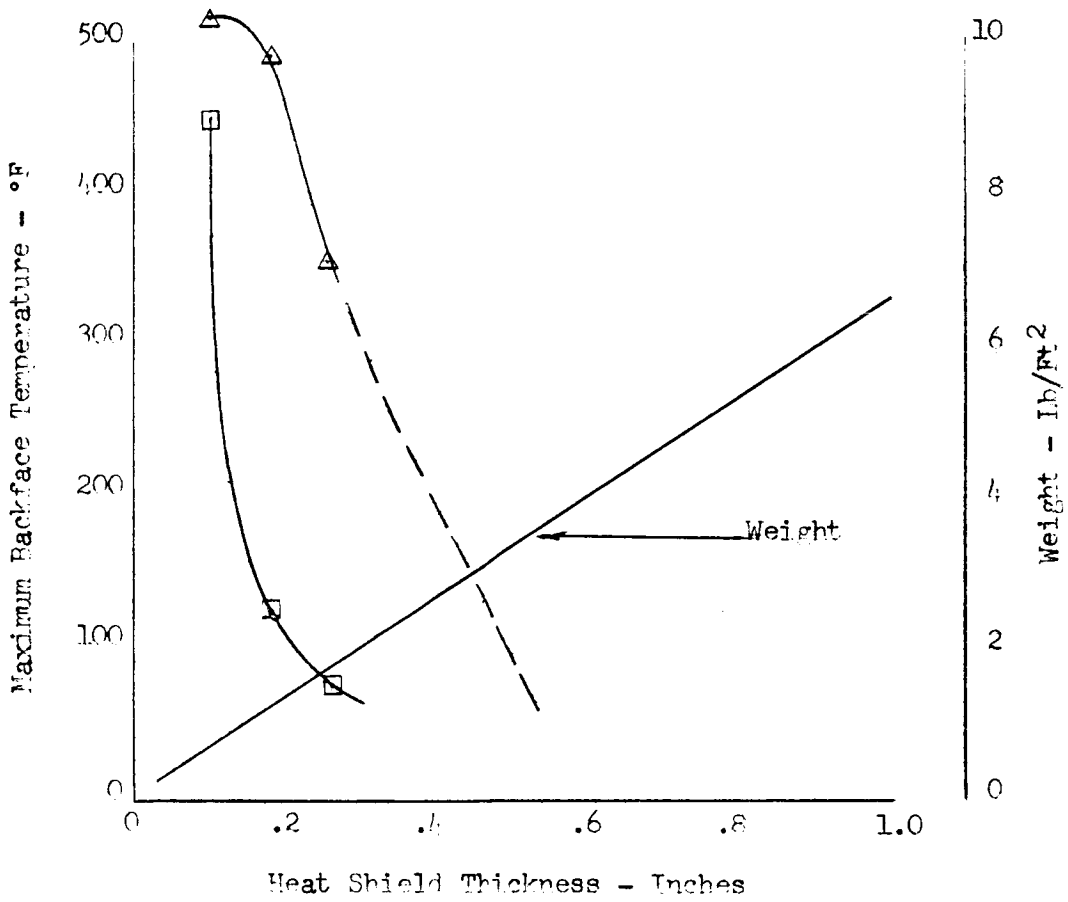

△ IBM analysis

□ IBM analysis

STRUCTURE TEMPERATURE VS THERMO-LAG T-500 THICKNESS

THERMO-LAG T-500

V_E = 25,000 fps
γ_E = -20°
M/C_DA = .2
Diam = 17 ft

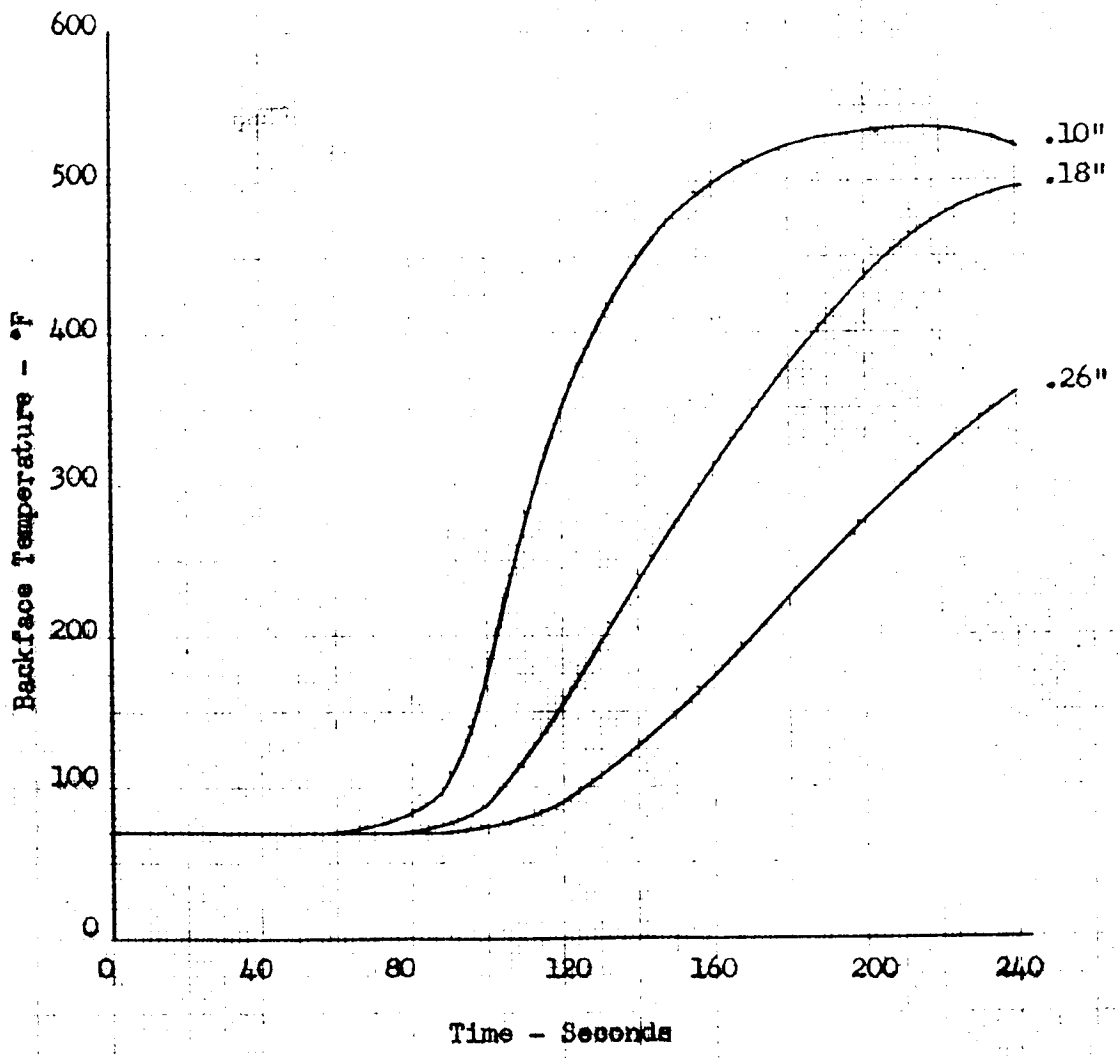

STRUCTURE TEMPERATURE VS THERMO-LAG T-500 THICKNESS

THERMO-LAG T-500

V_E = 25,000 fps
γ_E = -90°
M/C_DA = .2
Diam = 17 ft

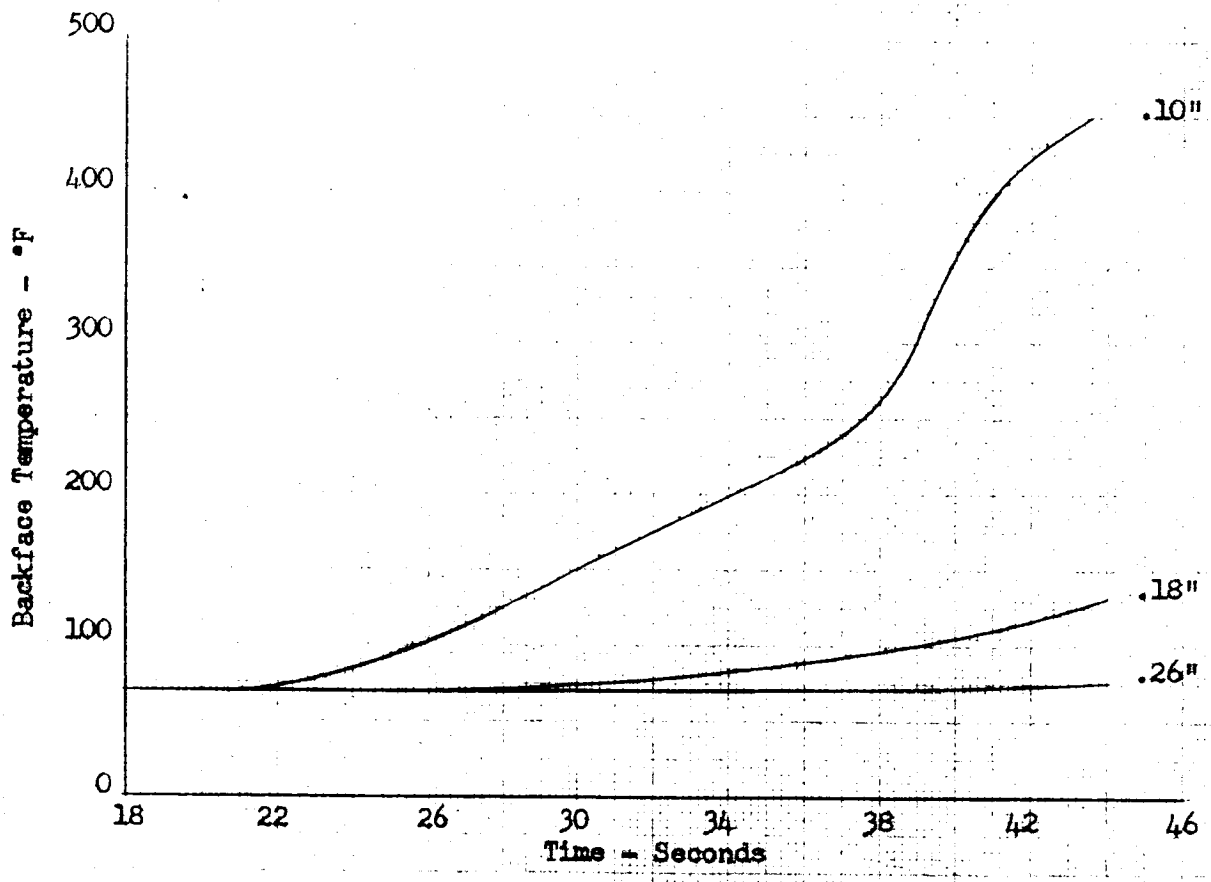

ABLATION HISTORY FOR THERMO-LAG T-500

V_E = 25,000 fps
γ_E = -20° & -90°
M/C_DA = .2
Diam = 17 ft

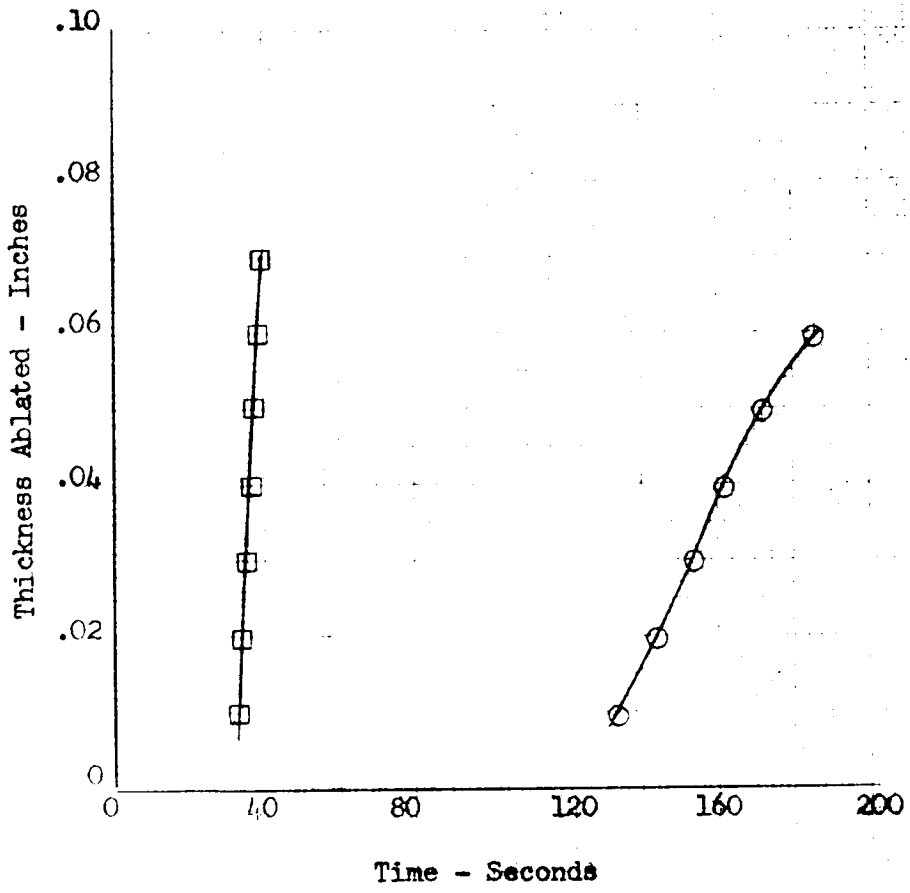

○ -20° entry - ablation rate = .000969 in/sec

□ -90° entry - ablation rate = .014 in/sec

MAXIMUM BACKFACE TEMPERATURE AS A FUNCTION OF TOTAL THICKNESS

AVCOAT 5026-39

V_E = 25,000 fps
γ_E = -20°
M/C_DA = .2
Diam = 7 ft & 17 ft

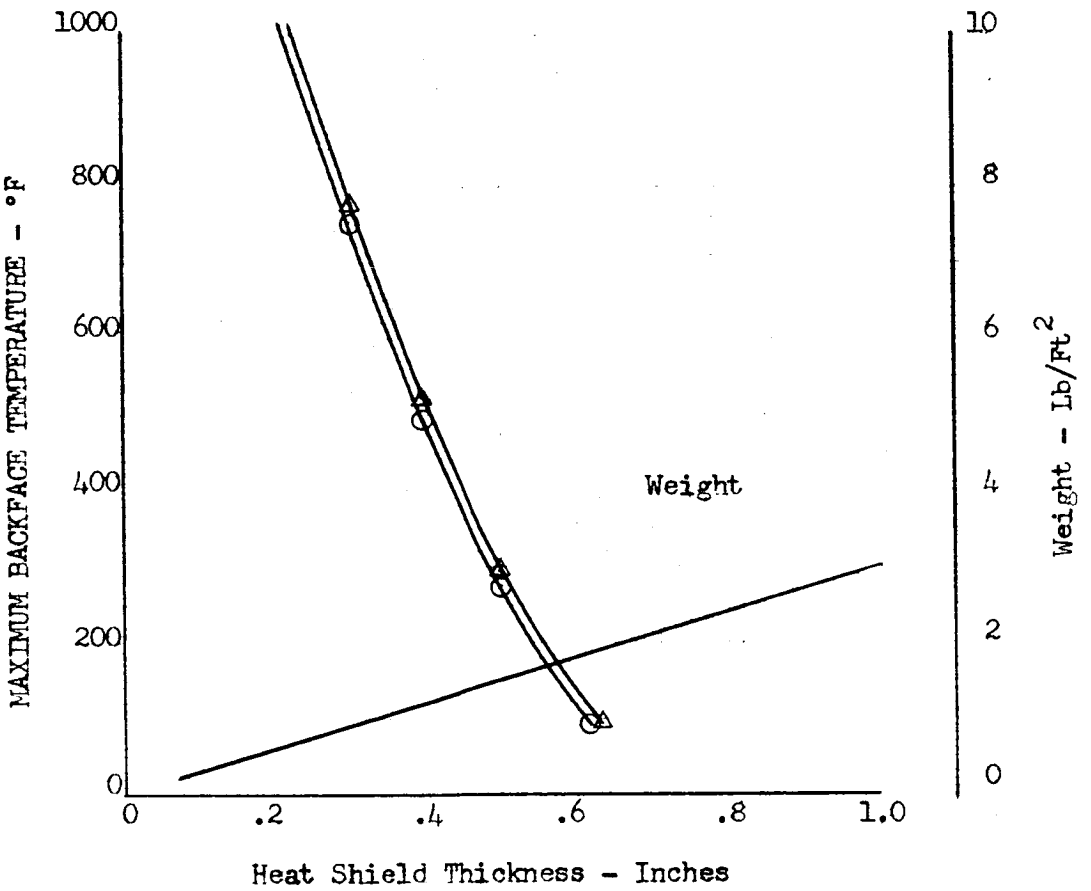

△ IBM analysis - small capsule

○ IBM analysis - large capsule

STRUCTURE TEMPERATURE VS AVCOAT THICKNESS

Avcoat 5026-39

V_E = 25,000 fps
γ_E = -20°
M/C_DA = .2
Diam = 17 ft

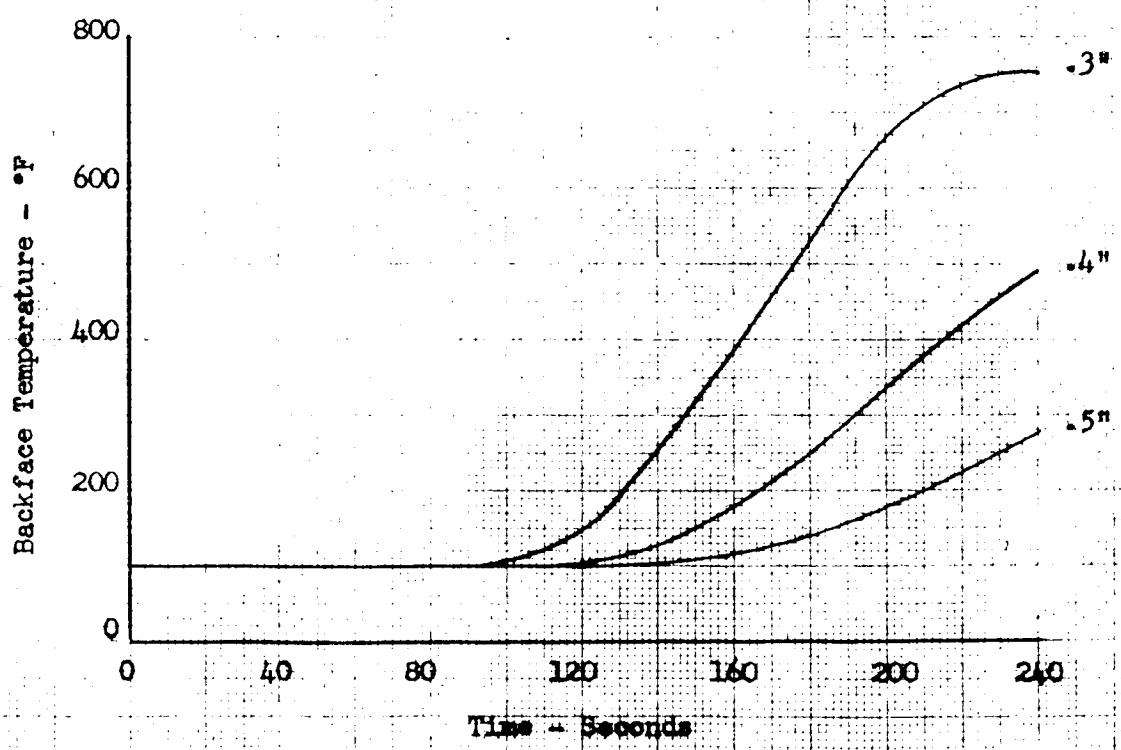

STRUCTURE TEMPERATURE VS AVCOAT THICKNESS

Avcoat 5026-39

V_E = 25,000 fps
γ_E = -20°
M/C_DA = .2
Diam = 17 ft

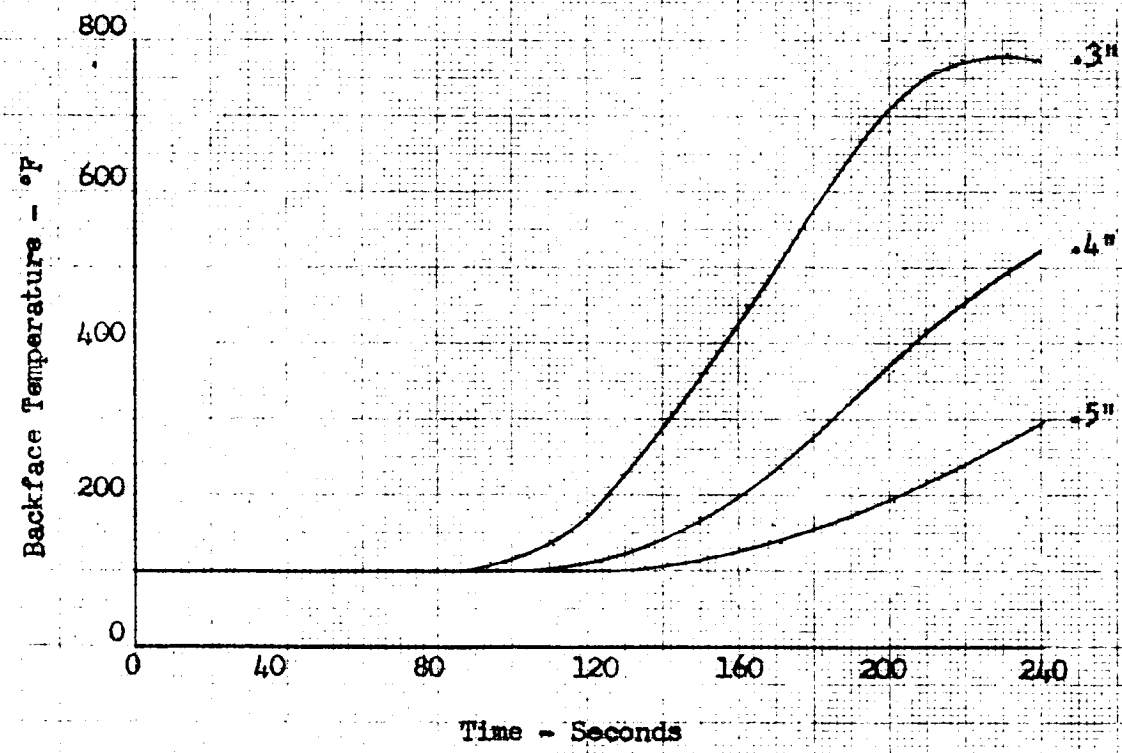

Figure 2.7-28

MAXIMUM BACKFACE TEMPERATURE AS A FUNCTION OF TOTAL THICKNESS

PHENOLIC GLASS WITH .02" ALUMINUM SUBSTRUCTURE

V_E = 25,000 fps
γ_E = -20° & -90°
W/C_DA = .2
Diam = 7 ft

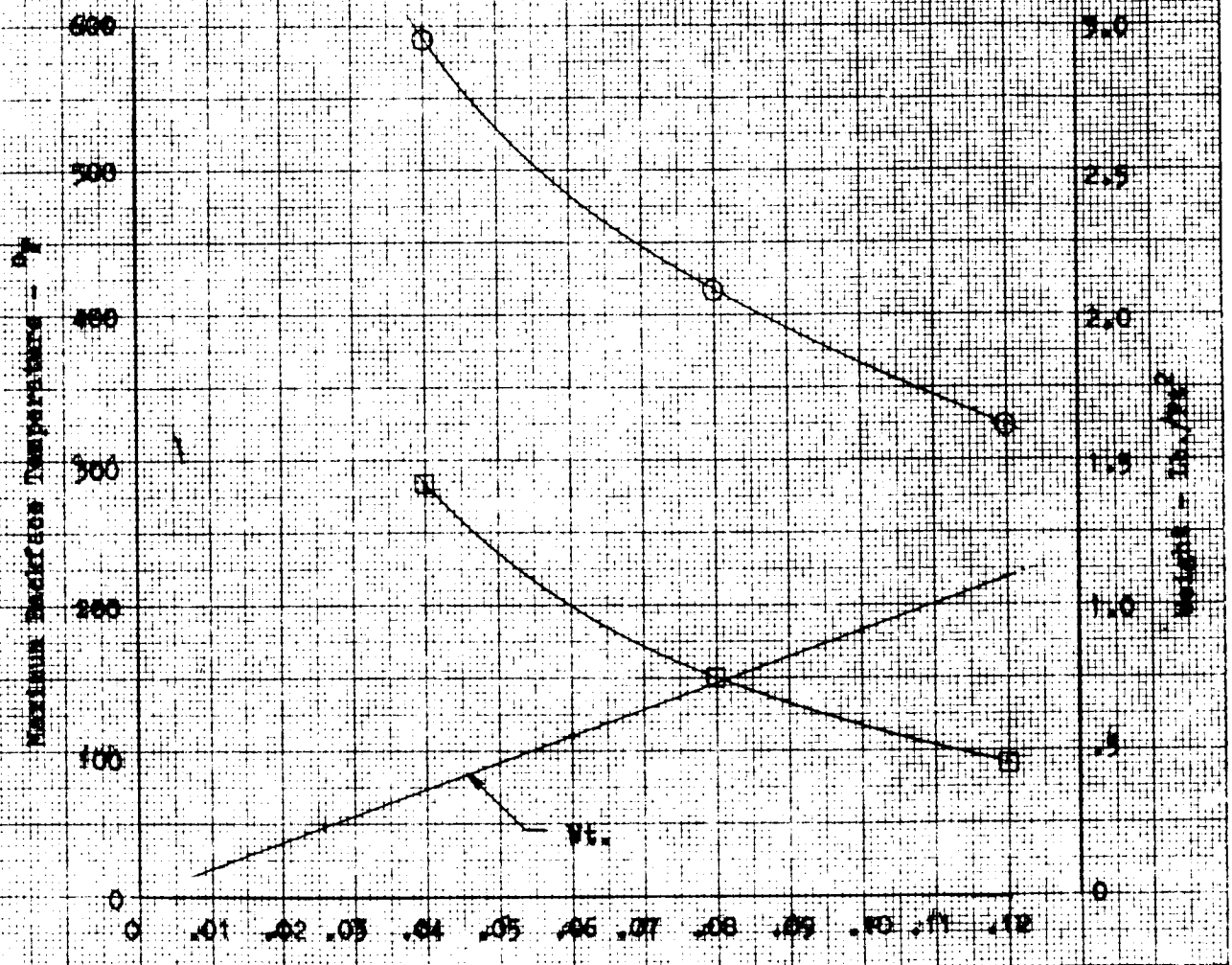

○ IBM analysis - -20° entry

□ IBM analysis - -90° entry

STRUCTURE TEMPERATURE VS PHENOLIC GLASS THICKNESS*

$V_E = 25{,}000$ fps
$\gamma_E = -20°$
$M/C_DA = .2$
Diam = 7 ft

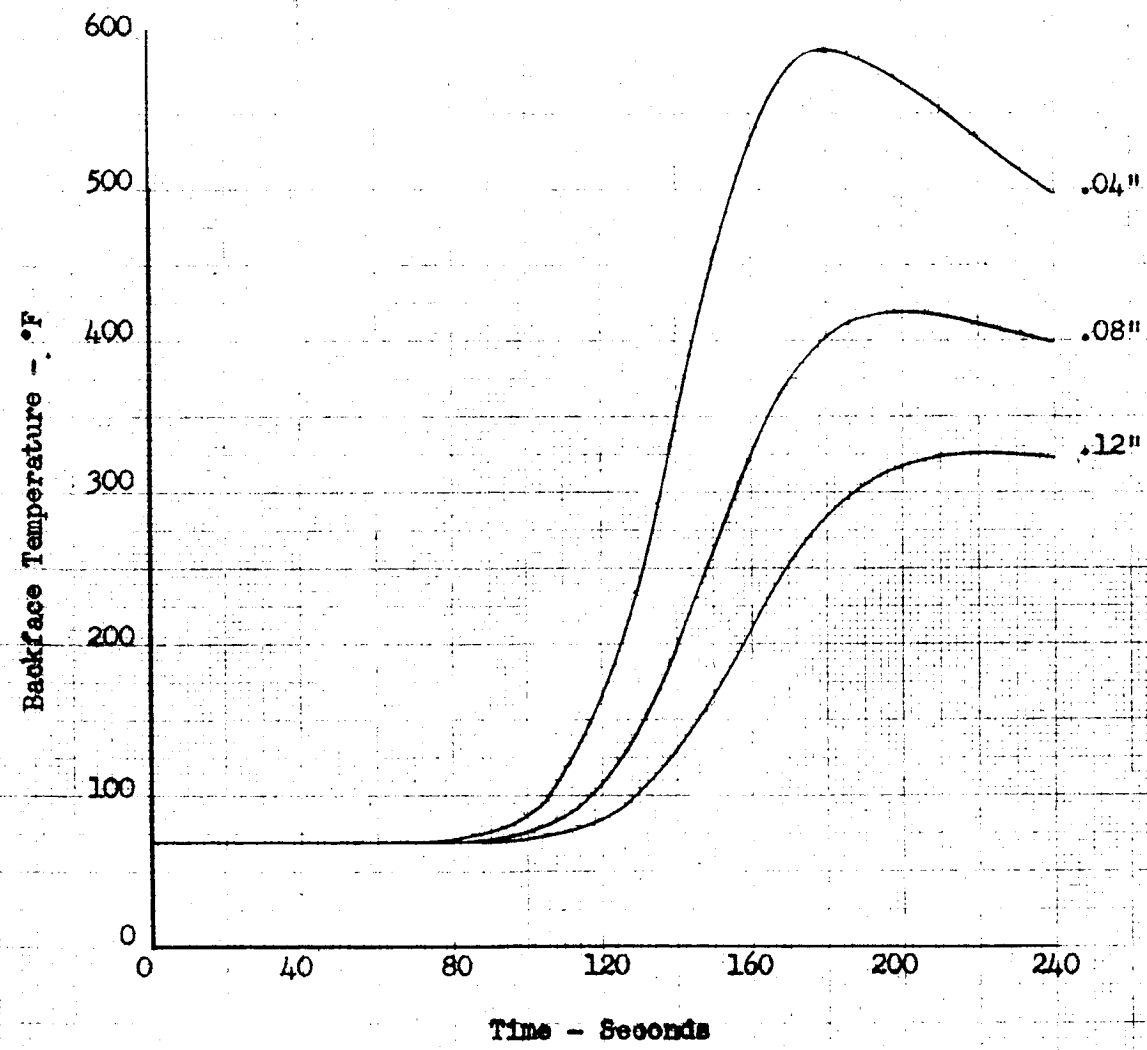

* .02" Aluminum Substructure

PREPARED BY:	NORTH AMERICAN AVIATION, INC. SPACE and INFORMATION SYSTEMS DIVISION	PAGE NO. OF
CHECKED BY:		REPORT NO.
DATE:	Figure 2.7-30	MODEL NO.

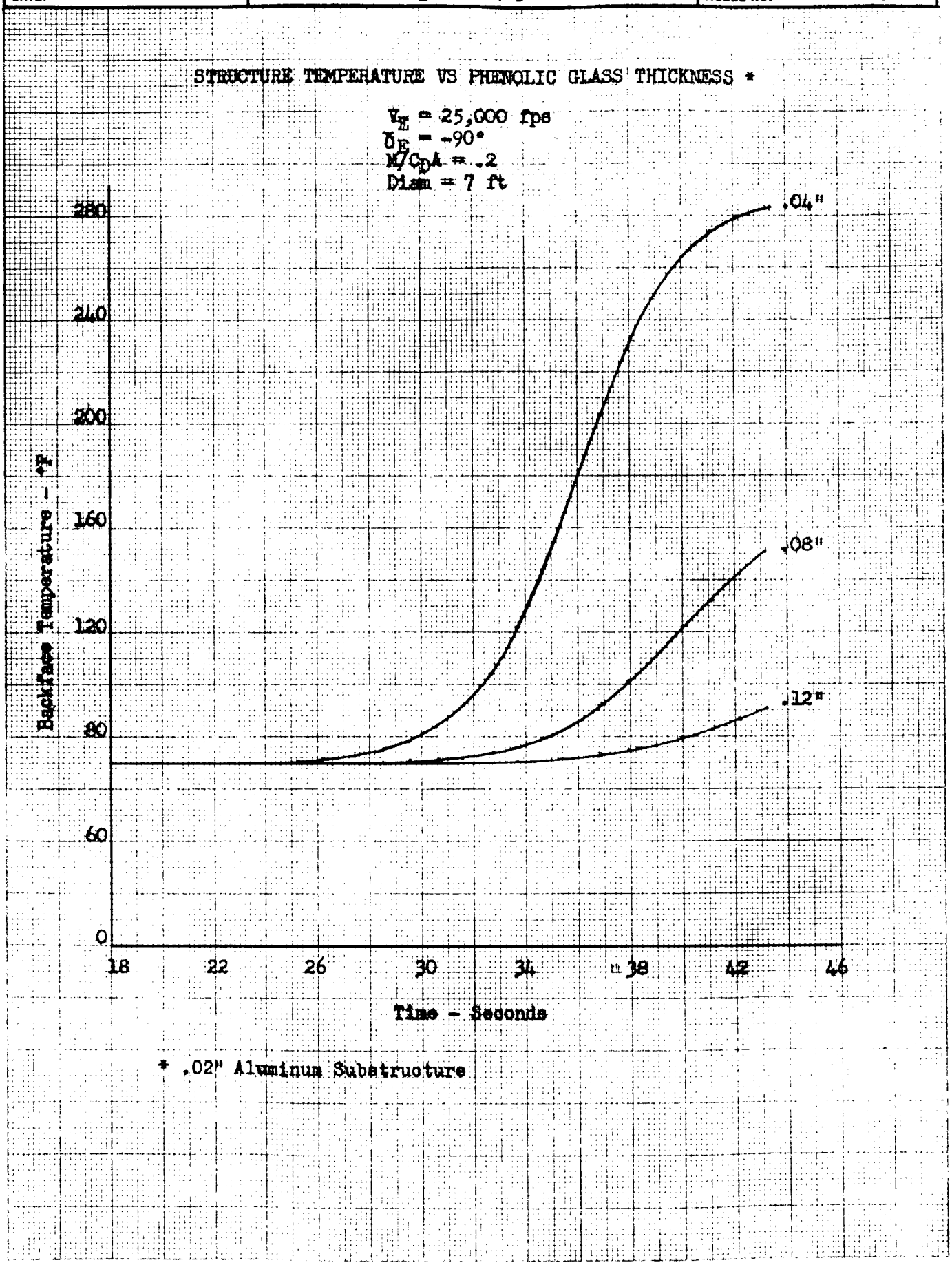

Figure 2.7-31

STRUCTURE TEMPERATURE VS PHENOLIC GLASS THICKNESS *

V_R = 25,000 fps
γ_R = -20°
M/C_DA = .2
Diam = 17 ft

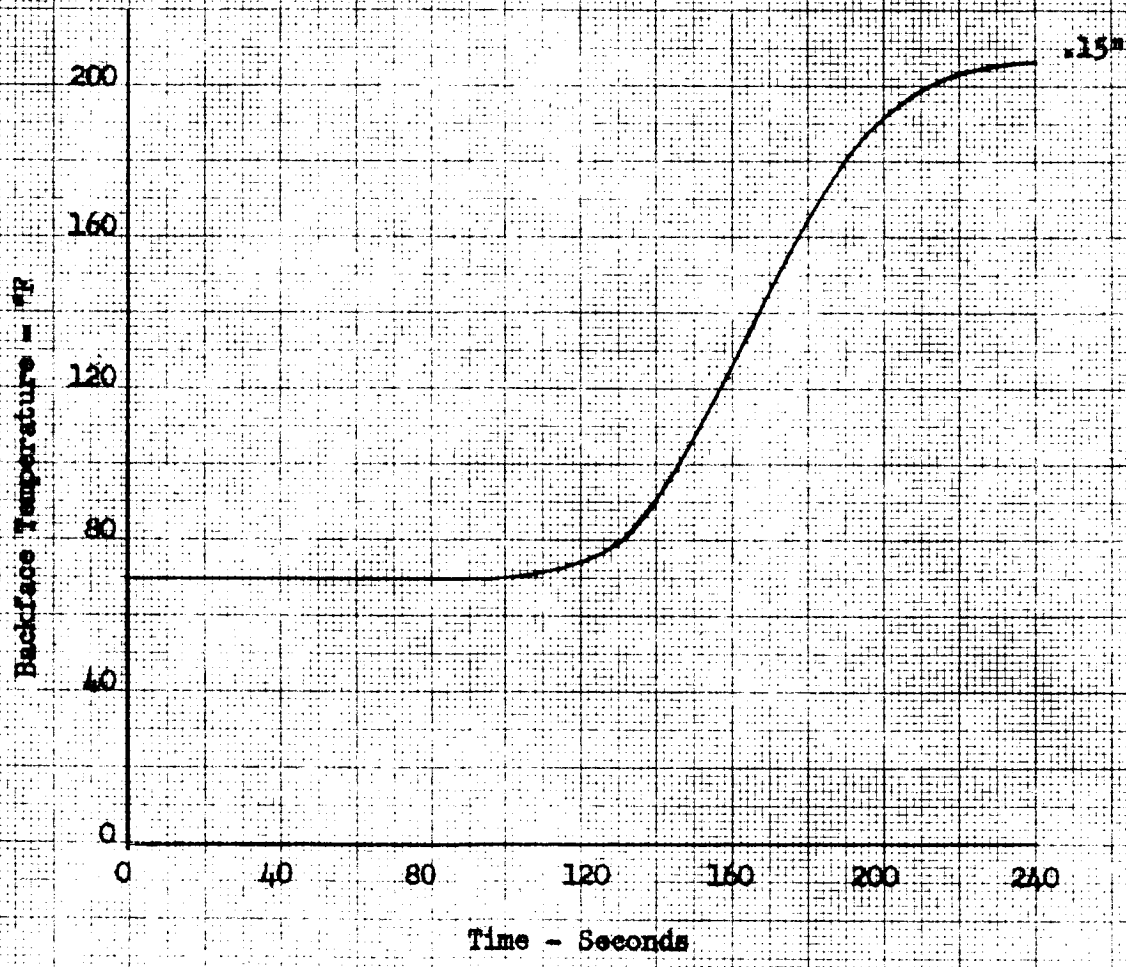

* .02" Aluminum Substructure

STRUCTURE TEMPERATURE VS PHENOLIC GLASS THICKNESS*

V_E = 25,000 fps
γ_E = -90°
M/C_DA = .2
Diam = 17 ft

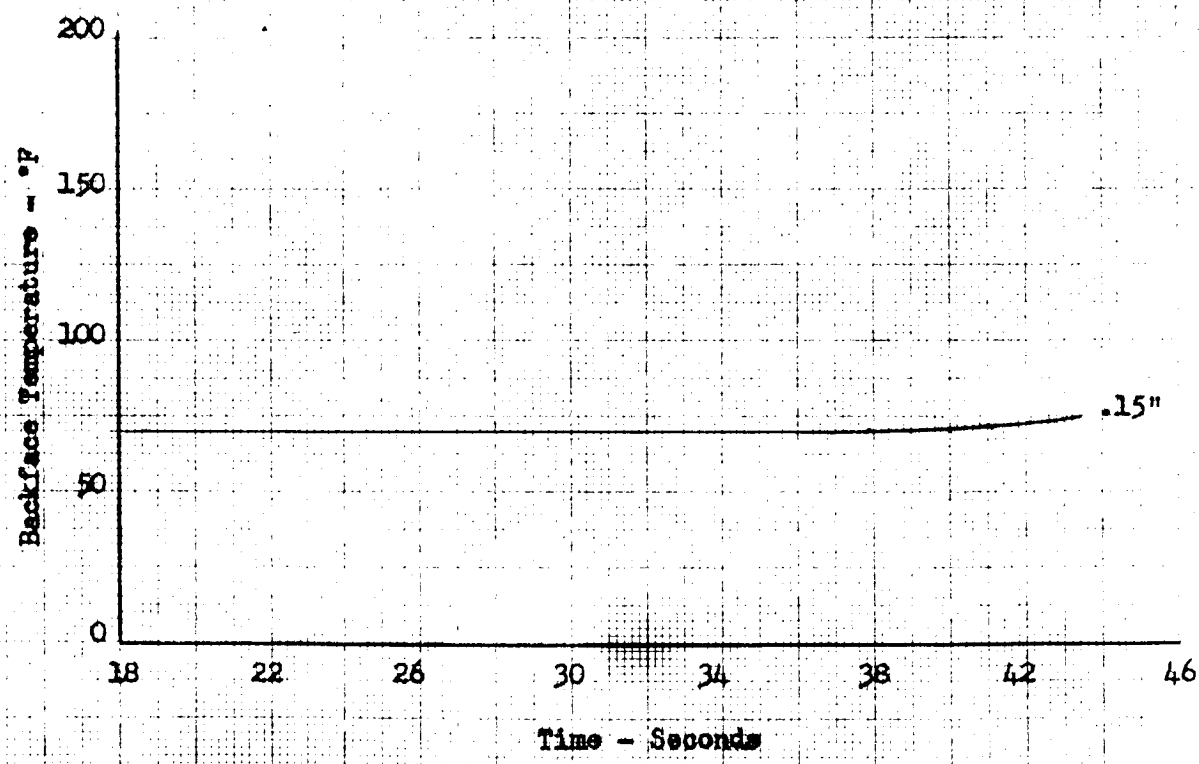

* .02" Aluminum Substructure

Figure 2.7-33

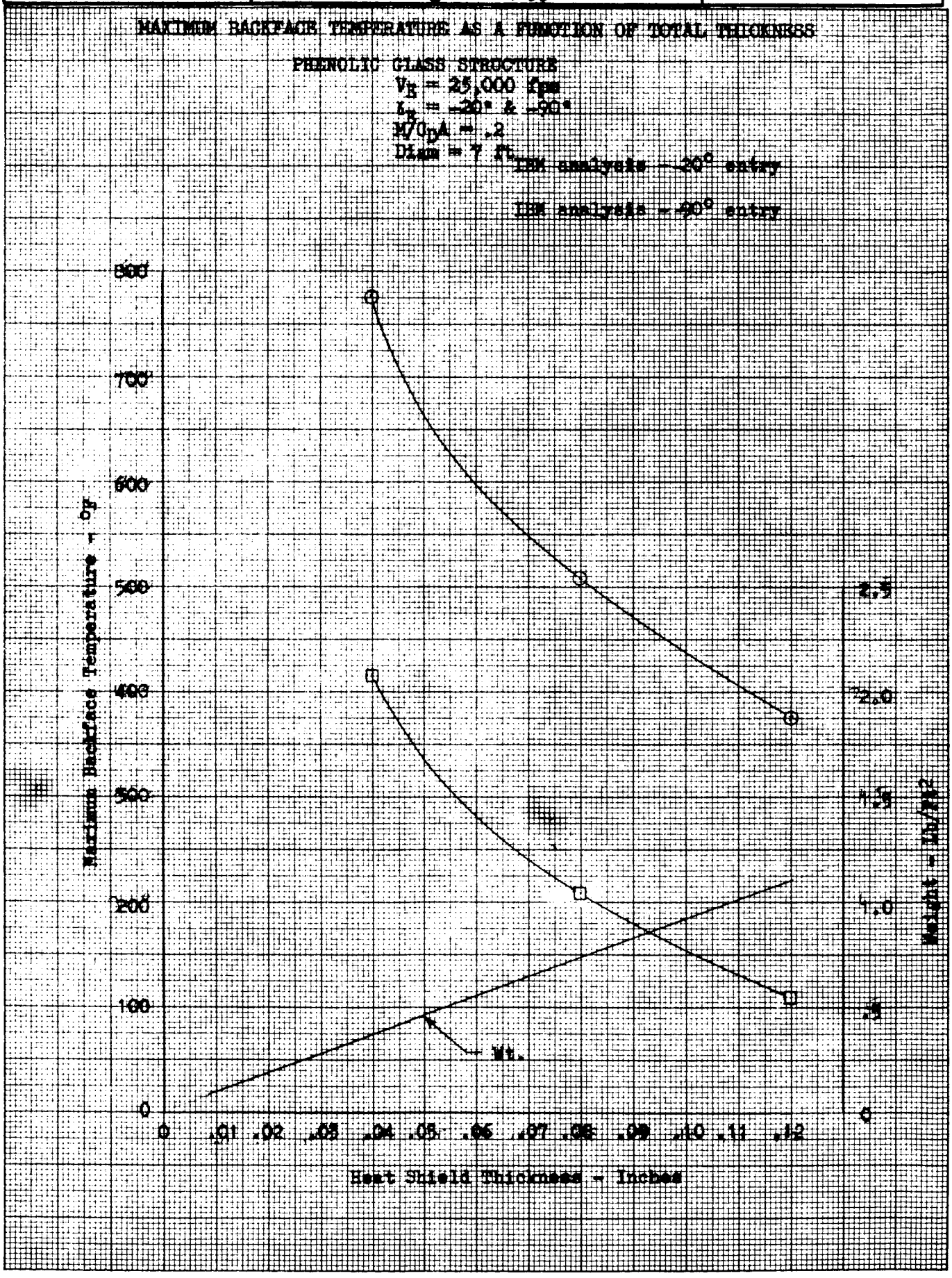
MAXIMUM BACKFACE TEMPERATURE AS A FUNCTION OF TOTAL THICKNESS
PHENOLIC GLASS STRUCTURE
V_E = 25,000 fps
γ_E = -20° & -90°
M/C_DA = .2
Diam = 7 ft
IBM analysis -20° entry
IBM analysis -90° entry
Maximum Backface Temperature - °F
800
700
600
500
400
300
200
100
0
Wt.
Weight - lb/ft²
2.5
2.0
1.5
1.0
.5
0
0 .01 .02 .03 .04 .05 .06 .07 .08 .09 .10 .11 .12
Heat Shield Thickness - Inches

Figure 2.7-34

BACKFACE TEMPERATURE HISTORY - PHENOLIC GLASS STRUCTURE

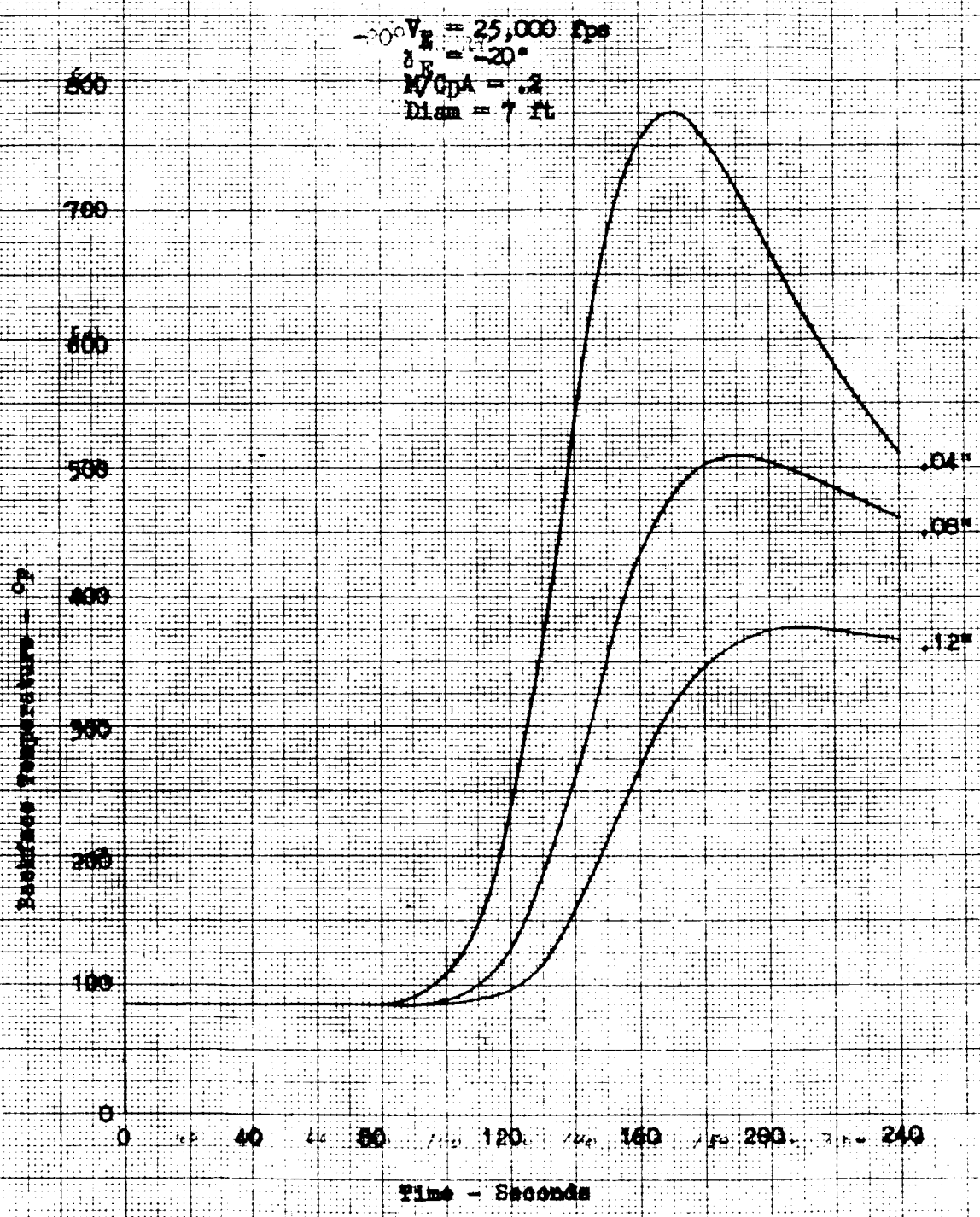

Figure 2.7-35

BACKFACE TEMPERATURE HISTORY - PHENOLIC GLASS STRUCTURE

V_E = 25,000 fps
γ_E = -90°
W/C_DA = .2
Diam = 7 ft

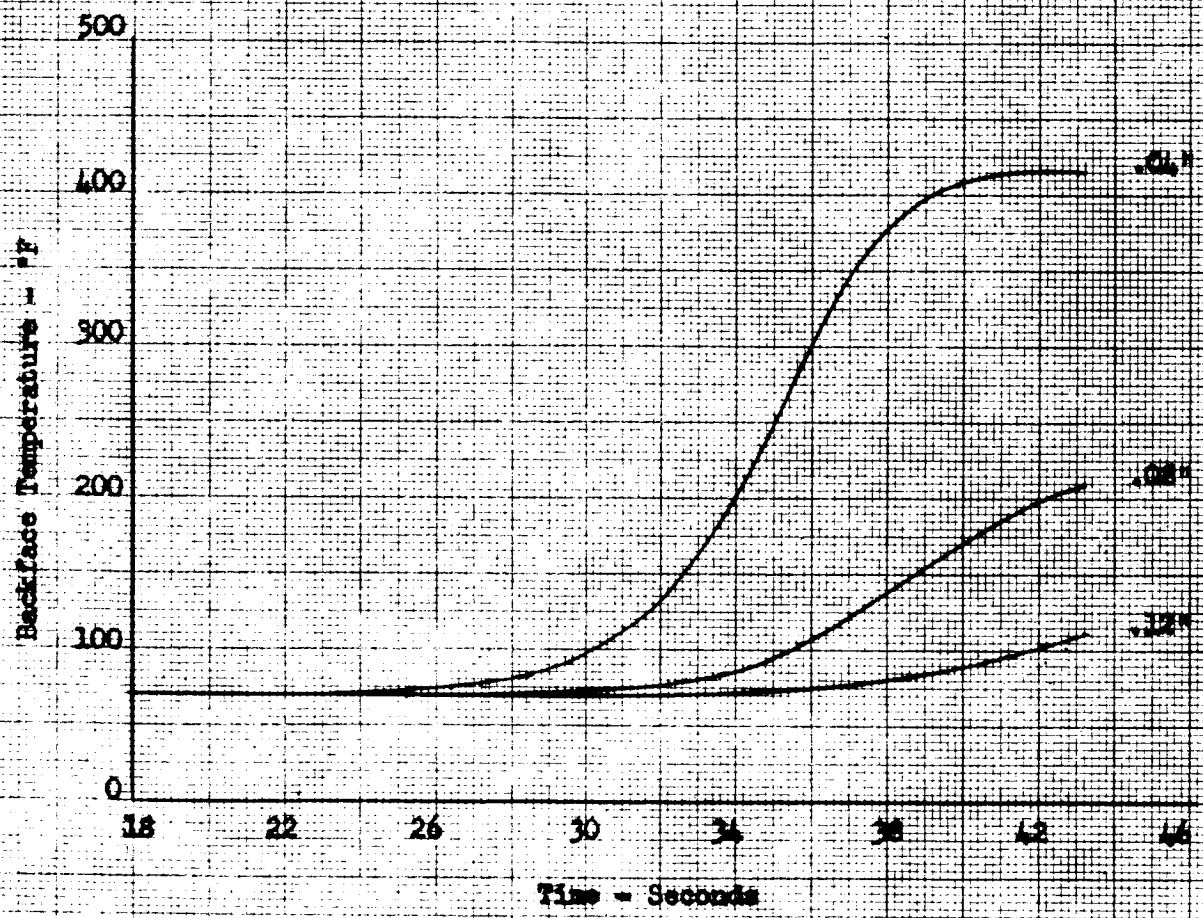

BACKFACE TEMPERATURE HISTORY - PHENOLIC GLASS STRUCTURE

V_E = 25,000 fps
γ_E = -20°
M/C_DA = .2
Diam = 17 ft

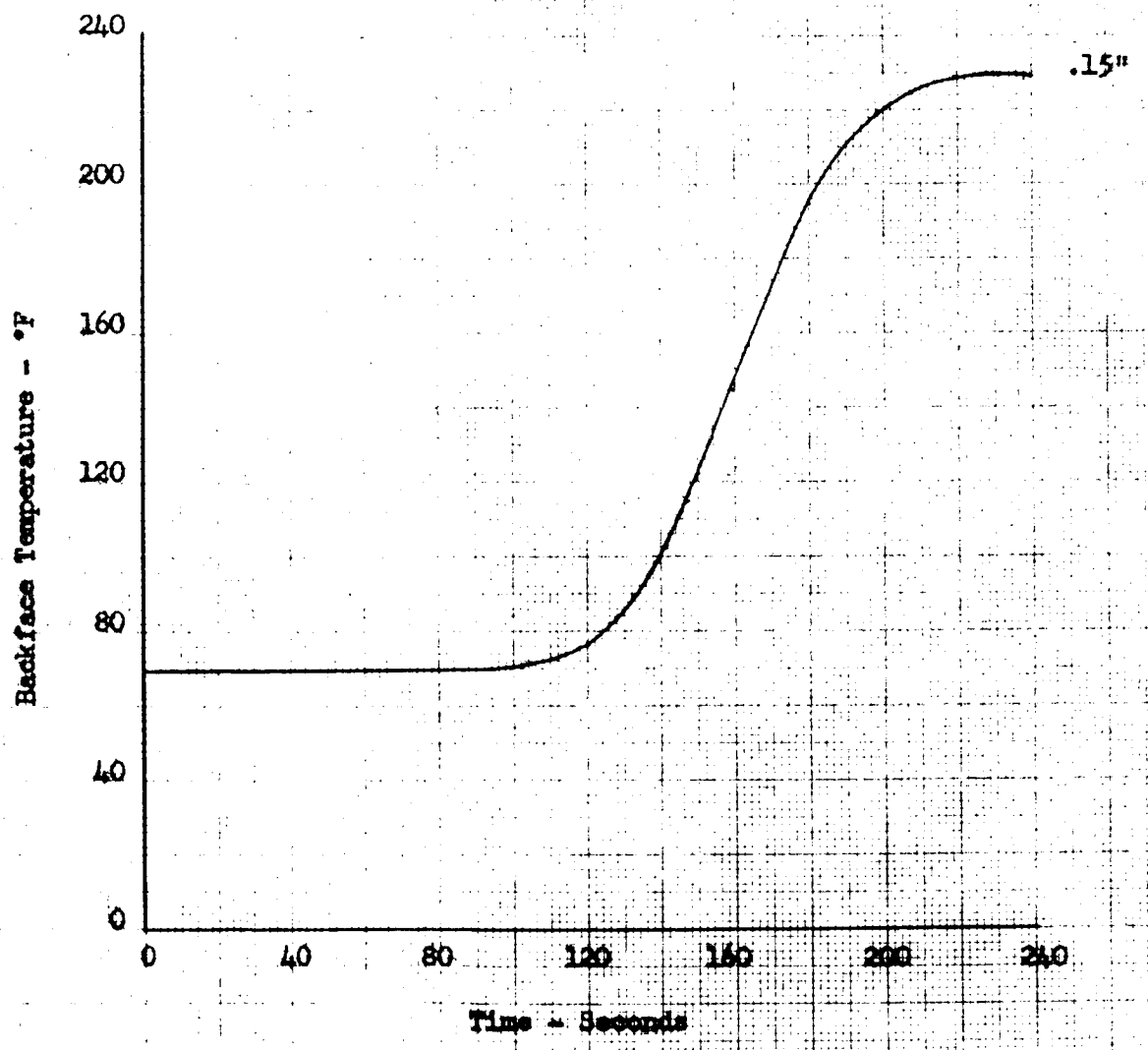

BACKFACE TEMPERATURE HISTORY - PHENOLIC GLASS

V_E = 25,000 fps
δ_E = -90°
M/C_DA = .2
Diam = 17 ft

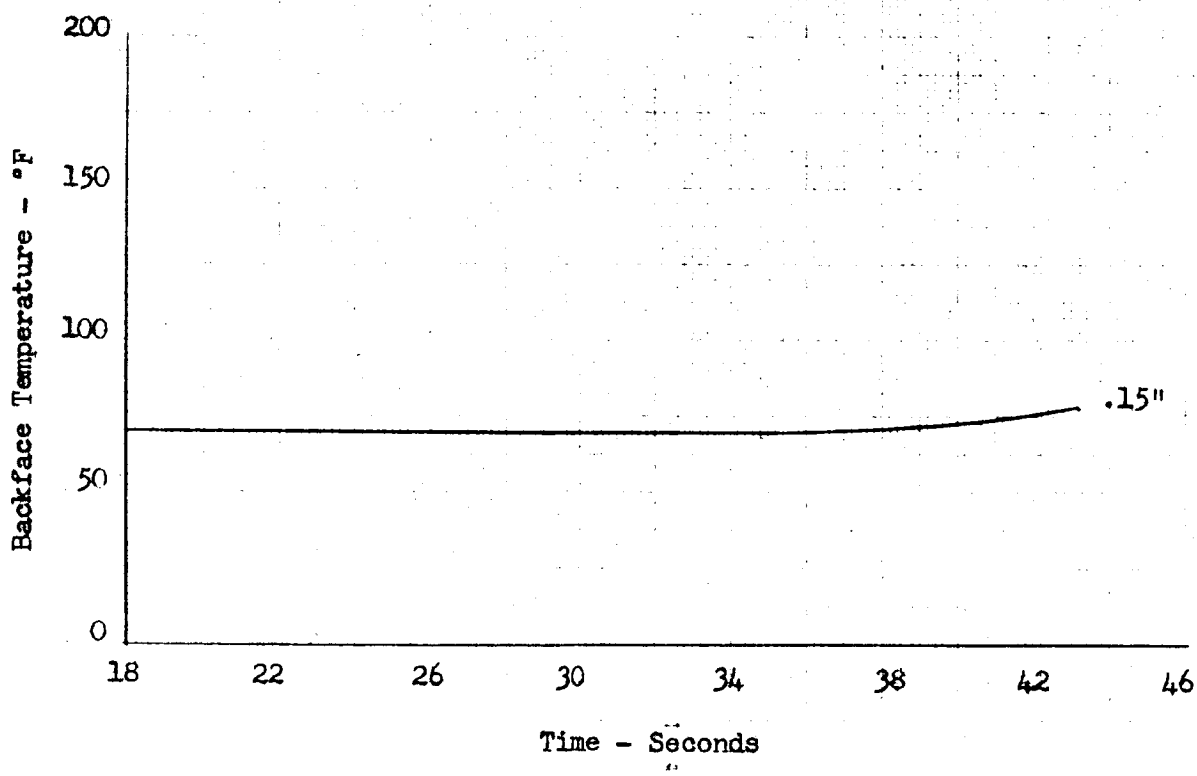

TEMPERATURE HISTORY OF SURFACE LAYER OF PHENOLIC GLASS

PHENOLIC GLASS STRUCTURE

V_E = 25,000 fps
γ_E = -20°
M/C_DA = .2
Diam = 7 ft

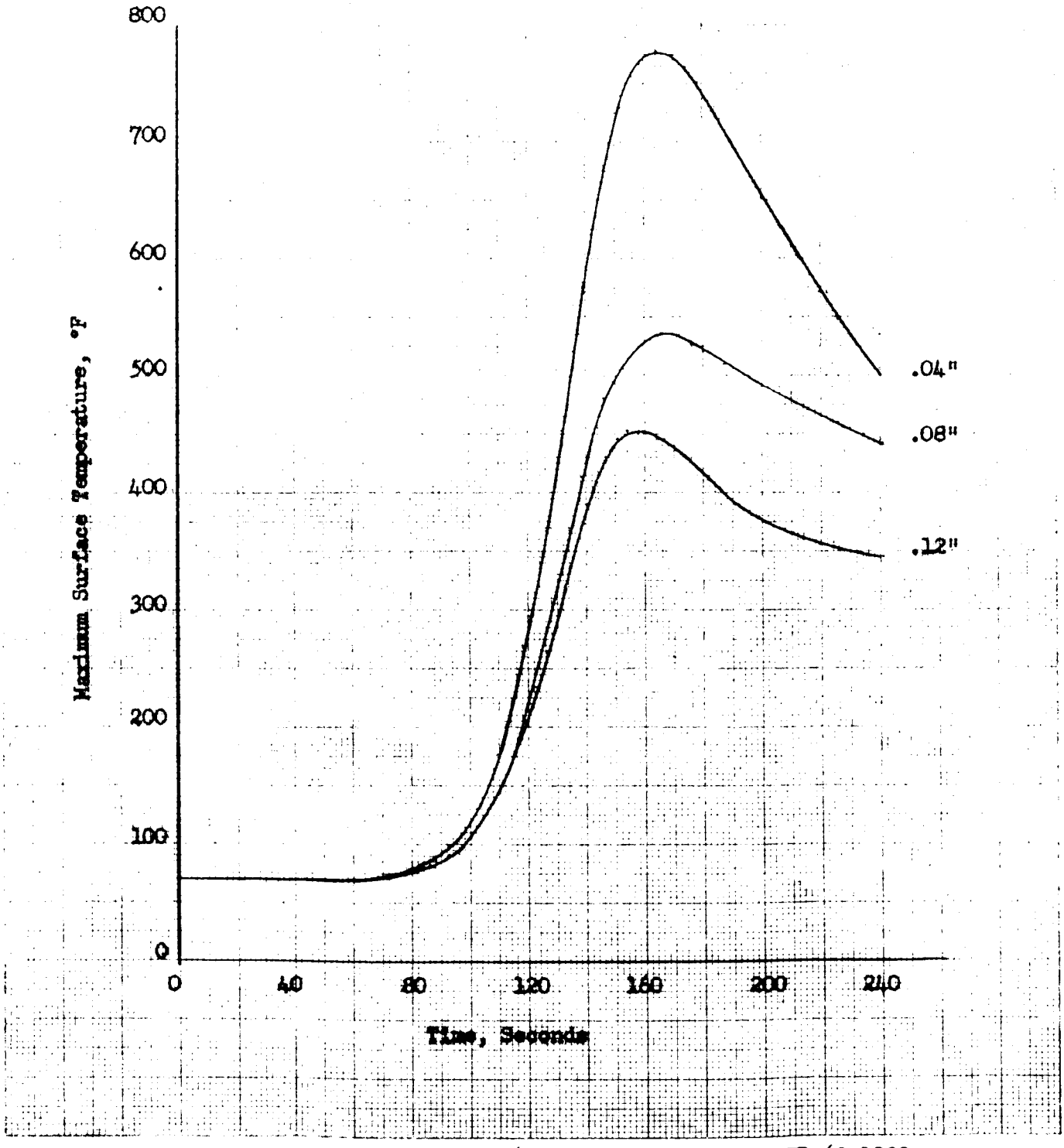

2.8 LANDING SYSTEM TRADEOFFS

This section presents the results of the landing-system parametric tradeoff study conducted by Space and Information Systems Division in conjunction with Cook Research Laboratories. The study involved the evaluation and selection of an effective system for landing a payload on the Martin surface. System concepts, which considered the let-down and landing of nominal 100 and 600 pound payloads for the large and small capsules, respectively, were analyzed. Recovery sequence programming and system deployment techniques were considered and are presented. The systems selected reflect state-of-the-art capability and, hence, provide the basepoint for a more detailed investigation.

2.8.1 Considerations and Constraints

The design information presented in Table 2.8-1 is the preliminary data used for establishing the performance of the landing system. Using this preliminary data, a series of curves were plotted to evaluate the parametric factors. Figure 2.8-1, which applies to the initially considered 400 pound Mariner B capsule with a 150 pound payload descending in the W_2 atmosphere shows the total descent time as a function of the ratio of second-stage parachute weight to the total parachute weight for three landing system weights of 25, 40, and 55 pounds, respectively. Similarly, Figure 2.8-2 shows the parachute weight ratio versus the starting altitude for sampling for the same conditions. (It is assumed that sampling begins at M = 0.9.) As may be seen from Figure 2.8-1, total maximum descent times of 116 seconds for the 25 pound landing system, 221 seconds for the 40 pound landing system, and 316 seconds for the 55 pound landing system can be achieved with optimum weight ratio of 0.3. From Figure 2.8-2, the same weight ratio of 0.3 will result in starting sampling at altitudes of 12,600 ft., 16,000 ft., and 18,500 ft. for the 25, 40 and 55 pound recovery systems. This curve also demonstrates that if only a single stage parachute system is utilized (weight ratio = 1.0) then sampling starting altitudes of 22,000 ft. for the 25 lb. system, 24,000 ft. for the 40 lb. system and 26,000 ft. for the 55 lb. system may be achieved.

These values are cross plotted in Figure 2.8-3 and show that as the landing system weight increases, sampling altitude and descent time rise in a nearly linear fashion. These values are plotted for a constant capsule and payload weight; they are intended to be only a parametric study tool.

Figure 2.8-4 shows the parachute weight ratio versus the descent time from first stage parachute deployment to second-stage parachute deployment for the B atmosphere for the 10% vehicle weight landing system. This curve is valid for both Mariner B and Voyager. The same relationship is shown for atmosphere W_2 in Figure 2.8-5.

TABLE 2.8-1 LANDING SYSTEM DESIGN REQUIREMENTS

	ITEM	MARINER "B"		VOYAGER
a)	Vehicle weight	350 lb		2000 lb
b)	Vehicle weight at first-stage parachute deployment	310 lb		1450 lb
c)	Vehicle weight at second-stage parachute deployment	310 lb		1450 lb
d)	Payload weight at impact	100-150 lb		600 lb
e)	Maximum permissible parachute load on vehicle	200 g's		200 g's
f)	Nominal vehicle $\frac{M}{C_D A}$ prior to first-stage deployment	0.2 slugs/ft^2		0.2 slugs/ft^2
g)	Maximum permissible recovery system weight, including sequencing, structure, parachute components, and impact attenuation (where applicable)	40 lb		200 lb
h)	Maximum first-stage parachute deployment velocity (Mach 4.5)	3750 ft/sec		3750 ft/sec
i)	Maximum first-stage parachute deployment altitude: For $_E$ = -90°	70,000 ft		70,000 ft
j)	Maximum dynamic pressure at first-stage deployment	190 psf 178 psf	(Atm W_2) (Atm B)	190 psf 178 psf
k)	Maximum deceleration force occurring on vehicle just prior to first-stage deployment	35 g's 30 g's	(Atm W_2) (Atm B)	35 g's 30 g's
l)	Maximum permissible parachute load exerted upon the vehicle at deployment	165 g's 170 g's	(Atm W_2) (Atm B)	165 g's 170 g's
m)	Maximum second-stage parachute deployment velocity	750 ft/sec		750 ft/sec
n)	Deployment altitude (based on point-mass trajectories)	37,500 ft 70,000 ft	(Atm W_2) (Atm B)	37,500 ft 70,000 ft
o)	Maximum descent velocity at impact	100 ft/sec		100 ft/sec

PREPARED BY: EP	NORTH AMERICAN AVIATION, INC. SPACE and INFORMATION SYSTEMS DIVISION	PAGE NO. OF
CHECKED BY:		REPORT NO.
DATE: 10/8/63		MODEL NO.

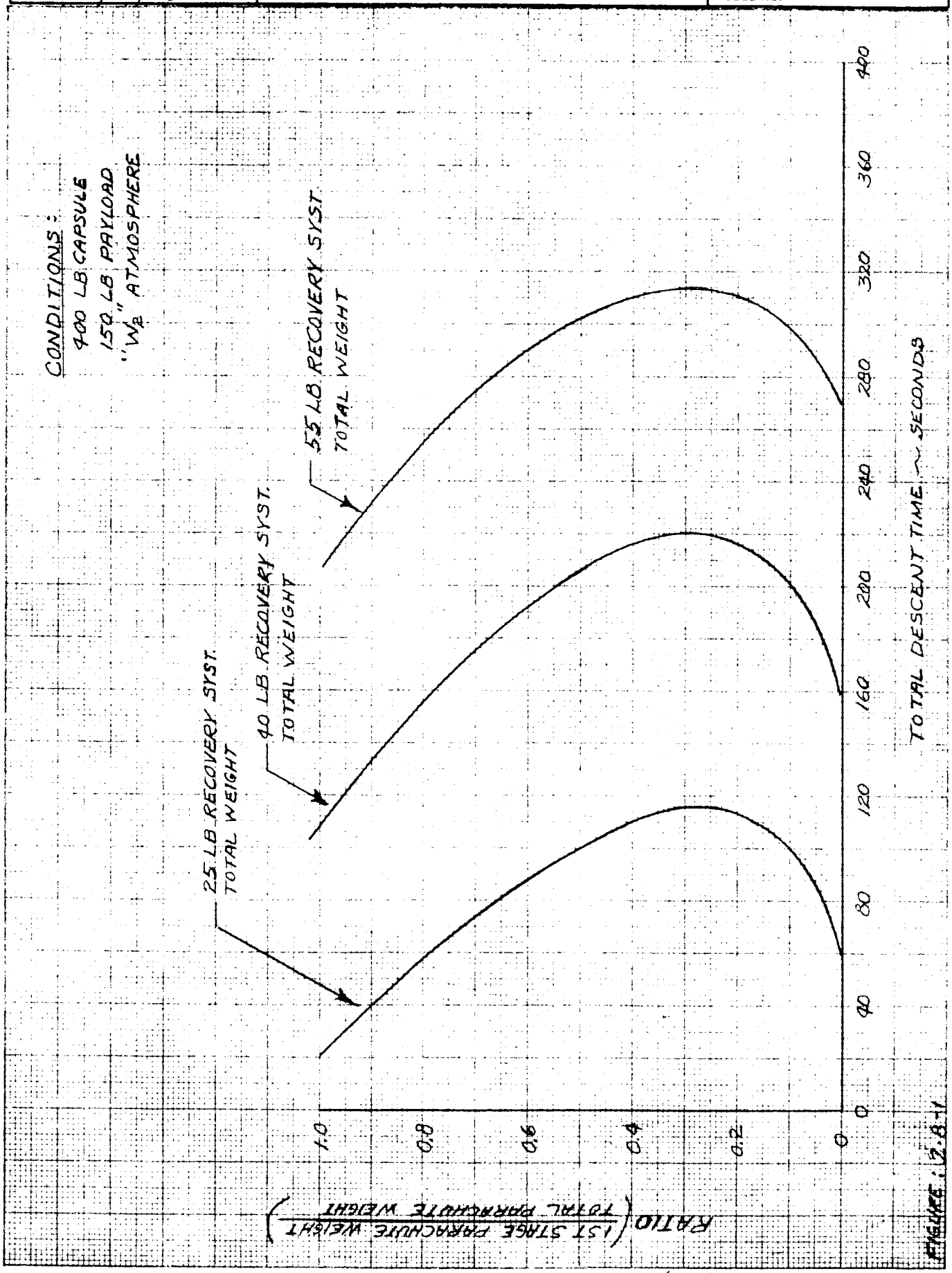

FIGURE 2.8-1

PREPARED BY: EP	NORTH AMERICAN AVIATION, INC. SPACE and INFORMATION SYSTEMS DIVISION	PAGE NO. OF
CHECKED BY:		REPORT NO.
DATE: 10/9/63		MODEL NO.

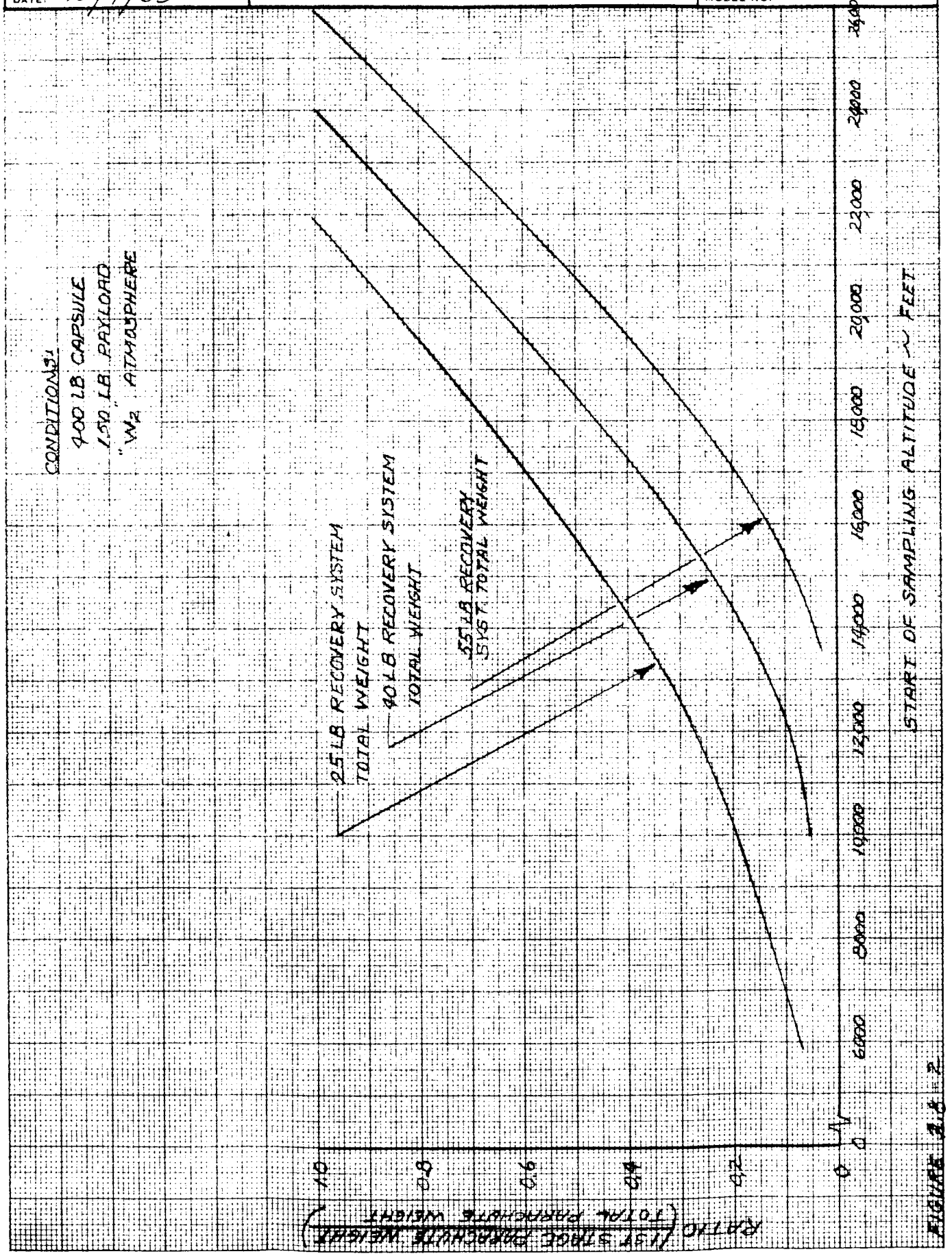

FIGURE 2.8.2

PREPARED BY: EP	NORTH AMERICAN AVIATION, INC. SPACE and INFORMATION SYSTEMS DIVISION	PAGE NO. OF
CHECKED BY:		REPORT NO.
DATE: 10/9/63		MODEL NO.

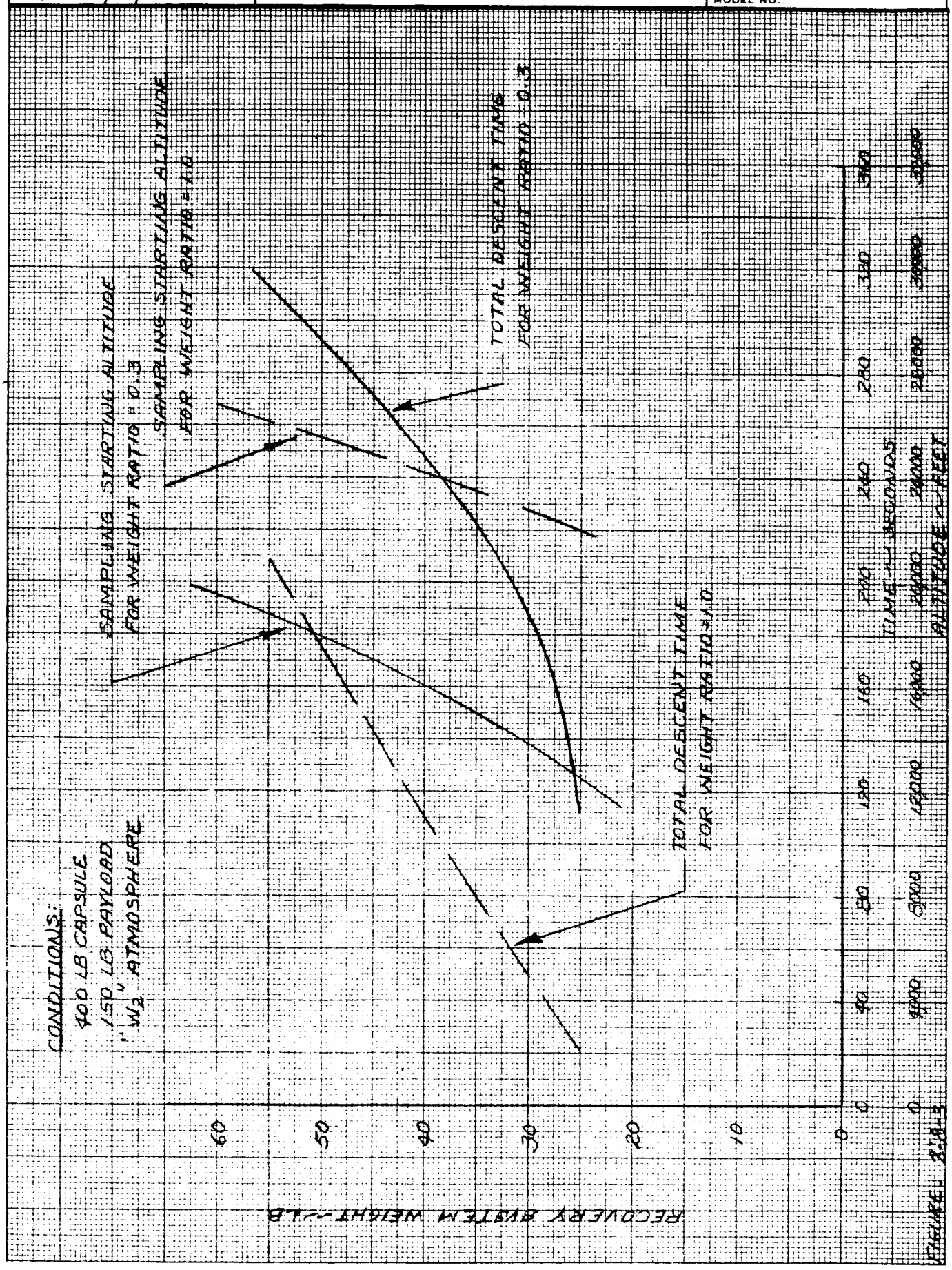

FIGURE 3.6.4-3

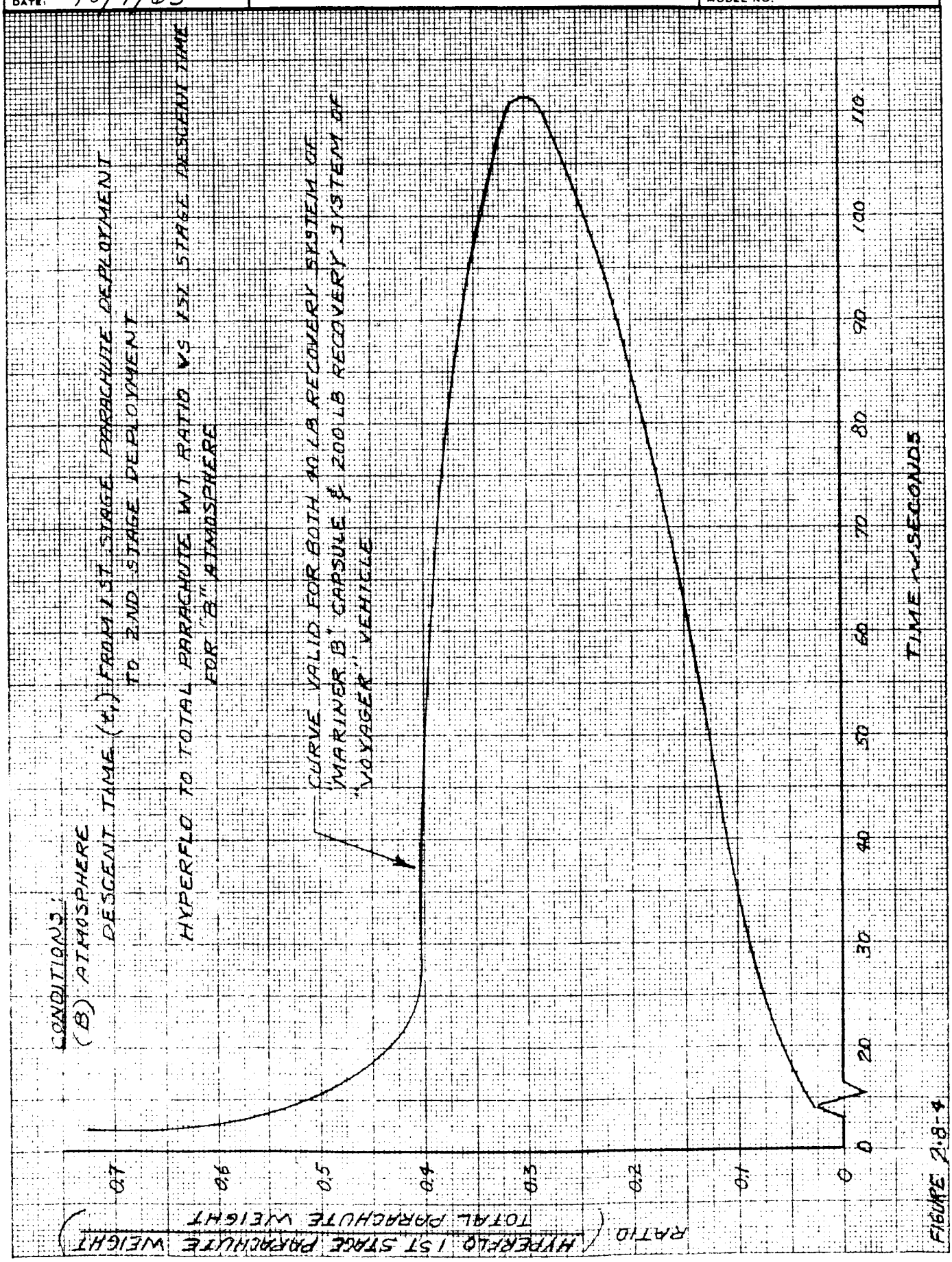
CONDITIONS:
(B) ATMOSPHERE
DESCENT TIME (t_1) FROM 1ST STAGE PARACHUTE DEPLOYMENT
TO 2ND STAGE DEPLOYMENT
HYPERFLO TO TOTAL PARACHUTE WT RATIO VS 1ST STAGE DESCENT TIME
FOR "B" ATMOSPHERE
CURVE VALID FOR BOTH 40 LB RECOVERY SYSTEM OF
"MARINER B" CAPSULE & 200 LB RECOVERY SYSTEM OF
"VOYAGER" VEHICLE
RATIO (HYPERFLO 1ST STAGE PARACHUTE WEIGHT / TOTAL PARACHUTE WEIGHT)
0.7
0.6
0.5
0.4
0.3
0.2
0.1
0
0
20
30
40
50
60
70
80
90
100
110
TIME ~ SECONDS

FIGURE 2.8-4

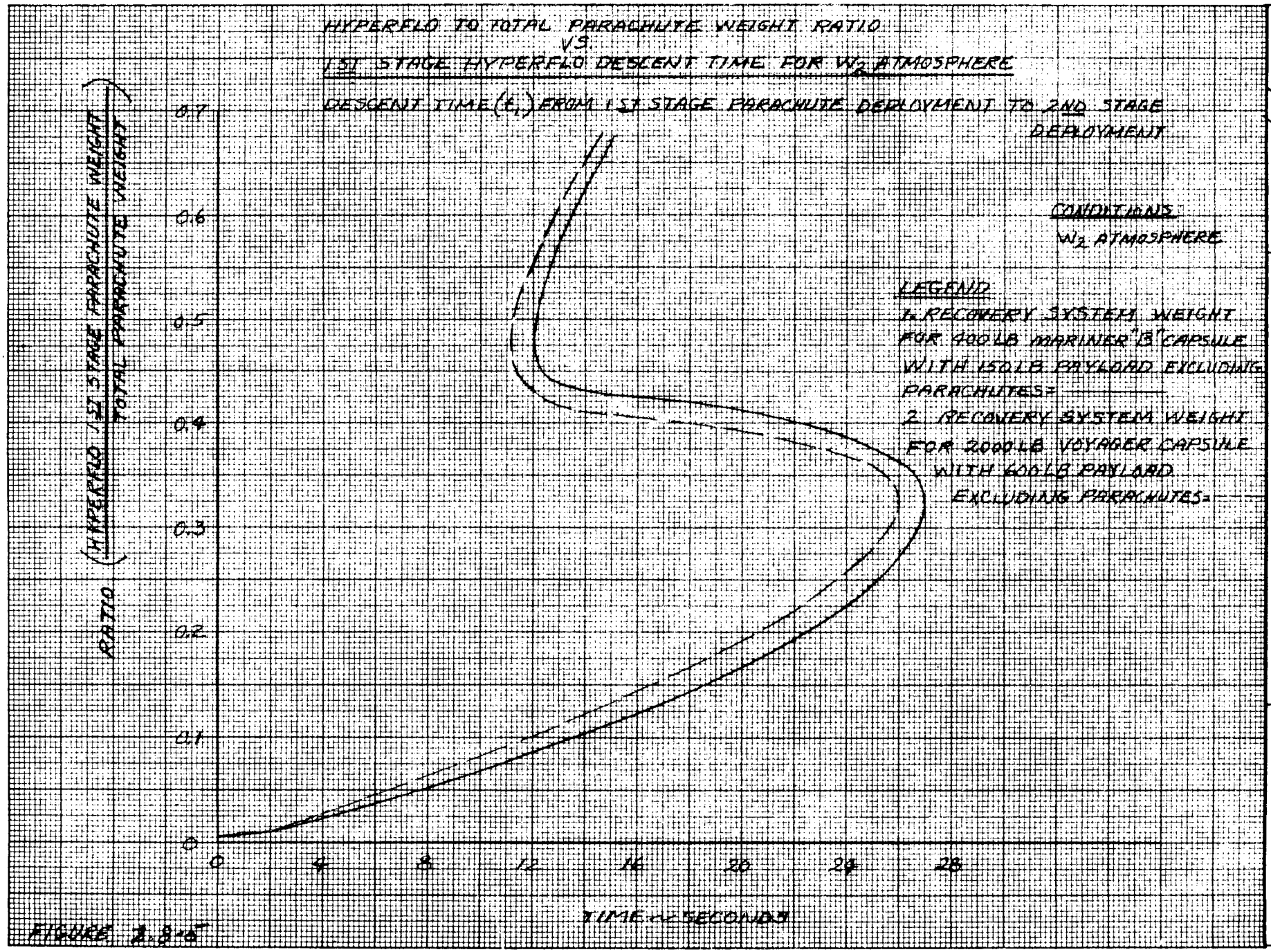

FIGURE 2.8-5

PREPARED BY: EP
CHECKED BY:
DATE: 10/9/63

NORTH AMERICAN AVIATION, INC.
SPACE and INFORMATION SYSTEMS DIVISION

MODEL NO.
REPORT NO.
PAGE NO. OF

Figure 2.8-6 plots starting altitude for sampling versus sampling time for both W_2 and B atmospheres for the 10% vehicle-weight landing systems.

It can be seen that both a one-stage parachute system and a two-stage system offer design advantages. The one-stage system is the least complex and, therefore, the most reliable; provisions for release of the first-stage, deployment of the second stage, and second-stage structure are not required. Moreover, the maximum spectrum of atmospheric samples can be achieved with this system. On the other hand, the two-stage system permits a longer period for data transmission and allows a longer dwelling time at the sampling altitudes. In addition, the resulting lower impact velocity requires less impact attenuation to permit landing survival and assure post-landing data transmission. Therefore, concepts encompassing these two approaches have been studied and appear in the following sections.

2.8.2 Parachute Design Concepts

The Hyperflo parachute being developed by Cook Electric Company was selected for the first-stage parachute. This parachute has been tested to the velocities equivalent to 3750 fps in the Martian atmosphere.

The second-stage parachutes which were considered were of solid construction and included both flat conical and extended skirt parachutes. The stability of solid parachutes increases as the dynamic pressure decreases. At the low dynamic pressures encountered in Martian entry, solid parachutes of the extended skirt type are stable to within $\pm 10°$ angle of attack, which is adequate for this application. The efficiency of the second-stage parachute can be measured as a function of the specific drag area (C_DS per pound of parachute weight). Efficiencies for candidate configurations are shown in Table 2.8-2.

TABLE 2.8-2 - SECOND STAGE EFFICIENCIES

Parachute Type	Drag Coefficient	Specific Drag Area $\frac{C_DS}{W_p}$ ft^2/lb
Solid Flat	0.7 to 0.8	50
Conical	0.75 to 0.85	55
Extended Skirt	0.75 to 0.85	60

PREPARED BY: EP	NORTH AMERICAN AVIATION, INC. SPACE and INFORMATION SYSTEMS DIVISION	PAGE NO. OF
CHECKED BY:		REPORT NO.
DATE: 10/9/63		MODEL NO.

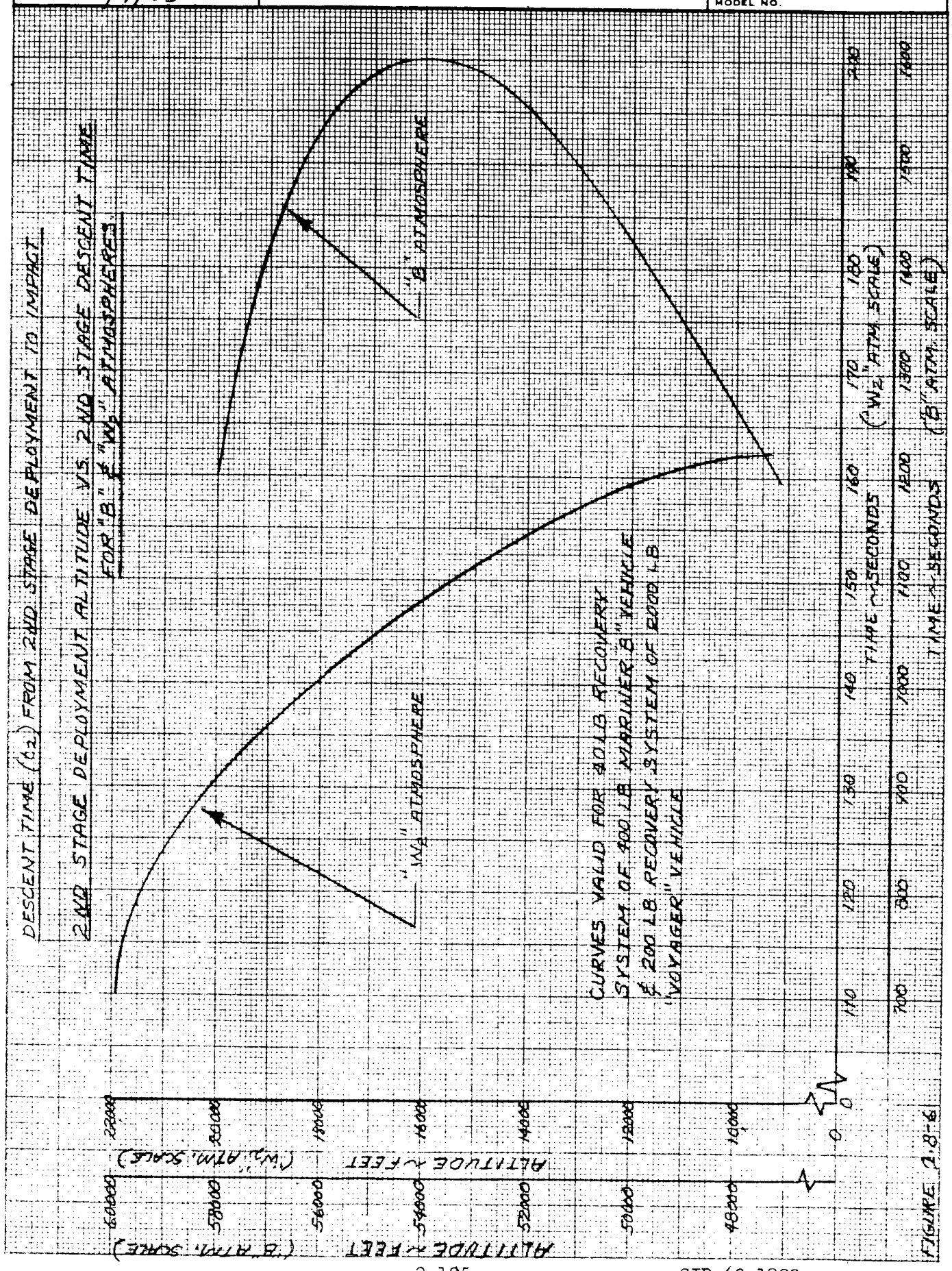

FIGURE 2.8-6

The extended skirt parachute is selected as the second stage because of its high specific drag ratio, its stability, and the high reliability as shown over a million times in paratrooper applications. A single parachute was chosen in preference to a cluster of parachutes because of its lighter weight. Although filling times of large single parachutes are longer than that required for clusters, in the rare Martian atmosphere filling times of only a few hundredths of a second are expected.

2.8.3 Parachute System Deployment Concepts

Candidate techniques considered for deployment of the first-stage parachute include:

(1) Releasing the aftcone and allowing it to extract the first-stage parachute.

(2) Using a pyrotechnic mortar to eject the parachute.

(3) Using a drogue gun and pilot chute to extract the parachute.

(4) Using a gas generator and ejector bag to eject the parachute.

The aftcone deployment concept envisaged jettisoning the aftcone by means of thrusters to a distance which would permit it to be carried away by the airflow. This system offers the advantage of not requiring additional components to accomplish first-stage deployment; however, the possibility of tumbling of the aftcone at separation leads to several disadvantages:

(1) Unpredictable drag characteristics.

(2) Possibility of parachute entanglement with the aftcone.

(3) Possibility of cutting or abrasion of the deployment bag bridle on the edge of the aftcone. Tests results on the Mercury, Gemini and Apollo recovery systems indicate this technique may not be sufficiently reliable without extensive testing.

The concept using a pyrotechnic-actuated mortar requires packaging the first-stage parachute in a mortar tube and ejecting the entire parachute and the risers clear of the vehicle. This concept has been proven and is presently employed on Apollo and Gemini. The principal advantage of the mortar system is that it is operative irrespective of the vehicle's attitude. However, this mission requires that the parachute be deployed in such a high g environment that the mortar required would be prohibitively heavy (in excess of 25 lbs) and would impose severe loads on the structure.

This disadvantage can be minimized by employing a small drogue gun to eject a slug which, in turn, extracts a pilot chute whose drag is sufficient to extract the first-stage parachute. This system is light in weight (total assembly, 4.2 lbs) and can successfully deploy the first stage even if the axis is oscillating as much as the vehicle $\pm$ 45 degrees. The slug can be fired straight aft, or off to a side, to get the pilot chute into the airflow. If fired to the side, a shorter bridle is required and the deceleration g's of the vehicle do not have to be overcome by the drogue gun.

The ejector-bag/gas-generator technique utilizes gas pressure to invert the bag in which the parachute is stored, thus ejecting the parachute pack. Because of the injection velocity required and the bag sealing problems under the extended space environment, this technique does not appear promising.

Considerations of the conditions at deployment (vehicle oscillations and high aerodynamic deceleration), and subsystem weight indicate that the drogue-gun and pilot-chute concept will accomplish first stage deployment most effectively. Deployment of a second stage, if employed, is best accomplished by disconnecting the first stage from the vehicle and letting it extract the second stage. These candidate deployment techniques are shown in their relation to overall landing system design in Section 2.8.3.

2.8.4 Landing System Concepts

The variety of landing system concepts that were considered are shown in six drawings for the small capsule and the one for the large capsule; these are summarized in Table 2.8-3 (Figures 2.8-7 through 2.8-14). All are based on a vehicle M/C_DA of 0.2 and landing system weights of 40 lbs. and 200 lbs. In Concept 1 (Figure 2.8-7) the parachute packs are mounted on the back of the heat shield below the antenna's radiation pattern. The aftcone is released and its drag extracts the first-stage parachute. Provisions for post-landing survival are shown. (Note that the first stage not only provides drag, but also aids in stabilization, hence the usage, "drogue chute".) Concept 2 (Figure 2.8-8) locates the first-stage parachute in the apex of the aftcone. This allows the mortar impulse to be directed through the vehicle's c.g. to minimize the dynamic perturbations; however, if interference with the antenna radiation pattern results (the dissipation factor of densely packed nylon may be relatively high) and, if transmission is required prior to parachute deployment, this method may prove objectionable.

In Concept 3 (Figure 2.8-9), the parachute mortar is located below the antenna and employs a potted "tear out" lanyard to allow side deployment with the parachute fix-point at the apex. A modification of Concept 4 (Figure 2.8-10) was chosen as the preferred configuration.

TABLE 2.8-3

LANDING SYSTEM CONCEPTS

	CONCEPT	PARACHUTE	IMPACT SURVIVAL	ANTENNA
350 lb. Capsule	No. 1	Two Stage (1)	yes	JPL
	No. 2	Two Stage (2)	yes	JPL
	No. 3	Two Stage (2)	yes	JPL
	No. 4	Two Stage (3)	yes	JPL
	No. 5	Two Stage (2)	yes	Exterior Cone
	No. 6	Single Stage (3)	no	JPL
2000 lb. Capsule	No. 1	Two Stage (3)	yes	JPL

(1) Aftcone released which extracts the parachute

(2) Mortar ejection with aftcone intact

(3) Aftcone released and mortar-ejected parachute

MARINER "B" 350 LB ENTRY CAPSULE
CONCEPT NO. 1

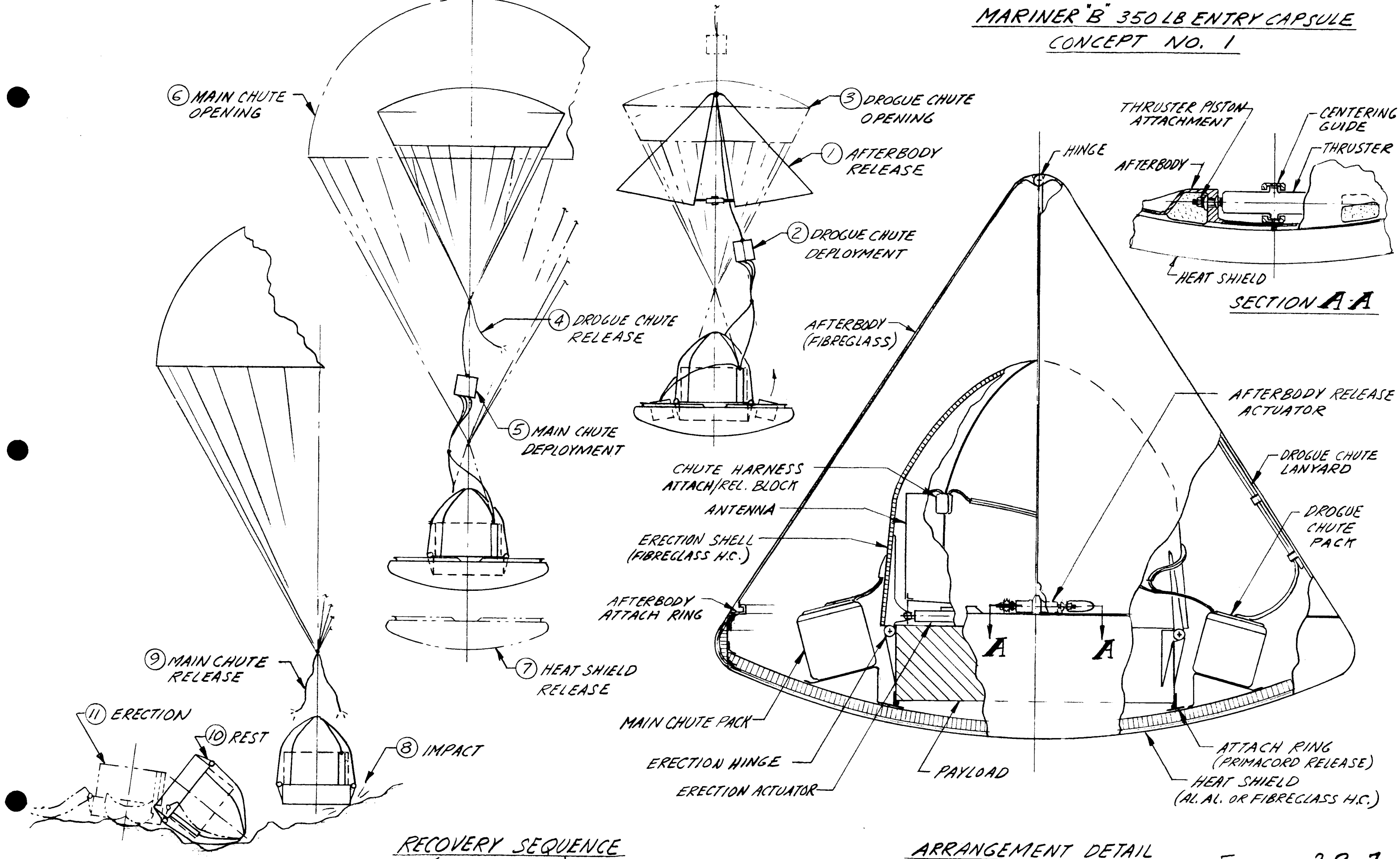

RECOVERY SEQUENCE (SCHEMATIC)

ARRANGEMENT DETAIL (1/10 SCALE)

FIGURE 2.8-7

MARINER "B" 350 LB ENTRY CAPSULE
CONCEPT NO. 2

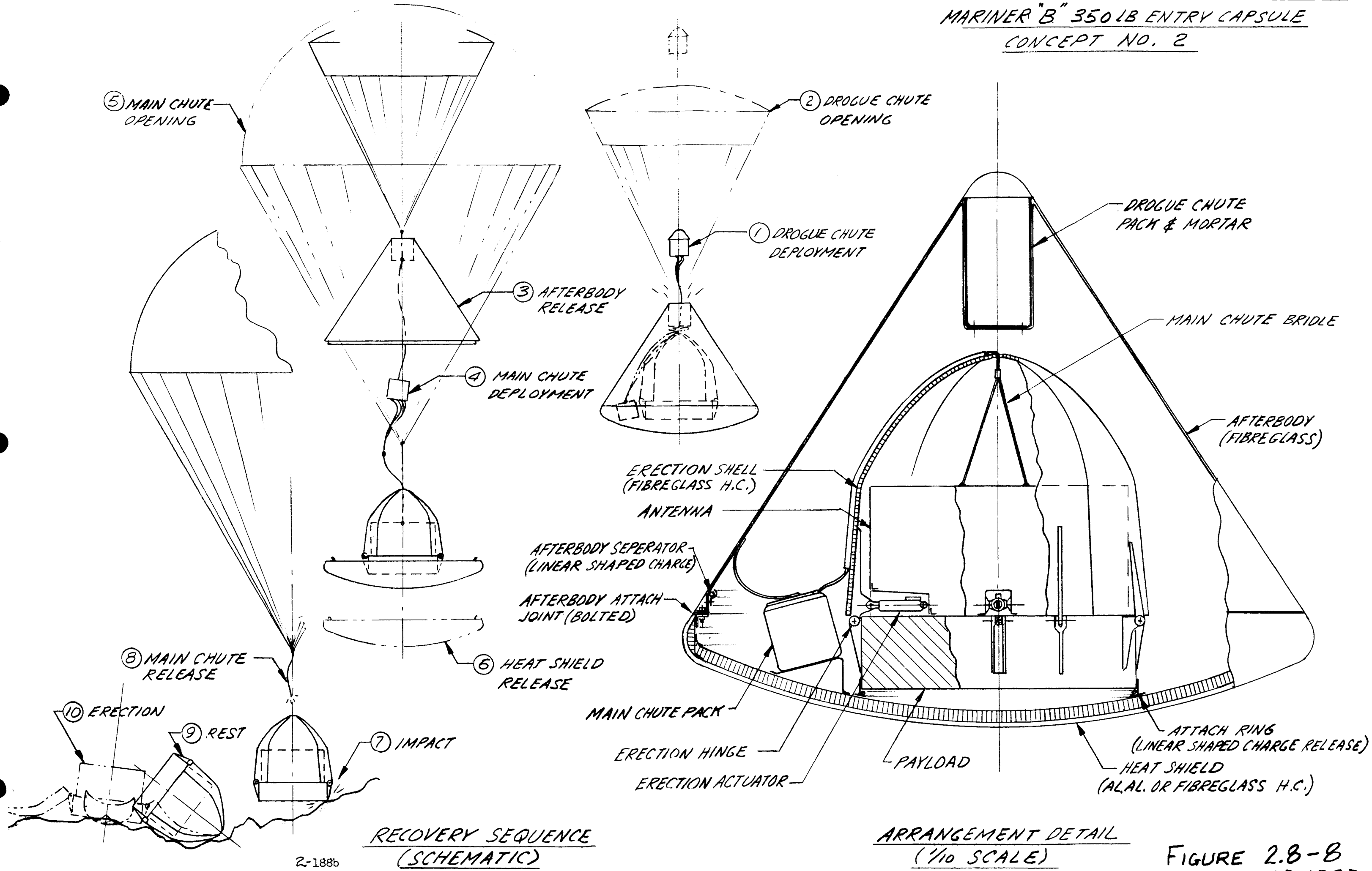

RECOVERY SEQUENCE (SCHEMATIC)

ARRANGEMENT DETAIL (1/10 SCALE)

FIGURE 2.8-8

MARINER "B" 350 LB ENTRY CAPSULE
CONCEPT NO. 3

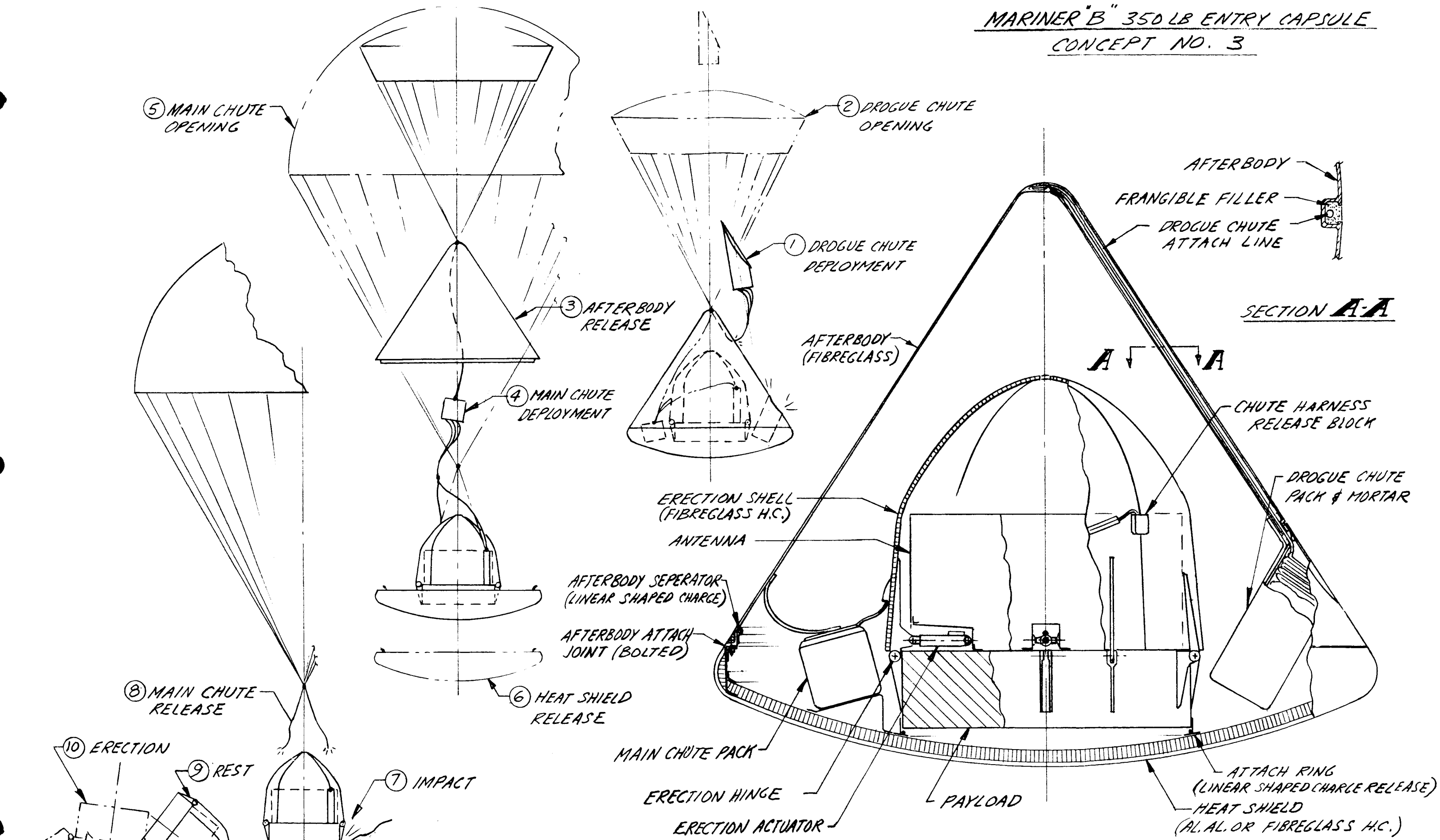

RECOVERY SEQUENCE (SCHEMATIC)

ARRANGEMENT DETAIL (1/10 SCALE)

FIGURE 2.8-9

MARINER "B" 350 LB ENTRY CAPSULE
CONCEPT NO. 4

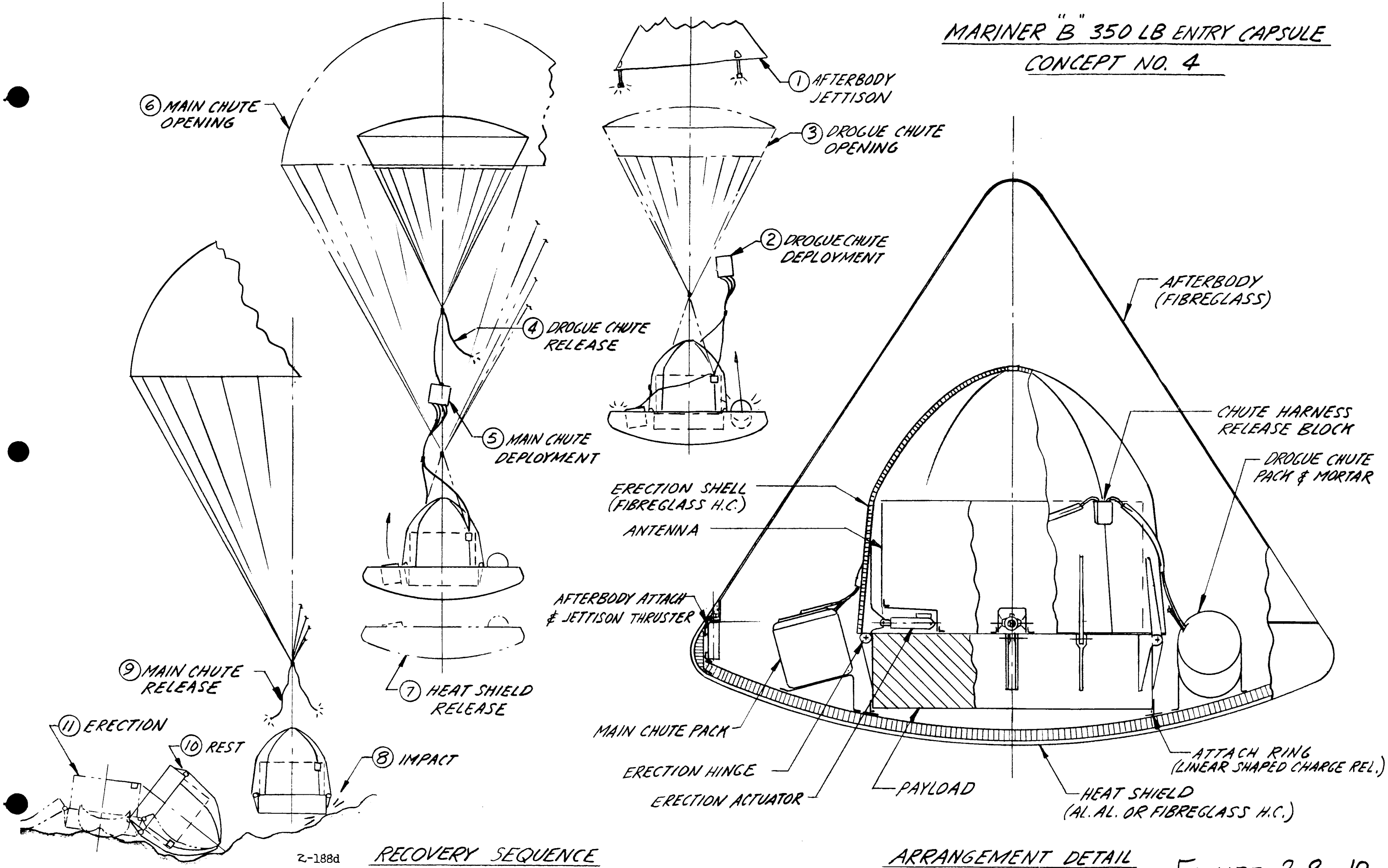

2-188d

RECOVERY SEQUENCE (SCHEMATIC)

ARRANGEMENT DETAIL (1/10 SCALE)

FIGURE 2.8-10

2-188d SID 63-1293

MARINER "B" 350 LB ENTRY CAPSULE
CONCEPT NO. 5 (CONICAL ANTENNA)

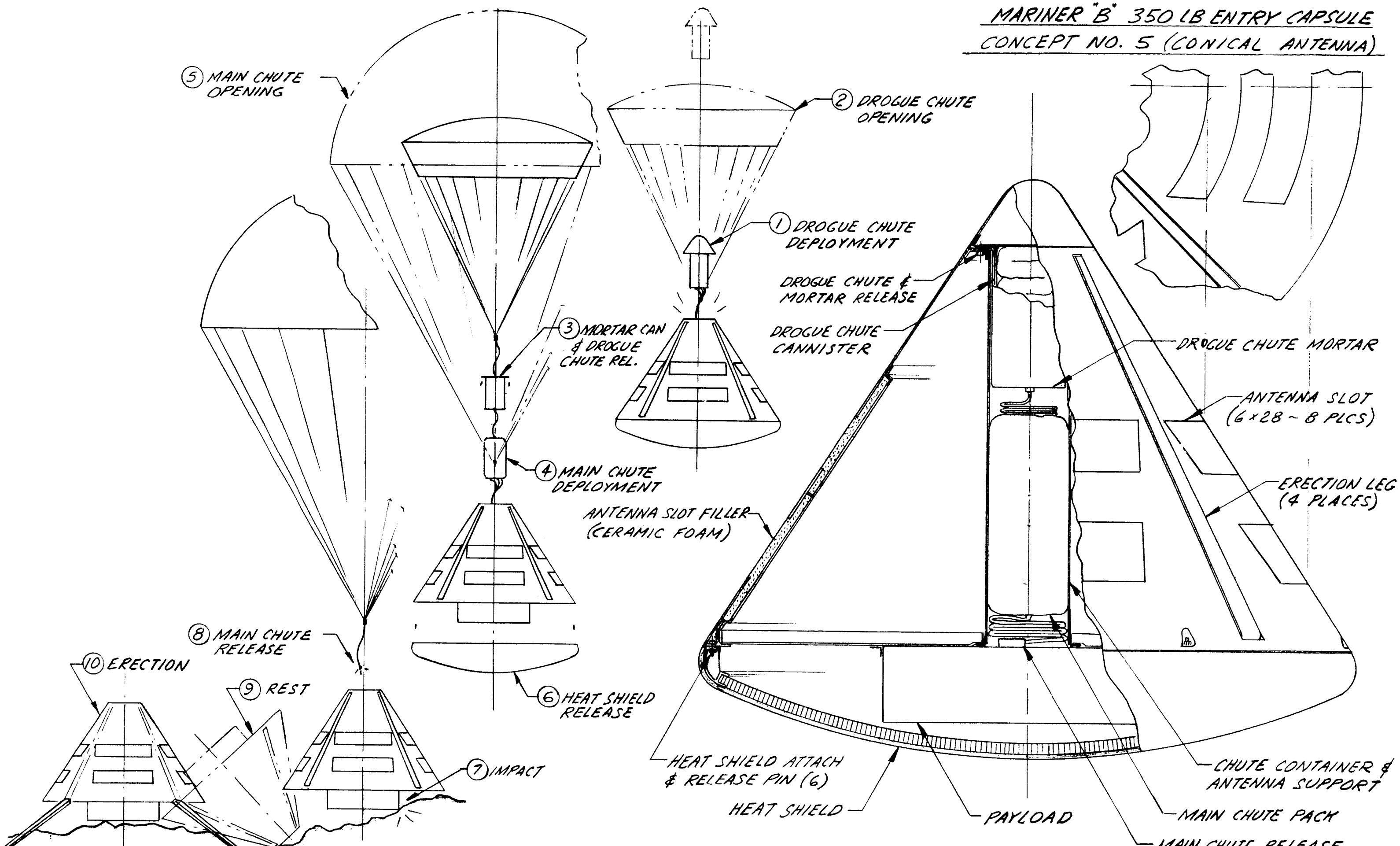

RECOVERY SEQUENCE (SCHEMATIC)

ARRANGEMENT DETAIL (1/10 SCALE)

FIGURE 2.8-11

MARINER "B" 350 LB ENTRY CAPSULE
(ALTERNATE CONCEPT NO. 5 (CONICAL ANTENNA)

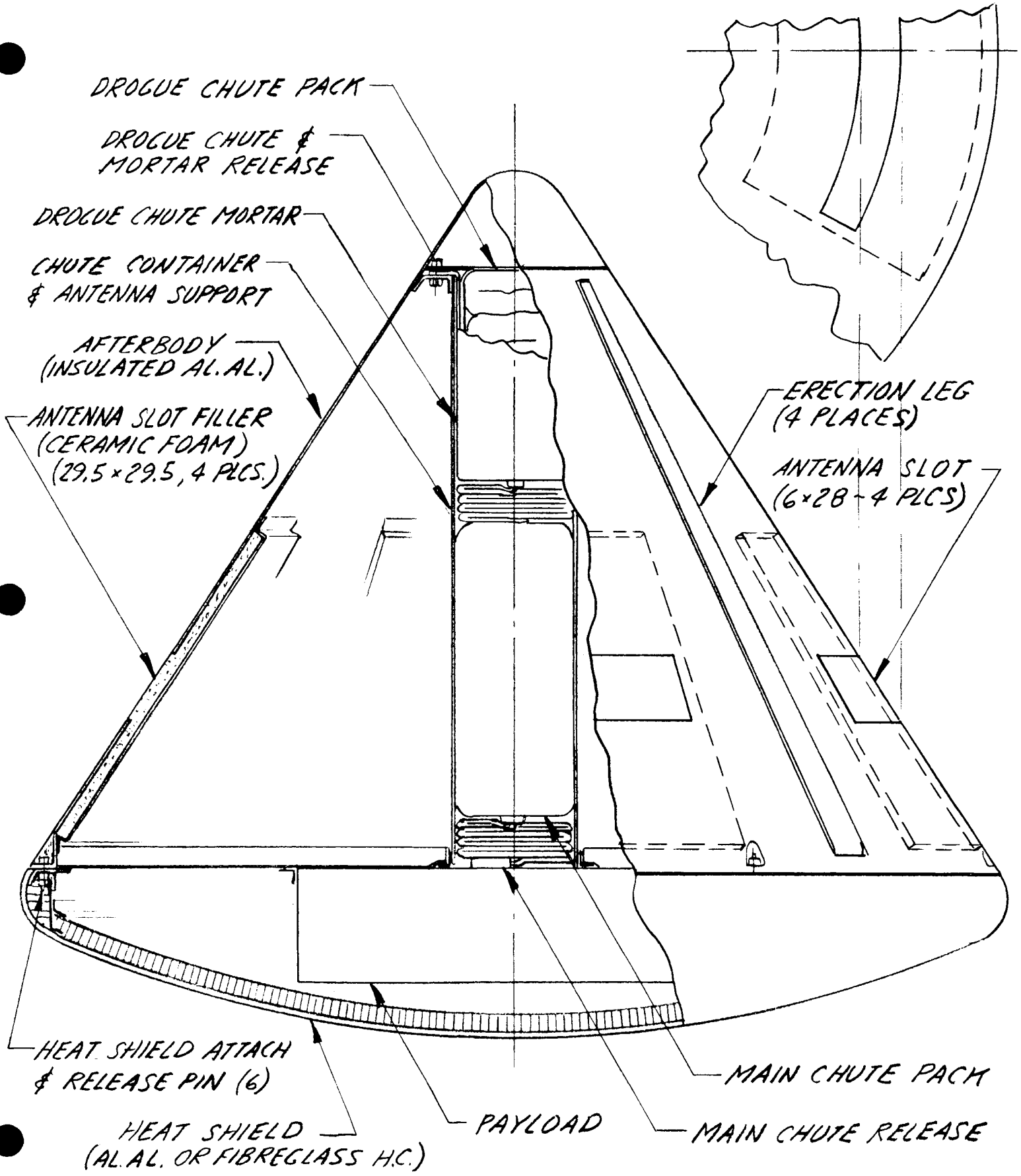

FIGURE 2.8-12
SID 63-1293

MARINER "B" 350 LB ENTRY CAPSULE
CONCEPT NO. 6

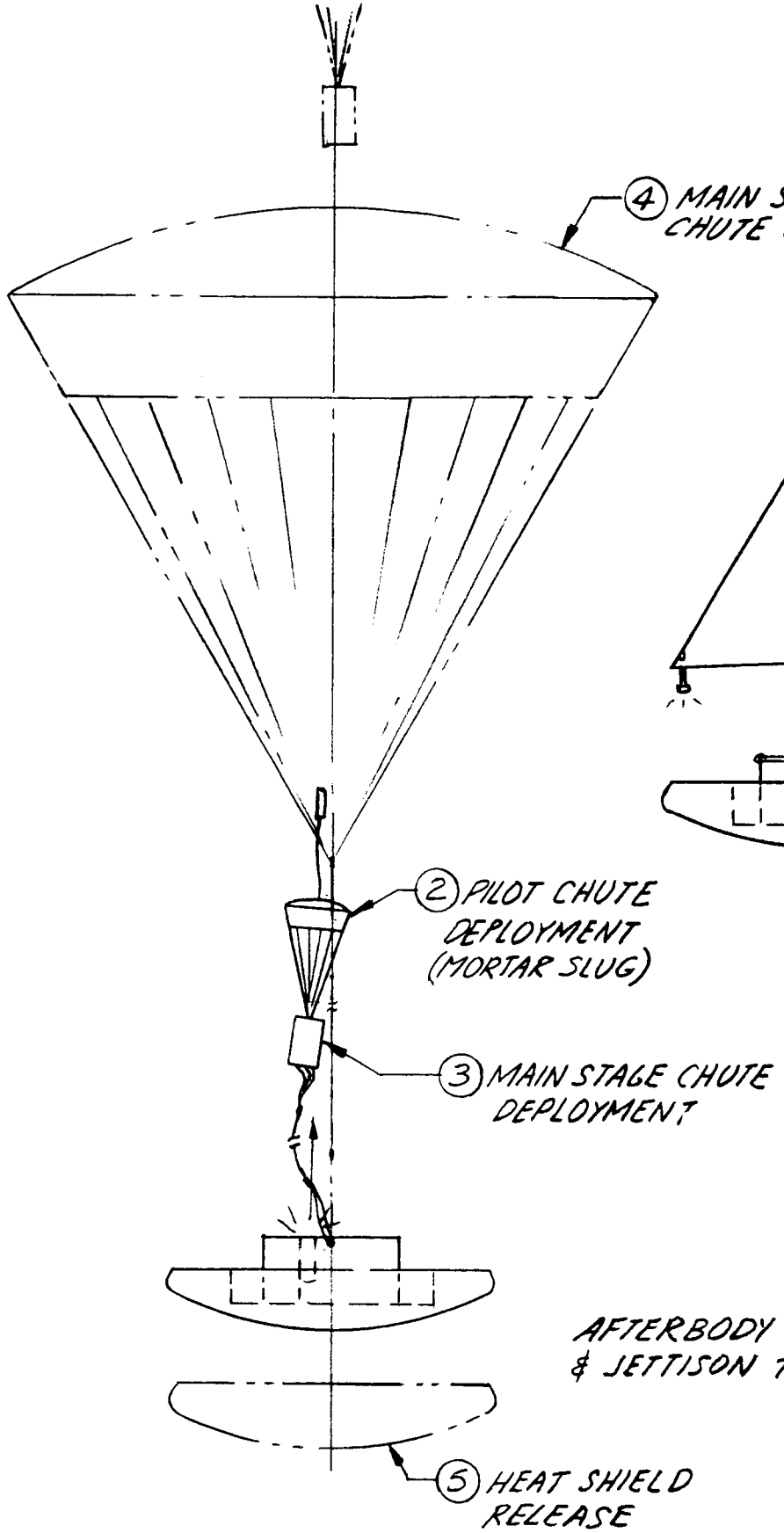

RECOVERY SEQUENCE
(NO LANDING SURVIVAL)
(SCHEMATIC)

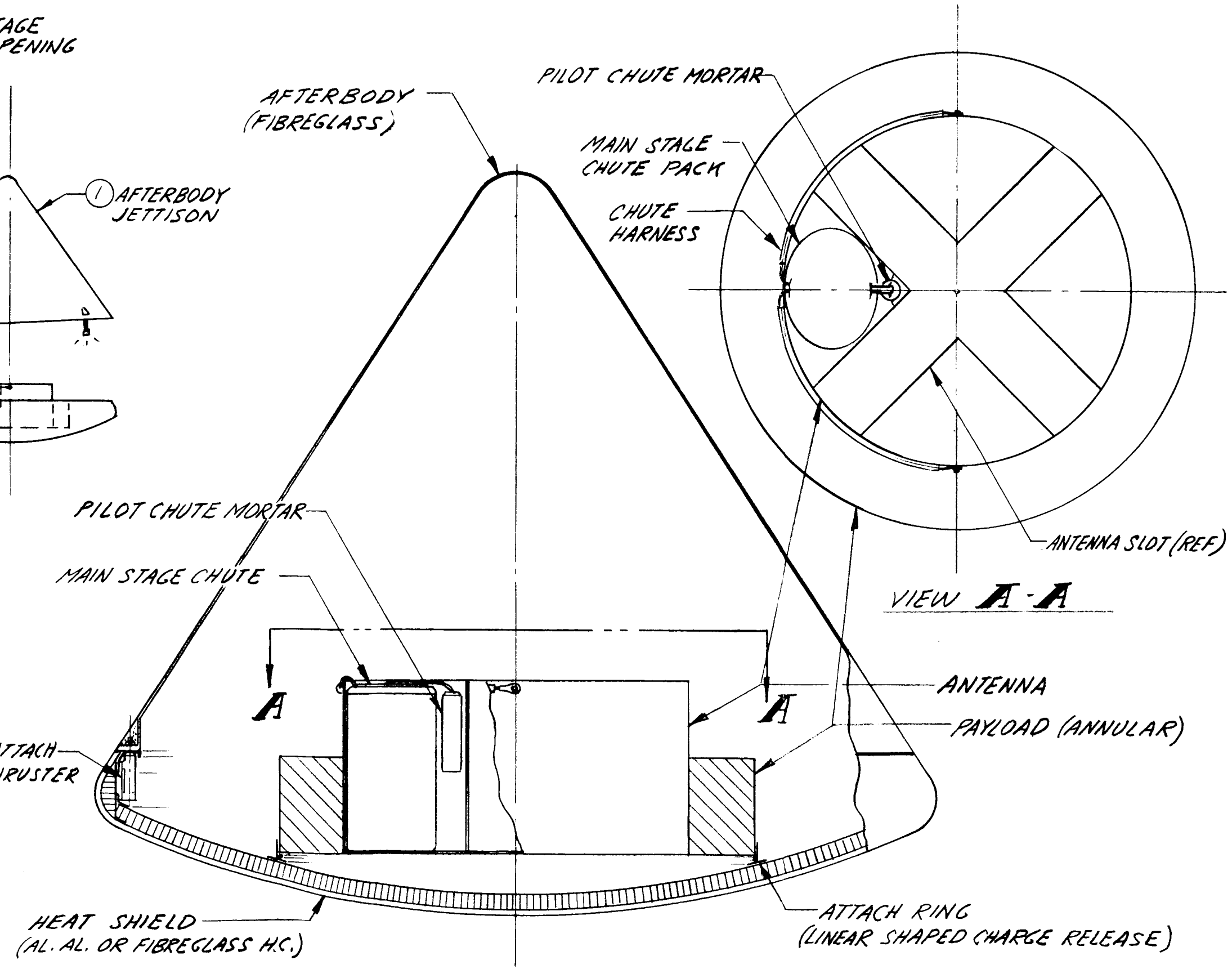

ARRANGEMENT DETAIL
(1/10 SCALE)

FIGURE 2.8-13

VOYAGER "2000" LB ENTRY CAPSULE
CONCEPT NO. 1

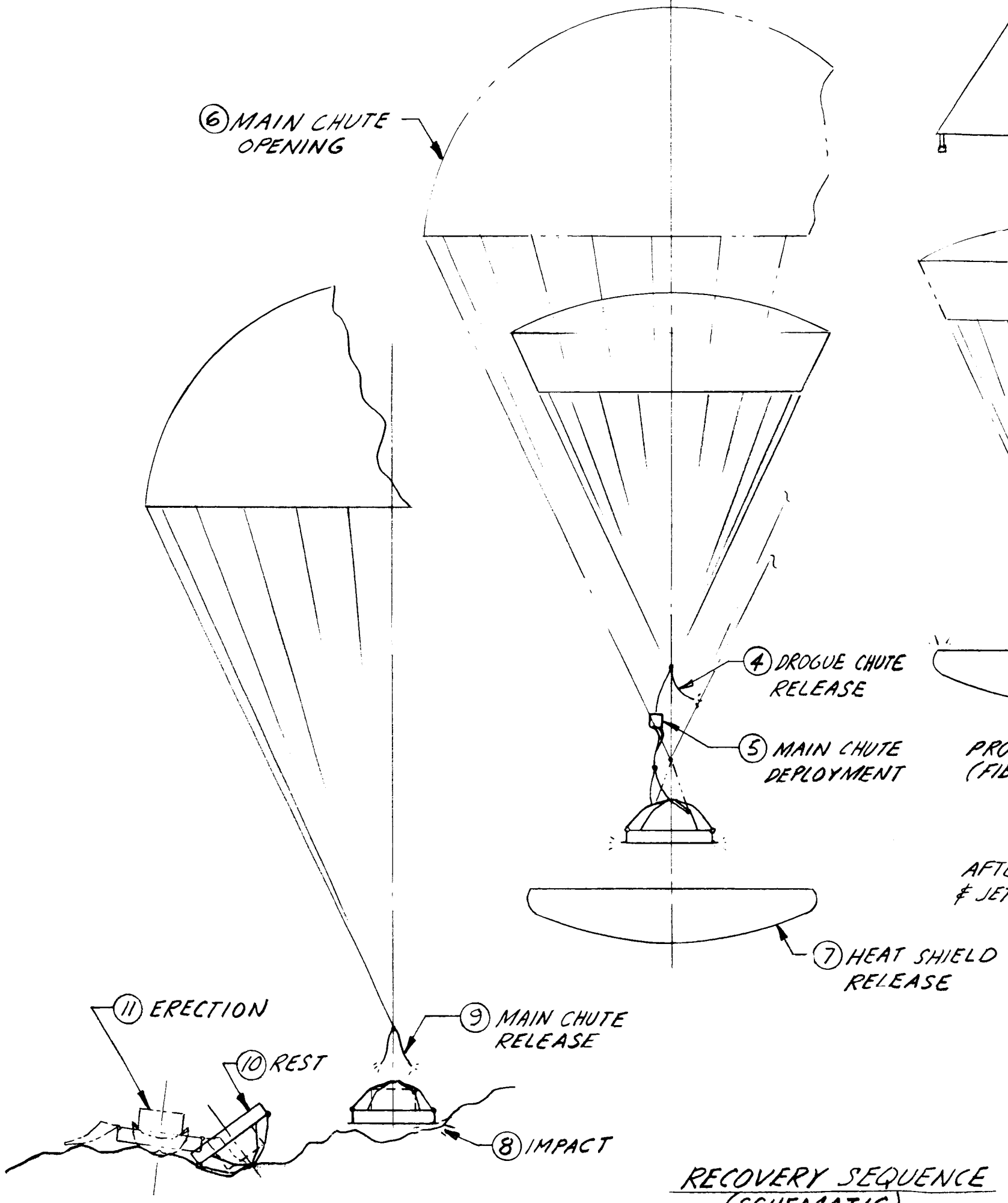

RECOVERY SEQUENCE
(SCHEMATIC)

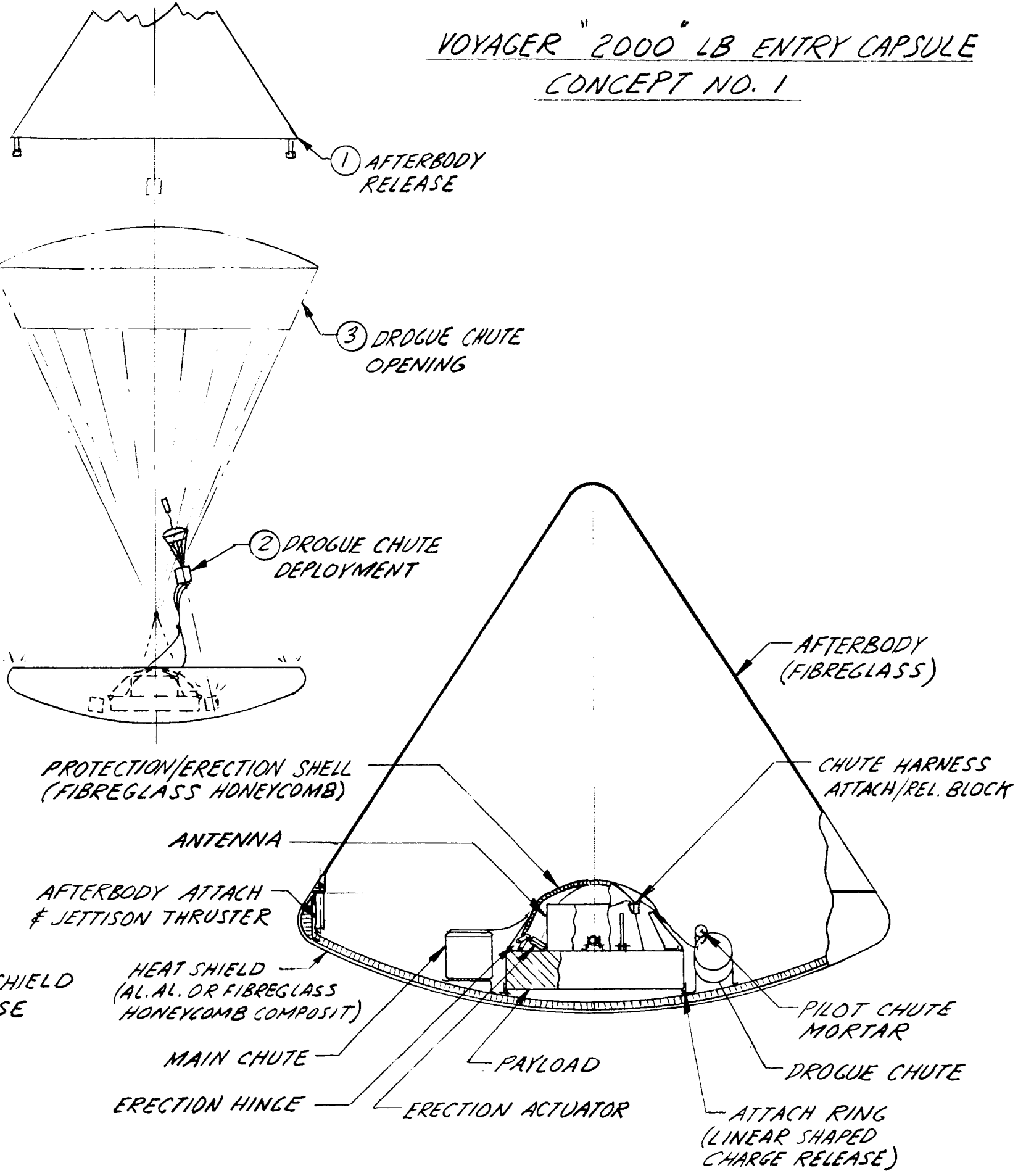

ARRANGEMENT DETAIL
(1/40 SCALE)

FIGURE 2.8-14

SID 63-1293

Although the parachute deployment sequence is shown using a mortar for first-stage deployment, the alternative of employing a drogue gun and pilot chute appears to be more favorable.

Small capsule Concept No. 5 (Figure 2.8-11) is based on an alternate antenna concept in which the afterbody serves to house a slotted antenna and is landed with the payload. Landing survival is assumed and is implemented by four erection legs mounted in the afterbody between the antenna slots. This concept allows a simple central parachute installation and is free of antenna interference and parachute deployment "kick" problems. Section 2.5.1 is a detailed description of this antenna configuration. The antenna shown in Figure 2.8-11 proved to be too heavy; Figure 2.8-12 shows an alternative antenna with fewer slots and lighter weight.

Concept 6 (Figure 2.8-13) for the small capsule respresents a "no landing survival" system. The JPL inboard antenna is employed with a single-stage recovery system to provide deceleration at maximum altitude. The parachutes are housed in the antenna voids (the space not occupied by the slots) to minimize deployment "kick" perturbations.

One concept for the large capsule is shown (Figure 2.8-14). It is similar to small capsule Concept No. 4. The alternative of using the slotted cone antenna is not applicable to the large capsule due to unfavorable weight and geometry. Design considerations prohibit the use of a one-stage system and mission requirements dictate that post-landing transmission is mandatory.

Two landing system design concepts were selected for the Mariner B and one for the Voyager. For the Mariner B, Concept 4 utilizes a two-stage parachute system to obtain maximum descent time. Concept 6 is also selected for its ability to provide the maximum sampling altitude with a less complex and more reliable single-stage parachute. Neither concept has impact attentuation; however, the requirements for post-landing data transmission were considered for Concept 4 and are discussed in paragraph 3.3. The concept recommended for the Voyager capsule utilizes a two-stage parachute system to obtain maximum descent time and incorporates impact attenuation.

2.8.5 Recovery System Events Sequencing & Actuation

The sequence of events during the landing phase are as follows:

(1) Afterbody jettison will be accomplished by thrusters which are initiated by a signal from the sensor.

(2) First-stage parachute mortar or drogue gun will be fired after a time delay of two seconds after jettison of the afterbody.

(3) First-stage parachute release will be activated by the sensor.

(4) Second stage parachute is deployed by the drag of the first-stage parachute.

(5) The heat shield is released through a time delay one second after first-stage parachute release.

(6) Data sampling and transmission is initiated by the same signal which releases the heat shield.

(7) Second-stage parachute release at impact is accomplished by a contact switch or state-of-the-art doppler altimeter prior to impact.

(8) Erection of the payload is then initiated.

Accurate sensing for initiation of these functions is complicated by the uncertainties in the atmospheric parameters and the trajectory variables. Conventional techniques such as baroswitches, dynamic pressure sensors, or timers are not applicable.

The altitude at which the hypersonic parachute can be deployed appears to be limited by the heating loads on the parachute. Inasmuch as the laminar heating rate is related to $\rho^{0.5} U^{3.19}$, it would appear that a velocity sensor could be used to deploy the first-stage parachute. A number of techniques for sensing velocity have been considered to provide an accurate signal for initial deployment of the first-stage parachute. Ratioing of Hyperflo parachute flight-test performance data obtained in the earth's atmosphere indicates that deployment can be initiated at a velocity of 3750 fps in the Martian atmosphere.

The techniques considered for sensing velocity include:

(a) An integrating accelerometer

(b) A "ratioing" accelerometer wherein the acceleration expected at a velocity of 3750 fps is picked off as a ratio or a fraction of the peak deceleration.

Both techniques require knowledge of the entry velocity so that the proper stop (in the case of the integrating accelerometer) or the proper ratio (in the case of the second concept) can be realized. This input can be made either at launch by estimating the entry velocity as a function of the projected trajectory parameters, and/or updated prior to separation by ground command utilizing smooth trajectory data acquired by the tracking network. The integrating accelerometer would be mounted on a "pendulum" so that the sensitive axis is always along

the resultant acceleration vector. If the entry attitude is not extreme the lift component of acceleration will be small and the resultant acceleration vector will be sufficiently well aligned with the velocity vector to provide an accurate signal. A suitable pendulus mount with sufficient angular freedom in two axes and the proper damping could be developed in a reasonably short time.

For extreme entry conditions, the vehicle will probably experience entry oscillations (and some lift) and the resultant accelerations recorded may be high by a factor of approximately 5 - 10%. Further analysis is required to ascertain the sensitivity and the tolerable errors. If greater accuracy is required, the 5-10% bias due to oscillations can be normalized by sensing the magnitude of the oscillation (e.g. a pendulum pickoff); however, this will obviously complicate the system. The integrating accelerometer would have to be of the pulse re-balanced type (forced balanced system) which is presently available with threshold levels that are more than adequate (one part in 10^5). An accelerometer of this type is manufactured by Bell Avionics for the Agena.

In the case of the "ratio" concept, the effect of oscillations may be self-cancelling inasmuch as only percentage pickoffs are employed. This system offers the promise of being somewhat simpler than the integrating accelerometer. It would have to be set up for the worst condition (i.e., 90° entry into any of the atmospheres) and would probably trigger at a velocity and/or altitude somewhat lower than the maximum capability of the system if entry is accomplished at angles less than -90°. However, the operational altitude band above ground level increases rapidly as the entry angle decreases and the decrease in sampling altitude due to non-optimum triggering may be less than that gained by the lower entry angle.

Other techniques considered for generating a signal for initial parachute deployment included measuring the temperatures behind the shock with a continuously fusible thermocouple (such as has been developed for the Dynasoar program) and relating these temperatures to velocity. Also considered was the possibility of using thermocouples embedded within the heat shield to measure ablation rates and temperature rise and relating this information to the velocity of the vehicle. However, an analysis quickly showed that, even if a direct temperature measurement of the invicid flow field behind the shock were possible, uncertainties of at least 30% would be encountered in relating the temperature measurement to velocity because of uncertainties in the nature and composition of the gas and its thermal real-gas properties (e.g., specific heat ratio). In the case of attempting to relate heat shield temperatures and ablation rates to velocity (and ultimately altitude), the unfeasibility of this approach becomes immediately

evident when one remembers that the temperature and ablation history are proportional to the entry angle (which is unknown), the atmosphere encountered and the radiative heating properties of the atmosphere.

2.8.6 Impact Attenuation

Impact attenuation may be required to provide for soft landing to assure post-landing data transmission. Candidate materials include pneumatic bags, metallic and non-metallic honeycomb structure, balsa wood, foamed plastics, hydraulic cylinders, deformable metal tubes and rocket propulsion. Airbags have successfully been utilized on Project Mercury and in the recovery of numerous drones and missiles. They have good vertical velocity attenuation characteristics but have no capability of absorbing shear loads. Furthermore, because of the extended period in the space environment and the exposure of the equipment to the thermal cycle required for sterilization, damage to the bag fabric is possible. Similarly, balsa wood and styrofoam cannot sustain the heat cycle and must be ruled out. This is discussed in detail in Section 2.4.

Active systems such as retrorockets were considered and eliminated because of the associated ground sensing, stowage and deployment problems. Furthermore, propulsion system weights are prohibitively high. (See Figures 2.8-15 and 2.8-16.) Hydraulic cylinders are precluded because of the oil-seal problems involved under extended space environments. The concentrated design and test effort required to qualify frangible metal tubes is prohibitive. Figure 2.8-17 shows the tradeoff developed early in the study; the size of the second-stage parachute and impact attenuation for 100 g's is shown.

Aluminum honeycomb was selected for impact attenuation because it is a passive material, it requires a minimum design effort, and it is capable of sustaining both the sterilization and space environments. This attenuator may be used in the form of struts where a specific stroke is required or, for higher energy absorption, as a solid block. The stroke required for the permissible 1000 g load at impact for 70% crush-up is about 1.7 inches.

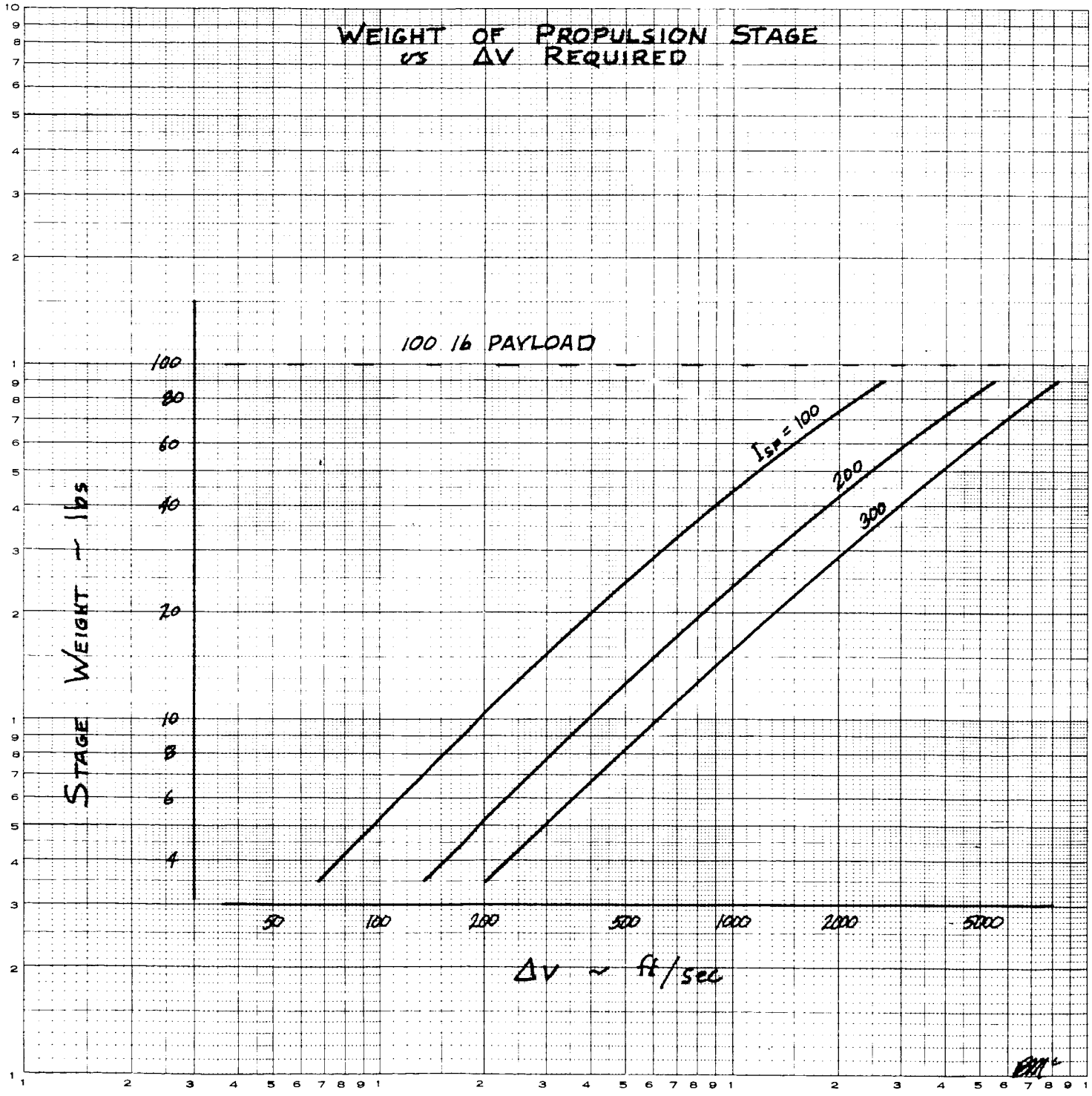
WEIGHT OF PROPULSION STAGE
vs ΔV REQUIRED
100 lb PAYLOAD
I_{SP} = 100
200
300
STAGE WEIGHT ~ lbs
100
80
60
40
20
10
8
6
4
50
100
200
500
1000
2000
5000
ΔV ~ ft/sec

FIGURE 2.8-15

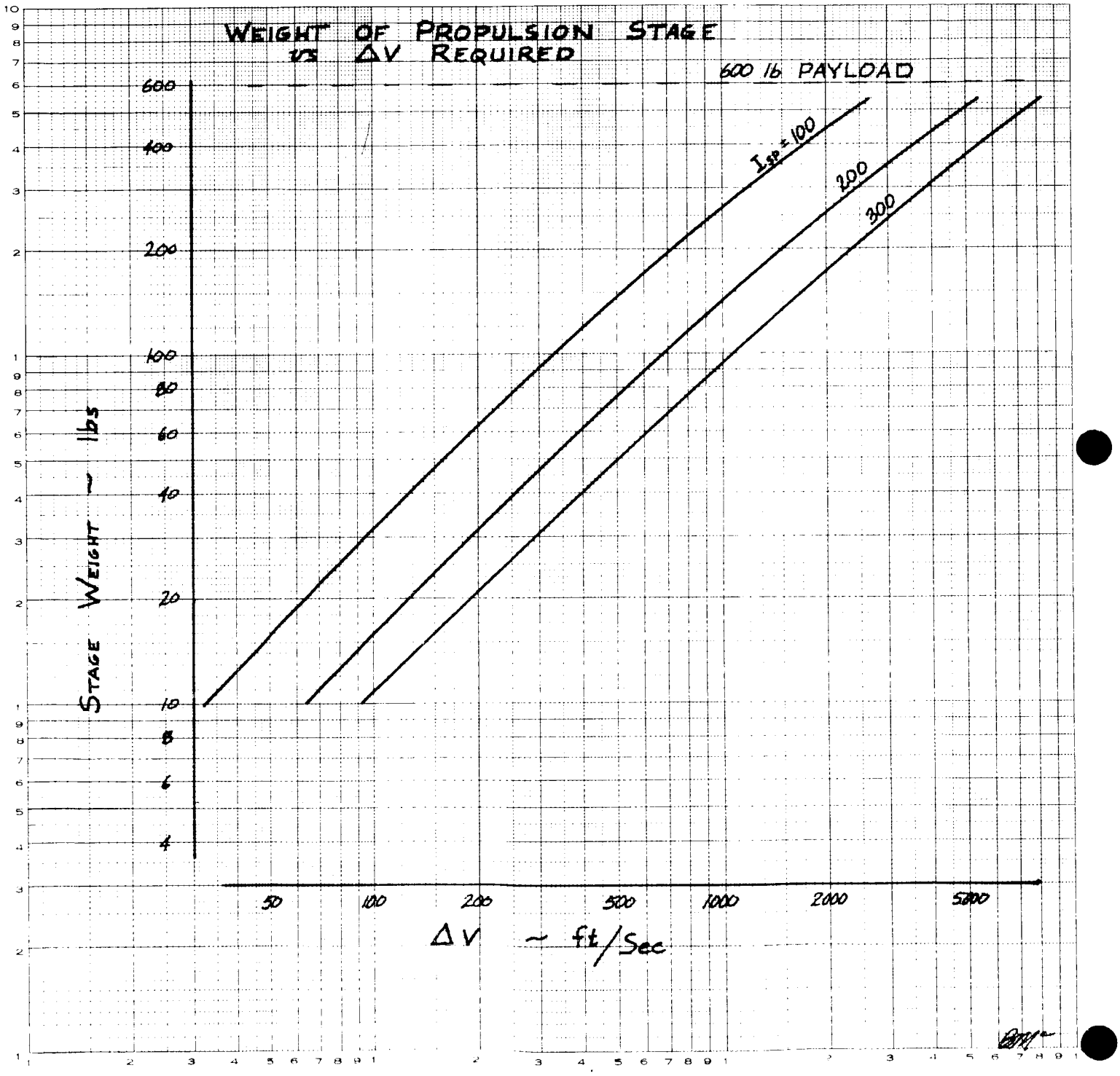
WEIGHT OF PROPULSION STAGE
VS ΔV REQUIRED
600 lb PAYLOAD
$I_{sp} = 100$
200
300
STAGE WEIGHT ~ lbs
600
400
200
100
80
60
40
20
10
8
6
4
50
100
200
500
1000
2000
5000
ΔV ~ ft/Sec

FIGURE 2.8-16

FIGURE 2.8-17

WEIGHT COMPARISON OF IMPACT ATTENUATION AND SECOND-STAGE PARACHUTE SIZE

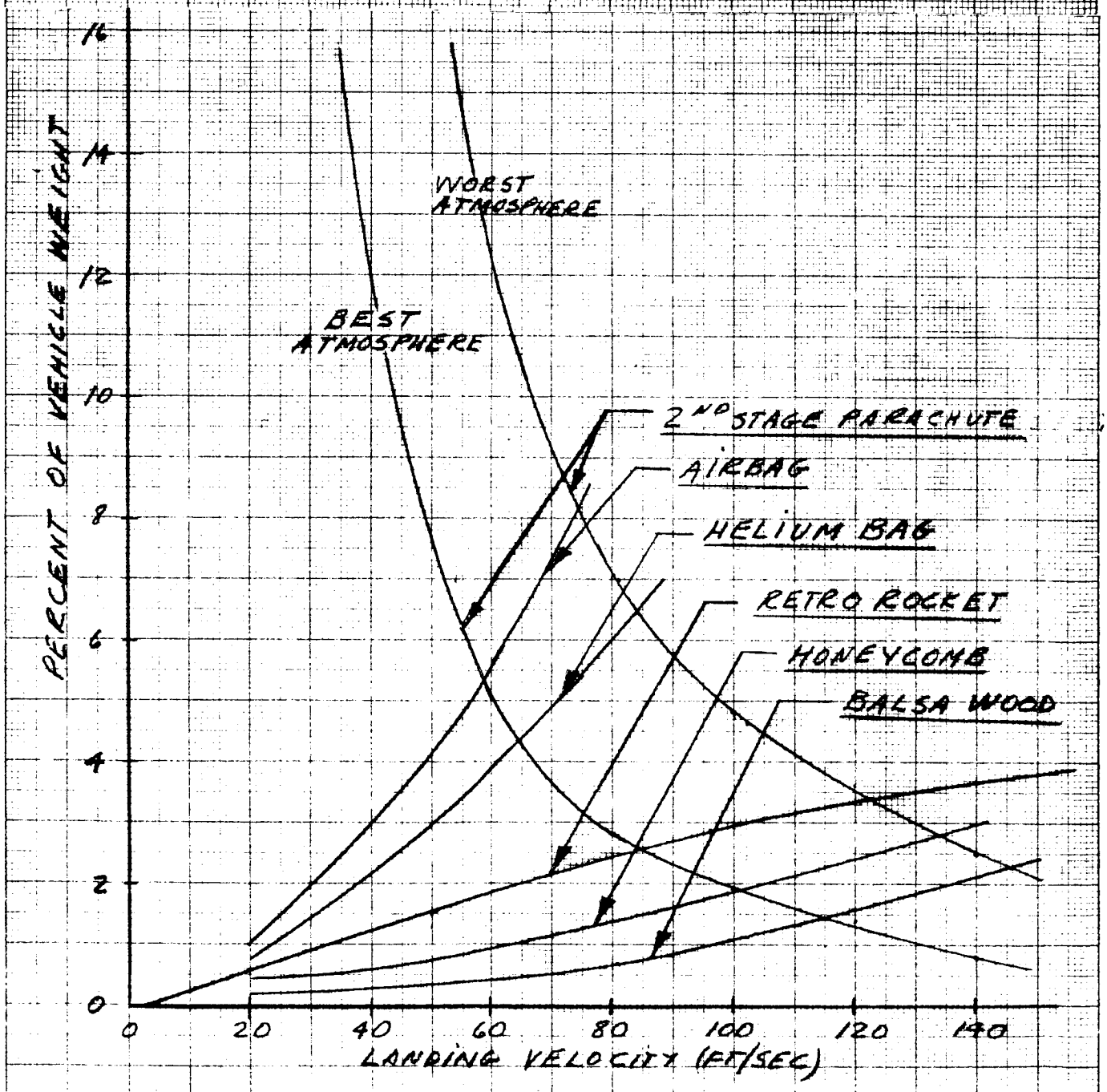

2.9 SYSTEM WEIGHTS TRADEOFFS AND INERTIAL PROPERTIES

2.9.1 System Weights Tradeoffs

The results of the various heat-shield, structural and landing system tradeoffs are summarized in Figures 2.9-1 through 2.9-4 for both the small (Mariner B) and large (Voyager) capsules for entry velocites of 22,000 and 25,000 fps. (The lower velocity was considered to evaluate its effect on payload and gross capsule weights.) The figures show the variation in capsule weight as a function of M/C_DA, payload weight, base diameter and the structural concept and material indicated. The Apollo configuration (66° included angle aftcone) with a nominal C_D of 1.5 entering at an angle of attack and L/D ratio of zero was assumed for both the small and large capsules.

The heat shield weights for the small capsule were developed by employing the results of the closed-form analyses, generated early in the study and described in Section 2.7. The weight of the structural system was derived from the data generated in Section 2.6. In the case of the landing system, nominal weights of 40 and 200 pounds were assumed for the small and large capsules, based on the results of preliminary parametric studies. The procedure employed was to assume an initial M/C_DA of 0.2, then calculate the heat loads, heat shield, and structural weights for a given size capsule. Successive iterations then were employed to re-compute the M/C_DA, heat load, and weights until the solution converged and M/C_DA and the weights computed were compatible.

For the reasons previously presented, Figures 2.9-1 and 2.9-2 considered only a phenolic-glass heat shield material. Although some weight saving would be possible with the more exotic ablators and/or employing "hotter" structures (as shown), really significant savings become apparent for the composite structure. Comparison of 22,000 and 25,000 fps entry velocities indicate potential gross capsule weight reductions in the order of 50 pounds for the small capsule having an M/C_DA of 0.2 and a 150 pound payload.

In the case of the large capsule, eight materials - structural combinations are shown. The composite structure is shown at a distinct weight disadvantage because of the large diameters required. Furthermore, the feasibility of fabricating structures of this magnitude today, which have the desired structural properties, has not been demonstrated. Phenolic glass also is heavy, and the weight advantages of the more advanced materials is apparent. The Voyager mission schedule is such that it is reasonable to assume that a number of these materials will be developed and qualified in time to be used.

Again, it should be noted that these curves were based upon preliminary data. However, they were most useful in selecting the

PREPARED BY:	NORTH AMERICAN AVIATION, INC. SPACE and INFORMATION SYSTEMS DIVISION	PAGE NO. OF
CHECKED BY:		REPORT NO.
DATE:	Capsule Weight vs M/C_dA	MODEL NO.

FIGURE 2.9-1

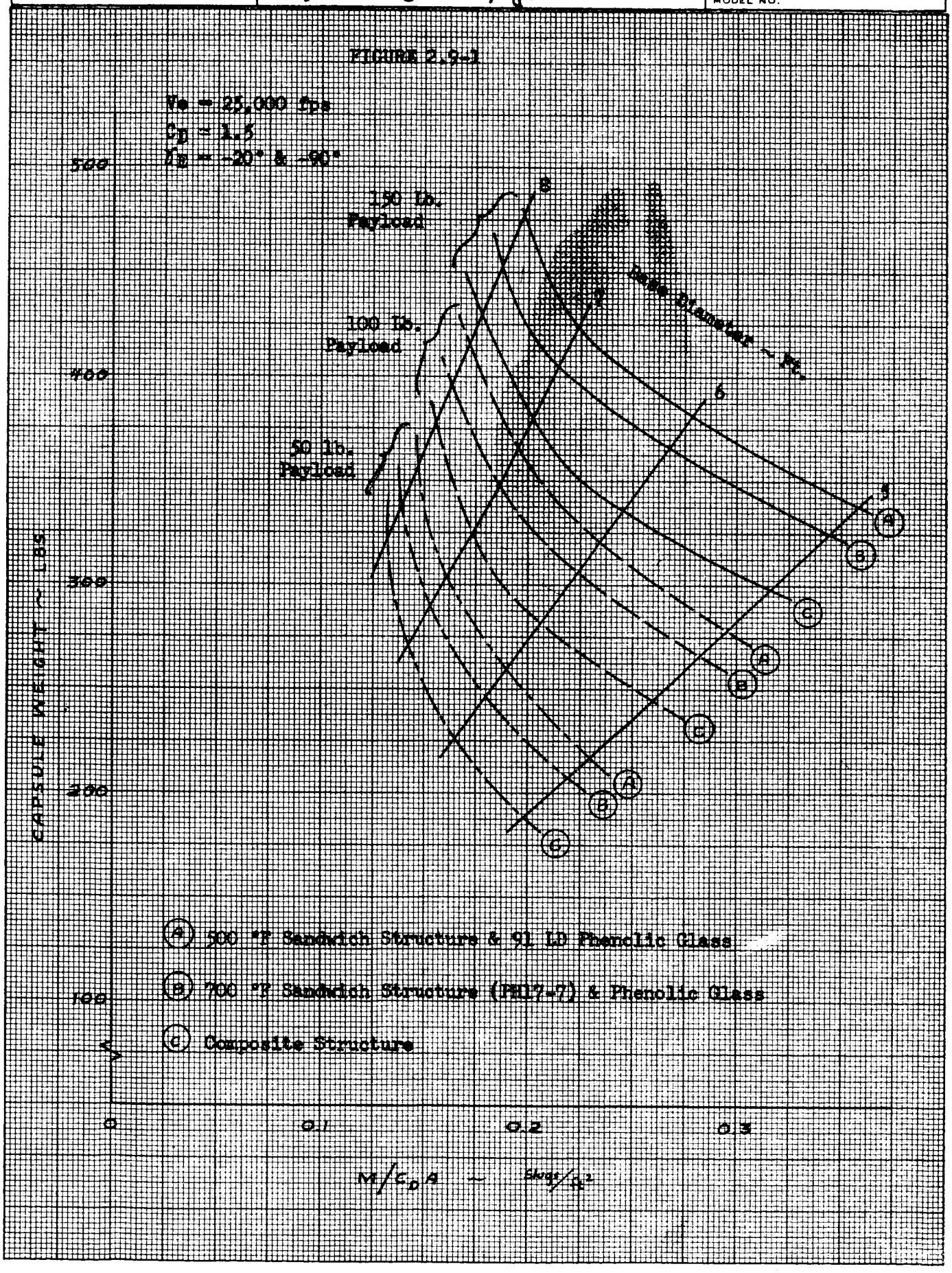

PREPARED BY:	NORTH AMERICAN AVIATION, INC. SPACE and INFORMATION SYSTEMS DIVISION	PAGE NO. OF
CHECKED BY:		REPORT NO. 2.9-2
DATE:	Capsule Weight vs. M/CDA	MODEL NO.

FIGURE 2.9-2

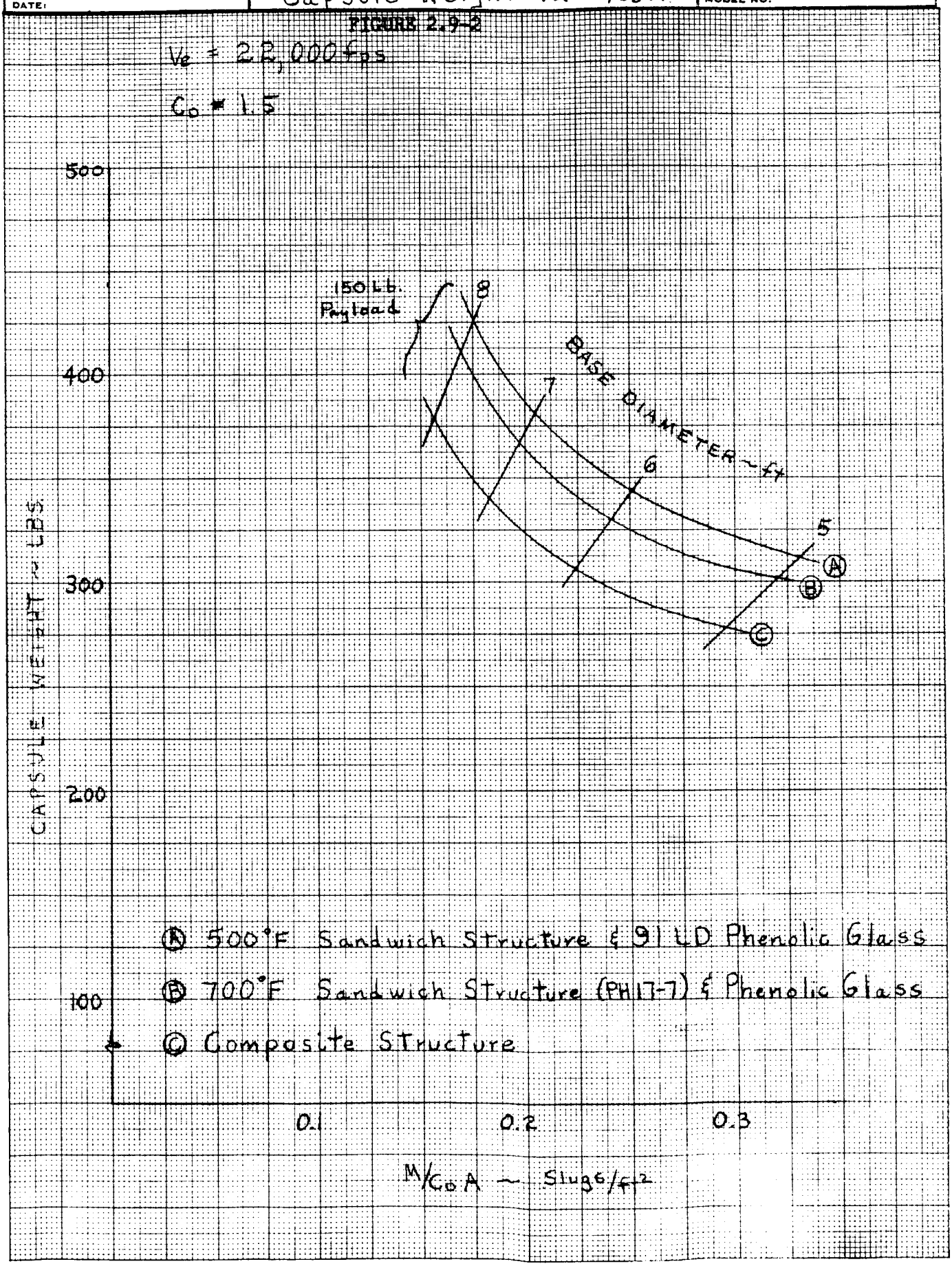

PREPARED BY:	NORTH AMERICAN AVIATION, INC. SPACE and INFORMATION SYSTEMS DIVISION	PAGE NO. OF
CHECKED BY:		REPORT NO.
DATE:	CAPSULE WEIGHT VS M/C_DA	MODEL NO.

FIGURE 2.9-3

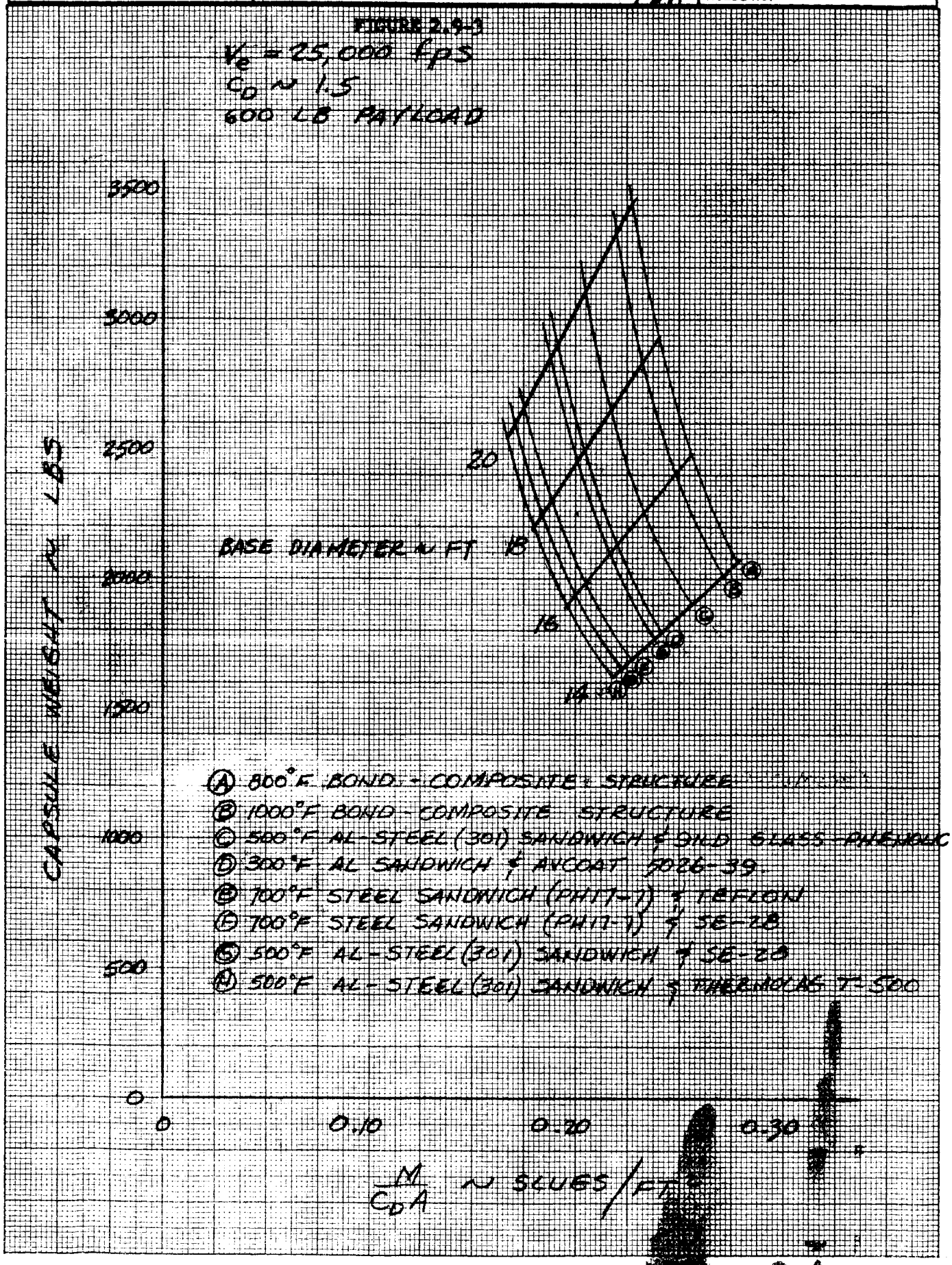

CAPSULE WEIGHT VS M/C_DA

FIGURE 2.9-4

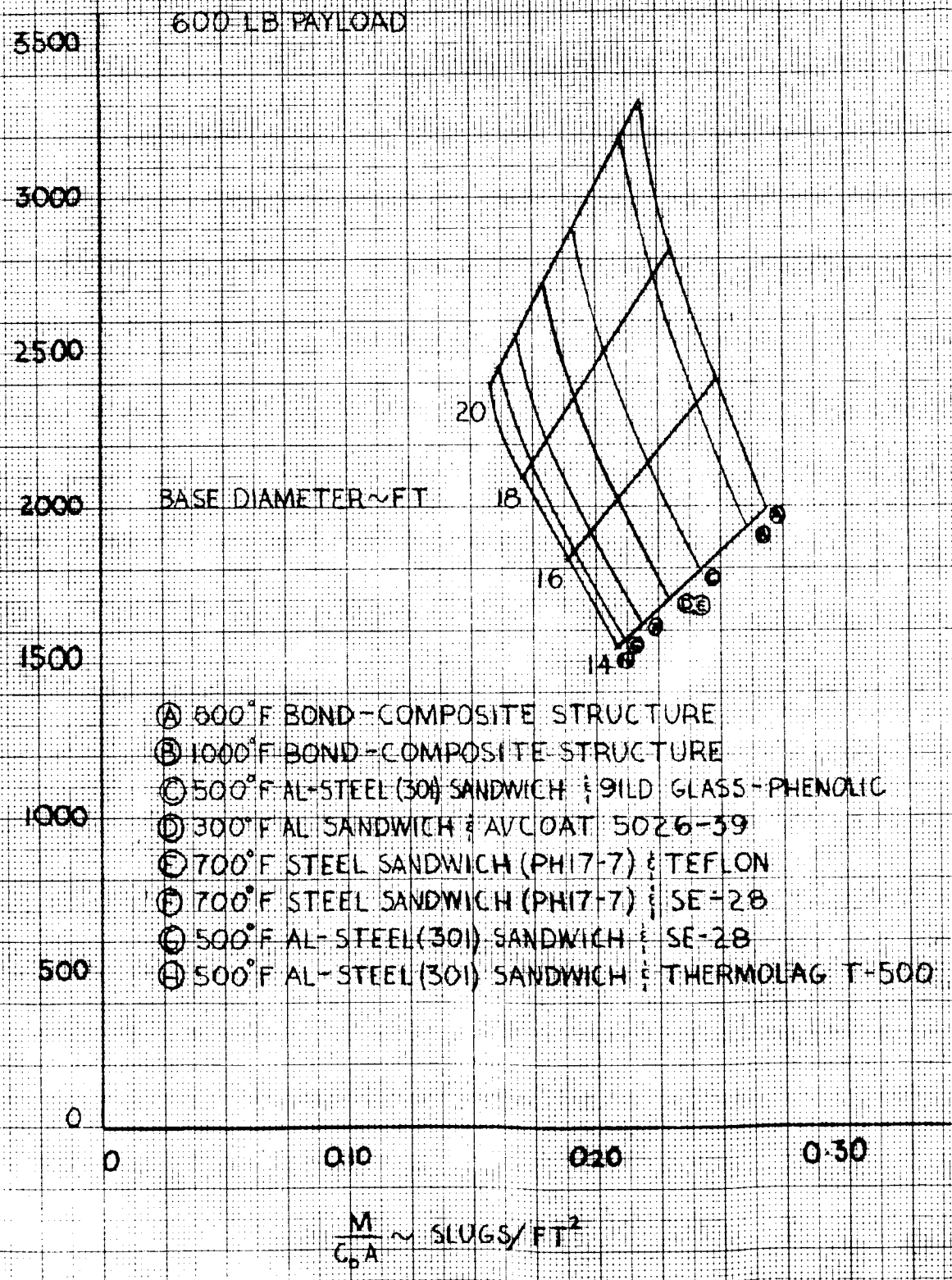

preliminary design configurations described in Section 3.0.

2.9.2 Preliminary Inertial Properties

Based upon the weights generated, a parametric survey was made to evaluate the range of c.g. locations and moments of inertia which might be expected for the several configurations in order to develop input data for the dynamic analysis.

The results of this analysis are presented in Figure 2.9-5 and Table 2.9-1. They indicated that it was reasonable to anticipate a horizontal c.g. location of within 0.2 D_B for both the Mariner and Voyager capsules, based upon the Apollo aerodynamic configuration and stowage of the recovery system at the apex of the cone. Relocation of the recovery system to a forward position with the payload and/or elimination of the aftcone in the case of the Voyager capsule will bring the c.g. forward.

The weights and centers of gravity were computed for the heat shield, structure, and payload weights shown for several diameters of interest. The payload was assumed to be located a maximum of six inches from the inner structural mold line for the small configuration and twelve inches for the large capsule. The moment-of-inertia data presented are for representative maximum and minimum weights and sizes for each configuration.

TABLE 2.9-1
PRELIMINARY INERTIA SUMMARY

DIAMETER (FT)	PAYLOAD (LBS)	HEAT SHIELD UNIT WT. (LBS/FT²)	CAPSULE GROSS WEIGHT (LBS)	ROLL INERTIA (SLUG-FT²)	PITCH & YAW INERTIA (SLUG-FT²)	C.G. % D.H.
6.5	150	3.0	375	33.2	38.8	20.6
7.5	100	3.9	420	64.7	69.1	17.6
14.0	600	2.5	1810	868.7	1090.9	21.4
18.0	600	5.6	2970	2852.4	2910.5	17.1

PREPARED BY:
CHECKED BY:
DATE:

NORTH AMERICAN AVIATION, INC.
SPACE and INFORMATION SYSTEMS DIVISION

MODEL NO.
REPORT NO. WA/63/152
PAGE NO. Enclosure (2) OF

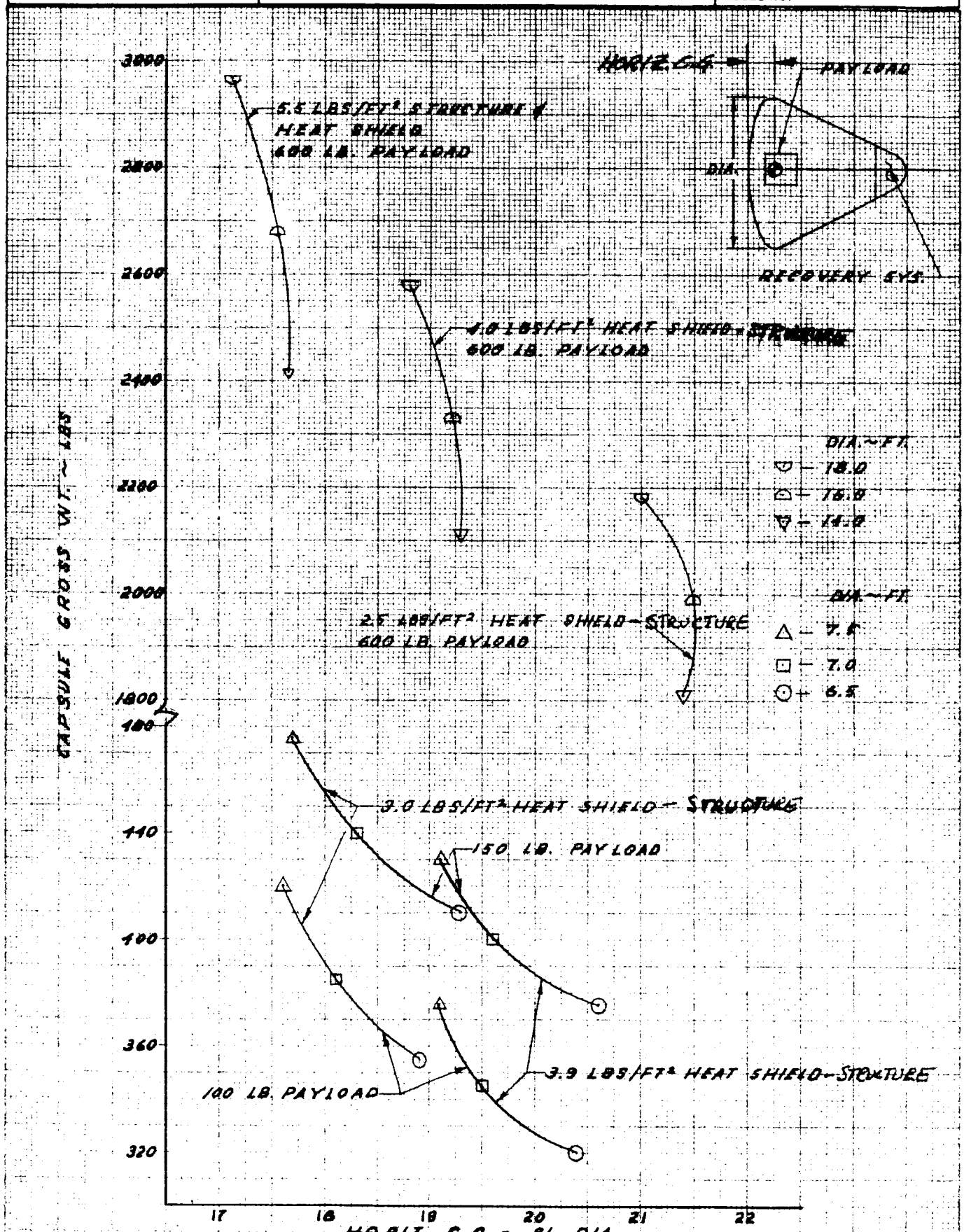

FIGURE 2.9-5
CAPSULE GROSS WT. vs. HORIZ. CENTER OF GRAVITY

2.10 DYNAMIC CONSIDERATIONS

2.10.1 Static Stability

The Apollo shape is statically stable in the heat shield forward position. Although the configuration has two trim points, the second point wherein the aftcone is in the forward position can be made unstable by moving the center of gravity sufficiently far away from the apex.

The geometry employed is defined in Figure 2.10.1. Wind-tunnel-derived pitching moment coefficients versus angle of attack are shown for three c.g. positions in Figures 2.10-2 through 2.10-4. It can be seen that for the c.g. located a distance .20 D_B back from the heat shield, the aftcone forward position exhibits neutral stability. To assure satisfactory entry, the initial angle of attack must be within ninety degrees of heat-shield forward to assure proper stabilization. The constraint on entry attitude is not as great, however, for c.g. locations closer to the heat shield.

Figures 2.10-3 and 2.10-4 show definite static instability at the aftcone forward trim point.

To provide reference data for evaluation of the stability of alternate large capsule configurations, pitching moment coefficients were computed as a function of the afterbody angle. Figure 2.10-5 shows the pitching moment coefficient for the 0.2 D_B c.g. location. These coefficients were obtained utilizing Newtonian flow theory. Although the results do not agree exactly with experimental wind-tunnel data, the trends are clearly shown. It can be seen that increasing the length of the afterbody can eliminate the aftcone forward trim point. Shortening the length of the afterbody (increasing θ_{AB}) leads to a greater possibility of stabilizing backwards. As is shown in the weight summary of the Design Section, elimination of the large capsule aftcone moves the c.g. to $< 0.1\ D_B$. There was insufficient time left on the program to analyze the combined effects on vehicle stability of removing the aftcone and moving the c.g. forward.

2.10.2 Dynamic Stability

Considerable data for the dynamic stability analysis was available from the Apollo program including the most recent theoretical and experimental wind-tunnel results at Mach numbers of 5.0 to 10.0 and hot-shot tests at Mach 18.7 (references 1 and 2). The detailed analyses of the vehicle stability characteristics were performed employing a digital computer solution of the general equations of motion for three degrees of freedom.

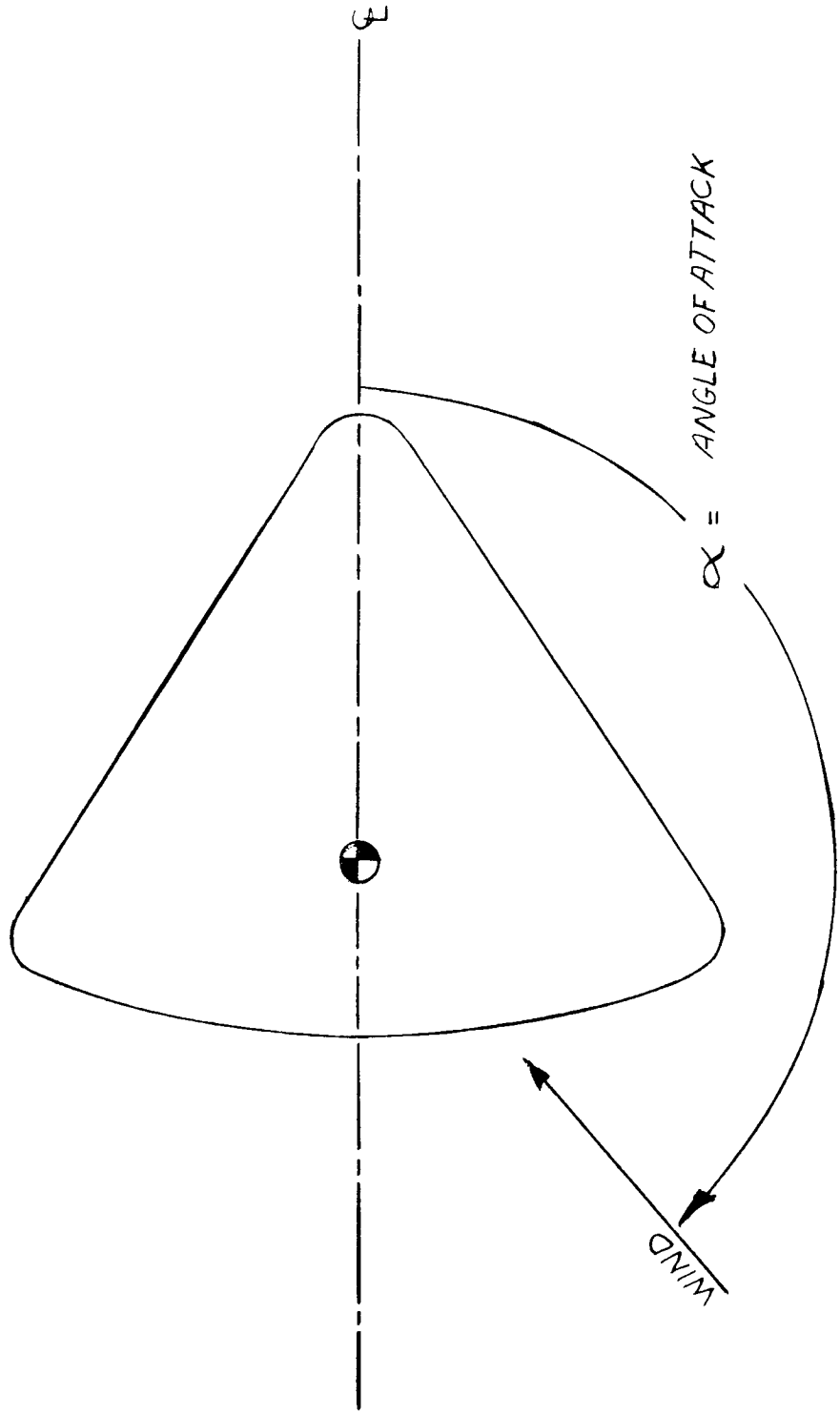

ANGLE OF ATTACK GEOMETRY

FIGURE 2.10-1

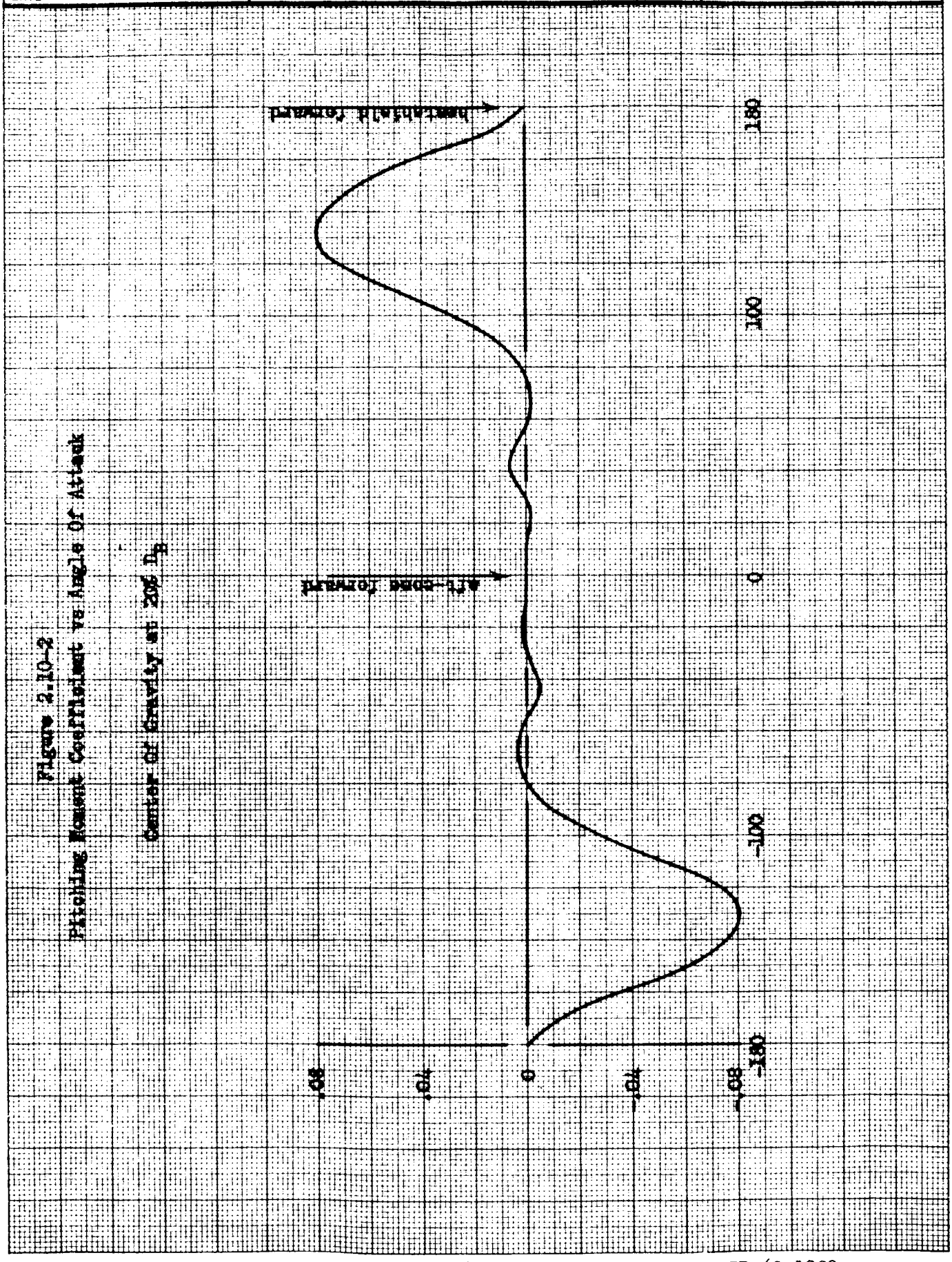

Figure 2.10-2
Pitching Moment Coefficient vs Angle Of Attack
Center Of Gravity at 20% D_B

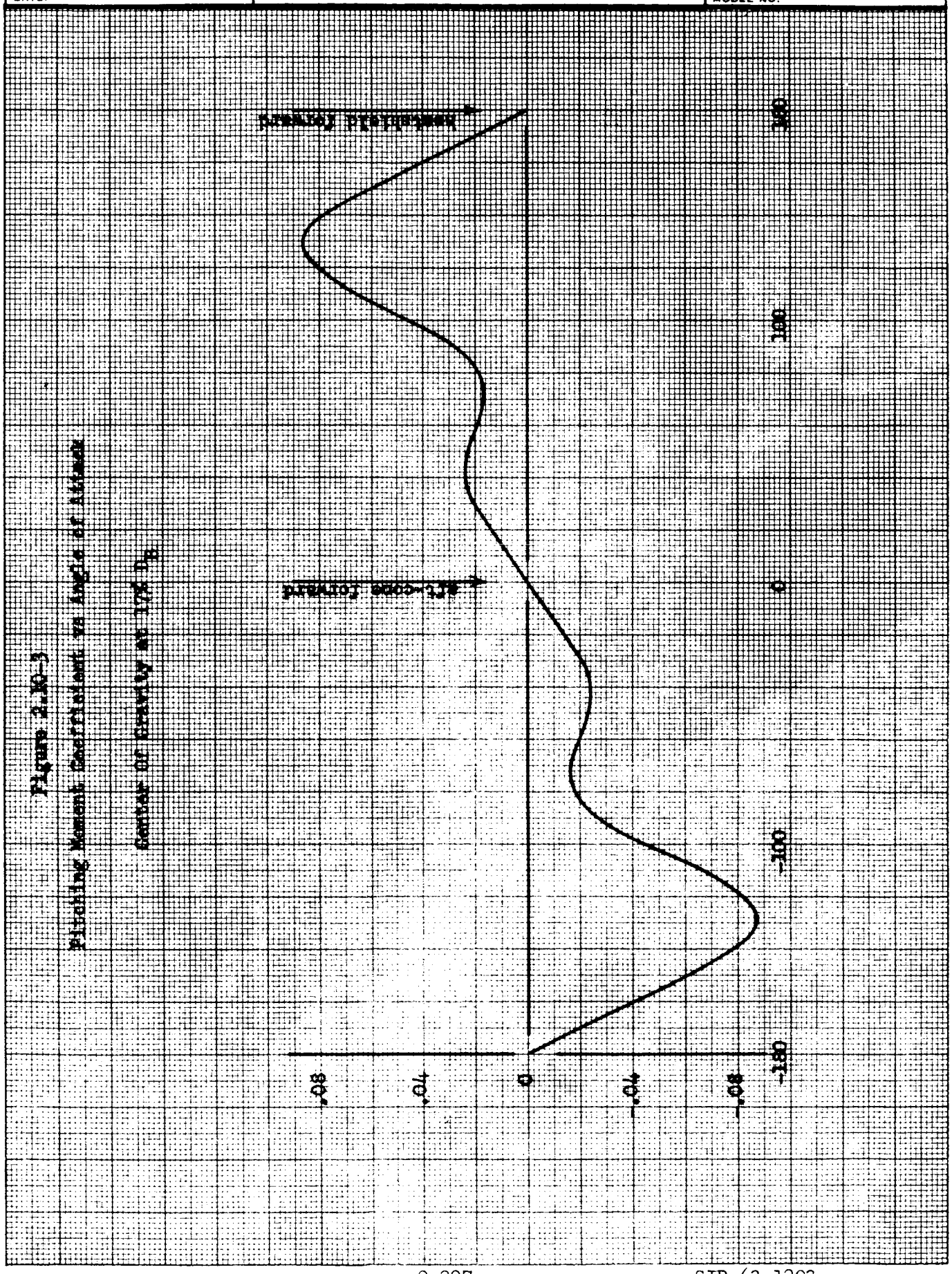

Figure 2.X-3

Pitching Moment Coefficient vs Angle of Attack

Center of Gravity at 1% D_B

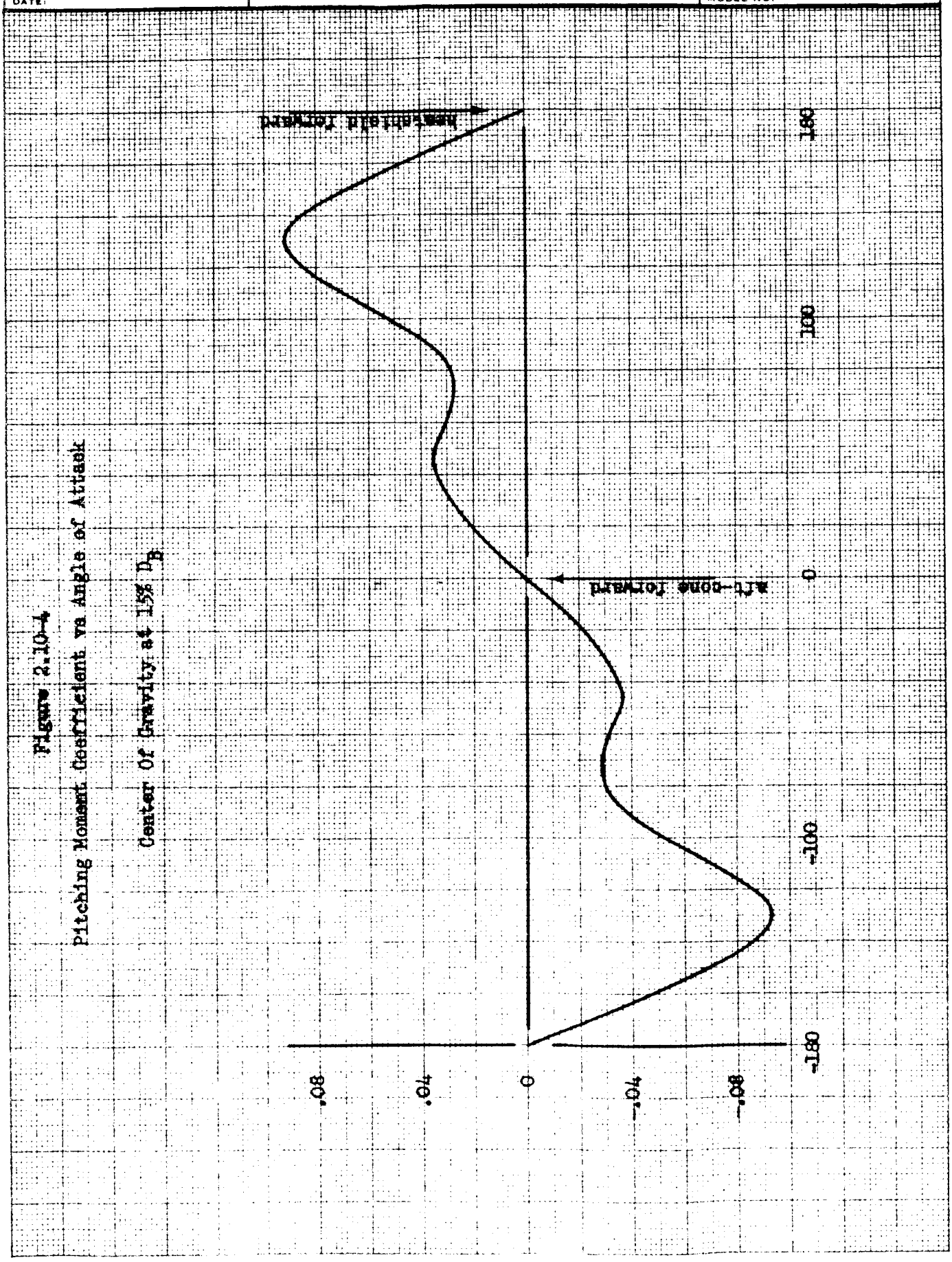

Figure 2.10-4

Pitching Moment Coefficient vs Angle of Attack

Center Of Gravity at 15% D_B

FIGURE 2.10-5

EFFECT OF AFTERBODY ANGLE ON PITCHING MOMENT COEFFICIENT

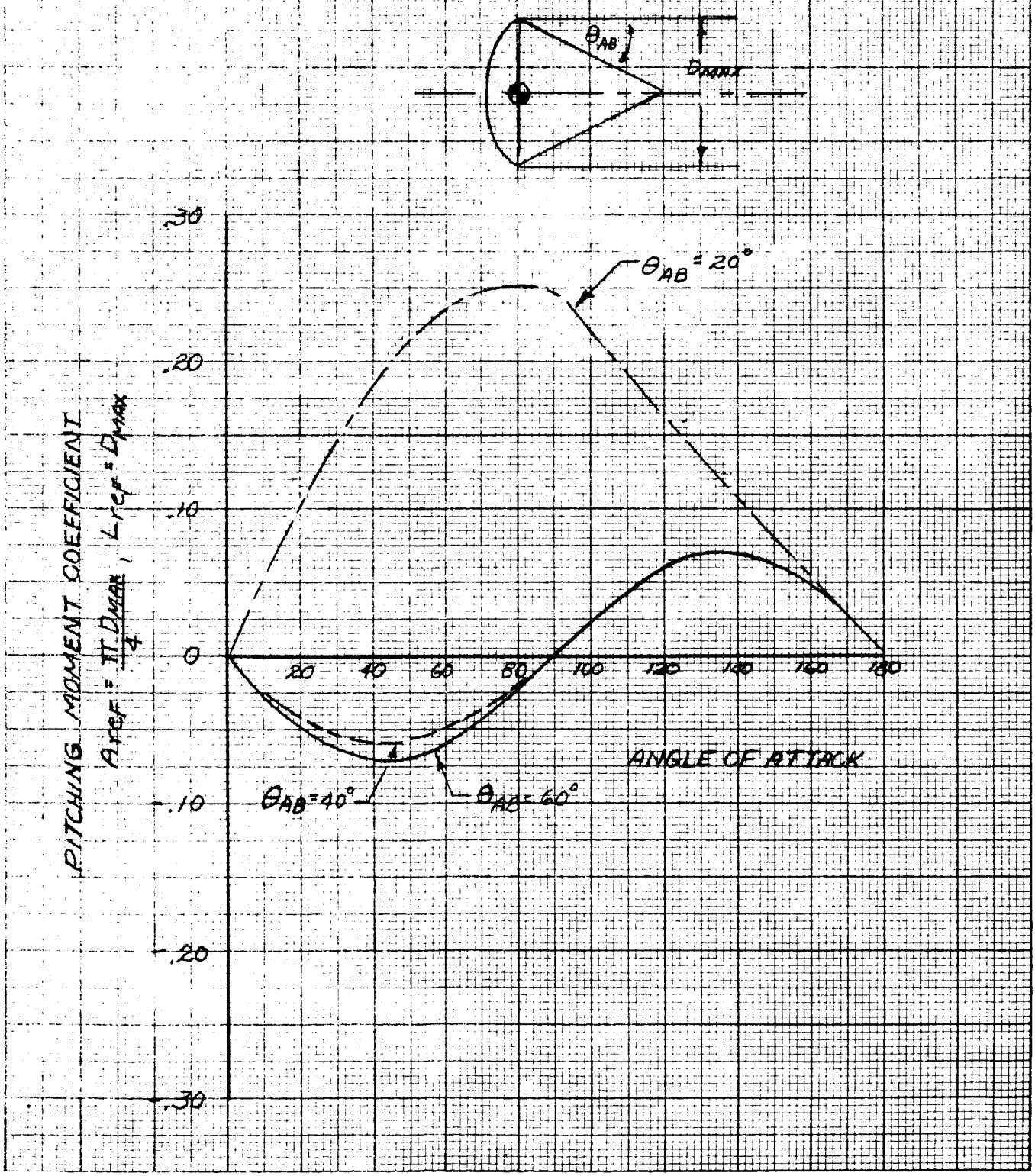

It was found that for vehicles entering the Martian atmosphere at other than $\alpha = 180°$ (heat shield forward) a pitch oscillation was observed. Typically as the dynamic pressure increases and the vehicle begins to be decelerated by the atmosphere, the vehicle oscillations decrease in amplitude whereas the frequency increases. This condition is attained before the times that peak heating and peak deceleration occur.

For entry angles approaching $\gamma = -90°$ (straight-in) the pulse of dynamic pressure experiences first a rapid increase, then a rapid decrease. In atmosphere W_2, the rate of decrease of dynamic pressure after peak deceleration is especially great. For these entry conditions, the small amplitude high frequency residual oscillation encountered at peak deceleration builds up as the dynamic pressure decreases because of the low viscous damping effects. It was found for certain extreme entry conditions that this oscillation could build up to the point that the probability of successful parachute deployment could be compromised (e.g., $\alpha \geq 45°$).

Two requirements on the amplitude of the angle of attack constrain the allowable entry conditions. First, the angle of attack during peak heating must not allow excessive heat loads on the aftcone. Atmosphere W_2 and an entry angle of -90° provided the least time for angle-of-attack oscillations to be damped. Apollo test data have shown that for $\alpha = 150°$, the convective heating rate will increase approximately by a factor of 1.7. However, the integrated convective rates should not exceed the calculated stagnation values on a time-average basis; on the other hand the radiative pulse might be expected to be somewhat lower than that calculated at the stagnation point because of the reduced effective R_n at the corners. The oscillation frequency is sufficiently high to preclude any local hot spots. It, therefore, appears that the heat shield is adequate for-90° entry angles where the oscillatory excursions do not exceed $\pm 30°$ of the nominal stagnation point. Amplitudes greater than this cannot be tolerated, however, due to excessive heating of the afterbody.

The second constraint of entry conditions is the amplitude of the oscillation of angle of attack at the time of parachute deployment. Tests performed during the Mercury program have shown that the drogue gun and pilot-chute method of parachute deployment can be used for instantaneous angles of attack of as much as 45 degrees from the heat shield forward position. However, at angles of attack greater than 45 degrees the lateral aerodynamic forces could interfere with positive first-stage deployment. Therefore, if the above two conditions on the amplitude of the angle of attack oscillation are met, a given entry attitude and tumbling rate may be considered allowable.

Thirty different entry conditions were analyzed for dynamic stability by the three degree-of-freedom digital simulation. Table

2.10-1 summarizes the range of entry conditions for the magnitude of the oscillations observed for each. Atmosphere W_2 was used in most of the cases; however, two cases also were run for Atmosphere B. A few results also are shown for a c.g. location offset of one inch from the symmetrical axis to assess the sensitivity to an unbalanced configuration.

The stability characteristics are summarized in Table 2.10-2. It was concluded that if the vehicle enters the atmosphere at an entry angle of -90° in a nearly apex forward attitude with no tumbling, the very low pitching moment may cause considerable delay in righting the vehicle. If some degree of tumbling can be assured, the possibility of remaining in the pitching-moment "deadband" is eliminated, if the c.g. is located less than 20 percent from the front face. As shown in Table 2.10-1, a c.g. location at 20% D_B was not sufficiently far forward to assure satisfactory entry for initial attitudes that were within 90° of apex forward or that were tumbling. However, for the c.g. located at 15% D_B, the angle-of-attack oscillations were within allowable limits for all tumbling rates checked. Furthermore for the c.g. at 15% D_B, non-tumbling entry attitudes to within five degrees of apex forward were found to result in angle-of-attack oscillations that were within allowable limits.

Figures 2.10-6 through 2.10-14 is a copy of the C.R.T. output of a representative run for an extreme entry condition. The variables plotted are for the small capsule (350 lbs.) having a base diameter of 6.75 ft., pitch moment of inertia 26.8 slug/ft.^{2}, and a c.g. location 13.8 in. aft of the front center of the heat shield. ($X_{c.g.}$ =17% D_B). This case shows the capsule to be tumbling at 6°/sec for entry into atmosphere W_2 at an angle of -90°, and with the aftcone oriented nearly forward (α = -5°) when the sensible atmosphere is penetrated. During peak heating and maximum deceleration, angle-of-attack oscillations with maximum amplitude of over 30° are observed. Although the capsule is at the maximum angle for only a short period of time, considerable increase in heating rate on the aftcone may result. During the period following peak heating, dynamic pressure decreases and, as shown in Figure 2.10-6, the angle-of-attack oscillation builds up to a maximum of 50° as the velocity for parachute deployment is reached (3750 fps). With the possibility for this high angle of attack as the drogue gun is fired, an excessive side aerodynamic force could interfere with positive deployment. Therefore, this entry trajectory again shows a slightly excessive amplitude of oscillation.

The condition illustrated obviously represents a limiting case. Entries into other atmospheres showed greater dynamic stability. As has been shown, the dynamic stability is very dependent upon c.g. location; for the small capsule, a c.g. location in the order of 15% appears feasible for the inboard antenna configuration (see Section 3.0). At lower entry angles, computer runs have confirmed that there is

TABLE 2.10-1

THREE DEGREE OF FREEDOM STABILITY RUNS

ATMOSPHERE W_2

LARGE CAPSULE

X_{cg}	α(Max) Entry	Initial $\dot{\theta}$	Entry γ	Heating Max $\Delta\alpha$	Parachute Max $\Delta\alpha$	Remarks
20	180	0	-90	0	0	
20	180	0	-90	0	.5	Z_{cg} = 1 in
20	160	0	-90	3	10	
20	135	0	-90	8	15	
20	90	0	-90	22	55	
20	207	1°/sec	-90	5	13	
20	207	1°/sec	-90	10	10	Z_{cg} = 1 in
20	6	6°/sec	-90	55	140	Z_{cg} = 1 in
20	180	0	-70	.15	.5	Z_{cg} = 1 in
20	180	0	-20	0	.1	

SMALL CAPSULE

20	180	0	-90	0	0	
20	135	0	-90	5	13	
20	90	0	-90	13	38	
20	160	0	-90	3	10	Atmos B
17	-5	0	-90	27	50	
17	-10	0	-90	19	44	
20	206	1°/sec	-90	5	10	
17	190	6°/sec	-90	1	3	
17	-5	6°/sec	-90	33	50	
17	207	12°/sec	-90	2	10	
17	-10	12°/sec	-90	32	50	
15	-5	0	-90	20	45	
15	-10	0	-90	20	40	
15	-16	12°/sec	-90	26	45	
15	-23	36°/sec	-90	23	45	
20	180	0	-20	0	0	
20	180	0	-20	0	0	Atmos B
20	160	0	-20	2	4	
20	160	0	-40	2	5	
20	160	0	-60	2	5	
17	90	6°/sec	-40	10	48	

TABLE 2.10-2

STABILITY SUMMARY

LOCATION	STATIC STABILITY	DYNAMIC STABILITY
20% D_B	Stable with heat shield forward Neutrally stable with apex forward	Heat shield forward will stabilize for $\alpha > 90°$ Apex forward ($-90° < \alpha < 90°$) Insufficient pitching moment to guarantee orientation in time for peak heating. Excessive oscillations in α possible.
17% D_B	Stable with heat shield forward Unstable with apex forward	For atmosphere W_2, $\gamma_E = -90°$, $\dot{\theta} = 0$ and $\alpha < 10°$, oscillation in during heating and parachute deployment may be excessive for this extreme entry condition. Other entry conditions show good dynamic stability, including tumbling at all α's.
15% D_B	Very stable with heat shield forward Very unstable with apex forward	Sufficient damping to assure acceptably small oscillations during peak heating, parachute deployment, and data transmission for all tumbling entries and, if $\alpha > 5°$ for non-tumbling entry.

sufficient time to damp the oscillations.

Figure 2.10-15 compares the relative altitudes obtained with the point mass and dynamic trajectory programs for the case shown. This effect has been taken into account in the design of the landing system wherein approximately a 10,000 foot altitude loss was introduced to account for the worst feasible deployment condition.

An alternative to tumbling entry is to assure that the vehicle does not enter with the apex directly forward. This could be done by spinning the capsule prior to separation from the spacecraft. A limited analysis of spinning entry was performed utilizing a six degree-of-freedom computer program. It was shown that using a spin rate of 15 rpm, a tip-off impulse of 6°/sec at separation allowed a negligible deviation (two degrees) in angle of attack at entry. However, spinning the capsule is not an obvious solution to the problem inasmuch as it introduces obvious problems in parachute deployment and stability.

Another alternative considered was active damping. Various techniques for actively establishing the desired attitude considered included mechanical and gyroscopic methods. It appears that a reaction control system (RCS) will readily meet the requirements for this mission. For a nitrogen cold-gas propulsion system, the total system weight as a function of initial angular rate to be damped is shown in Figure 2.10-17. The system was sized to damp the angular velocity within 2π radians. Two rate gyros would be required as sensors. Other alternative RCS techniques were considered for the larger capsule to see if the system weight could be reduced. Many of these were summarily rejected because of lack of demonstrated reliability. As a group, the monopropellants have been plagued with a tendency toward detonation in use. Some monopropellants, such as hydrogen peroxide or hydrazine, will not comply with the anticipated nine-month storability requirement without taking extensive precautionary measures. Bi-propellants require essentially twice the plumbing of a gaseous system for a negligible saving in weight. Some new monopropellants with allegedly high stabilities and performance (Rocket Research Inc., Monex propellant family) have recently been announced but insufficient experience has been obtained with these to date to consider their application at this time.

2.10.3 REFERENCES

1. S&ID Internal Letter 223-130-63-021, Dept. 695-223, Comparison of FS-4 AEDC Hotshot II Data with FS-3 Continuous Flow Data and Newtonian Flow Theory (Confidential).

2. S&ID Internal Letter 223-130-63-033, Dept. 695-223, Command Module Pitching Moment, Axial Force and Normal Force Coefficient Curves (Confidential).

PREPARED BY:	NORTH AMERICAN AVIATION, INC. SPACE and INFORMATION SYSTEMS DIVISION	PAGE NO. OF
CHECKED BY:		REPORT NO.
DATE:	Figure 2.10-6	MODEL NO.

ALTITUDE vs TIME

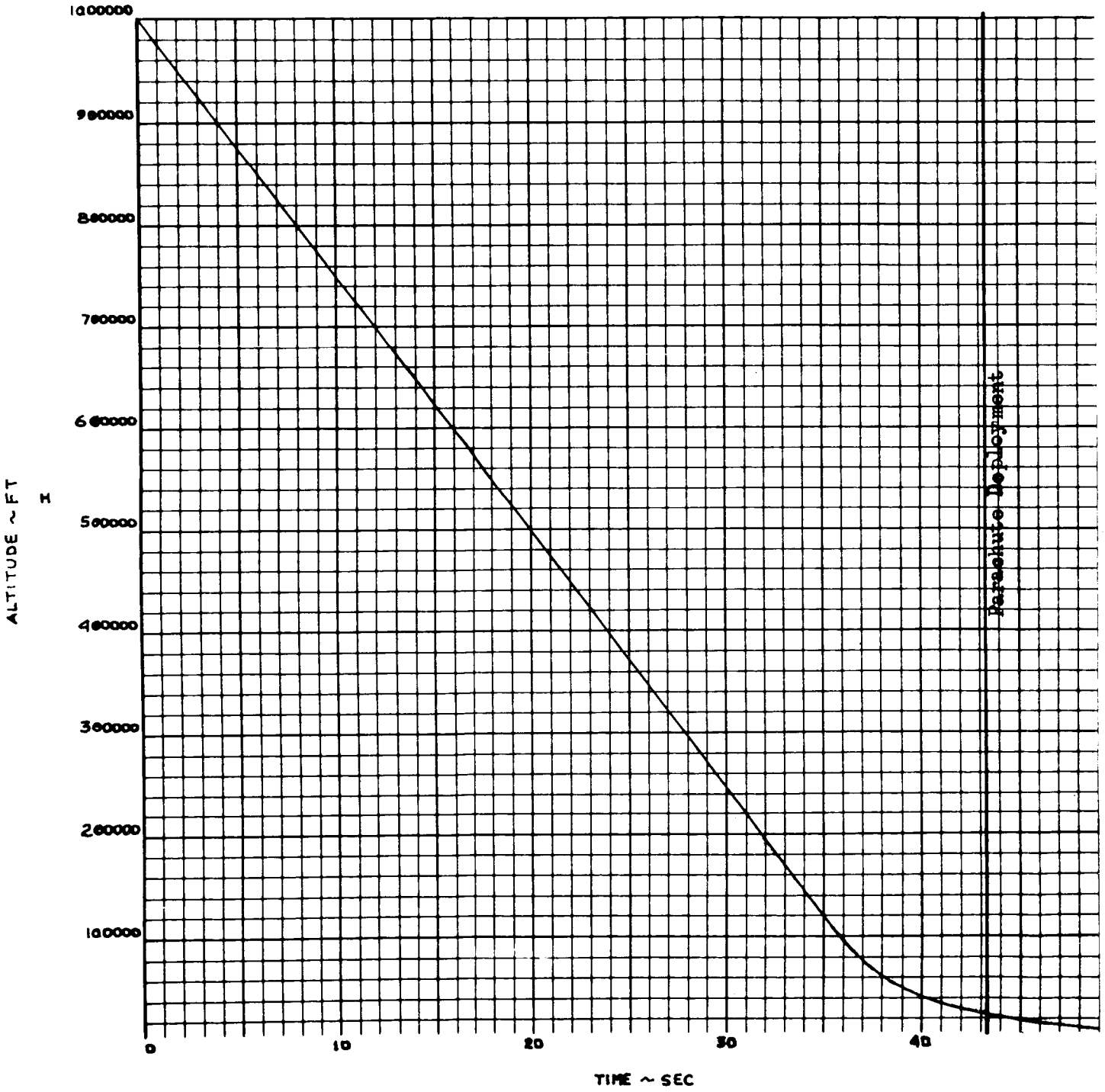

Figure 2.10-7

MACH NUMBER vs TIME

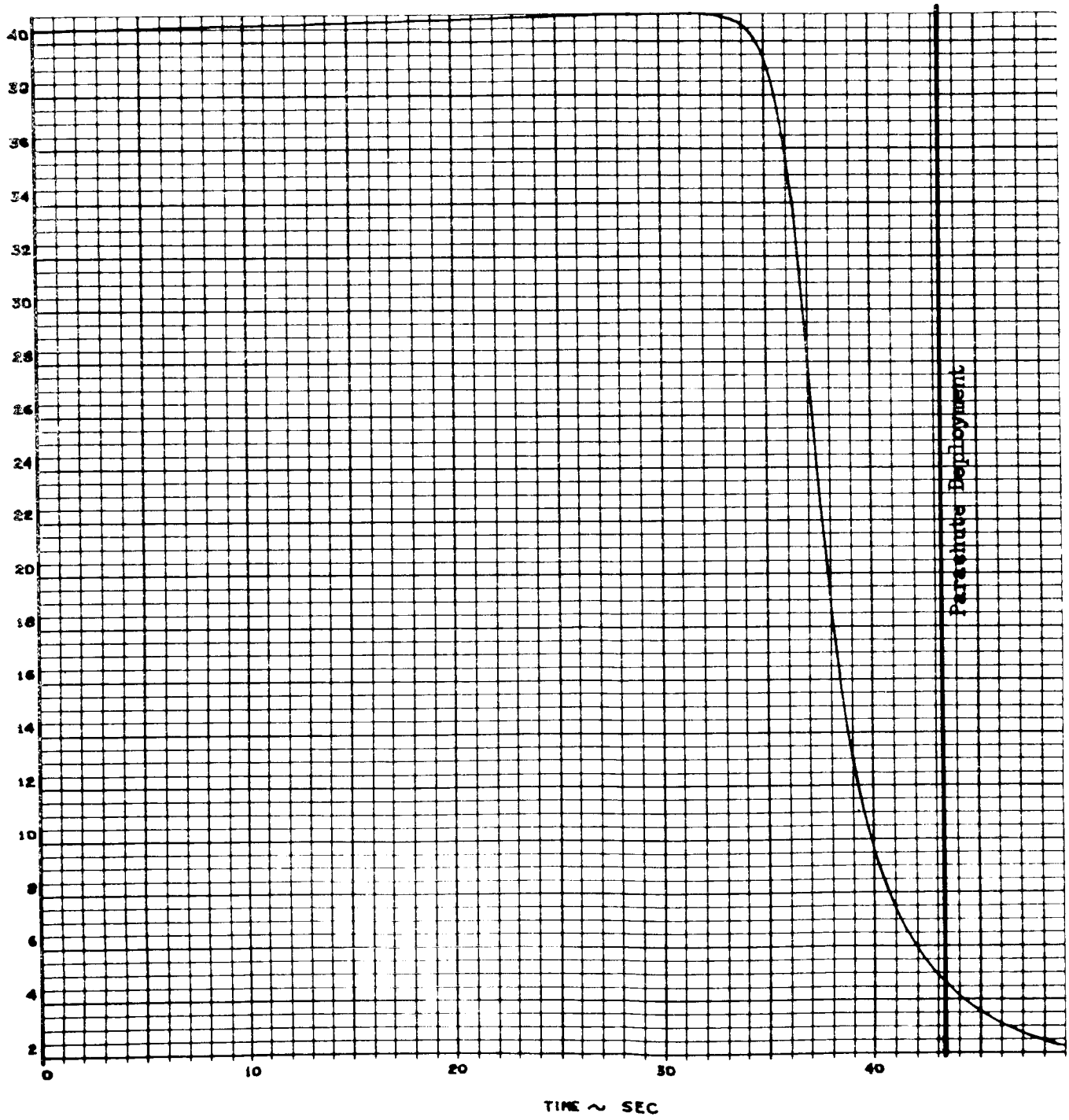

PREPARED BY:	NORTH AMERICAN AVIATION, INC. SPACE and INFORMATION SYSTEMS DIVISION	PAGE NO. OF
CHECKED BY:		REPORT NO.
DATE:	Figure 2.10-8	MODEL NO.

ALTITUDE vs MACH NUMBER

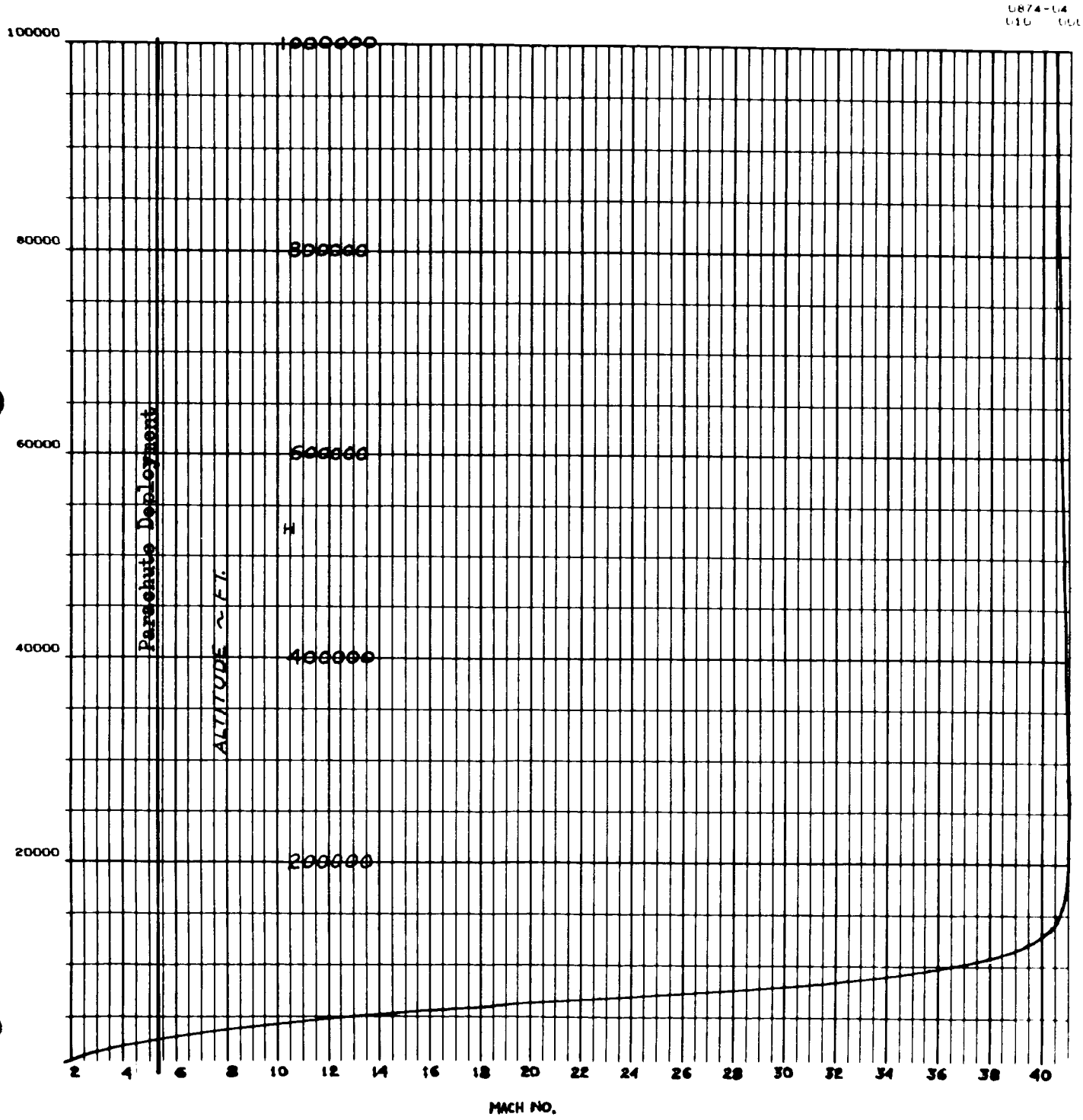

Figure 2.10-9

DYNAMIC PRESSURE vs TIME

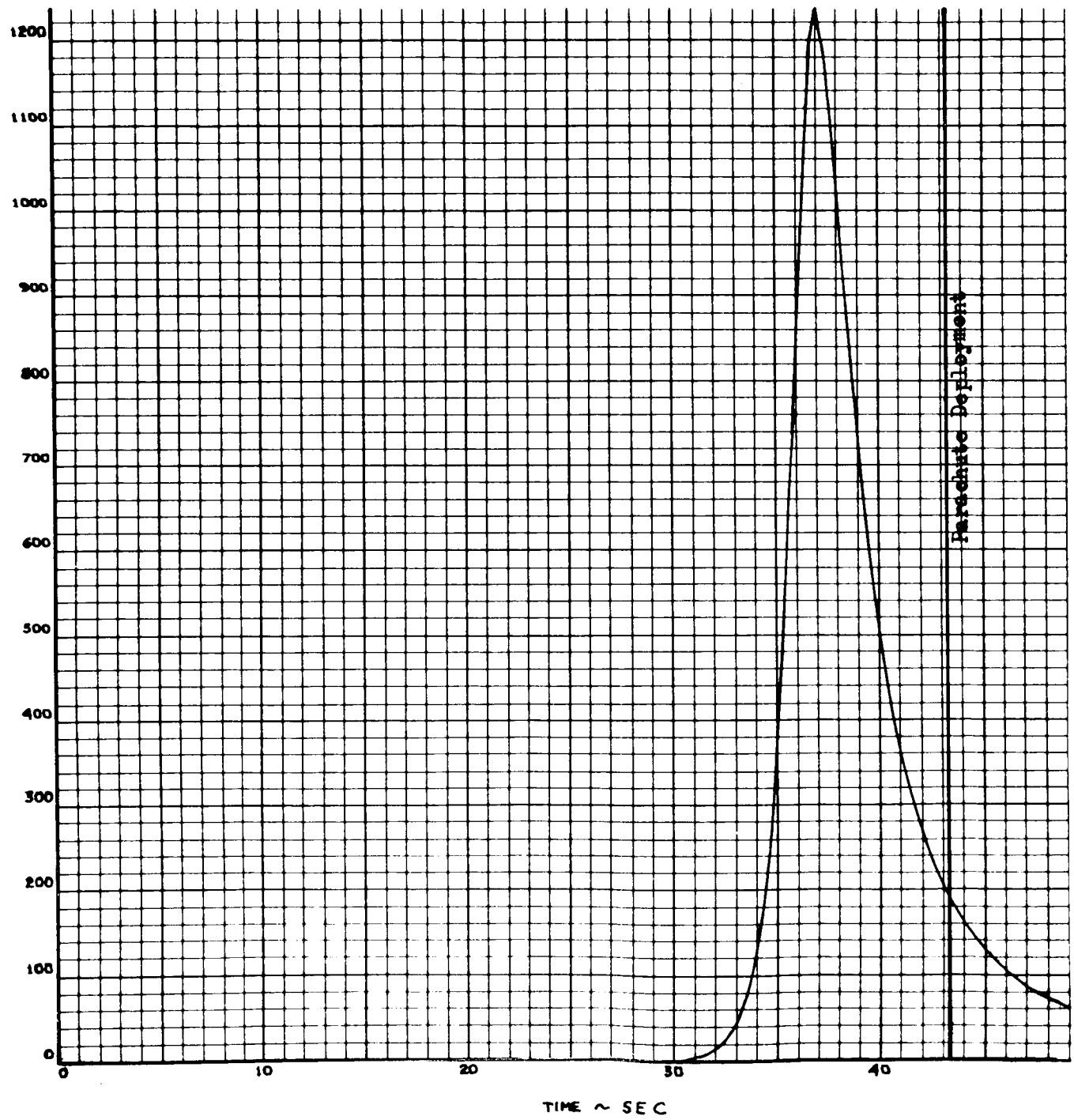

PREPARED BY:	NORTH AMERICAN AVIATION, INC. SPACE and INFORMATION SYSTEMS DIVISION	PAGE NO. OF
CHECKED BY:		REPORT NO.
DATE:	Figure 2.10-10	MODEL NO.

PITCH ANGLE vs TIME

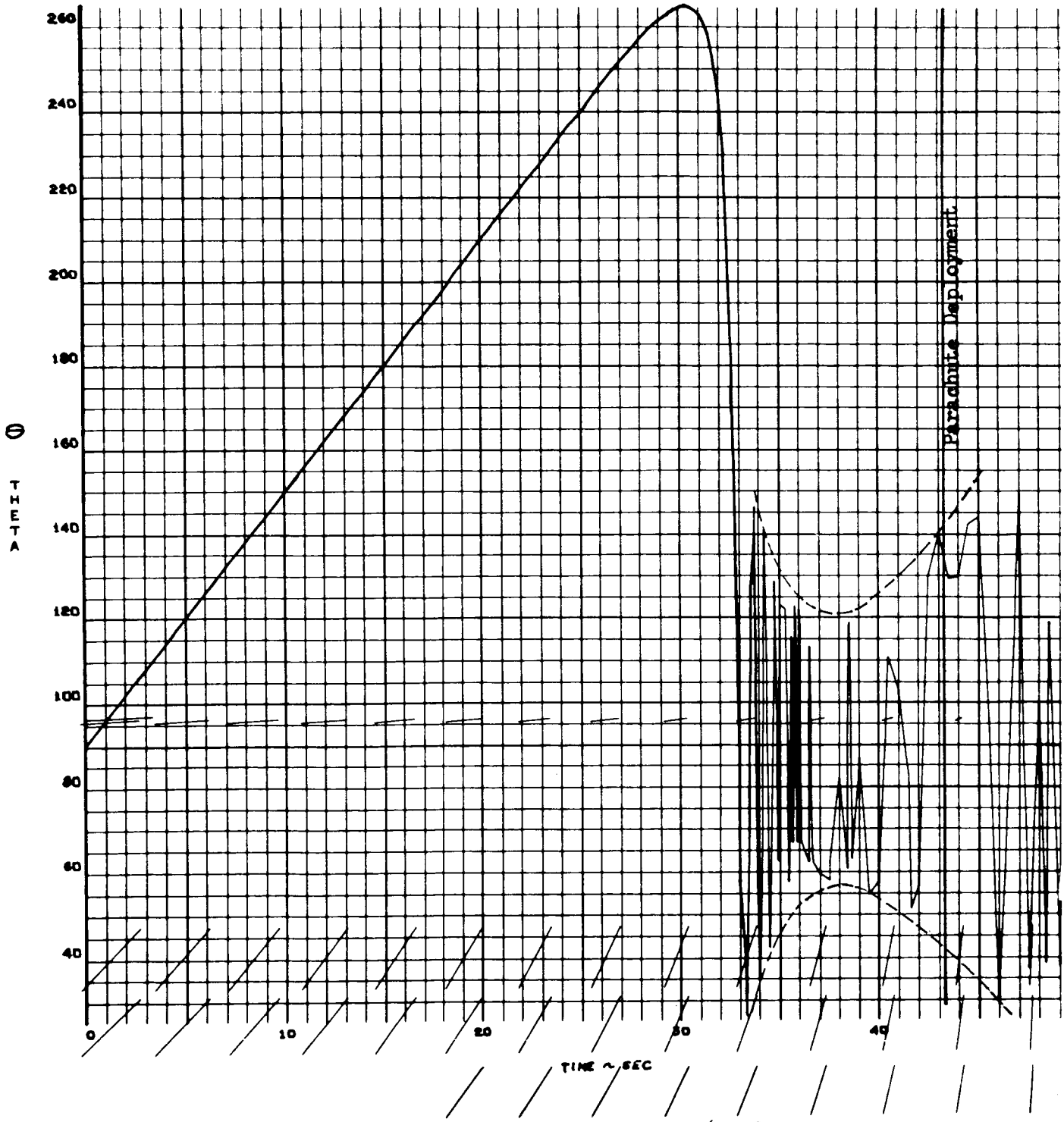

Figure 2.10-11

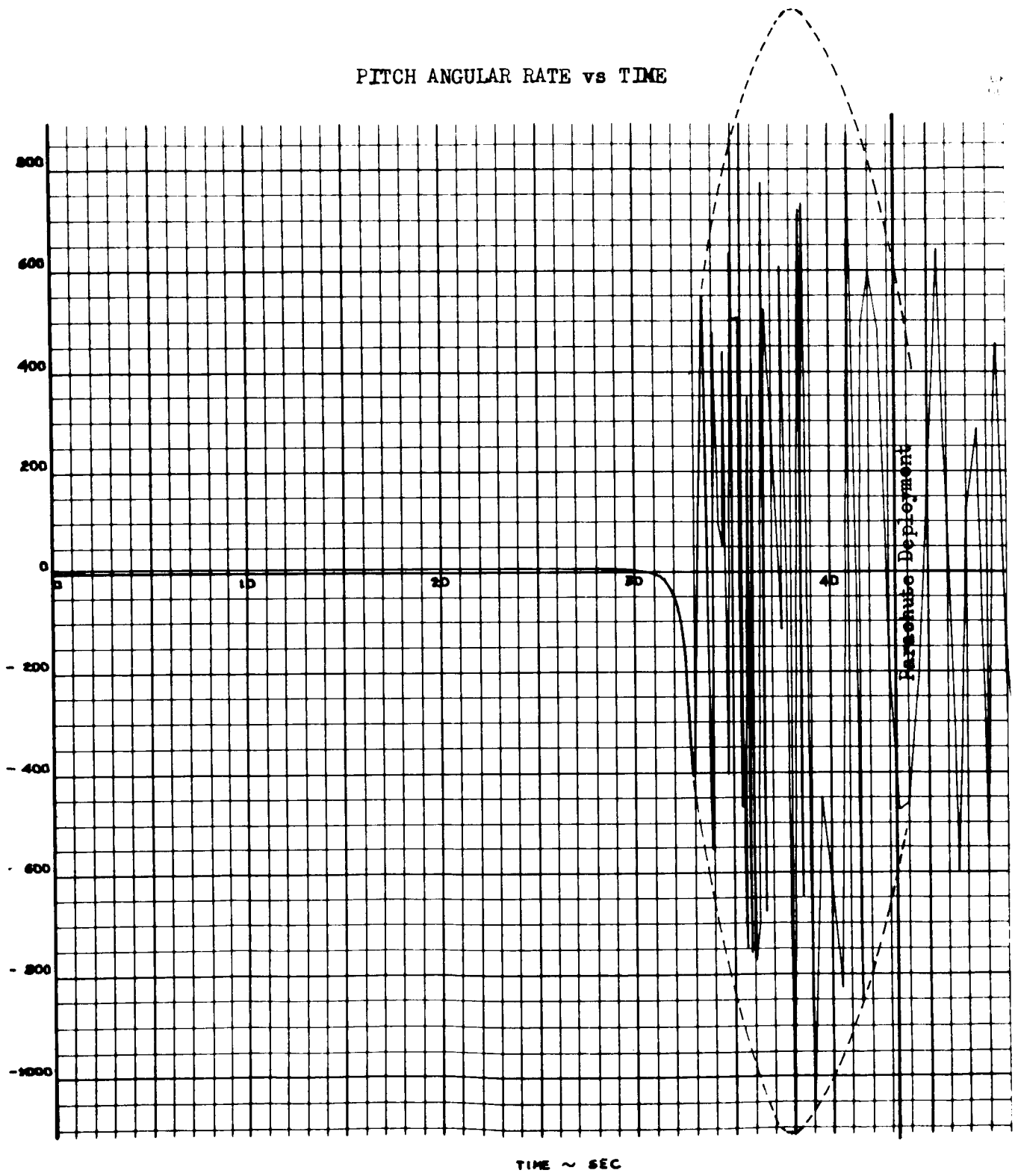

Figure 2.10-12

PITCH ANGULAR ACCELERATION vs TIME

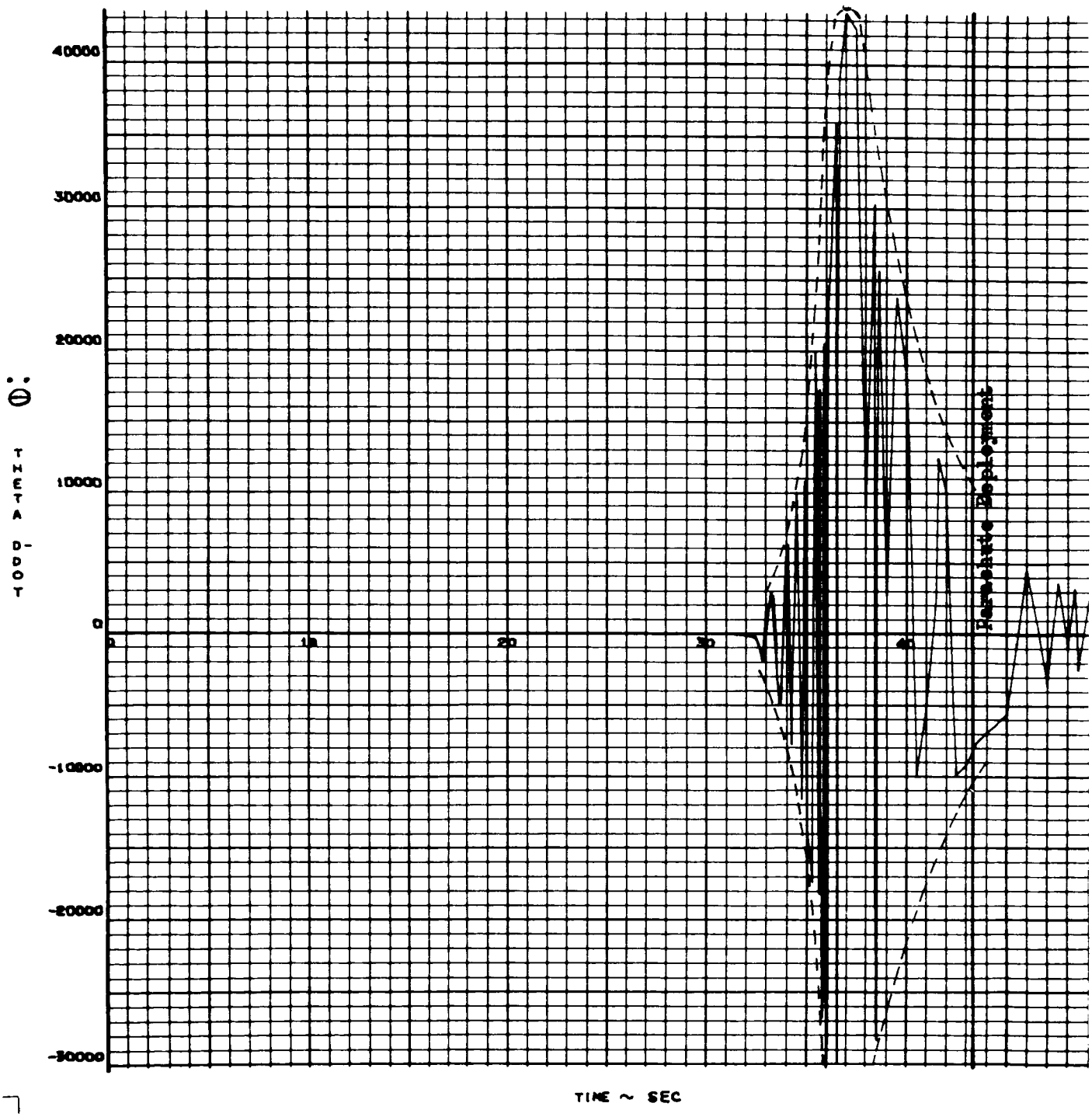

Figure 2.10-13

FLIGHT PATH ANGLE vs TIME

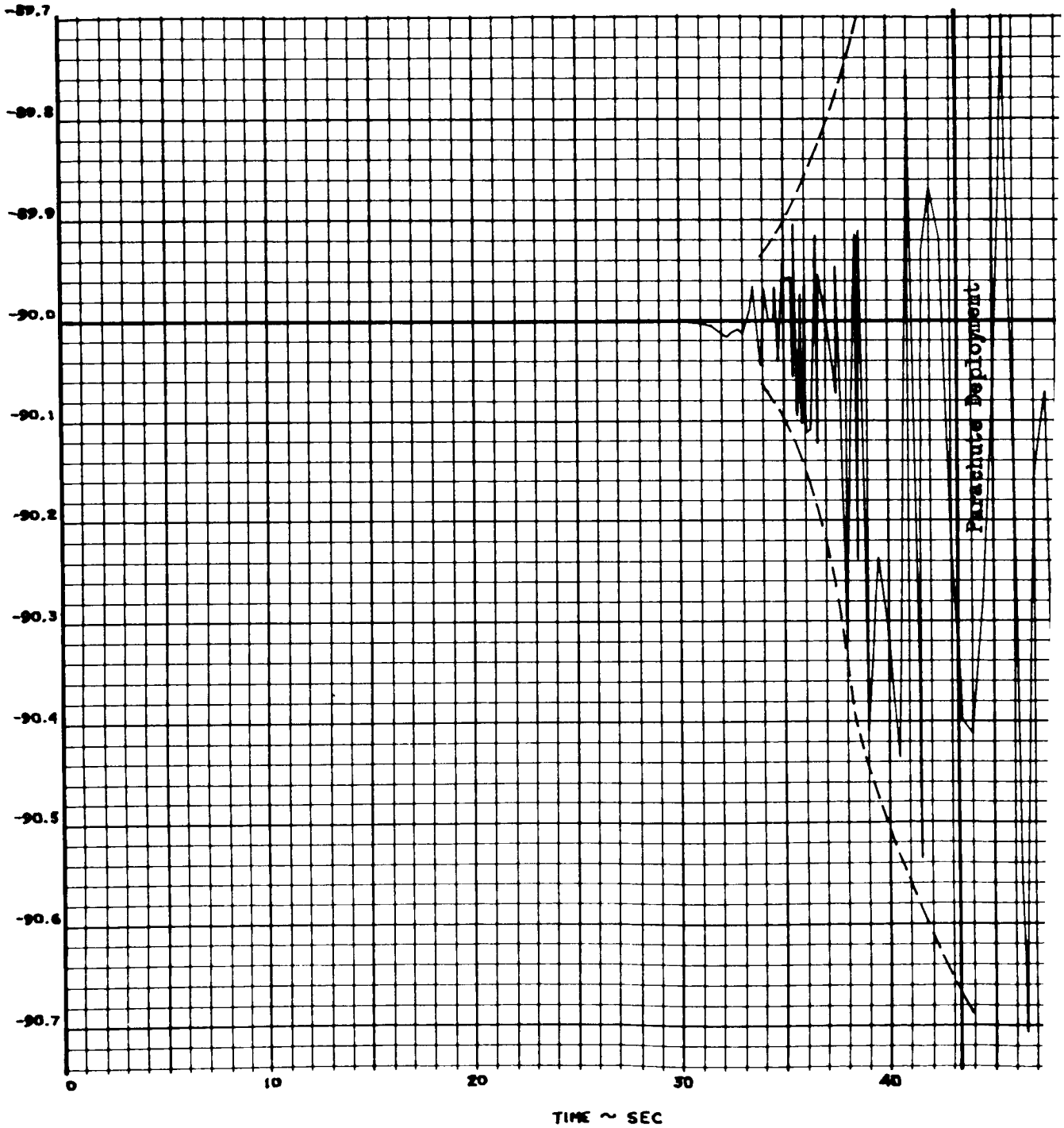

PREPARED BY:	NORTH AMERICAN AVIATION, INC. SPACE and INFORMATION SYSTEMS DIVISION	PAGE NO. OF
CHECKED BY:		REPORT NO.
DATE:	Figure 2.10-14	MODEL NO.

ANGLE OF ATTACK vs TIME

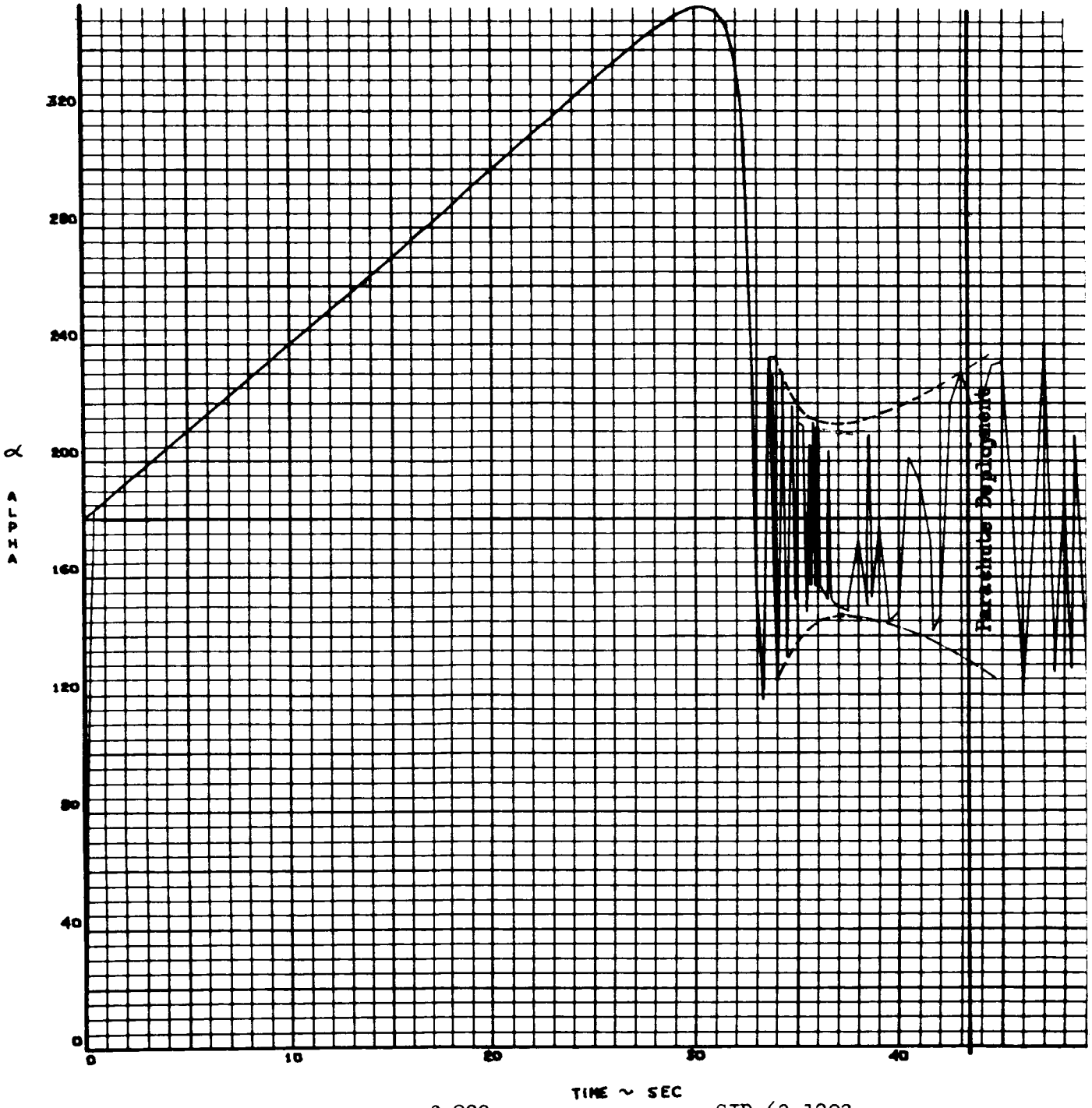

Figure 2.10-15

COMPARISON OF POINT-MASS TRAJECTORY
AND
THREE-DEGREE-OF-FREEDOM TRAJECTORY
Atmosphere W_2
$\gamma_E = -90°$

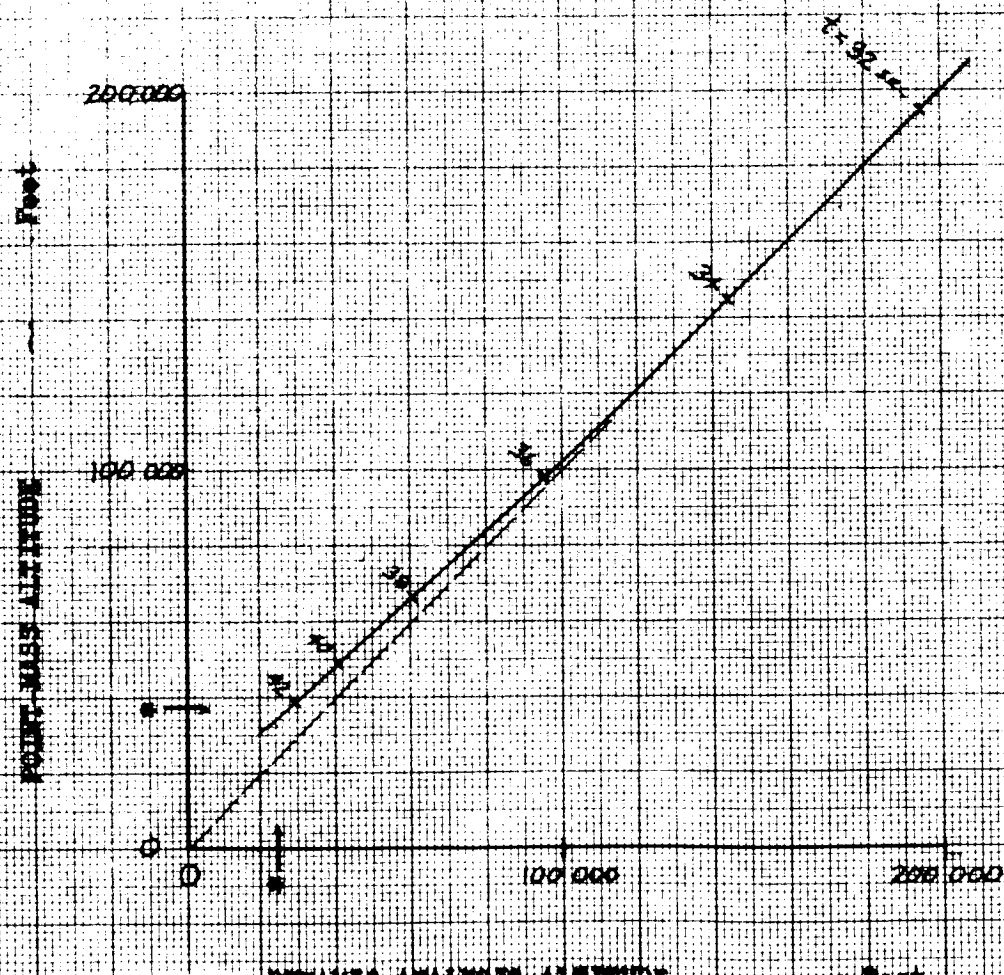

* Parachute Deployment (V ~ 3750 fps)

Figure 2.10-16

TOTAL SYSTEM WEIGHT OF REACTION CONTROL SYSTEM FOR SEVERAL VOYAGER CAPSULE CONFIGURATIONS.

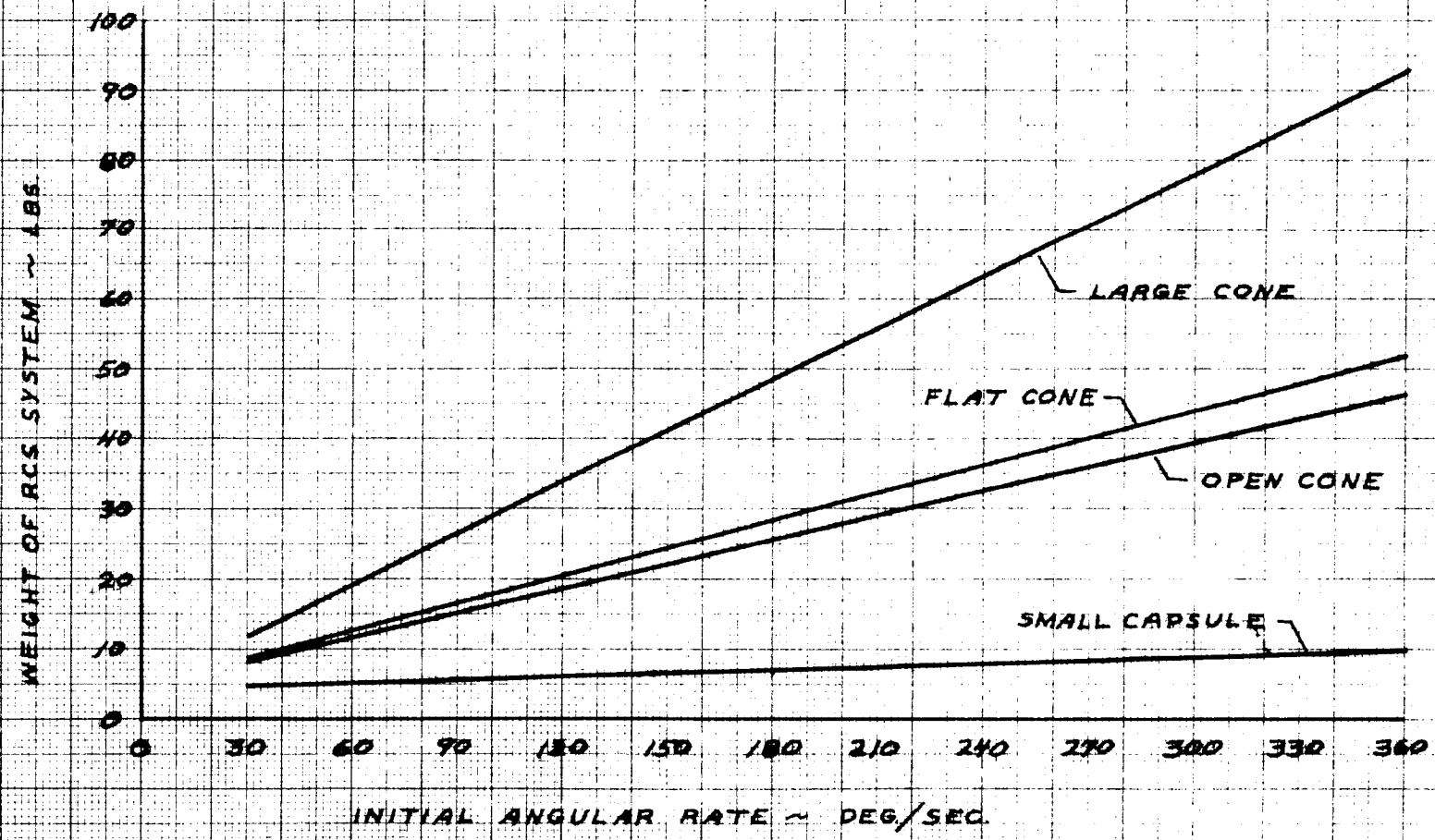

3.0 PRELIMINARY DESIGN

The sections which follow describe the Mariner and Voyager capsule configurations selected for the design phase of the study and discusses the heat shield, structural and landing systems. Finally, the preliminary design, including the summary of the weights and inertial properties, is presented.

3.1 CONFIGURATION SELECTION

The configurations selected for the preliminary design included consideration of the entry trajectories and parachute deployment requirements as they constrain M/C_DA (Sections 2.2, 2.8, and 2.10) capsule weight limitations; capsule geometric constraints imposed by shroud and spacecraft bus geometries (Section 2.5); present and projected state-of-the-art in materials and fabrication techniques, including sterilization and the space environment (Sections 2.4, 2.6, and 2.7); as well as the constraints imposed by dynamic considerations (Section 2.10). The configurations selected for both the small and large capsules are described in the sections which follow.

3.1.1 Mariner B Capsule

The weight of the Mariner B capsule was defined as 350 pounds by the ground rules of the study. The results of the parametric point-mass trajectory studies, landing system tradeoffs, and dynamic considerations all indicated that the M/C_DA of the capsule should be in the order of 0.2, or less, for the Apollo configuration to meet the minimum mission objectives of deploying a parachute, sampling the atmosphere, and transmitting prior to impact both the data acquired during entry blackout (presumed to be stored) and the atmospheric data attained.

Based upon the system weight tradeoffs described in Section 2.9, a base diameter of 6.75 feet was selected for further study. This size was compatible with both the shroud geometry and volumes required for payload, antenna, and landing system stowage (Section 2.5) for the reasons previously described (e.g., short development schedule; backlog of development data; flight tested and qualified for similar entry conditions on the Mercury program; well-known, widely used material, etc.); phenolic glass was selected as the forebody heat-shield material (sections 2.4, 2.6, and 2.7). An aluminum sandwich honeycomb was selected as a base point for the forebody structure; however, the discussions with two prominent manufacturers indicated that it would be feasible to fabricate a forebody composite out of a homogeneous glass-reinforced phenolic plastic using conventional materials of commerce (e.g., GILD phenolic resin and #181 glass fibres) to meet both the heat protection and structural requirements in an integrated structure. The weight savings in bonding materials, both in the core and heat

shield structure interface are significant; these coupled with the elimination of differential thermal expansion and bond-line temperature problems would tend to enhance reliability and make the latter concept extremely attractive (Section 2.6). Before firming up a final design, it is further recommended that progress in beryllium fabrication be reviewed inasmuch as there is much current activity to develop the technology of beryllium sandwich structure fabrication (e.g., at North American, Space and Information Systems Division), which could afford some weight saving if available in time.

A GILD, #181 phenolic resin-glass afterbody was selected for the small capsule to meet the pre-entry transmission requirement and still be compatible with the inbased antenna system suggested by Jet Propulsion Laboratories (Section 1.0 and 2.6). This shield would be jettisoned prior to initial parachute deployment (Section 2.8). An alternate antenna concept considered included slot antennas mounted on the aftcone (Section 2.5).

Two parachute concepts were considered for the preliminary design (Section 2.8). These included a single stage system to afford maximum sampling altitude and a two-stage system for maximum time on the parachute for data transmission. Both systems considered initial deployment at supersonic velocities. In the doubly unlikely event that the capsule both entered at -90° and encountered the worst atmosphere, in the order of 500 to 1,000 bits could be transmitted from the time of achieving subsonic velocity to impact at a bit rate of 5 B/sec. For a very nominal weight penalty, HT-1 nylon (Du Pont NOMEX - high temperature nylon) was selected as the parachute material to obviate sterilization problems (Section 2.4) and to afford an additional margin of safety in the event of premature parachute deployment.

Except for the condition of backward entry with an angle of attack of less than 5° <u>and no tumbling</u> into the worst atmosphere (W_2) at $\gamma_E = -90°$; the capsule appears stable for all entry conditions, including tumbling up to rates of 36°/sec (the upper limit explored, as shown in Section 2.10 for realistic c.g. locations). Entry into the other atmospheres or at other entry angles improves the dynamic behavior. Thus, it would appear that the capsule should be separated from the spacecraft bus in such a manner as to impart a tumbling rate. Furthermore, the need for spinning up the capsule after separation to enhance stability is obviated; indeed this may be a serious disadvantage if the capsule were to come in at and hold an angle of attack inasmuch as this would enhance the probability of skip-out at low entry angles and could increase the probability of aftcone failure through overheating if the angle of attack were maintained at greater than 30° through peak heating. Section 2.10 also described a relatively simple, lightweight (i.e., less than 10 pounds) active cold-gas system which could be considered for auxilliary, or back-up purposes.

Three cycle sterilization of the Mariner B capsule at 145° C for 36 hours, and the effects of the space environment, also were considered (Section 2.4). There were no obvious problems with materials selected for the heat shield structure, or landing system. If Primacord, or an RDX based explosive, were employed as explosive charges to separate the heat shield after parachute deployment, the 145° C (i.e., 300° F) sterilization temperature could not be attained inasmuch as its ignition point is 285° F. However, there are other high temperature explosives (e.g., Du Pont TACOT) with service temperatures to 350° C. HT-1 nylon, suggested for the parachutes, will withstand up to 500° F.

3.1.2 Voyager Capsule

A nominal target weight of 2,000 pounds was suggested for the Voyager capsule; however, the "electronic" payload was fixed at 600 pounds. Preliminary weights tradeoff data (Section 2.9) showed that depending upon the materials selected a capsule diameter of 16 to 18 feet, weighing in the order of 2,000 to 2,400 pounds, was indicated for the Apollo configuration in order to achieve an M/C_DA of 0.2. (Atmospheric data acquired by the Mariner B presumably will be available for the Voyager design so that some of the uncertainties will have been resolved and a higher degree of confidence can be enjoyed in the design phase for this mission.)

The design and geometric considerations (Section 2.5) showed that the volume available within the Apollo shape, was far in excess of that required to house the payload. Two alternate configurations therefore were considered. These included (a) replacement of the aftcone by a "flat plate" enclosure for the payload and (b) enshrouding the payload and landing system in a form-fitting protective enclosure. Unavailability of sufficient aerodynamics data and time did not permit a thorough analysis of the dynamic behaviour of the latter two configurations; however, preliminary analytical considerations of static stability indicate that the configurations are statically stable (Section 2.10). Again, a simple relatively-lightweight active system has been described for augmentation purposes.

As discussed previously (Sections 2.6 and 2.9), the composite structural concept is not applicable to the Voyager capsule because of the large diameters required and the weight penalties for phenolic glass are high; therefore, the more advanced heat shield materials must be considered on the assumption that they will be available in time for the mission. These include the Avcoat, SE 28, and Thermo-Lag types of materials. For the forebody, aluminum sandwich again was selected with the possibility of employing beryllium if the technology advances sufficiently (Section 2.6). For the afterbody, phenolic fibreglass again seems to be the preferred material (for any of the three afterbody configurations), unless a slot antenna is installed on the aftcone.

A single parachute for the large capsule is precluded by size considerations and the state of the art, therefore, a two-stage system was considered (Section 2.8). Post landing operational capability for the large capsule is a prerequisite and suitable designs for righting the capsule were investigated.

Instructions received during the course of the study were to place greater emphasis on the Mariner B design; thus the detailed attention devoted to the Voyager capsule was less than that accorded to the Mariner B in a number of areas, including materials compatibility, etc. The sections which follow present the heat shield structural design, landing system designs, and preliminary design drawings and weights summary.

3.2 HEAT SHIELD-STRUCTURAL DESIGN

3.2.1 Mariner B Capsule

3.2.1.1 Forebody

As described in Sections 2.3 and 2.7, the design criteria for the heat shield are defined by the heating loads encountered at -20° entry. Figure 3.2-1 shows the thickness and weight of phenolic glass (30% 91-LD resin and 70% #181 fibreglass) required for heat protection. For -20° entry, the machine calculations indicated a requirement of 0.3 inches (2.8 lb/ft^2) for a backface temperature of 530° F. (There should be no bond-line temperature problem at these temperatures.) Figure 3.2-2 shows the temperature rise as a function of time and thickness for both -20° and -90° entry. (These data were developed early in the program for a 7 foot diameter capsule; however, the difference in heat loads between a 6.75 foot base diameter capsule are in the order of one percent and, therefore, the 7 foot diameter capsule data are applicable.)

The structural weight requirements for the forebody have been defined in Section 2.6. At -20° entry, the highest structural and heating loads are encountered in atmosphere B. Figure 3.2-2 presents an analysis of the load-backface temperature histories for heat shield thickness of 0.25 and 0.35 inches. Tables 3.2-1 (a) and (b) present the calculations for the forebody structure at -20° entry. It can be seen an aluminum substructure limited to a maximum temperature of 530° F (to maintain minimum gages and still prevent core collapse) would weigh 0.493 lb/ft^2; the heat shield thickness required would be approximately 0.30 inches and weigh 2.8 lb/ft^2. It also can be seen that the maximum inertial load of 14 g's has decayed significantly before the backface temperature rises to its maximum value.

As described in Section 2.7, composite structures can sustain load at temperatures to approximately 900° F for short periods of time. This would permit the heat shield thickness to be reduced to 0.25 inches. The equivalent minimum structural requirement for -20° entry is 2.3 lb/ft^2.

The minimum structural requirements, however, are defined by entry into atmosphere W_2 at -90°. Thus the structure must be designed for an inertial load of 200 g's and heavier structural sections must be employed (e.g., core and facing sheets). However, because of the short heating times (Figures 3.2-3), there is no significant temperature rise for -90° entry and, therefore, a cold structure can be assumed.

The heat shield structural design requirements are summarized in Table 3.2-2. The weights shown for the composite structure are conservative inasmuch as the heat shield and structural requirements were computed separately and the load carrying capability of the heat shield was ignored. (No load carrying capability was assumed for the heat in the case of the aluminum substructure.) The weights shown do not include any of the supports and/or attachments required for the payload, landing system, or afterbody.

3.2.1.2 Payload Support

During the parametric study, the forebody structure was assumed to be loaded by uniformly-distributed aerodynamic pressure and reacted upon by the inertial force of the afterbody, payload, and landing system simply supported at the edges. The dynamic analyses indicated that the most critical load condition encountered will occur during entry into atmosphere W_2 when the vehicle undergoes peak deceleration while simultaneously experiencing a lateral oscillation at a maximum frequency in the order of 5 cps and an amplitude of less than $\pm 30°$. The maximum lateral accelerations do not exceed 40 g's.

For the case of simple forward entry at zero angle of attack into atmosphere W_2 with no lateral oscillations, the following preliminary weight apportionment may be made to each subsystem and/or component.

	Percent
Afterbody	10
Forebody	41
Payload	35
Landing System	11
Fittings	3

For an ideally designed sandwich dome, the forebody mass inertia will compensate 41 percent of the point-to-point aerodynamic load without introducing shear or bending in the structure. When the payload plus landing system and fittings are supported directly by the shell, shear and bending are introduced. A ring support, or crushable pad, therefore, is required to support this mass. A ring support (to be sheared by a shaped-charge explosive after second-stage parachute deployment in order to drop the heat shield) appeared to offer the lightest and most reliable solution in this preliminary design study for a reliable, single separation device.

Assuming a total flange width of three inches for the support ring and employing the payload diameter plus one inch as the ring diameter, the stresses on the shell may be computed as follows:

TABLE 3.2-2

FOREBODY HEAT SHIELD STRUCTURAL DESIGN REQUIREMENTS

Conditions	Aluminum Sandwich Substructure			Composite Structure		
	Max. Temp.	Max. Load	Design	Max. Temp.	Max. Load	Design
Temperature, °F	530	100	530*/100**	830	100	830*/100**
Time, sec	240	30	240**	240	30	240*
Maximum Load, g's	14	200	200*	14	200	200**
E	-20°	-90°	-	-20°	-90°	-
Weights, lb/ft^2						
Heat Shield	2.80	1.40	2.80	2.30	1.30	2.30
Silicone Bond	.35	.35	.35	-	-	-
Structure	.493***	.78	.78	.25	.82	.82
TOTALS	3.64	3.53	3.93	2.55	2.15	3.12
Total Forebody Wt, lbs	160	156	173	112	95	138

* Heat shield
** Structure
*** Minimum gage limited

(a) O.D. of support ring = 38 inches

(b) I.D. of support ring = 32 inches

(c) Payload support ring area = $.785 \left[(38)^2 - (32)^2\right] = 330 \text{ in}^2$

(d) Load density = $\sigma_c^{1} = \dfrac{(.35)\ (350 \text{ lb})\ (200 \text{ g's})}{330 \text{ in}^2}$

$$\simeq 74 \text{ psi}$$

Assuming that the lateral load is 50 g's and it is reacted over two opposite quadrants, and further assuming that the distance of the payload c.g. to the plane of the support ring is eleven inches (an unlikely condition even with a 30 pound erection mechanism and bumper atop the payload, the turning moment stress is:

$$\sigma_c^{11} = \frac{11}{38}\ (.35)\ (350 \text{ lb})\ (50 \text{ g's}) \frac{4}{330}$$

$$21 \text{ psi}$$

and

$$\sigma_c^{1} + \sigma_c^{11} \simeq 95 \text{ psi}$$

Reference 4 of Section 2.6 indicates that this value is less than the minimum bare flatwise compression strength capability of a minimum density (c.a., 3 lb/ft^3) aluminum core. Similar data are available for plastic sandwich structures. In the detailed design phase, the shear and moment distributions must be analyzed after all the systems and components are located on the shell, as a function of the anticipated loading conditions. This analysis must include a point-to-point study of core and skin stability and suitable provision then will be made for local reinforcement (e.g., doublers, local increase in core density or height, etc.) where indicated. Inasmuch as these reinforcements will encompass relatively small areas, only minor changes in the overall vehicle weight are expected. This vehicle is unique in concept and production will be limited, therefore, considerable "custom" fabrication to incorporate these <u>local</u> requirements appears economically feasible in order to achieve the requisite weight efficiencies desired. An experimental test program will be required to substantiate the analysis. Due to the limited scope of the study, such an analysis obviously was not attempted.

3.2.1.3 Afterbody

As described in Section 2.6, both reinforced fibreglass and aluminum monocoque afterbody structures were considered. The structural weight requirement for both was nearly the same.

These calculations were based upon the requirement that the monocoque structure supports only its own mass in a manner to preclude buckling under an entry deceleration load of 200 g's, exclusive of any lateral and/or vibrational loads. The structural weight must be supplemented by the heat protection subsystem weight to maintain rational structural temperatures. In the case of the aluminum aftcone, 0.055 inches of phenolic glass (or its equivalent) would be required to maintain the aluminum below 530° F as described in Section 2.7. In the case of the reinforced fibreglass shield, the total thickness required is 0.06 inches. It should be noted that no internal insulation requirements were considered for either the fore- or afterbodies, for either the plastic or aluminum structural concepts, to restrict the internal temperatures during entry, inasmuch as one of the ground rules presented at an early meeting by JPL stated that the payload would have its own environmental control system and that capsule temperature rise during entry would present no problems.

Due to time limitations, the effect of dynamic loads (e.g., lateral forces, vibrations, accoustic pressure, etc.) during both launch and entry received meagre attention; however, the requirement for additional stabilizing structure (e.g., webs, rings, stiffeners, etc.)in the aftcone has been recognized and provision was made in the weights statement for their incorporation.

3.2.2 Voyager Capsule

3.2.2.1 Forebody

Because of the sizes required, only the "conventional" ablator-insulator/ metal substructural type of arrangement was considered. Projected or existing facilities do not appear capable of providing the pressures required to attain the requisite properties in a composite structure and, therefore, this concept was not considered for the large capsule.

The heat shield design considered the following materials and thicknesses which would afford a backface temperature of 530° F (See Section 2.7).

Material	Thickness (in)	Wt. lb/ft^2
Avcoat #5026-39	0.393	1.2
Thermolag T 500	0.19	1.3
SE 28	0.3	1.2

A value of 1.3 lb/ft^2 was adopted as representative for these materials. As discussed previously in Sections 2.4 and 2.7, although these materials are not considered state-of-the-art today, it is anticipated that they will be by 1969 inasmuch as they are undergoing rapid development under the Apollo and other high-performance entry vehicle programs.

The same structural design conditions considered for the smaller Mariner B capsule were assumed for the Voyager i.e., that there will have been no substantial temperature rise when the maximum load (200 g's) is applied and that temperatures as high as 530° will be realized only for the low load conditions experienced for the -20° entry trajectory.

Assuming an initial capsule weight of 2500 pounds and a load of 200 g's, the following unit weights will apply for the 5052 H-39 aluminum sandwich structure at 100° for a Wg of 500,000 pounds.

Component	Wt. lb/ft^2
Structure	1.65
Silicone Rubber Bond	3.5
Heat Shield	1.30
Total	3.30

For a 17 foot diameter forebody, this will result in a total forebody weight of 925 pounds.

These weights are representative of the simple sandwich structure plus heat shield. No provision for mounting the payload and landing system has been made. As was the case of the Mariner B capsule, the payload size as compared to the vehicle diameter is small and, therefore, these loads must be applied directly to the sandwich shell. Again, two methods were considered to distribute this load and to avoid local stress concentrations on the shell. These were:

(a) A supporting ring to be sheared by a shaped explosive charge after final parachute deployment to separate the heat shield.

(b) Employing a crushable pad.

The estimated weights of the payload support structure are shown in the weights analysis. Again, a more detailed design study must consider the problem of local sandwich reinforcement employing local doublers and/or local increases in the core density and height. The weight increase due to these deviations from the ideal model should be nominal inasmuch as the area involved is small.

3.2.2.2 Afterbody

As described in Section 2.6 only monocoque construction for the design of an Apollo afterbody was considered. An Apollo type capsule, 17 to 18 feet in diameter, has a far greater volume than is required to house the payload. It, therefore, became apparent that the weight economies might be realized by considering other configurations and a weight comparison was made between:

(a) A 0.15 inch thick conical Apollo-type aftcone of monocoque construction, plus local reinforcements required to counter the lateral load and vibrational stresses.

(b) A flat-plate type afterbody to cover the payload which is supported at a point one-half its radius by a drum type support and a ring, or pad, to distribute the inertial loads on the forebody.

(c) Elimination of the afterbody and provision of a form-fitting glass phenolic shroud to protect the payload, landing system, and inner face of the forebody.

The results of these comparisons are given in the weights summary.

MAXIMUM BACKFACE TEMPERATURE AS A FUNCTION OF TOTAL THICKNESS

Phenolic Glass

V_E = 25,000 fps
γ_E = -20° & -90°
M/C_DA = .2
Diam = 7 ft

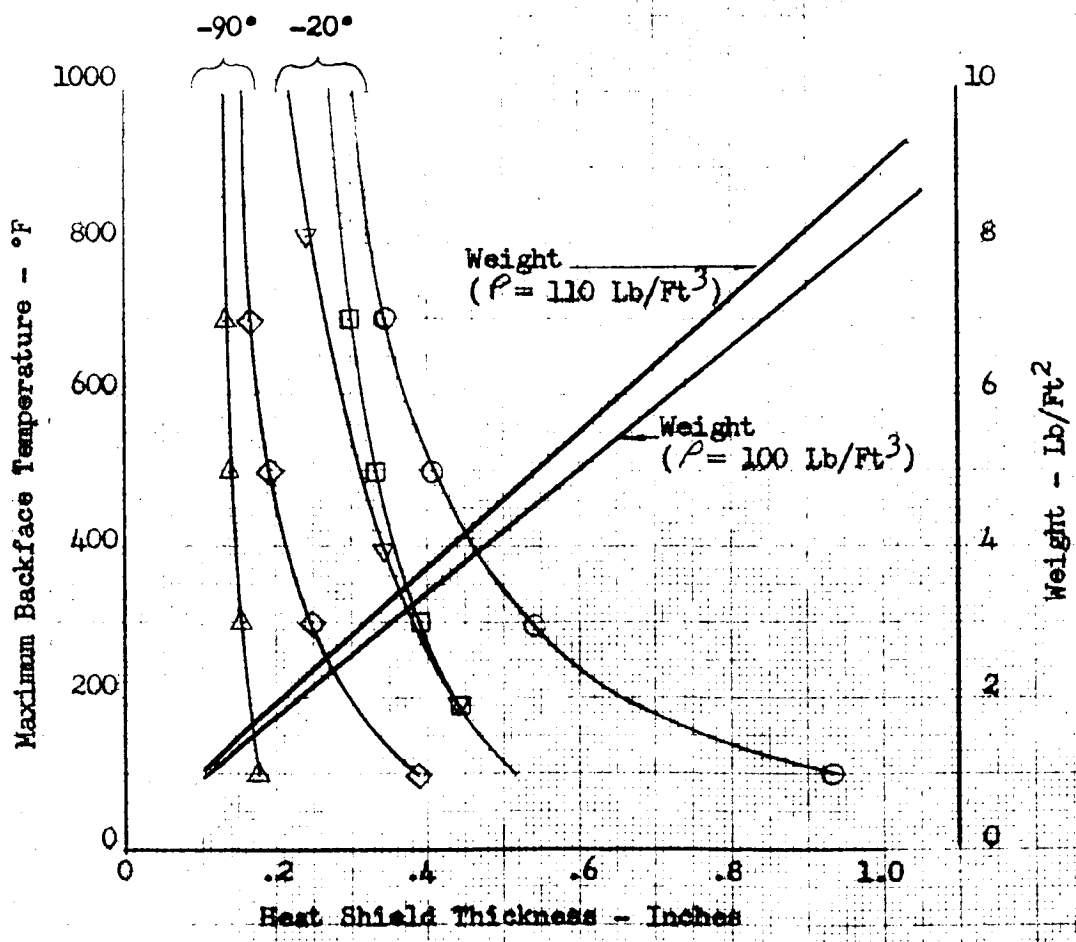

○ Hand Calculations - Swann - γ = -20°

□ Hand Calculations - Adams - γ = -20°

▽ IBM Analysis - γ = -20°

◇ Hand Calculations - Swann - γ = -90°

△ Hand Calculations - Adams - γ = -90°

STRUCTURE TEMPERATURE VS PHENOLIC GLASS THICKNESS

Phenolic Glass

V_E = 25,000 fps
——— γ_E = -20°
– – – γ_E = -90°
M/C_DA = .2
Diam = 7 ft

30% 911D Resin
70% 181 Glass Fiber Reinforcement

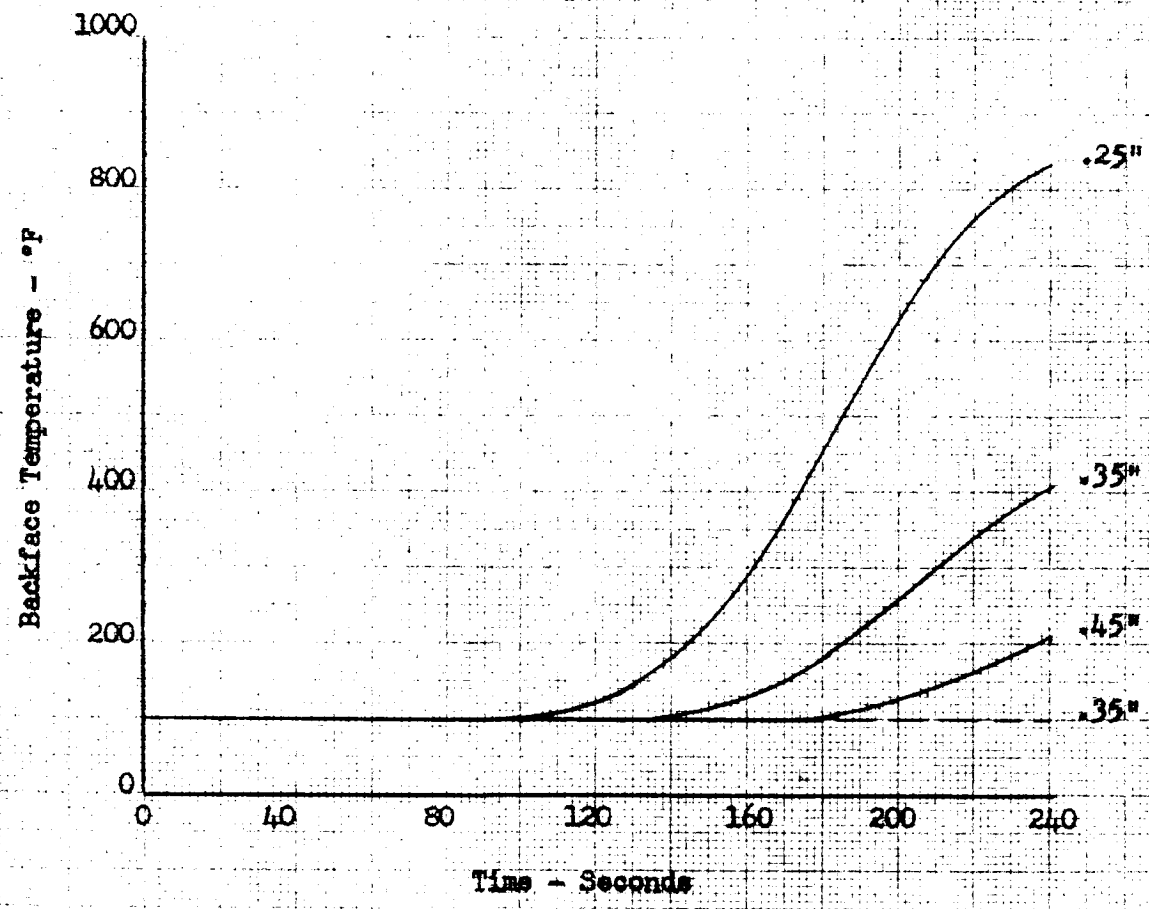

PREPARED BY:	NORTH AMERICAN AVIATION, INC. SPACE and INFORMATION SYSTEMS DIVISION	PAGE NO. OF
CHECKED BY:		REPORT NO.
DATE:	Voyager Entry Capsule Design Study Load & H.S. Backface Temp. vs. Entry Time	MODEL NO.

Fig. 3.2-3

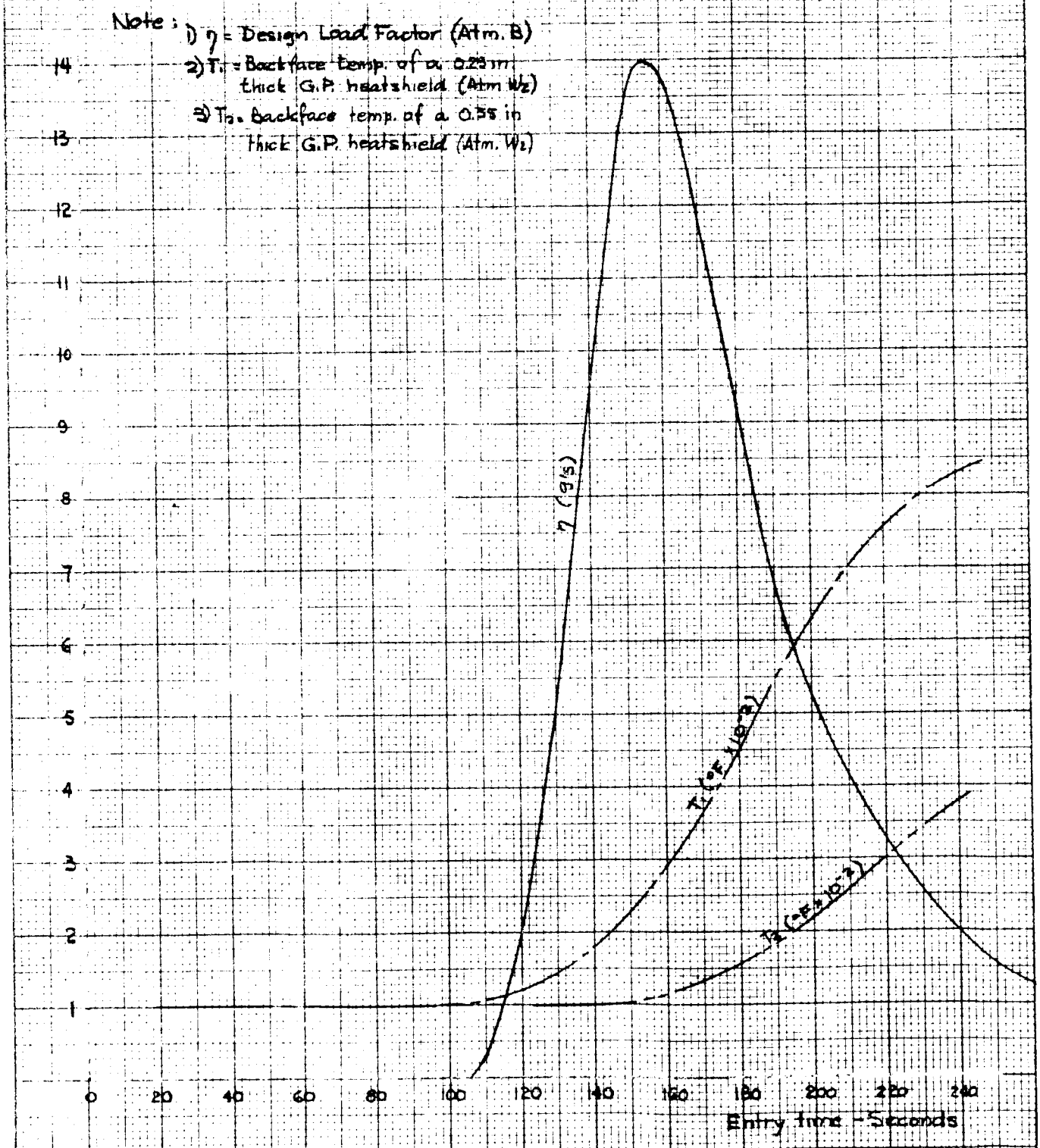

PREPARED BY: ASM	NORTH AMERICAN AVIATION, INC. SPACE and INFORMATION SYSTEMS DIVISION	PAGE NO. OF
CHECKED BY:		REPORT NO.
DATE: 9/27/63	Table 3.2-1 (a)	MODEL NO. Voyager

Determination of minimum heat shield requirements, for Phenolic Glass ablator, 20° entry angle and Atmosphere B accelerations (plus 25% Margin of Safety) for conventional aluminum structure

①	②	③	④	⑤	⑥	⑦	⑧	⑨	⑩
Time	$\eta_{atm.B}$	Backface Temp.	Al sandw. $K_1 \times 10^3$	Wg	$\sqrt{Wg}$	W_{CALC} (1)	W_{min} (3)	Backface Temp.	$W_{CALC.}$ (3)
Sec.	$\times 1.25$ g's	$t_{AB.} = .25 t_{GP}$ °F				#/ft² (1)	#/ft² (3)	$t_{AB} = .35$ °F	
20	—	100	1.97	—	—	—	.493		
40	—	100		—	—	—			
60	—	100		—	—	—			
80	—	100		—	—	—			
100	—	100		—	—	—			
120	2.0	120	1.97	700	27	.313			
140	9.5	180	1.98	3320	58	.370			
155	14.0	260	2.01	4900	70	.400			
160	13.75	290	2.03	4800	69	.395			
180	9.25	450	2.25	3420	59	.380		155	.375
200	5.25	630	2.70	1840	43	.345		220	.340
220	3.25	760	—	1040	32			300	.325
240	2.00	830	—	700	27		.493	380	.313
260	1.25			440	21				
280	1.00			350	19				
300	.75			260	16				

JUST IFIED

2 DT

OVER MAX. TEMP. FOR ALUMINUM

(1) Of this weight, .260 #/ft² are for adhesive film between facings and core

(2) Corresponds to h = .25 & t = .006 for each facing with 3#/cuft core

(3) These weights do not include weight of bond between heat shield and structure

PREPARED BY: ASM	NORTH AMERICAN AVIATION, INC. SPACE and INFORMATION SYSTEMS DIVISION	PAGE NO. OF
CHECKED BY:		REPORT NO.
DATE: 9/27/63	Table 3.2.-1(b)	MODEL NO. Voyager

Determination of minimum heat shield requirements, for Phenolic Glass ablator, 20° entry angle γ_E and Atmosphere B accelerations (plus 25% Margin of Safety) for 91 LD, #181 Composite Structure

①	②	③	④	⑤	⑥	⑦	⑧	⑨	⑩
Time	η atm B	Backface temp	#181/91LD $K_1 \times 10^3$	W_g	$\sqrt{W_g}$	$\omega_{calc.}$	ω_{min}		
sec	x 1.25 g's	t_{AB} = .25 GP °F				#/ft²	#/ft²		
20	–	100	3.16	0	0		.250		
40	–	100							
60	–	100							
80	–	100							
100	–	100	3.16	0	0				
120	2.0	120	3.20	700	27	.08			
140	9.5	180	3.31	3320	58	.192			
155	14.0	260	3.43	4900	70	.241			
160	13.75	290	3.50	4800	69	.241			
180	9.25	450	3.67	3420	59	.216			
200	5.25	630	5.30	1840	43	.228			
220	3.25	760	5.90	1040	32	.190			
240	2.00	830	6.66 (1)	700	27	.180			
260	1.25			440	21				
280	1.00			350	19				
300	.75			260	16		.250		

(1) K_1 values are extended above 550°F using data from Ref 7 for very short exposures (.5 hr) for reduction of compressive strength vs. temperature

(2) ω_{min} is calculated on the base of a composite structure with .50 in between facings, 3.5 Lb/ft³ core and t_f = .010 (each) No adhesive weight needs to be added since the concept consists in laminating all parts together.

3.3 LANDING SYSTEM DESIGN

Two landing system concepts which were selected during the parametric study (Section 2.8) were analyzed for the 100 pound Mariner B payload. The first, Concept 6 (Mariner B), consists of a single stage parachute system, to provide the maximum permissible initial drag and to afford atmospheric data measurements over the greatest altitude range. Landing survival to permit post-impact transmission was not considered. The second, Concept 4, provides an optimum combination of first stage and second stage parachutes to yield the maximum descent time. In this concept, soft landing is provided to permit post-impact data transmission.

Only one concept (Concept 1) is analyzed for landing the 600 pound Voyager payload. Weight, volume, and deployment limitations preclude the use of a single-stage parachute system for this payload. Consequently, only a two-stage system capable of yielding maximum descent time and of providing soft landing is considered. For the second stage, a single parachute was selected for its lighter weight over the alternative of using a cluster.

3.3.1 Concept 6 (Mariner B)/Maximum Altitude

The parachute-system weight breakdown for Concept 6 is as follows:

		Weight, Pounds
Parachute (D_p = 13.8 ft.)	=	24.6
Parachute riser	=	6.1
Added structure	=	4.3
Sequencing system	=	5.0
TOTAL		40.0

where D_p is the projected diameter of the inflated parachute.

It has been assumed that atmospheric data sampling will not start until subsonic velocity has been achieved. In resolving the question of when to release the heat shield, it was found that releasing it with first-stage deployment is in keeping with the optimization criterion for this concept, minimum altitude loss. The heat shield should separate cleanly from the vehicle at opening of the first stage, as the heat shield M/C_DA is three times that of the vehicle on the parachute.

The opening force is 11,900 pounds and the total deceleration on the payload due to parachute drag and the vehicle drag is 154 g's. The terminal ground-impact velocity ($C_D = 1.0$) is 204 ft/sec. The altitude-time relationship for worst-case initial conditions ($V_o = 3750$ fps, $H_o = 28{,}000$ ft., Atmosphere W_2, $\gamma_E = -90°$) is described in Table 3.3-1. For this worst entry condition, the total time for subsonic sampling is 88 seconds. The initial sampling altitude is 20,045 ft.

TABLE 3.3-1

Concept 6 Landing System Deployment Trajectory

	Time	Altitude Lost
Deployment and inflation time (experimental data)	0.5 sec.	1,875 ft.
Deceleration time to V = 750 fps	5.0	6,080
Deceleration time to equilibrium velocity (See Figure 3.3-1)	0.5	225
Descent at equilibrium to impact	87.5	19,820

3.3.2 Concept 4 (Mariner B)/Maximum Time

Digital computation conducted by Cook Research in support of this analysis has shown that an optimum weight ratio (first-stage parachute weight to total parachute system weight) of 0.28 yields the maximum descent time (See Figure 3.3-2). The system weight breakdown for Concept 4 is as follows:

		Weight, Pounds
First stage parachute ($D_p = 7.12$ ft.)	=	5.6
First stage parachute riser	=	2.7
First stage structure	=	3.0
Sequencing system	=	5.0
Second stage parachute ($D_p = 28$ ft.)	=	16.0
Second stage parachute riser	=	2.0
Second stage structure	=	2.0
Impact attenuation	=	3.7
TOTAL		40.0

PREPARED BY: EP	NORTH AMERICAN AVIATION, INC. SPACE and INFORMATION SYSTEMS DIVISION	PAGE NO. OF
CHECKED BY:		REPORT NO.
DATE: 10/9/63		MODEL NO.

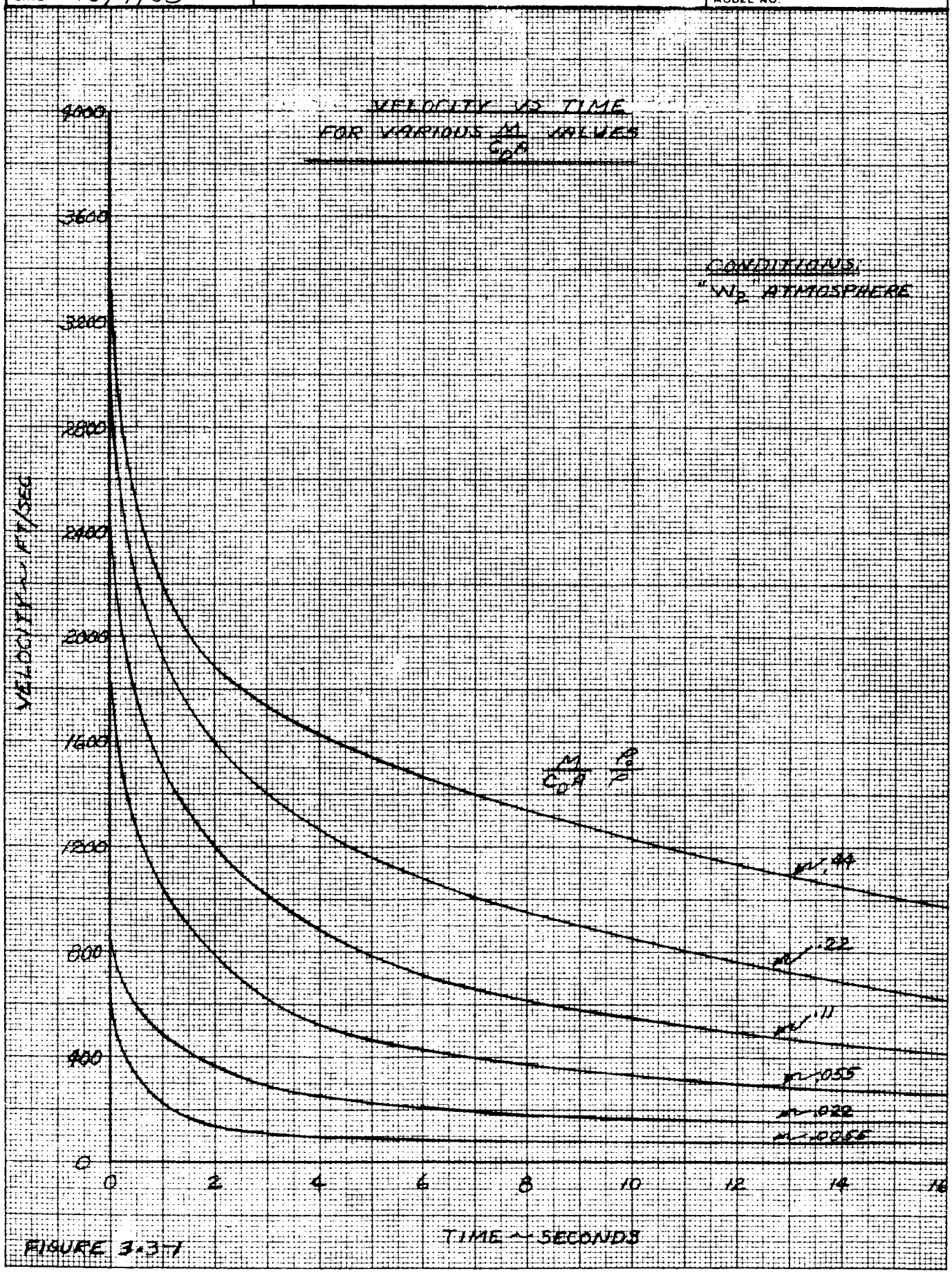

FIGURE 3-3-1

PREPARED BY: EP	NORTH AMERICAN AVIATION, INC. SPACE and INFORMATION SYSTEMS DIVISION	PAGE NO. OF
CHECKED BY:		REPORT NO.
DATE: 10/9/63		MODEL NO.

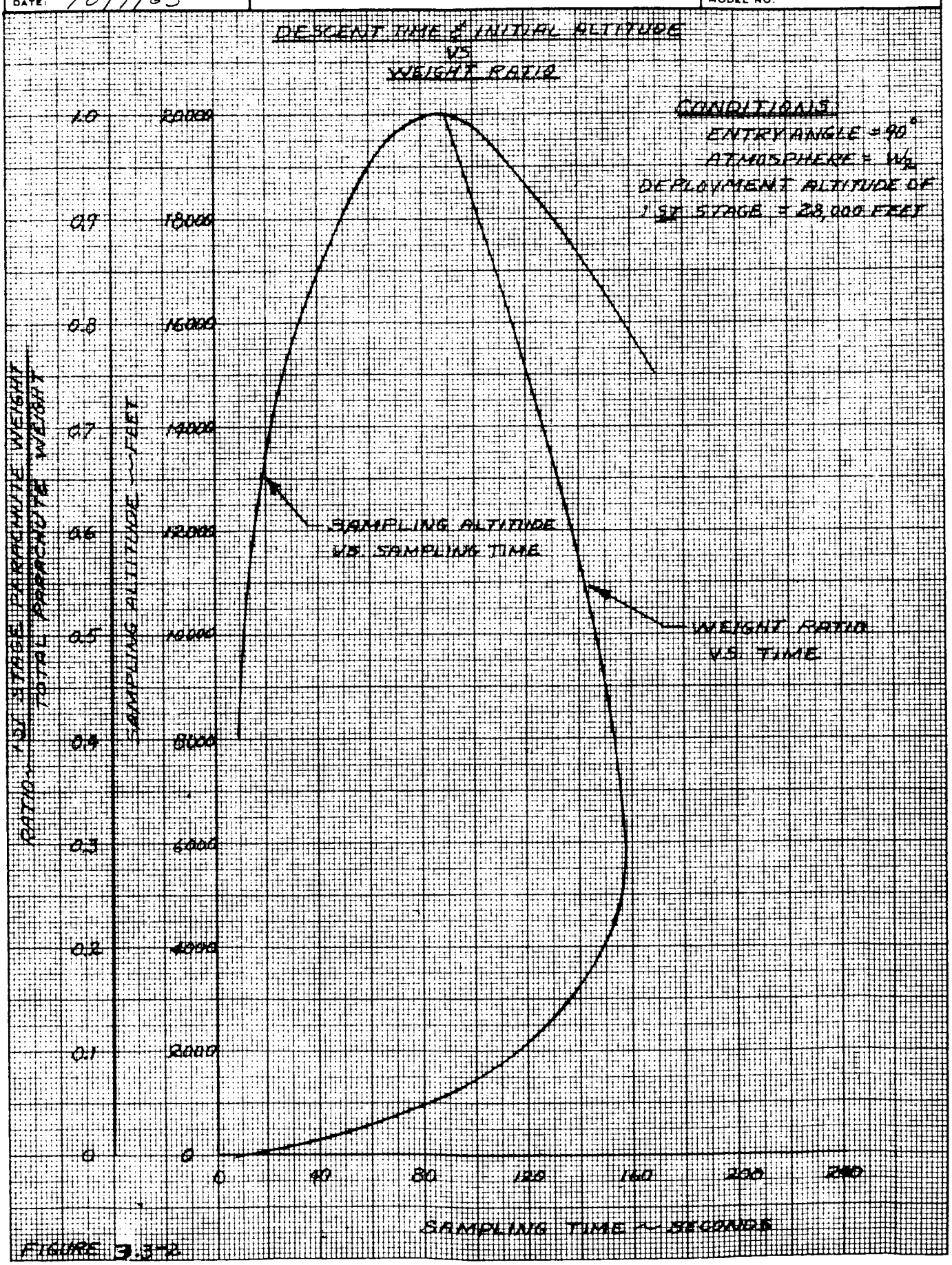

FIGURE 3.3-2

Since this concept utilizes a two-stage system, the first stage is deployed at 3750 fps and allowed to decelerate the vehicle to 750 fps. At that time, the first stage is released from its fixpoint and extracts the second stage. At second stage opening, the force generated initiates separation of the payload from the heat shield and the atmospheric data sampling is initiated. The first stage opening force is 8000 pounds. The ground-impact velocity was constrained to <100 fps. The altitude time relationship for worst-case initial conditions (V_o = 3750 fps, H_o = 28,000 ft., Atmosphere W_2, $\gamma_E = -90°$) is described in Table 3.3-2. For this extreme entry condition, the total time for subsonic sampling is 170 seconds. The initial sampling altitude is 15,110 feet.

TABLE 3.3-2

Concept 4 Landing Trajectory

	Time	Altitude loss
Deployment and inflation time (experimental data)	0.4 sec.	1500 ft.
Deceleration to 750 fps (See Figure 3.3-1, adjusted M/C_DA = .190)	11	11,000
Deploy second stage	0.5	
Fill second stage (1)	.02	390
Time to achieve equilibrium velocity (See Figure 3.3-1, M/C_DA = .0056)	5.0	750
Descent time to impact	165	14,360

Note (1) This extremely fast filling time is a result of the low density. The parachute opening force is 11,900 pounds which is within allowable limits; reefing of the parachute is not required.

This concept incorporates impact attenuation. For 1000 g's on the payload, the stroke required for 70% crush is .143 feet. The aluminum-honeycomb attenuator required weighs 3.52 pounds and occupies 1.01 cubic feet.

3.3.3 Concept 1 (Voyager)/Recovery

The maximum descent time obtainable is achieved with a weight ratio of 0.28. The weight breakdown for the system components is as follows:

	Weight, Pounds
First stage parachute (D_p = 17 ft.) =	40
First stage riser	20
First stage structure	10
Sequencing system	5
Second stage parachute(D_o = 90 ft.)	100
Second stage riser	5
Second stage structure	10
Impact attenuation	10
TOTAL	200

where D_o is the developed diameter of the parachute.

The first stage opening force is 18,200 pounds and the total deceleration on the payload due to parachute drag and the vehicle drag is 47.6 g's. The altitude time relationship for worst-case initial conditions (V_o = 3750 fps, H_o = 28,000 ft., Atmosphere W_2, $\gamma_E = -90°$) is described in Table 3.3-3. For this extreme entry condition, the total time for subsonic sampling is 159 seconds. The initial sampling altitude is 15,750 feet.

TABLE 3.3-3

Voyager Landing Trajectory

	Time	Altitude loss
Deployment and inflation time	0.5	1,875
Deceleration to 750 fps (adjusted M/C_DA = 0.186)	10	10,000
Deploy second stage	0.5	375
Fill second stage (1)	0.03	
Deceleration with second stage reefed (Figure 3.3-1)	2.0	1,100
Deceleration from 550 fps to equilibrium velocity	2.0	400
Descent time to impact	155	14,250

Note (1) This is an extremely fast time to inflate; to prevent uneven deployment it is advisable to reef the parachute to 10% of its C_DA for two seconds.

The Voyager mission requires impact attenuation. For 1000 g's on the payload, the stroke required is .115 feet. The aluminum-honeycomb attenuator required weighs 11 pounds and occupies 3.2 cubic feet spread uniformly over the five foot diameter base of the payload.

All of the above calculations are based on the worst combination of entry conditions (90° entry into the W_2 atmosphere assuming that the capsule is oscillating). Under any other entry angle or less severe atmospheric density conditions both the sampling altitude ceiling and the available sampling time will increase greatly. Figure 3.3-3 shows the sampling altitude and descent time versus the weight ratio for 90° entry into atmosphere B. A large improvement in the altitude and time factors may be noted.

The final choice of the most suitable parachute system can only be made after a thorough review is made of the data-telemetering requirements in terms of transmission rate and the amount of stored and acquired data to be transmitted. If all of the data can be gathered in slightly less than 100 seconds for the extreme entry condition, it is then quite advantageous to select the one-stage parachute system inasmuch as it offers the maximum altitude capability with a less complex and more reliable system.

The subsystems recommended, regardless of which concept is ultimately selected are:

TASK	SUBSYSTEM
Sensing and Landing events sequencing	Integrating accelerometer from which velocity is derived
Deployment of first stage parachute	Pyrotechnic-actuated drogue gun and pilot chute
First stage parachute	Hyperflo ribbon parachute
Second stage parachute	Extended skirt parachute
Impact attenuation	Aluminum honeycomb

Because of factors such as the very low deployment altitudes involved, high deployment velocities, steep entry angles, and terrain uncertainties, a detailed analysis of the sensing and sequencing system should be conducted in the future to determine error margins, tolerance buildups, etc. and their effect upon the design.

PREPARED BY: EP	NORTH AMERICAN AVIATION, INC. SPACE and INFORMATION SYSTEMS DIVISION	PAGE NO. OF
CHECKED BY:		REPORT NO.
DATE: 10/9/63		MODEL NO.

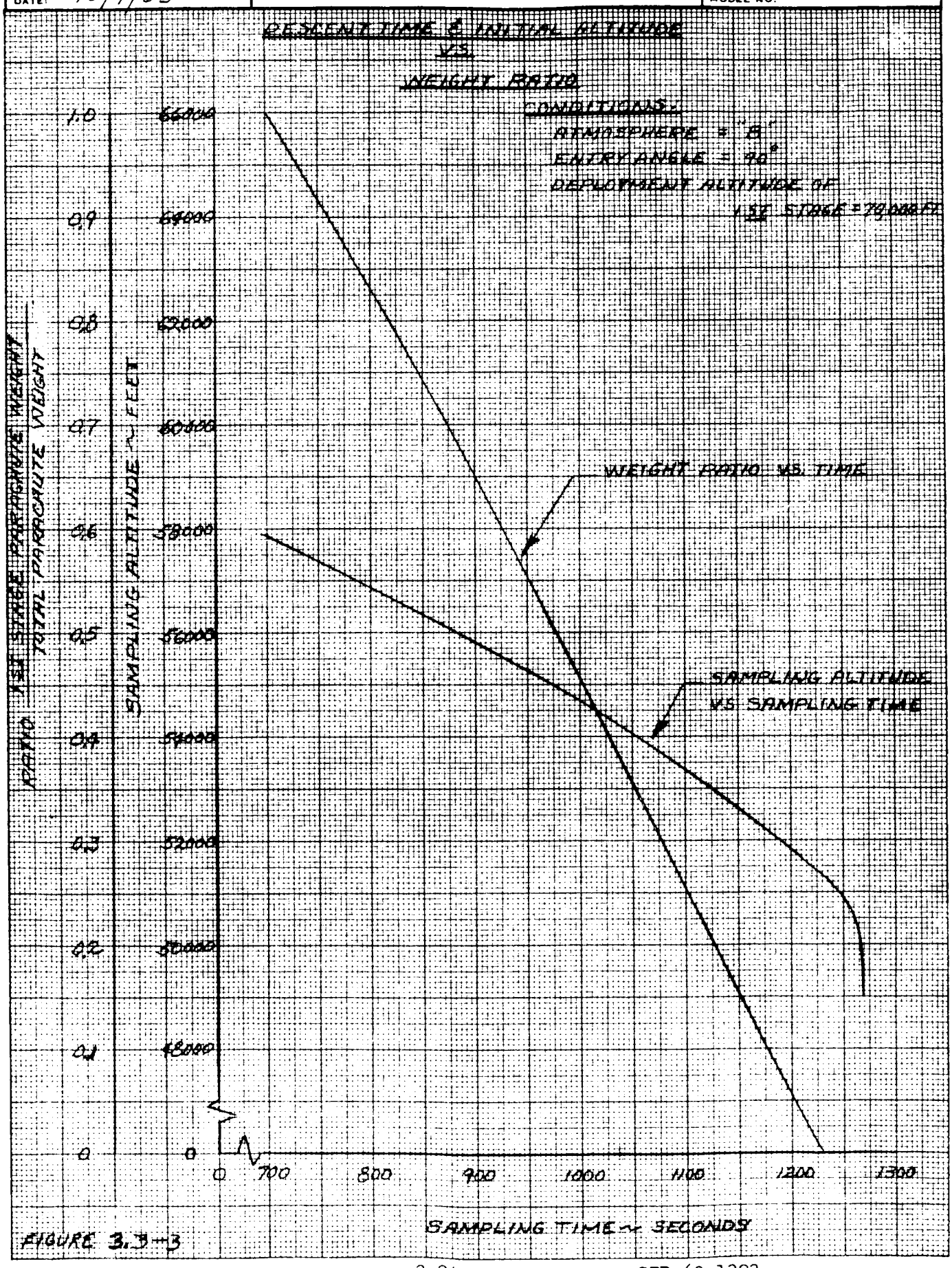

FIGURE 3.3-3

3.4 CONFIGURATION DRAWINGS

The initial design phase of this study yielded several feasible concepts which served as a basis for generating preliminary configuration drawings. The primary structural element considered was a spherical-segment forebody of aluminum alloy honeycomb sandwich construction. The inner surface of this structure provides the mounting surface for the payload and landing system. The edge of the segment serves as an attachment point for the capsule afterbody. As described previously, a phenolic fiberglass heat shield is employed for heat protection in the case of the smaller capsule and the more advanced ablater-insulator materials were considered for the large capsule. An aft cone, fabricated entirely of fiberglass, was considered for the case of the inboard antenna configuration, and an aluminum-fiberglass structure was employed for the flush-mounted slot antenna.

Only the most promising variations for each of the two configurations (i.e., the small, Mariner B and large, Voyager capsules) are presented. In the case of the Mariner B, the capsules shown differ only with respect to the type of antenna employed and the provisions made for post-impact survival. In the case of the Voyager capsule, the differences between the various concepts shown primarily reflect possible variations in afterbody geometry.

It should be noted that although this investigation demonstrated the feasibility of employing the configurations selected for the Mariner B mission, **with the given initial conditions (and also demonstrates the feasibility of** the Voyager configurations, if Mariner B confirms the assumptions made about the atmosphere), it is obvious that the detailed definition of many of the design elements will require additional study. The inter-relationship between the design elements and their integration into the system to insure compatibility with the mission requirements is complex and requires a series of successive iterations before the final design emerges. The constraints of time, as well as the unavailability at the beginning of study of clearly defined mission objectives and payload and spacecraft-bus interface requirements, limited the number and depth of those iterations.

3.4.1 Mariner B Capsule

The basic configurations selected for the 350 pound capsule represent designs which incorporate: (1) JPL's cylindrical inboard antenna with post-impact survival, (2) JPL's cylindrical inboard antenna with no post-impact survival, and (3) a slotted antenna mounted in the afterbody with no post-impact survival.

The capsule showing provisions for post-impact survival is composed of three basic elements. These are the base, the afterbody, and the encapsulated payload. The base structure provides for attachment and/or mounting of the

electronic payload, parachute landing system, heat shield and afterbody. The structural element consists of a spherical segment fabricated of a bonded aluminum honeycomb sandwich bonded by a toroidal segment of the same construction. These two sections are riveted together to form the forebody structure. The fiberglass heat shield is bonded to the outer face of the sandwich structure to provide the necessary thermal barrier. Fittings and mounting flanges are located on the inner face of the structure for the installation of the electronic payload and parachute canister. The peripherical sandwich structure terminates in a ring flange that mates with the afterbody cone as shown in Section C-C of Figure 3.4-1. The afterbody is secured to the base structure by means of ballistically actuated thrusters that are used to jettison the afterbody prior to parachute deployment. The thrusters are hermetically sealed to endure the prolonged space environment and they have provisions for adjustment so that the afterbody may be secured rigidly to the base and still permit the thrust section required for separation. The electronic payload is bolted directly to a mounting ring, as shown in detail B-B. Separation is achieved by a linear shaped change that severs the mounting ring. In the event that a localized separation device may be desirable, an alternate method employing explosive studs is shown. Either of these methods provides for a uniform load at the sandwich-structure inner face.

The afterbody structure shown is fabricated entirely of a fiberglass layup to accommodate the pre-entry transmission requirement and to provide thermal protection. It is attached to the base structure by means of the thruster studs.

The electronic payload is assumed to be packaged in a cylindrical container and capable of withstanding 1000 earth g's. However, since the cylindrical antenna shown mounted atop the electronic payload is assumed not to be designed to resist any other than the impact force, it is shown to be protected by a fiberglass honeycomb structure for post-impact survival. This structure is made up of four identical "tulip petal" shaped assemblies. Each assembly is hinged to the electronic payload canister in a manner to provide protection for the antenna when they are in the closed position. Each segment is individually operated by a gas actuator that is triggered by a device that senses the cessation of movement and erects, or rights the payload to afford directional transmission.

The parachute system shown consists of a first-stage or drogue parachute and a second-stage main parachute. The drogue parachute is shown packaged in a container for mortar deployment. The drogue parachute canister is so located as to minimize the mortar's reaction on the capsule's dynamic behavior. The drogue parachute extracts and deploys the second-stage parachute from its canister. At the time of second-stage deployment, a signal is generated to fire a linear shaped charge which severs the electronic payload mounting ring and thus jettisons the base structure and heat shield. Release of the forebody

reduces the weight on the parachute and generally enhances its characteristics. As the payload impacts on the planet surface, the main-chute bridle is released to permit the capsule to tumble free of the parachute and thus prevent entanglement and subsequent failure of the erection mechanism. The principal feature of this configuration is the survival of impact and the self-erecting device to permit post-impact operation.

The configuration showing the use of JPL's inboard antenna, but no post-impact survival (Figure 3.4-1) also is comprised of the same three basic elements. The base is constructed of aluminum alloy honeycomb sandwich with a bonded fiberglass heat shield as previously described. The afterbody is made of fiberglass and is attached to the base by ballistically operated thrusters, as shown on the previous configuration. The arrangement of the payload differs considerably in that there is no provision for continued operation after impact. The electronic equipment therefore is located in an annular canister that surrounds the cylindrical antenna, and is attached to the base by a peripheral mounting flange. A single-stage parachute system is shown which is stowed within one of the antenna quadrants.

In the deployment sequence, the afterbody is jettisoned first by activating the thrusters. This uncovers the payload package and permits the parachute to be deployed by a mortar fired pilot chute. The pilot chute extracts the main parachute at which time a signal activates the linear shaped charge to sever the payload mounting flange and drop the forebody. The payload is designed to transmit data to point of impact only. The significant feature of this configuration is that there is no post-impact survival, thus eliminating the need for encapsulative payload and the self-erecting system.

The third configuration (Figure 3.4-1) departs from the previous concepts in that it employs a slotted antenna that is an integral part of the afterbody. This configuration again incorporates the same three basic capsule elements. The base structure is similar to the two configurations previously described in that it is fabricated of aluminum-alloy honeycomb sandwich with a bonded-in-place fiberglass heat shield. The afterbody is of thermally-insulated aluminum-alloy monocoque construction with built-in antenna slots located peripherally near the center of the cone. The apex of the cone is capped with a cover that is an integral part of the drogue-chute deployment canister. The base of the afterbody cone is made up of a bulkhead assembly that provides a mounting for the electronic payload on the bottom side and forms the lower end of the parachute canister. The parachute canister is a tubular member running lengthwise and located on the capsule centerline. The entire afterbody structure is attached to the forebody by a series of explosive bolts. The landing parachute system is housed on the centerline of the capsule and is activated by firing the drogue-chute mortar which in turn deploys the second stage parachute. After second stage has reached full deployment a signal triggers the explosive bolts releasing the forebody. The capsule is designed to operate to the time of impact only. This configuration represents the simplest system since it requires only the parachute deployment and heat-shield separation systems. In addition the parachute is located on the centerline of the capsule so that perturbations due to parachute deployment are minimized.

3.4.2 Voyager Capsule

The configuration selected for the large capsule shown in Figure 3.4-2 represents designs incorporating: (1) the Apollo shape, (2) Apollo forebody with flat-plate aft-closing, and (3) Apollo forebody with payload shroud. All these configurations assume post-impact survival.

The basic configuration shown is similar to the smaller 350 pound capsule, wherein the major components are the base, the afterbody, and the electronic payload. The base structure is fabricated of aluminum alloy honeycomb sandwich with a bonded-in-place heat shield. The afterbody cone is made of fiberglass to facilitate transmission. The afterbody is secured to the base structure by a series of ballistically operated thrusters that are capable of jettisoning the afterbody to permit parachute deployment. The payload is encapsulated for post-impact survival in a manner similar to that of the 350 pound capsule and features a self-righting device for post-impact transmission of data.

The alternative configurations represent afterbody modifications only. The electronic payload and parachute landing system remain the same as in the basic configuration. The method of payload extraction in the case of flat aft-closure is to jettison the payload cover-plate with ballistic thrusters, deploy the parachute system and then jettison the forebody structure. In the case of the shrouded payload, the same sequence is followed.

In all cases the electronic payload was assumed to be capable of withstanding a vertical impact of 100 earth g's. The recovery system was designed to survive tumbling and to have the capability to right itself for surface operations.

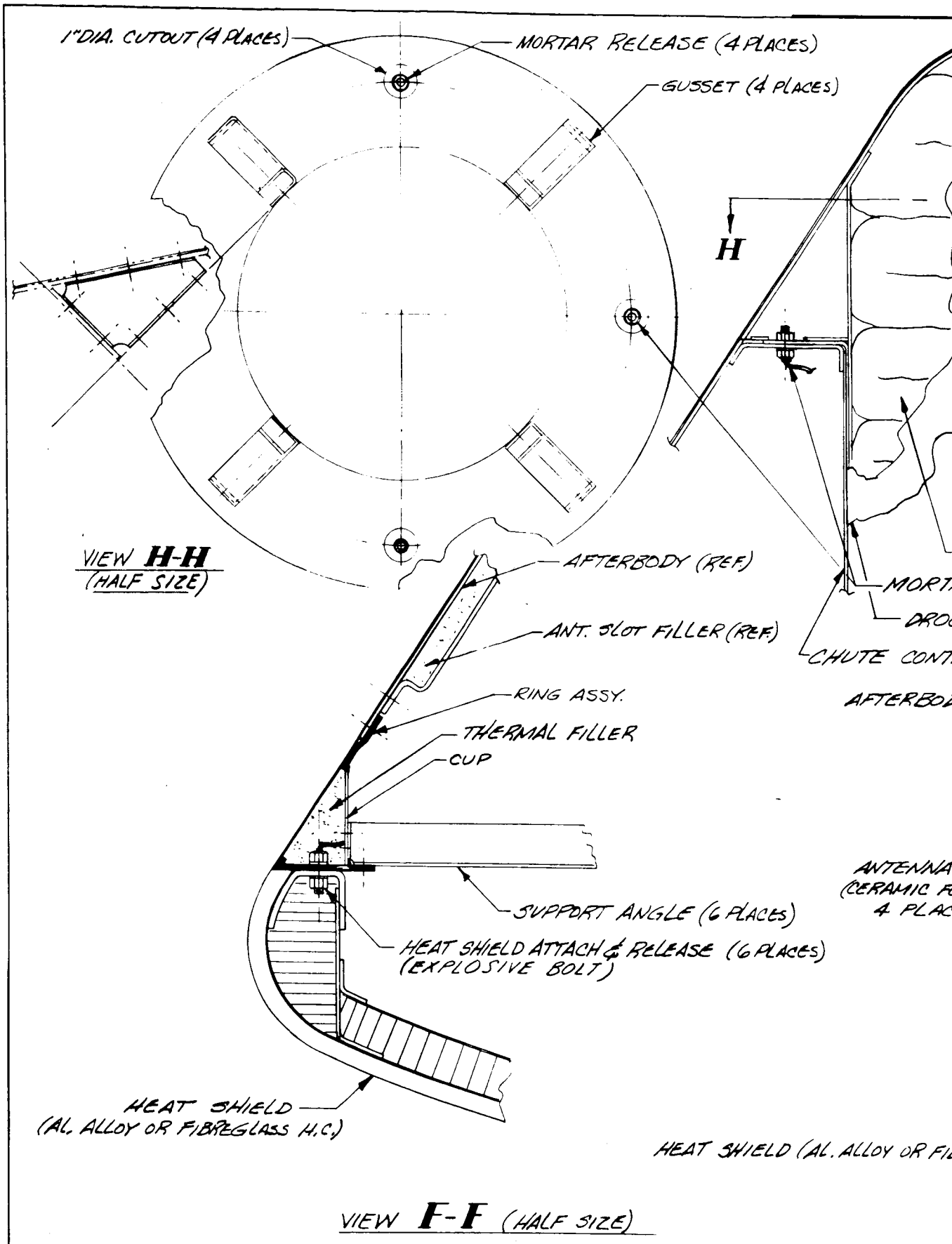
1" DIA. CUTOUT (4 PLACES)
MORTAR RELEASE (4 PLACES)
GUSSET (4 PLACES)
H
VIEW H-H
(HALF SIZE)
AFTERBODY (REF)
ANT. SLOT FILLER (REF)
RING ASSY.
THERMAL FILLER
CUP
SUPPORT ANGLE (6 PLACES)
HEAT SHIELD ATTACH & RELEASE (6 PLACES)
(EXPLOSIVE BOLT)
HEAT SHIELD
(AL. ALLOY OR FIBREGLASS H.C.)
CHUTE CONT
AFTERBOD
ANTENNA
(CERAMIC F
4 PLAC
HEAT SHIELD (AL. ALLOY OR FI
VIEW F-F (HALF SIZE)

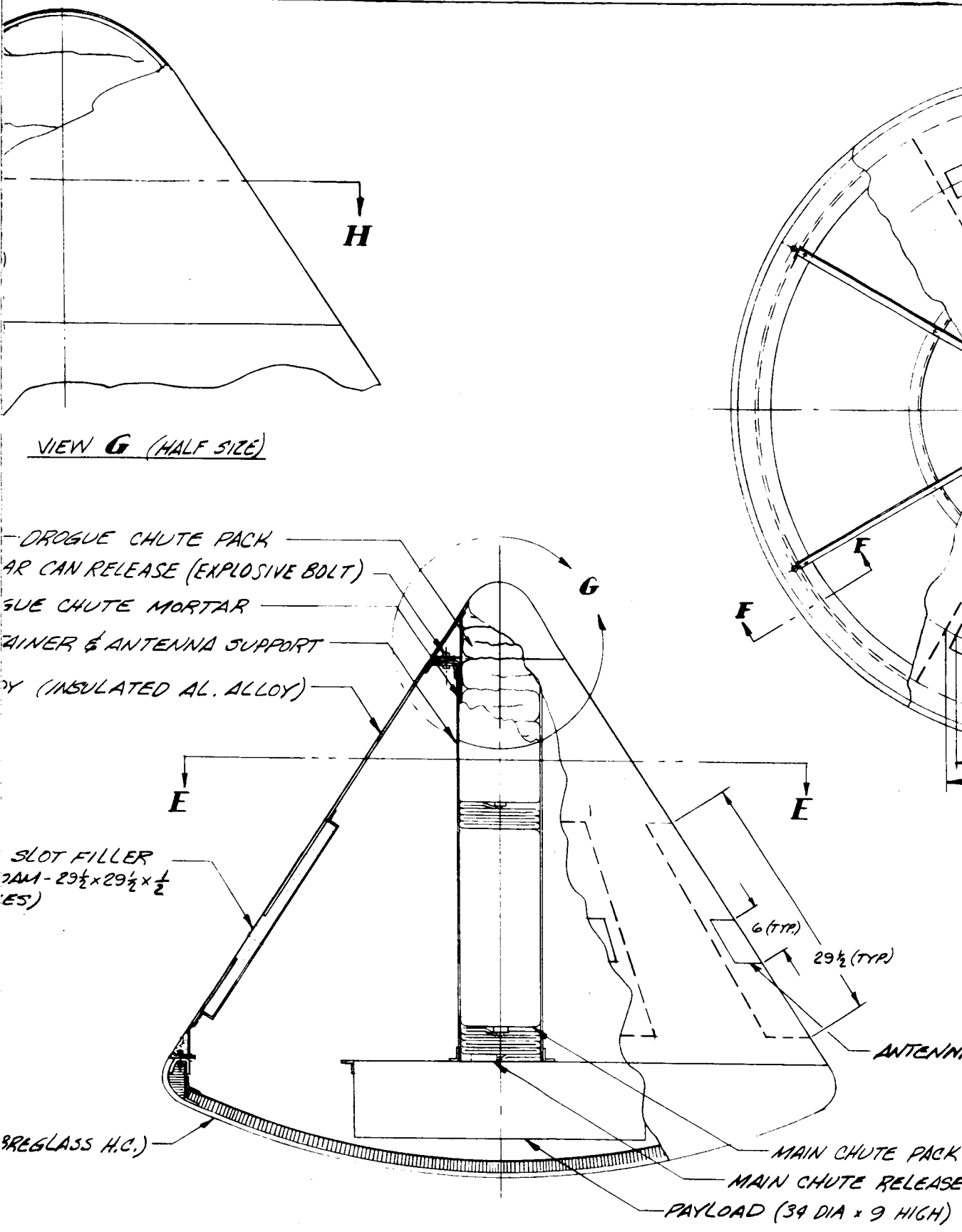

ARRANGEMENT & DETAIL (1/8 SCALE)
SLOTTED CONE ANTENNA ~
NO LANDING SURVIVAL PROVISIONS

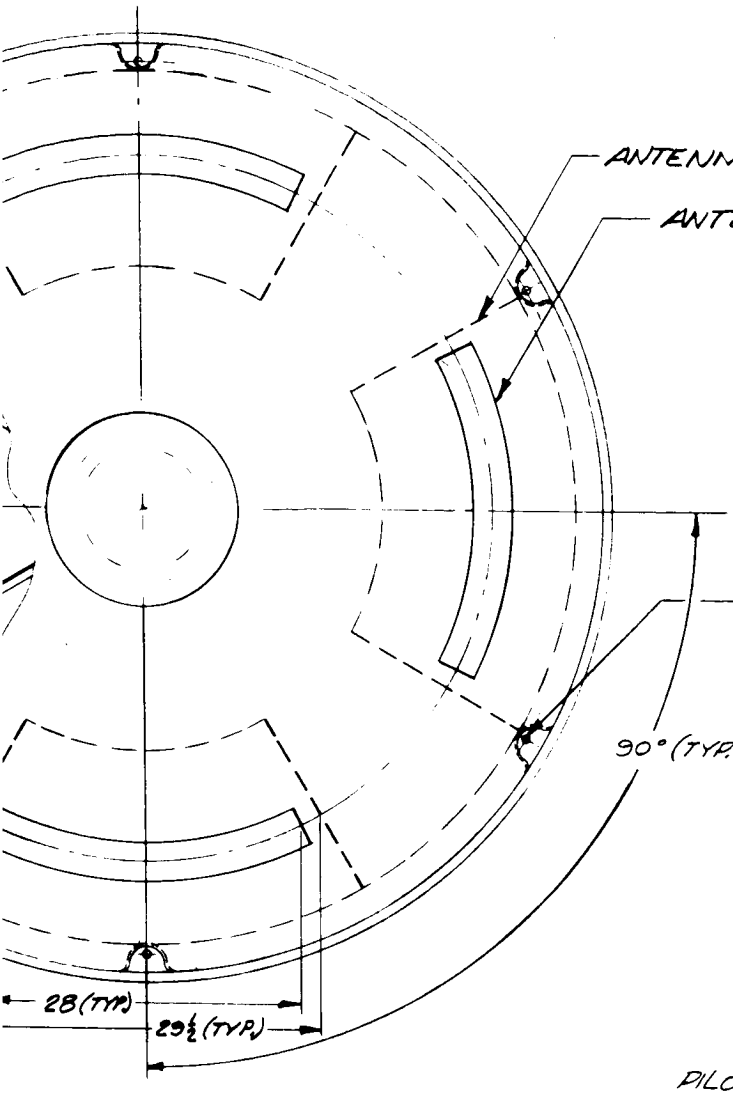

VIEW E-E (1/8 SCALE)

A SLOT (6 × 28 4 PLACES)

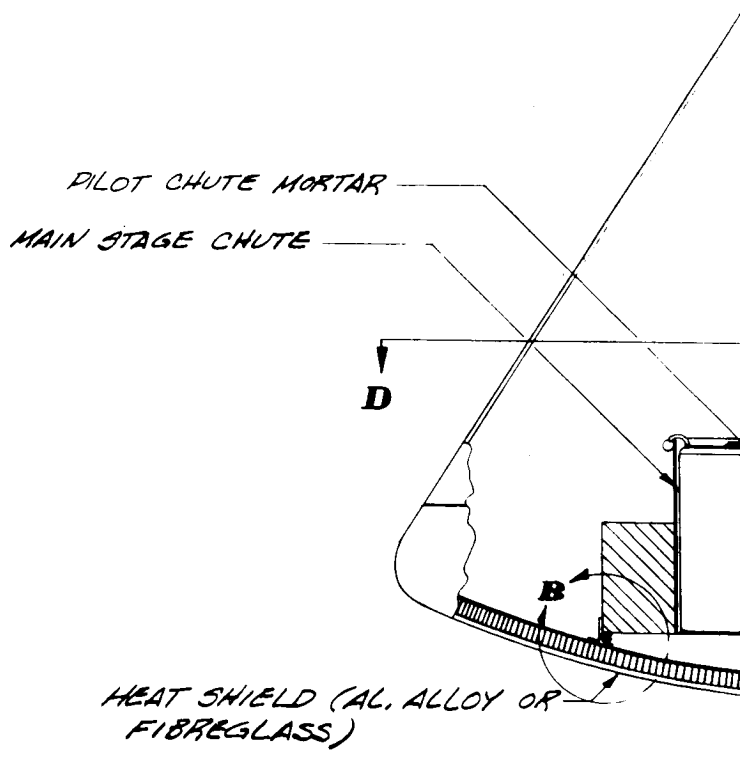

ARRA
JPL TYPE A

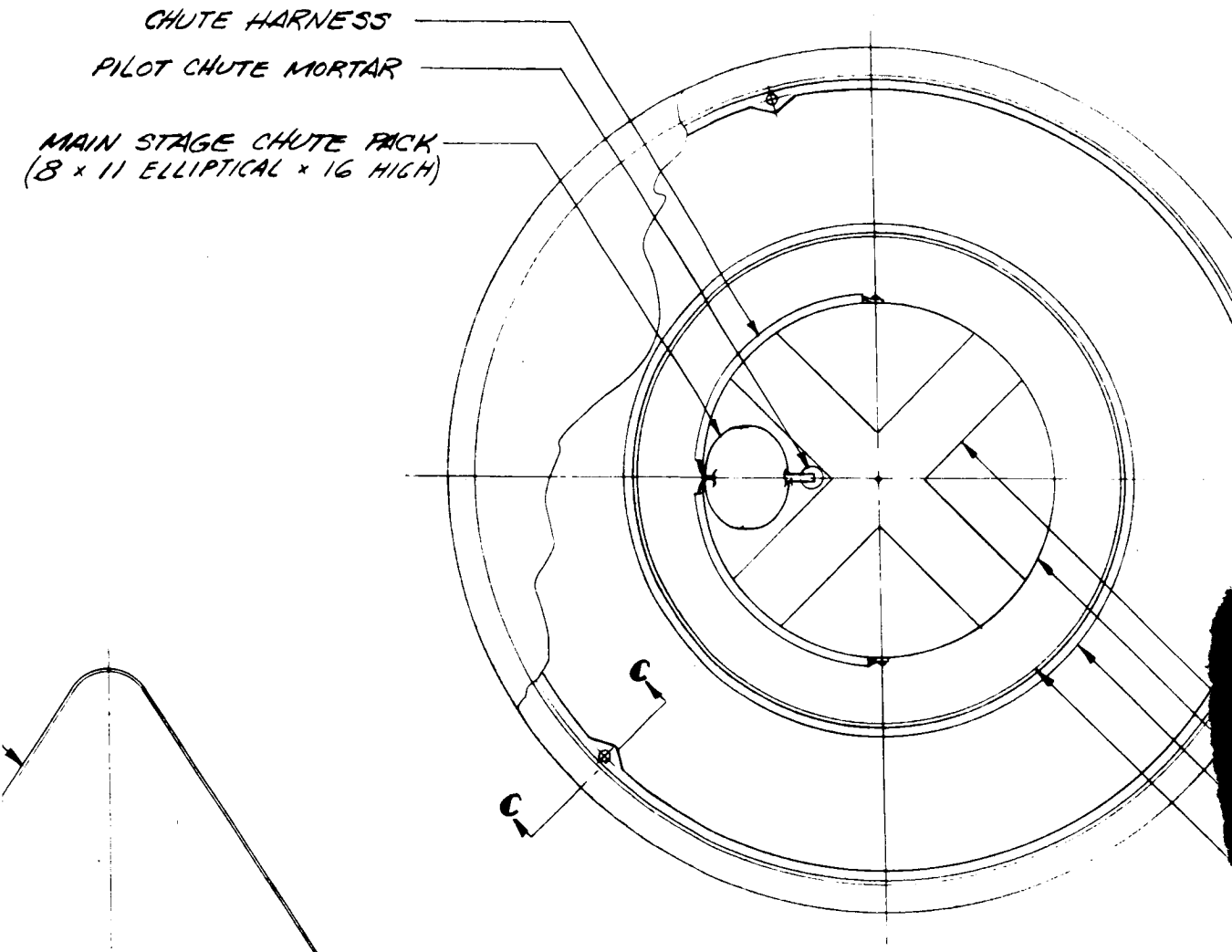

VIEW **D-D** (1/8 SCALE)

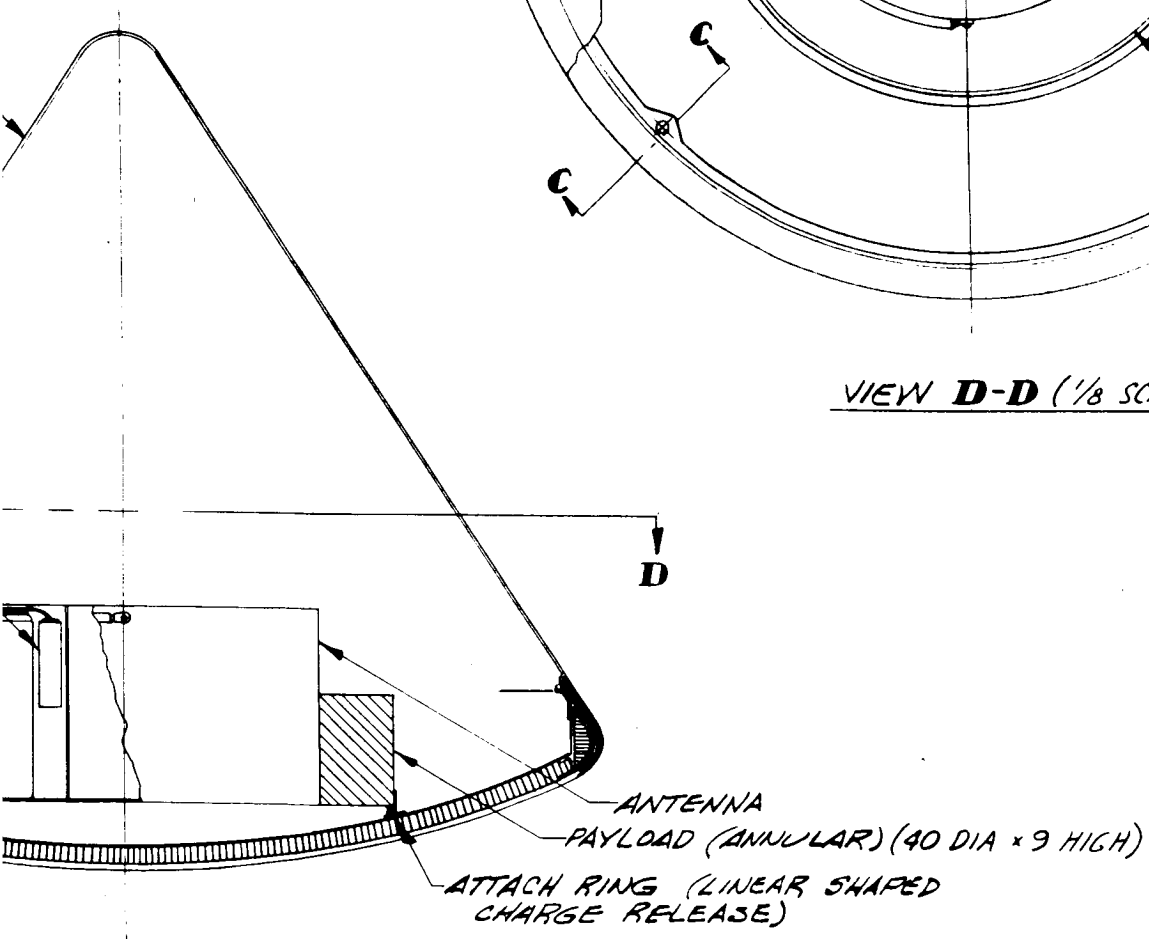

GEMENT & DETAIL (1/8 SCALE)
TENNA – NO LANDING SURVIVAL

Y

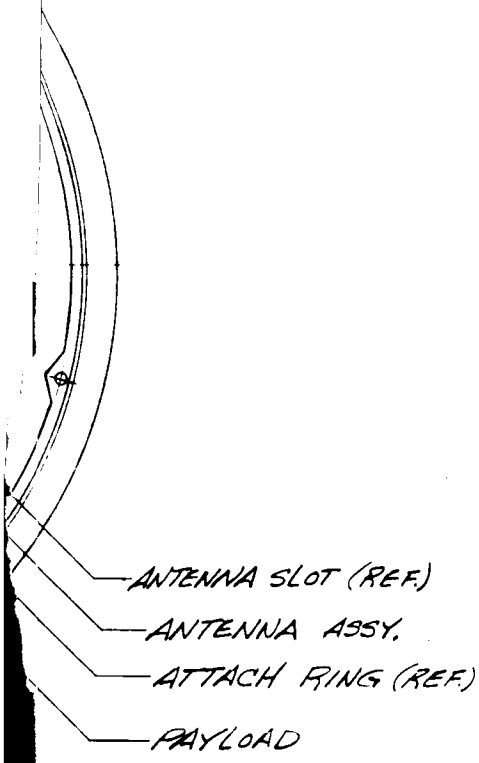

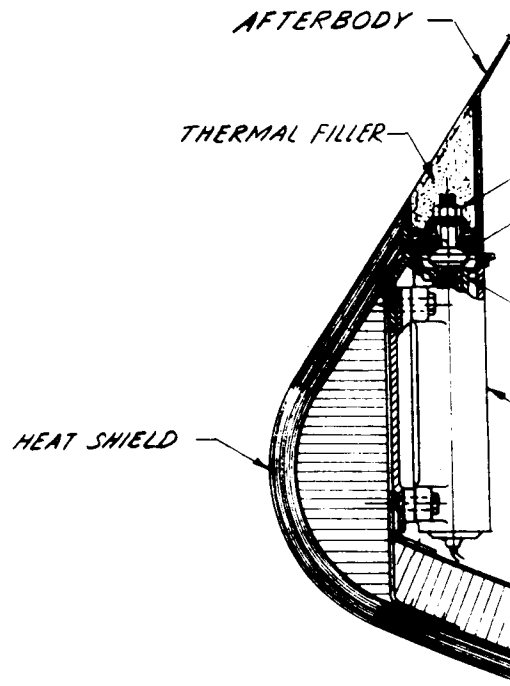

SECTION C-
AFTERBODY ATTACH / SEP

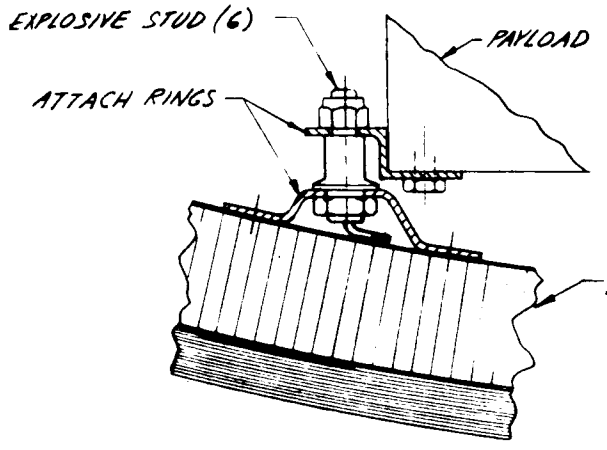

ALTERNATE DETAIL B-B

H

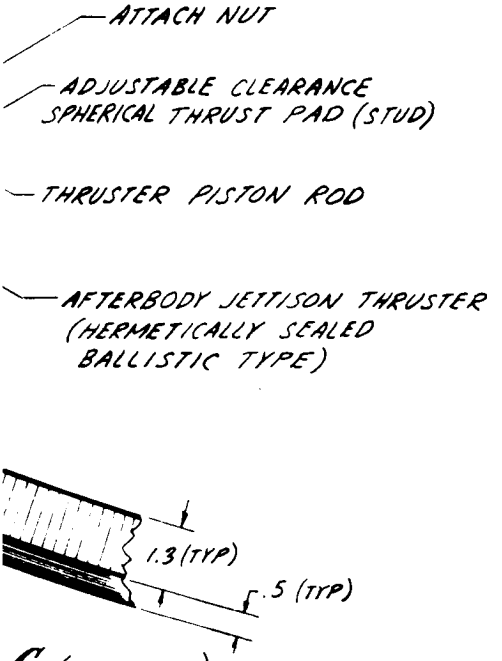

C (HALF SIZE)
ARATION DETAIL

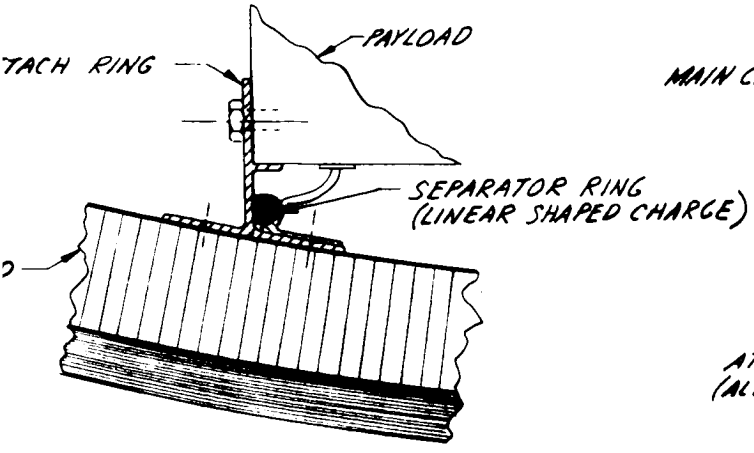

DETAIL B-B (FULL SIZE)
EAT SHELD ATTACH / SEPARATION DETAIL

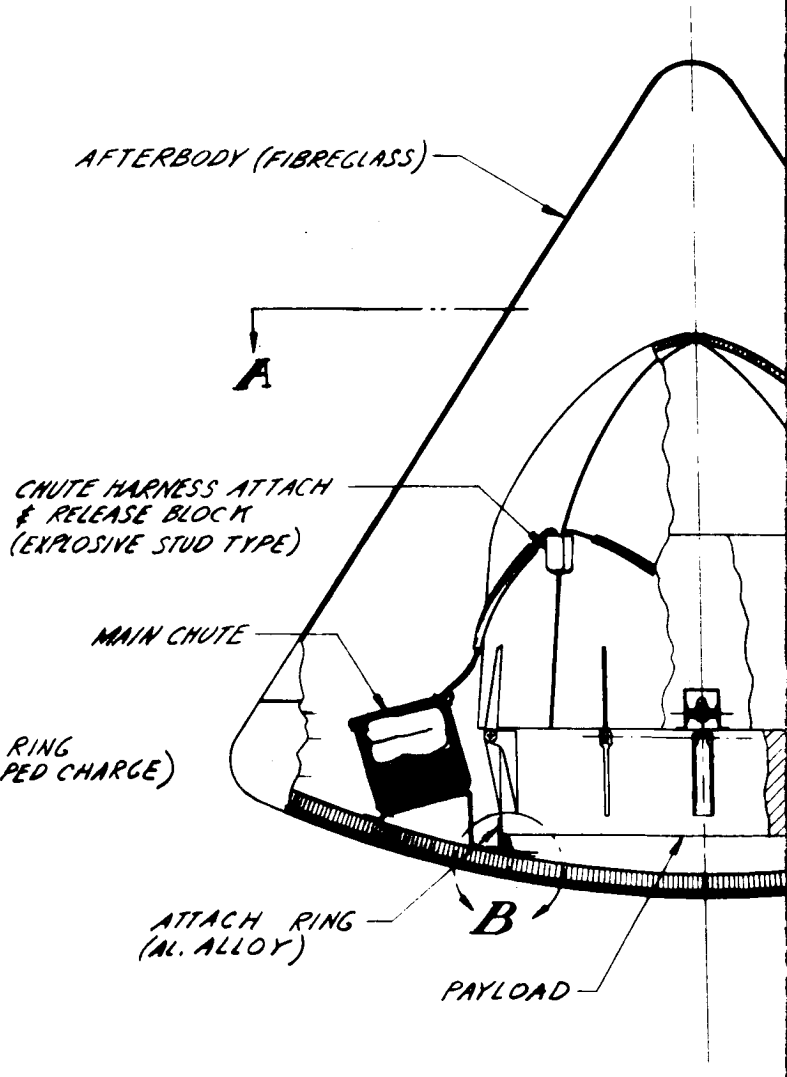

TYPICAL ARRANGEME
JPL TYPE ANTENNA ~ F

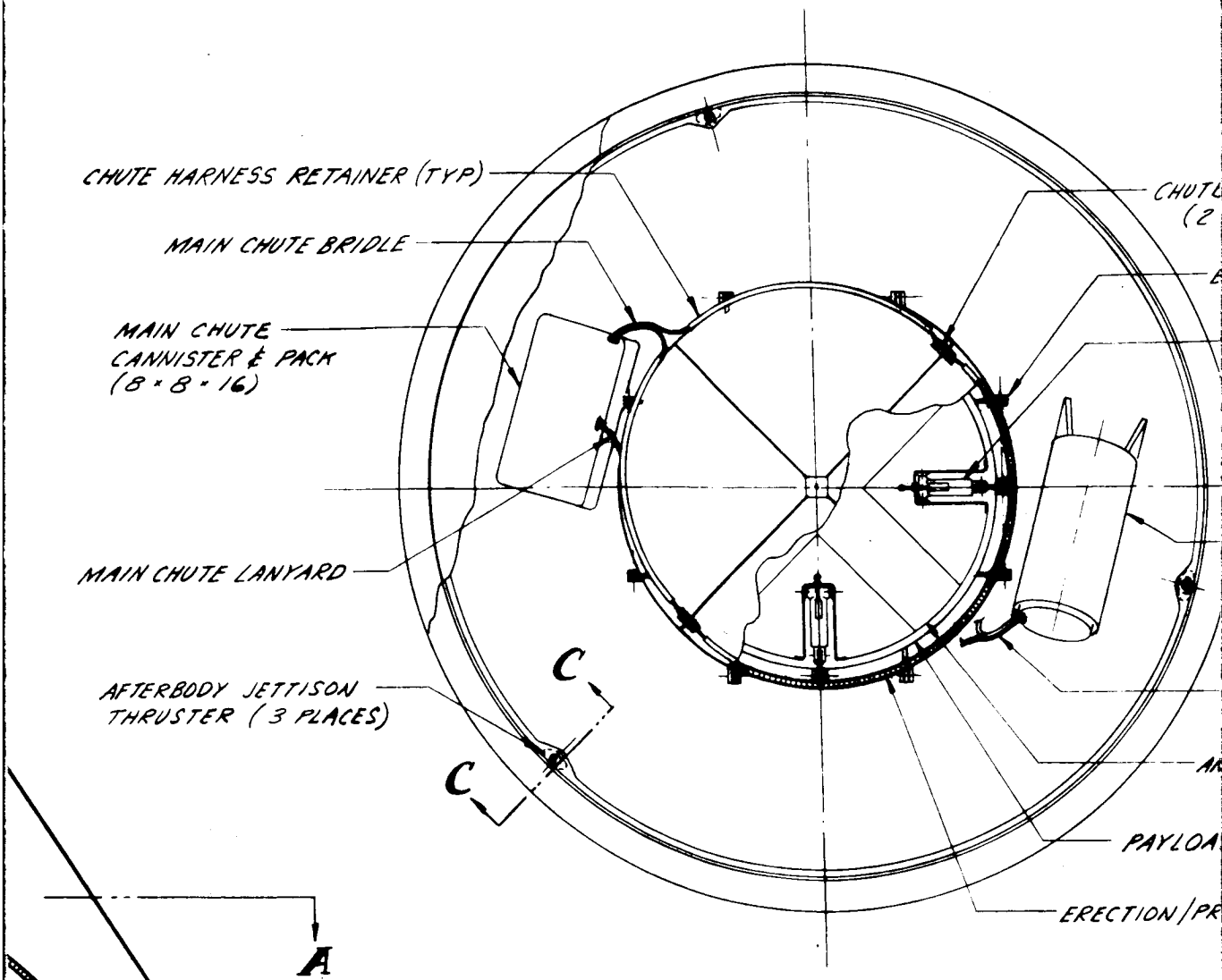

TOP SECTIONAL VIEW A-A (1/8 SIZE)

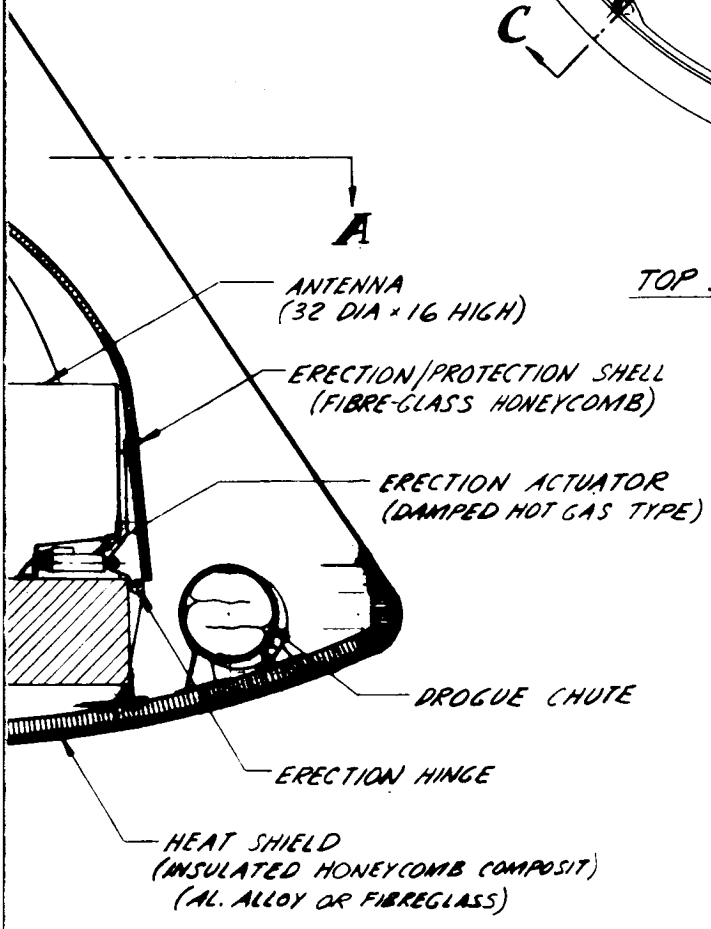

NT & DETAIL (1/8 SCALE
POST LANDING SURVIVAL

= BRIDLE ATTACH/RELEASE BLOCK
PLACES)

RECTION HINGE (12 PLACES)

—ERECTION ACTUATOR
(4 PLACES)

— DROGUE CHUTE
PACK & MORTAR
(8 DIA × 16 LONG)

— DROGUE CHUTE BRIDLE

NTENNA (32 DIA × 16 HIGH)

D (34 DIA × 9 HIGH)

OTECTION SHELL SEGMENT (4)

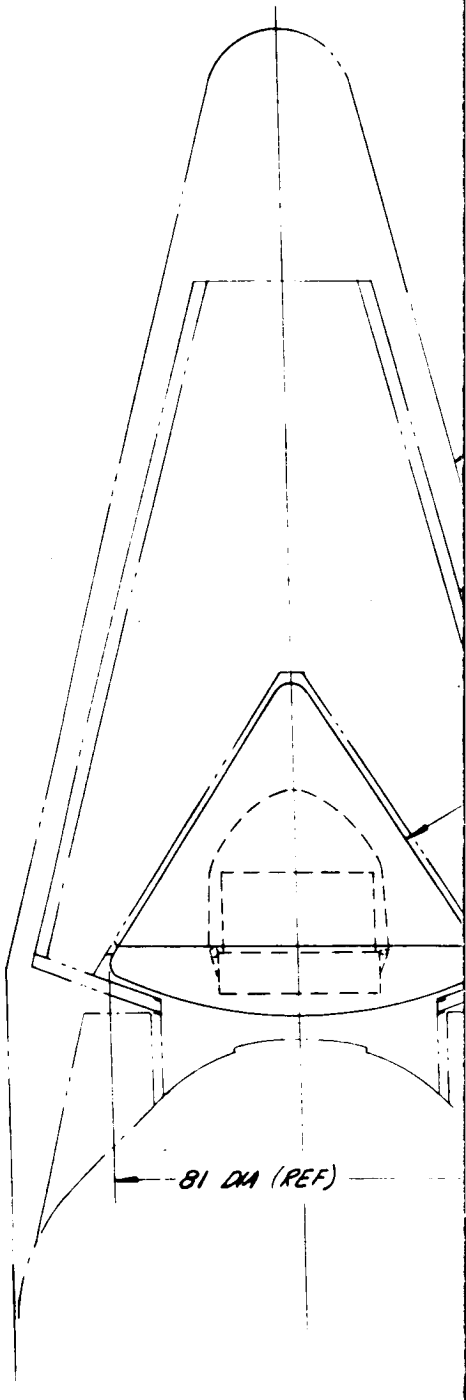

TYPICAL INSTALLAT
(1/80 SCALE)

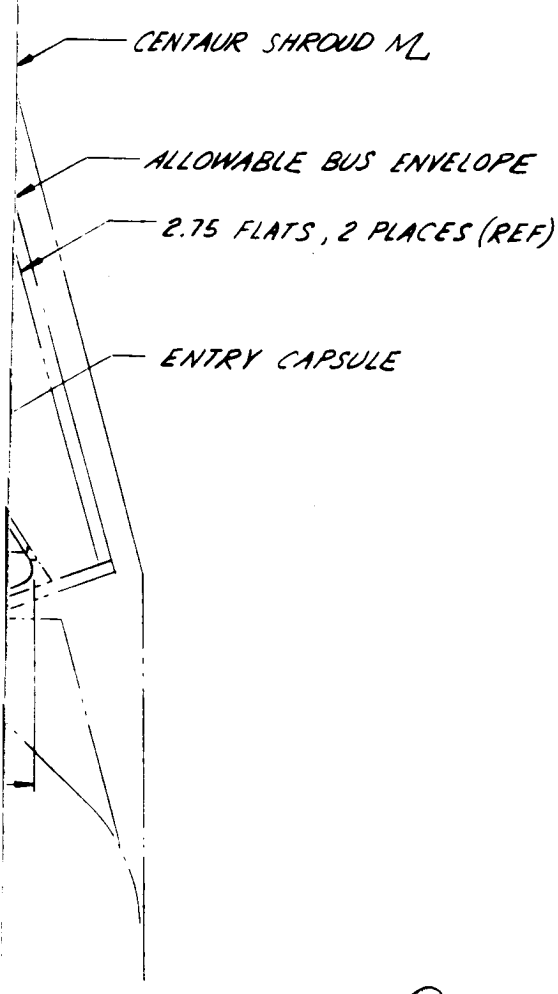

9

ION

SCALE NOTED	DR. A. CUMMINGS	NORTH AMERICAN AVIATION, INC. SPACE and INFORMATION SYSTEMS DIVISION 12214 LAKEWOOD BLVD. DOWNEY, CALIFORNIA
	DATE 9-24-63	
	MODEL	

FIGURE 3.4-1

MARINER "B" 350 LB ENTRY CAPSULE
SELECTED CONFIGURATIONS

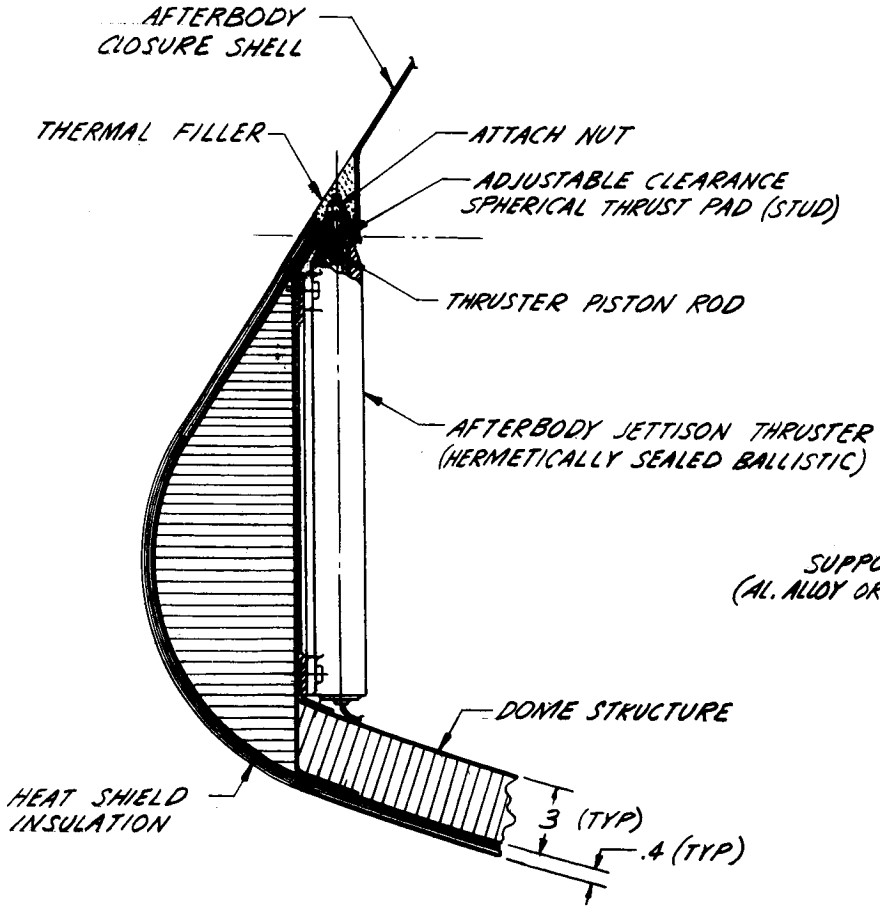

SECTION C-C (1/4 SIZE)

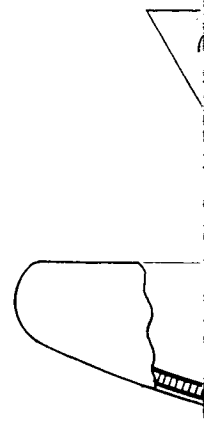

(RA

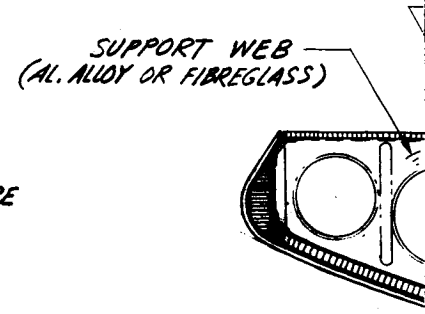

(RAD

/

COVER JETTISON THRUSTER (3 OR 4)
(HERMETICALLY SEALED BALLISTIC)
(SEE SECTION C-C)

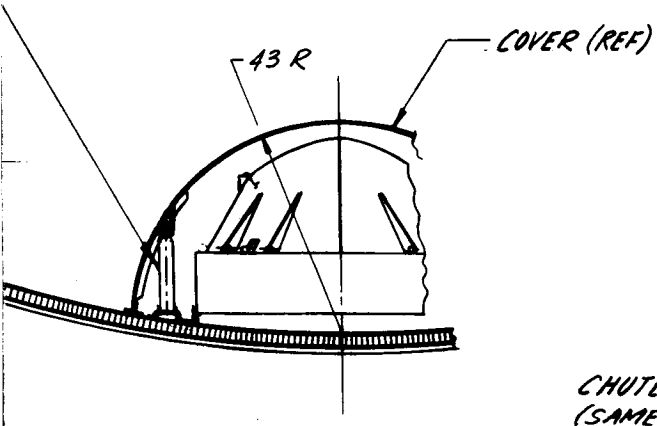

SECTION F-F (1/20 SCALE)
DIAL SECTION THRU COVER THRUSTER)

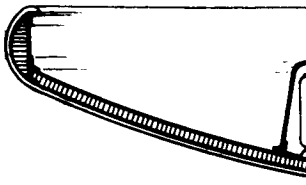

CHUTE & PAYLOAD INSTALLATION
(SAME AS BASE POINT)

ALTE
LO

COVER JETTISON THRUSTER (4)
(HERMETICALLY SEALED BALLISTIC)
(SEE SECTION C-C)

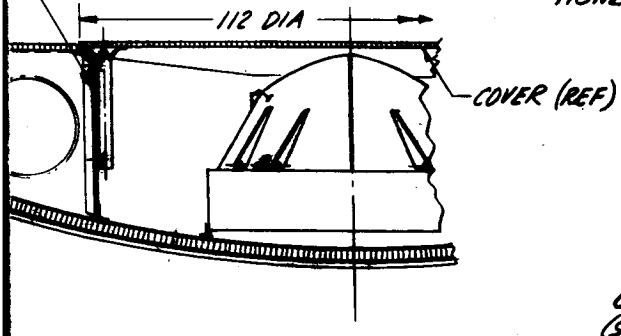

SECTION E-E (1/20 SCALE)
IAL SECTION THRU COVER THRUSTER)

FIXED BACK COVER
(AL. ALLOY OR FIBREGLASS ~
HONEYCOMB OR FRAMED)

BACK
(AL. AL

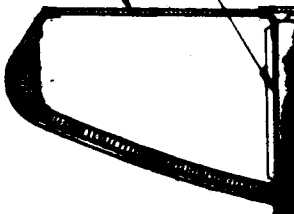

CHUTE & PAYLOAD INSTALLATION
(SAME AS BASE POINT CONFIGURATIO
EXCEPT FOR DROGUE CHUTE ATTITUD

A

PROTECTION/E
(4 SEGMEN

ERECTION A

MAIN C

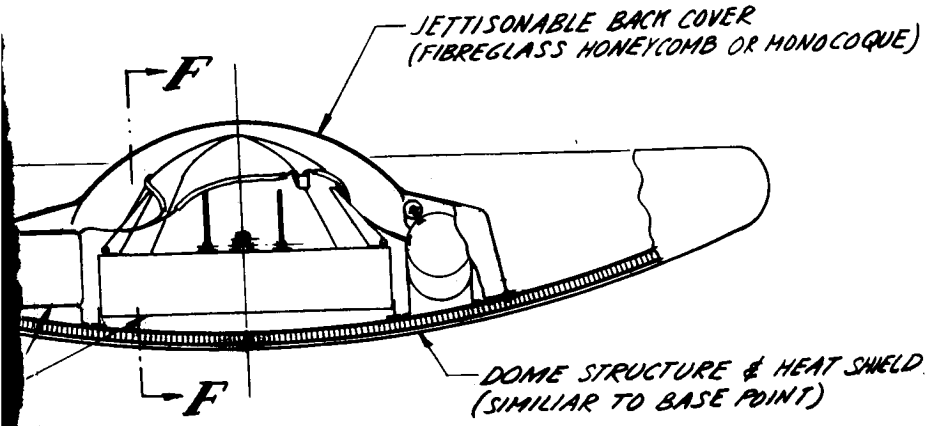

F

PNATE CAPSULE CONFIGURATION (1/20 SCALE)
CAL CLOSURE (OPEN DOME) TYPE

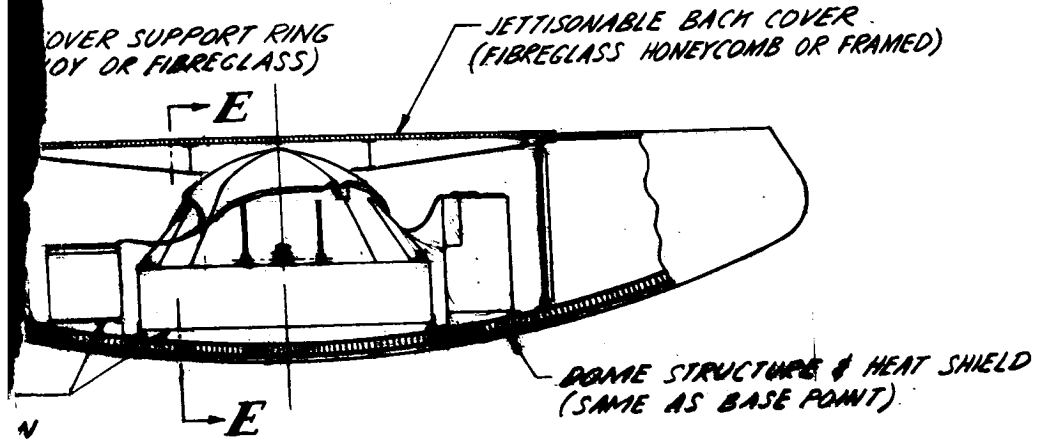

ATTAC

N
E)

TERNATE CAPSULE CONFIGURATION (1/20 SCALE)
FLAT CLOSED DOME TYPE

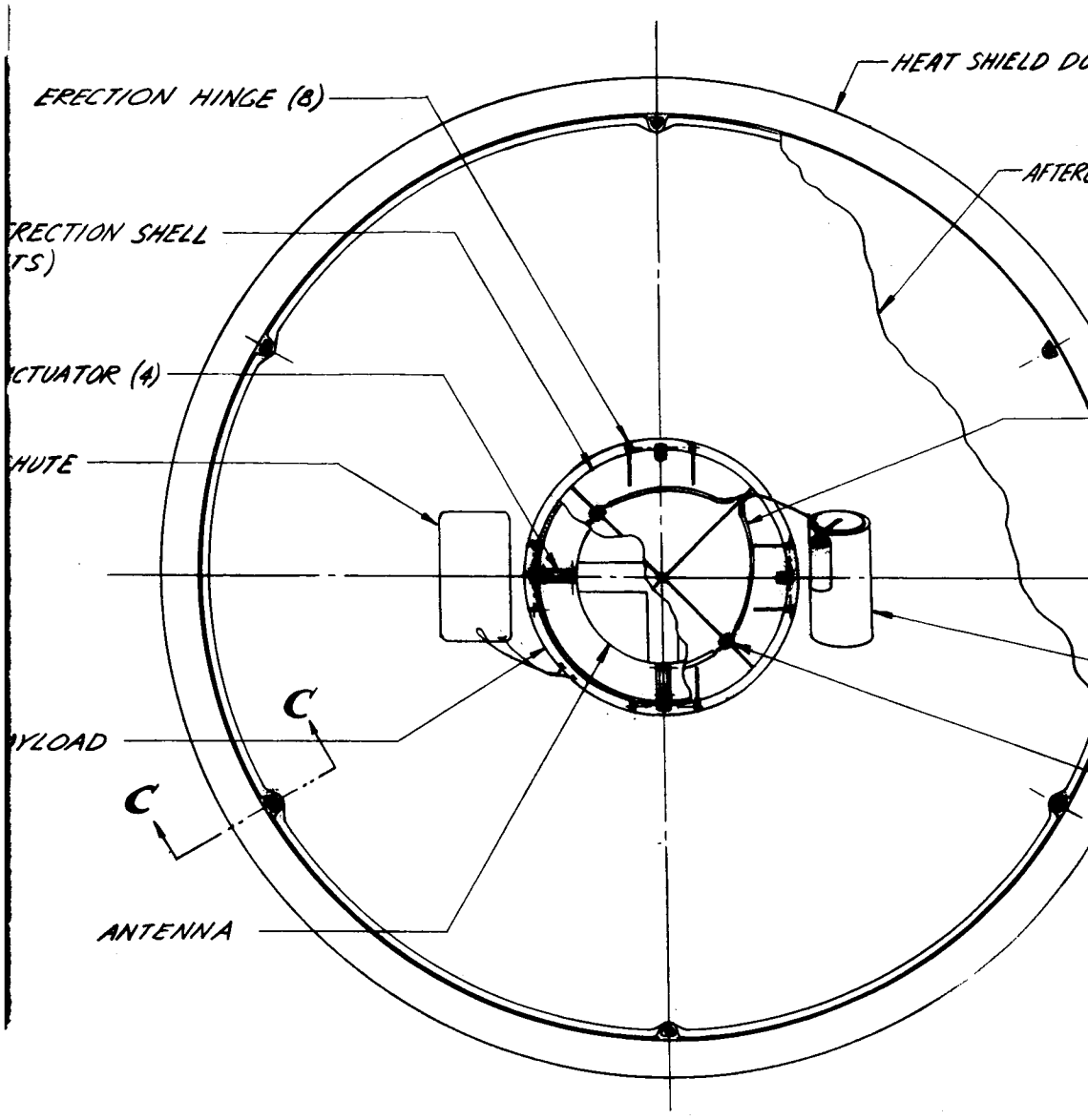

VIEW A-A (1/20 SIZE)
(TYPICAL PLAN ARRANGEMENT)

ERECTION
(FIBREGL

ERECTION

MAIN C
(16 × 16 × 28

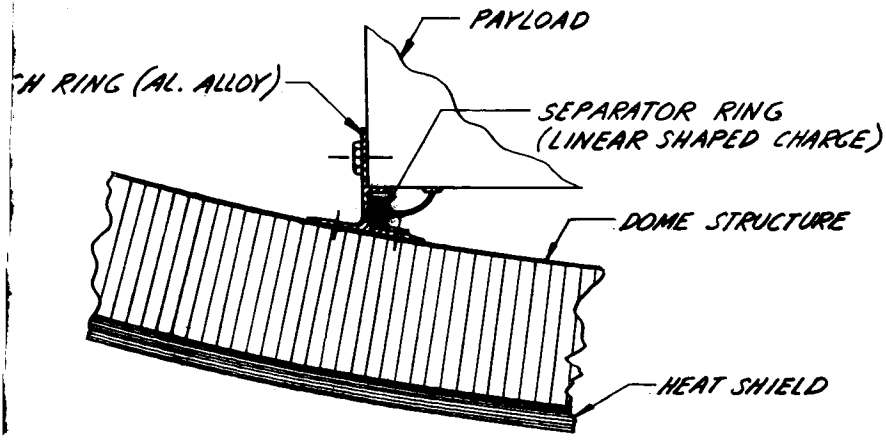

DETAIL B (1/2 SIZE)
(HEAT SHIELD DOME ATTACH/RELEASE)

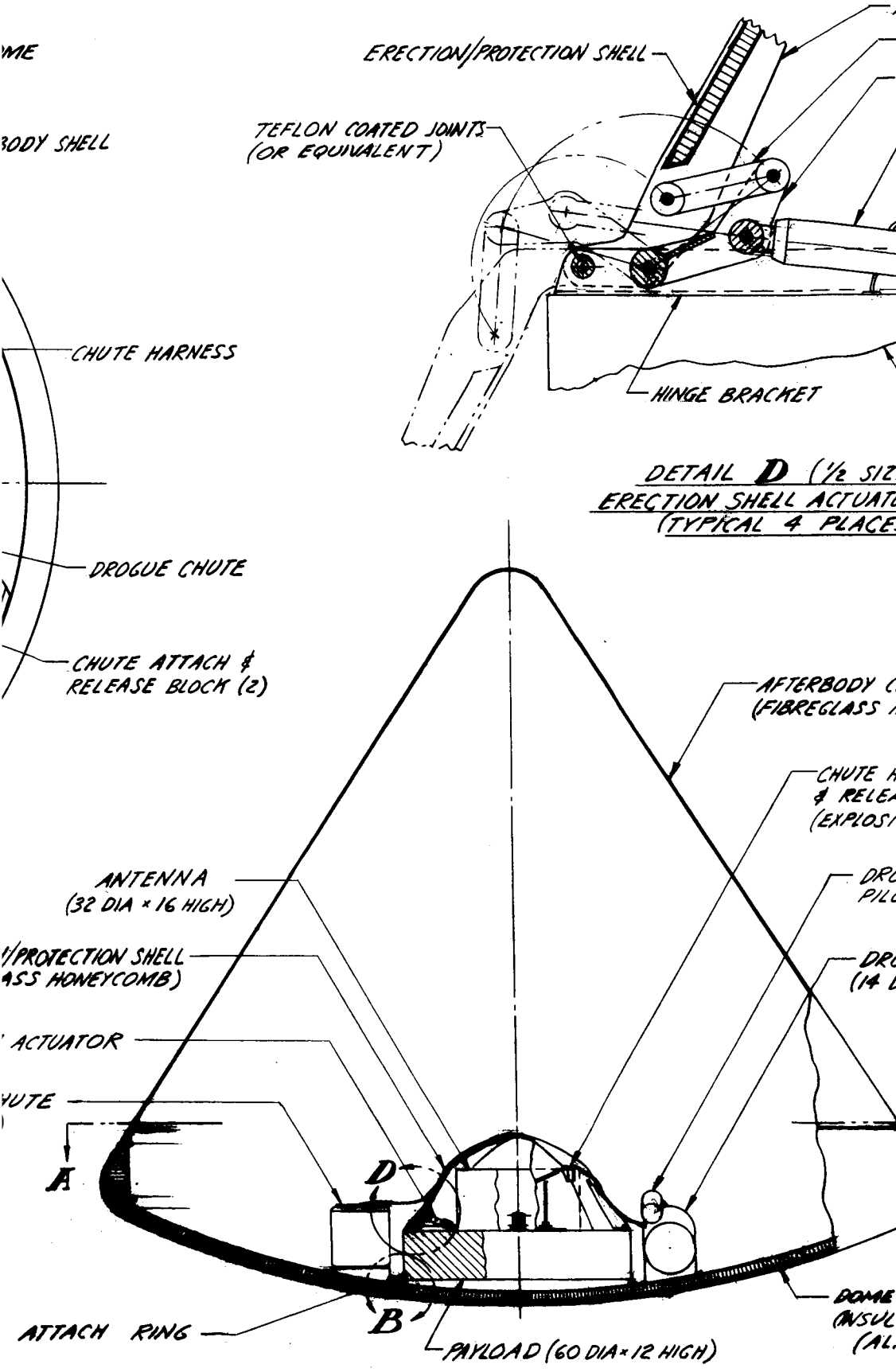

BASE POINT CONFIGURATION
SIDE SECTIONAL VIEW (1/20 SCALE)
CONICALLY CLOSED DOME (FULL APOLLO) TYPE

5

HINGE ARM
LINK
WALKING BEAM

E)
OR & HINGE
S)

LOSURE SHELL (JETTISONABLE)
HONEYCOMB OR MONOCOQUE)

HARNESS ATTACH
ASE BLOCK
VE STUD)

OGUE CHUTE
OT MORTAR

OGUE CHUTE
DIA × 24 LONG)

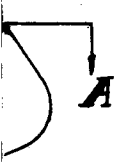

STRUCTURE & HEAT SHIELD
ATED HONEYCOMB)
ALLOY OR FIBREGLASS)

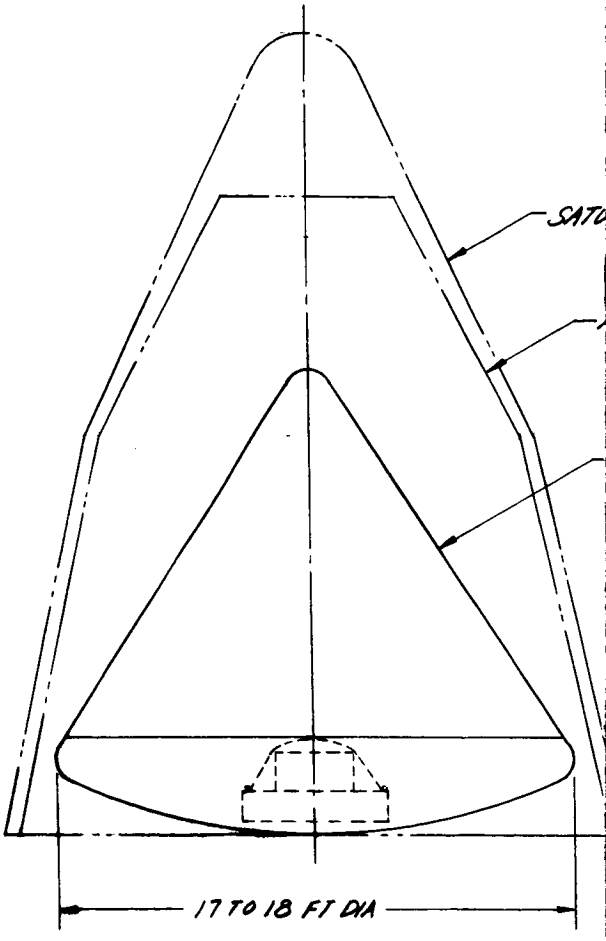

TYPICAL INSTALLATION
1/40 SCALE

RN SHROUD ML

ALLOWABLE BUS ENVELOPE

-ENTRY CAPSULE

NOTED	DR. A. CUMMINGS DATE 10/4/63	NORTH AMERICAN AVIATION, INC. SPACE and INFORMATION SYSTEMS DIVISION 12214 LAKEWOOD BLVD., DOWNEY, CALIFORNIA

FIGURE 3.4-2

VOYAGER "2000" LB ENTRY CAPSULE
SELECTED CONFIGURATIONS

3.5 WEIGHT AND MASS PROPERTIES

Summary weight statements for the small capsule are presented in Tables 3.5-1 and 3.5-2. (In all cases the gross weight is defined as a maximum of 350 pounds.) The major difference between the two sets of data is the trade-off between forebody structural weight and payload weight; i.e., the composite forebody structure has a lighter structural weight and therefore yields larger payload weight.

Two candidate afterbody materials are shown. The first is phenolic glass which is compatible with the r.f. transmission requirements for the inboard antenna and is sized to withstand both the structural loads and the thermal environment. The second material shown is an aluminum shell with phenolic glass (of the required thickness for the thermal environment) bonded in place. The afterbody is modified structurally to accommodate a surface-mounted slot antenna. The increase in weight of the slot antenna installation, however, exceeds the weight available for the payload. The landing system weight is assumed to be constant for all the configurations.

A summary of the centers of gravity and the moments of inertia for these four variations are presented in Table 3.5-3. The centers of gravity are given as a function of the distance from the exterior mold line of the vehicle. The lateral centers of gravity are on the center line of symmetry of the vehicle. The moments of inertia are given in slug-ft.^{2} about the centers of gravity. The pitch plane is defined as the plane in which the landing system components are contained. Since the maximum gross weight is defined as 350 pounds, the nominal M/C_DA is 0.2 for a base diameter of 6.75 feet.

The small-capsule configurations discussed thus far have no provisions for survival after impact. In order to protect the payload from landing loads and to right the capsule after impact, an erection/protection system has been evaluated. This system will weigh approximately 30 pounds for the in-board antenna configuration and 20 pounds in the slot antenna configuration, (see Section 3.4). This weight must be subtracted from the payloads noted in Tables 3.5-1 and 3.5-2 to obtain the available payload weight. A summary of the remaining payload weight associated with each version of the small capsule assuming a 350 pound gross weight limit is presented in Table 3.5-4.

Summary weight statements together with the computed values of M/C_DA for the large capsule configurations are presented in Table 3.5-5 and 3.5-6. Three versions are presented which vary in afterbody configuration and base diameter. First is the 33° half-angle aftcone which was derived from the standard Apollo configuration. However, the volume contained within this cone is greater than necessary; therefore, two alternate configurations are considered. The "flat-plate afterbody" has a plate closing the exposed aft surface of the forebody with an internal annular ring for support. This ring must be broken during afterbody-forebody separation, and therefore, an increase weight for the separation device is required.

TABLE 3.5-1

SUMMARY WEIGHT STATEMENT

SMALL CAPSULE - ALUMINUM FOREBODY STRUCTURE

Antenna Type	Inboard Antenna		Slot Antenna	
Afterbody Material	Glass Phenolic		Aluminum	
	Jettisoned	Retained	Jettisoned	Retained
Component				
Afterbody Structure & Heat Protection	40	-	2	80
Forebody Structure & Heat Shield	173	-	173	-
Thrusters, Latches	5	-	2	1
Payload Support Ring	3	2	3	2
Landing System	40	-	40	-
Antenna (JPL)	-	12	-	-
Payload (JPL)	-	(1) 75	-	(2) 47
SUB-TOTAL	261	89	220	130
GROSS WEIGHT	350		350	

(1) Reduce this payload by 30# for impact survival.

(2) Reduce this payload by 20# for impact survival.

TABLE 3.5-2

SUMMARY WEIGHT STATEMENT

SMALL CAPSULE - COMPOSITE FOREBODY STRUCTURE

Antenna Type	Inboard Antenna		Slot Antenna	
Afterbody Material	Glass Phenolic		Aluminum	
	Jettisoned	Retained	Jettisoned	Retained
Component				
Afterbody Structure & Heat Protection	40	-	2	80
Forebody Structure & Heat Shield	138	-	138	-
Thrusters, Latches	5	-	2	1
Payload Support Ring	3	2	3	2
Landing System	40	-	40	-
Antenna (JPL)	-	12	-	-
Payload (JPL)	-	(1) 110	-	(2) 82
SUB-TOTAL	226	124	185	165
GROSS WEIGHT	350		350	

(1) Reduce this payload by 30# for impact survival.

(2) Reduce this payload by 20# for impact survival.

TABLE 3.5-3

CENTER OF GRAVITY AND MOMENT OF INERTIA SUMMARY

SMALL CAPSULE

	Weight-Pounds	C.G. - Distance from base		Moment of Inertia - Slug/Ft.^{2}		
		Inches	*% Base diameter	Roll	Pitch	Yaw
Composite Forebody Structure						
Glass Phenolic Afterbody and Inboard Antenna	350	12.1	14.9	40.1	25.9	28.6
Aluminum Afterbody Structure and Slot Antenna	350	14.6	18.0	44.3	33.5	36.2
Aluminum Forebody Structure						
Glass Phenolic Afterbody and JPL Drum Antenna	350	11.7	14.4	45.3	28.7	31.4
Aluminum Afterbody and Slot Antenna	350	14.1	17.4	49.5	36.4	39.1

*Base diameter = 81"

TABLE 3.5-4

PAYLOAD SUMMARY FOR A MAXIMUM

CAPSULE WEIGHT OF 350 POUNDS

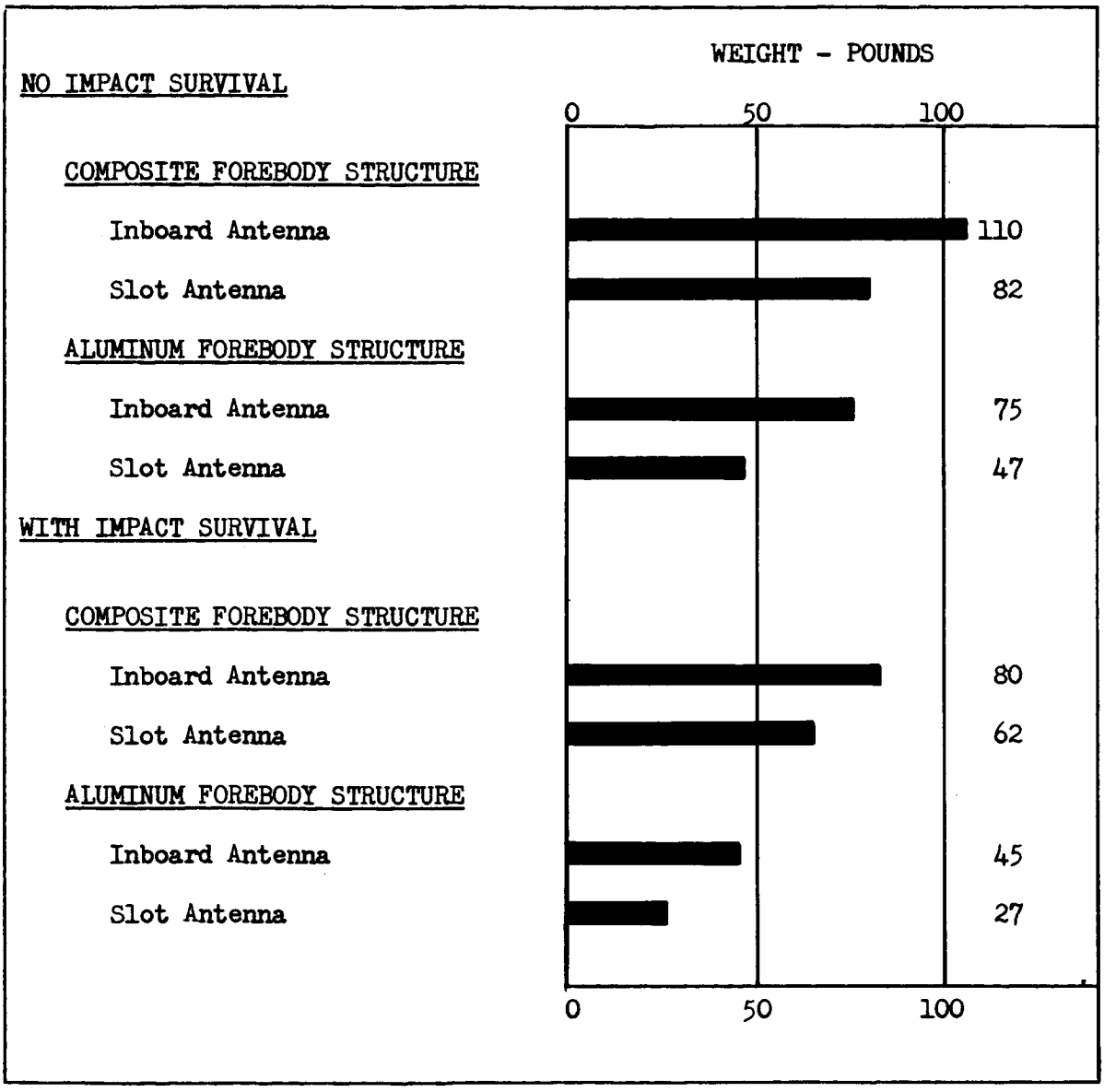

TABLE 3.5-5

SUMMARY WEIGHT STATEMENT

17 FOOT DIAMETER

COMPONENT	WEIGHT - POUNDS					
	33° Half Angle Cone Afterbody		Flat Plate Afterbody		Open Afterbody	
	Jettisoned	Retained	Jettisoned	Retained	Jettisoned	Retained
Afterbody Structure & Heat Shield	545	-	405	-	(1) 240	-
Forebody Structure & Heat Shield	970	-	970	-	970	-
Thrusters, Latches, etc.	25	-	35	-	-	-
Payload Support	20	10	20	10	20	10
Landing System	200	-	200	-	200	-
Payload (Including Inboard Antenna)	-	600	-	600	-	600
Erection System	-	90	-	90	-	120
SUB-TOTAL	1760	700	1630	700	1430	730
GROSS WEIGHT	2460		2330		2160	
M/C_DA	0.224		0.213		0.197	

(1) Heat Shield & Bond Line Only - No Structure

TABLE 3.5-6

SUMMARY WEIGHT STATEMENT

18 FOOT DIAMETER CAPSULE

Component	WEIGHTS - POUNDS					
	33° Half Angle Cone Afterbody		Flat Plate Afterbody		Open Afterbody	
	Jettisoned	Retained	Jettisoned	Retained	Jettisoned	Retained
Afterbody Structure & Heat Shield	610	-	445	-	(1) 270	-
Forebody Structure & Heat Shield	1090	-	1090	-	1090	-
Thrusters, Latches, Etc.	25	-	35	-	-	-
Payload Support	20	10	20	10	20	10
Landing System	200	-	200	-	200	-
Payload (Including Inboard Antenna)	-	600	-	600	-	600
Erection System	-	90	-	90	-	120
SUB-TOTAL	1,945	700	1,790	700	1,580	730
GROSS WEIGHT	2,645		2,490		2,310	
M/C_DA	0.215		0.203		0.188	

(1) Heat Shield & Bond Line Only - No Structure

The "open afterbody" has no structural cover and consists only of the required heat shield and a bond line for attachment to the aft face of the forebody structure. Thermal protection is added to the erection/protection system (described in Section 3.4) to protect the payload. In the case of the large capsule, the payload is defined as weighing 600 pounds and the gross weights of the configurations are, therefore, different. Summary center-of-gravity, moment-of-inertia data for the six versions are presented in Table 3.5-7.

TABLE 3.5-7

CENTER OF GRAVITY & MOMENT OF INERTIA SUMMARY

LARGE CAPSULE

BASE DIAMETER (ft)	AFTERBODY CONFIGURATION	WEIGHT (lb)	CENTER OF GRAVITY DISTANCE FOR BASE		MOMENT OF INERTIA Slug - Feet^2		
			Inches	% Base Diameter	Roll	Pitch	Yaw
17.0	Open	2,160	14.2	7.00	1,490	780	780
	Flat Plate	2,330	16.9	8.65	1,620	880	880
	33° Half Angle	2,460	30.5	14.91	1,830	1,615	1,615
18.0	Open	2,310	14.5	6.70	1,875	985	985
	Flat Plate	2,490	17.4	8.06	2,030	1,100	1,100
	33° Half Angle	2,645	31.8	14.71	2,245	1,980	1,980